Experimental Characterisation of Fuel Blends

By

Richard David Mumby

Submitted in accordance with the requirements for the degree of

Doctor of Philosophy

The University of Leeds

School of Mechanical Engineering

Institute of Thermofluids

January 2016

Intellectual Property and Publications Statements

The candidate confirms that the work submitted is his own, except where work which has formed part of jointly-authored publications has been included. The contribution of the candidate and the other authors to this work has been explicitly indicated below. The candidate confirms that appropriate credit has been given within the thesis where reference has been made to the work of others.

- T. Al-Mughanam, D. Bradley, M. Lawes, R. Mumby, (2015), "Burning Velocity Blending Laws for Methane/Air and Hydrogen/Air Blends", 25th International Colloquium on the Dynamics of Explosions and Reactive Systems. Paper 212.
  The author of the present thesis was responsible for the numerical evaluation of the different blending laws. Other authors to this publication provided technical discussions and guidance.
- D. Bradley, M. Lawes, R. Mumby, (2015), "Cellular Flame Instabilities", 8th International Seminar on Fire and Explosion Hazard. USTC Press. In press.
  The author of the present thesis was responsible for the experimental acquisition of data and numerical analysis. Other authors to this publication provided technical discussions and guidance.
- D. Bradley, M. Lawes, R. Mumby, (2016), "Burning Velocity and Markstein Length Blending Laws for Methane/Air and Hydrogen/Air Blends". Pending submission to Fuel Journal.
  The author of the present thesis was responsible for numerical analysis and development of new blending laws. Other authors to this publication provided technical discussions and guidance.

In memory of my father,

David John Mumby

Acknowledgements

The value of achievement lies in the achieving – Albert Einstein

Never, have such words resonated with me more. The course of my PhD has been a tremendously enlightening journey, filled with peaks and troughs, there has been little plain sailing, though, every wave worth its while.

Thanks and appreciation is given to Dr. Gary Sharpe for giving me the opportunity to set sail with my studies at Leeds, and the EPSRC for providing my Scholarship.

My sincere admiration and thanks are undoubtedly given to my supervisors, Prof. Derek Bradley and Dr. Malcolm Lawes. It has been a privilege and pleasure to work alongside them both. Their immense contribution towards my academic, intellectual and professional development is truly unrivalled and always kept me on course.

As an experimentalist, much of my time was spent in the Thermofluids Laboratory. My sincere thanks and appreciation are given to laboratory technicians, Mark Batchelor, Brian Leach and Paul Banks, for their friendly advice, regardless of how many times I badgered them.

Through this journey, there is no doubt family and friends have helped me keep afloat. In particular, I thank friends, Luke Bates, Myeji Materego and Ben Thorne, for those countless inspiring conversations over lunch, and the many moral boosting laughs over a few drinks after a hard day's work. Furthermore, special thanks are given to my mother, with a heart of gold, she has always unreservedly supported and encouraged me through highs and lows, whatever my path.

Finally, I would like to acknowledge my heartfelt appreciation for my fiancée, Kylie. She has the patience and empathy of a saint, and has relentlessly provided the wind in my sails, to which I am eternally indebted – I wholeheartedly thank you.

Abstract

In the quest to mitigate demand for conventional petroleum derived transportation fuels and reduce their associated CO_2 emissions, there are an increasing number of alternative fuels being proposed. Blending of such alternatives necessitates a comprehensive understanding of their combustion behaviour for effective and efficient commercial deployment. Therefore, characterisation of such blends fundamental combustion parameters relative to their constituents, under different operational conditions, is of essential importance. Two key parameters are that of laminar burning velocity and ignition delay time.

The present work predominately focused on investigations of the former and the theoretical development of a universal predictive laminar burning velocity blending law, suitable for all commercial fuel types and those from chemically dissimilar families, such as methane and hydrogen. Aiding this development, an array of pure fuel/air mixtures and their blends burning velocities were measured by means of a constant volume combustion vessel, at a temperature of 360K, for pressures of 0.1, 0.5 and 1.0 MPa, at equivalence ratios from 0.8 to 1.3. Blends comprised of pure fuels representative of the major chemical families found within Fischer-Tropsch synthetic gasoline, namely, *iso*-octane, *n*-heptane, toluene, *1*-hexene, and that of promising bio-derived alcohols, namely, ethanol and *n*-butanol.

A proposed laminar burning velocity blending law was evaluated against existing laws, using the measured blend data, and existing data from other researchers, and on average, outperformed all. The acquired data also allowed investigations into linear and nonlinear flame speed/stretch relationships, and correlations between the critical Peclet and Karlovitz numbers with Markstein numbers, as a function of fuel type, pressure and equivalence ratio.

Furthermore, during the present work, considerable efforts were made towards commissioning a rapid compression machine, which served to allow the concurrent collection of ignition delay data for the same blends by other researchers. This gave the opportunity for a conjoint investigation into the comparative effects of ethanol and *n*-butanol addition to a TRF gasoline surrogates burning velocity and ignition delay behaviour.

Table of Contents

Chapter 1 - Introduction 1
1.1 General Overview and Motivation 1
1.2 Conventional and Alternative Transportation Fuel Sources 3
1.2.1 Conventional Fuels 3
1.2.2 Fisher-Tropsch Synthetic Fuels 3
1.2.3 Bio-Fuels 6
1.3 Key Combustion Characteristics of Fuel Blends 8
1.4 Laminar Premixed Flames and Burning Velocity 9
1.4.1 Historical Perspectives 9
1.4.2 Flame Structure 10
1.4.3 Flame Stretch 11
1.4.4 Determination of Unstretched Burning Velocity 12
1.4.4.1 Flat Flame Burners 12
1.4.4.2 Counter Flow Stagnation Burners 13
1.5.4.3 Spherical Combustion Vessels 15
1.5.4.3.1 Linear Extrapolation Methodology 16
1.5.4.3.2 Nonlinear Extrapolation Methodology 17
1.5.4.3.3 Accounting for Expansion of Combustion Products 17
1.4.5 Development of Flame Instabilities 17
1.5 Autoignition and Ignition Delay Time 21
1.5.1 Determination of Ignition Delay Time 22
1.5.1.1 Flow Reactors 23
1.5.1.2 Shock Tubes 24
1.5.1.3 Rapid Compression Machines 26
1.6 Aims and Objectives 27
1.7 Thesis Structure 28
Chapter 2 - Review of Laminar Burning Velocity Analytical Approaches and Blending Laws 30
2.1 Introduction 30
2.2 Analytical Approaches to Laminar Burning Velocity 30
2.2.1 Spalding Expressions for Laminar Burning Velocity 30
2.2.2 Zel’dovich and Frank-Kamenetskii Approximations 33

2.2.3 Activation Temperature influence on Laminar Burning Velocity 35
2.3 Blending Relationships and Stoichiometry 36
2.4 Laminar Burning Velocity Blending Laws 39
2.4.1 Mole Blending Law of Payman and Wheeler 40
2.4.2 Mass Blending Law of Lipzig 40
2.4.3 Le Châtelier based Blending Law of Di Sarli 40
2.4.4 Equal Adiabatic Temperature Assumption Blending Law of Spalding 41
2.4.5 Activation Temperature Blending Law of Hirasawa 42
2.4.6 Molar Heat of Reaction Correlations of Bradley et al. 42
2.4.7 *Q/k* Blending Law of Present Work 44
2.5 Review of Markstein Parameter Blending Laws 45
2.5.1 Deficient Reactant Blending Law 46
2.5.2 xu_lL_b Blending Law 46
Chapter 3 - Experimental Apparatus, Operating Techniques and Data Processing 47
3.1 Introduction 47
3.2 Experimental Apparatus 48
3.2.1 Combustion Vessel 50
3.2.2 Auxiliary Systems 52
3.2.2.1 Pressure Measurement 52
3.2.2.2 Heating System and Temperature Control 52
3.2.2.3 Ignition System 53
3.2.2.4 High Speed Digital Schlieren Photography 55
3.2.2.4.1 Schlieren Calibration 58
3.2.2.5 Triggering and Synchronisation System 58
3.3 Operating Techniques 59
3.3.1 Fuel Handling and Preparation 59
3.3.2 Experimental Procedure 60
3.4 Data Processing 62
3.4.1 Thermodynamic Properties of Burned and Unburned Gases 62
3.4.2 Schlieren Image Processing 62
3.4.3 Acquisition of u_l and L_b 65
3.5 Verification of Improvements due to Vessel Modifications 67

3.5.1 Heating System Upgrade 67
3.5.2 Air Supply System Upgrade 80
Chapter 4 - Experimental Laminar Burning Velocity and Markstein Length Measurements of Pure Fuel/Air Mixtures and Blends 82
4.1 Introduction 82
4.2 Pure Liquid Hydrocarbon Fuels 82
4.3 Binary Equimolar Liquid Hydrocarbon Blends 111
4.4 TRF and Alcohol Blends 133
4.5 Methane and Hydrogen Blends 143
Chapter 5 - Discussions of Measured Pure Fuel/Air Mixtures and Blend Behaviour 147
5.1 Introduction 147
5.2 Linear and Nonlinear Flame Speed vs. Stretch Rate Relationships 147
5.3 Cellular Instabilities 150
5.4 Comparisons of Measured u_l and L_b Values to Existing Data 156
5.5 Comparative Effects of Ethanol and *n*-Butanol Addition to TRF/Air Mixtures u_l and τ_i Behaviour 165
5.5.1 Analysis of Measured u_l and L_b Data 166
5.5.2 Analysis of τ_i Data 171
5.5.3 Summary of Investigation 172
5.6 Investigation into Methane/Air Mixtures Energy Flux Variations with Hydrogen Addition. 173
Chapter 6 - Predictive Performance of Laminar Burning Velocity and Markstein Length Blending Laws 176
6.1 Introduction 176
6.2 Equimolar Binary Blends 177
6.3 TRF and Alcohol Blends 178
6.4 Methane and Hydrogen Blends 179
6.5 Overall Evaluation 180
Chapter 7 - Conclusions and Recommendations for Future Research 190
7.1 Conclusions 190
7.1.1 Measurements of u_l and L_b for Pure Hydrocarbon/Air Mixtures and Blends 190
7.1.1.1 Pure Fuels 190

7.1.1.2 Equimolar Binary Blends 191
7.1.1.3 Gasoline Surrogate/Alcohol Blends 191
7.1.2 Error Analysis of Linear S_n-α Methodology 192
7.1.3 Cellular Instability Phenomena 193
7.1.4 u_l Blending Laws 193
7.1.5 L_b Blending Laws 195
7.2 Recommendations for Future Research 195
7.2.1 Further Research Paths 195
7.2.2 Experimental Apparatus - The Leeds CV2 Bomb 196
Appendix A - Blending Law Performance League Tables 197
Appendix B - Commissioning a Rapid Compression Machine 228
B.1 Introduction 228
B.2 Ideal and Real RCM Behaviour 228
B.3 The Leeds RCM 232
B.3.1 Configuration and Operation Overview 233
B.3.2 Pneumatic Driving Reservoir 236
B.3.3 Hydraulic Locking and Damping Chamber 236
B.3.4 Combustion Chamber and Cylinder 238
B.3.5 Piston Assembly 239
B.4 Modifications and Developments 239
B.4.1 Aims and Objectives 239
B.4.2 Initial Performance 240
B.4.3 Generation of Virtual Model 243
B.4.4 Piston Position Monitoring 244
B.4.5 Increasing Piston Driving Pressure 247
B.4.6 Adaptable Piston Damping 249
B.4.7 Investigation into Thermal Shock Error of Dynamic Pressure Transducers 253
B.4.7.1 Quantification of Thermal Shock Error 257
B.4.7.2 Flush Mounting with Coatings 257
B.4.7.3 Recessed Mounting with Silicone Fillings 261
B.4.8 Combustion Chamber Heating and Temperature Control 263
B.4.9 Fuel/Oxidiser/Diluent Mixing Chamber and Delivery System 267
B.4.10 Triggering, Synchronisation and Data Acquisition System 268

B.5 Experimental Procedure 269
B.5.1 Mixture Preparation 269
B.5.2 Operating Technique 271
B.6 *Iso*-Octane Ignition Delay Data for International Collaborative 272
Appendix C - Stress Calculations for RCM Mixing Chamber 275
References 278

List of Figures

Figure 1.1: Concentration and temperature profiles associated with one-dimensional, premixed, adiabatic flame (Barnard, 1995).....11
Figure 1.2: Schematic of one-dimensional planar flame, indicating the unstretched burning velocity, u_l, the unstretched flame speed, S_s, and the gas expansion velocity, u_g (Lawes, 2002). 11
Figure 1.3: Schematic of typical flat flame burner, with perforated burner plate (Bosschaart and De Goey, 2003). 13
Figure 1.4: Schematic of typical twin-flame counter flow stagnation burner (Tripathi, 2012). 14
Figure 1.5: Typical axial velocity for one of the flames corresponding to Fig. 1.6 (Tripathi, 2012). 14
Figure 1.6: Variation of flame speed, S_n, with flame stretch rate, α, for *iso*-octane/air at 1.0 MPa, 360K and ϕ = 1.0, taken from the present work. 18
Figure 1.7: Schematic of the hydrodynamic instability mechanism (Law, 1989). 19
Figure 1.8: Schematic of the thermo-diffusive instability mechanism (Law, 1989). 20
Figure 1.9: Typical operational boundaries of shock-tubes, rapid compression machines, and flow reactors. A comparison to a representative ignition delay curve of *iso*-octane is included; ignition delay of *iso*-octane is obtained from the reduced mechanism of Pepiot-Desjardins and Pitsch (2008) at an equivalence ratio of 0.6 and a pressure of 2.0MPa (Grogan et al., 2015).....23
Figure 1.10: Schematic of a typical flow reactor (Beerer et al., 2009). 23
Figure 1.12: Schematic of a typical shock (http://www.ucalgary.ca/johansen/node/7.).25
Figure 1.13: Wave system in the shock tube (Campbell et al., 2015).....26
Figure 2.1: Computed heat release profiles for different CH4, CH3OH, H2 + air mixtures at initial temperatures and pressures of 300K and 0.1 MPa respectively. The full line curves are indicative of computations and the dotted of fitted algebraic expressions, where $\theta = c$. (Bradley et al., 1991). 32
Figure 2.2: Variation of centroid position and heat release rate integral with the product Qu_l for different fuel/air mixtures. Initial temperatures and pressures are shown in bracket (Bradley et al., 1991). 33
Figure 2.3: u_l of different fuels under lean conditions at an initial temperature of 300K. Symbols are experimental data, with the full lines indicating computations. A1, A2

and A3 denote CH4 and CH3OH at 0.01, 0.1 and 1.0 MPa respectively. Alkene experiments are represented by B at 0.1MPa, whilst C, D, E1 and E2 denote C2H4, C2H2, H2 and H2 at 0.1 MPa respectively. (Bradley et al., 1991). 43
Figure 2.4: Variation of k_u with ϕ, for methane/air, hydrogen/air, and their blends at 303K. 45
Figure 3.1: Schematic of vessel and auxiliary systems. 49
Figure 3.2: The Leeds CV2 – external view. 51
Figure 3.3: The Leeds CV2 – internal view. 51
Figure 3.4: Custom made mini sparkplug assembly. 54
Figure 3.5: Schlieren images of iso-octane/air taken at r = 65mm, ϕ = 1, P_i = a) 0.1 MPa, b) 0.5 MPa, c) 1.0 MPa, T_u = 360K. 57
Figure 3.6: Sequence of triggering for camera, sparkplug and dynamic pressure transducer. 59
Figure 3.7: a) Schlieren image, b) Digitised image with sparkplug masking, c) Best fit circle to digitised flame front edge. 64
Figure 3.8: a) r variation with t, b) S_n variation with r, c) S_n variation with α, for *iso*-octane at P_i = 0.1 MPa, T_u = 360K for ϕ = 1 and 1.3. Solid red and blue lines denote linear and nonlinear relationships to L_b across used data points respectively. 66
Figure 3.9: Temperature measurements of vessel surface as a function of time during initial heating stage, using: a) 2kW heater, b) 8kW booster heater and 2kW heater. 68
Figure 3.10: Custom made K-type thermocouple probe for internal temperature measurement at elevated pressure, with fans running. 70
Figure 3.11: Dashed red lines represent track of thermocouple probe from each of the four positions, denoted by P1, P2, P3 and P4. 71
Figure 3.12: Temperature measurements at each probe insertion position, denoted by P1, P2, P3 and P4, as a function of time after turning off the fans and heater, through r = 0-190mm, where r = 0 denotes the vessel centre. T_u = 360K. P_i = 0.1 MPa. 73
Figure 3.13: Temperature measurements at each probe insertion position, denoted by P1, P2, P3 and P4, as a function of time after turning off the fans and heater, through r = 0-190mm, where r = 0 denotes the vessel centre. T_u = 360K. P_i = 0.5 MPa. 74

Figure 3.14: Temperature measurements at each probe insertion position, denoted by P1, P2, P3 and P4, as a function of time after turning off the fans and heater, through r = 0-190mm, where r = 0 denotes the vessel centre. T_u = 393K. P_i = 0.1 MPa. 75
Figure 3.15: Temperature measurements at each probe insertion position, denoted by P1, P2, P3 and P4, as a function of time after turning off the fans and heater, through r = 0-190mm, where r = 0 denotes the vessel centre. T_u = 393K. P_i = 0.5 MPa. 76
Figure 3.16: Symbols denote the average temperature measurement for all positions within r = 75mm, at a) 360K and 0.1 MPa, b) 360K and 0.5 MPa, c) 393K and 0.1 MPa, d) 393K and 0.5 MPa. Dashed lines and error bars indicate target temperatures and the minimum and maximum recorded temperatures respectively. 78
Figure 3.17: Variation of u_l with T_u for stoichiometric *iso*-octane/air mixtures. Each symbol denotes the average of three experiments, with the accompanying red error bars indicating the minimum and maximum values. 80
Figure 3.18: Variation of u_l with different air supplies for stoichiometric ethanol/air mixtures. Each symbol denotes the average of three experiments, with the accompanying red error bars indicating the minimum and maximum value. 81
Figure 4.1: a) S_n variation with α, b) S_n variation with r, for *iso*-octane/air mixtures at P_i = 0.1 MPa, T_u = 360K and ϕ = 0.8-1.3. Solid red and blue lines denote linear and nonlinear relationships for L_b through data points, dashed lines indicate their extrapolation to zero stretch rate and red crosses indicate r_c. 85
Figure 4.2: a) S_n variation with α, b) S_n variation with r, for *n*-heptane/air mixtures at P_i = 0.1 MPa, T_u = 360K and ϕ = 0.8-1.3. Solid red and blue lines denote linear and nonlinear relationships for L_b through data points, dashed lines indicate their extrapolation to zero stretch rate and red crosses indicate r_c. 86
Figure 4.3: a) S_n variation with α, b) S_n variation with r, for toluene/air mixtures at P_i = 0.1 MPa, T_u = 360K and ϕ = 0.8-1.3. Solid red and blue lines denote linear and nonlinear relationships for L_b through data points, dashed lines indicate their extrapolation to zero stretch rate and red crosses indicate r_c. 87
Figure 4.4: a) S_n variation with α, b) S_n variation with r, for *1*-hexene/air mixtures at P_i = 0.1 MPa, T_u = 360K and ϕ = 0.8-1.3. Solid red and blue lines denote linear and

nonlinear relationships for L_b through data points, dashed lines indicate their extrapolation to zero stretch rate and red crosses indicate r_c. 88
Figure 4.5: a) S_n variation with α, b) S_n variation with r, for ethanol/air mixtures at P_i = 0.1 MPa, T_u = 360K and ϕ = 0.8-1.3. Solid red and blue lines denote linear and nonlinear relationships for L_b through data points, dashed lines indicate their extrapolation to zero stretch rate and red crosses indicate r_c. 89
Figure 4.6: a) S_n variation with α, b) S_n variation with r, for *n*-butanol/air mixtures at P_i = 0.1 MPa, T_u = 360K and ϕ = 0.8-1.3. Solid red and blue lines denote linear and nonlinear relationships for L_b through data points, dashed lines indicate their extrapolation to zero stretch rate and red crosses indicate r_c. 90
Figure 4.7: a) S_n variation with α, b) S_n variation with r, for *iso*-octane/air mixtures at P_i = 0.5 MPa, T_u = 360K and ϕ = 0.8-1.3. Solid red and blue lines denote linear and nonlinear relationships for L_b through data points, dashed lines indicate their extrapolation to zero stretch rate and red crosses indicate r_c. 91
Figure 4.8: a) S_n variation with α, b) S_n variation with r, for *n*-heptane/air mixtures at P_i = 0.5 MPa, T_u = 360K and ϕ = 0.8-1.3. Solid red and blue lines denote linear and nonlinear relationships for L_b through data points, dashed lines indicate their extrapolation to zero stretch rate and red crosses indicate r_c. 92
Figure 4.9: a) S_n variation with α, b) S_n variation with r, for toluene/air mixtures at P_i = 0.5 MPa, T_u = 360K and ϕ = 0.8-1.3. Solid red and blue lines denote linear and nonlinear relationships for L_b through data points, dashed lines indicate their extrapolation to zero stretch rate and red crosses indicate r_c. 93
Figure 4.10: a) S_n variation with α, b) S_n variation with r, for *1*-hexene/air mixtures at P_i = 0.5 MPa, T_u = 360K and ϕ = 0.8-1.3. Solid red and blue lines denote linear and nonlinear relationships for L_b through data points, dashed lines indicate their extrapolation to zero stretch rate and red crosses indicate r_c. 94
Figure 4.11: a) S_n variation with α, b) S_n variation with r, for ethanol/air mixtures at P_i = 0.5 MPa, T_u = 360K and ϕ = 0.8-1.3. Solid red and blue lines denote linear and nonlinear relationships for L_b through data points, dashed lines indicate their extrapolation to zero stretch rate and red crosses indicate r_c. 95
Figure 4.12: a) S_n variation with α, b) S_n variation with r, for *n*-butanol/air mixtures at P_i = 0.5 MPa, T_u = 360K and ϕ = 0.8-1.3. Solid red and blue lines denote linear and nonlinear relationships for L_b through data points, dashed lines indicate their extrapolation to zero stretch rate and red crosses indicate r_c. 96

Figure 4.13: a) S_n variation with α, b) S_n variation with r, for *iso*-octane/air mixtures at P_i = 1.0 MPa, T_u = 360K and ϕ = 0.8-1.3. Solid red and blue lines denote linear and nonlinear relationships for L_b through data points, dashed lines indicate their extrapolation to zero stretch rate and red crosses indicate r_c. 97
Figure 4.14: a) S_n variation with α, b) S_n variation with r, for *n*-heptane/air mixtures at P_i = 1.0 MPa, T_u = 360K and ϕ = 0.8-1.0. Solid red and blue lines denote linear and nonlinear relationships for L_b through data points, dashed lines indicate their extrapolation to zero stretch rate and red crosses indicate r_c. 98
Figure 4.15: a) S_n variation with α, b) S_n variation with r, for toluene/air mixtures at P_i = 1.0 MPa, T_u = 360K and ϕ = 0.8-1.0. Solid red and blue lines denote linear and nonlinear relationships for L_b through data points, dashed lines indicate their extrapolation to zero stretch rate and red crosses indicate r_c. 99
Figure 4.16: a) S_n variation with α, b) S_n variation with r, for *1*-hexene/air mixtures at P_i = 1.0 MPa, T_u = 360K and ϕ = 0.8-1.0. Solid red and blue lines denote linear and nonlinear relationships for L_b through data points, dashed lines indicate their extrapolation to zero stretch rate and red crosses indicate r_c. 100
Figure 4.17: a) S_n variation with α, b) S_n variation with r, for ethanol/air mixtures at P_i = 1.0 MPa, T_u = 360K and ϕ = 0.8-1.0. Solid red and blue lines denote linear and nonlinear relationships to L_b across used data points, with dashed lines indicating their extrapolation to zero stretch rate. Red crosses indicate r_c. 101
Figure 4.18: a) S_n variation with α, b) S_n variation with r, for *n*-butanol/air mixtures at P_i = 1.0 MPa, T_u = 360K and ϕ = 0.8-0.9. Solid red and blue lines denote linear and nonlinear relationships to L_b across used data points, with dashed lines indicating their extrapolation to zero stretch rate. Red crosses indicate r_c. 102
Figure 4.19: Variation of r_c, with ϕ, for all pure liquid fuel/air mixtures, at a) 0.5 MPa and b) 1.0 MPa. 103
Figure 4.20: Schlieren images of *iso*-octane/air mixtures, f = 5400 fps, ϕ = 0.8, T_u = 360K, P_i = 0.1, 0.5 and 1.0 MPa. 105
Figure 4.21: Schlieren images of *iso*-octane/air mixtures, f = 5400 fps, ϕ = 1.0, T_u = 360K, P_i = 0.1, 0.5 and 1.0 MPa. 106
Figure 4.22: Schlieren images of *iso*-octane/air mixtures, f = 5400 fps, ϕ = 1.3, T_u = 360K, P_i = 0.1, 0.5 and 1.0 MPa. 107
Figure 4.23: Schlieren images of *iso*-octane/air mixtures, f = 5400 fps, r = 65 mm, ϕ = 0.8-1.3, T_u = 360K, P_i = 0.1, 0.5 and 1.0 MPa. 108

Figure 4.24: Variation of u_l with ϕ for all pure liquid fuel/air mixtures, P_i = a) 0.1 MPa, b) 0.5 MPa, c) 1.0 MPa, T_u = 360K. 109
Figure 4.25: Variation of L_b with ϕ for all pure liquid fuel/air mixtures, P_i = a) 0.1 MPa, b) 0.5 MPa, c) 1.0 MPa, T_u = 360K. 110
Figure 4.26: Variation of u_l with ϕ for *iso*-octane/air, toluene/air and their relative equimolar binary blend, P_i = a) 0.1 MPa, b) 0.5 MPa, c) 1.0 MPa, T_u = 360K. ... 113
Figure 4.27: Variation of L_b with ϕ for *iso*-octane/air, toluene/air and their relative equimolar binary blend, P_i = a) 0.1 MPa, b) 0.5 MPa, c) 1.0 MPa, T_u = 360K. ... 114
Figure 4.28: Variation of u_l with ϕ for *iso*-octane/air, *1*-hexene/air and their relative equimolar binary blend, P_i = a) 0.1 MPa, b) 0.5 MPa, c) 1.0 MPa T_u = 360K. 115
Figure 4.29: Variation of L_b with ϕ for *iso*-octane/air, *1*-hexene/air and their relative equimolar binary blend, P_i = a) 0.1 MPa, b) 0.5 MPa, c) 1.0 MPa, T_u = 360K. ... 116
Figure 4.30: Variation of u_l with ϕ for *iso*-octane/air, ethanol/air and their relative equimolar binary blend, P_i = a) 0.1 MPa, b) 0.5 MPa, c) 1.0 MPa, T_u = 360K. ... 117
Figure 4.31: Variation of L_b with ϕ for *iso*-octane/air, ethanol/air and their relative equimolar binary blend, P_i = a) 0.1 MPa, b) 0.5 MPa, c) 1.0 MPa, T_u = 360K. ... 118
Figure 4.32: Variation of u_l with ϕ for *iso*-octane/air, *n*-heptane/air and their relative equimolar binary blend, P_i = a) 0.1 MPa, b) 0.5 MPa, c) 1.0 MPa, T_u = 360K. ... 119
Figure 4.33: Variation of L_b with ϕ for *iso*-octane/air, *n*-heptane/air and their relative equimolar binary blend, P_i = a) 0.1 MPa, b) 0.5 MPa, c) 1.0 MPa, T_u = 360K. ... 120
Figure 4.34: Variation of u_l with ϕ for toluene/air, *1*-hexene/air and their relative equimolar binary blend, P_i = a) 0.1 MPa, b) 0.5 MPa, c) 1.0 MPa, T_u = 360K. ... 121
Figure 4.35: Variation of L_b with ϕ for toluene/air, *1*-hexene/air and their relative equimolar binary blend, P_i = a) 0.1 MPa, b) 0.5 MPa, c) 1.0 MPa, T_u = 360K. ... 122
Figure 4.36: Variation of u_l with ϕ for toluene/air, ethanol/air and their relative equimolar binary blend, P_i = a) 0.1 MPa, b) 0.5 MPa, c) 1.0 MPa, T_u = 360K. ... 123
Figure 4.37: Variation of L_b with ϕ for toluene/air, ethanol/air and their relative equimolar binary blend, P_i = a) 0.1 MPa, b) 0.5 MPa, c) 1.0 MPa, T_u = 360K. ... 124
Figure 4.38: Variation of u_l with ϕ for toluene/air, *n*-heptane/air and their relative equimolar binary blend, P_i = a) 0.1 MPa, b) 0.5 MPa, c) 1.0 MPa, T_u = 360K. ... 125
Figure 4.39: Variation of L_b with ϕ for toluene/air, *n*-heptane/air and their relative equimolar binary blend, P_i = a) 0.1 MPa, b) 0.5 MPa, c) 1.0 MPa, T_u = 360K. ... 126
Figure 4.40: Variation of u_l with ϕ for *1*-hexene/air, ethanol/air and their relative equimolar binary blend, P_i = a) 0.1 MPa, b) 0.5 MPa, c) 1.0 MPa, T_u = 360K. ... 127

Figure 4.41: Variation of L_b with ϕ for *1*-hexene/air, ethanol/air and their relative equimolar binary blend, P_i = a) 0.1 MPa, b) 0.5 MPa, c) 1.0 MPa, T_u = 360K. ... 128
Figure 4.42: Variation of u_l with ϕ for *1*-hexene/air, *n*-heptane/air and their relative equimolar binary blend, P_i = a) 0.1 MPa, b) 0.5 MPa, c) 1.0 MPa, T_u = 360K. ... 129
Figure 4.43: Variation of L_b with ϕ for *1*-hexene/air, *n*-heptane/air and their relative equimolar binary blend, P_i = a) 0.1 MPa, b) 0.5 MPa, c) 1.0 MPa, T_u = 360K. ... 130
Figure 4.44: Variation of u_l with ϕ for ethanol/air, *n*-heptane/air and their relative equimolar binary blend, P_i = a) 0.1 MPa, b) 0.5 MPa, c) 1.0 MPa, T_u = 360K. ... 131
Figure 4.45: Variation of L_b with ϕ for ethanol/air, *n*-heptane/air and their relative equimolar binary blend, P_i = a) 0.1 MPa, b) 0.5 MPa, c) 1.0 MPa, T_u = 360K. ... 132
Figure 4.46: Variation of a) u_l and b) L_b with ethanol addition to TRF/air mixtures, P_i = 0.1 MPa and T_u = 360K. ... 137
Figure 4.47: Variation of a) u_l and b) L_b with ethanol addition to TRF/air mixtures, P_i = 0.5 MPa and T_u = 360K. ... 138
Figure 4.48: Variation of a) u_l and b) L_b with ethanol addition to TRF/air mixtures, P_i = 1.0 MPa and T_u = 360K. ... 139
Figure 4.49: Variation of a) u_l and b) L_b with *n*-butanol addition to TRF/air mixtures, P_i = 0.1 MPa and T_u = 360K. ... 140
Figure 4.50: Variation of a) u_l and b) L_b with *n*-butanol addition to TRF/air mixtures, P_i = 0.1 MPa and T_u = 360K. ... 141
Figure 4.51: Variation of a) u_l and b) L_b with *n*-butanol addition to TRF/air mixtures, P_i = 1.0 MPa and T_u = 360K. ... 142
Figure 4.52: Variation of u_l with hydrogen addition to methane/air mixtures, P_i = 0.1 MPa, T_u = 303K, a) ϕ = 0.6-0.9, b) ϕ = 1-1.3. ... 145
Figure 4.53: Variation of L_b with hydrogen addition to methane/air mixtures, P_i = 0.1 MPa, T_u = 303K, a) ϕ = 0.6-0.9, b) ϕ = 1.0-1.3. ... 146
Figure 5.1: Variation of a) u_l and b) L_b percentage increase by linear extrapolation relative to nonlinear extrapolation with ϕ, for all pure liquid fuel/air mixtures, P_i = 0.1 MPa and T_u = 360K. ... 149
Figure 5.2: Variation of Pe_{cl} with Ma_b for different liquid pure fuel/air mixtures measured in the Leeds CV2, at a) 0.5 MPa and b) 1.0 MPa. Alongside corresponding data of large-scale atmospheric explosions for methane/air and propane/air mixtures. The solid black curve shows the best fit through the Leeds CV2 data. ... 152

Figure 5.3: Variation of K_{cl} with Ma_b for different liquid pure fuel/air mixtures measured in the Leeds CV2, at a) 0.5 MPa and b) 1.0 MPa. Alongside corresponding data of large-scale atmospheric explosions for methane/air and propane/air mixtures. The solid black curve shows the best fit through the Leeds CV2 data. 154
Figure 5.4: Variation of K_{cl} with Ma_{sr}, for ethanol/air mixtures at different elevated pressures, measured in the Leeds CV2 by Bradley et al. (2009). Alongside corresponding data of large-scale atmospheric explosions for methane/air and propane/air mixtures. The solid black curve shows the best fit through the Leeds CV2 data. 155
Figure 5.5: Comparison of a) u_l and b) L_b measurements for *iso*-octane/air mixtures at 0.1 MPa, 360K, across ϕ = 0.8-1.3. Solid black curves shows best fit through present data..... 157
Figure 5.6: Comparison of a) u_l and b) L_b measurements for *iso*-octane/air mixtures at 0.5 MPa, 360K, across ϕ = 0.8-1.3. Solid black curves shows best fit through present data..... 158
Figure 5.7: Comparison of a) u_l and b) L_b measurements for *iso*-octane/air mixtures at 1.0 MPa, 360K, across ϕ = 0.8-1.3. Solid black curves shows best fit through present data..... 159
Figure 5.8: Comparison of a) u_l and b) L_b measurements for ethanol/air mixtures at 0.1 MPa, 360K, across ϕ = 0.8-1.3. Solid black curves shows best fit through present data. 161
Figure 5.9: Comparison of a) u_l and b) L_b measurements for ethanol/air mixtures at 0.5 MPa, 360K, across ϕ = 0.8-1.3. Solid black curves shows best fit through present data. 162
Figure 5.10: Comparison of a) u_l and b) L_b measurements for ethanol/air mixtures at 1.0 MPa, 360K, across ϕ = 0.8-1.3. Solid black curves shows best fit through present data. 163
Figure 5.11: Comparison of u_l measurements for a) *n*-heptane/air and b) toluene/air mixtures at 0.1 MPa, 360K, across ϕ = 0.8-1.3. Solid black curves shows best fit through present data. 164
Figure 5.12: Variation of volumetric energy with alcohol addition to TRF. 166
Figure 5.13: Variation of a) u_l and b) L_b with P_i, at ϕ = 0.8, for all TRF/alcohol/air mixtures. 167

Figure 5.14: Variation of a) u_l and b) L_b with P_i, at ϕ = 1.0, for all TRF/alcohol/air mixtures. 168
Figure 5.15: Variation of a) u_l and b) L_b with P_i, at ϕ = 1.2, for all TRF/alcohol/air mixtures. 169
Figure 5.16: Variation of ignition delay with temperature, for TRF/air mixtures at 2.0 MPa and ϕ = 1 (Materego, 2015). 171
Figure 5.17: Difference in ignition delay between the TRF and the TRF/alcohol blends as a function of temperature, at 2.0 MPa and ϕ = 1 (Materego, 2015). 172
Figure 5.18: Variation of energy flux as a function of hydrogen addition to methane/air mixtures, $\bar{x}_{H2}$, P_i = 0.1 MPa, T_u = 303K, a) ϕ = 0.6-0.9, b) ϕ = 1.0-1.3. 175
Figure 6.1: Predictive performance of a) u_l and b) L_b laws for blends of methane/hydrogen/air mixtures as a function of $\bar{x}_{fH2}$, P_i = 0.1 MPa, T_u = 303K, ϕ = 0.6. 182
Figure 6.2: Predictive performance of a) u_l and b) L_b laws for blends of methane/hydrogen/air mixtures as a function of $\bar{x}_{fH2}$, P_i = 0.1 MPa, T_u = 303K, ϕ = 0.7. 183
Figure 6.3: Predictive performance of a) u_l and b) L_b laws for blends of methane/hydrogen/air mixtures as a function of $\bar{x}_{fH2}$, P_i = 0.1 MPa, T_u = 303K, ϕ = 0.8. 184
Figure 6.4: Predictive performance of a) u_l and b) L_b laws for blends of methane/hydrogen/air mixtures as a function of $\bar{x}_{fH2}$, P_i = 0.1 MPa, T_u = 303K, ϕ = 0.9. 185
Figure 6.5: Predictive performance of a) u_l and b) L_b laws for blends of methane/hydrogen/air mixtures as a function of $\bar{x}_{fH2}$, P_i = 0.1 MPa, T_u = 303K, ϕ = 1.0. 186
Figure 6.6: Predictive performance of a) u_l and b) L_b laws for blends of methane/hydrogen/air mixtures as a function of $\bar{x}_{fH2}$, P_i = 0.1 MPa, T_u = 303K, ϕ = 1.1. 187
Figure 6.7: Predictive performance of a) u_l and b) L_b laws for blends of methane/hydrogen/air mixtures as a function of $\bar{x}_{fH2}$, P_i = 0.1 MPa, T_u = 303K, ϕ = 1.2. 188
Figure 6.8: Predictive performance of a) u_l and b) L_b laws for blends of methane/hydrogen/air mixtures as a function of $\bar{x}_{fH2}$, P_i = 0.1 MPa, T_u = 303K, ϕ = 1.3. 189

List of Tables

Table 2.1: Assigned symbols for the different weighting factors used in the forthcoming blending laws. 39
Table 3.1: Summary of all liquid fuels used in the present work. 60
Table 3.2: Summary of average temperature measurements and the maximum positive and negative temperature deviations from T_u within r = 75mm, t = 15s. 79
Table 4.1: List of all pure liquid hydrocarbon based fuels studied and their basic properties. 83
Table 4.2: Binary equimolar constituent mixtures showing different constituent ratios as discussed in Chapter 2, Section 2.3. Densities for all fuels are shown in Table 4.1. 112
Table 4.3: Composition of TRF Blend, showing the different fractional proportions of each constituent within the blend, as discussed in Chapter 2, Section 2.3. Densities for all fuels are shown in Table 4.1. 134
Table 4.4: Effects on various mixture fractions of increasing liquid volume of ethanol and *n*-butanol to the base TRF liquid Fuel. All fractional calculations are as discussed in Chapter 2, Section 2.3. Densities for all fuels are shown in Table 4.1. 134
Table 4.5: A compositional list of the CH4/H2/air blends, showing the proportion of each constituent within the blend by different units of measurement, as discussed in Chapter 2, Section 2.3. 144
Table 6.1: Summary of all existing and proposed u_l blending laws investigated. 177
Table 6.2: Summary of all proposed L_b blending laws investigated. 177
Table 6.3: Average u_{lp}/u_l and L_{bp}/L_b values of each u_l and L_b blending law, for all blends studied. 181
Table 6.4: Average u_l and L_b blending law performances (u_{lp}/u_l and L_{bp}/L_b), all methane and hydrogen Blends, ϕ = 0.6-1.3, T_u = 303K, P_i = 0.1 MPa. 181

Nomenclature

A	Area	m^2
c	Reaction Progress Variable	-
c_c	Horizontal Position of Area Centroid beneath R Curve	-
c_p	Specific heat capacitance at constant pressure	J/mol/K
c_v	Specific heat capacitance at constant volume	J/mol/K
D	Mass Diffusivity	m^2/s
h	Enthalpy	J/mol
h_f	Enthalpy of Formation	J/mol
K	Karlovitz Number	-
k	Thermal Conductivity	J/m/K/s
L_b	Burned Gas Markstein Length	m
Le	Lewis Number	-
m	mass	kg
Ma_b	Burned Gas Markstein Number	-
Ma_{sr}	Markstein Strain Rate Number	-
Pe	Peclet Number	-
P_i	Initial Pressure	MPa
Q	Mass Heat of Reaction	J/kg
$\bar{Q}$	Molar Heat of Reaction	J/mol
q	Heat Release Rate	J/s
q_m	Maximum Heat Release Rate	J/s
R	Universal Gas Constant	J/mol/K
r_u	unburned radius	m
S_n	Stretched Flame Speed	m/s
S_s	Unstretched Flame Speed	m/s
t	Time	s
T_u	Unburned Gas Temperature	K
u_g	Gas Velocity ahead of Flame	m/s
u_l	Unstretched Laminar Burning Velocity	m/s
u_n	Stretched Laminar Burning Velocity	m/s
$\bar{x}$	Mixture Mole Fraction	-
x	Mixture Mass Fraction	-
$\bar{x}_d$	Deficient Mole Fraction	-
x_d	Deficient Mass Fraction	-
$\bar{x}_f$	Fuel Mole Fraction	-
x_f	Fuel Mass Fraction	-
x_v	Fuel Volume Fraction	-

Greek Symbols

α	Flame Stretch Rate, Thermal Diffusivity	1/s, m^2/s
β	Zeldovich Number	-
γ	Heat Capacity Ratio (c_p/ c_v)	-
δ	Flame Thickness	m
λ	Eigenvalue for burning velocity = 0.5	-
v	Kinematic Viscosity	m^2/s
ρ	Density	kg/m^3
σ	Unburned to Burned Gas Density Ratio	-
τ_i	Ignition Delay Time	s
τ_e	Excitation Time	s
ϕ	Equivalence Ratio	-

Subscripts and Superscripts

a	Activation
b	Burned Gas
cl	Critical
i	*i*'th Constituent
l	Laminar
P	Products
R	Reactants
sch	Schlieren
u	Unburned Gas

Acronyms

ADC	Analogue to Digital Convertor
CR	Compression Ratio
SOC	Start of Compression
EOC	End of Compression
FT	Fisher-Tropsch
GHG	Green House Gases
LV	Liquid Volume

Chapter 1 - Introduction

1.1 General Overview and Motivation

Over 66% of current World energy demands are met by an infrastructure based on the finite resource of fossil fuels, of which approximately 40% is consumed by the vastly expanding transportation sector (IEA, 2015). The transportation sectors energy demands are largely in the form of liquefied hydrocarbons derived from crude oil, which have traditionally served as the energy source of choice due to their high energy density, abundant low cost supply, relatively safe nature and ease of transportation and storage. However, the need to divert from such traditions is increasingly evident from dwindling supplies becoming harder to extract, the theory of peak oil, unsecure and capricious supply chains and the disconcerting environmental effects of combustion emissions such as carbon dioxide, nitrogen oxides, smog and soot (Minns, 2005).

In the hope of mitigating such concerns, there is much research and development exploring the possibilities of optimising existing engine technologies and diverting to other potentially viable alternative fuels that can partially, if not fully, substitute conventional petroleum derived fuels. Ideally, alternative fuels should at least reduce the dependency on fossil based fuels and the release of noxious emissions, be fungible with existing infrastructure, of similar energy density, be scalable to demand, and offer potential for carbon neutral cycles. Promising alternatives to conventional fuels are first, that of Fisher Tropsch (FT) synthetic fuels, available from a multitude of feedstock's, such as coal, gas, shale, biomass, waste or any other carbonous material. Second, are bio-fuels, such as ethanol and *n*-butanol, which are typically fermented from high starch content biomass. Such alternative fuels are already being phased into many commercial fuel blends, with the likelihood of increasing proportions.

Characterisation of the combustion performance for blends comprised of alternative fuels in varying proportions, under different operational pressures and temperatures, is of vital importance to their effective use and optimisation within modern engines. They must therefore be properly assessed and understood, before their commercial deployment.

Two fundamental areas for combustion characterisation within all engines are that involving burning velocity and autoignition. The former, is the rate of burn, and

characterised by the unstretched laminar burning velocity, u_l, a fundamental phyiso-chemical parameter of a propagating flame, which depends upon chemical reaction kinetics, exothermicity and molecular transport processes within the reaction zone. The latter, autoignition, is the sudden exothermic heat release from the oxidisation of a fuel under the influence of heat and pressure, via the establishment of a self-heating chemical mechanism. It is characterised by the ignition delay time, τ_i, defined as the period of time taken for the onset of combustion at a given pressure and temperature. Both u_l and τ_i are dependent upon fuel/air mixture composition, pressure and temperature.

In the case of spark ignition (SI) engines, both parameters are critically interrelated. The spark initiated flame duration is governed by u_l and, autoignition, as pressure and temperature increase, can only occur if τ_i is shorter than the time required for the complete burn by the spark initiated flame front. Strong autoignition within SI engines gives rise to the phenomenon known as “knock”, which can potentially lead to severe engine damage due to high oscillating pressure rises. Furthermore, the volumetric efficiency of SI engines is knock limited via the compression ratio, thus limiting fuel efficiency and the potential emission reductions. Conversely, compression ignition (CI) engines rely on autoignition, in which again, τ_i is critical to efficiency and performance.

Collaboration agreements between Shell Global Solutions UK, Sasol SA, the University of Leeds, and University of Cape Town, supported investigations into the u_l and τ_i behaviour of blends of fuels relative to their constituents, under different conditions. The present work predominately focused on u_l behaviour, as a function of pressure and equivalence ratio, and the development of a universal predictive u_l blending law. Measurements of u_l were performed using a spherical combustion vessel, for blends comprised of constituents representative of the major fuel groups found within commercial FT synthetic gasoline, namely, *iso*-octane, *n*-heptane, toluene and *1*-hexene, and that of promising alternative bio-alcohols, namely, ethanol and *n*-butanol. Furthermore, blends comprised of the more chemically dissimilar fuels of methane and hydrogen, were also investigated to further aid the development of a universal predictive u_l blending law.

1.2 Conventional and Alternative Transportation Fuel Sources

The following subsections introduce the main implications of conventional and promising alternative transportation fuel sources.

1.2.1 Conventional Fuels

Conventional fuels are considered as those derived from petroleum, also known as crude oil. It is essentially a mixture of liquefied hydrocarbons and the result of anaerobic decomposition of organic matter. Primarily found trapped beneath sedimentary rock layers, the exposure to great pressure, temperature, time and lack of oxygen cause a chemically transforming process known as catagenesis to occur within the organic matter, creating the production of solid, liquid and gaseous hydrocarbons. Within which holds the captured energy the transportation sector has predominately exploited for over 100 years. Geologists perform seismic surveys where sound waves are projected into the earth generating feedback that is interpreted by computers producing three dimensional images that show the exact location and quantity of any oil pockets available for extraction. Drilling to such pockets is then carried out by 10-100cm diameter drills creating high flow rate extraction paths that are typically lined with steel and concrete reinforcements, allowing petroleum to be pumped through pipe work or transported via road or rail to a refinery. At refineries the petroleum is heated up to temperatures of over 850K allowing separation of different molecular weight hydrocarbons with different boiling points in a fractionating column, the higher sections of the column capturing the more volatile products and vice versa. The heavier alkanes are often processed further by cracking, this producing more useful lighter alkanes and alkenes. With such refining and reforming, petroleum is transformed into a vast array of end products such as liquid petroleum gas (LPG), gasoline, naphtha, kerosene, diesels, heavy fuel oils, lubricants, waxes, solvents, petroleum coke and other products (Speight, 2008).

1.2.2 Fisher-Tropsch Synthetic Fuels

Fisher-Tropsch (FT) synthetic fuels represent an array of fuels that share the common factor of being derived through catalytic chemical reaction conversions of one carbonaceous material to another via the gasification and FT processes. Production can stem from such feedstocks as tar sand, coal, natural gas, oil shale, biomass and waste,

where coal-to-liquid (CTL), gas-to-liquids (GTL) and biomass-to-liquids (BTL) are now coined terms representing various synthetic fuel types relative to their initial feedstock (Speight, 2008).

Gasification is the first major chemical process for production, which serves to thermo-chemically decomposes the feedstock, initially by pyrolysis to be followed by various other gas thermal upgrading steps under controlled oxygen conditions and high temperatures (>950K). This primarily produces a mixture of carbon monoxide and hydrogen, known as syngas. Further gas conditioning purifies the syngas mixture by the removal of contaminants such as sulphur, nitrogen and particulates which may be used as fertilisers. This gives major environmental benefits through substantially cleaner combustion of both syngas and end product fuels. Syngas is a valuable product in itself, providing a relatively clean fuel for gas turbines powering electrical generators in FT production, with only carbon dioxide and water vapour as combustion products, but typically contains less than half the energy density of natural gas. Heat recovery systems also power steam turbines generating more electricity for the overall process. Syngas also serves as an intermediate feedstock in the manufacture of fertilisers such as ammonia and the production of methane via the Sabatier process, via a nickel or ruthenium catalyst which may lead to the production of methanol and hydrogen (Speight, 2008).

The syngas then undergoes a form of synthesis by the German originated Fischer-Tropsch (FT) process pioneered by Franz Fischer and Hans Tropsch in 1925, which serves as the second major chemical process in the overall production. Although other synthesis processes exist such as the Bergius, Mobil and Karrick processes, the FT has become most favoured following its refinements in coal rich Germany during World War II and South Africa during apartheid. The FT process takes the syngas over a selected catalyst generating chemical reactions that form specific length hydrocarbon chains, the length of which is determined primarily by the catalyst material and temperature. For example, a cobalt based catalyst in the region of 500K can create high cetane number diesel and jet fuels, whilst an iron based catalyst at 610K can create the more challenging gasoline fuels. Such processes can offer high potential for a broad range of petroleum fuel, lubricant, solvent and waxes (Speight, 2008).

The following formula represents the main chemical reactions during the FT process, where carbon monoxide and hydrogen are converted to water and the desired hydrocarbons:

$$n\mathrm{CO} + (2n+1)\mathrm{H_2} \rightarrow \mathrm{C}_n H_{(2n+2)} + n\mathrm{H_2O} \quad (1.1)$$

The prior endothermic gasification process can simply be represented by the carbonenaous feedstock and water being converted into syngas:

$$\mathrm{C} + \mathrm{H_2O} \rightarrow \mathrm{H_2} + \mathrm{CO} \quad (1.2)$$

Energy to support gasification is often generated from the simple exothermic combustion of carbon and oxygen:

$$2\mathrm{C} + \mathrm{O_2} \rightarrow \mathrm{CO} \quad (1.3)$$

In addition, partial combustion of the feedstock may also serve as a means of syngas production too:

$$\mathrm{C}_n\mathrm{H}_{(2n+2)} + {}^1\!/_2\, n\mathrm{O_2} \rightarrow (n+1)\mathrm{H_2} + n\mathrm{CO} \quad (1.4)$$

Historically, FT synthetic fuels have received little interest due to the low cost of abundant petroleum reserves such as in the Middle East, compared to the relatively high costs and increased complexities of synthetic fuel production. However, as production techniques are optimised and petroleum prices rise, alongside concerns of security and environmental impact, the viability of FT synthetic fuels increases. Feedstock flexibility alone forms an attractive factor that can potentially take advantage of vast coal, natural gas and tar sand reserves, although such feedstock's increase the overall carbon cycle compared to conventional petroleum based fuels. That said, various forms of non-food biomass are often combined or totally substitute, offering much reduced carbon cycles, but often at the expense of increased costs. Carbon capture and storage (CCS) technologies also offer potential to drastically reduce onsite carbon emissions. A further significant advantage over many other competing alternative energy sources comes from being fully fungible with existing infrastructure and with little or no modification required on existing engine technologies (Speight, 2008).

Sasol, has the World's largest commercially based CTL plant in Secunda, South Africa, producing 160,000 barrels of oil equivalent per day (BOE/D), whilst Shell has the World's largest GTL plant in Ras Laffan Industrial City, Qatar producing 140,000 BOE/D and 120,000 BOE/D of natural gas liquids (NGL) and ethane. Both companies

have other GTL facilities and have expansion plans into USA and Canada, where the process can take direct advantage of abundant natural gas reserves.

Shell has also developed three pioneering technologies that make use of the sulphur by-product:

- Shell Thiocrete - a cement replacement, not requiring water, with superior compressive strength and durability properties.
- Shell Thiopave – a partial substitute for bitumen in asphalt mixtures to give increased load bearing roads with improved durability, whilst reducing green house gas (GHG) emissions through lower temperature production.
- Shell Thiogro – sulphur based fertilisers that increase crop yields.

Overall, FT synthetic fuel is an energy source that offers the prospect of a potentially sustainable, stable and secure supply with environmental benefits that can be immediately implemented into today's transportation energy infrastructure, whilst concurrently producing many other petroleum based substitutes and useful end products.

1.2.3 Bio-Fuels

A bio-fuel may be gaseous, liquid or solid and is defined as being derived from biomass. This may constitute of any recent living organism or its metabolic by-products to qualify as a renewable energy source. A bio-fuel has been defined as "any fuel with an 80 percent minimum content by volume of materials derived from living organism harvested within the 10 years preceding its manufacture" Speight (2008). Photosynthesis is responsible for capturing more carbon dioxide from the atmosphere than any other natural or industrial process in the world. Around one seventh of carbon dioxide in the atmosphere is fixed by photosynthesis in terrestrial biomass forms each year, if as little as 7.5% of this was utilised to form feasible biofuels it would eradicate all carbon dioxide annually emitted to the atmosphere by fossil based fuels (Lee, 2012). Biofuels are considered to be relatively clean fuels, with lower sulphur dioxide, nitrogen oxides and soot emissions than conventional fossil fuels (Speight, 2008).

Liquid biofuels were the initial fuels of choice of internal combustion engine inventor, Nikolaus August Otto, and the inventor of the diesel engine, Rudolf Diesel, who selected ethanol and peanut oil, respectively (Speight, 2008). However, again, the abundant discoveries of relatively cheap petroleum soon made them undesirable

options, with any further interest in biofuels coinciding with that of petroleum prices for most of the 20th century.

Biofuels can be categorised into three main groups of first, second and third generation. First generation are considered conventional biofuels which are primarily derived from sugars, starches and vegetable oils from arable land crops such as wheat, corn, sugar cane and sugar beat. Example end product fuels include: biodiesel, biogasoline, green diesel, bioethers, biogas, bioalcohols and syngas. However, production is limited by thresholds on the amount of arable land available for this purpose relative to that for food production, whilst still requiring high amounts of potentially noxious fertilisers. Recent studies suggest relative reductions in overall GHG emissions by such means are often only marginal after allowances for processing, production and transportation. Therefore, their implementation can only fractionally reduce dependence on petroleum based fuel, whilst threatening to increase the cost of basic food supplies, as land is competed for, and with limited environmental benefit (Gnansounou et al., 2009; Lee and Lavoie, 2013).

Second generation are considered advanced biofuels producing much the same end products as first generation but derived from only sustainable feedstock's that do not significantly impose on arable land or negatively impact on the environment. Thus second generation biofuels solve many issues associated with first generation biofuels, often with the prospect of much larger yields. Non-food biomass may take the form of residuals from current crops such as leaves, stems and husks, industrial waste such as pulp and skins or specifically grown crops such as jatropha, miscanthus and switchgrass (Lee and Lavoie, 2013; Speight, 2008).

There are two main streams of development for second generation biofuels, involving either thermochemical or biochemical processing. The former employs such methods as pyrolysis, gasification and torrefaction for the production of syngas and other hydrocarbons, which may be directly used as fuels, or produce an array of fuels via FT processing and thus essentially be considered synthetic BTL fuels. The latter focuses on chemically induced biological reactions that separate the complex carbohydrates of lignin, hemicellulose and cellulose found in all plant life. These may then undergo fermentation and other processes to produce such alcohols as ethanol, methanol and butanol (Lee and Lavoie, 2013; Speight, 2008).

Third generation are considered to be those derived from algal biomass with substantially higher yields compared to classical lignocellulosic biomass. These types of algae can again produce oil that can be refined into diesel fuels, however, they can also be genetically modified to directly produce ethanol, *n*-butanol and other fuels (Lee and Lavoie, 2013). Advancements in genetically modified algae have allowed *n*-butanol production to be potentially scalable to demand and therefore a serious contender to ethanol. Benefits include, a higher volumetric energy density, less corrosion and swelling to engines parts, without being hygroscopic. Furthermore, algae offers great diversity in terms of its cultivation, typically by means of opens ponds, closed loop systems or photo-bioreactors. The latter two techniques are both closed systems that allow the direct connection to CO_2 sources which significantly increase growth. However, the large scale production of algae requires substantial quantities of water, nitrogen and phosphorus and the current energy input associated with their use often counters any CO_2 reduction. Much on-going research continues towards biofuel technologies, with an increasing number of production techniques alongside new feedstock possibilities such as microalgae and fungi, all with the aims of increasing production efficiency, sustainability and yields (http://biofuel.org.uk/third-generation-biofuels.html, 2015; Lee and Lavoie, 2013).

1.3 Key Combustion Characteristics of Fuel Blends

Blends of such conventional and alternative fuels necessitate an understanding of their combustion performance to ensure they are not only suitable for their intended application, but optimal. Furthermore, due to the synergistic nature of fuels and engines, there is potential for engines to be optimised to specific combustion characteristics of specific blends for increased efficiency. For example, in the case of an SI engine, a gasoline blend with a higher octane rating would potentially allow for a higher compression ratio, thus, giving higher volumetric efficiency and potentially, reduced fuel consumption.

The science of combustion invokes a multitude of disciplines, including, thermodynamics, chemistry, physics and fluid mechanics. It may be defined as a self-supporting exothermic chemical reaction between that of a fuel and oxidant, which includes the principle physical processes of mass and energy transportation, resulting in the liberation of heat and conversion of chemical species (Barnard, 1995).

In the case of engines and turbines, there are two primary modes of combustion, that of propagating deflagration flames, driven by the molecular transport processes of conduction and diffusion of species within a thin reaction zone, and autoignition, induced by reactant composition, temperature and pressure, typically as a result of localised hot spots. Flames can be categorised as either premixed or diffusion, the former with flame propagation through a homogenous fuel/air mixture, the latter with the mixing of fuel and air within the reaction zone. Flame propagation and autoignition are characterised by the laminar burning velocity, u_l, and ignition delay time, τ_i. These key parameters are discussed in the following sections, with techniques for their acquisition reviewed.

1.4 Laminar Premixed Flames and Burning Velocity

Premixed laminar flames are prevalent in an array of applications from residential cookers and heaters, to industry furnaces and burners. Whilst, the study of laminar flames has importance in its own right, their theoretical understanding serves as a vital prerequisite to the study of turbulent combustion, in which stretched laminar flamelets are considered in turbulent flows. This section introduces the concepts and assumptions surrounding the structure and dynamics of laminar premixed flames and the determination of the inherent physiochemical parameter of unstretched laminar burning velocity, u_l.

1.4.1 Historical Perspectives

Mallard and Le Chatelier (1883) pioneered laminar flame speed theory, on the assumption of heat conduction from hot reaction gases to the unburned cold reactant mixture governing the rate of flame propagation. Thus, concluding the unstretched laminar flame speed was a function of the square root of the product of the reactant mixture thermal diffusivity, the reaction rate and the temperature gradient through the flame. Over five decades later, Zeldovich and Frank-Kamenetskii (1938) then emphasised the need to account for molecular diffusion of the reactants, alongside thermal conduction, and further introduced a temperature dependant reaction rate. Seminal studies of Semenov (1935) and Hinshelwood (1940) lead to a greater appreciation of chemical kinetic steps and the intrinsic formation and consumption of intermediate radicals. Later, Dixon-Lewis and Williams (1963) pioneered the computation of a laminar hydrogen/air flame structure, accounting for conduction,

chemical and chain reactions and species diffusion. Thus, elucidating the molecular diffusion and transportation properties within the flame. Concurrently, an analytical expression for laminar burning velocity was also proposed by Zeldovich and Barenblatt (1959).

1.4.2 Flame Structure

A premixed laminar flame is a thin self-propagating exothermic reaction zone within the flow field of reactants and products. Figure 1.1 shows the reactant and product concentrations, temperature profiles through an ideal premixed, laminar, one-dimensional and adiabatic flame. It comprises four zones as the flame moves right to left: the cold reactant zone, the preflame zone, the reaction zone, and finally the product zone (Barnard, 1995). Heat conduction and the mass diffusion dominate the reactants in the preflame zone, whilst chemical reaction and mass diffusion dominate the reaction zone. As reactants in the preflame approach the reaction zone they are heated by conductive heat transfer, before further heating from chemical reaction. This process takes the unburned cold zone reactants, T_u to the adiabatic burned gas temperature, T_b in the product zone. The resulting nonlinear temperature profile is primarily caused by the nonlinear heat release and transport process.

The laminar flame thickness, as denoted by $\delta_{l,}$ maybe described as the distance between the unburned gas at T_u, and the completely burned gas at T_b (Tripathi, 2012). There are many different definitions of laminar flame thickness (Gillespie et al., 2000; Haq, 1998; Poinsot and Veynante, 2005). In the present work, it is defined as a hydrodynamic length, given by:

$$\delta_l = \frac{\nu_u}{u_l}, \tag{1.5}$$

where, ν_u, denotes the reactants kinematic viscosity.

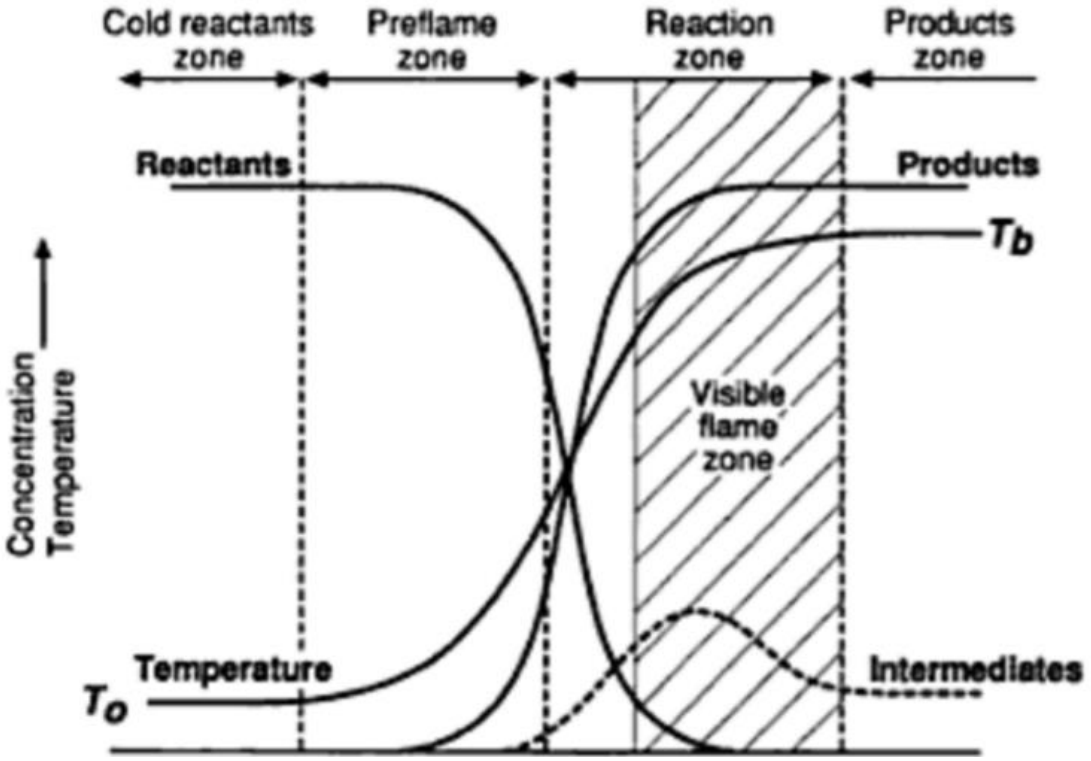

Figure 1.1: Concentration and temperature profiles associated with one-dimensional, premixed, adiabatic flame (Barnard, 1995).

1.4.3 Flame Stretch

Figure 1.2 shows an ideal planar flame in which the flame front travels from right to left, whereby the unburned reactants enter the reaction zone at u_l and the products exit at the flame speed, S_s. The difference being, u_g, caused by the expansion of the hot product gases, hence:

$$S_s = u_l + u_g \tag{1.6}$$

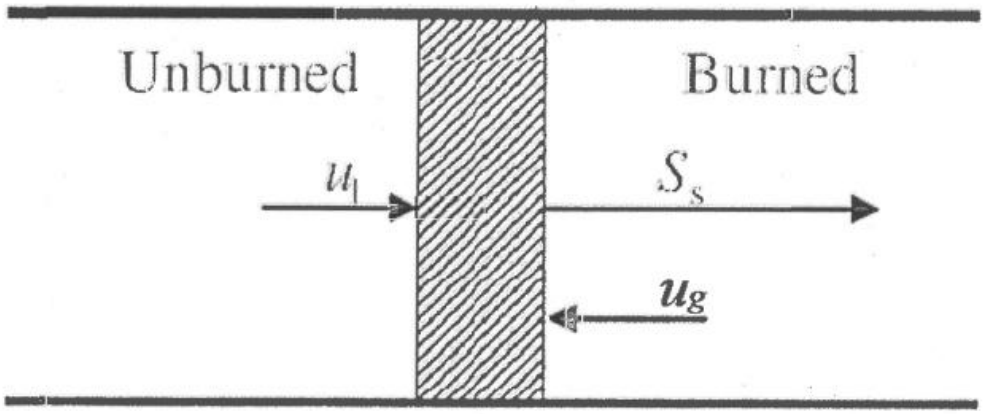

Figure 1.2: Schematic of one-dimensional planar flame, indicating the unstretched burning velocity, u_l, the unstretched flame speed, S_s, and the gas expansion velocity, u_g (Lawes, 2002).

Practical flames are seldom in such an ideal form, and are often within unsteady and non-uniform flow systems, subjecting the flame to transverse and tangential velocity components, alongside flame curvature, that "stretch" the flame. This causes changes to the frontal area of the flame which, in turn, affects the species concentrations and temperature profile through the flame, and subsequently, the flame thickness and burning velocity.

The phenomenon of stretch was first investigated by Karlovitz et al. (1953) who interpreted its effect on flame extinction. Markstein (1964) followed with an investigation into the relationship between stretch and flame curvature. Williams (1985) defines the total stretch rate, α, as the time derivative of area, *A*, of an infinitesimal element over the area:

$$\alpha = \frac{1}{A}\frac{dA}{dt} \tag{1.7}$$

1.4.4 Determination of Unstretched Burning Velocity

The unstretched laminar burning velocity, u_l, is defined as the velocity of a plane flame front moving normal to its surface through adjacent unburned reactants which are converted to products (Barnard, 1995). It is a fundamental physio-chemical parameter of a flame, and dependent upon: the reaction chemical kinetics, exothermicity, molecular transport processes, equivalence ratio, pressure and temperature.

Over the past fifty years or more, many experimental techniques have been developed and refined for the determination of unstretched laminar burning velocity. The following subsections serve to introduce those that have become well established and proven to be relatively accurate.

1.4.4.1 Flat Flame Burners

A schematic of a typical flat flame burner is shown in Figure 1.3. Premixed fuel/air flow through a perforated plate, ignites, and adjusted such that a flat flame is stabilised, normal to the upstream mixture flow, and located above the plate. Inert gases are often used to shroud the flame and reduce potential of any environmental influences. The burning velocity of the mixture can then be deduced by dividing the volumetric mixture flow rate by the area of the flame. However, due to heat transfer to the burner, the flame is not adiabatic, and therefore values of u_l are reduced. Heat loss can be minimised by

high mixture flow rates, however, this is limited by the need to maintain a stable flame surface free from distortion.

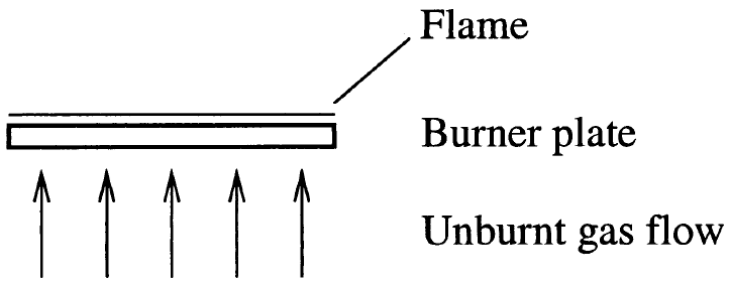

Figure 1.3: Schematic of typical flat flame burner, with perforated burner plate (Bosschaart and De Goey, 2003).

In efforts to decouple this undesirable heat loss effect, Botha and Spalding (1954) introduced the concept of measuring the required cooling rate to achieve a flat flame for different mixture flow rates, such that a flow rate without heat loss could be estimated by extrapolating to a cooling rate of zero, yielding a u_l without heat loss. Much development has since refined the technique, improving its accuracy, with advances in highly thermally insulating materials and more efficient perforated plate designs (Bosschaart and De Goey, 2003).

1.4.4.2 Counter Flow Stagnation Burners

Counter flow stagnation burners have been used in the measurement of many combustible mixture u_l values (Hirasawa et al., 2002; Jayachandran et al., 2015; Yamaoka and Tsuji, 1985). Figure 1.4 shows a schematic of a typical counter flow stagnation burner. The premixed combustible mixture is fed through two opposing jets and ignited, the mixture flow rates to each jet are then adjusted such that a planar stagnation flame is created equidistant from the nozzle of each jet, where y = 0. Different size flames are created by different mixture flow rates, in each case the velocity of each jet is the same, such that the point of stagnation remains central.

Figure 1.5 shows a typical profile of the normal velocity component, v, where the stretch rate is given by $a = dv/dy$. The larger the gradient, the greater the stretch. From left to right, a linear decrease in velocity is shown prior to the main preheat zone. This is then reversed as the flame enters the main preheat zone due to intense heating and therefore thermal expansion. Finally, the velocity decreases again towards completion of heat release in the approach to the stagnation point. The flame is stabilised at the boundary of the main preheat zone. At this point the stretched burning velocity is

approximately the local burning velocity, u_n. With different mixture flow rates, different a and u_n values are measured. Plotting of these u_n values as a function a, allows the extrapolation to the point of zero a, thus, allowing for the determination of u_l. (Tripathi, 2012).

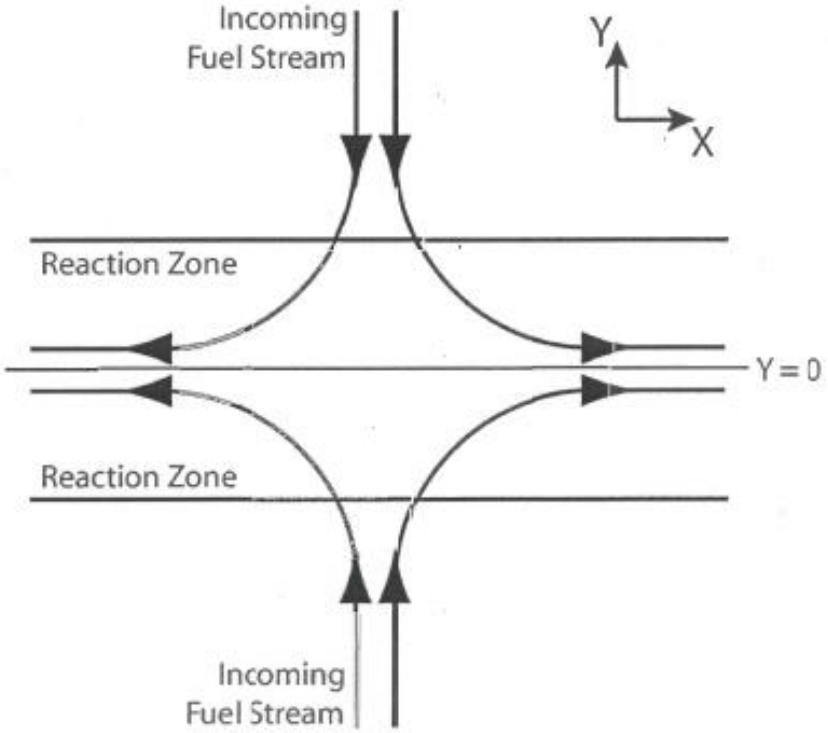

Figure 1.4: Schematic of typical twin-flame counter flow stagnation burner (Tripathi, 2012).

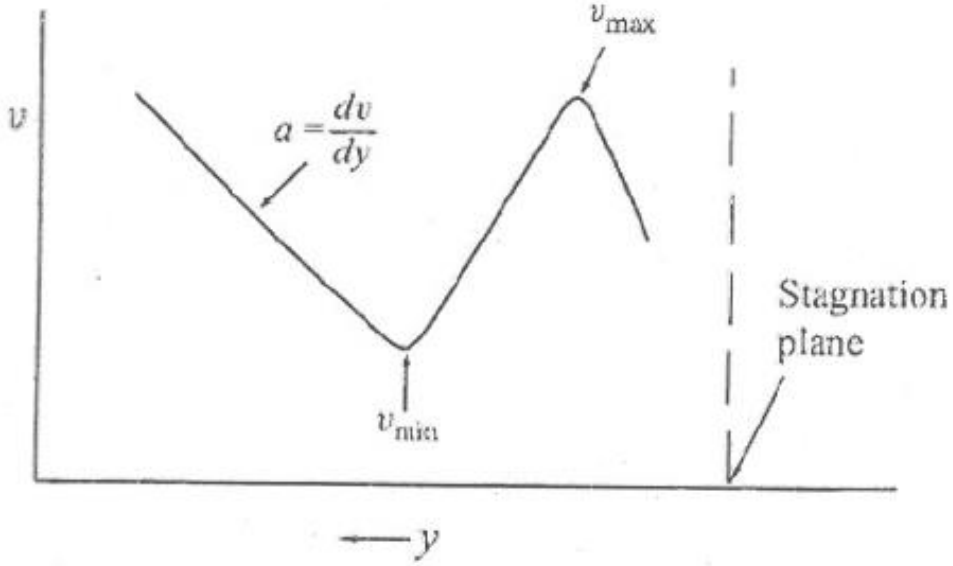

Figure 1.5: Typical axial velocity for one of the flames corresponding to Fig. 1.6 (Tripathi, 2012).

1.5.4.3 Spherical Combustion Vessels

Spherical combustion vessels containing quiescent, premixed, homogenous mixtures, when centrally ignited, typically by an electrode or laser beam, create an outwardly propagating spherical flame. A distinct advantage over flat flame burner and counter flow stagnation jet methods is the potential for u_l measurements at elevated pressures. Dependent upon the vessel design and ability for optical access, there are two techniques which are commonly used to deduce u_l.

First, the constant volume technique, this does not require optical access and u_l is deduced from the pressure trace history from each explosion. Accuracy of this technique is limited by the neglection of flame stretch and/or instability influences. Hill and Hung (1988) outlined the main assumptions: the flame is taken to be spherical, smooth and thin; with spatially uniform pressure; both unburned and burned gases conform as ideal; equilibrium of the dissociation products; compression of the unburned mixture is isentropic; and buoyancy effects are negligible.

Second, the constant pressure technique, was that used for all u_l measurements in the present work by use of the Leeds CV2, as described in Chapter 3. The technique requires optical access such that the evolution of the outwardly propagating flame front can be observed. This allows the flame morphology to be studied, such that any deviation from a spherical and smooth flame can be detected. For example, the former could arise from the buoyancy of a slow burning mixture and the latter from cellular instabilities, as discussed in Section 1.5.5. In the case of the present work, high speed digital schlieren photography, described in Chapter 3, was employed to give a definitive and measureable flame edge.

This allows for measured radii as a function of time, thus the stretched flame speed, S_n, is calculated by:

$$S_n = \frac{dr}{dt} \tag{1.8}$$

Asides the merits of visual flame morphology, further merit of the technique, particularly with large vessels, such as the Leeds CV2, results from the negligible pressure and temperature rise and boundary influence, such that, the outwardly propagating spherically flame can be assumed to be under both isobaric and adiabatic conditions, and purely a function of stretch.

For spherically expanding flames the total flame stretch rate is defined by:

$$\alpha = \frac{1}{A}\frac{dA}{dt} = \frac{1}{4\pi r^2}\frac{(8\pi r)dr}{dt} = \frac{2}{r}\frac{dr}{dt} = \frac{2}{r}S_n \qquad (1.9)$$

Bradley et al., (1996) showed the total stretch rate may be split into two separate stretch rate components, one associated with flame curvature, α_c, and the other with aerodynamic strain, α_s, hence:

$$\alpha = \alpha_c + \alpha_s \qquad (1.10)$$

The curvature stretch rate is an inevitable result of a finite flame thickness, in which the outer boundary is larger than the inner. The ratio between the outer and inner boundary at small radii is large relative to that at larger radii, thus curvature stretch rate is most dominant at smaller radii and tends to unity at larger radii to become negligible. The curvature of a flame consequently bears transverse and tangential velocity components that strain the flame, and account for the aerodynamic strain. However, the present work does not consider the separate effects of α_c and α_s, only their sum, α.

The following subsections introduce methods to decouple the effects of α on S_n, to yield the unstretched flame speed S_s, and then u_l, by accounting for the expansion of the combustion products.

1.5.4.3.1 Linear Extrapolation Methodology

In the stable regime of a flame, the Markstein theory (1964), and its later generalisation and extension Clavin (1985) neglected higher order terms and suggested a linear relationship between S_n and α, with L_b the gradient. Extrapolation of this relationship to the point of zero α, then yields a theoretical unstretched flame speed, S_s:

$$S_s - S_n = L_b\alpha \qquad (1.11)$$

This linear methodology has been employed within many combustion studies. Larger vessels with larger windows, allow for measurement of larger flame radii with reduced stretch, thus reducing the extent of extrapolation required and therefore increasing the accuracy of S_s.

Ideally, stretch rates should be as small as possible, such that the deviation from the measured S_n values to that of S_s is correspondingly small. However, this deviation can be large for flames subjected to high degrees of stretch and Lewis numbers. The Lewis number, Le, is defined by the ratio of thermal to mass diffusivity of a mixture, $Le = \alpha/D$.

In such a case flames can exhibit nonlinear behaviour between S_n and α, which this methodology does not take account of, thus, leading to erroneous over estimations of S_s.

1.5.4.3.2 Nonlinear Extrapolation Methodology

A nonlinear methodology was presented by Kelley and Law (2009) from the seminal work of Ronney and Sivashinsky (1989). It accounts for deviation from the non-adiabatic, planar and small stretch rate assumption of the linear approach for flames exhibiting nonlinear S_n and α behaviour, which are generally subjected to high degrees of stretch:

$$\left(\frac{S_n}{S_s}\right)^2 \ln\left(\frac{S_n}{S_s}\right)^2 = -2\frac{L_b \alpha}{S_s} \tag{1.12}$$

It is becoming widely accepted that the use of this nonlinear approach will reduce the over estimation error incurred by the linear approach for flames exhibiting high stretch rate behaviour. As part of the present study, all u_l measurements employed both methodologies to quantify any overestimation error associated with the linear approach and identify the influence of fuel type, pressure and ϕ.

1.5.4.3.3 Accounting for Expansion of Combustion Products

In the case of either of the above methodologies, the determination of u_l is the same, via multiplying S_s by the thermal expansion factor. As the flame is under isentropic conditions within the view of the vessel windows, the thermal expansion factor of the flame is given by the ratio of burned, ρ_b, to unburned, ρ_u, gases:

$$u_l = S_s\left(\frac{\rho_b}{\rho_u}\right) \tag{1.13}$$

In the present work, both ρ_u and ρ_b were obtained from the chemical equilibrium program, GasEq (Morley, 2005).

1.4.5 Development of Flame Instabilities

Instabilities within flame fronts have a significant influence on the burning rate of premixed laminar flames. Their form maybe characterised by cells, cracks or ridges within the flame front and their development is dependent upon L_b. Bradley et al., (1996) showed that low L_b values reduce flame stability, whilst high values increase it. With the use of schlieren photograph, Fig. 3.5, in Chapter 3 demonstrates a stable smooth flame and that of unstable flames with high cellularity for stoichiometric *iso-*

octane/air mixtures. The high cellularity serves to increase the flame front surface area, resulting in a relative increase in S_n. Figure 1.6 demonstrates this using an S_n vs. α plot for a stoichiometric *iso*-octane/air flame at 1.0 MPa, with transition to instability and flame cellularity.

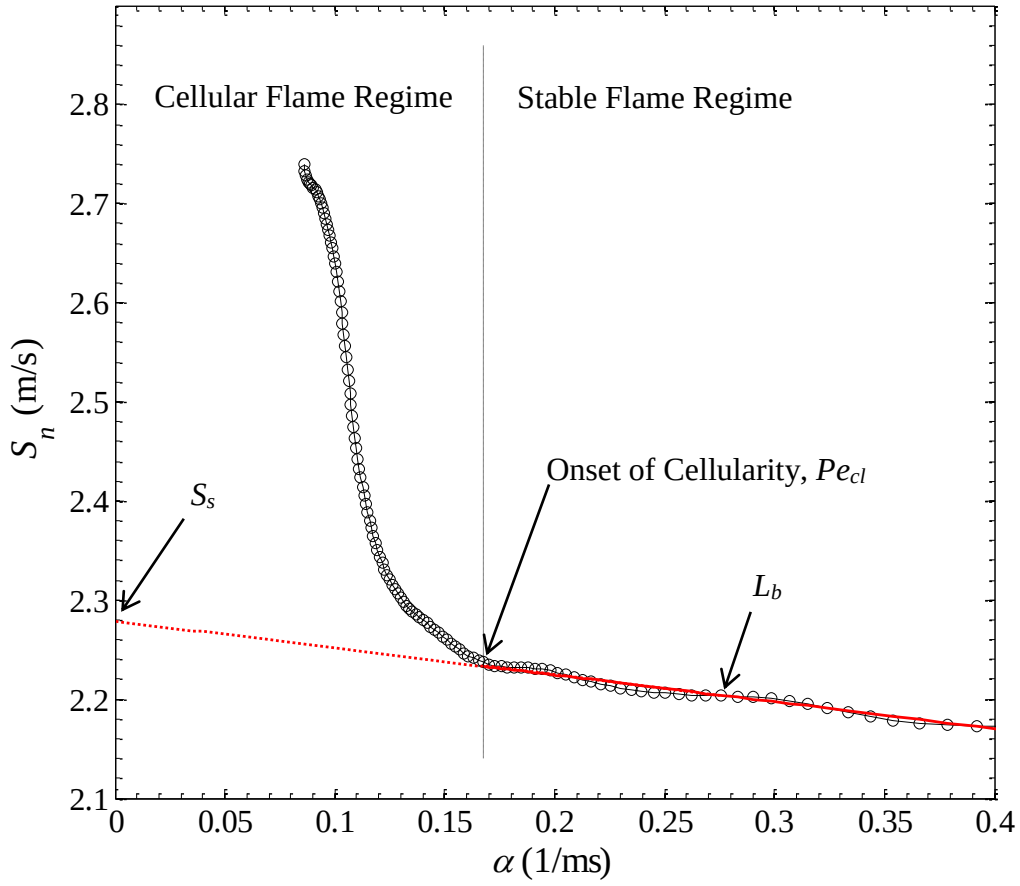

Figure 1.6: Variation of flame speed, S_n, with flame stretch rate, α, for *iso*-octane/air at 1.0 MPa, 360K and ϕ = 1.0, taken from the present work.

The point at which S_n rapidly deviates from its prior response to stretch is known as the critical radius, r_c. This is commonly defined in terms of the dimensionless critical Peclet number, Pe_{cl}, where $Pe_{cl} = r_c/\delta_l$, with δ_l the flame thickness. However, because of the importance of a necessary minimal stretch rate to stabilise a flame, a more logical stability criterion is one based on the Karlovitz stretch factor, the minimal value of which for flame stability, K_{cl} is given by (Bradley et al., 2009):

$$K_{cl} = (2\sigma/Pe_{cl})[1 + (2Ma_b/Pe_{cl})]^{-1} \qquad (1.14)$$

Beyond Pe_{cl}, the flame speed increases due to wrinkling by flame instabilities and L_b becomes meaningless. For most hydrocarbon fuels, as pressure and equivalence ratio increase, the stable regime in which L_b can accurately be measured becomes increasingly limited, between the minimum unaffected spark radius and the onset of cellularity, at the critical radius, r_c. In extreme cases, r_c can nearly occur instantaneously, hence, the measurement of L_b and u_l becomes impossible. In the present study, instabilities occurred for all pure fuel/air mixtures and their blends under elevated pressure, particularly under rich conditions, such that measurements at 1.0 MPa were limited to stoichiometric conditions.

These instabilities are indicative of the Darrieus-Landau (D-L) effect which accounts for the inevitability of hydrodynamic instability within a planar laminar flame (Darrieus, 1938; Landau, 1944). The flame is considered as a wave of density discontinuity with hydrodynamic disturbances creating the instabilities. The disturbances are a result of hot expanding products and vortices that develop within the reaction zone of the flame. Figure 1.7 shows a simplified schematic of a flame propagating at u_n. On the right side, reactants enter a convex flame front section which serves to slow their flow through divergence, however, as the burning velocity remains constant, a dynamic imbalance is induced which increases the protrusion. Similarly, on the left side, the reactants enter a concave flame front section causing a contrasting receding effect. The net result significantly deforms the overall flame surface, such that its area increases and subsequently increases the rate of reaction (Tripathi, 2012).

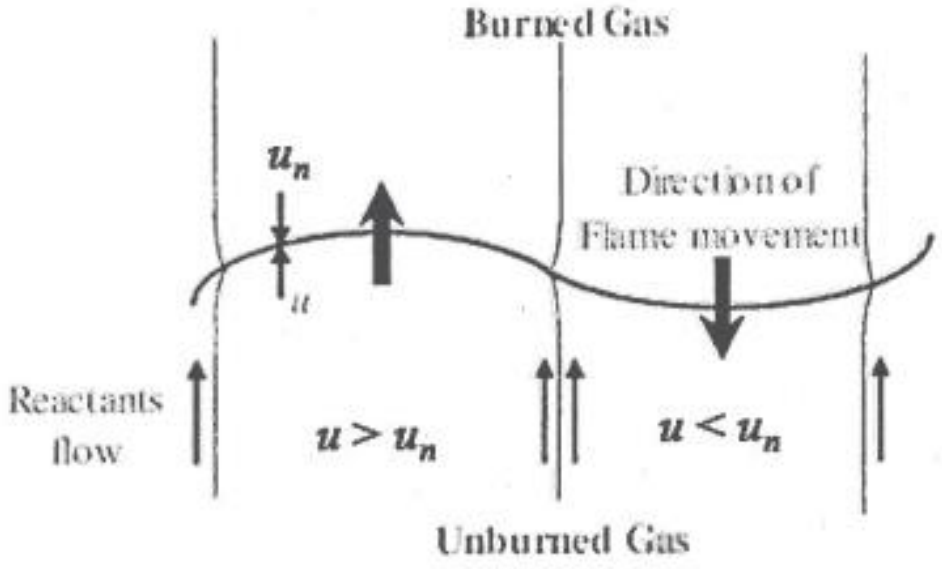

Figure 1.7: Schematic of the hydrodynamic instability mechanism (Law, 1989).

These hydrodynamic instabilities can be augmented or countered by thermal and mass diffusive mechanisms, the ratio of their fluxes being represented by the Lewis number, *Le*, which can determine whether a flame is stable or unstable. A Lewis number of less than unity implies dominance of mass diffusion, which is indicative of an unstable flame, whilst if it is greater than unity it implies dominance of thermal diffusion, which is indicative of a stable flame. Figure 1.8 illustrates a stable and unstable flame front, in the case of the unstable flame, mass diffusion dominates, as indicated by the larger arrows, such that, at the crest convergence of the flame front occurs which increase the local enthalpy and burning velocity, in contrast, at the trough, divergence to the flame front occurs which decrease local enthalpy and burning velocity. Thus, the crest propagates faster relative to the trough and increases the amplitude of the flame, which serves to destabilise it.

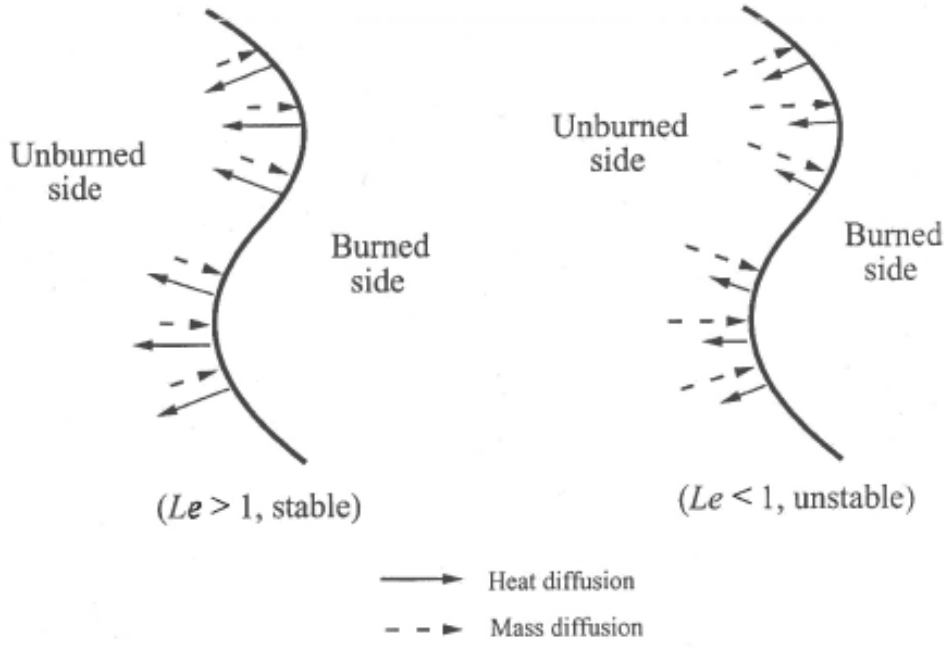

Figure 1.8: Schematic of the thermo-diffusive instability mechanism (Law, 1989).

Conversely, in the case of the stable flame, thermal diffusion dominates, such that, at the crest divergence to the unburned gas occurs, which decrease the local enthalpy and burning velocity, in contrast, at the trough, convergence to the unburned gas occurs, which increase the local enthalpy and burning velocity. Thus, a flattening effect of the wavelike profiles occurs which serves to stabilises the flame.

1.5 Autoignition and Ignition Delay Time

The phenomenon of autoignition occurs when a potentially reactive mixture of fuel and oxidiser is subjected to a sufficient magnitude of temperature, pressure and time to initiate sustained oxidisation of the fuel, via a self-heating manor. The period of time in which this happens is known as the ignition delay time. Autoignition is often assessed by this inherent property, which may be specifically defined as the duration between the time of sufficient autoignition conditions being met and the onset of actual ignition. Investigations into the ignition delay behaviour of different fuel blends play a vital role in their characterisation and mapping for optimum performance and efficiency in the modern reciprocating engines and turbines that employ them. Studies have also gained greater understanding of the potential risks and hazards associated with modern industrial processes that may lead to spontaneous combustion.

The understanding of autoignition with regards to SI engines is of great importance as its occurrence becomes a limiting factor of performance, whereby part or all the fuel/air mixture ignite independently of the timed spark ignition, typically the end gas ignites before the arrival of the spark ignited flame front. This can lead to severe pressure oscillations within the cylinder that can cause serious engine damage, a phenomenon known as knock. Fuels used in spark ignition engines are therefore designed to resist ignition under engine conditions until a spark occurs, with the octane rating dictating the extent of the fuels ability, i.e. a higher octane number gives a higher resistance to autoignition and vice versa. The actual octane number corresponds to autoignition performance relative to the ratio of *iso*-octane and heptane in a specific test engine, where *iso*-octane gives very high resistance and heptane very low, a typical octane rating of 95 would equate to 95% octane and 5% heptane. Therefore, SI engine efficiency is knock limited, as their volumetric efficiency is largely dependent upon CR, the extent of which is dictated by the intended fuels ability to resist autoignition at high pressures and temperatures, before SI.

Compression engines such as diesel engines on the other hand rely on autoignition to achieve combustion. Diesel engines compress air and then add high pressure vaporised fuel to the cylinder to initiate combustion via autoignition. This method allows much higher CR’s to be achieved hence increasing volumetric and thermal efficiency with reduced risk of autoignition. However, this is at the expense of much stronger components and slower engine response times. The cetane number is used as a measure

of diesels ignition delay and corresponds to the ignition delay time relative to the ratio of cetane and alpha-methylnapthalene in a specific test engine. Whereby a higher percentage of cetane produces shorter ignition delay times, thus a higher cetane number gives better performance as the shorter ignition delay allows more time for combustion within a cycle.

1.5.1 Determination of Ignition Delay Time

Autoignition behaviour is often characterised by the experimental measurement of the ignition delay time, τ_i. Another parameter of interest, within τ_i, is the excitation time, τ_e, this is the period of time in which the majority of heat release occurs. However, whereas τ_i is typically measured in the order of milliseconds, τ_e values are in the order of microseconds, making there accurate experimental measurement impossible due to insufficient response times achievable from dynamics pressure transducers, particularly under such high pressures and temperatures, where thermal shock becomes an issue.

There have been many measurements of τ_i for a variety of fuels and blends under different equivalence ratios, temperatures and pressures using a variety of techniques and apparatus, reference to which are given in the following subsections for three of the most common experimental techniques.

The complex flow fields within engines and turbines serve to obscure τ_i measurements, therefore a common theme amongst typical τ_i measuring apparatus is to negate such effects by simplification of the environment in which it is measured. Three common techniques are introduced below: Flow reactors, shock-tubes and that used in the present work, rapid compression machines. Figure 1.9 shows their typical operational boundaries.

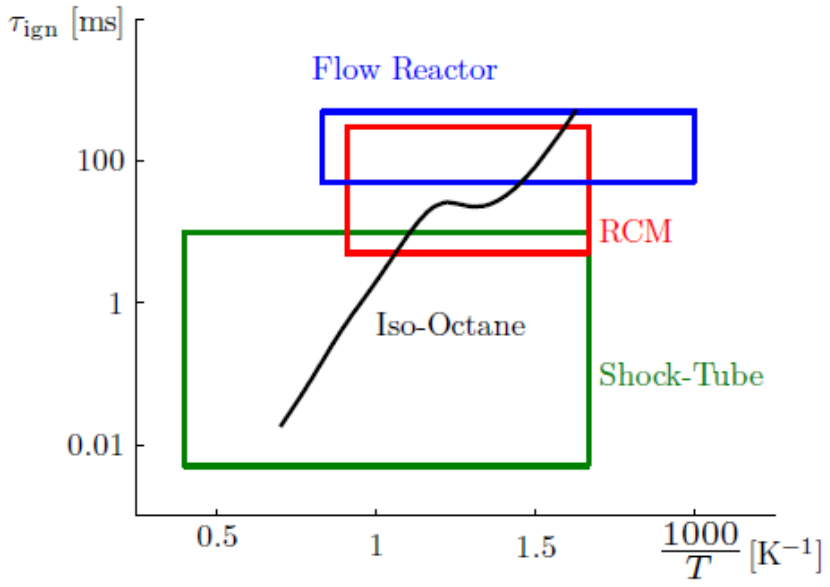

Figure 1.9: Typical operational boundaries of shock-tubes, rapid compression machines, and flow reactors. A comparison to a representative ignition delay curve of *iso*-octane is included; ignition delay of *iso*-octane is obtained from the reduced mechanism of Pepiot-Desjardins and Pitsch (2008) at an equivalence ratio of 0.6 and a pressure of 2.0MPa (Grogan et al., 2015).

1.5.1.1 Flow Reactors

Flow reactors have been successfully employed in the measurement of τ_i values for many years, with Mullins (1951), Lezberg (1957) Chang et al., (1958) and Miller (1958) acquiring some of the earliest data. Figure 1.10 shows a schematic of typical flow reactor. Essentially, they comprise of a cylinder duct in which a preheated turbulent oxidiser (usually air) flow mixes with fuel that is usually radially injected, slightly downstream, this creates a homogeneous premixed combustible mixture, and under the heat and pressure of the flow, ignition of the combustible mixture occurs sometime further downstream.

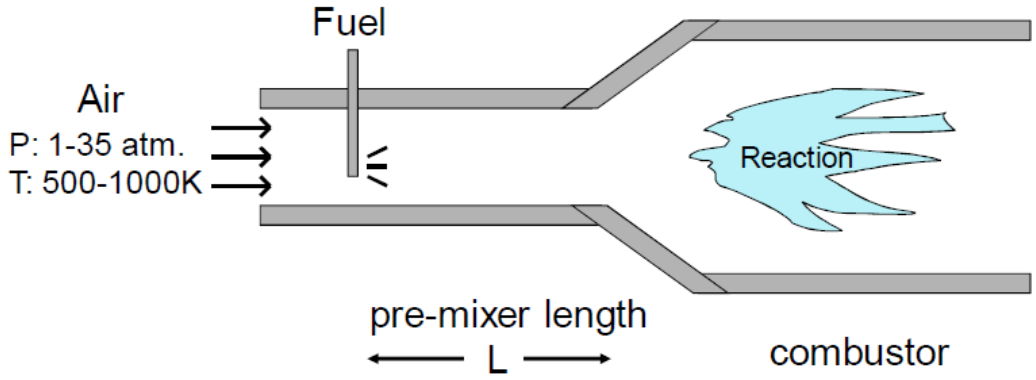

Figure 1.10: Schematic of a typical flow reactor (Beerer et al., 2009).

The measurement of τ_i is defined between the point at which the fuel and oxidiser are sufficiently mixed and the point at which ignition occurs, which is usually detected by light emission or a pressure spike. Heating is usually limited to 1000K and most systems operate in the range of 0.1-3.0 MPa. Using optical access, Beerer et al., (2009) employ a laser/photo-detector system to accurately detect the premixed charge just after the fuel is injected and photodiodes to detect luminescence at the onset of combustion. Fig. 1.11 shows a typical measurement of τ_i for a methane/air mixture using this setup.

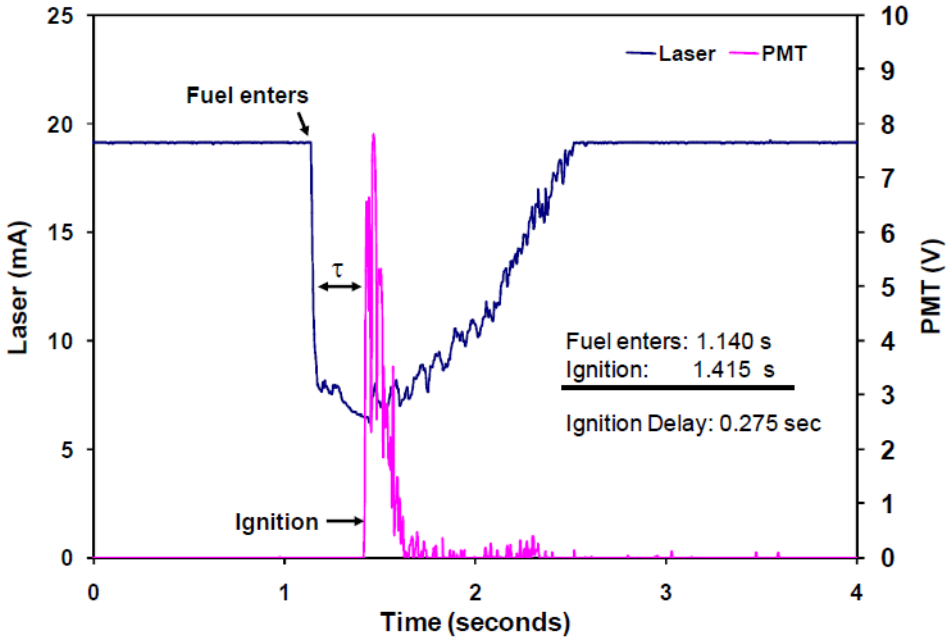

Figure 1.11: Measurement of τ_i for methane/air mixture using laser detection for entering mixture and photodiode detection for luminous from onset of combustion (Beerer et al., 2009).

1.5.1.2 Shock Tubes

Shock tubes are generally used in the measurement of relatively short τ_i values under the high temperatures (Campbell et al., 2015; Davidson et al., 2005; Hawthorn and Nixon, 1966; Zhu et al., 2015). Figure 1.12 shows an operational schematic of a typical shock tube. They comprise of a length cylindrical duct in which an inert high pressure driving gas is separated from a relatively low pressure combustible test mixture via a thin diaphragm. Depending on the pressure ratio between the two gases, this is typically made from aluminium, copper or steel. Upon rupturing the diaphragm, usually by means of an electronically operated needle, a shock wave is generated by the high pressure driving gas as it enters the low pressure mixture zone. This shock wave, known as the incident shock wave, compresses the mixture up to a high autoignition pressure

and temperature to allow ignition to take place, with a reflective shock wave returning down the duct.

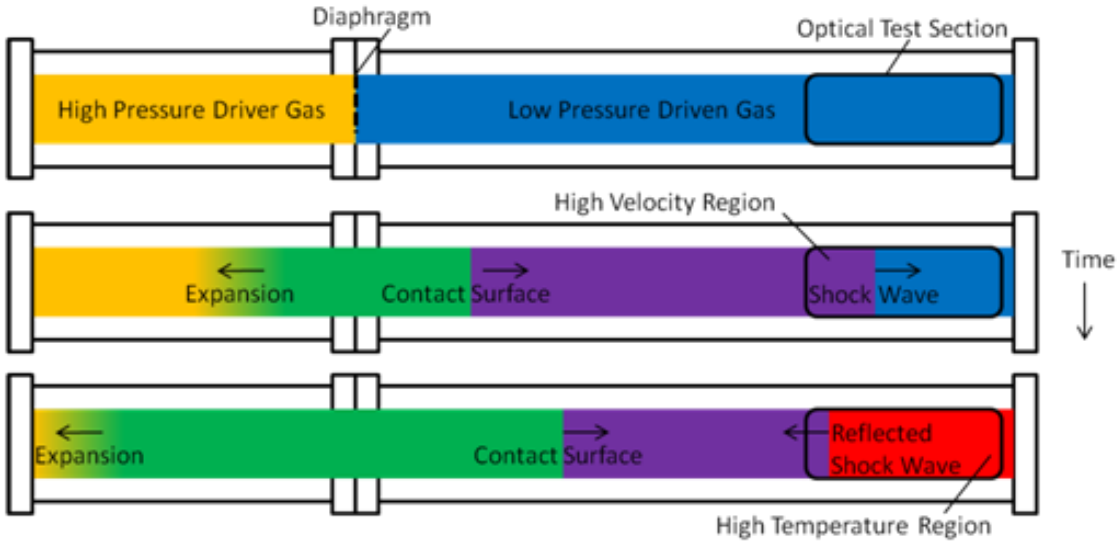

Figure 1.12: Schematic of a typical shock (http://www.ucalgary.ca/johansen/node/7.)

As indicated by the number five in Fig. 1.13 measurements of τ_i values are limited by the time between the point at which the incident shock wave compresses the mixture to sufficient pressure and temperature within the test zone and the return of the reflective shockwave, which is a function of the contact surface between that of the inert driving gas and the test mixture. Thus, only measurements of τ_i values shorter than this duration are possible and are typically within the range 1-3ms.

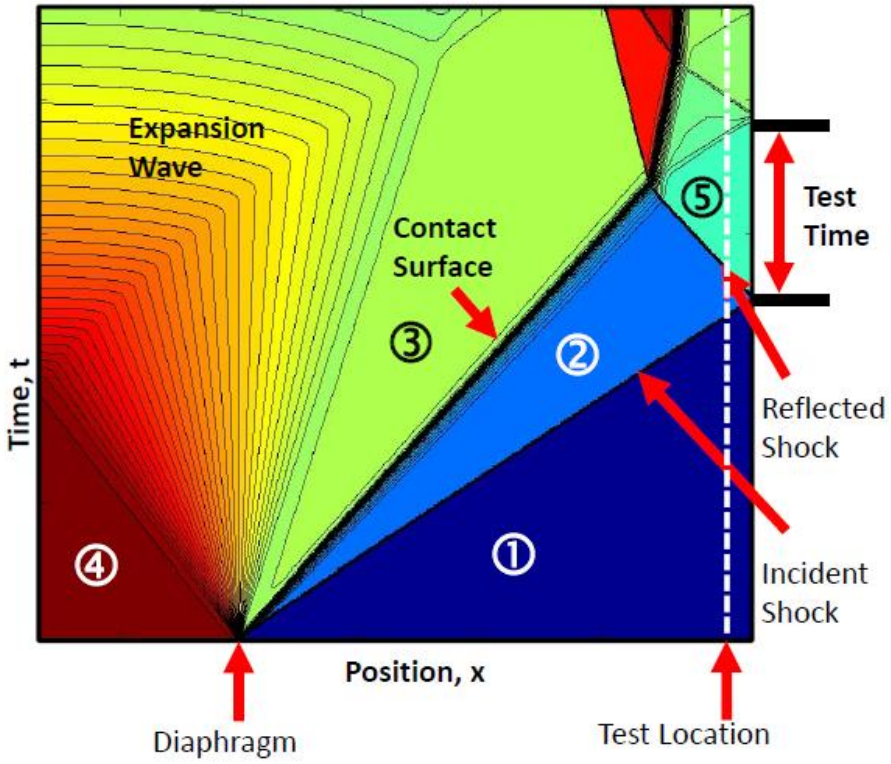

Figure 1.13: Wave system in the shock tube (Campbell et al., 2015).

However, recent developments have successfully increased this range by methods such as specifically tailored driving gases and extended driving gas sections, this has shown to increase the distance between the shock wave and the driving gas contact surface, resulting in increased times up to 55ms (Campbell et al., 2015).

1.5.1.3 Rapid Compression Machines

Many τ_i values for a variety of fuels over an array of conditions have been measured using rapid compression machines (Affleck and Thomas, 1968; Griffiths et al., 1993; Grogan et al., 2015; Mittal et al., 2014). They have since undergone much refinement with advances in technology allowing for higher pressures and temperatures to be achieved, typically in the region of 2.0-4.0 MPa and 900-1500K, and are responsible for a vast array of τ_i measurements for a large variety of fuels. Regardless of different operating mechanisms, a common theme to all RCM's is the simplistic nature of rapidly compressing a premixed combustible mixture within a cylinder via a piston to a constant end of compression (EOC) volume. The compression increases the mixture pressure and temperature to autoignition conditions at EOC, and a pressure spike indicates the onset of ignition.

The value of τ_i is generally defined as the duration between the EOC and the point of the maximum rate of pressure rise (Griffiths and Nimmo, 1985; Mittal, 2006; Westbrook et al., 1998). Rapid compression is essential to reduce the likelihood of any pre-reactions during the pressure and temperature rise of compression. RCM's are generally well suited to the measurement of longer τ_i values due to their ability to hold the required autoignition EOC pressures and temperatures for relatively long periods, typically over 100ms, which is typically two fold that of shock tubes (Mittal and Bhari, 2013).

1.6 Aims and Objectives

An increased array of alternative fuels has subsequently led to an increased number of potential fuel blends. Developing understanding of different fuel blends behaviour relative to their constituents, particularly, key combustion parameters, u_l and τ_i, under different operational conditions is imperative within commercial fuel blending, to ensure blends are not only effective, but optimised for their intended conditions. Thus, the ability to accurately predict such parameters for different blends, regardless of their constituent chemical families is highly desirable.

The present work aims to investigate the u_l and associated Markstein length, L_b, behaviour of blends, relative to their constituents, which are representative of the major chemical families found within FT synthetic gasoline, and promising bio-alcohols, as a function of pressure and equivalence ratio. Thus, facilitating the development of universal predictive u_l and L_b blending laws.

Furthermore, the present work aims to revise the well-established Leeds CV2 auxiliary systems and operations, in the quest for higher fidelity u_l measurements, and aid the commissioning of an RCM, to allow the concurrent collection of τ_i data by M. Materego (2015) for fuels and blends also studied by the author in the Leeds CV2.

Subsequently, the objectives of the present work may be summarised as follows:

- Aid the commissioning of an RCM to achieve SI engine like pressures and temperatures in the region of 2.5 MPa and 1000K, and the accurate acquisition of τ_i values for premixed fuel/air mixtures, as studied in the Leeds CV2.
- Upgrade the Leeds CV2 auxiliary systems to attain higher accuracy u_l and Markstein length, L_b, data acquisition. Investigating the heating system and the internal gas temperature uniformity, as a function of initial pressure and temperature.

- Perform measurements of u_l and L_b for pure fuels representative of the major fuel groups used within commercial FT synthetic gasoline and their binary equimolar blends, across ϕ = 0.8-1.3 for initial pressures of 0.1, 0.5 and 1.0 MPa. Thus, allowing examination of blend behaviour relative to their constituents and the influence of pressure and equivalence ratio.
- Perform measurements of u_l and L_b for a high octane gasoline surrogate and the comparative effect of ethanol and *n*-butanol addition, across the same conditions as above - Forming part of a joint study with M. Materego (2015) measuring the corresponding τ_i behaviour for the same blends.
- Investigate flame speed/stretch rate behaviour, and the effect of using linear and nonlinear extrapolation methodologies, and correlations between critical Peclet and Karlovitz numbers with Markstein numbers, as a function of pressure and equivalence ratio, for all measured constituent fuel/air mixtures and their blends.
- Develop u_l and L_b predictive blending laws, for chemically dissimilar fuels, including, multicomponent fuel blends, in which constituents may themselves be blends, thus on a 'blends of blends' basis of significant relevance to commercial fuel blending.
- Analyse predictive performance of existing and any proposed u_l and L_b blending laws, using data from the aforementioned binary blends, multicomponent gasoline surrogate/alcohol blends, and methane and hydrogen blends from other researchers.

1.7 Thesis Structure

- Chapter 2 reviews u_l analytical approaches, which serve as foundations to many u_l blending laws. Furthermore, a review of blending relations and stoichiometry is given, and existing and proposed u_l and L_b blending laws are presented.
- Chapter 3 describes the experimental apparatus, operating techniques and data processing involved to acquire u_l and L_b for premixed fuel/air mixtures at elevated pressure and temperature. Verification of an array of upgrades to the Leeds CV2 and auxiliary systems are made, alongside, significant refinements to the previous operating techniques and data processing protocols.
- Chapter 4 presents a substantial range of experimentally measured u_l and L_b data for both liquid and gaseous fuel/air mixtures and their blends, over a wide equivalence ratio range at both elevated pressures and temperatures. The liquid

fuel/air mixtures are categorised into three groups: pure fuel constituents, binary equimolar blends, and TRF/Alcohol blends. The gaseous fuel/air mixtures are exclusively methane, hydrogen and their blends.

- Chapter 5 presents discussions based on the measured data presented in Chapter 4. These include:
    i. An assessment of linear and nonlinear extrapolation methodologies in deducing u_l from S_n/α plots.
    ii. Observed correlations between the critical Peclet and Karlovitz numbers with Markstein numbers.
    iii. Comparisons to existing u_l and L_b data.
    iv. The comparative effects of ethanol and *n*-butanol addition to a TRF gasoline surrogate blend, in terms of u_l, L_b and τ_i.
    v. The influence of hydrogen addition to premixed methane/air mixtures energy flux.
- Chapter 6 presents the predictive performance of each u_l and L_b blending law as presented in Chapter 2, for all blends presented in Chapter 4, with an overall evaluation of the most successful law.
- Chapter 7 concludes the main discussions and findings, and makes recommendations for further work.
- Appendix A presents the performance league tables for each blending law examined, for all blends studied.
- Appendix B presents technical details on the commissioning of the Leeds RCM.
- Appendix C presents stress calculations for the RCM fuel/air mixing chamber.

Chapter 2 - Review of Laminar Burning Velocity Analytical Approaches and Blending Laws

2.1 Introduction

Since the 1960's advances in digital computing have allowed significant progress in the development of fully detailed chemical kinetic modelling of laminar flame reactions and laminar burning velocity. Such models are exemplified in programs such as CHEMKIN, which enables a range of burning velocities to be computed over a range of conditions. However, blends of different pure fuels, as with real commercial fuels, particularly when of dissimilar nature, can result in significantly more complex chemistry, not always fully understood, and thus not accurately modelled. Consequently, relatively simple blending laws for the prediction of the unstretched laminar burning velocity, u_l, and other parameters such as the associated burnt gas Markstein length, L_b, of blends of the constituent mixtures, which may themselves be blends, are invaluable. This is particularly so with the present availability of ranges of petroleum, Fischer-Tropsch, and bio-fuels (Broustail et al., 2011; van Lipzig et al., 2011). Such laws are typically based on traditional analytical approaches utilising various thermodynamic parameters. They usually assume a linear relationship between properties of constituent mixtures and their blends. This Chapter introduces the analytical foundations of u_l blending laws in Section 2.2. Section 2.3 introduces the blending and stoichiometric relationships. Section 2.4 reviews existing and presents a proposed u_l blending law, and finally, Section 2.5 presents proposed blending laws for L_b.

2.2 Analytical Approaches to Laminar Burning Velocity

Prominent analytical expressions for laminar burning velocity are reviewed in the following subsections.

2.2.1 Spalding Expressions for Laminar Burning Velocity

A useful starting point is the analytical expression for the laminar burning velocity, u_l, derived by Spalding (1957a, b) for a flat, one dimensional, premixed flame. This followed earlier pioneering work by Zeldovich and Frank-Kamenetskii, ZF-K (1938). The flame equations with molecular diffusion of reactants and thermal conduction,

together with a temperature explicit reaction rate, and the energy and mass conservation equations yielded the expression (Spalding, 1957a):

$$u_l = \left[\frac{1}{\lambda} \frac{k_u \int_0^1 R(c)dc}{(T_b - T_u)\bar{c}_p^2 \rho_u^2} \right]^{0.5}, \qquad (2.1)$$

where u_l is the laminar burning velocity, k_u the thermal conductivity of unburned gas, T_b the adiabatic burned gas temperature, T_u the initial temperature, $\bar{c}_p$ the mean specific heat and ρ_u is the density of unburned gas. The progress of the reaction at a temperature, T, is indicated by a reaction progress variable, *c*, given by $\frac{T - T_u}{T_b - T_u}$. $\int_0^1 R(c)dc$ is the heat release rate source term integrated over the reaction, in which $R(c) = (k/k_u)H\dot{m}$, where, *H* is the heat of reaction of the fuel, $\dot{m}$ its mass volumetric rate of burning. λ is a burning velocity eigenvalue with $\lambda = k_u \bar{R}/(T_b - T_u)c_p^2 G$, where k_u is unburned thermal conductivity, $\bar{R}$ the area under the $R(c)$ curve and *G* the mass flow rate per unit area.

Equation 2.1 assumes a Lewis number, $Le = k/\rho C_p D$, of unity, where *D* is the diffusion coefficient of the deficient reactant. Spalding (1957a) employs a parameter δ, which is Le^{-1}, in which normal diffusion is characterised by $\delta = 1$. If the deficient reactant is of low molecular mass, δ is greater than unity. If it is of high molecular mass, δ is less than unity. Spalding (1957a) shows how Eq. 2.1 is modified by a non–unity δ. A large δ increases λ and subsequently decreases u_l. The value of λ was related to the centroid of the heat release rate versus reaction progress variable profiles. By considering various profiles numerically he derived an empirical expression for λ, in which,

$$\lambda = \frac{1}{2} - 0.6604(1 - c_c) - 0.4283(1 - c_c)^2. \qquad (2.2)$$

Here c_c is the value of c at the centroid of the area under the heat release rate curve, given by:

$$c_c = \frac{\int_0^1 c\, R(c) dc}{\int_0^1 R(c) dc}. \qquad (2.3)$$

Because of the influence of the profile of the heat release rate against c, it is instructive to study profiles for different mixtures, computed by detailed chemical kinetics. Shown in Fig. 2.1, taken from Bradley et al (1991), are some numerically computed heat release rates q/q_{max}, namely $H\dot{m}$ normalised by its maximum value, plotted against c, which is θ in the original figure. The profiles for H_2 and CH_4 are in sharp contrast: that for H_2 peaks at a lower value of c than those for CH_4 and CH_3OH. Clearly, c_c is smaller for the H_2 mixture, and λ also will be smaller.

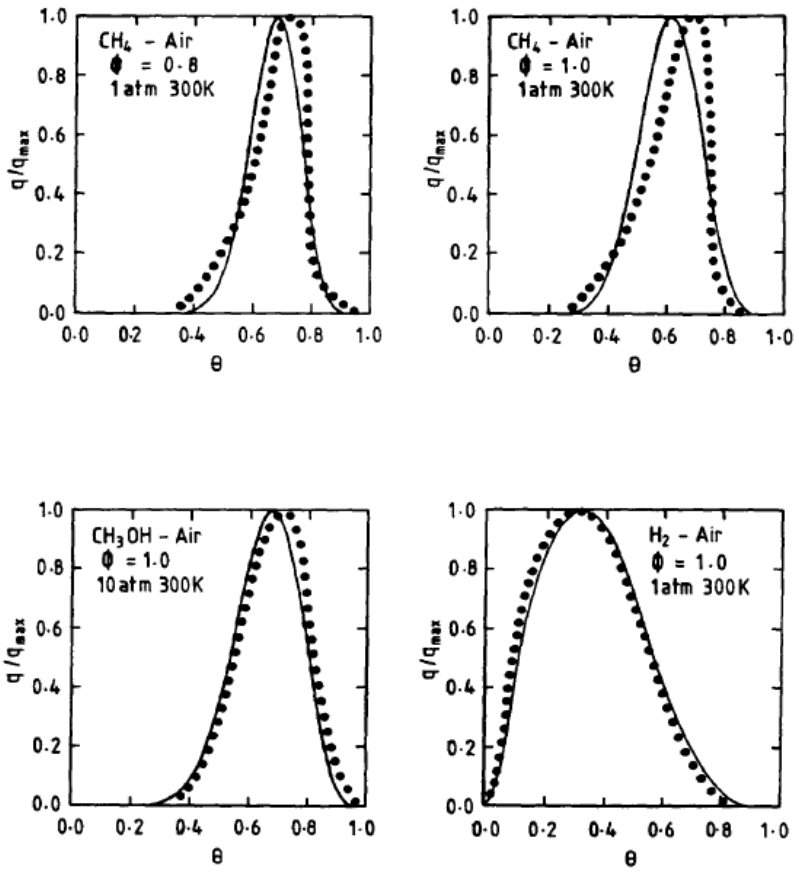

Figure 2.1: Computed heat release profiles for different CH4, CH3OH, H2 + air mixtures at initial temperatures and pressures of 300K and 0.1 MPa respectively. The full line curves are indicative of computations and the dotted of fitted algebraic expressions, where θ = *c*. (Bradley et al., 1991).

A heat release rate that is weighted towards lower values of c will on this count, give, from Eq. 2.1, a higher value of u_l. In Fig. 2.2, Bradley et al (1991), shows the variation of centroid position and heat release rate integral with the product Qu_l for different fuel/air mixtures.

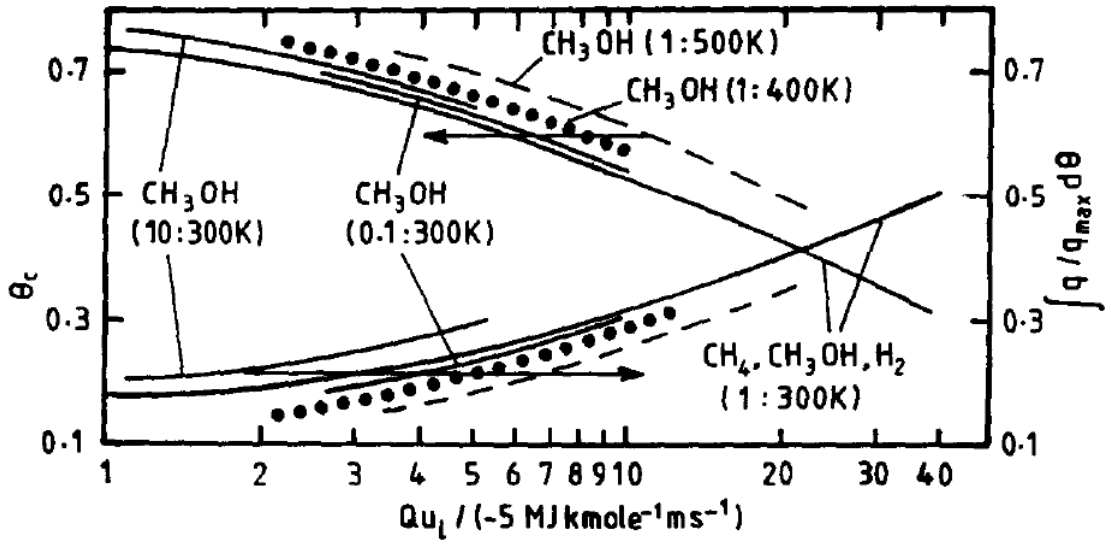

Figure 2.2: Variation of centroid position and heat release rate integral with the product Qu_l for different fuel/air mixtures. Initial temperatures and pressures are shown in bracket (Bradley et al., 1991).

2.2.2 Zel'dovich and Frank-Kamenetskii Approximations

The chemical reaction rates that generate $q = \dot{m}H$ are complex. Globally, they might be expressed by a term representing reactant concentrations and a rate constant, an Arrhenius "A" value multiplied by an exponential terms, $\exp(-E/RT)$, in which E is a global activation energy and E/R an activation temperature, T_a , with R the ideal gas constant. In practice, reactants are consumed and eventually, at c = 1.0, q = 0. However, the fall in concentration of the reactant is countered in the Arrhenius term by the increase in T. ZF-K (1938) showed that, if all the heat release occurred at c = 1 then, c_c = 1.0 and λ = 0.5. This follows from Eq. 2.2, which gives c_c = 1.0. If $S(c)$ represents the product of concentrations, Arrhenius "A" values, heat of reaction, k/k_u , and any effect of non-unity Le, then

$$R(c) = S(c)\exp(-E/RT). \qquad (2.4)$$

Hence,

$$\int_0^1 R(c)dc = \int_0^1 S(c)\exp(-E/RT)dc. \tag{2.5}$$

Now,

$$dc/dT = (T_b - T_u)^{-1}, \tag{2.6}$$

and,

$$\int_0^1 R(c)dc = \int_0^1 S(c)\exp(-E/RT)(T_b - T_u)^{-1}dT \tag{2.7}$$

with,

$$\frac{d\exp(-E/RT)}{dT} = \frac{E}{RT^2}\exp(-E/RT), \tag{2.8}$$

therefore,

$$\int_0^1 R(c)dc = \int_0^1 S(c)\left[\frac{E}{RT^2}(T_b - T_u)\right]^{-1} d\exp(-E/RT) \tag{2.9}$$

.

With the ZF-K high activation energy, asymptotic, assumption that all the heat release occurs at T_b.

$$\begin{aligned}\int_0^1 R(c)dc &= S(1)\left[\frac{E(T_b - T_u)}{RT_b^2}\right]^{-1} d\exp(-E/RT)\\ &= S(1)\left[\frac{E(T_b - T_u)}{RT_b^2}\right]^{-1}\exp(-E/RT_b).\end{aligned} \tag{2.10}$$

The value of *E/R* is the activation temperature, T_a and β is the Zel'dovich number, given by the square bracketed term in Eq. 2.10, so that

$$\beta = (T_a/T_b^2)(T_b - T_u). \tag{2.11}$$

The value of $S(1)\exp(-E/RT_b)$ represents the maximum volumetric heat release rate, $q_{\max}$, and consequently, bearing in mind $R(c) = (k/k_u)H\dot{m}$,

$$\int_0^1 R(c)dc = (k/k_u)q_{\max}/\beta. \tag{2.12}$$

In Eq. (2.1), with c_c = 1 and λ = 0.5:

$$u_l = \left[\frac{2k_u q_{\max}}{\beta(T_b - T_u)\bar{c}_p^2 \rho_u^2}\right]^{0.5}. \tag{2.13}$$

The expressions from ZF-K (1938) and Semenov (1942) assume Le = 1 and all the heat release to occur at T_b. This is more valid at high T_a/T_b and β, but the computed heat release rate profiles in Fig. 2.1 show the assumptions limitations. This approach was, however, a significant advance on the earlier simplified one of Mallard and Chatelier (1883), which neglected molecular transport. Kuo (2005) presents extensions to Eq. 2.13 that allow for a greater variety of conditions, such as differences in Le, order of reaction and mole densities of reactants, n_r, and products, n_p. For a first-order reaction he gives:

$$u_l = \sqrt{\frac{2k_b c_{pb} A}{\rho_u \bar{c}_p^2}\left(\frac{T_u}{T_b}\right)\left(\frac{n_r}{n_p}\right)\frac{Le}{\beta^2}\exp(-E/RT_b)}, \tag{2.14}$$

where *A* is the Arrhenius factor. For a second-order reaction he gives:

$$u_l = \sqrt{\frac{2k_b (c_{pb})^2 A a_0}{\rho_u \bar{c}_p^3}\left(\frac{T_u}{T_b}\right)\left(\frac{n_r}{n_p}\right)^2\frac{Le^2}{\beta^3}\exp(-E/RT_b)}, \tag{2.15}$$

with a_0 the number of molecules of reactant per unit volume.

2.2.3 Activation Temperature influence on Laminar Burning Velocity

With $q_{\max} = S(1)\exp(-T_a/T_b)$ for the ZF-K assumptions, together with Eq. 2.13,

$$u_l \rho_u = \left[\frac{2k_m S(1)\exp(-T_a/T_b)}{\beta(T_b - T_u)\bar{c}_p^2}\right]^{1/2}, \tag{2.16}$$

therefore,

$$u_l\rho_u = \exp\left(-T_a/2T_b\right)\exp\ln\left(\frac{2k_m S(1)}{\beta\left(T_b-T_u\right)\bar{c}_p^2}\right)^{1/2},$$

and,

$$u_l\rho_u = \exp-\left[\left(T_a/2T_b\right)-\ln\left(\frac{2k_m S(1)}{\beta\left(T_b-T_u\right)\bar{c}_p^2}\right)^{1/2}\right].$$

Let,

$$T_{al} = T_a - 2T_b\ln\left(\frac{2k_m S(1)}{\beta\left(T_b-T_u\right)\bar{c}_p^2}\right)^{1/2}. \tag{2.17}$$

Therefore,

$$u_l\rho_u = \exp\left(-T_{al}/2T_b\right). \tag{2.18}$$

Here T_{al} is an activation temperature for the laminar burning mass flux. However, it is clear that T_{al} is dependent upon pressure, P, Lewis number, Le, and temperature change, $\Delta T = \left(T_b - T_u\right)$ and, in practice, the variation of q with c. It follows from Eq. 2.18 that,

$$2\ln u_l\rho_u = -T_{al}/T_b, \tag{2.19}$$

and,

$$\frac{d\,2\ln u_l\rho_u}{d\,1/T_b} = -T_{al}, \tag{2.20}$$

This is a frequently used expression in asymptotic analyses (Peters and Williams, 1987) and (Bradley et al., 1998b).

2.3 Blending Relationships and Stoichiometry

The composition of a blend may be expressed in a number of formats, and often by the fractional concentration of each constituent within the blend. Concentrations can be in terms of the fuel and air mole fraction of each constituent within the total moles of the blend, or by the fuel mole fraction of each constituent within the total fuel moles of the

blend. Alternatively, mass fractions may be used. Commercially, for practicality, blends are usually expressed in terms of the fuel volume fraction of each constituent within the total fuel volume of the blend. A clear understanding of such relations and blend stoichiometry is paramount when assessing any blending law, and consequently a generalised overview is presented of the constituent relations within a blend.

A generalised reaction for each pure constituent fuel is given by:

$$\mathrm{C}_x\mathrm{H}_y\mathrm{O}_Z + a(0.21\mathrm{O}_2 + 0.79\mathrm{N}_2) \rightarrow x\mathrm{CO}_2 + \left(\frac{y}{2}\right)\mathrm{H}_2\mathrm{O} + 0.79\mathrm{N}_2 \quad (2.21)$$

Where *a* denotes the number of air moles per mole of fuel, thus balancing Eq. 2.21 gives:

$$a = x + \frac{y}{4} - \frac{z}{2} \quad (2.22)$$

Let subscript *s* denote stoichiometric conditions. If *f* represents the number of fuel moles, the equivalence ratio maybe expressed as:

$$\phi = \frac{f/a}{(f/a)_s}, \qquad \therefore\ a = \frac{f/\phi}{(f/a)_s}, \quad (2.23)$$

to give:

$$f + a = f + \frac{f/\phi}{(f/a)_s} \quad (2.24)$$

Thus, one mole of a fuel and air mixture compromises of:

$$\left[\frac{f}{f + (f/\phi)/(f/a)_s}\right]_{fuel} + \left[\frac{(f/\phi)/(f/a)_s}{f + (f/\phi)/(f/a)_s}\right]_{air} = 1 \quad (2.25)$$

Which may be simplified to:

$$\left[\frac{\phi}{\phi + (a/f)_s}\right]_{fuel} + \left[\frac{(a/f)_s}{\phi + (a/f)_s}\right]_{air} = 1 \quad (2.26)$$

Generalised blend expressions are now given to demonstrate how the proportion of each constituent within a blend is calculated, in terms of the five aforementioned units of measurement: moles of fuel and air, moles of fuel, mass of fuel and air, mass of fuel, and liquid volume of fuel.

First, consider one mole of a binary blend, where $\bar{x}_i$ denotes the fuel and air mole fraction of the *i'*th constituent within the total moles of the blend. (e.g. $\bar{x}_1 + \bar{x}_2 = 1$).

This may be expressed by:

$$\sum_{i=1}^{n} \left\{ \left[\frac{\phi}{\phi + (a/f)_s} \right]_{fuel} + \left[\frac{(a/f)_s}{\phi + (a/f)_s} \right]_{air} \right\}_i \bar{x}_i \tag{2.27}$$

Therefore, $\bar{x}_i$is given by:

$$\bar{x}_i = \frac{\left\{ \left[\frac{\phi}{\phi + (a/f)_s} \right]_{fuel} + \left[\frac{(a/f)_s}{\phi + (a/f)_s} \right]_{air} \right\}_i}{\left\{ \sum_{i=1}^{n} \left\{ \left[\frac{\phi}{\phi + (a/f)_s} \right]_{fuel} + \left[\frac{(a/f)_s}{\phi + (a/f)_s} \right]_{air} \right\}_i \right\}^{-1}} \tag{2.28}$$

For blends considered in terms of solely their fuel moles, as is the case with CH_4 and H_2 blends studied in forth coming Chapters, the fuel mole fraction of the *i'*th constituent within the total fuel moles of the blend is expressed by, $\bar{x}_{f,i}$:

$$\bar{x}_{f,i} = \left[\frac{\phi \bar{x}}{\phi + (a/f)_s} \right]_{fuel\ i} \left\{ \sum_{i=1}^{n} \left[\frac{\phi \bar{x}}{\phi + (a/f)_s} \right]_{fuel\ i} \right\}^{-1} \tag{2.29}$$

Mass based equivalents of Eq. 2.28 and 2.29 are simply calculated by applying the following relationship:

$$m = nM_w \tag{2.30}$$

Thus, the fuel and air mass fraction of the *i'*th constituent within the total mass of the blend is given by, x_i:

$$x_i = \frac{\left\{ \left[\frac{\phi M_f}{\phi + (a/f)_s} \right]_{fuel} + \left[\frac{(a/f)_s M_a}{\phi + (a/f)_s} \right]_{air} \right\}_i \bar{x}_i}{\left\{ \sum_{i=1}^{n} \left\{ \left[\frac{\phi M_f}{\phi + (a/f)_s} \right]_{fuel} + \left[\frac{(a/f)_s M_a}{\phi + (a/f)_s} \right]_{air} \right\}_i \bar{x}_i \right\}^{-1}} \tag{2.31}$$

Where, M_f and M_a denote the molecular mass of fuel and air respectively. And, the fuel mass fraction of the *i'*th constituent within the total fuel mass of the blend is given by, $x_{f,i}$:

$$x_{f,i} = \left[\frac{\phi M_f \bar{x}}{\phi + (a/f)_s}\right]_{fuel,i} \left\{\sum_{i=1}^{n} \left[\frac{\phi M_f \bar{x}}{\phi + (a/f)_s}\right]_{fuel,i}\right\}^{-1} \quad (2.32)$$

Commercially, liquid fuels are usually blended by volume for practicality, as is the case with the TRF and alcohol blends studied in forth coming Chapters. The liquid volume of a fuel is related to the number of moles, *n*, and mass by:

$$V = \frac{m}{\rho} = \frac{nM_f}{\rho} \quad (2.33)$$

Where, ρ denotes the liquid fuel density at 298K. Thus, the fuel liquid volume fraction of the *i'*th constituent within the total fuel liquid volume of the blend is found by, $x_{v,i}$:

$$x_{v,i} = \left[\frac{\phi M_f \bar{x}}{\phi + (a/f)_s \rho_f}\right]_{fuel,i} \left\{\sum_{i=1}^{n} \left[\frac{\phi M_f \bar{x}}{\phi + (a/f)_s \rho_f}\right]_{fuel,i}\right\}^{-1} \quad (2.34)$$

The corresponding fuel liquid volume percentage of the *i'*th constituent can then simply be found by, $LV\%_i$:

$$LV\%_i = 100 x_{v,i} \quad (2.35)$$

2.4 Laminar Burning Velocity Blending Laws

This Section presents the existing and proposed u_l blending laws. As discussed in Section 2.3, the fractional amounts of each constituent within a blend can be expressed in terms of moles of fuel and air, moles of fuel, mass of fuel and air, mass of fuel, and liquid volume of fuel. The following blending laws often make use of such fractional concentrations as weighting factors against various other parameters. Table 2.1 summarises these different weighting factors and symbols:

Weighting by Fractional Concentration of:	Corresponding Equation	Symbol
(Fuel + Air Moles)/Total Moles	Eq. 2.28	$\bar{x}$
Fuel Moles/Total Fuel Moles	Eq. 2.29	$\bar{x}_f$
(Fuel + Air Mass)/Total Mass	Eq. 2.31	x
Fuel Mass/Total Fuel Mass	Eq. 2.32	x_f
Fuel Liquid Volume/Total Fuel Liquid Volume	Eq. 2.34	x_v

Table 2.1: Assigned symbols for the different weighting factors used in the forthcoming blending laws.

In all cases, subscripts *i* and *bl* denote the *i*'th constituent and blend. Throughout this thesis the constituent fuel/air mixtures that constitute a blend have the same ϕ.

2.4.1 Mole Blending Law of Payman and Wheeler

Perhaps the most rudimentary of blending laws is that proposed by Payman and Wheeler (1922), who investigated hydrogen, methane and carbon dioxide blends u_l, using a flat plate burner at the initial pressure and temperature of 0.1 MPa and 298K. This led to the simple expression of weighting each constituent mixtures u_l by that of its mole fraction within the blend, to yield the $u_{l,bl}$ of the blend:

$$u_{l,bl} = \sum_{i=1}^{n} (\bar{x} u_l)_i, \tag{2.36}$$

where, $\bar{x}$, denotes the mole fraction of the *i'*th constituent mixture within the total moles of the blend.

2.4.2 Mass Blending Law of Lipzig

Lipzig *et al*. (2010) investigated a mass based version of the above blending law, thus weighting each constituent mixtures u_l by its mass fraction within the blend, to yield the $u_{l,bl}$ of the blend:

$$u_{l,bl} = \sum_{i=1}^{n} (x u_l)_i. \tag{2.37}$$

Here, x, denotes the mass fraction of the *i'*th constituent mixture within the total mass of the blend.

2.4.3 Le Châtelier based Blending Law of Di Sarli

Using the CHEMKIN PREMIX code with the GRI kinetic mechanism, Di Sarli and Benedetto (2007) studied methane and hydrogen blends, with hydrogen fractions between 0.1-0.95, over an extensive range of ϕ from 0.5 to 3, at an initial temperature and pressure of 300K and 0.1 MPa. A Le Châtelier rule-like formula was developed:

$$u_{l,bl} = \frac{1}{\sum_{i=1}^{n} \left(\frac{\bar{x}_f}{u_l} \right)_i} \tag{2.38}$$

Where $\bar{x}_f$ denotes the fuel mole fraction of the *i'*th constituent within the total fuel moles of the blend.

2.4.4 Equal Adiabatic Temperature Assumption Blending Law of Spalding

Uniquely, Spalding (1956) proposed a blending law that relies on the assumption that if the adiabatic flame temperature, $T_{b,}$ of the constituents and blend are the same, then their corresponding q_{max}/β will be very similar. It can be seen from ZF-K's earlier work, Eq. 2.13 that mixtures may be differentiated by:

$$I = \left[u_l(T_b - T_u)\bar{c_p}\rho_u\right]^2 \tag{2.39}$$

Later Spalding (1957a) presents a revised expression for *I*:

$$I = u_l(T_b - T_u)^{0.5}\bar{c_p}\rho_u \tag{2.40}$$

Thus, with all mixtures under the same T_b, Spalding proposed:

$$I_{bl} = k_{bl}\sum_{i=1}^{n}\left(\frac{xI}{k}\right)_i, \tag{2.41}$$

where, x, denotes the mass fraction of the *i'*th constituent mixture within the total mass of the blend.

With I_{bl} known, the u_l of blend can be found by rearranging Eq. 2.40:

$$u_{l,bl} = \left[\frac{I}{(T_b - T_u)^{0.5}\bar{c_p}\rho_u}\right]_{bl} \tag{2.42}$$

All present values for T_b, c_p, k and ρ_u were obtained from the GasEq code (Morley, 2005).

However, for radically dissimilar fuels with large differences in T_b, such as methane and hydrogen, matching the T_b of both constituents and blend is often not possible without significantly varying at least one of the constituent equivalence ratios. This study focuses solely on blends and constituents at the same equivalence ratio. Hence this method was not possible to apply to the methane and hydrogen blends investigated in subsequent Chapters.

2.4.5 Activation Temperature Blending Law of Hirasawa

Hirasawa et al. (2002) propose a blending law based on the fractional mole weighting the burning velocity activation temperature, $\tilde{T}_a$, of each constituent in the blend. However, $\tilde{T}_a$ is not based on mass flux, as discussed in section 2.2.3, but on u_l:

$$\tilde{T}_a = -T_b \, ln(u_l). \tag{2.43}$$

Hence, the activation temperature of the blend, $\tilde{T}_{a,bl}$, is derived from:

$$\tilde{T}_{a,bl} = \sum_{i=1}^{n} [\bar{x} T_b \, ln(u_l)]_i. \tag{2.44}$$

Here, $\bar{x}$, denotes the mole fraction of the *i*'th constituent mixture within the total moles of the blend. All T_b values were obtained from GasEq (Morley, 2005). Finally, the blend laminar burning velocity, $u_{l,bl}$, is derived via the inverse of Eq. 2.44:

$$u_{l,bl} = exp\left(\frac{-\tilde{T}_a}{T_b}\right)_{bl} \tag{2.45}$$

2.4.6 Molar Heat of Reaction Correlations of Bradley et al.

Although no direct blending law was proposed, Bradley *et al*. (1991) observed correlations between u_l and heats of reaction per mole of reactants, $\bar{Q}$, for an array of different fuels under lean conditions at different initial and pressures, as shown in Fig. 2.3.

The correlations show an approximate linear relationship, but only within specific fuel families and are pressure dependent. It was recognised that such a relationship may potentially lend itself to the development of a blending law for fuels within the same family. The resulting blending law involves plotting the $\bar{Q}$ value of each constituent linearly against their respective u_l and thus the u_l of the blend can be deduced from the known value of its $\bar{Q}$ and the linear relationship between its constituents. However, this approach was anticipated to fail with constituents from radically dissimilar chemical families such as methane and hydrogen, where the values of u_l and chemical kinetics are very different.

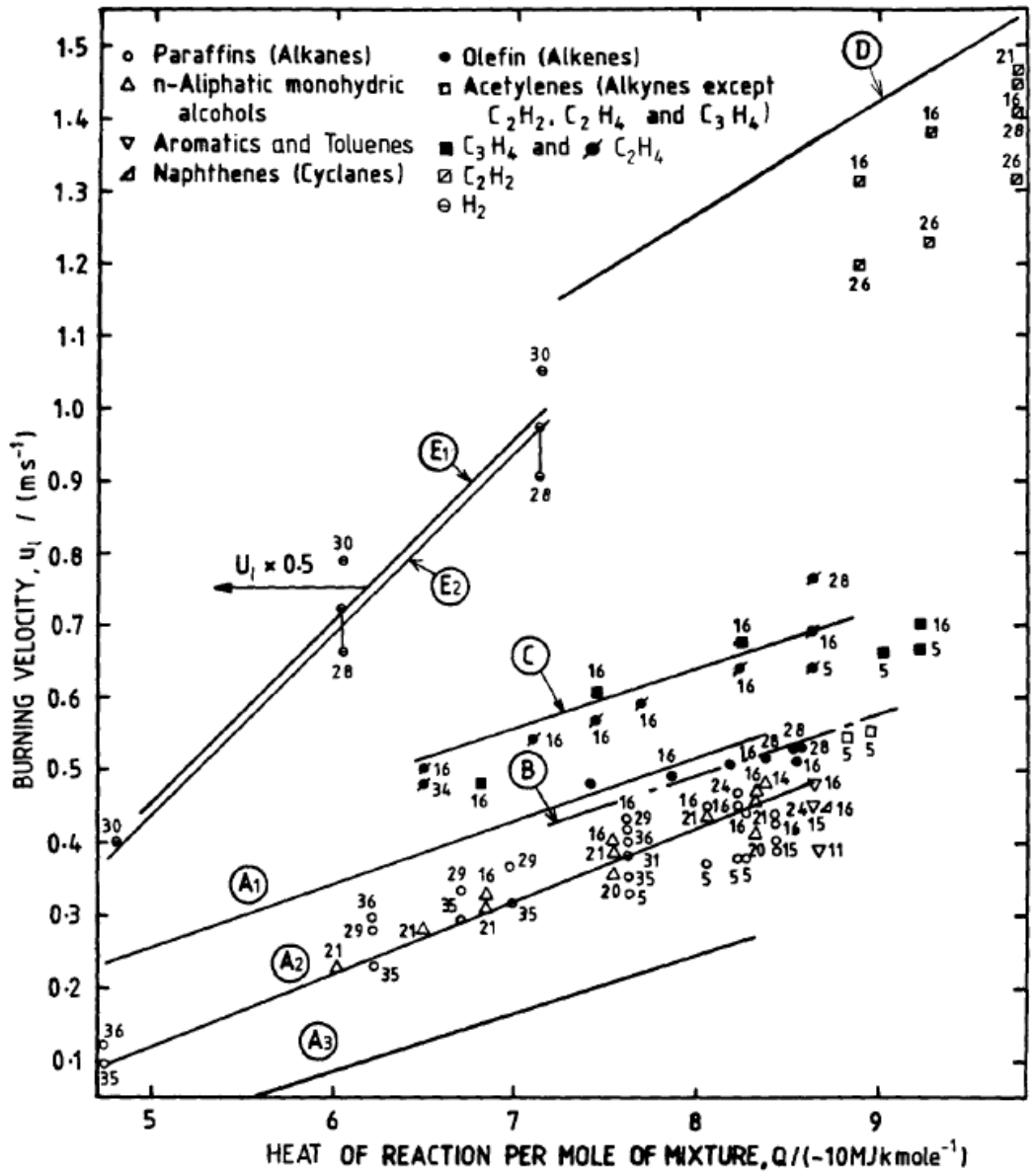

Figure 2.3: u_l of different fuels under lean conditions at an initial temperature of 300K. Symbols are experimental data, with the full lines indicating computations. A1, A2 and A3 denote CH4 and CH3OH at 0.01, 0.1 and 1.0 MPa respectively. Alkene experiments are represented by B at 0.1MPa, whilst C, D, E1 and E2 denote C2H4, C2H2, H2 and H2 at 0.1 MPa respectively. (Bradley et al., 1991).

Here, $\bar{Q}$ for all fuel/air mixtures were calculated using:

$$\bar{Q} = \sum_{P} n(h_f - \Delta h) - \sum_{R} n(h_f - \Delta h), \tag{2.46}$$

where, subscripts R and P denote the reactants and products respectively, $\bar{Q}$ the heat of reaction per mole of the reactants, n the number of moles, h_f the enthalpy of formation at the standard state conditions of 298K and 0.1 MPa, and Δh the sensible enthalpy,

which is the difference in enthalpy between any given state and the enthalpy at standard state conditions. In this study $\bar{Q}$ is based on the lower heating value, LHV, where the product H_2O is assumed to be fully vaporised. Utilising the GasEq code, all fuel and species h_f and Δh values were obtained, alongside values of n for a comprehensive range of product species, leading to more accurate values of $\bar{Q}$ under lean conditions, where NO and O_2 become significant, and rich conditions where CO and H_2 become significant. Theses product species comprised: N_2, H_2O, CO_2, CO, O_2, OH, H, O, H_2 and NO.

2.4.7 *Q/k* Blending Law of Present Work

Finally, the proposed blending law from the present work is based on a reformulation of Spaldings analytical expression for u_l as shown in Eq. 2.1. Such that, the macro parameters of u_l, Q, k_u, $\bar{c}_p$ and ρ_u are utilised to one side, where Q is the heat of reaction per mass of the reactants, whilst the remainder represent a measure of reactivty by describing the volumetric heat release rate profile through the flame:

$$u_l \rho_u \left(\frac{Q \bar{c}_p}{k_u}\right)^{0.5} = \left[\frac{\int_0^1 R(c)dc}{\lambda}\right]^{0.5} \tag{2.47}$$

On the assumption that the fractional mass weighted integrated volumetric heat release rate profile terms in c for the constuent mixtures can be added, to give a compararble term for blends comprising of i'th constituents, Eq. 2.47 then yeilds:

$$\left[u_l \rho_u \left(\frac{Q c_p}{k_u}\right)^{0.5}\right]_{bl} = \left[\frac{\int_0^1 R(c)dc}{\lambda}\right]_{bl}^{0.5} = \sum_{i=1}^{n} x_i \left[\frac{\int_0^1 R(c)dc}{\lambda}\right]_i^{0.5}, \tag{2.48}$$

whereby, x, denotes the mass fraction of each consituent mixture within the total mass of the blend. Applying the fractional mass weigting to the corresponding macro parameters, yields the blending law:

$$\left[u_l \rho_u \left(\frac{Q c_p}{k_u}\right)^{0.5}\right]_{bl} = \sum_{i=1}^{n} \left[x u_l \rho_u \left(\frac{Q c_p}{k_u}\right)^{0.5}\right]_i \tag{2.49}$$

The law implies the u_l of any blend is ultimately dependant upon the volumetric heat release rate profile through the flame, which is assumed to be the sum of the fractional mass weighted constituent mixture volumetic heat relase rates. During the present work, Q, k_u and $\bar{c}_p$ values for all mixtures were aquired via the use of GasEq (Morley, 2005).

Uniquely, this law accounts for the influence of consituent mixutres with marked differences in thermal conductivity. The majority of liquid hydrocarbon/air mixtures have negligible difference in thermal conductivity, being similar with ϕ. However for gaseous mixtures, such as CH_4/air and H_2/air there are significant difference between their thermal conductivies. Figure 2.4 shows how k_u values vary with ϕ for mixtures of CH_4/air, H_2/air and their blends. The k_u values for CH_4/air mixtures remain relatively similar across ϕ = 0.6-1.3, in significant contrast to those for H_2/air which exhibit a strong linear increase with ϕ, in which the k_u value of H_2/air become over double that of CH_4/air under stoichiometric conditions. The values of k_u for all pure fuel and blend mixtures were obtained using the thermal equilibrium program GasEq (Morley, 2005).

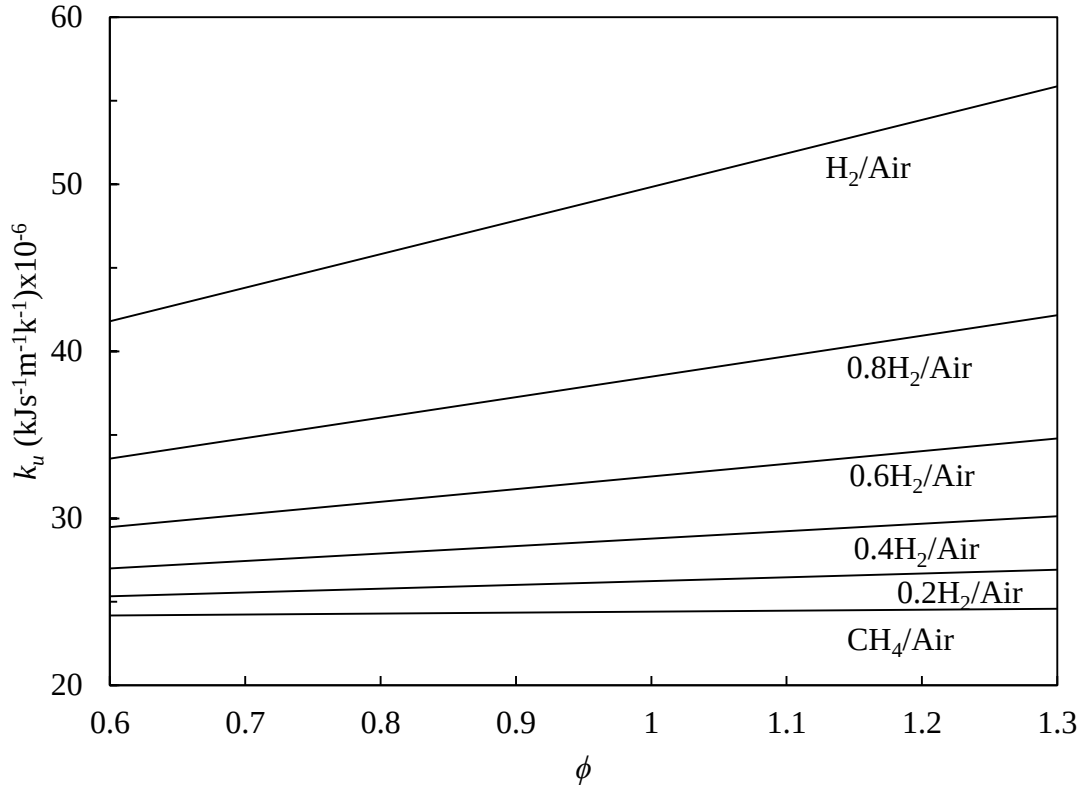

Figure 2.4: Variation of k_u with ϕ, for methane/air, hydrogen/air, and their blends at 303K.

2.5 Review of Markstein Parameter Blending Laws

As introduced in Chapter 1, the Markstein length, L_b, is an intrinsic property of any flame, describing the influence of stretch upon u_l, thus being an important parameter in the study of fundamental combustion, and making a L_b blending law highly desirable. Whilst there are a number of u_l blending laws proposed in literature, no L_b blending

laws were found. Three possible approaches were considered in the present work and are detailed in the following subsections.

2.5.1 Deficient Reactant Blending Law

The first L_b law was inspired by the role of the Lewis number in determining the Markstein number, in particular that of the deficient reactant. It involves weighting the value of L_b of each constituent mixture by the deficient reactant mole fraction. Under lean conditions the value of $L_{b,bl}$ for the blend is found by weighting the L_b for each constituent mixture by the fuel mole fraction and under rich conditions by the oxygen mole fraction:

$$L_{b,bl} = \sum_{i=1}^{n} (\bar{x}_d L_b)_i, \tag{2.50}$$

where, $\bar{x}_{d,i}$, denotes the deficient reactant mole fraction of the *i'*th constituent within the total deficient reactant moles of the blend. Hence, under lean conditions, where solely the fuel moles are considered, $\bar{x}_{d,i} = \bar{x}_{f,i}$, as per Eq. 2.29. However, under rich conditions, where solely the oxygen moles are considered, $\bar{x}_{d,i}$, becomes:

$$\bar{x}_{d,i} = 0.21 \left[\frac{(a/f)_s \bar{x}}{\phi + (a/f)_s} \right]_i \left\{ \sum_{i=1}^{n} 0.21 \left[\frac{(a/f)_s \bar{x}}{\phi + (a/f)_s} \right]_i \right\}^{-1} \tag{2.51}$$

Similarly, the equivalent mass based version was also trialled during the present work.

2.5.2 xu_lL_b Blending Law

This law involves a more empirical approach by the fractional mass weighting of the product xu_lL_b for each constituent mixture:

$$L_{b,bl} = \sum_{i=1}^{n} \frac{(xu_l L_b)_i}{u_{l,bl}}, \tag{2.52}$$

where, x, denotes the mass fraction of the *i'*th constituent mixture within the total mass of the blend.

Chapter 3 - Experimental Apparatus, Operating Techniques and Data Processing

3.1 Introduction

The measurement of both laminar and turbulent burning velocities of both liquid and gaseous fuels at various initial temperatures, pressures and equivalence ratios, have been made using a variety of experimental methods and apparatus (Broustail et al., 2011; Saeed and Stone, 2004; van Lipzig et al., 2011). Many of these have become well established for combustion studies. Common examples include constant volume combustion vessels (Hu et al., 2009; Jerzembeck et al., 2009; Marshall et al., 2011), adiabatic perforated plate burners (Dirrenberger et al., 2014; Konnov et al., 2011; Sileghem et al., 2013) and the twin counter flame stagnation technique (Egolfopoulos et al., 1992; Yamaoka and Tsuji, 1985).

Various imagining techniques are used; typically high speed digital schlieren and shadowgraphy (Broustail et al., 2011; Ormsby, 2005), and flow field imagining such as digital particle image velocimetry (DPIV) (Hirasawa et al., 2002; Jayachandran et al., 2015). Selection of apparatus and technique is often influenced by the fuel type, desired initial conditions, diagnostic ability, setup complexity, operation practicality and required accuracy.

In particular, constant volume combustion vessels have become popular due to their flexibility in allowing a range of combustion fundamentals to be studied over a wide range of variables: fuel type, blend and phase, including two phase mixtures (Bradley et al., 2014), temperature, pressure, equivalence ratio, r.m.s turbulence and its length scale.

Furthermore, they allow experimentation in a convenient and simplified manner. Flame front measurements taken within the core region have no surface interaction with the vessel walls, and in the case of larger vessels, also remain under the constant initial pressure, allowing for the assumption of all thermodynamic properties to be under adiabatic and isobaric conditions. Also, the flame is not moored, as would be the case with burners, thus the operating range is not limited by flashback or blow off. Generated turbulence can usually be assumed to be homogenous and isotropic with no mean fluid

motion. These significant benefits make the constant volume combustion vessel the choice for the present work.

The combustion vessel and accompanying auxiliary systems are presented in Section 3.2, with the fuel handling and experimental procedures in Section 3.3. Section 3.4 presents the various data processing operations and finally Section 3.5 presents a verification of the modifications made to the vessel during the present work.

3.2 Experimental Apparatus

A schematic of the apparatus used in the present work is shown in Fig. 3.1. Also shown is the inter-connectivity of its systems. The vessel is known as the Leeds Mk 2 combustion vessel (CV2), or the "bomb" and has been extensively used in the acquisition of both laminar and turbulent burning velocities. Examples include (Al-Shahrany et al., 2005; Bradley et al., 1998b; Bradley et al., 2009; Haq, 1998; Harker, 2009; Mansour, 2011; Ormsby, 2005; Tripathi, 2012).

However, the present work included significant upgrades to the auxiliary systems and refinements to the operating techniques in the quest for higher fidelity results. Physical upgrades to the auxiliary systems are discussed within Section 3.5, whilst refinements to operating techniques and procedures are discussed in Section 3.3.

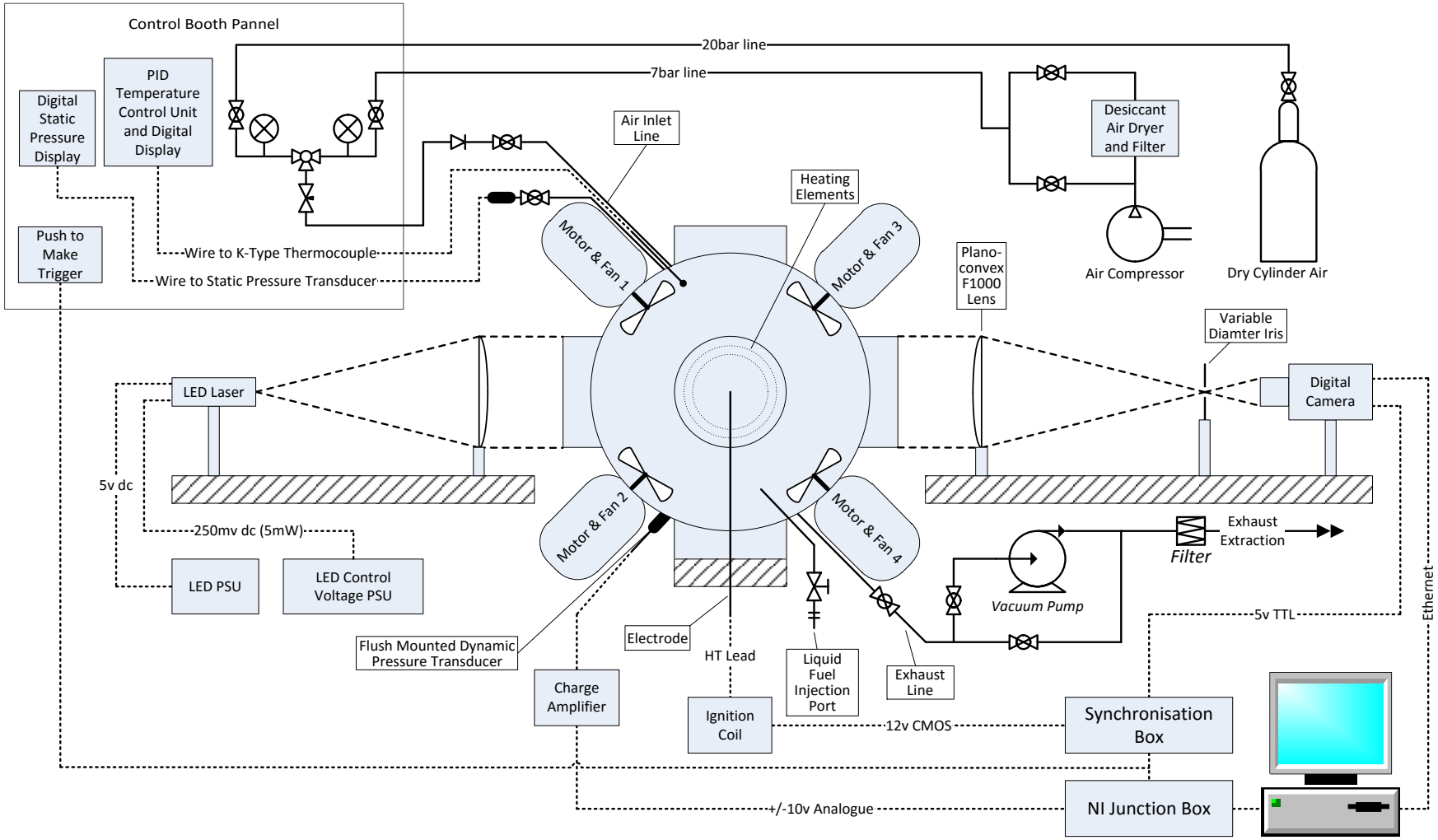

Figure 3.1: Schematic of vessel and auxiliary systems.

3.2.1 Combustion Vessel

Commissioned in 1991 by the Leeds combustion group, the Leeds CV2 as shown in Fig. 3.2 is a unique modular designed fan stirred combustion vessel (Bradley et al., 1998b). Figure 3.3 shows an internal view with the main access port removed. The vessel is capable of withstanding temperatures and pressures associated with the combustion of mixtures at initial temperatures and pressure of up to 600K and 1.5 MPa, respectively. Comprising a stainless steel SAE316 spherical body with an internal diameter of 380mm, and three pairs of orthogonally opposed ports that allow for an array of auxiliary systems to be employed. These ports allow exceptional optical access via 150mm diameter quartz windows, allowing a range of imagining techniques to be employed. High speed digital schlieren photography was used in the present work. However, such techniques as DPIV (Larsson, 2008) and a laser swinging sheet system (Harker, 2009) have also been used.

Turbulence was generated by four identical eight bladed fans, symmetrically disposed in a regular tetrahedron configuration, powered by four 8kW three phase motors, each controlled by individual solid states variable frequency convertors with a speed control range of 200-10,000rpm (3.3-176Hz). All work reported in this thesis was under laminar conditions and the fans were used only for mixing prior to ignition. However, they have also frequently been used for turbulent combustion studies (Harker, 2009; Mansour, 2011; Ormsby, 2005).

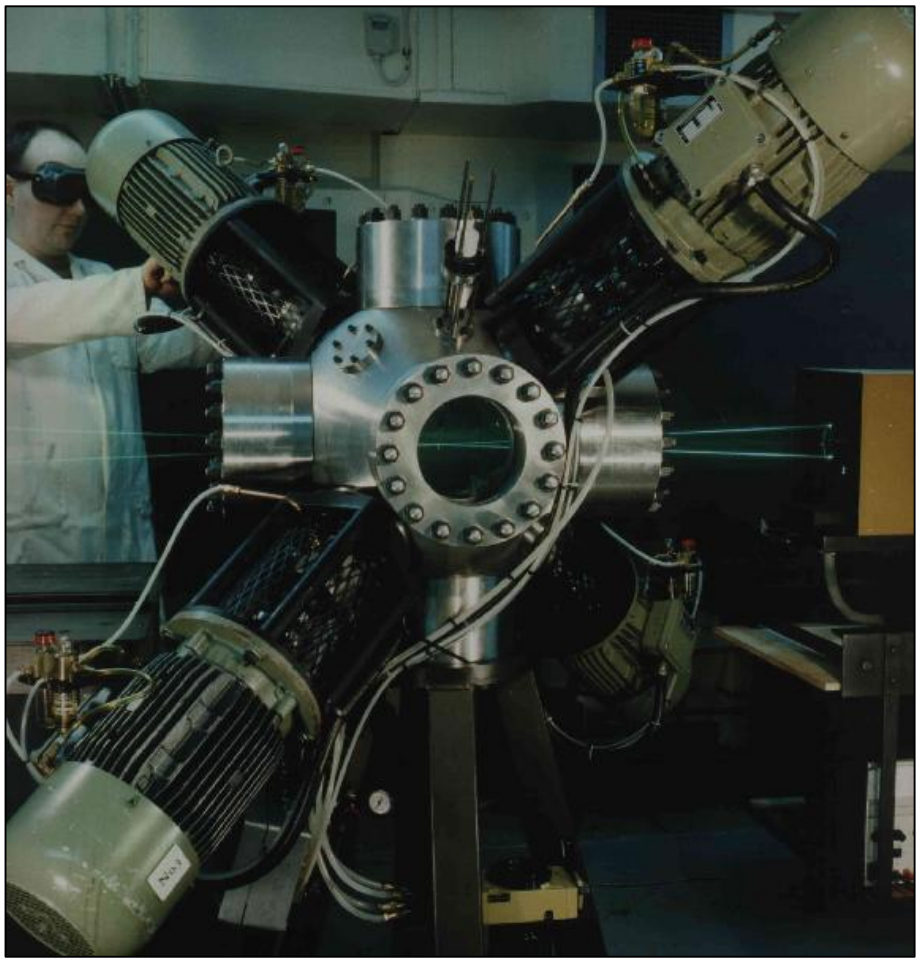

Figure 3.2: The Leeds CV2 – external view.

Figure 3.3: The Leeds CV2 – internal view.

3.2.2 Auxiliary Systems

Several auxiliary systems were employed on the combustion vessel for the present work. These included: static and dynamic pressure measurement systems; a heating and temperature control system; an ignition system; a high speed digital schlieren system and a triggering and synchronisation system. These are discussed in detail in the following subsections.

3.2.2.1 Pressure Measurement

Two pressure transducers were employed, one for static measurements and the other for dynamic measurements. The static pressure transducer (Druck PDCR 911) had a range of 0-1.5 MPa and was connected to a four digit digital display within the control booth. It measured absolute pressure and was used in mixture preparation to monitor vacuum, partial pressures and final pressure. Prior to ignition it was isolated for protection via a swage lock ball valve.

Variation in atmospheric pressure can strongly influence the mixture preparation hence calibration of the transducer was performed on a daily basis by taking readings from a mercury barometer. This helped reduce any error in the mixture equivalence ratio. During combustion of the mixture the associated pressure rise was measured by a dynamic pressure transducer (Kistler 701A) which was flush mounted to the vessel inner wall surface and had a range of 0-25 MPa. The charge from the transducer was then converted via a charge amplifier (Kistler 5007) to a +/- 10v analogue signal. An analogue to digital convertor (ADC) (Microlink 4000), then digitised the signal, which was interpreted by a virtual instrument (VI) panel using LabVIEW software to graphically display and record the pressure trace, at a sampling frequency of 50kHz.

In order to optimise the voltage range for the associated pressure increase during combustion, the charge amplifier volts/pressure range was adjusted to 5v/bar for initial pressures of 0.1 and 0.5 MPa and 10v/bar for the initial pressure of 1.0 MPa. Typically, the maximum pressure rise from combustion was around six times the initial pressure of the mixture. Calibration of the static transducer was performed via a dead weight tester and found to be within ±0.25%. Calibration of the dynamic transducer was outsourced to Kistler Instruments Ltd.

3.2.2.2 Heating System and Temperature Control

The existing heating system was upgraded for the present work and a demonstration of the improvement is discussed in Section 3.5.1. As shown by Fig. 3.3, heating of the

vessel was performed by two internal 2kW coiled heating elements, one attached to the inside of the access cover and the other attached to the inside of the opposing port cover. The temperature was set, controlled and displayed by a PID controller (CAL Controls, CAL3200) mounted in the control panel, using feedback via a K type thermocouple (25μ chromel-alumel wire) sheathed by a 1.5mm stainless steel casing and positioned such that the junction end was 75mm away from the vessels inner wall surface. During heating, convective heat transfer was aided by turbulence generated by the four fans, this helped maintain a more uniform temperature across the vessel, ensured the elements did not over heat and reduced the risk of any pre-combustion reactions of the mixture due to excessive hot spots (Mandilas, 2008). A safe guard mechanism was employed which prevented heating unless the fans were activated.

During the initial heating phase of the vessel, the set point temperature of the PID controller was set considerably higher than the desired initial mixture temperature, thus causing a more aggressive rate of heat transfer that significantly reduced the heat up time. Ceasing heating then lowered the vessel temperature towards the desired target while thermal conduction ensured a uniform temperature distribution as discussed in Section 3.5. The temperature was then maintained by the PID controller with the set point a few degrees above the desired mixture temperature. Depending on the heat of reaction generated by combustion and frequency of experiments, the vessel temperature could also be manipulated by either significantly increasing the set point temperature to give a higher heating rate or by flushing the vessel with air for longer periods after each experiment to increase cooling.

3.2.2.3 Ignition System

All mixtures were ignited with a centrally positioned spark plug within the vessel using a variable arc discharge ignition system. As shown in Fig. 3.4, a miniaturised spark plug assembly, developed at Leeds, was used to minimise aerodynamic influences on flame propagation.

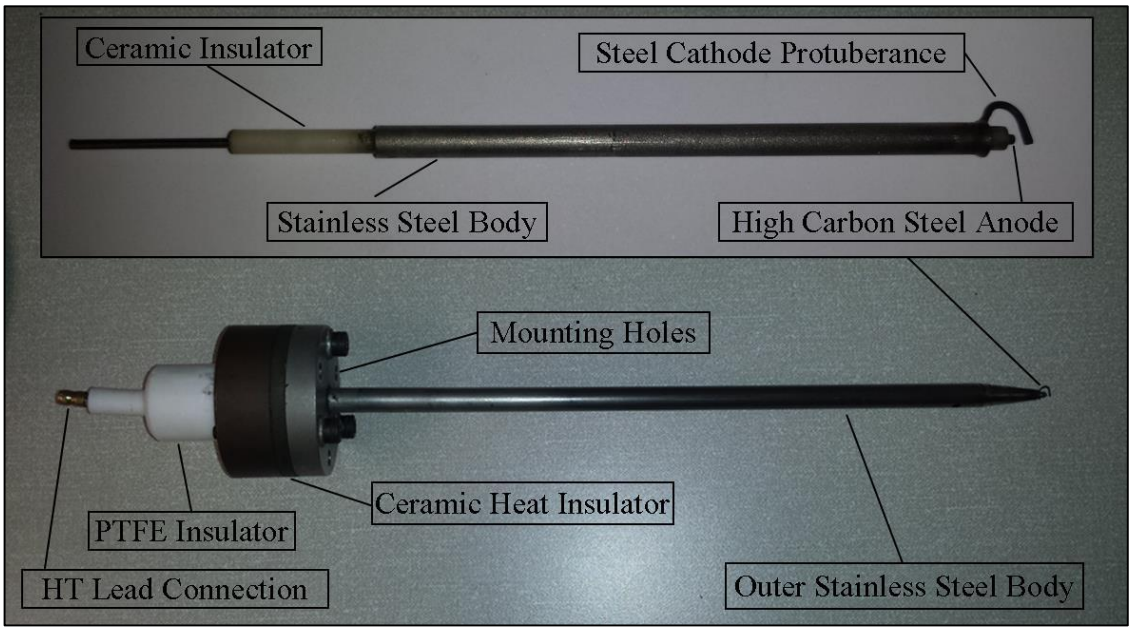

Figure 3.4: Custom made mini sparkplug assembly.

This compromised a central 1.5mm diameter high carbon steel electrode serving as the anode, being insulated by a ceramic sheath within a stainless steel tube with a protuberance to serve as the corresponding cathode. This assembly was then secured into an internally PTFE insulated 6.35mm stainless steel tube and mounted through the vessel wall. This grounded the outer stainless steel section to earth for the cathode side of the circuit, with an external standard male HT cable connection attached to the internal anode rod. This setup ensured the risk of uncontrolled ignition from residual ignition energy was avoided (Kondo et al. 1997).

The central anode electrode was connected to the secondary coil windings on one side of a double ended VW ignition coil via a high tension (HT) cable, with the other side earthed to increase the original charge of the unit. The primary coil windings were supplied with a 12v supply and broken by a 12v CMOS signal to induce the spark. The spark energy was kept to the minimum ignition energy (MIE) required to initiate a sustained reaction. This minimised the influence of spark assisted flame propagation (Tripathi, 2012). This minimum energy was a function of fuel, equivalence ratio and initial pressure. In particular, the minimum energy reduced with increasing pressure. Suitable ignition energy variation was achieved by altering the spark plug gap and, hence, dissipation of the spark. For all mixtures, the spark plug gap was set to 1.5, 1 and 0.5mm for initial pressures of 0.1, 0.5 and 1.0 MPa respectively.

3.2.2.4 High Speed Digital Schlieren Photography

High speed schlieren cine photography was employed to track the development of spherically expanding flames within the vessel. The technique allowed the visual detection of the flame front through the density gradients between the burnt and un-burnt mixtures that cause varying degrees of light refraction. The technique was first used at Leeds by Bradley and Hundy (1971) and has become well established for combustion studies at Leeds (Al-Shahrany et al., 2005; Ormsby, 2005; Tripathi, 2012) and at many other institutes (Broustail et al., 2011; Hu et al., 2009; Jerzembeck et al., 2009).

Figure 3.1 shows a schematic of the schlieren optical configuration. A near point source of light was provided by a 20mW (regulated to 5mW), 635nm LED laser, this expanded onto a f-1000mm plano-convex lens, collimating a 150mm beam through the vessel and its contents to another f-1000mm plano-convex lens, which focused the beam onto a variable diameter iris (1-15mm). A high speed digital Phantom M310 camera using an 80mm Nikon lens, then recorded the resulting image to its internal memory of 512MB. The camera was positioned such that the maximum field of view of 150mm diameter, limited by the vessel windows, took full advantage of the camera resolution of 768 x 768 pixels. This resulted in a recorded square view of 159 x 159mm and thus 0.20708mm/pixel. This resolution was more than sufficient to capture a defined flame edge and detailed flame cellularity, whilst allowing the ample sampling rate of 5400 fps.

The exposure time was set to 6μs. Phantom software controlled the camera via an Ethernet cable and allowed the recorded images to be converted from the standard ".cine" format to a string of ".bmp" images for interpretation by an automated image processing program, as discussed in Section 3.4.2. The software also featured an 'extreme dynamic range' (EDR) function. This involved a pre-set pixel saturation threshold that, once exceeded, reset the exposure time within the global exposure time of 6μs. This essentially slowed down pixels that were charging so fast they would become saturated before the global exposure time expired, thus allowing much better definition of images featuring both low and high intensity light.

The schlieren technique benefits from a relatively simple setup and allows quick and effective adaptation of the system sensitivity via variation of the iris diameter. At the smallest diameter of 1mm, the system was highly sensitive, giving true schlieren images. Increasing the iris diameter desensitises the system, whereby an intermediate between schlieren and shadowgraphy was reached. This allowed the system to be

optimised for different mixture conditions, of varying density, to show the maximum amount of surface detail, whilst ensuring a clearly definable flame front edge was always observed. Iris diameters of 1, 5 and 12.5mm were found to be best suited for initial pressures of 0.1, 0.5 and 1.0 MPa.

Figure 3.5 demonstrates typical schlieren image quality at r = 65mm, for stoichiometric iso-octane/air at the three initial pressures used in the present work. A limitation of any schlieren setup is the 2D projection of a 3D flame, rendering an image overlapping effect. However, as long as the flame edge was clearly defined, the rate of propagation could be observed.

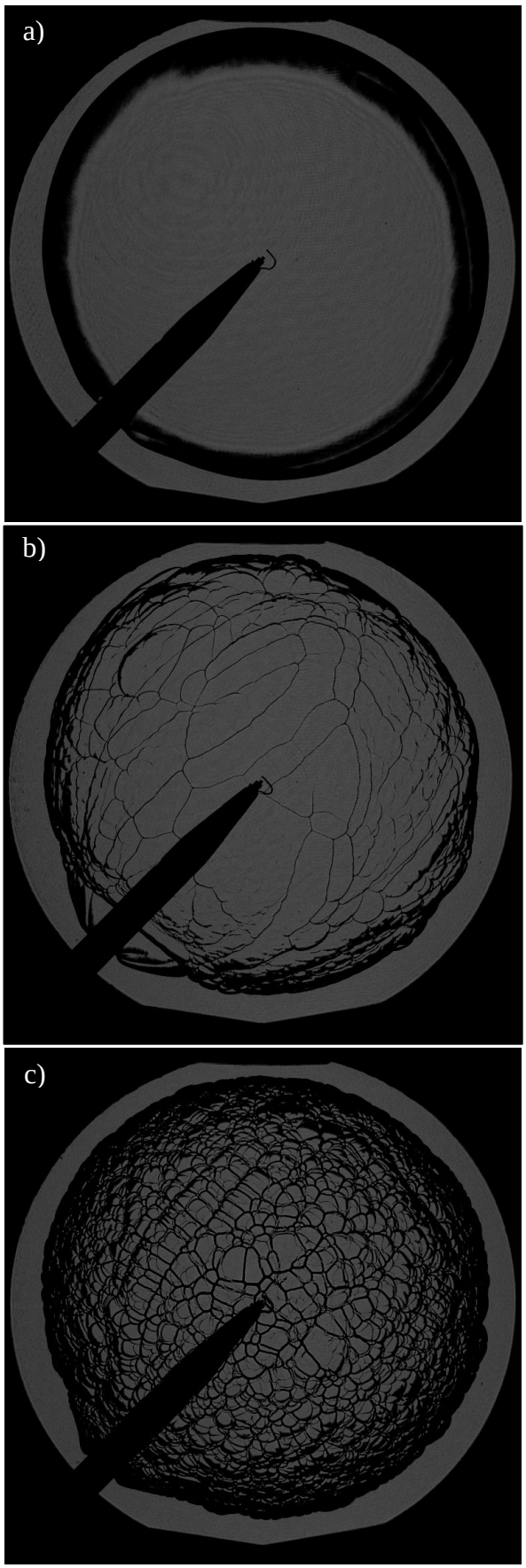

Figure 3.5: Schlieren images of iso-octane/air taken at r = 65mm, ϕ = 1, P_i = a) 0.1 MPa, b) 0.5 MPa, c) 1.0 MPa, T_u = 360K.

3.2.2.4.1 Schlieren Calibration

At the start and end of every day of experiments, confirmation of the beam collimation and pixel resolution was achieved through recording an image, via the high speed camera, of a mounted transparent Perspex sheet with an imprinted $10mm^2$ grid within a section of the collimated beam on either side of the vessel. It was ensured that the beam was correctly adjusted such that both images displayed the same size grid, thus confirming a collimated bean through the vessel. The pixel size was confirmed by an image analysis tool developed in MATLAB, this allowed a computer generated best fit grid of known size and pixel resolution to be superimposed over each image of the Perspex grid. The average of both sides was taken, with variation typically within 0.1%.

3.2.2.5 Triggering and Synchronisation System

In order to simultaneously capture the schlieren images of the propagating flame and the associated pressure rise, synchronisation of the high speed camera, dynamic pressure VI and spark system was required. This was achieved via a purpose built triggering system, following the sequence of operation as shown by Fig 3.6. Upon pressing the 'push to make' ignition switch, a +5v TTL trigger signal was generated. Its rising edge triggered the start of both the camera and dynamic pressure transducer recording systems. The corresponding falling edge then initiated a +12v CMOS pulse to break the primary side of the coil, thus generating a spark. This sequence of operations ensured that all flame data were captured together with a small amount of reference data prior to ignition.

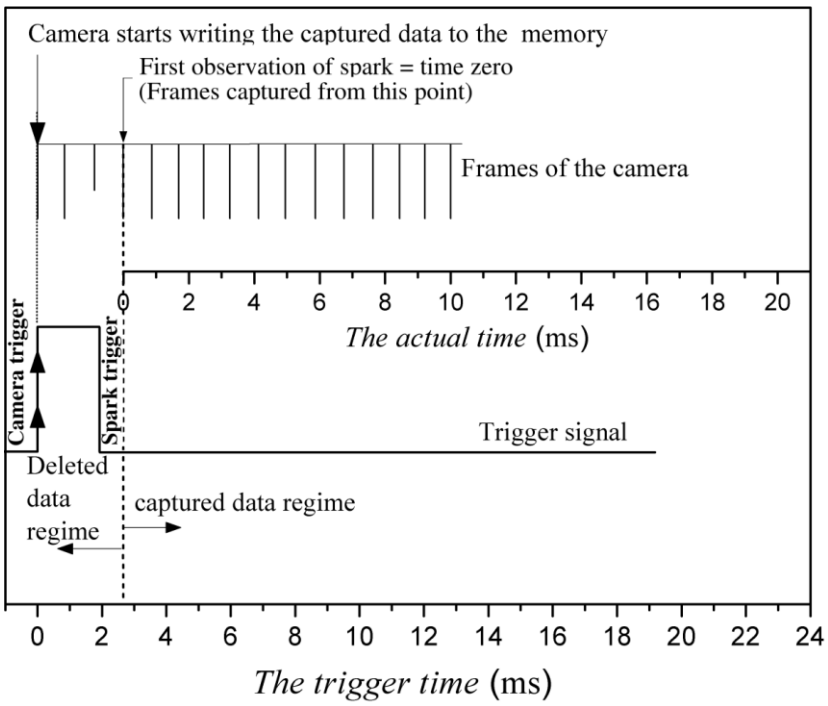

Figure 3.6: Sequence of triggering for camera, sparkplug and dynamic pressure transducer.

3.3 Operating Techniques

Past procedures for both fuel handling and rig operations have been revised within the present work in the quest for increased safety, reduced experimental time and higher fidelity data acquisition. These are detailed in the following subsections.

3.3.1 Fuel Handling and Preparation

A summary of all fuels used in the present work is given in Table 3.1. In accordance with University health and safety regulations, and operating in a fume cupboard, all fuels were decanted into 250ml narrow necked glass bottles and stored in a refrigerator at 5°C. Due to the hygroscopic nature of ethanol, the precaution of decanting the entire 2.5litre supply bottle into ten 250ml bottles at once was taken to reduce its exposure time to atmospheric air. As a further precaution to minimise fumes, all fuel bottles had a silicone septum cap fitted, which was pierced by a 1mm diameter stainless steel Luer lock needle with the appropriately sized syringe attached. Therefore, it was not necessary to open any fuel bottle within the laboratory outside the fume cupboard. Any fuel required was taken from the refrigerator at least 30 minutes before use to allow equalisation to room temperature (25°C) to ensure its density corresponded to that used in calculations for subsequent syringe volume measurements.

Fuel	Supplier	Purity (ppm)	Density (g/ml @ 25°C)	Molecular Mass (g)
iso-Octane	Fisher Scientific	99.91%	0.619	114.23
n-Heptane	Fisher Scientific	99%	0.683	100.23
Toluene	Fisher Scientific	99.8%	0.867	92.14
1-Hexene	Sigma-Aldrich	99%	0.678	84.16
Ethanol	Fisher Scientific	99.8%	0.7897	46.07
n-Butanol	Fisher Scientific	99.89%	0.810	74.14

Table 3.1: Summary of all liquid fuels used in the present work.

For a fuel to fully vaporise its vapour pressure, which is a function of temperature, must be equal to or greater than its partial pressure, which is a function of the total pressure within a system. The initial temperature of all experiments in the present work was 360K. This was selected on the basis of being sufficient to ensure complete vaporisation of all fuels, within a practical time, across an equivalence ratio range of, ϕ = 0.8-1.3, at initial pressures of 0.1, 0.5 and 1.0 MPa. It also facilitated a saturated steady state, with low risk of pre-combustion reactions on the vessel walls. Furthermore, a large number of previous burning velocity studies carried out at Leeds and other institutes were at the same temperature, which serve as means of comparison, as discussed in Chapter 5. However, the exception to this was *n*-butanol which was found to have an insufficient vapour pressure for complete vaporisation at the high pressure of 1.0MPa, Indeed, at ϕ = 1.0, droplets were visible on known cooler regions of the combustion vessel such as the quartz windows. Therefore, for this fuel, ϕ was limited to 0.9 at 1.0 MPa.

In all cases the vessel fans were in operation during mixture preparation to improve mixing. Typically the fans were operated at 1000rpm, but for the alcohols, ethanol and *n*-butanol, the fan speed was increased to 2500rpm to increase convection and decrease vaporisation time.

3.3.2 Experimental Procedure

After the vessel had been sufficiently heated, as discussed in Section 3.2.2.2, an initial sealing test was performed, where the vessel was pressurised with dry air to the intended initial pressure of the mixture and monitored for at least five minutes to ensure

no leakage. This test was performed whenever the initial temperature or pressure of the mixture was altered. To ensure the vessel was free from any unwanted gaseous residuals from previous experiments, the vessel was vacuumed down to 0.05 MPa from atmospheric pressure, filled with dry air to 2 MPa, and again vacuumed down to 0.05 MPa. This ensured any gaseous residuals were kept to a maximum of 0.3%.

With the fuel at room temperature, the assumption of the ideal gas law, known volume of the vessel, fuel composition and density, the liquid volume of fuel required for each mixture was calculated. A Hamilton glass gas tight syringe, with an accuracy stated by the manufactures of 0.5% at full scale, was equipped with a Luer locked needle to pierce the silicone septum of the fuel bottles. Detaching the needle then allowed the syringe to be connected to the vessel's gated Luer lock liquid fuel delivery port. With the vessel under vacuum at 0.05 MPa, the port valve was then opened and the fuel drawn in by the difference in room and vessel pressure. This significantly aided fuel vaporisation rate and initiated mixing with a small quantity of air. The valve was then closed and the associated partial pressure from evaporation of the fuel was confirmed via the digital static pressure gauge. Dry air was then added to the desired initial mixture pressure whilst ensuring the mixture temperature had stabilised to the desired initial mixture temperature. At this point, the fans were switched off and a 15s time period given to allow the mixture to equilibrate and become quiescent. This also allowed sufficient time to arm the triggering system, perform a final brief visual inspection and return to the protected control booth. Ensuring the initial mixture temperature and pressure were as desired, the inlet air supply and static pressure transducer were isolated by remotely closing ball valves and finally, the ignition button pressed.

After combustion the resulting products were exhausted via a remotely operated exhaust valve, this ensured the vessel was depressurised to a safe level before leaving the protection of the control booth. The fans and heaters were then reactivated, the inlet air supply and static pressure transducers isolation valves reopened, and the vessel flushed with dry air for at least one minute to aid the evacuation of combustion products. During this time the acquired data was saved and the LabVIEW and Phantom programs reset. The vacuuming and dry air filling procedure as described above was then repeated to prepare the vessel for the next experiment.

3.4 Data Processing

This Section serves to highlight the various stages of processing the acquired experimental data. First, the required thermodynamic data and assumptions are addressed in Section 3.4.1. Second, the schlieren image digitalisation technique and acquisition of the average flame front radius are discussed in Section 3.4.2. Finally, the automated technique of deducing u_l via both linear and nonlinear approaches to measuring L_b, are discussed in Section 3.4.3.

3.4.1 Thermodynamic Properties of Burned and Unburned Gases

All Schlieren images used to deduce u_l and L_b were taken with the full spherical flame front visible through the vessel windows. During this period any pressure rise is negligible such that constant pressure was assumed. Therefore all thermodynamic properties of the mixture during this stage were considered to be under isobaric and adiabatic conditions. As discussed in Chapter 1, Section 1.5, the calculation of u_l requires the thermal expansion factor, which is the ratio of the burned to unburned density, ρ_b and ρ_u. These densities were obtained from the thermal equilibrium program GasEq, developed by Morley (2005). The program offers the calculation of thermodynamic and combustion parameters at a variety of conditions. However, for the present work the constant pressure and adiabatic temperature assumption was deemed most sufficient.

3.4.2 Schlieren Image Processing

The present work involved a large number of experiments and thus many thousands of flame images were processed. This, coupled with the subjective nature of defining a flame edge, particularly when faint and or with emerging cellularity, warranted the use of a partially automated and systematic image processing technique for the analysis of flame propagation. Software for this was developed by (Sharpe, 2011), using the MATLAB programming environment. During the present work the program has been refined and optimised for increased speed and the ability to deal with images of high cellularity.

Figure 3.7 illustrates some of the steps undertaken to process a schlieren image. Figure 3.7a shows an image of a typical cellular flame. The flame is essentially cellular except for a disturbance caused by the spark plug. Therefore, for accurate calculations it was necessary to eliminate the influence of this disturbance as follows. Initially, using the

schlieren image immediately prior to ignition, the outer edge of the window and spark plug tip position was identified. A circa 20 degree section from the tip on either side of the spark plug probe was then masked off as shown in Fig 3.7b to negate the accelerative effects of its presence. The resulting coordinates were then saved to file and applied to every subsequent image as a frame of reference.

The process of identifying the flame edge starts with the last fully observable flame front schlieren image within the vicinity of the window such as that in Fig 3.7a. The outer window edge, sparkplug tip position and mask coordinates were then superimposed onto the image. A level set approach was then initiated from the window outer edge frame of reference towards the inner burnt gas region. The identified flame front was then highlighted, as shown in Fig. 3.7b by a black outline that neighbours the unburned mixture region highlighted in blue, with the burned gas region highlighted in grey. A best fit circle was then applied to the flame front as illustrated by the blue line in Fig. 3.7c. Hence, the average flame radius was calculated and saved to file. This process was then repeated for every image back to the point of ignition, with each previous flame front serving as an initial level set starting point. Details of this level set technique are given in (Sethian, 1999; Tripathi, 2012).

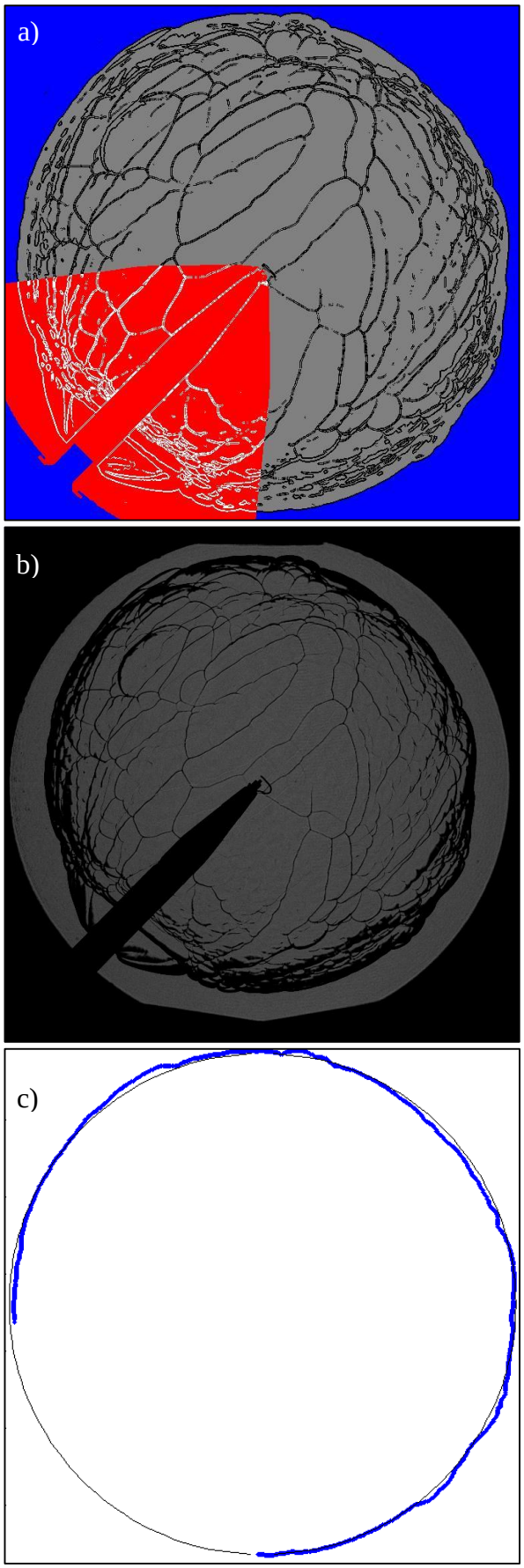

Figure 3.7: a) Schlieren image, b) Digitised image with sparkplug masking, c) Best fit circle to digitised flame front edge.

3.4.3 Acquisition of u_l and L_b

From the process discussed above, each experiment resulted in a series of radii as a function of the time of each captured image. Subsequently, the stretched flame speed as a function of radius and stretch rate was calculated, as discussed in Chapter 1, Section 1.5. These calculations were performed in a further MATLAB code that automatically generated plots of: r vs. t, S_n vs. r and S_n vs. α. Figure 3.8 shows typical examples of these.

As also, discussed in Chapter 1, Section 1.5, both linear and nonlinear approaches to measuring L_b were automatically applied to S_n vs. α data in order to deduce u_l via extrapolation to zero stretch rate, with the selected data range overseen at every stage to ensure a realistic fit and application only within the stable regime of the flame. Figure 3.8c illustrates distinct linear and nonlinear behaviour, for rich and stoichiometric *iso*-octane/air mixtures respectively. In cases such as the rich mixture, where no differences between the approaches occurred or were within the experimental error, the linear approach was assumed sufficient. However, in cases such as the stoichiometric mixture, where distinct nonlinear behaviour occurs, the linear approach is clearly inadequate, causing an over prediction of u_l. Thus, the nonlinear u_l value was used. Throughout the present work, solid red and blue lines on all S_n vs. α plots denote the linear and nonlinear approaches respectively, whilst highlighting the selected stable flame regime used.

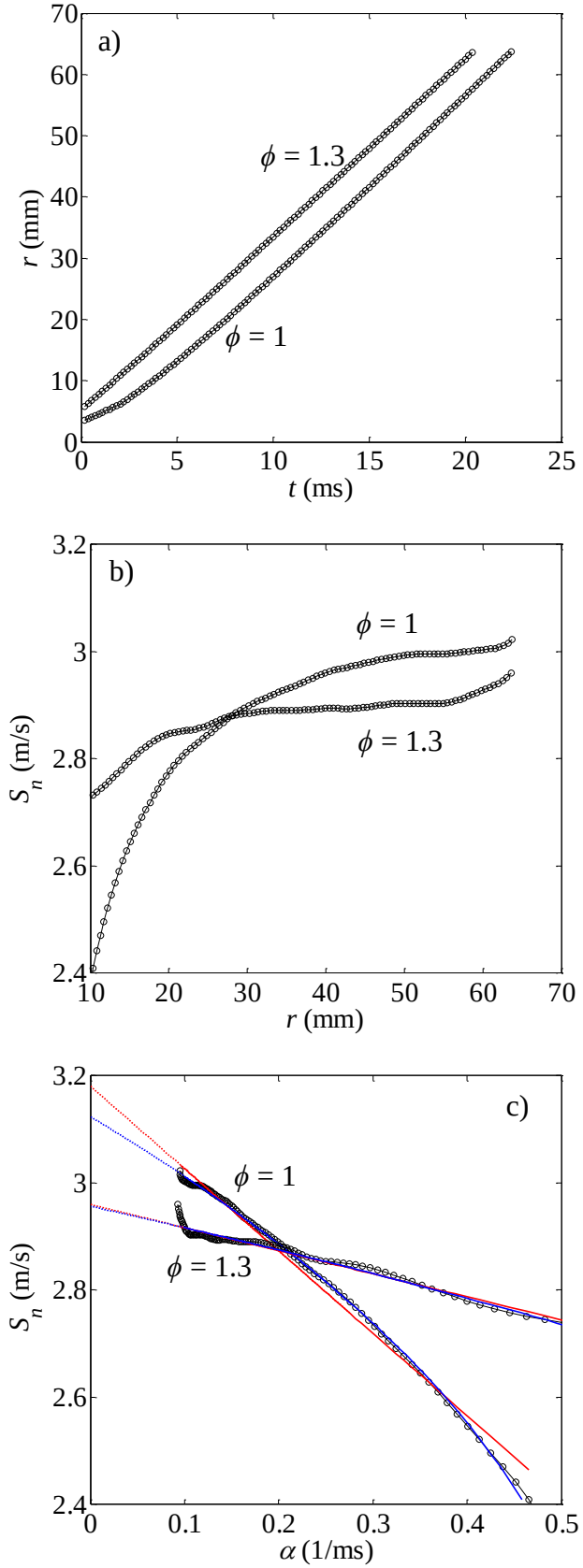

Figure 3.8: a) r variation with t, b) S_n variation with r, c) S_n variation with α, for *iso*-octane at P_i = 0.1 MPa, T_u = 360K for ϕ = 1 and 1.3. Solid red and blue lines denote linear and nonlinear relationships to L_b across used data points respectively.

3.5 Verification of Improvements due to Vessel Modifications

During the present work, an array of modifications to the vessel and its auxiliary systems was carried out in order to improve safety, experimental efficiency and accuracy. These included, a new ignition system that allowed considerably higher spark energy, with controlled spark duration, a higher flow rate vacuum system, which reduced vacuuming time by around 70%, a revised schlieren system with significantly improved versatility and sensitivity, a more powerful and uniform heating system with improved temperature uniformity, and the introduction of a desiccant dryer to the main compressor air supply for improved air quality and reduced cylinder air use. The latter two modifications required some preliminary experimentation in order to verify their performance, which is presented in the following subsections.

3.5.1 Heating System Upgrade

Originally, the initial heating of the vessel was done either by the internal 2kW heating element attached to the access port, or by an independent 8kW heating element for reduced heating time and/or higher temperature, which was inserted via the access port. Both methods used running fans forcing convection to aid more uniform heating. In the case of the independent 8kW heating element, once the vessel reached the desired temperature it was removed and the internal 2kW heating element reattached, which was deemed sufficient to maintain spatially uniform temperature.

Figure 3.9a shows temperature measurements taken by M. Lawes, from the vessel outer body surface, on the heater side and opposing side, using solely the 2kW heating element to initially heat the vessel from room temperature. The internal gas temperature target was set to 150°C. After the target temperature was reached and stabilised, at around 200 minutes, a mixture was added, hence, the slight fall in readings as the mixture heated. The mixture was then left for over an hour, with the PID temperature controller maintaining the target temperature. During this period, a circa 15°C temperature differential existed between either side of the vessel outer surface. Figure 3.9b shows the corresponding temperature measurements using the 8kW heating element to initially heat the vessel. This was attached with the internal gas temperature target set to 150°C, for around an hour.

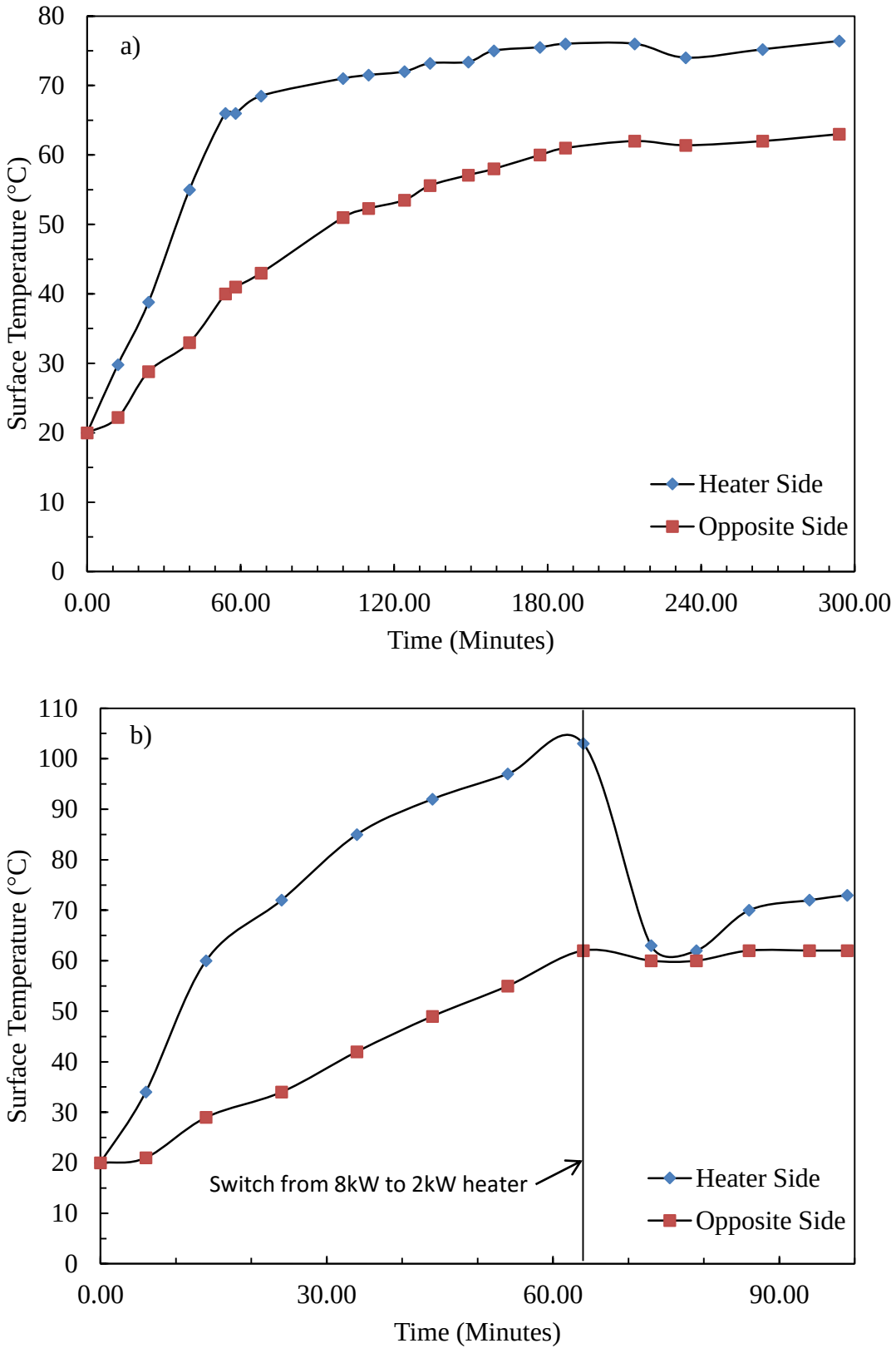

Figure 3.9: Temperature measurements of vessel surface as a function of time during initial heating stage, using: a) 2kW heater, b) 8kW booster heater and 2kW heater.

As expected, a much higher rate of heat transfer was observed. A 15 minute period was then required to remove the 8kW heater and install the 2kW heater. A rapid decrease in temperature readings on the heater side was then observed as the 2kW heating element and mounting plate absorbed heat from the vessel body. This caused the surface temperature readings on either side to nearly equalise at circa 75 minutes. However, this could not be maintained as the internal gas temperature dropped below target, activating the 2kW heater, causing surface readings on the heater side to rise again and depart from equalisation with the opposite side. Shortly after, the heater was switched off to try and counter this effect, but again, it was found that the internal gas temperature could not be maintained without having a relatively large temperature differential between either side of the vessel.

As discussed in Section 3.2.2.2, the degree of temperature maintenance was influenced by the nature of the experiments. Preliminary experiments, also found low heat of reaction mixtures and/or relatively long periods between combustion events significantly destabilised the vessels heat saturation, even at relatively low initial gas temperatures of 360K. This, indicates that a single 2kW heating element was not sufficient to maintain spatially uniform temperature of the vessel during the course of a typical day of experimentation.

In an effort to both reduce the time required to pre-heat the vessel and to improve temperature uniformity, the single 2kW heating element was removed and two new larger surface area 2kW heating elements were installed, as shown in Fig. 3.3. One was attached in the original position inside of the access port cover and the other symmetrically opposing it on the other port cover. In turn, these new heating elements fractionally reduced the internal volume of the vessel.

To quantify the new internal volume, a measured quantity of water was carefully poured into the top access port of the vessel, with the heaters and electrode in place, until the level became flush with the top internal surface. The required water volume was 30.372l, hence, the corresponding new internal volume of the combustion vessel was found to be $0.030372m^3$.

The new heating system proved to be more effective in initially heating the vessel to the target initial mixture temperature of 360K than the independent 8kW heating element, reducing the initial heating time by around 20 minutes. This was particularly advantageous, as further time was saved by not having to install and remove the

independent heater, which subsequently eliminated the hazardous exposure to the large hot heating element upon its removal.

A series of experiments was then conducted in order to quantify temperature distribution within the vessel and to ensure a stable and uniform core region (within the field of view through the windows) exists prior to ignition, at both elevated temperatures and pressures. For laminar studies, the fans were switched off prior to ignition giving a period of time to allow the mixture to become quiescent, arm systems and retreat to the safety of the main control booth.

Thus, to quantify the effect on temperature uniformity from switching off the fans, initial measurements with them switched on were first required. As shown in Fig. 3.10, a custom made temperature measurement probe was manufactured in order to conduct such experiments.

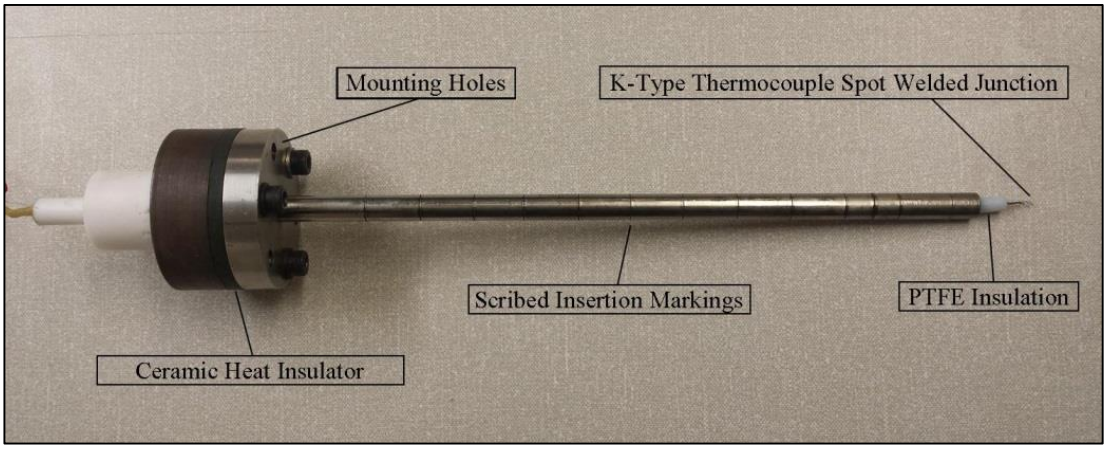

Figure 3.10: Custom made K-type thermocouple probe for internal temperature measurement at elevated pressure, with fans running.

This allowed safe and measureable insertion of a K type thermocouple into the vessel with running fans and at elevated pressure. Fig. 3.11 illustrates the track of the probe via the four existing ports that oppose the centre of each fan.

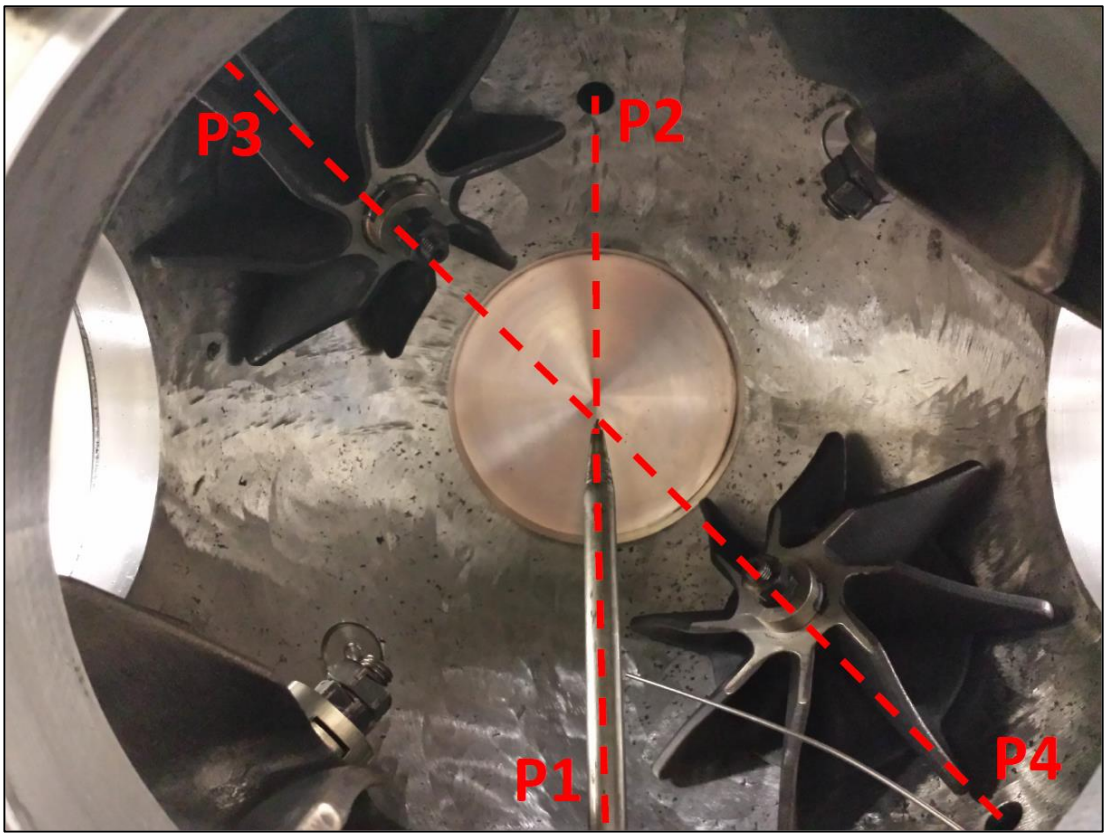

Figure 3.11: Dashed red lines represent track of thermocouple probe from each of the four positions, denoted by P1, P2, P3 and P4.

Ensuring the vessel was fully heated, such that the desired internal air temperature was stable with the fans running, a series of temperature measurements were made from the inner wall surface, in 20mm increments to the vessel centre, from each of the four symmetrically disposed positions. Then, for every position the fans were turned off and the temperature recorded every 5 seconds up to one minute. This procedure was carried out at initial temperatures of 360 and 393K for both initial pressures of 0.1 and 0.5 MPa.

Thus, these four conditions allowed the effects of elevated temperature and pressure on internal gas temperature uniformity to be observed, whilst fans were on and after they were switched off. Figures 3.12-3.15 show the recorded temperature measurements for each position, across r = 0-190mm, relative to the time from the fans being switched off, for each of the four conditions. In all cases, with the fans running, all measurements taken within r = 175mm were within 1.5K of the target temperature.

However, measurements at r = 190mm were significantly varied and considered to be within the thermal boundary layer of the inner wall surface. In all cases after the fans were switched off, measurements taken from positions 1 and 4 had a tendency to become lower with an increased rate at larger radii. This was anticipated as in both

positions the probe tracked downwards into cooler regions caused by heat rising. This effect for position 4 was further augmented by the cooler quartz window. In contrast, measurements from positions 2 and 3 had a tendency to become higher, with an increased rate at larger radii. Again this was anticipated as the probe tracks upwards into hotter regions due to heat rise. In particular measurements from position 2 at larger radii became very high due to heat radiation from the close proximity of the 2nd heating element.

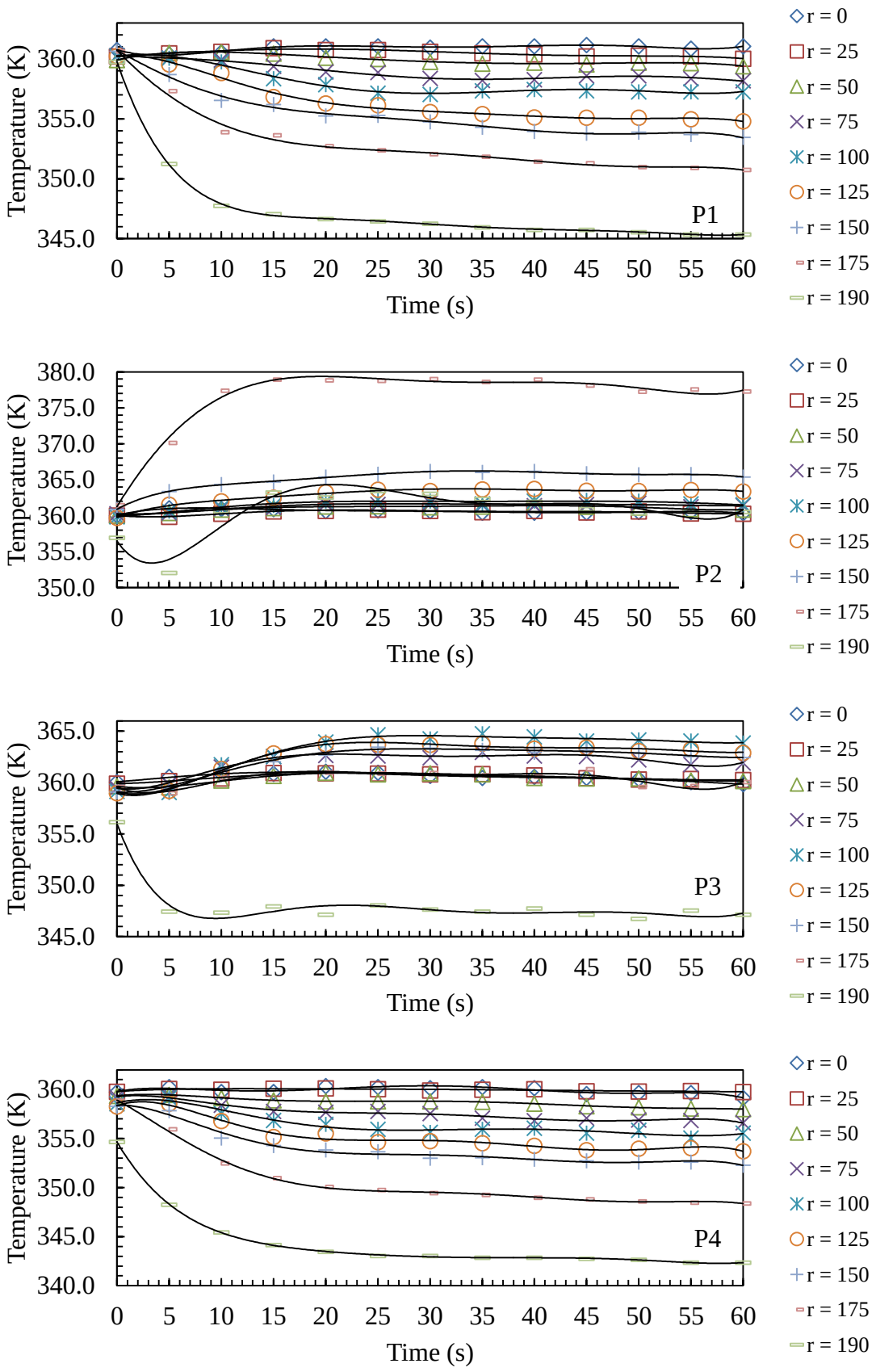

Figure 3.12: Temperature measurements at each probe insertion position, denoted by P1, P2, P3 and P4, as a function of time after turning off the fans and heater, through r = 0-190mm, where r = 0 denotes the vessel centre. T_u = 360K. P_i = 0.1 MPa.

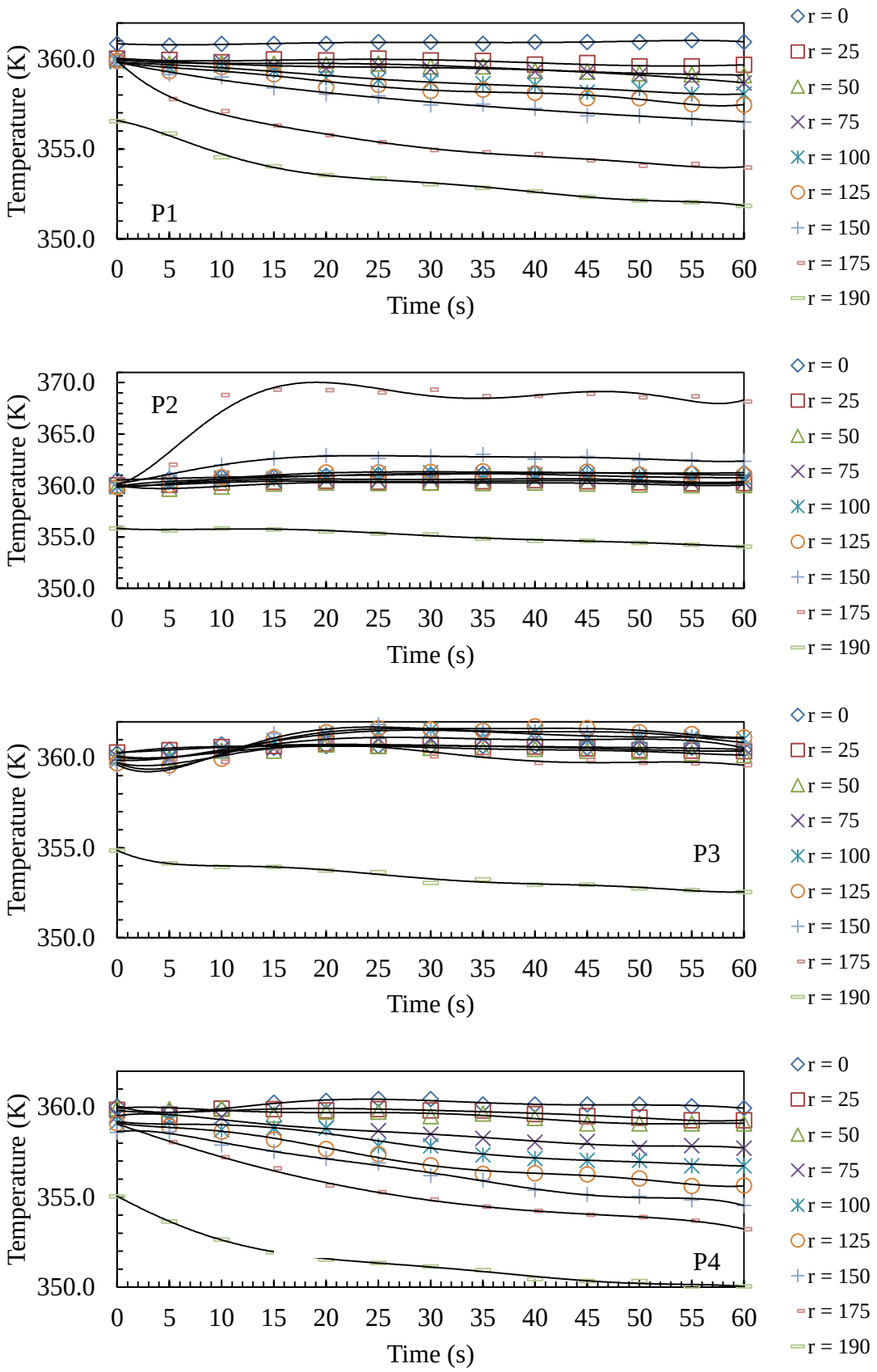

Figure 3.13: Temperature measurements at each probe insertion position, denoted by P1, P2, P3 and P4, as a function of time after turning off the fans and heater, through r = 0-190mm, where r = 0 denotes the vessel centre. T_u = 360K. P_i = 0.5 MPa.

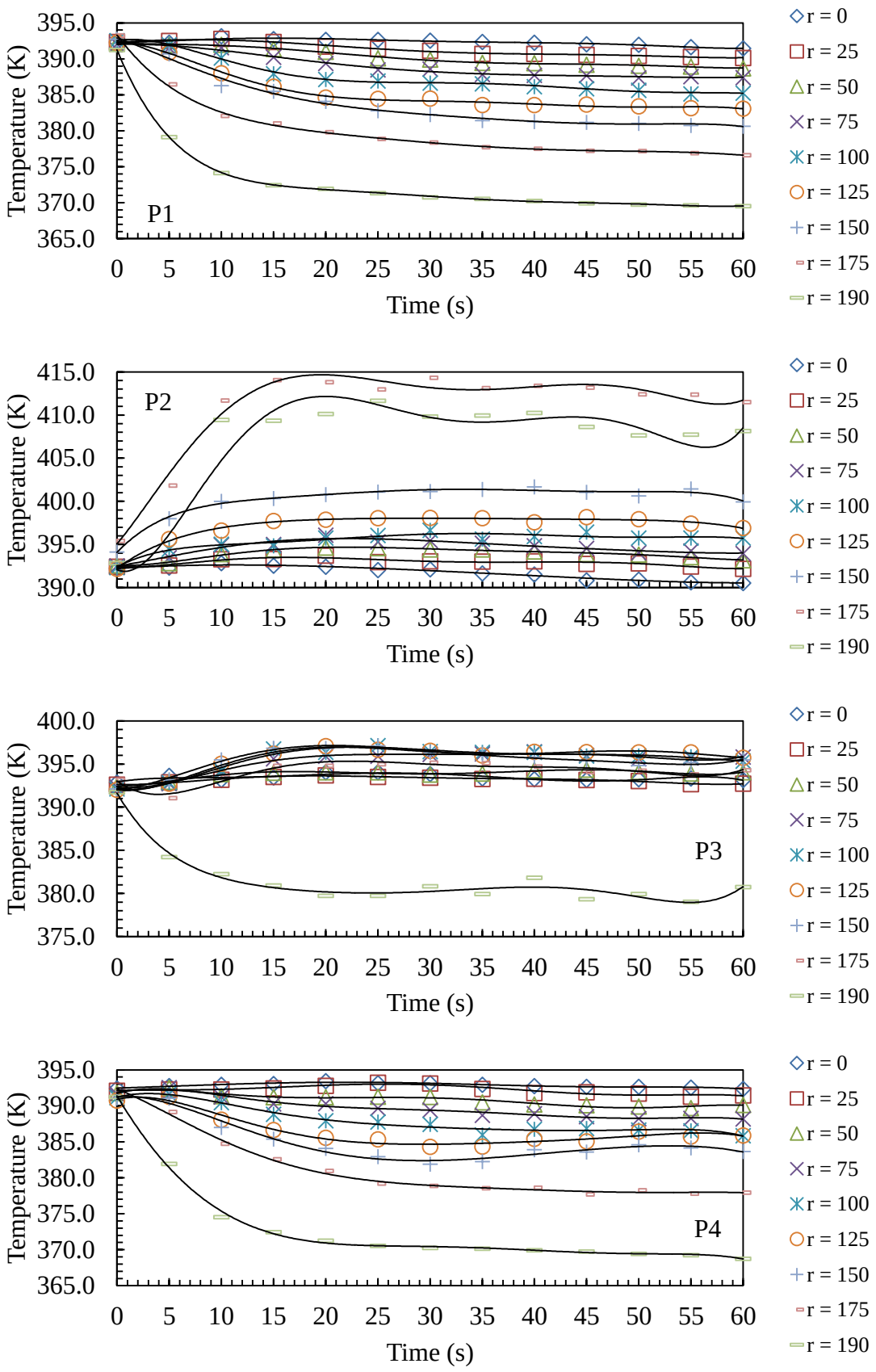

Figure 3.14: Temperature measurements at each probe insertion position, denoted by P1, P2, P3 and P4, as a function of time after turning off the fans and heater, through r = 0-190mm, where r = 0 denotes the vessel centre. T_u = 393K. P_i = 0.1 MPa.

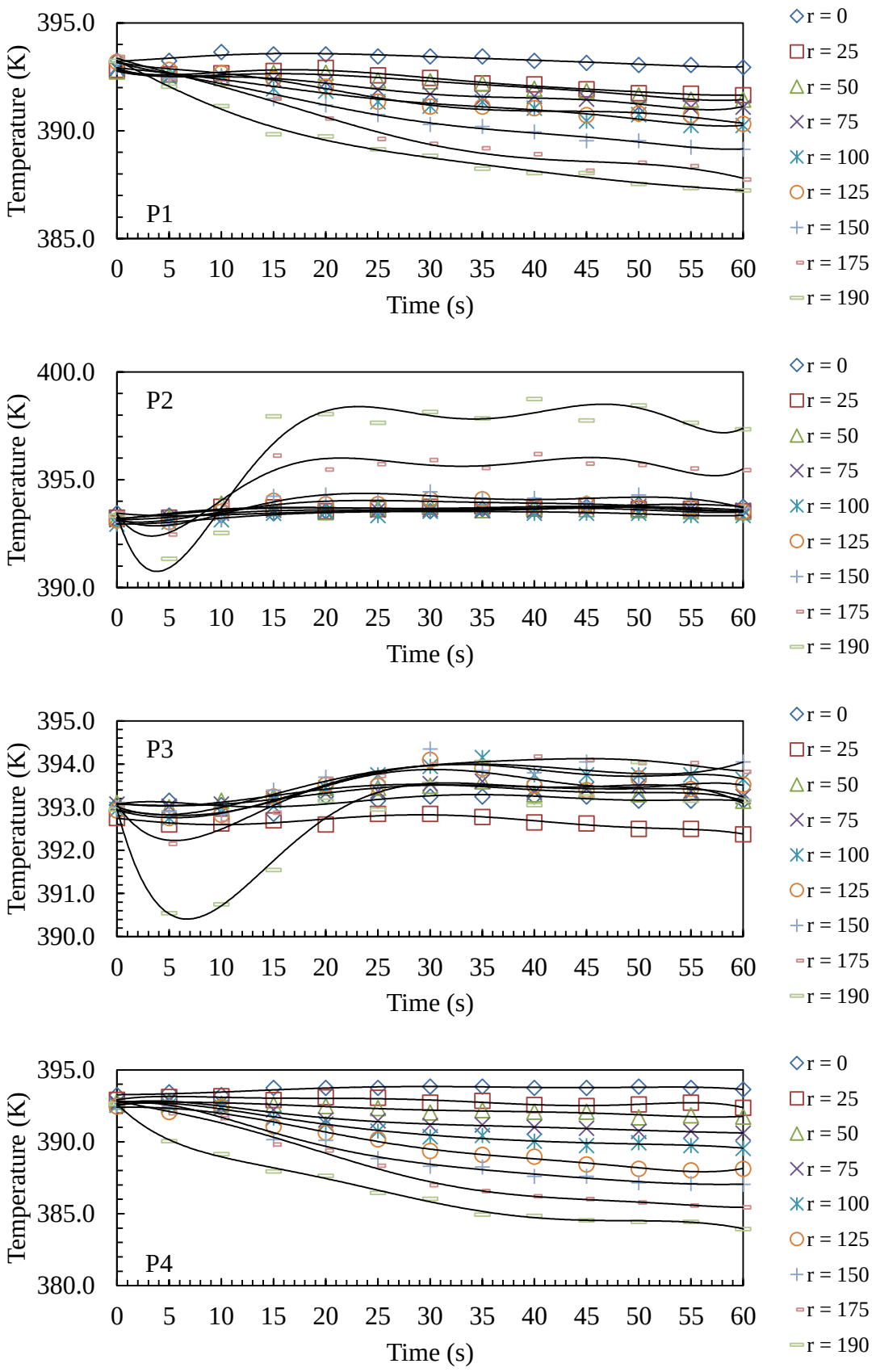

Figure 3.15: Temperature measurements at each probe insertion position, denoted by P1, P2, P3 and P4, as a function of time after turning off the fans and heater, through r = 0-190mm, where r = 0 denotes the vessel centre. T_u = 393K. P_i = 0.5 MPa.

In summary, Fig. 3.16 shows the average temperature measurements from all positions relative to the time after switching off the fans, at each condition. It can be seen that the overall temperature uniformity of the air within the vessel improved by the elevated initial pressure of 0.5 MPa for both initial temperatures of 360K and 393K. This increased stability at higher pressure was likely due to the increased density and thus thermal mass within the vessel. In contrast, deterioration of temperature uniformity occurred when increasing the initial temperature to 393K for both initial pressures of 0.1 and 0.5 MPa. This was most likely due to increased heat transfer rates associated with the higher temperature differentials, the effects of which were exasperated at larger radii. However, the critical radius of interest was that of the windows in which flame front images were used, r = 75mm.

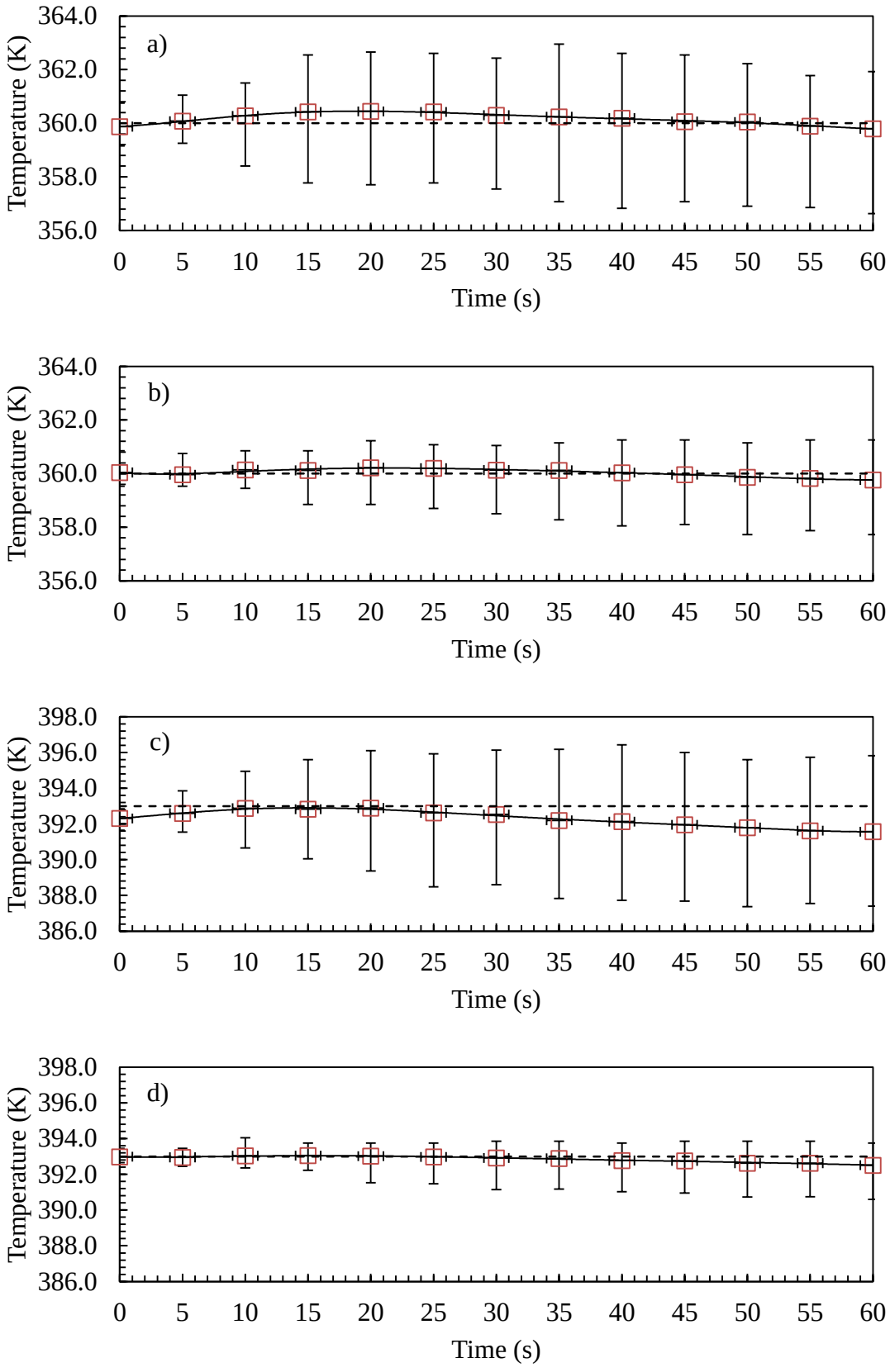

Figure 3.16: Symbols denote the average temperature measurement for all positions within r = 75mm, at a) 360K and 0.1 MPa, b) 360K and 0.5 MPa, c) 393K and 0.1 MPa, d) 393K and 0.5 MPa. Dashed lines and error bars indicate target temperatures and the minimum and maximum recorded temperatures respectively.

Temperature uniformity within this radius was significantly better for all conditions. Table 3.2 below summarises the average measured temperature for each condition, with the maximum positive and negative temperature deviations from the target temperature, T_u, , within the core region of r = 75mm and typical required time prior to ignition, after switching off the fans, t = 15s.

P_i (MPa)	T_u (K)	Average Measured Temp. within r = 75mm, t = 15s. (K)	Max. Positive Temp. Deviation from T_u (K)	Max. Negative Temp. Deviation From T_u (K)
0.1	360	360.4	2.6	2.2
0.5	360	360.1	0.9	1.1
0.1	393	392.8	2.6	2.9
0.5	393	393	0.8	0.8

Table 3.2: Summary of average temperature measurements and the maximum positive and negative temperature deviations from T_u within r = 75mm, t = 15s.

With the exception of the u_l vs. T_u benchmarking experiments discussed below, all u_l experiments within the present work were fixed at T_u = 360K. However, P_i was varied: 0.1, 0.5 and 1.0 MPa. The vessel gas temperature uniformity analysis has showed an increase in P_i improves temperature uniformity, hence the condition of T_u = 360K and P_i = 1.0 MPa was assumed to be well within acceptable tolerances.

As a benchmark, a further series of experiments was then carried out to examine the effect of T_u on the u_l of stoichiometric *iso*-octane at 0.1 MPa, from 300K to 400K in 10K intervals. Figure 3.17 shows the variation of measured u_l values as a function of T_u, indicating an approximate linear relationship equating to 0.002m/s/K.

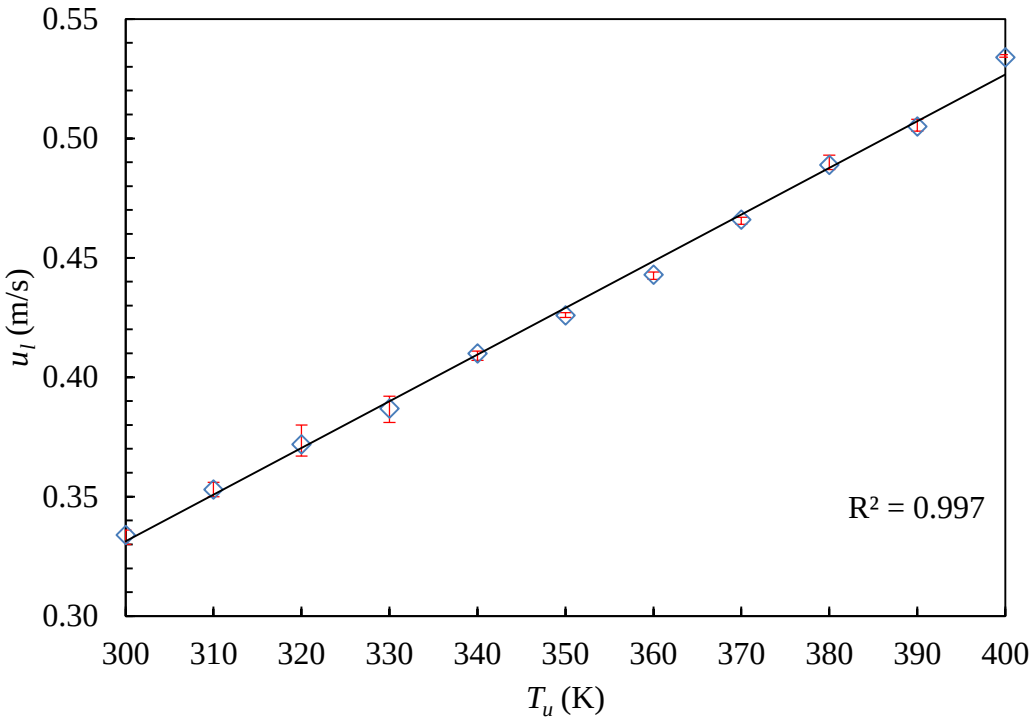

Figure 3.17: Variation of u_l with T_u for stoichiometric *iso*-octane/air mixtures. Each symbol denotes the average of three experiments, with the accompanying red error bars indicating the minimum and maximum values.

3.5.2 Air Supply System Upgrade

The combustion laboratory offered three sources of air for experimentation purposes: BOC dried cylinder air at 20 bar, filtered compressor air at 7 bar and filtered compressor air via the new automated desiccant dryer at 7 bar. The need for consistent high quality dry air is imperative for high fidelity experimentation, particularly when dealing with such notoriously hygroscopic fuels as ethanol. The use of compressor air via the desiccant dryer to flush, purge and fill the combustion vessel at low initial pressures, sparing the BOC dried cylinder air for higher pressure work was most pragmatic. However, to ensure such a method was sufficient in minimising water vapour in air to the point of negligible effect on u_l values, a series of experiments were performed using the most hygroscopic fuel in the study, ethanol, to quantify any changes in u_l between the sole uses of the different air sources.

Figure 3.18 shows u_l measurements of stoichiometric mixtures of ethanol with each air source, each condition was repeated three times. There was negligible difference between the use of cylinder air and filtered compressor air via the desiccant dryer, however, the use of just filtered compressor air has a notable lowering effect on the

measured u_l values. This air source was anticipated to contain the most water vapour out of the three available, and its consistent lowering effect on ethanol's u_l serves as an indication that only cylinder air or compressor air via the desiccant dryer are sufficient for consistent high fidelity u_l ethanol measurements.

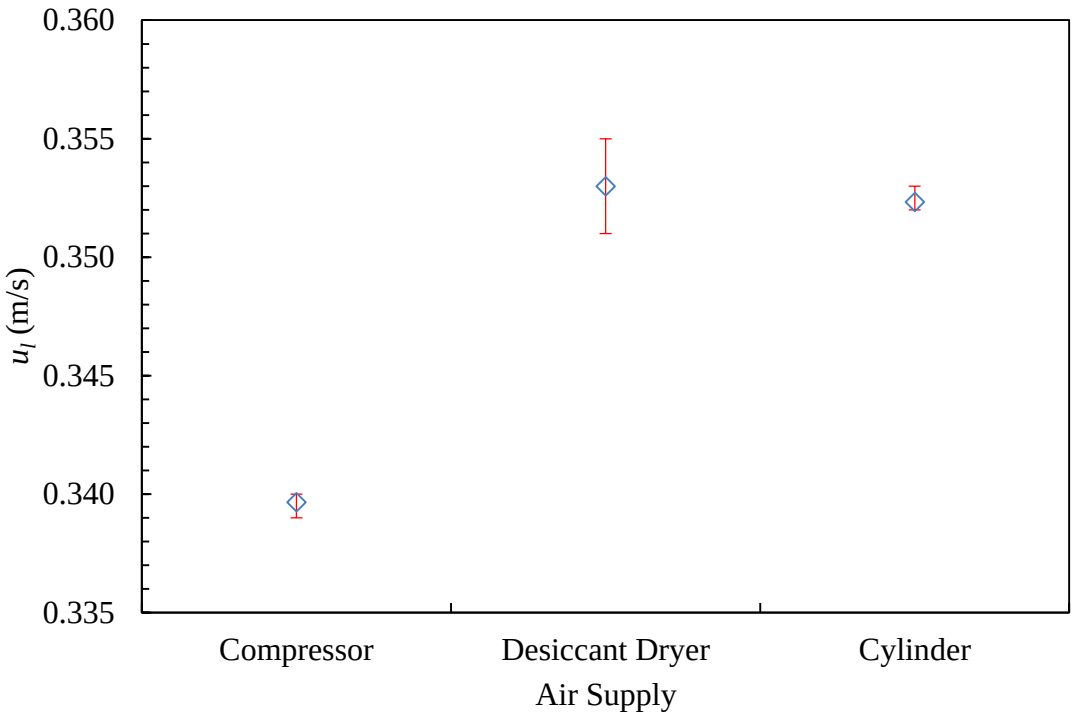

Figure 3.18: Variation of u_l with different air supplies for stoichiometric ethanol/air mixtures. Each symbol denotes the average of three experiments, with the accompanying red error bars indicating the minimum and maximum value.

Chapter 4 - Experimental Laminar Burning Velocity and Markstein Length Measurements of Pure Fuel/Air Mixtures and Blends

4.1 Introduction

This Chapter presents measured values of laminar burning velocities and their associated Markstein lengths for all the pure liquid hydrocarbon fuel/air mixtures and their blends, using the numerical and experimental techniques outlined in Chapters 1 and 3. Also presented are existing laminar burning velocities and Markstein lengths for methane/air, hydrogen/air and their blends measured by other researchers. The liquid hydrocarbon pure fuels and their related blend behaviour are considered over equivalence ratios from 0.8 to 1.3, at pressures of 0.1, 0.5 and 1.0 MPa at 360K. For methane/air and hydrogen/air blends the equivalence ratio ranged from 0.6 to 1.3, at 0.1 MPa and 303K.

The liquid hydrocarbon fuel blends are classified into two groups comprising binary equimolar blends and toluene reference fuel (TRF) blends. The latter allows examination of blending law performance on a 'blends of blends' basis and the comparative effects of ethanol and *n*-butanol addition to a TRF. The laminar burning velocities and Markstein lengths for the pure liquid fuel/air mixtures are presented first in Section 4.2 and their binary equimolar and TRF/Alcohol blends in Sections 4.3 and 4.4. Finally, the laminar burning velocities and Markstein lengths for methane/air and hydrogen/air and their blends are presented in Section 4.5.

Subsequent discussions from the experimental data within this Chapter are presented in Chapter 5. An evaluation of the predictive performance of the different blending laws outlined in Chapter 2, is given in Chapter 6, by comparing the predicted values with the experimental values of this Chapter.

4.2 Pure Liquid Hydrocarbon Fuels

The pure liquid hydrocarbon fuels are listed in Table 4.1 and were selected as representatives of the major fuel groups of alkanes, alkenes, aromatics and alcohols, typically found within modern day commercial gasoline fuels. Their chemically

dissimilar compositions facilitate identification of any unique traits of a particular fuel group, which may be of significant interest to those concerned with commercial fuel blending.

Fuel	*iso*-Octane	*n*-Heptane	Toluene	*1*-Hexene	Ethanol	*n*-Butanol
Composition	C_8H_{18}	C_7H_{16}	C_7H_8	C_6H_{12}	C_2H_5OH	C_4H_9OH
M_w	114.26	100.23	92.15	84.18	46.08	74.14
ρ @ 298.15K	0.6919	0.683	0.867	0.678	0.7897	0.810
Supplier	Fisher Scientific	Fisher Scientific	Fisher Scientific	Sigma-Aldrich	Fisher Scientific	Fisher Scientific

Table 4.1: List of all pure liquid hydrocarbon based fuels studied and their basic properties.

Figures 4.1-4.18 show the measured stretched laminar flame speed, S_n, variation with stretch rate, α, and corresponding S_n variation with r, for all the pure liquid fuel/air mixtures, at P_i = 0.1, 0.5, across ϕ = 0.8-1.3, and 1.0 MPa, across ϕ = 0.8-1.0. As discussed in Chapters 1 and 3, all u_l measurements employed both linear and nonlinear flame speed/stretch rate extrapolation methodologies, in the measurement of L_b, within the stable regime of the flame. The solid red and blue lines indicate the linear and nonlinear stable regimes in which data points were used, and the corresponding dashed lines indicate their extrapolation to zero stretch rate. At P_i = 0.1 MPa, where ϕ = 0.8-1.2, distinct nonlinearity for all pure fuel/air mixtures was observed, particularly for *iso*-octane/air mixtures, the slowest burning fuel/air mixtures studied here. In such cases, the linear approach consistently yielded higher values of L_b and subsequently u_l, with the difference decreasing with ϕ. In contrast, at P_i = 0.5 and 1.0 MPa, linear behaviour was dominant for all fuel/air mixtures across the full equivalence ratio range, with negligible differences between the linear and nonlinear approaches, with any differences being within the margin of experimental error.

In all cases, as both pressure and equivalence ratio increase, the stable regime in which L_b can accurately be measured becomes increasingly limited, between the minimum unaffected spark radius of r = 10 mm and the onset of cellularity, at the critical radius, r_c, as indicated by red crosses. As previously discussed in Chapter 1, r_c is defined as the radius above which, the flame speed sharply accelerates, deviating from the earlier

response to the stretch rate, due to the increasing rate of generation of surface area. At P_i = 0.1 MPa, with ϕ = 0.8-1.2, all pure fuel/air mixtures were observed to be stable. However under the richest condition where ϕ = 1.3, all became unstable at approximately r_c = 60 mm.

Figures 4.19a and b show the variation of r_c with ϕ for all pure fuel/air mixtures at 0.5 and 1.0 MPa. At this increased pressure, with the exception of *iso*-octane/air, *n*-heptane/air and ethanol/air mixtures, at P_i = 0.5 MPa and ϕ = 0.8, all pure fuel/air mixtures became unstable within the observable window radius of 75 mm. For ϕ = 1.1-1.3, at P_i = 1.0 MPa, the accurate measurement of L_b became impossible, as the stable range between the minimum unaffected spark radius and r_c was too narrow. This phenomenon was observed for all pure fuel/air mixtures, consequently limiting the accurate acquisition of u_l data at P_i = 1.0 MPa to ϕ = 0.8-1.0.

A low vapour pressure can also limit u_l data at the higher values of P_i and ϕ, where a completely gaseous mixture is unattainable. In the case of *n*-butanol/air mixture, the maximum ϕ at 1.0 MPa was limited to 0.9 at T_u = 360K. Beyond this, its required partial pressure would become higher than its vapour pressure, and vaporisation would be insufficient.

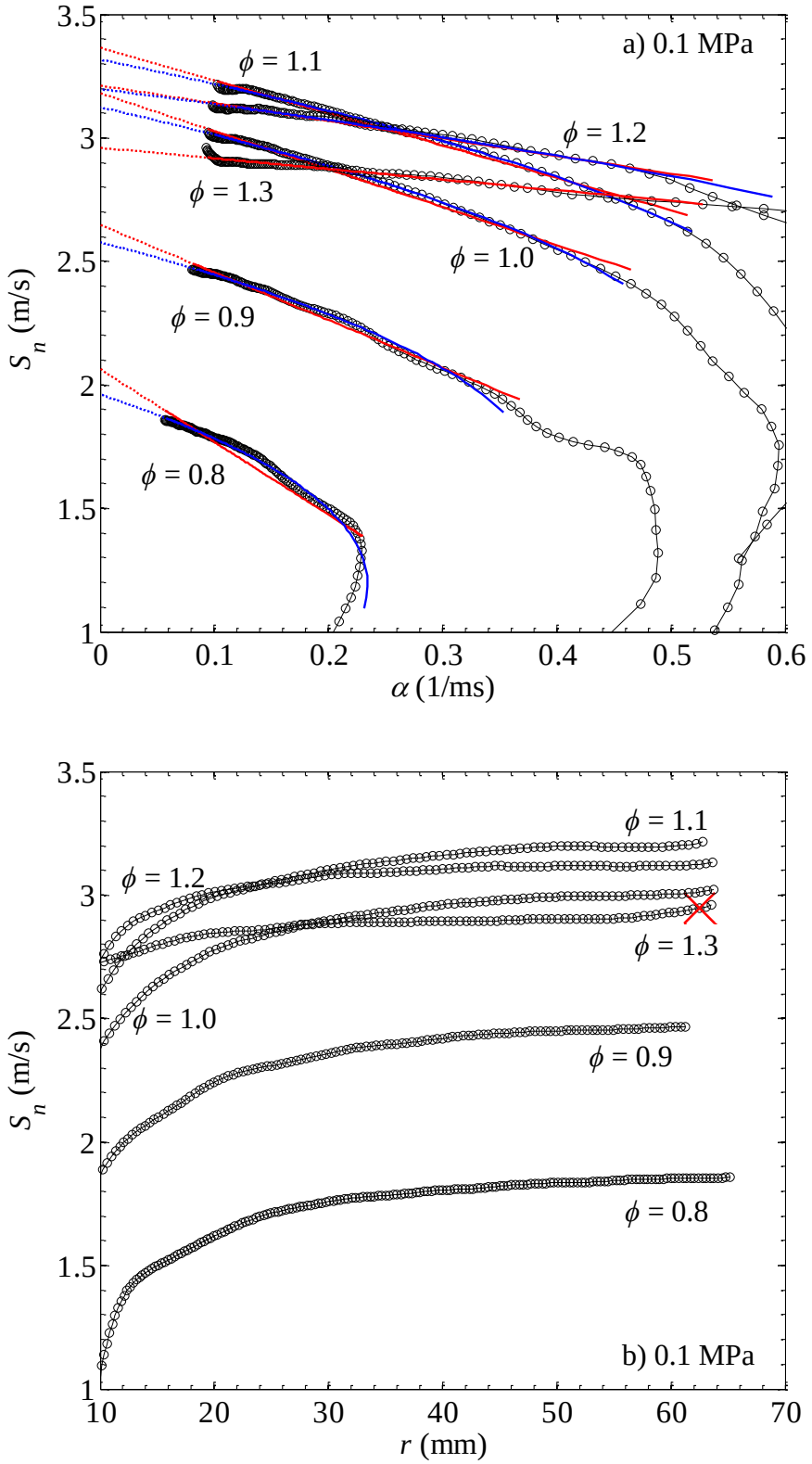

Figure 4.1: a) S_n variation with α, b) S_n variation with r, for *iso*-octane/air mixtures at P_i = 0.1 MPa, T_u = 360K and ϕ = 0.8-1.3. Solid red and blue lines denote linear and nonlinear relationships for L_b through data points, dashed lines indicate their extrapolation to zero stretch rate and red crosses indicate r_c.

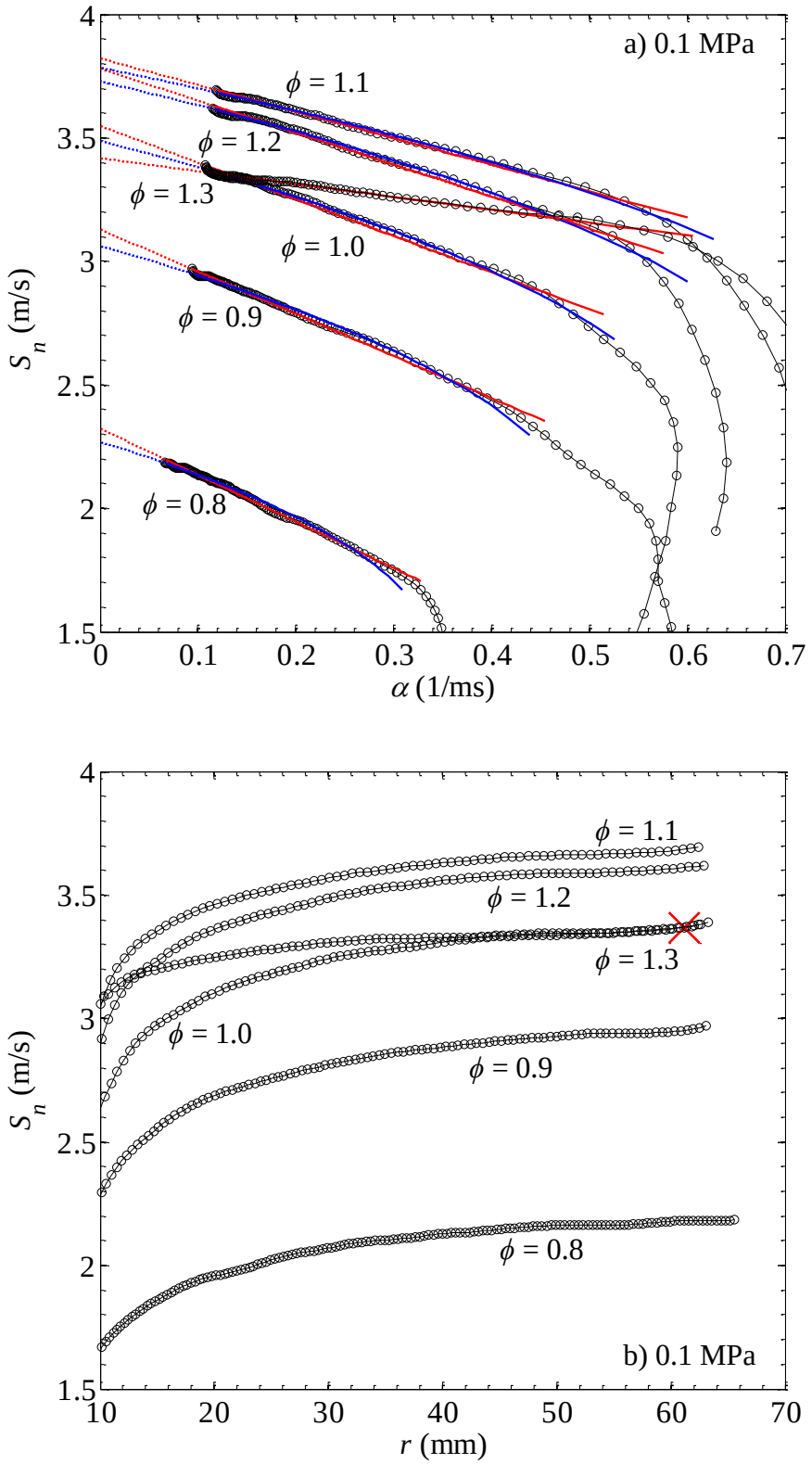

Figure 4.2: a) S_n variation with α, b) S_n variation with r, for n-heptane/air mixtures at P_i = 0.1 MPa, T_u = 360K and ϕ = 0.8-1.3. Solid red and blue lines denote linear and nonlinear relationships for L_b through data points, dashed lines indicate their extrapolation to zero stretch rate and red crosses indicate r_c.

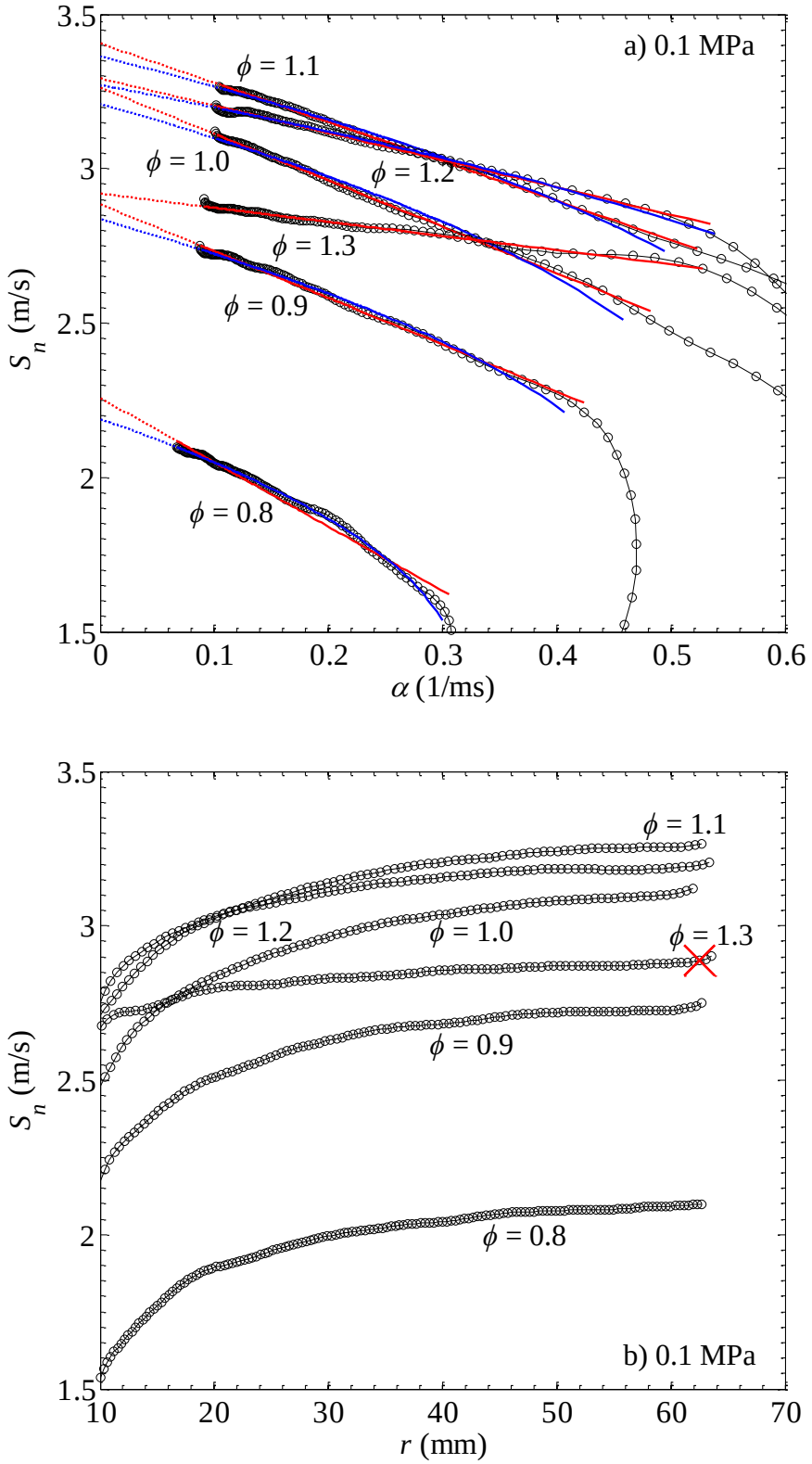

Figure 4.3: a) S_n variation with α, b) S_n variation with r, for toluene/air mixtures at P_i = 0.1 MPa, T_u = 360K and ϕ = 0.8-1.3. Solid red and blue lines denote linear and nonlinear relationships for L_b through data points, dashed lines indicate their extrapolation to zero stretch rate and red crosses indicate r_c.

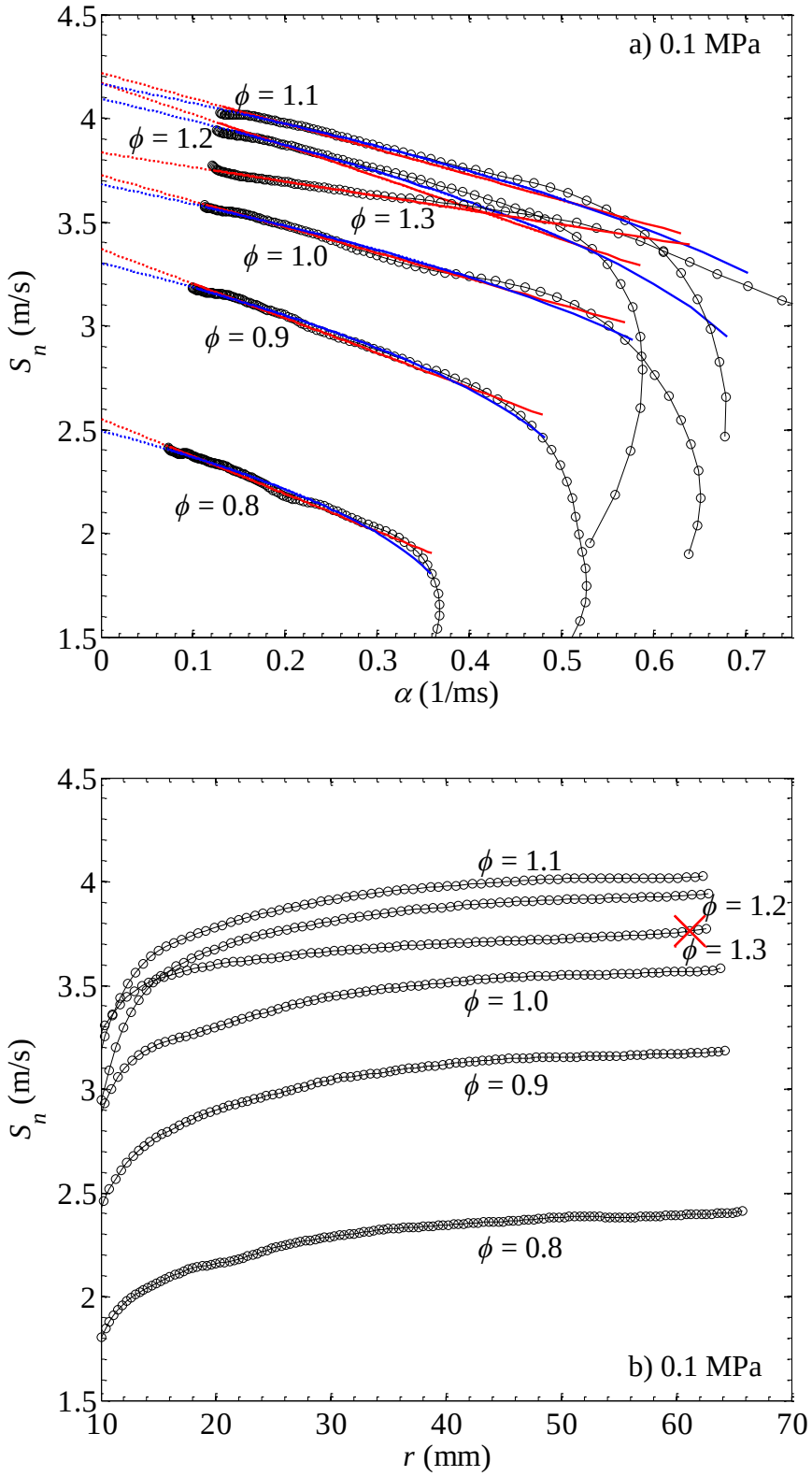

Figure 4.4: a) S_n variation with α, b) S_n variation with r, for *1*-hexene/air mixtures at P_i = 0.1 MPa, T_u = 360K and ϕ = 0.8-1.3. Solid red and blue lines denote linear and nonlinear relationships for L_b through data points, dashed lines indicate their extrapolation to zero stretch rate and red crosses indicate r_c.

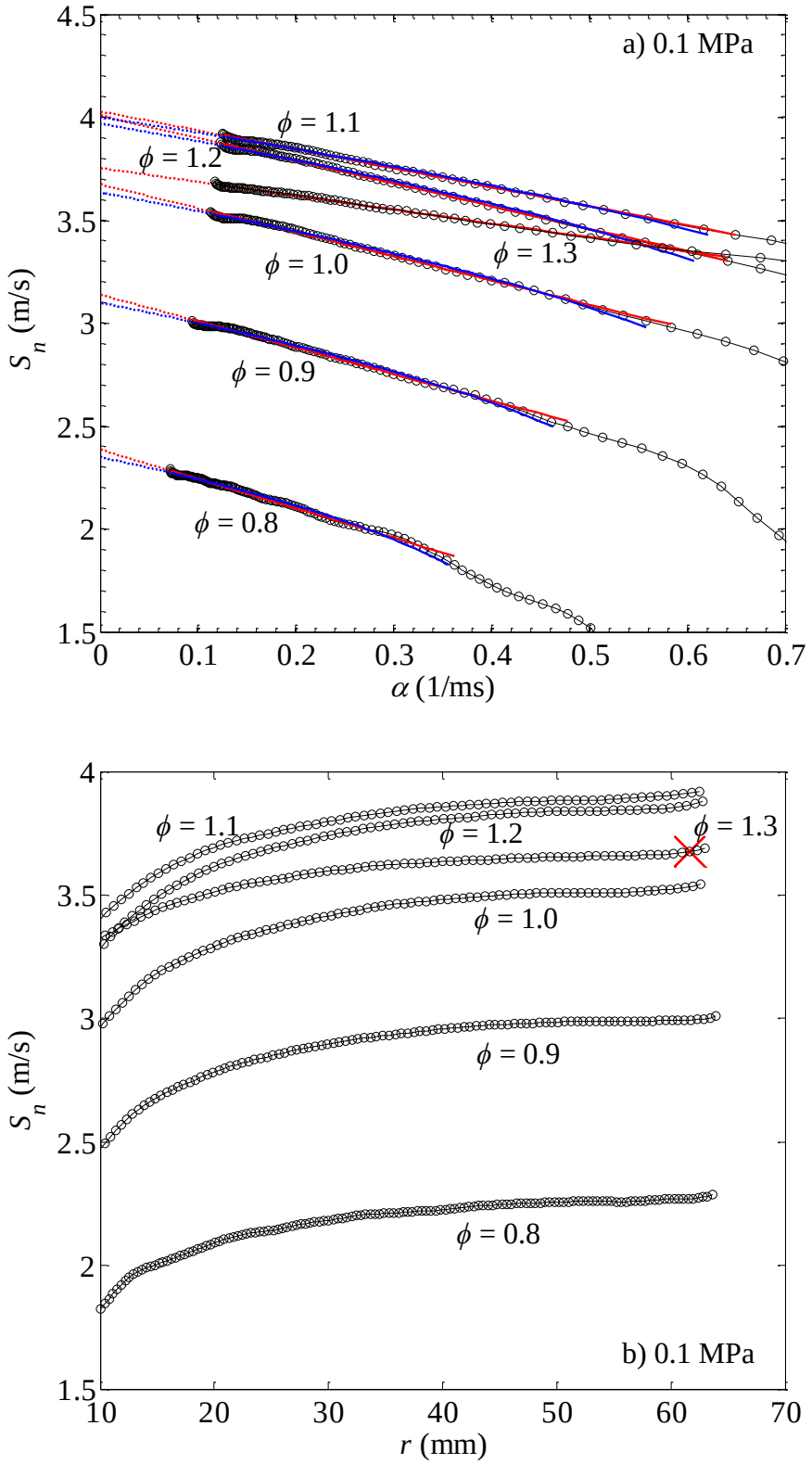

Figure 4.5: a) S_n variation with α, b) S_n variation with r, for ethanol/air mixtures at P_i = 0.1 MPa, T_u = 360K and ϕ = 0.8-1.3. Solid red and blue lines denote linear and nonlinear relationships for L_b through data points, dashed lines indicate their extrapolation to zero stretch rate and red crosses indicate r_c.

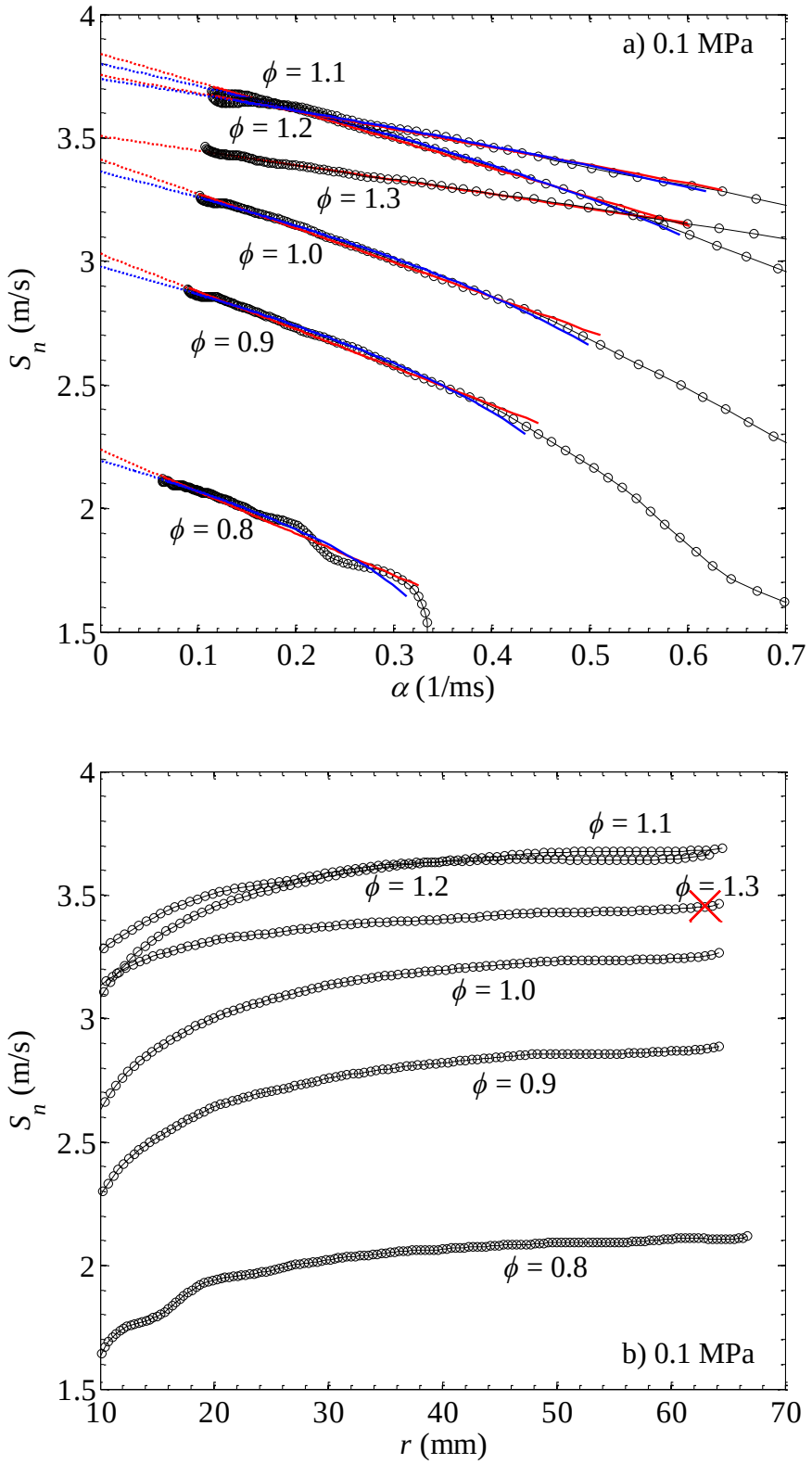

Figure 4.6: a) S_n variation with α, b) S_n variation with r, for n-butanol/air mixtures at P_i = 0.1 MPa, T_u = 360K and ϕ = 0.8-1.3. Solid red and blue lines denote linear and nonlinear relationships for L_b through data points, dashed lines indicate their extrapolation to zero stretch rate and red crosses indicate r_c.

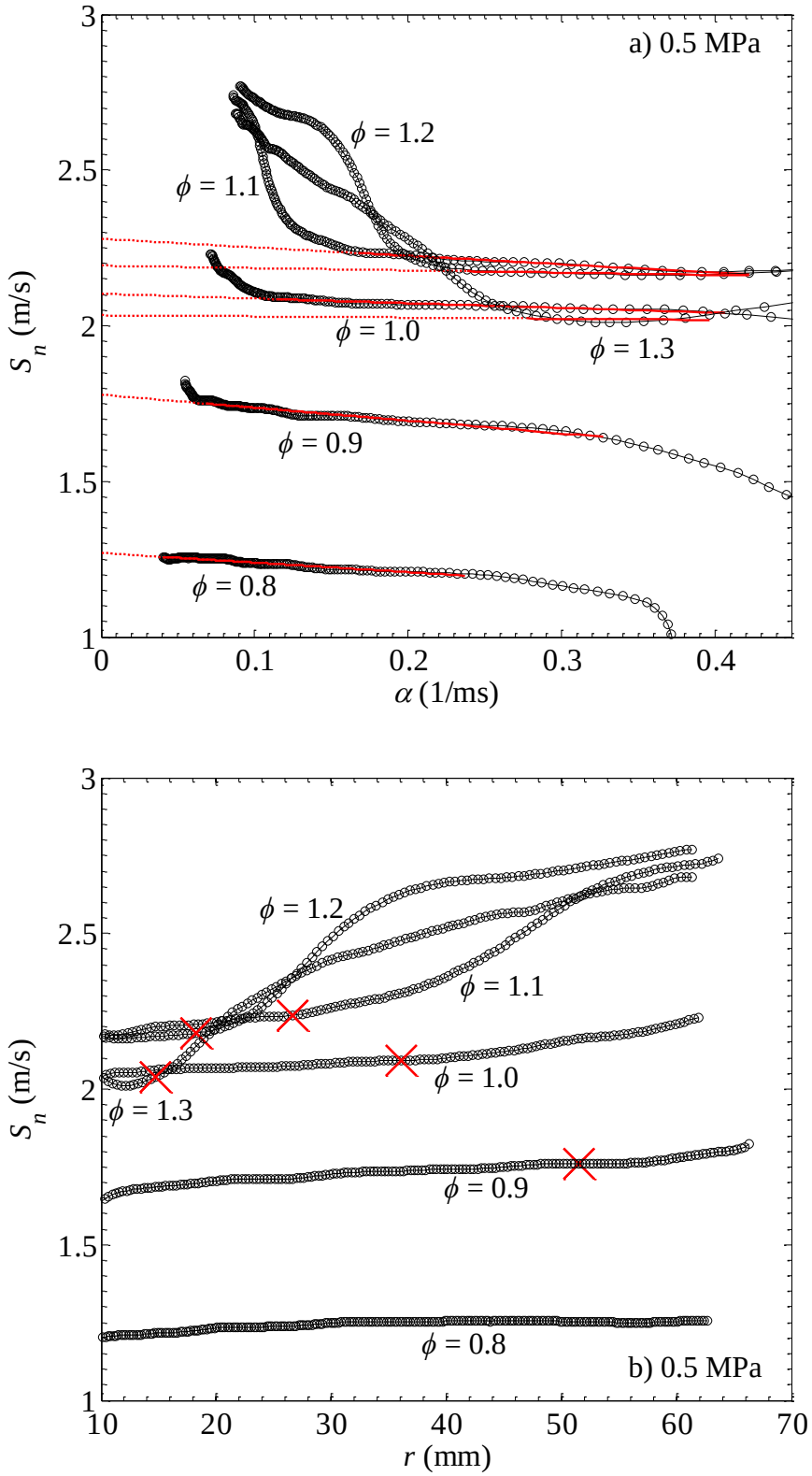

Figure 4.7: a) S_n variation with α, b) S_n variation with r, for *iso*-octane/air mixtures at P_i = 0.5 MPa, T_u = 360K and ϕ = 0.8-1.3. Solid red and blue lines denote linear and nonlinear relationships for L_b through data points, dashed lines indicate their extrapolation to zero stretch rate and red crosses indicate r_c.

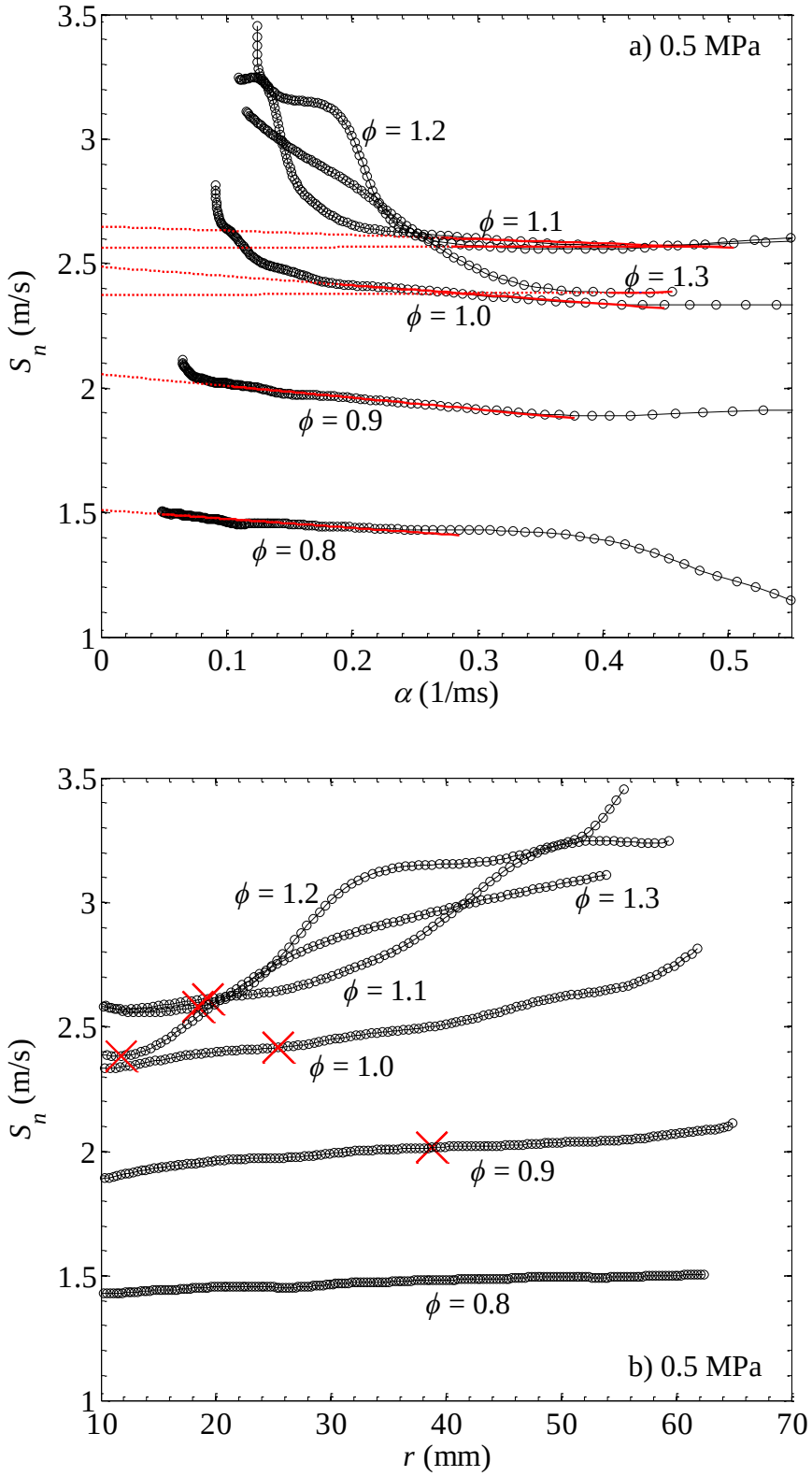

Figure 4.8: a) S_n variation with α, b) S_n variation with r, for n-heptane/air mixtures at P_i = 0.5 MPa, T_u = 360K and ϕ = 0.8-1.3. Solid red and blue lines denote linear and nonlinear relationships for L_b through data points, dashed lines indicate their extrapolation to zero stretch rate and red crosses indicate r_c.

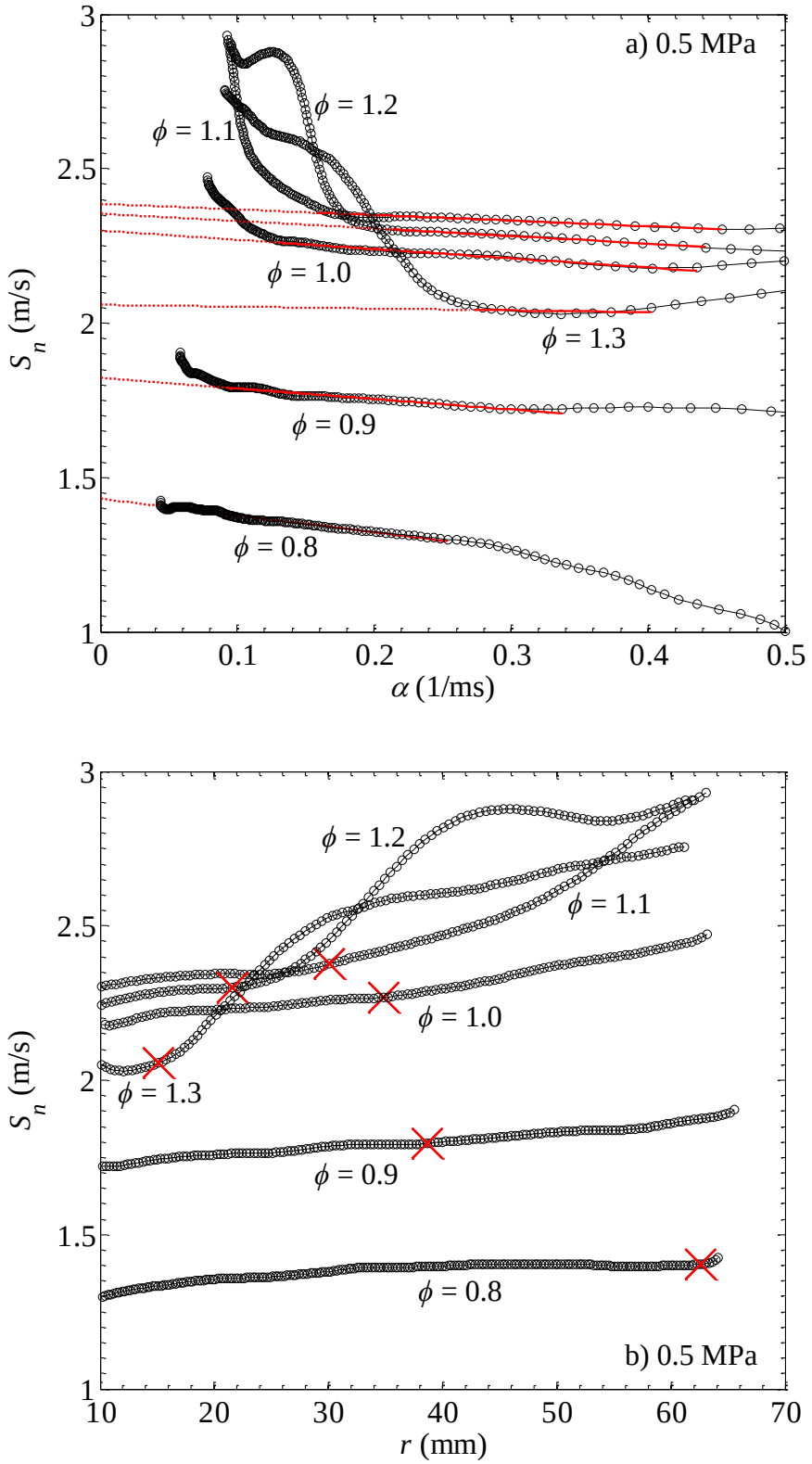

Figure 4.9: a) S_n variation with α, b) S_n variation with r, for toluene/air mixtures at P_i = 0.5 MPa, T_u = 360K and ϕ = 0.8-1.3. Solid red and blue lines denote linear and nonlinear relationships for L_b through data points, dashed lines indicate their extrapolation to zero stretch rate and red crosses indicate r_c.

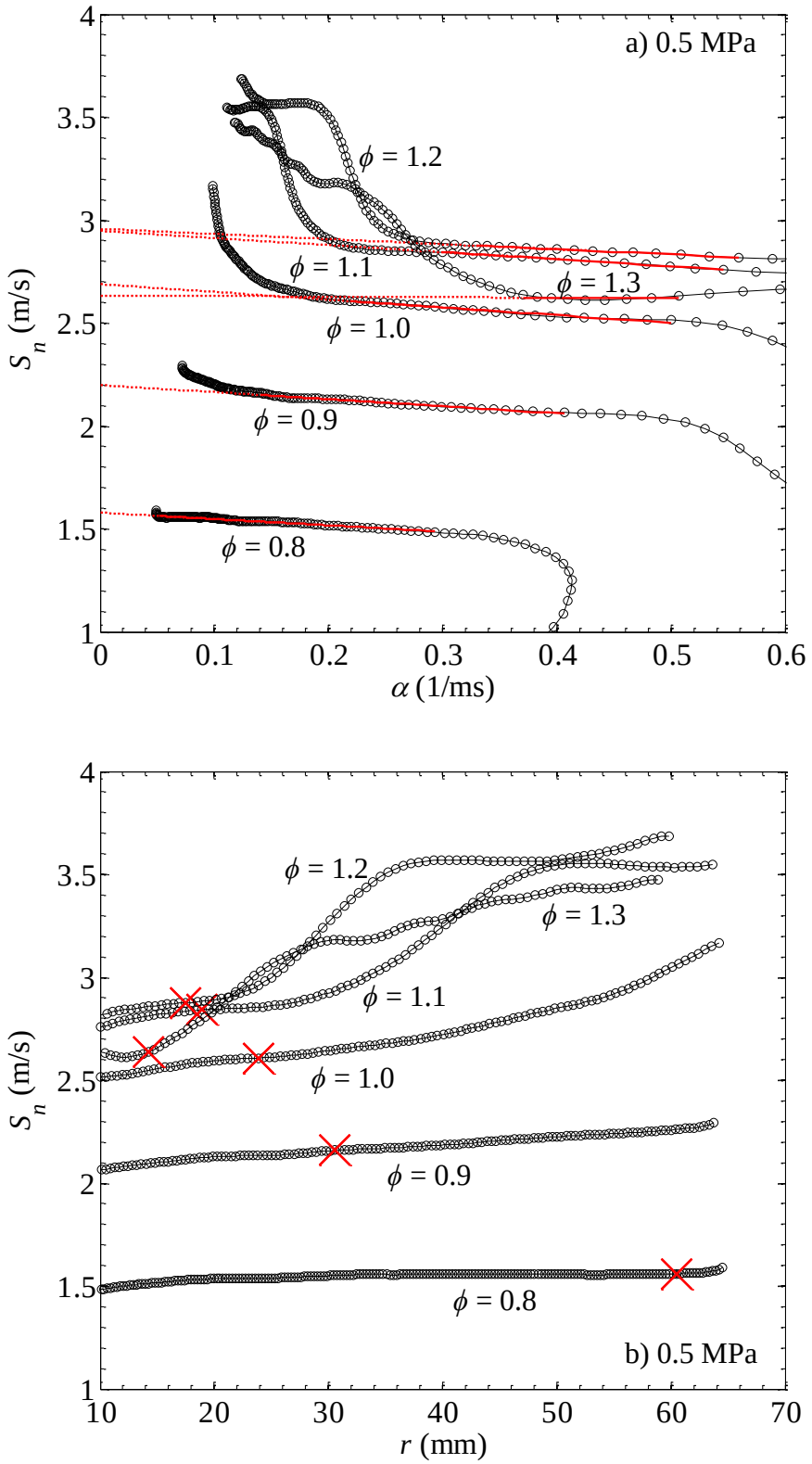

Figure 4.10: a) S_n variation with α, b) S_n variation with r, for *1*-hexene/air mixtures at P_i = 0.5 MPa, T_u = 360K and ϕ = 0.8-1.3. Solid red and blue lines denote linear and nonlinear relationships for L_b through data points, dashed lines indicate their extrapolation to zero stretch rate and red crosses indicate r_c.

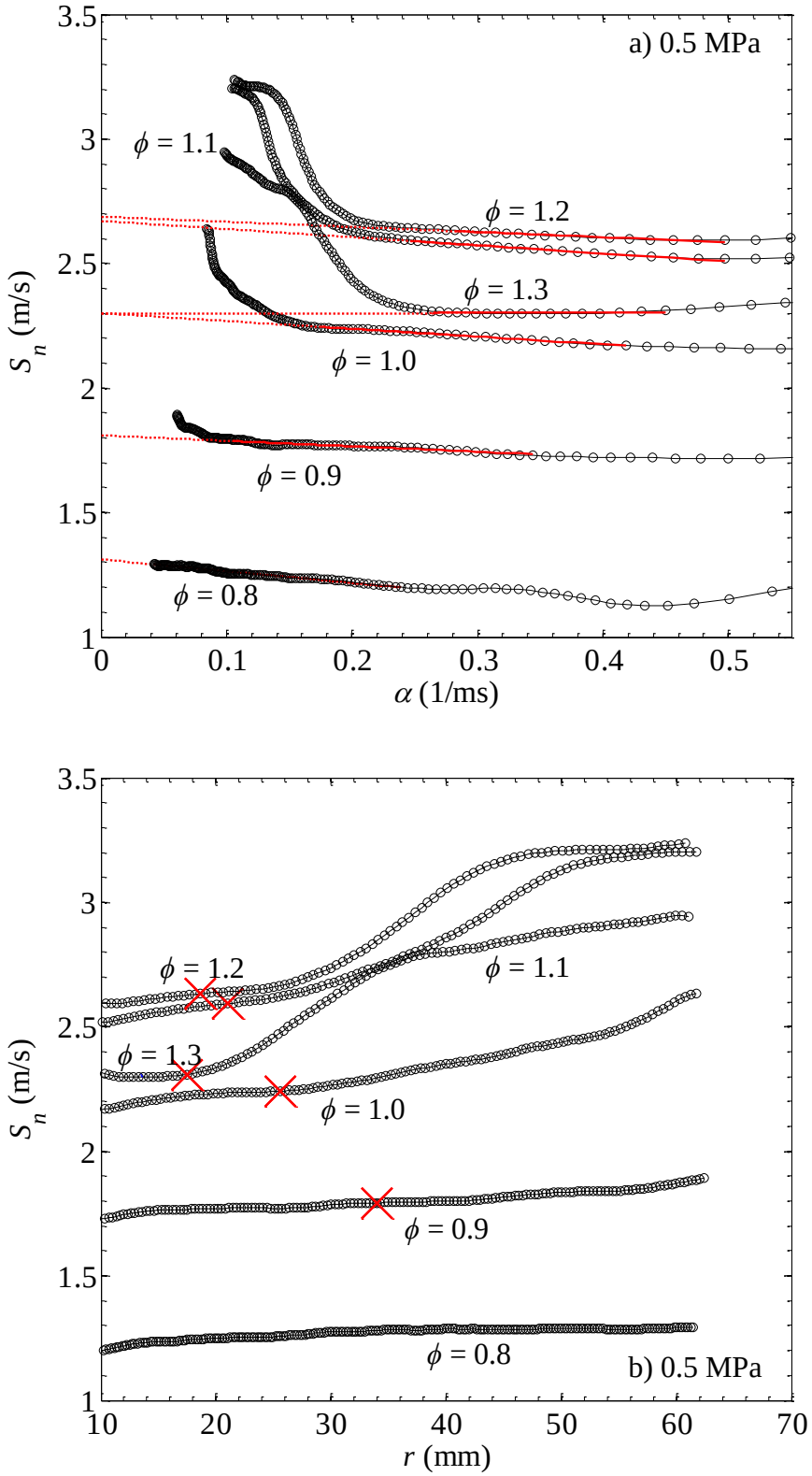

Figure 4.11: a) S_n variation with α, b) S_n variation with r, for ethanol/air mixtures at P_i = 0.5 MPa, T_u = 360K and ϕ = 0.8-1.3. Solid red and blue lines denote linear and nonlinear relationships for L_b through data points, dashed lines indicate their extrapolation to zero stretch rate and red crosses indicate r_c.

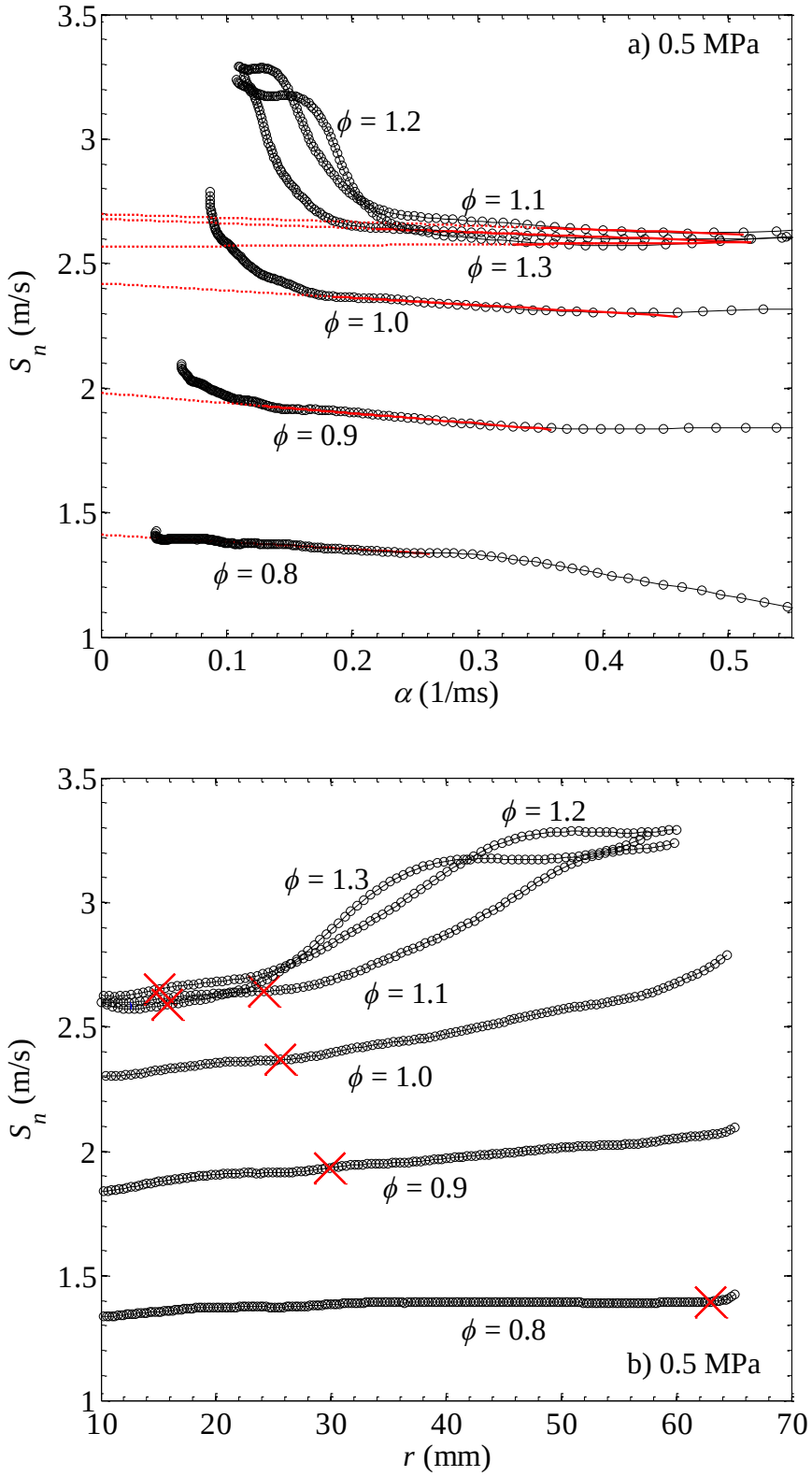

Figure 4.12: a) S_n variation with α, b) S_n variation with r, for n-butanol/air mixtures at P_i = 0.5 MPa, T_u = 360K and ϕ = 0.8-1.3. Solid red and blue lines denote linear and nonlinear relationships for L_b through data points, dashed lines indicate their extrapolation to zero stretch rate and red crosses indicate r_c.

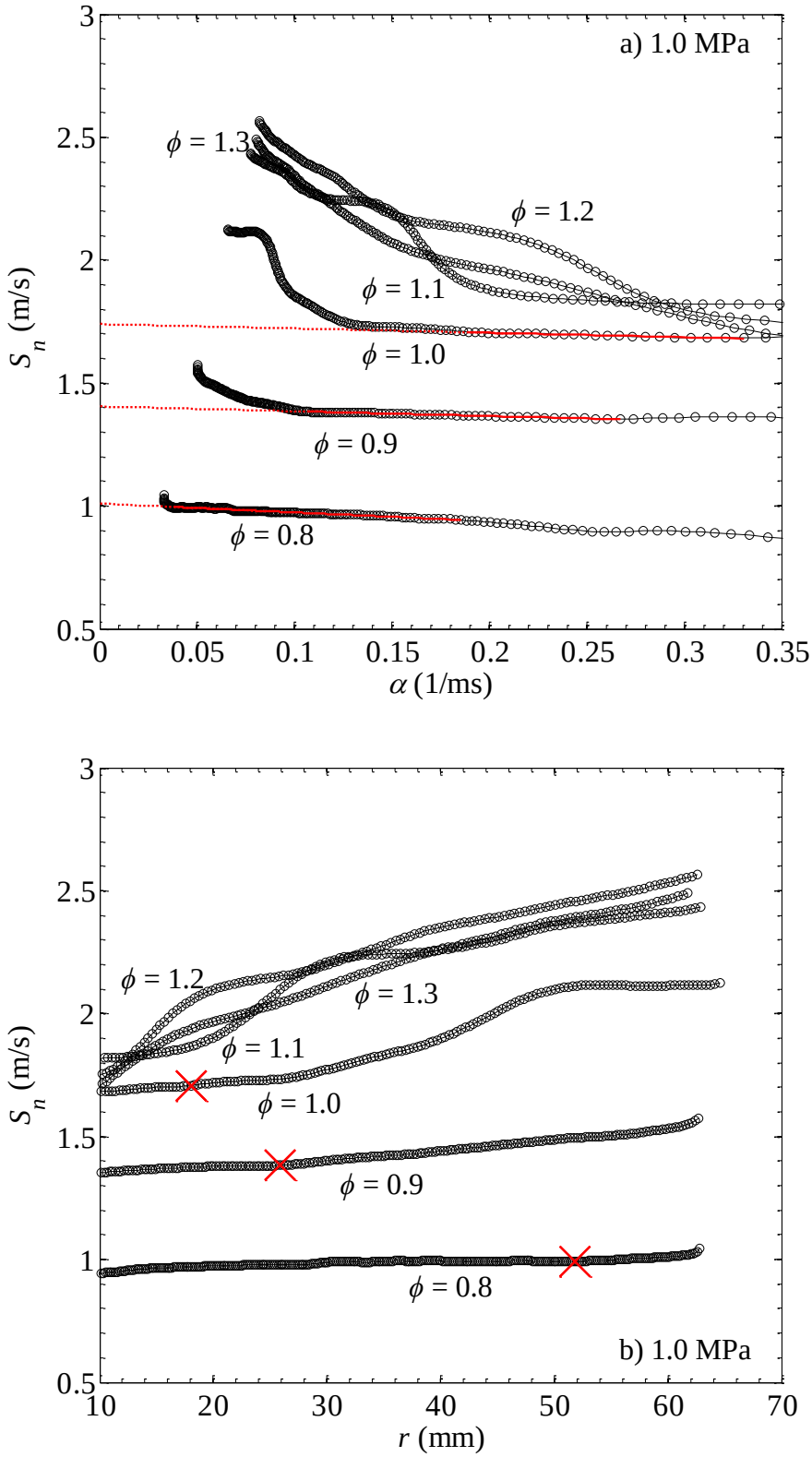

Figure 4.13: a) S_n variation with α, b) S_n variation with r, for *iso*-octane/air mixtures at P_i = 1.0 MPa, T_u = 360K and ϕ = 0.8-1.3. Solid red and blue lines denote linear and nonlinear relationships for L_b through data points, dashed lines indicate their extrapolation to zero stretch rate and red crosses indicate r_c.

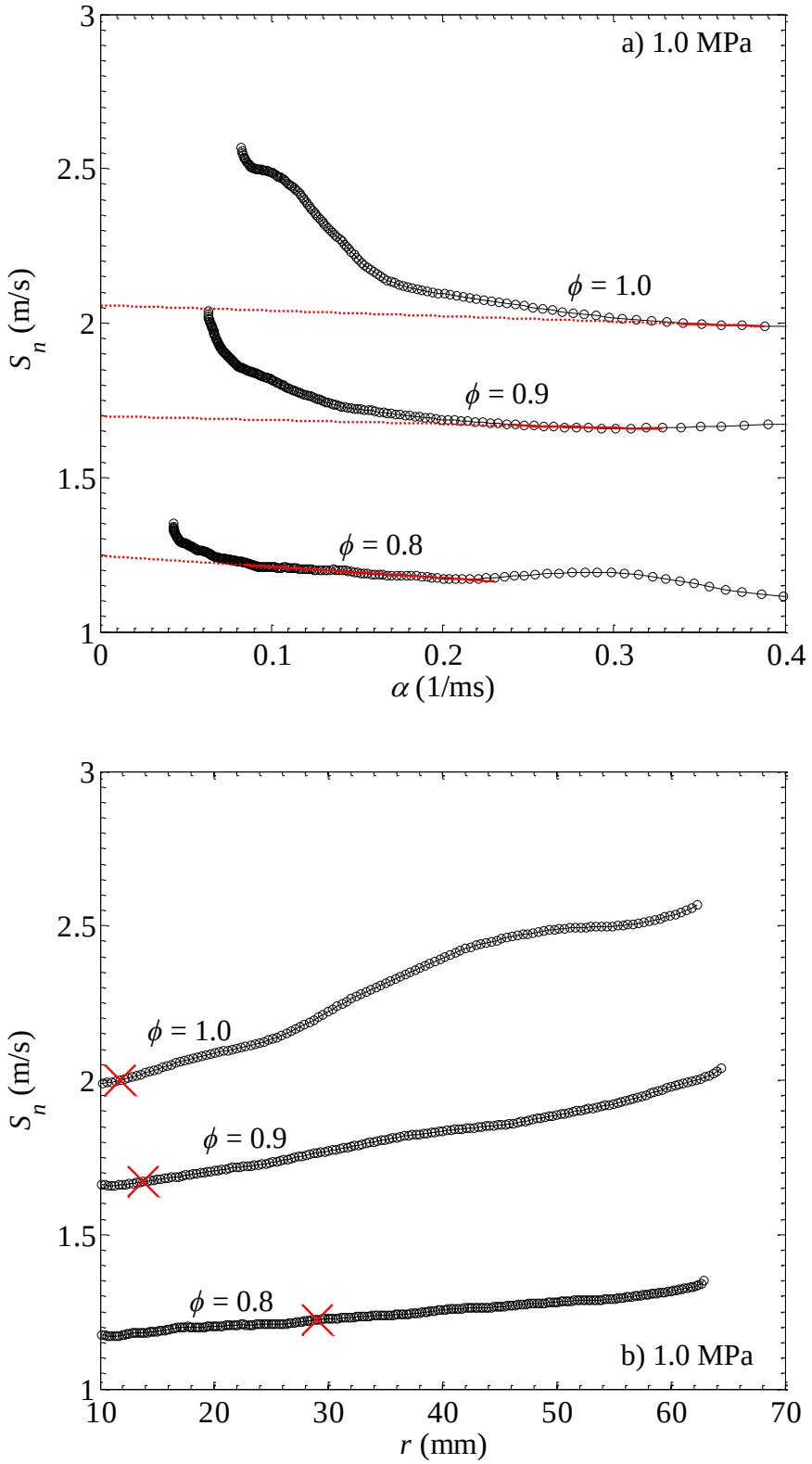

Figure 4.14: a) S_n variation with α, b) S_n variation with r, for n-heptane/air mixtures at P_i = 1.0 MPa, T_u = 360K and ϕ = 0.8-1.0. Solid red and blue lines denote linear and nonlinear relationships for L_b through data points, dashed lines indicate their extrapolation to zero stretch rate and red crosses indicate r_c.

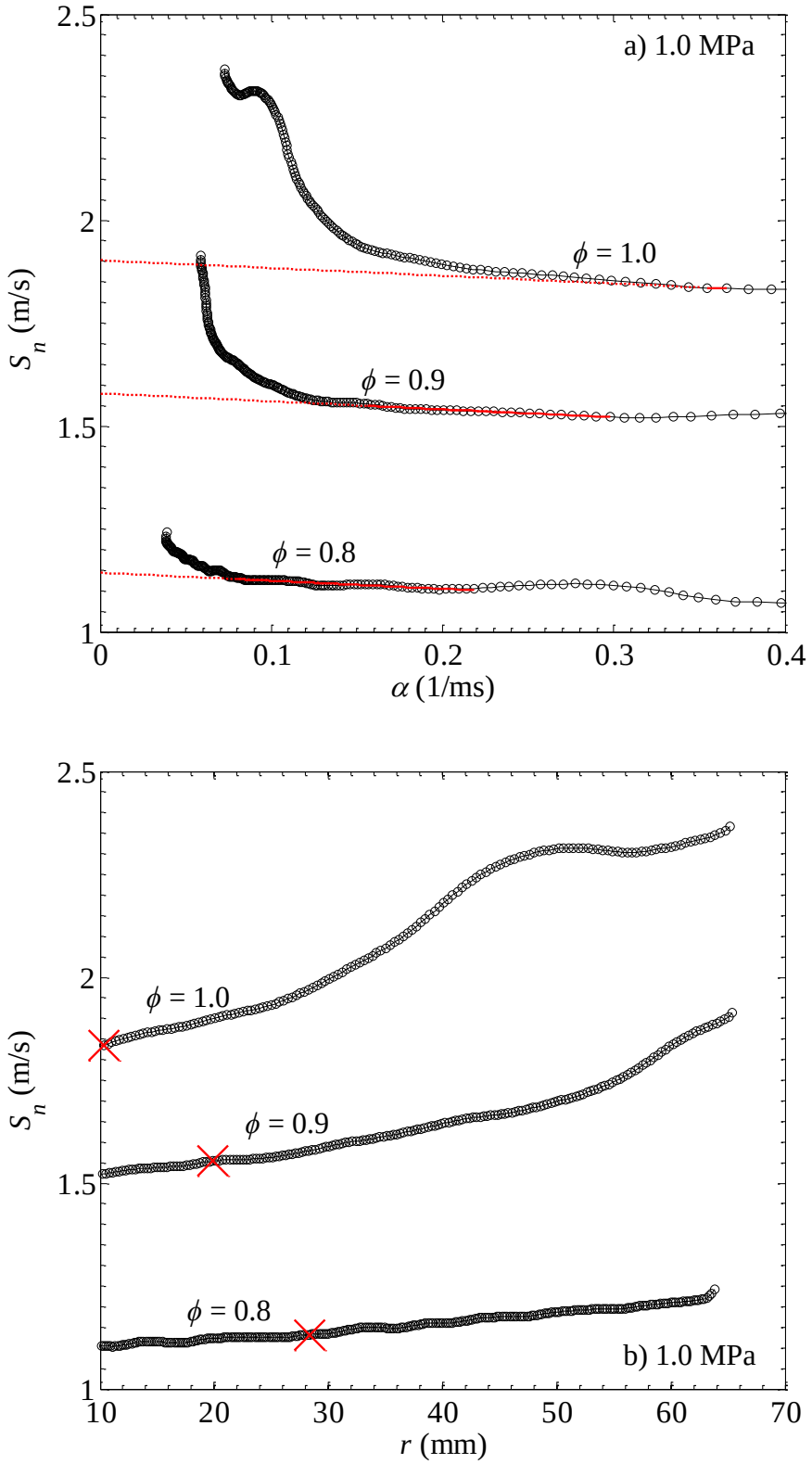

Figure 4.15: a) S_n variation with α, b) S_n variation with r, for toluene/air mixtures at P_i = 1.0 MPa, T_u = 360K and ϕ = 0.8-1.0. Solid red and blue lines denote linear and nonlinear relationships for L_b through data points, dashed lines indicate their extrapolation to zero stretch rate and red crosses indicate r_c.

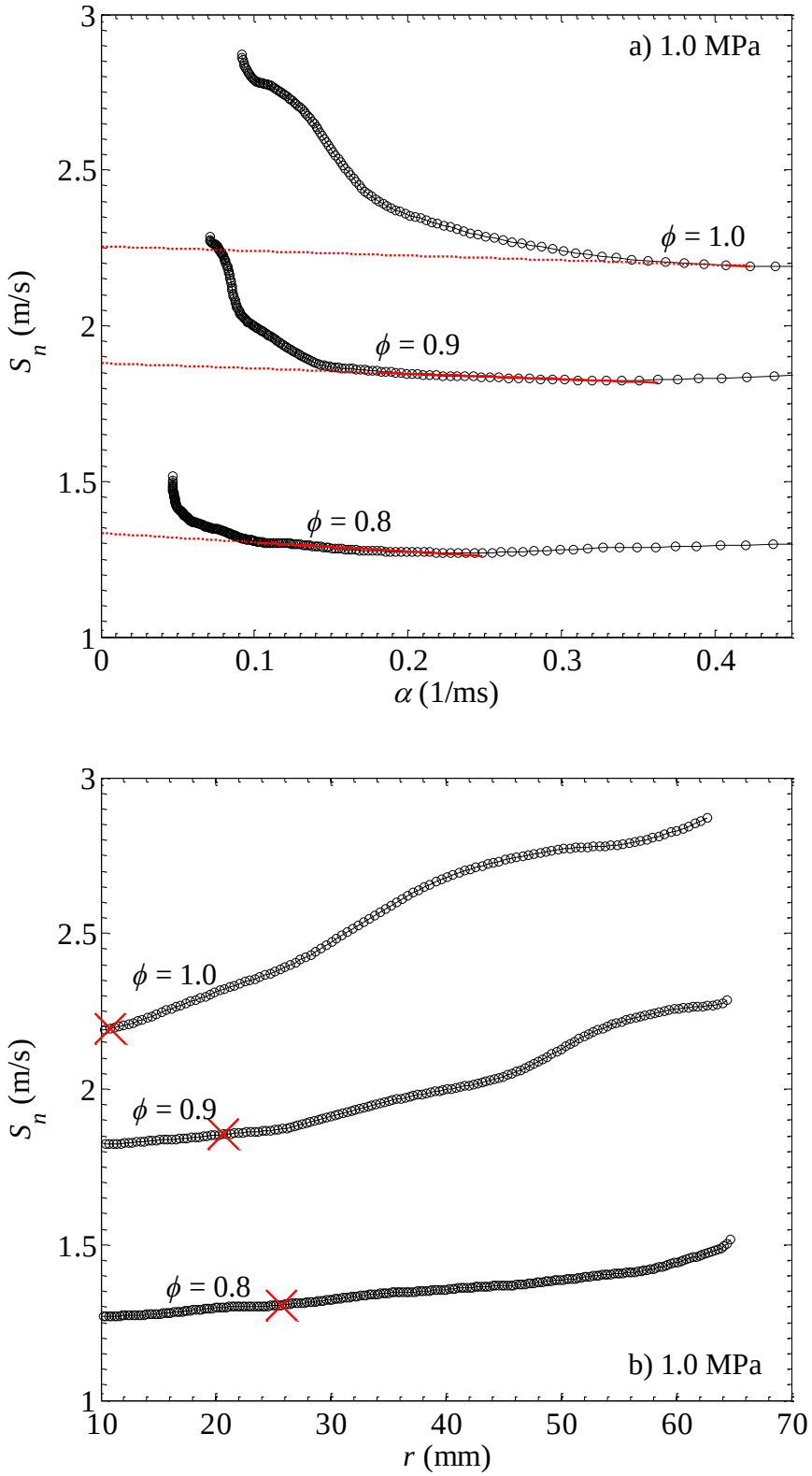

Figure 4.16: a) S_n variation with α, b) S_n variation with r, for *1*-hexene/air mixtures at P_i = 1.0 MPa, T_u = 360K and ϕ = 0.8-1.0. Solid red and blue lines denote linear and nonlinear relationships for L_b through data points, dashed lines indicate their extrapolation to zero stretch rate and red crosses indicate r_c.

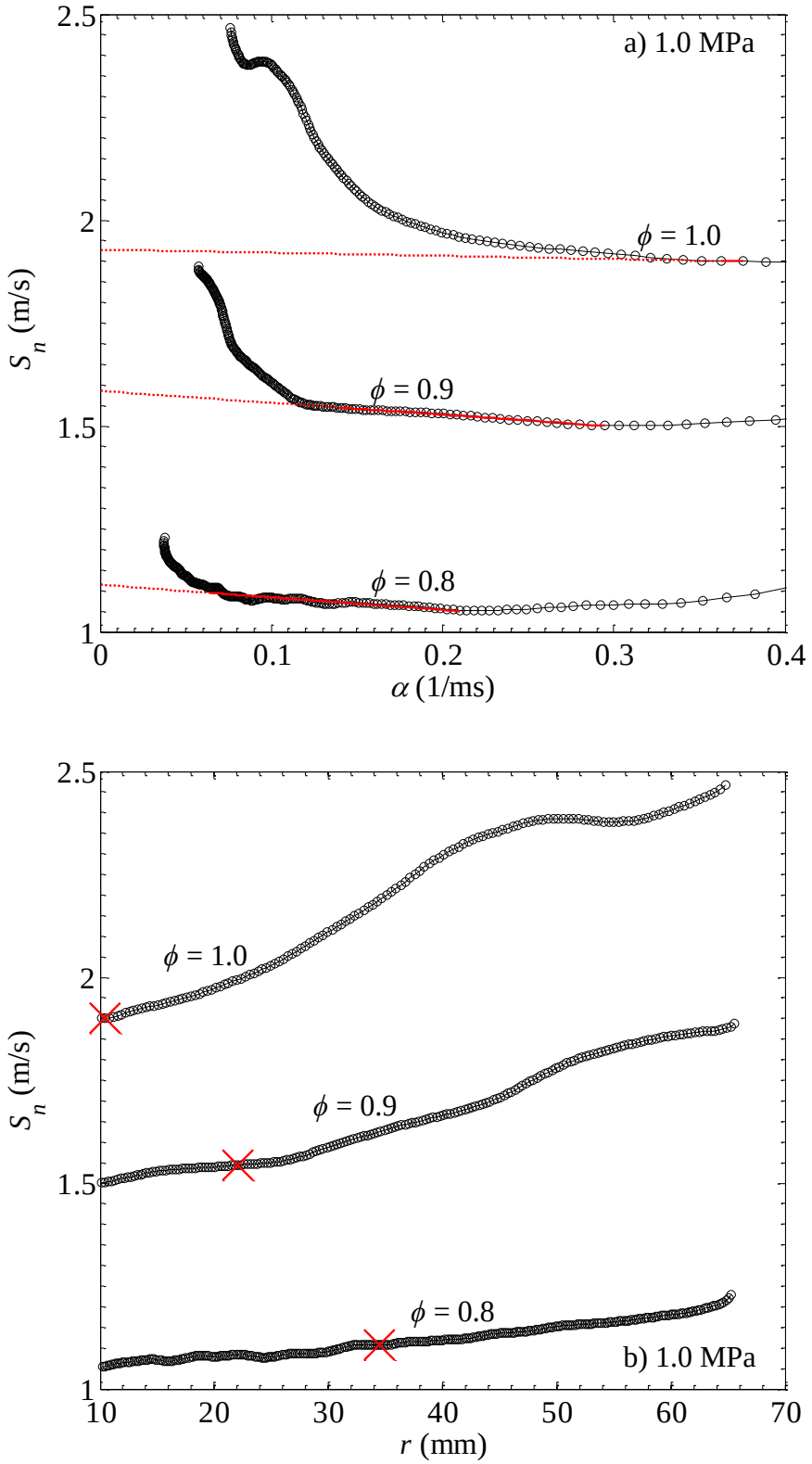

Figure 4.17: a) S_n variation with α, b) S_n variation with r, for ethanol/air mixtures at P_i = 1.0 MPa, T_u = 360K and ϕ = 0.8-1.0. Solid red and blue lines denote linear and nonlinear relationships to L_b across used data points, with dashed lines indicating their extrapolation to zero stretch rate. Red crosses indicate r_c.

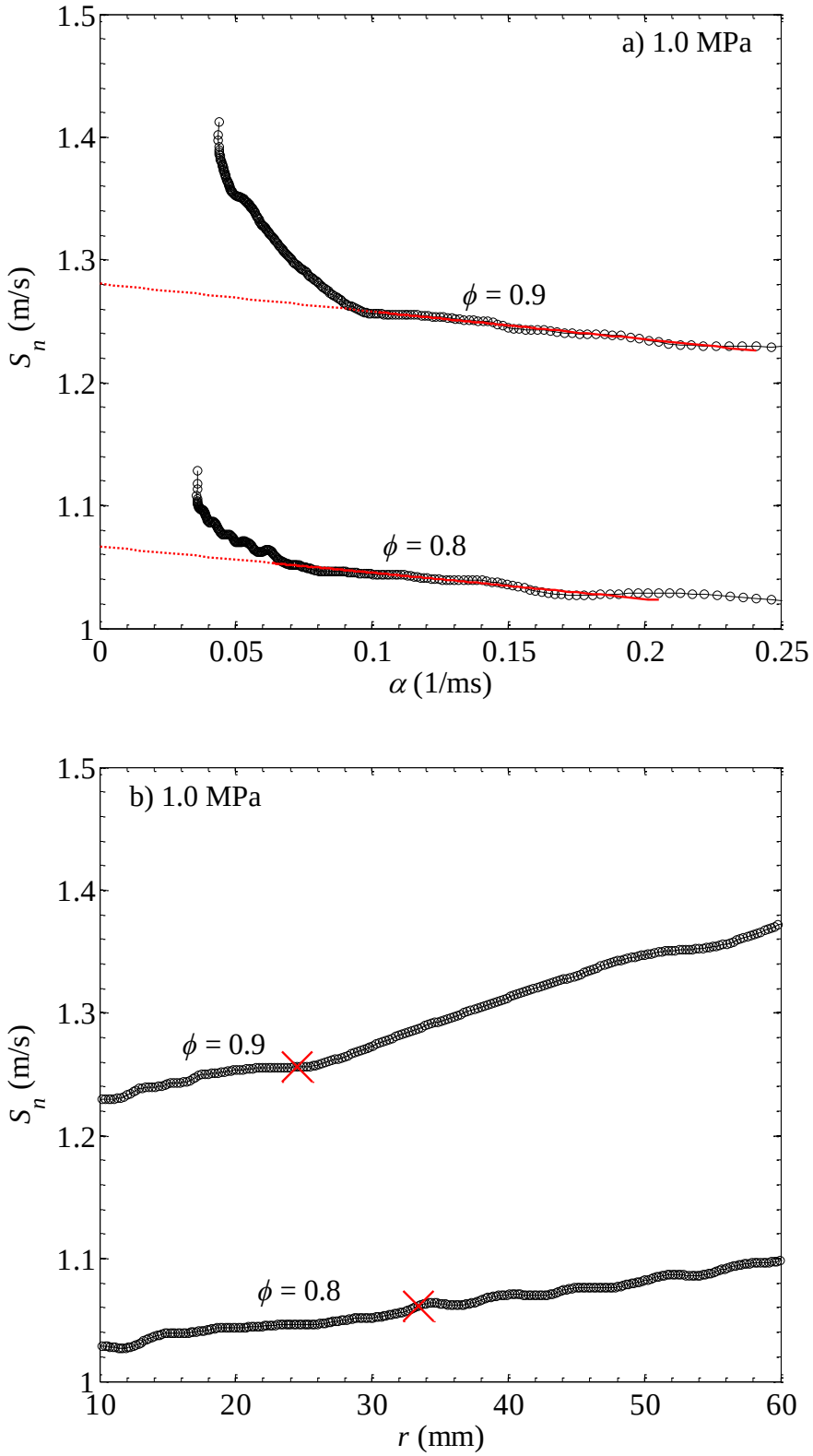

Figure 4.18: a) S_n variation with α, b) S_n variation with r, for n-butanol/air mixtures at P_i = 1.0 MPa, T_u = 360K and ϕ = 0.8-0.9. Solid red and blue lines denote linear and nonlinear relationships to L_b across used data points, with dashed lines indicating their extrapolation to zero stretch rate. Red crosses indicate r_c.

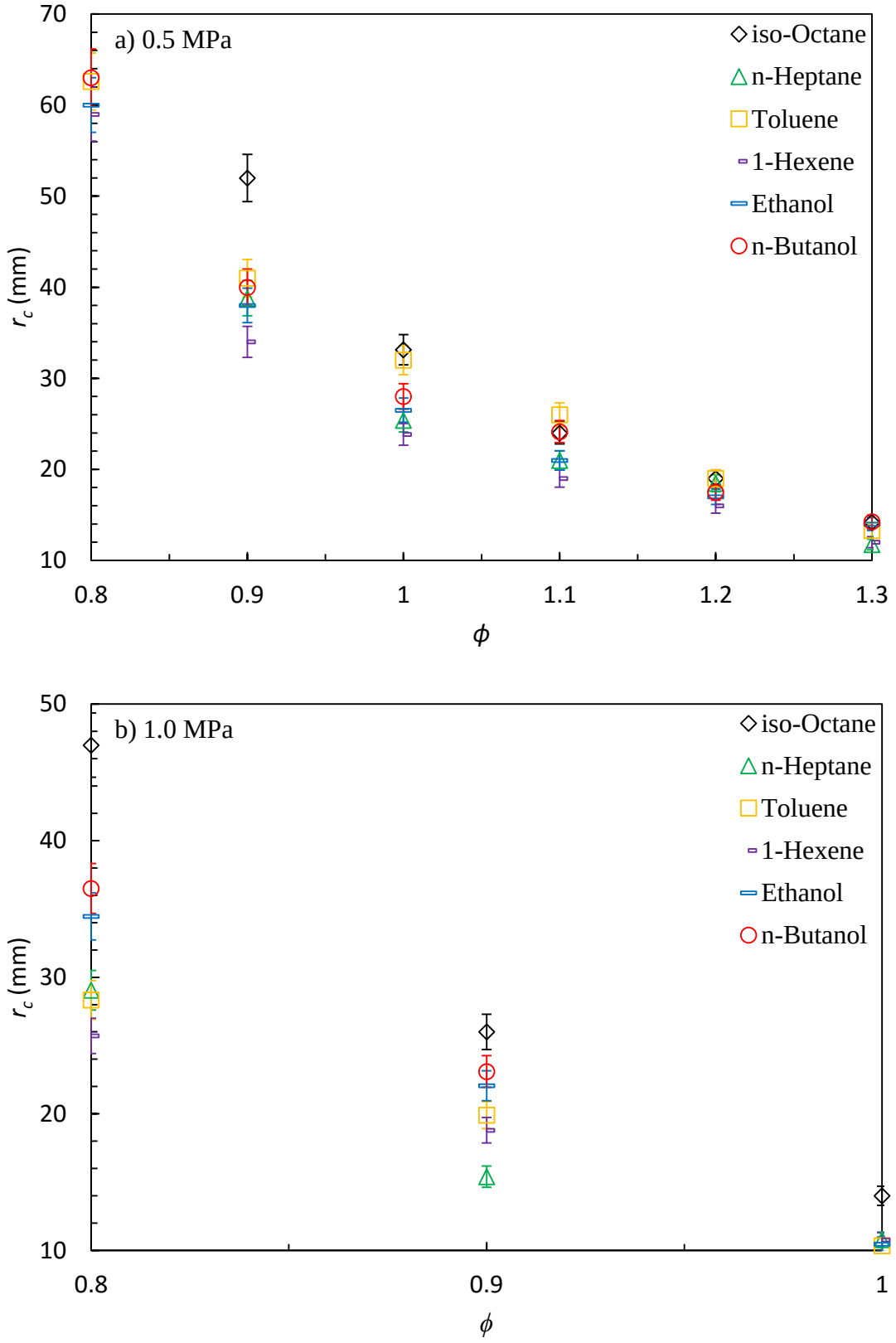

Figure 4.19: Variation of r_c, with ϕ, for all pure liquid fuel/air mixtures, at a) 0.5 MPa and b) 1.0 MPa.

Figures 4.20, 4.21 and 4.22 present a selection of schlieren images showing the flame front evolution and the transition to cellularity of *iso*-octane/air mixtures at ϕ = 0.8, 1 and 1.3, respectively, at P_i = 0.1, 0.5 and 1.0 MPa. The full extent of cellularity for each condition can be observed in Fig. 4.23 in the schlieren images, all at r = 65 mm. In all cases, it can be seen that the number of cracks or cells increases with radius, initial pressure and equivalence ratio, particularly with the latter.

Measurements of u_l and L_b for each pure fuel/air mixture are shown in Figs. 4.24 and 4.25, respectively, at T_u = 360K, P_i = 0.1, 0.5 and 1.0 MPa, and ϕ = 0.8-1.3. During the present work, all experimental values indicated by symbols are the average of at least three experiments with the accompanying error bars indicating the scatter. The repeatability for all the results was good, with u_l and L_b generally within 2 and 5%, respectively. To differentiate between u_l measurements derived using either the linear or nonlinear approach, all unfilled symbols denote a justifiable linear approach and all filled symbols a necessary nonlinear approach.

In general, the u_l values of each pure fuel/air mixture in decreasing order are given by: *1*-hexene, ethanol, *n*-heptane, *n*-butanol, toluene and *iso*-octane. However, ethanol was observed to be differently pressure sensitive, with u_l decreasing in relative rank as the initial pressure increased. Across all pressures the highest and lowest burning velocities are exhibited by *1*-hexene and *iso*-octane, respectively. Peak burning velocities for all fuels at pressures of 0.1 and 0.5 MPa occur between ϕ = 1.1-1.2, although for the three fastest burning fuels, ethanol, *n*-butanol and *1*-hexene this occurs closer to ϕ = 1.2 at 0.1 MPa, with the two alcohols continuing this trend at the increased initial pressure of 0.5 MPa. The relative difference in u_l between the pure fuel/air mixtures is greatest at 0.1 MPa and decreases as the pressure increases. All fuels share the common trend of a decrease in Markstein length as the equivalence ratio and pressure increase.

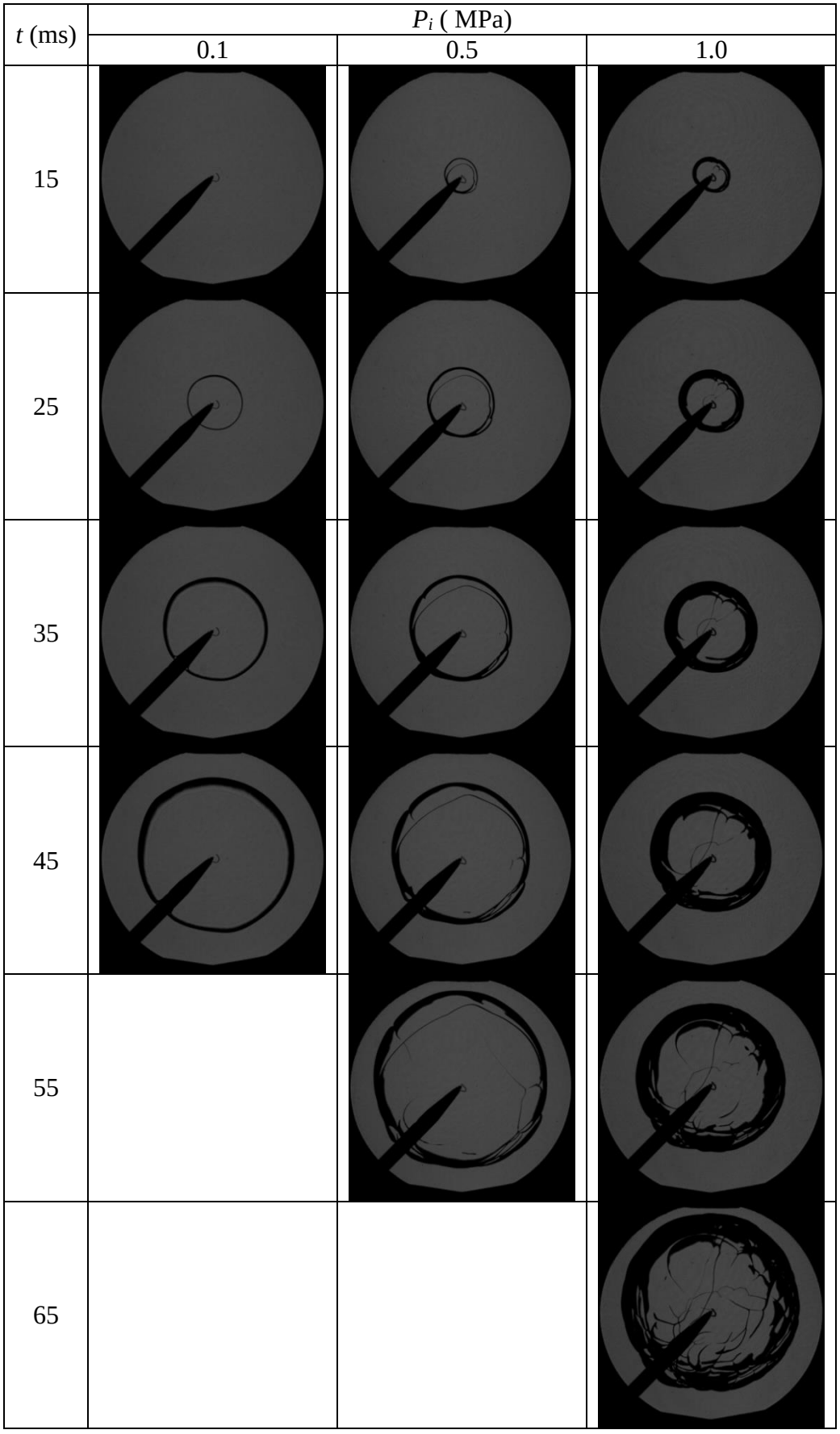

Figure 4.20: Schlieren images of *iso*-octane/air mixtures, f = 5400 fps, ϕ = 0.8, T_u = 360K, P_i = 0.1, 0.5 and 1.0 MPa.

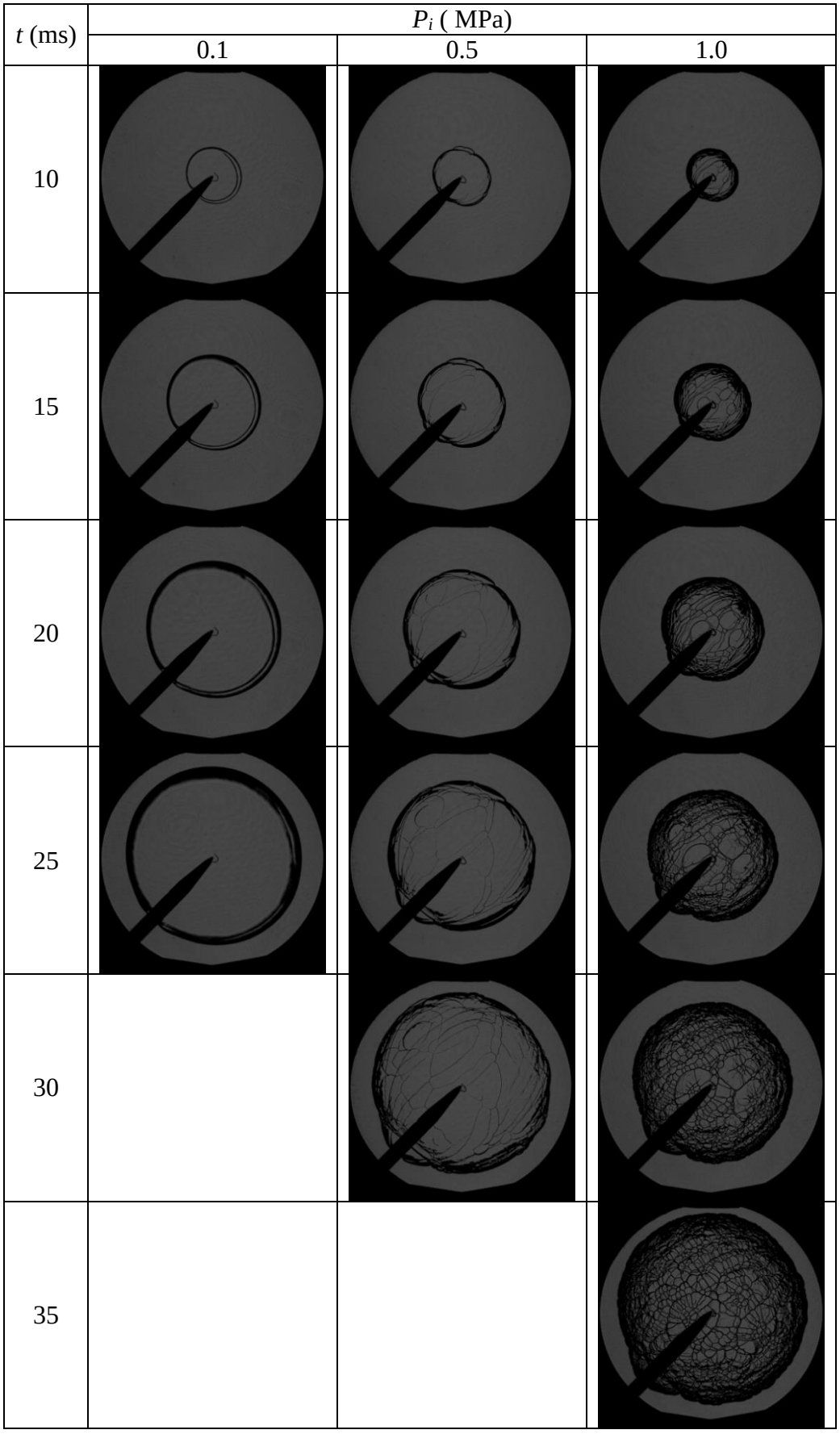

Figure 4.21: Schlieren images of *iso*-octane/air mixtures, f = 5400 fps, ϕ = 1.0, T_u = 360K, P_i = 0.1, 0.5 and 1.0 MPa.

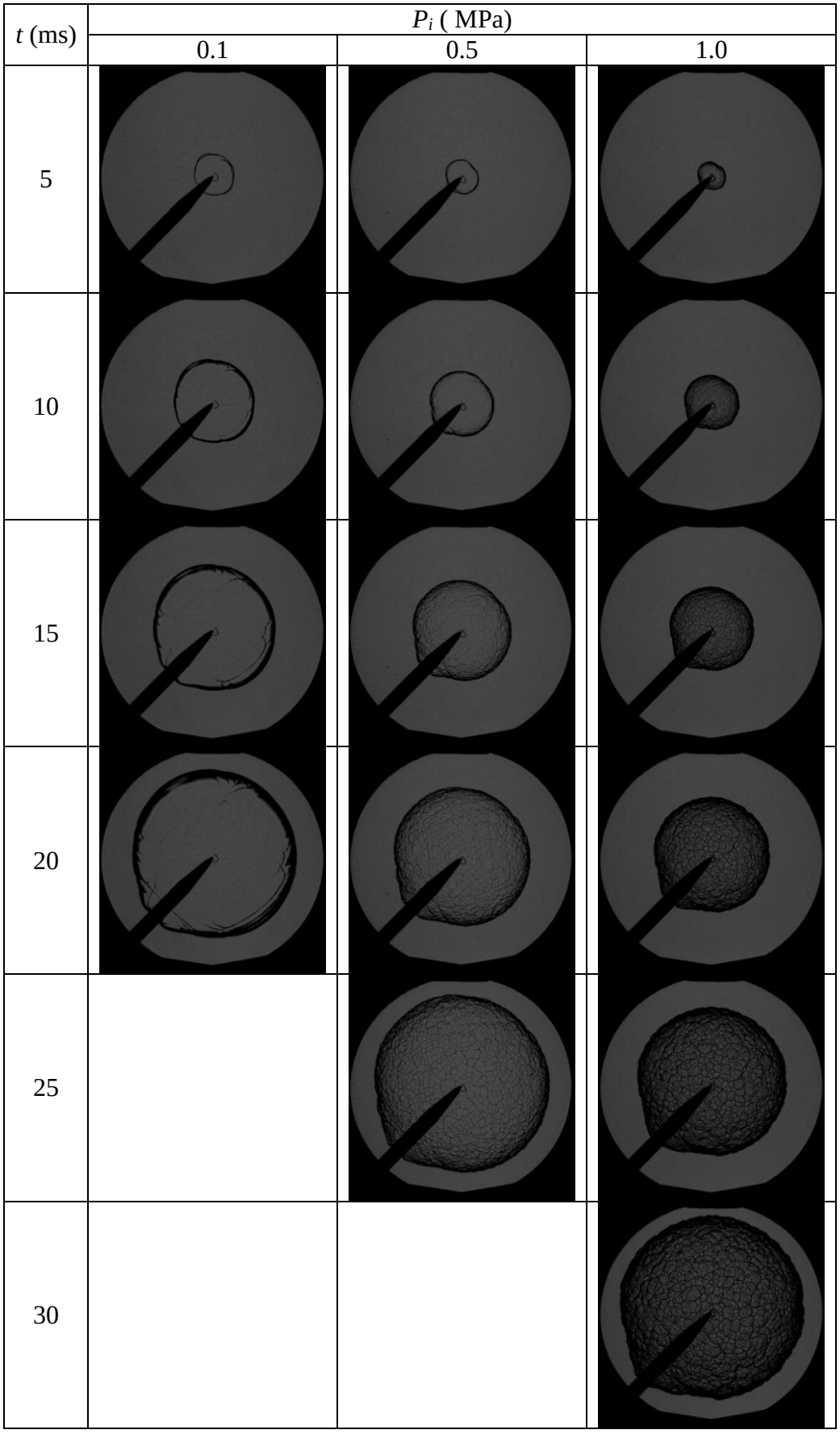

Figure 4.22: Schlieren images of *iso*-octane/air mixtures, f = 5400 fps, ϕ = 1.3, T_u = 360K, P_i = 0.1, 0.5 and 1.0 MPa.

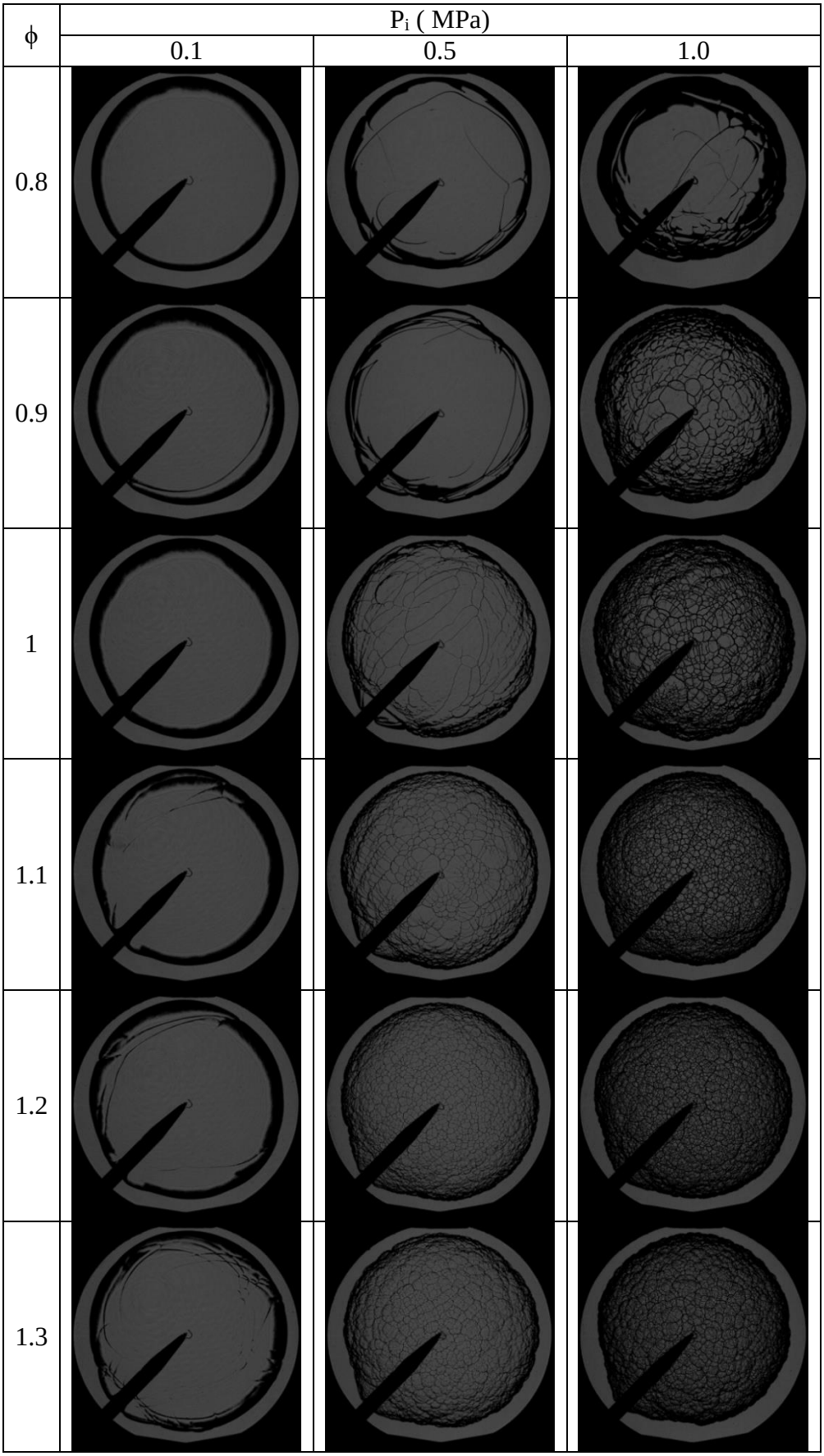

Figure 4.23: Schlieren images of *iso*-octane/air mixtures, f = 5400 fps, r = 65 mm, ϕ = 0.8-1.3, T_u = 360K, P_i = 0.1, 0.5 and 1.0 MPa.

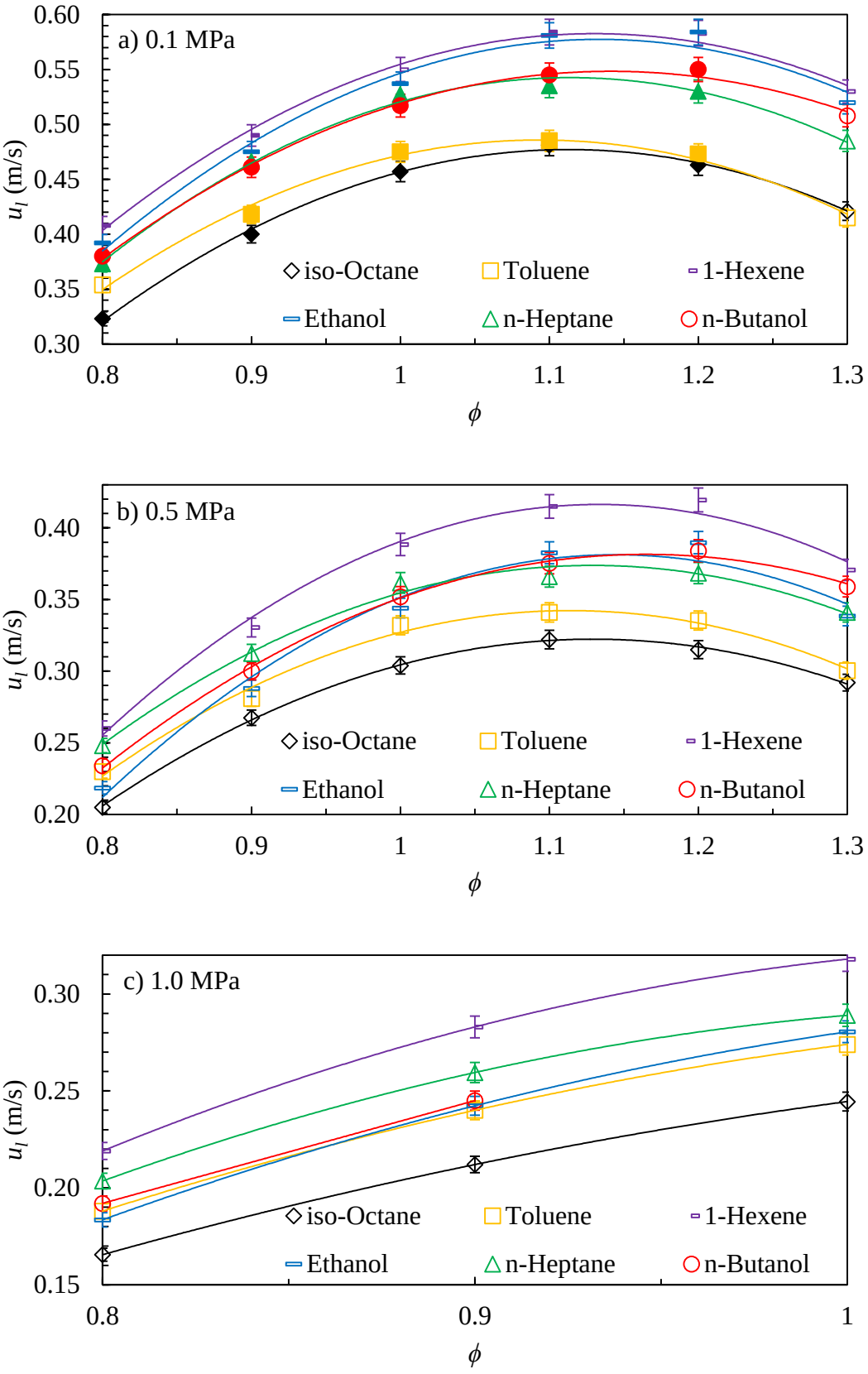

Figure 4.24: Variation of u_l with ϕ for all pure liquid fuel/air mixtures, P_i = a) 0.1 MPa, b) 0.5 MPa, c) 1.0 MPa, T_u = 360K.

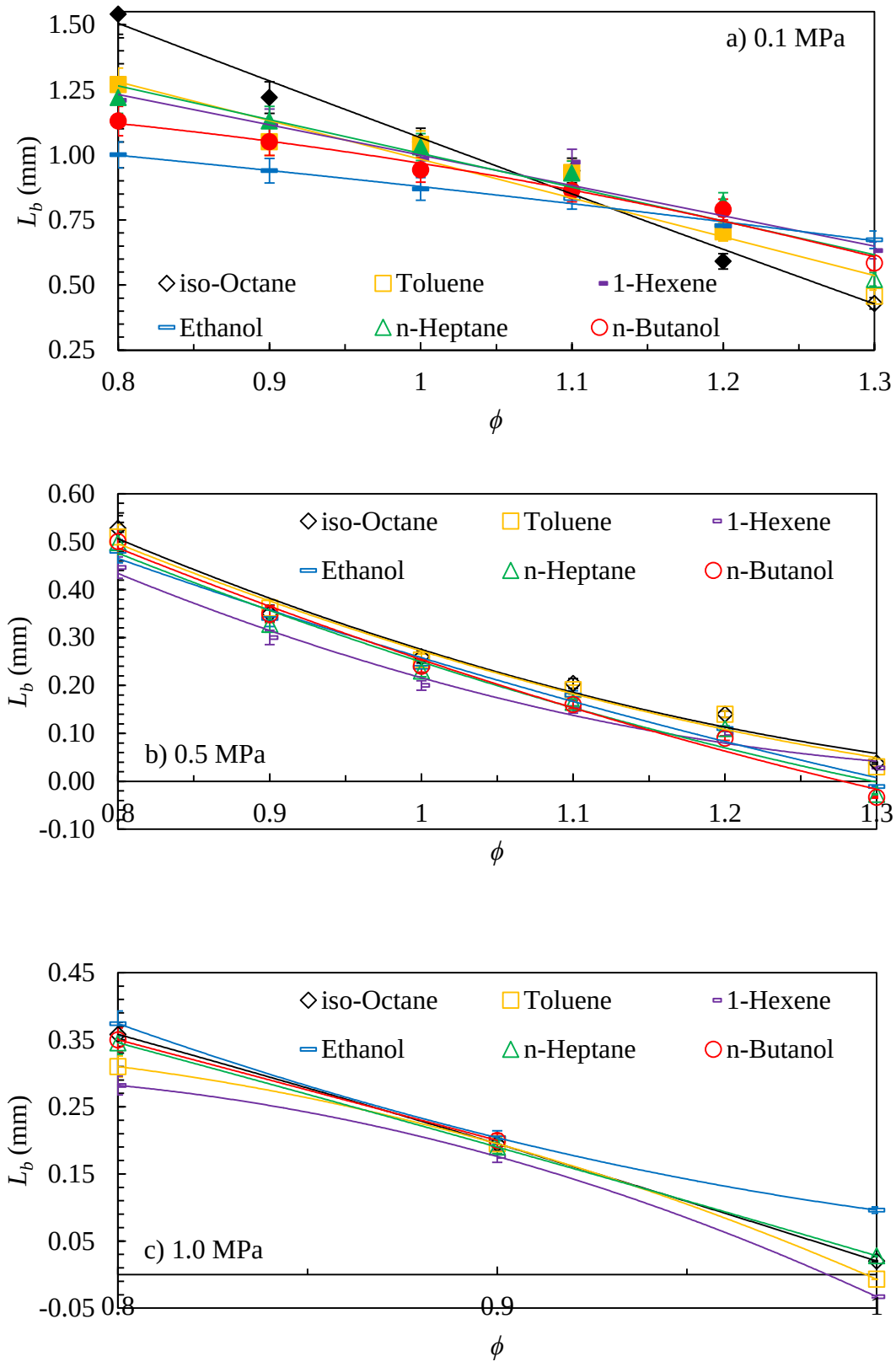

Figure 4.25: Variation of L_b with ϕ for all pure liquid fuel/air mixtures, P_i = a) 0.1 MPa, b) 0.5 MPa, c) 1.0 MPa, T_u = 360K.

4.3 Binary Equimolar Liquid Hydrocarbon Blends

Binary equimolar constituent mixture blends are a good starting point to identify any fuel groups or particular blends that behave in an unexpected manner relative to their constituent fuels and thus might challenge any blending laws. As discussed in Chapter 2, Section 2.3, and illustrated by Eq. 2.28, the constituent mixtures always have the same equivalence ratios. From the five pure fuels chosen to represent the major fuel groups of gasoline, ten binary equimolar blends were investigated. Table 4.2 summarises the composition of each binary blend, showing the relevant mole, mass, and liquid fuel fractions, based on the expressions in Chapter 2.

The alcohols, ethanol and *n*-butanol, contain oxygen and therefore, for a given ϕ, generally require less air to oxidise their elemental carbon and hydrogen. Uniquely, the blend of toluene/1-hexene has the same fractional fuel and air moles, at a given ϕ, the result of both fuels requiring the same amount of air. Liquid volume fractions depend on the constituent fuel densities.

Figures 4.26-4.45 show the values of u_l and L_b for each blend, and those of their constituent mixtures at P_i = 0.1, 0.5 and 1.0 MPa. Again, whether a linear or nonlinear extrapolation to zero stretch rate was used is indicated by the symbols employed. Unfilled symbols denote a justifiable linear extrapolation, and filled symbols denote a necessary nonlinear extrapolation. For all blends, as with the pure fuel/air mixtures, nonlinear flame speed/stretch rate behaviour was only observed at 0.1 MPa between ϕ = 0.8-1.2. At the elevated pressures of 0.5 and 1.0 MPa there was dominant linear behaviour across all equivalence ratios.

In all cases, the u_l and L_b behaviour of the blend relative to its constituents is best observed at 0.1 MPa, where the relative differences between the constituent u_l and L_b values are greatest. In general there was a tendency for the blend mixtures u_l and L_b values to be closer to the slower burning constituent, particularly under lean conditions and with *iso*-octane/ethanol/air and toluene/*n*-heptane/air blends, as shown in Figs. 4.30-4.31 and Figs. 4.38-4.39.

Equimolar Blends of Constituent Fuel/Air Mixtures	Fuel/Air Mass Ratio of Constituent Mixtures	Fuel Mole Ratio of Constituent Fuels	Fuel Mass Ratio of Constituent Fuels	Fuel Liquid Volume Ratio of Constituent Fuels
iso-Octane /Toluene	1.004	0.724	0.901	1.128
iso-Octane /*1*-Hexene	1.004	0.724	0.984	0.965
iso-Octane /Ethanol	1.008	0.253	0.626	0.715
iso-Octane /*n*-Heptane	1.004	0.883	1.004	0.992
Toluene /*1*-Hexene	1.008	1	1.092	0.855
Toluene /Ethanol	1.012	0.348	0.695	0.634
Toluene /*n*-Heptane	1.004	1.217	1.123	0.883
1-Hexene /Ethanol	1.004	0.348	0.637	0.742
1-Hexene /*n*-Heptane	0.996	1.217	1.02	1.028
Ethanol /*n*-Heptane	0.992	3.484	1.604	1.387

Table 4.2: Binary equimolar constituent mixtures showing different constituent ratios as discussed in Chapter 2, Section 2.3. Densities for all fuels are shown in Table 4.1.

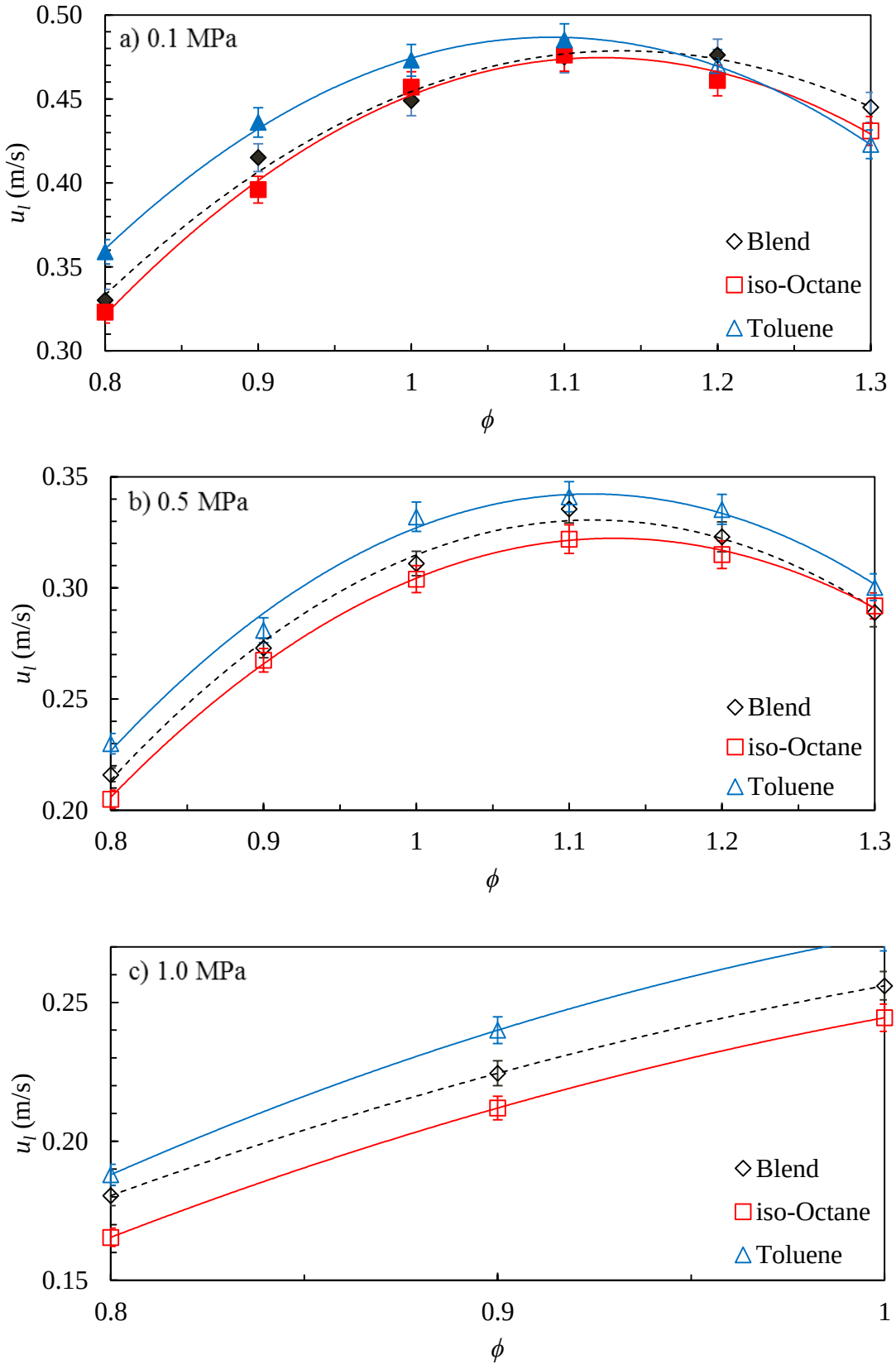

Figure 4.26: Variation of u_l with ϕ for *iso*-octane/air, toluene/air and their relative equimolar binary blend, P_i = a) 0.1 MPa, b) 0.5 MPa, c) 1.0 MPa, T_u = 360K.

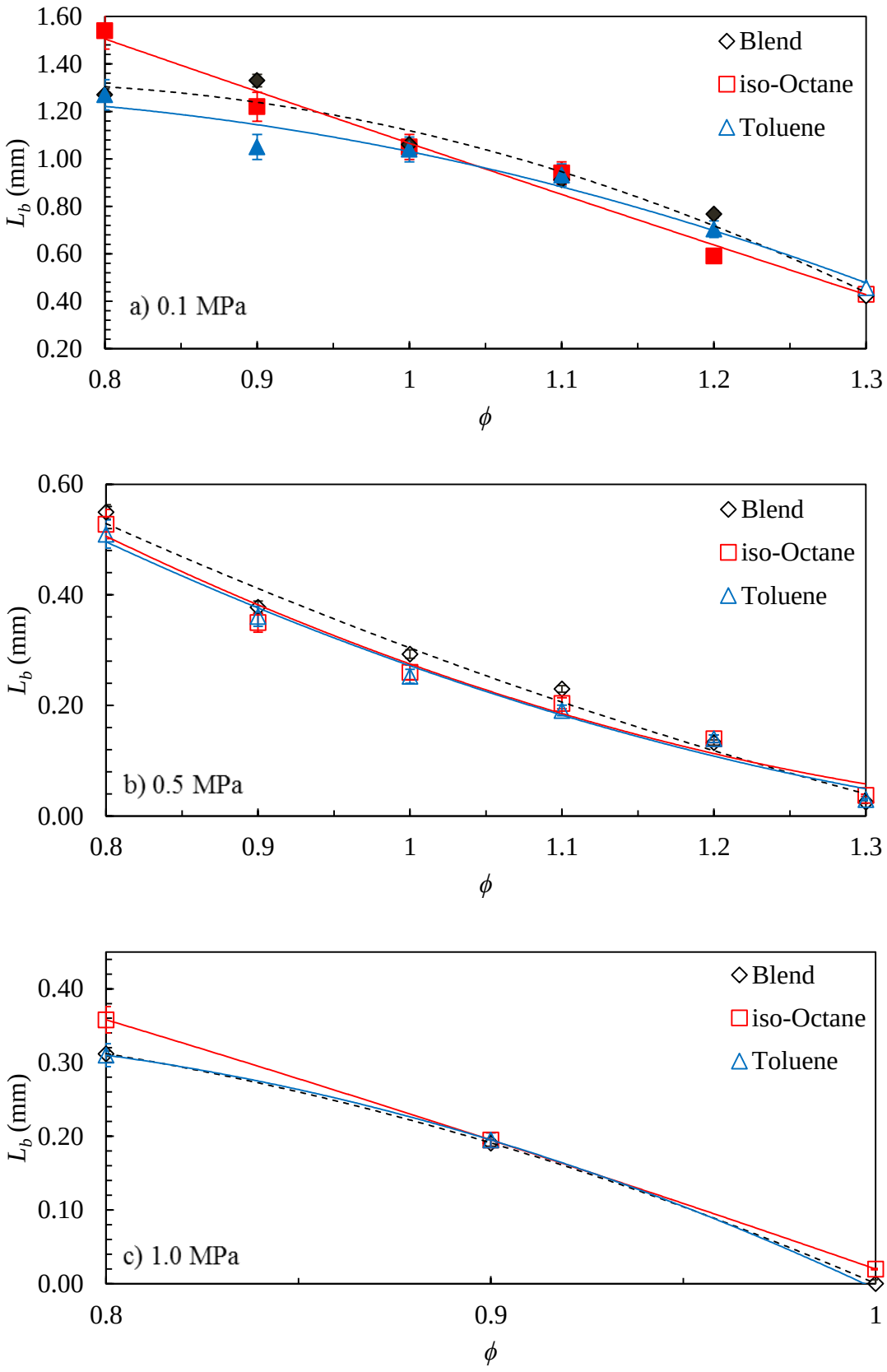

Figure 4.27: Variation of L_b with ϕ for *iso*-octane/air, toluene/air and their relative equimolar binary blend, P_i = a) 0.1 MPa, b) 0.5 MPa, c) 1.0 MPa, T_u = 360K.

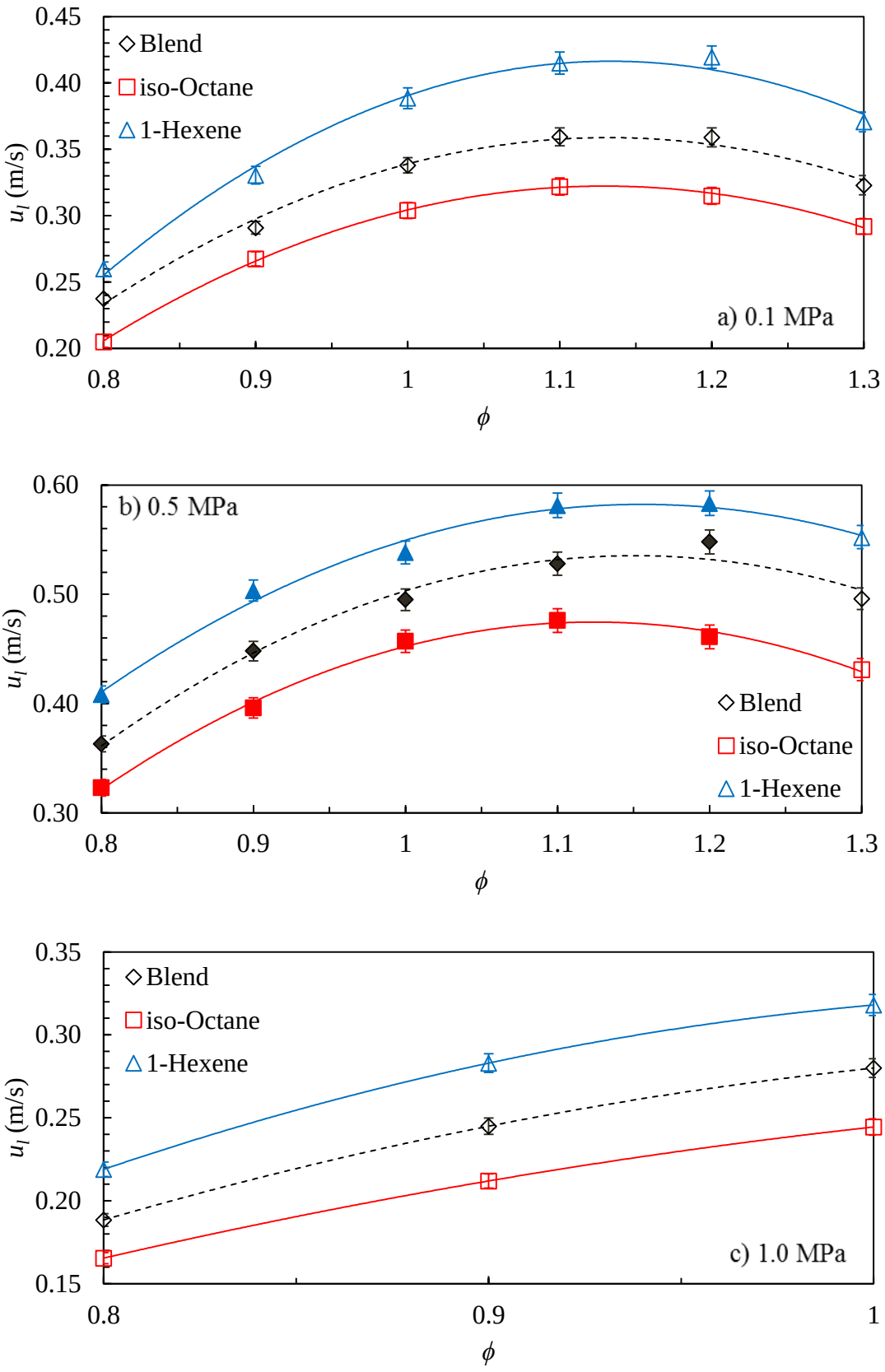

Figure 4.28: Variation of u_l with ϕ for *iso*-octane/air, *1*-hexene/air and their relative equimolar binary blend, P_i = a) 0.1 MPa, b) 0.5 MPa, c) 1.0 MPa T_u = 360K.

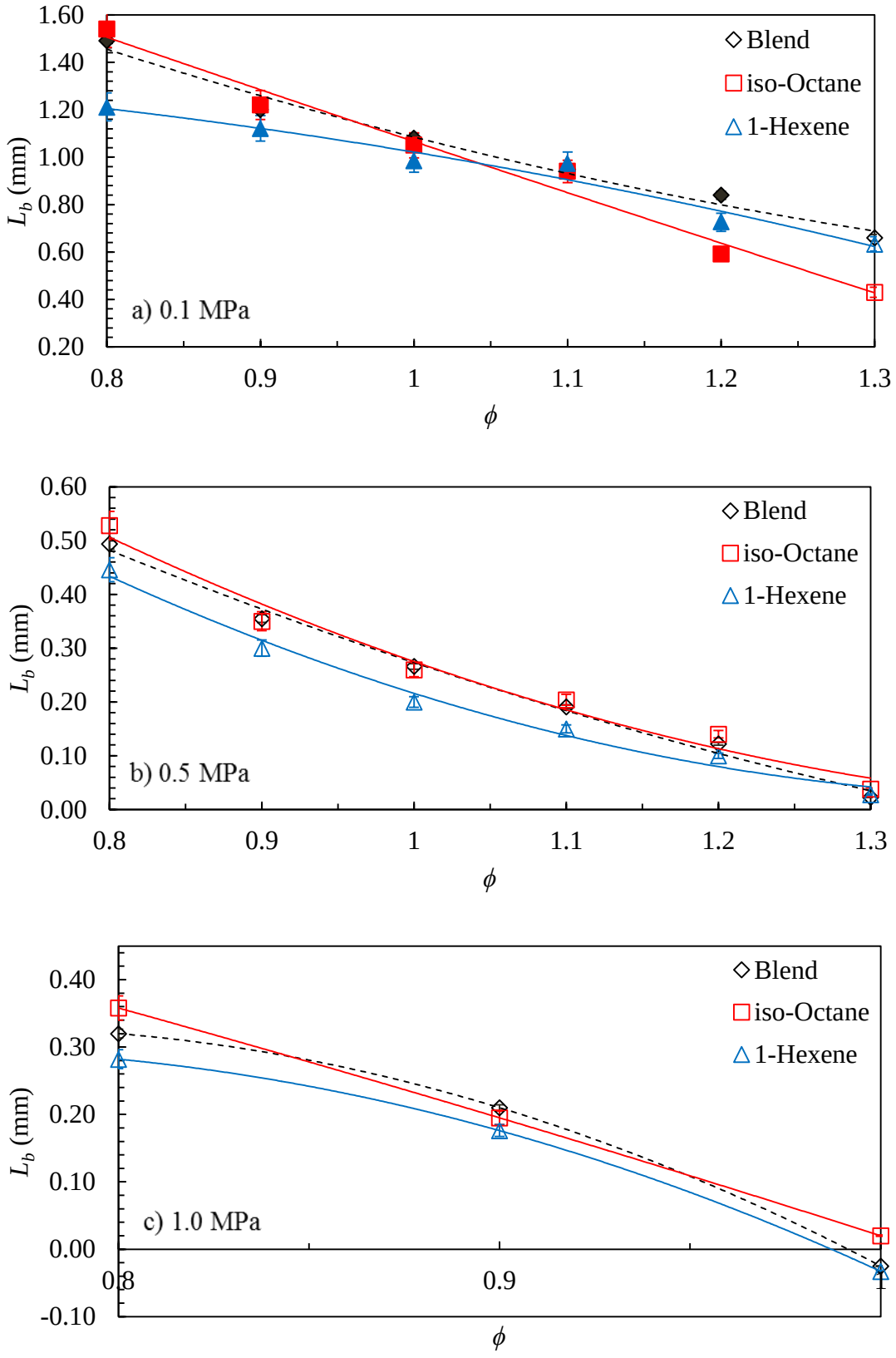

Figure 4.29: Variation of L_b with ϕ for *iso*-octane/air, *1*-hexene/air and their relative equimolar binary blend, P_i = a) 0.1 MPa, b) 0.5 MPa, c) 1.0 MPa, T_u = 360K.

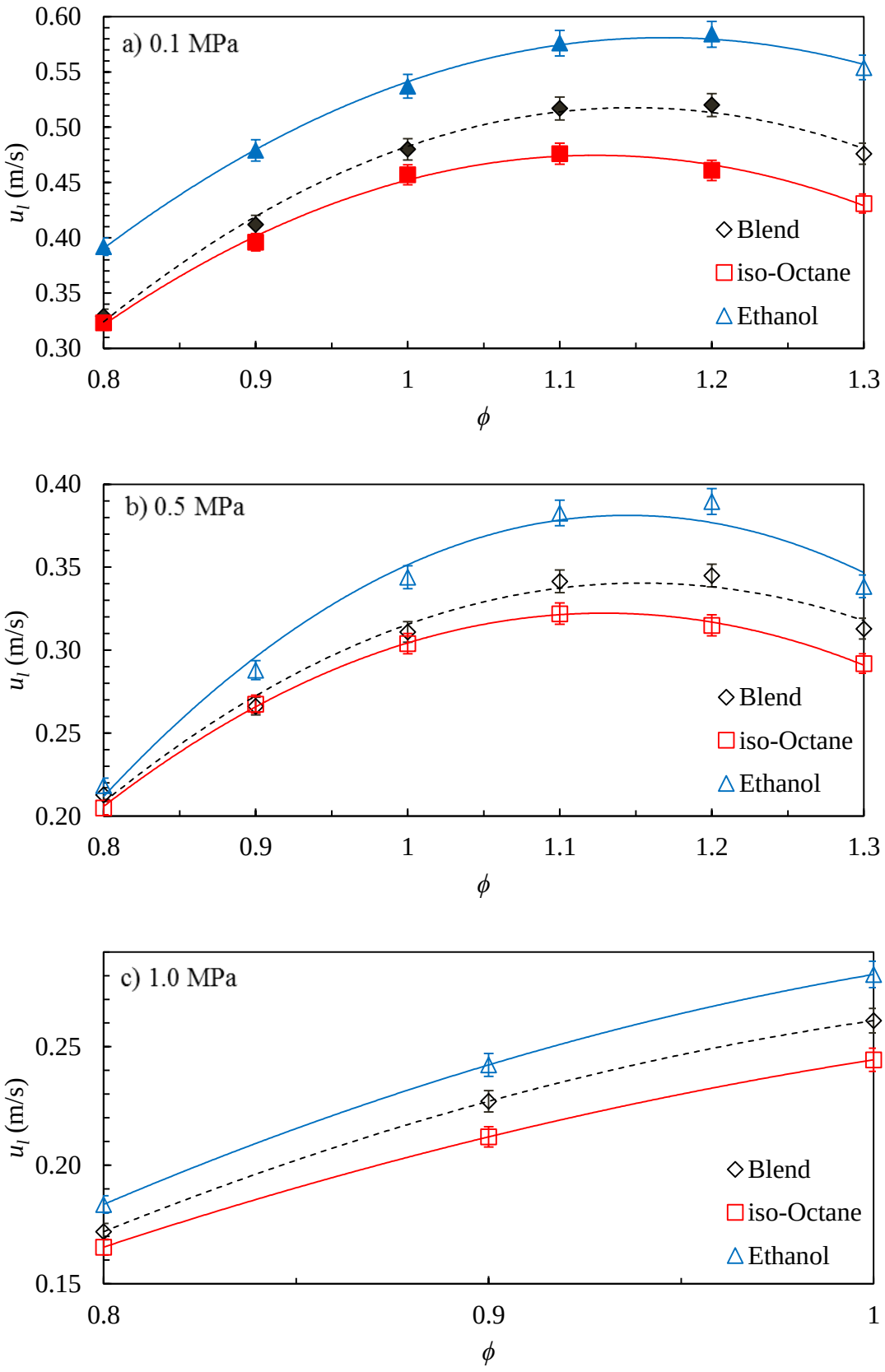

Figure 4.30: Variation of u_l with ϕ for *iso*-octane/air, ethanol/air and their relative equimolar binary blend, P_i = a) 0.1 MPa, b) 0.5 MPa, c) 1.0 MPa, T_u = 360K.

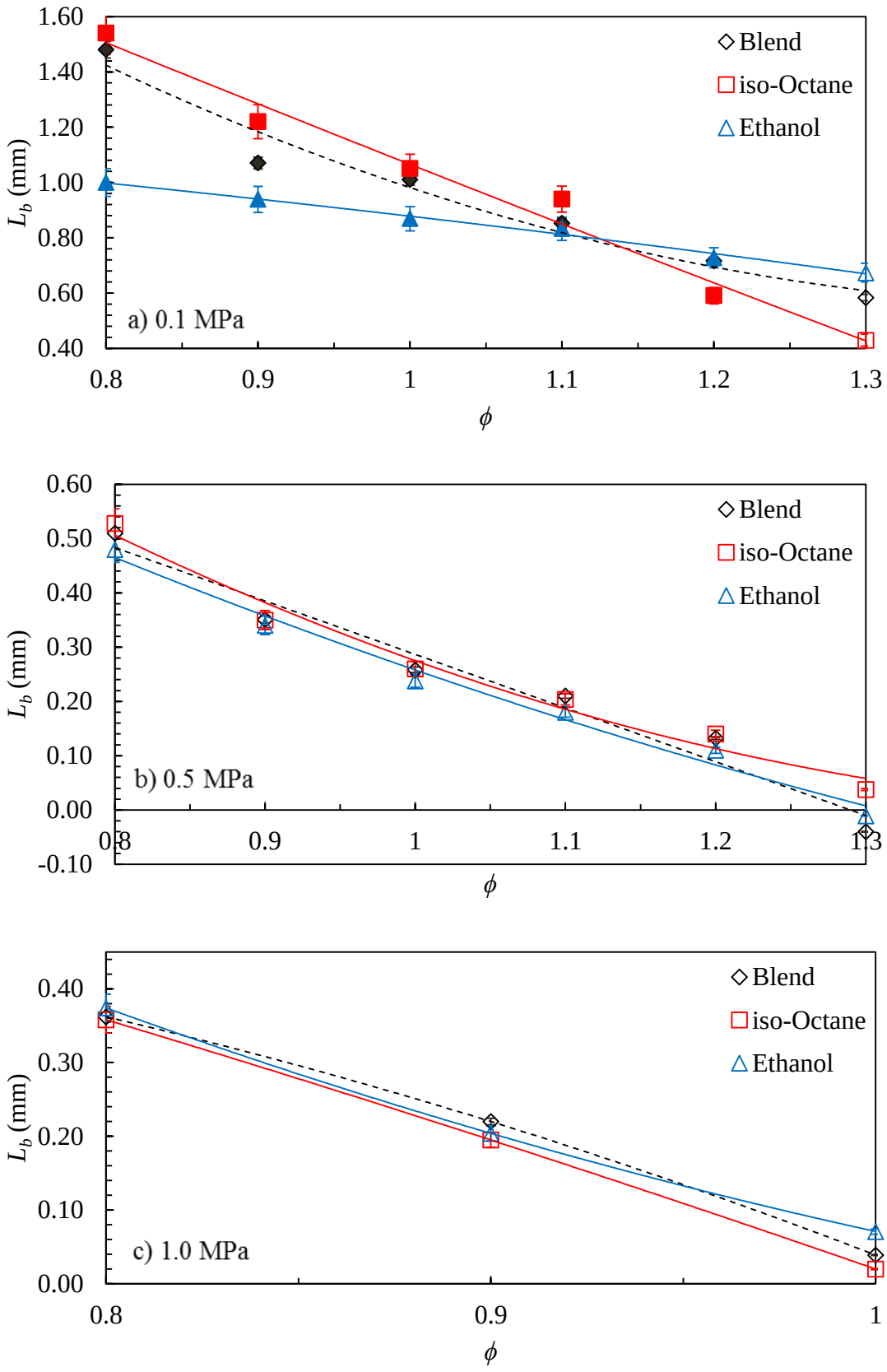

Figure 4.31: Variation of L_b with ϕ for *iso*-octane/air, ethanol/air and their relative equimolar binary blend, P_i = a) 0.1 MPa, b) 0.5 MPa, c) 1.0 MPa, T_u = 360K.

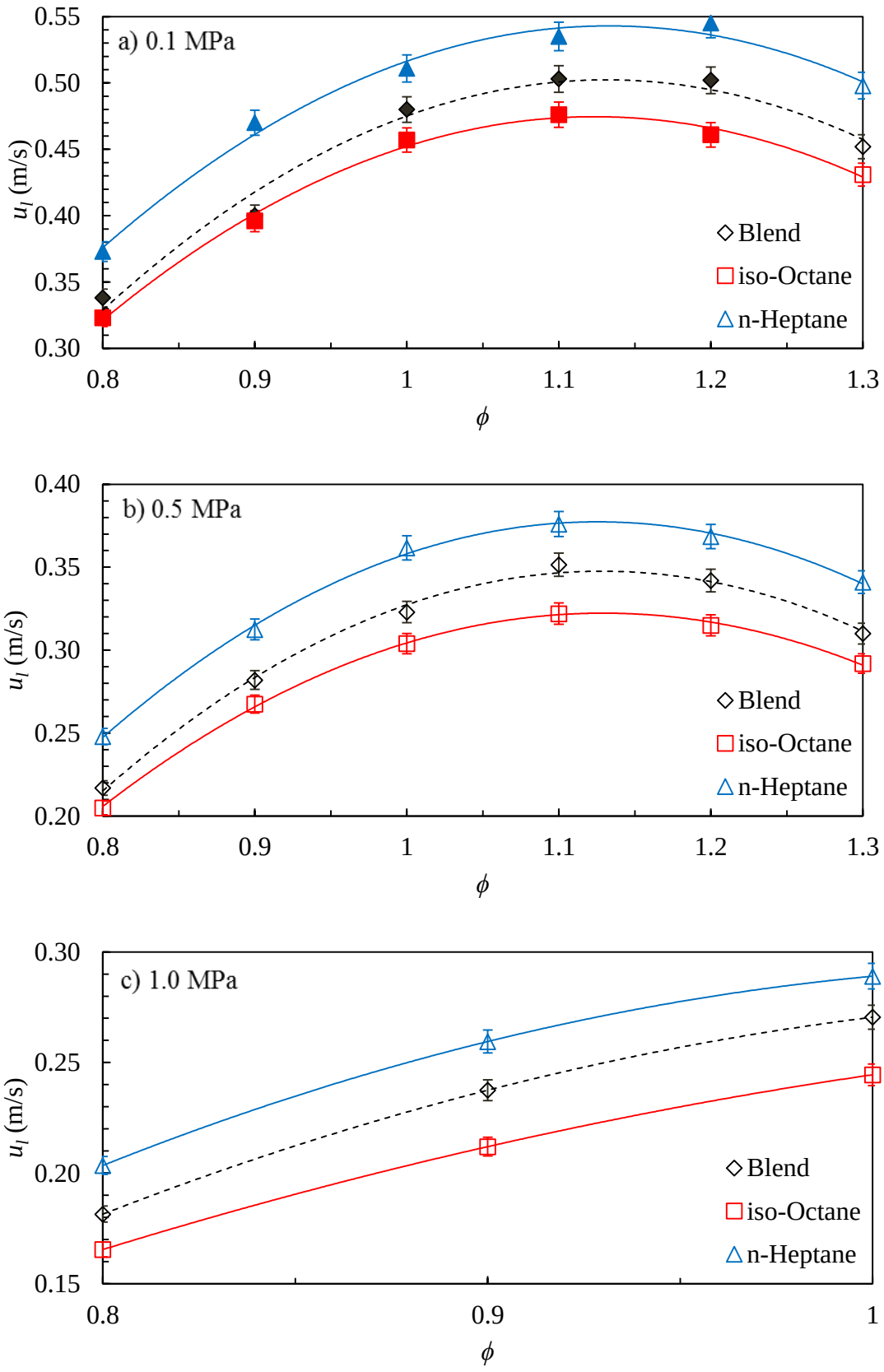

Figure 4.32: Variation of u_l with ϕ for *iso*-octane/air, *n*-heptane/air and their relative equimolar binary blend, P_i = a) 0.1 MPa, b) 0.5 MPa, c) 1.0 MPa, T_u = 360K.

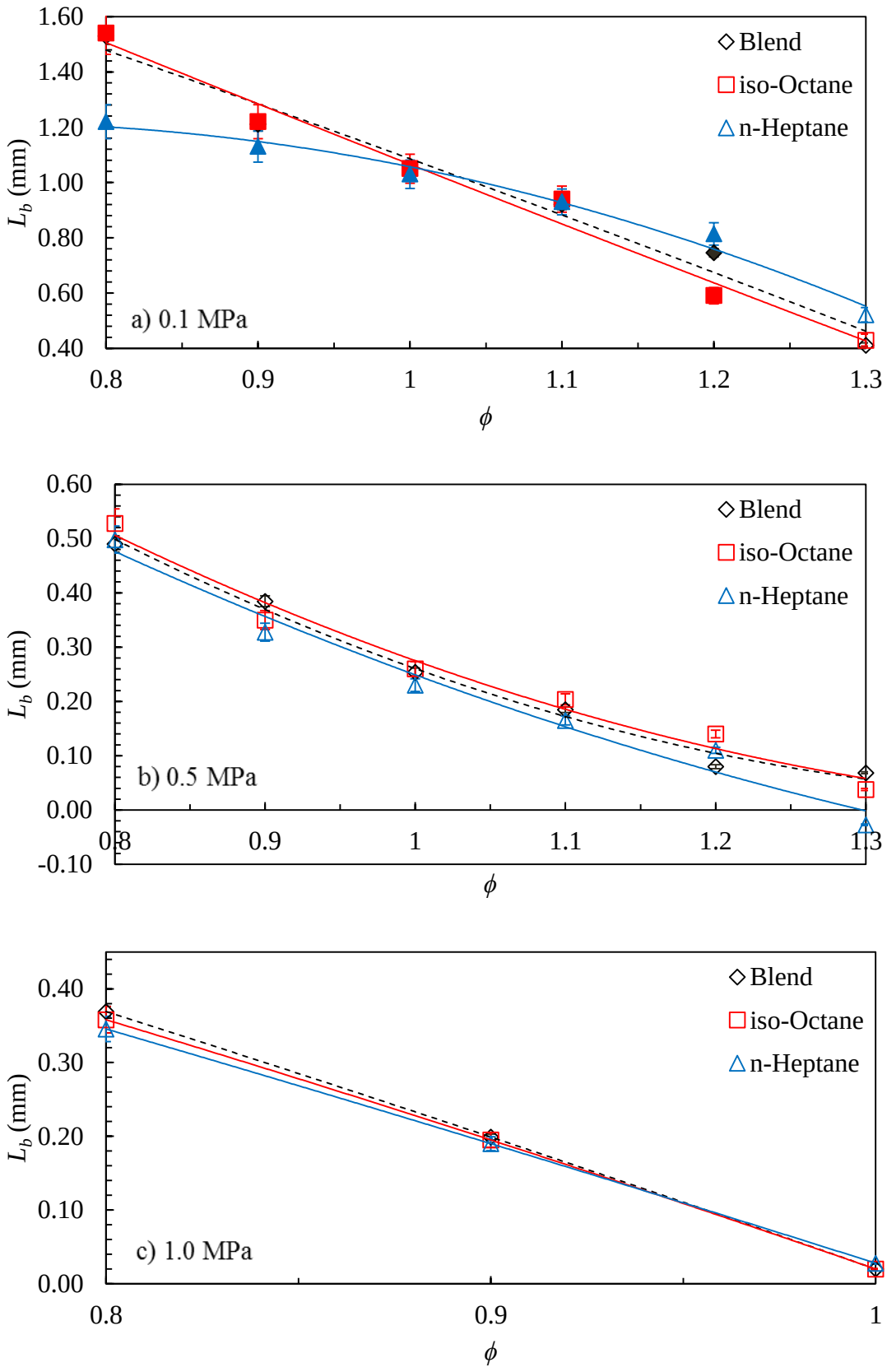

Figure 4.33: Variation of L_b with ϕ for *iso*-octane/air, *n*-heptane/air and their relative equimolar binary blend, P_i = a) 0.1 MPa, b) 0.5 MPa, c) 1.0 MPa, T_u = 360K.

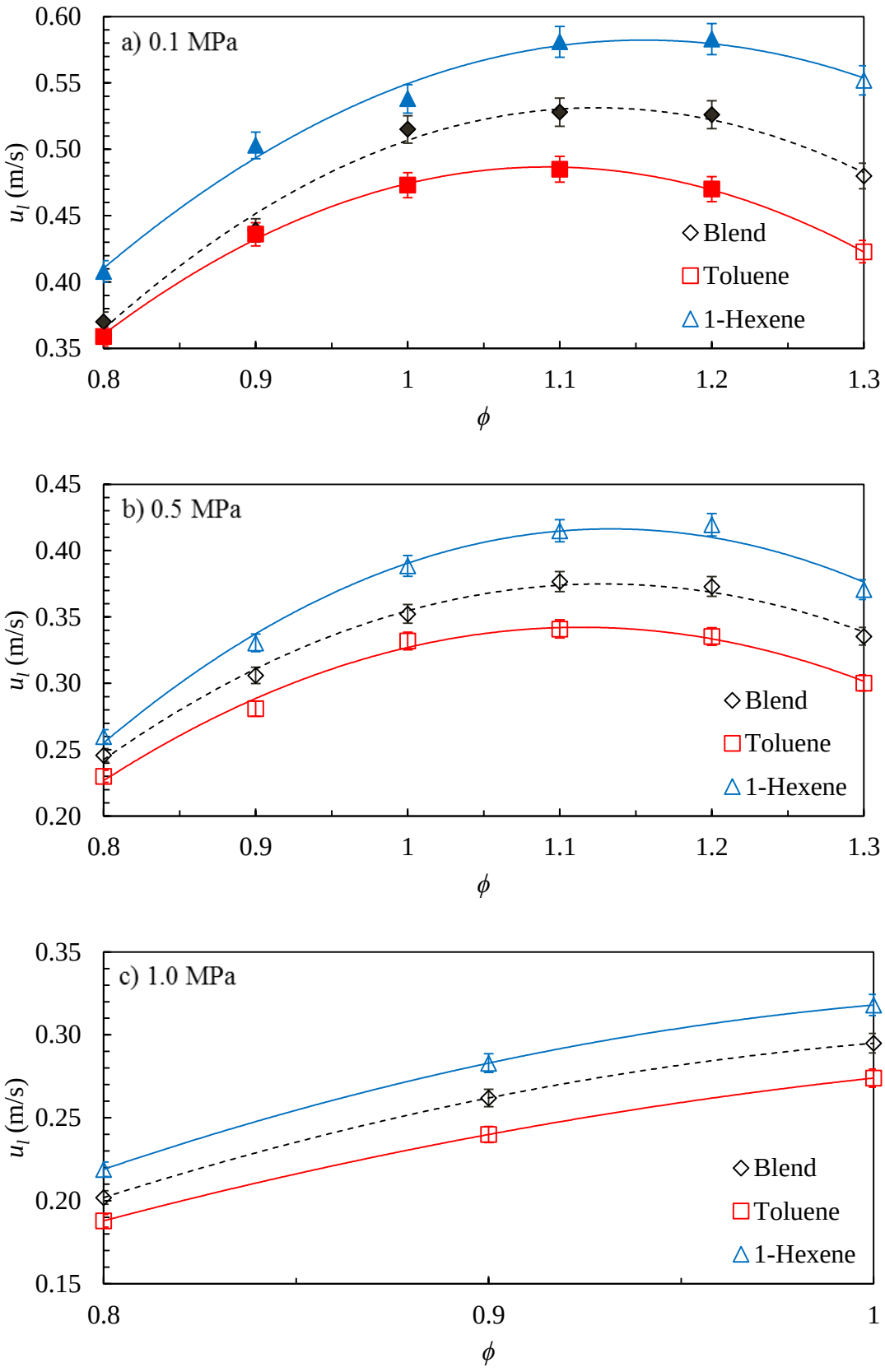

Figure 4.34: Variation of u_l with ϕ for toluene/air, *1*-hexene/air and their relative equimolar binary blend, P_i = a) 0.1 MPa, b) 0.5 MPa, c) 1.0 MPa, T_u = 360K.

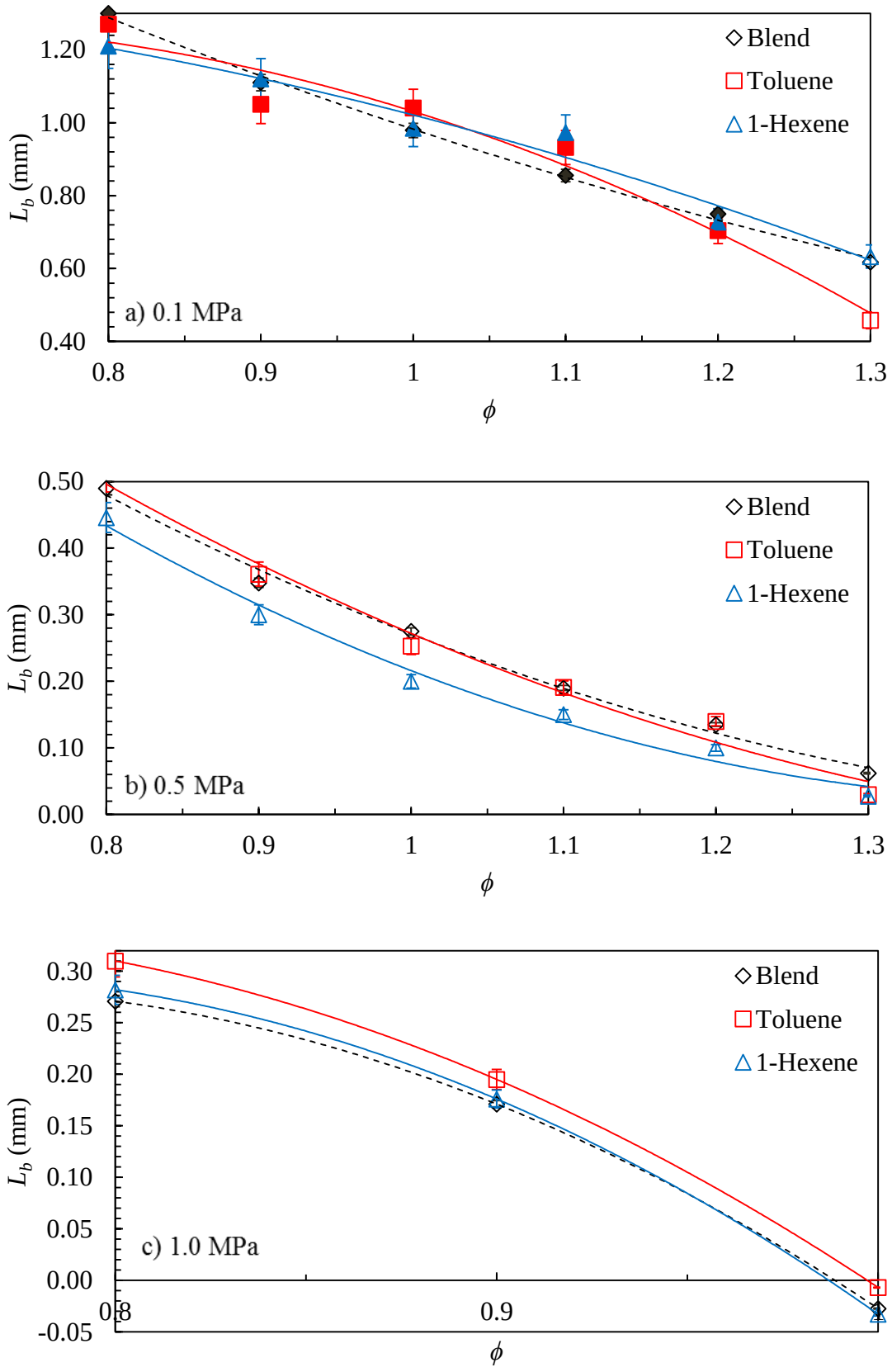

Figure 4.35: Variation of L_b with ϕ for toluene/air, *1*-hexene/air and their relative equimolar binary blend, P_i = a) 0.1 MPa, b) 0.5 MPa, c) 1.0 MPa, T_u = 360K.

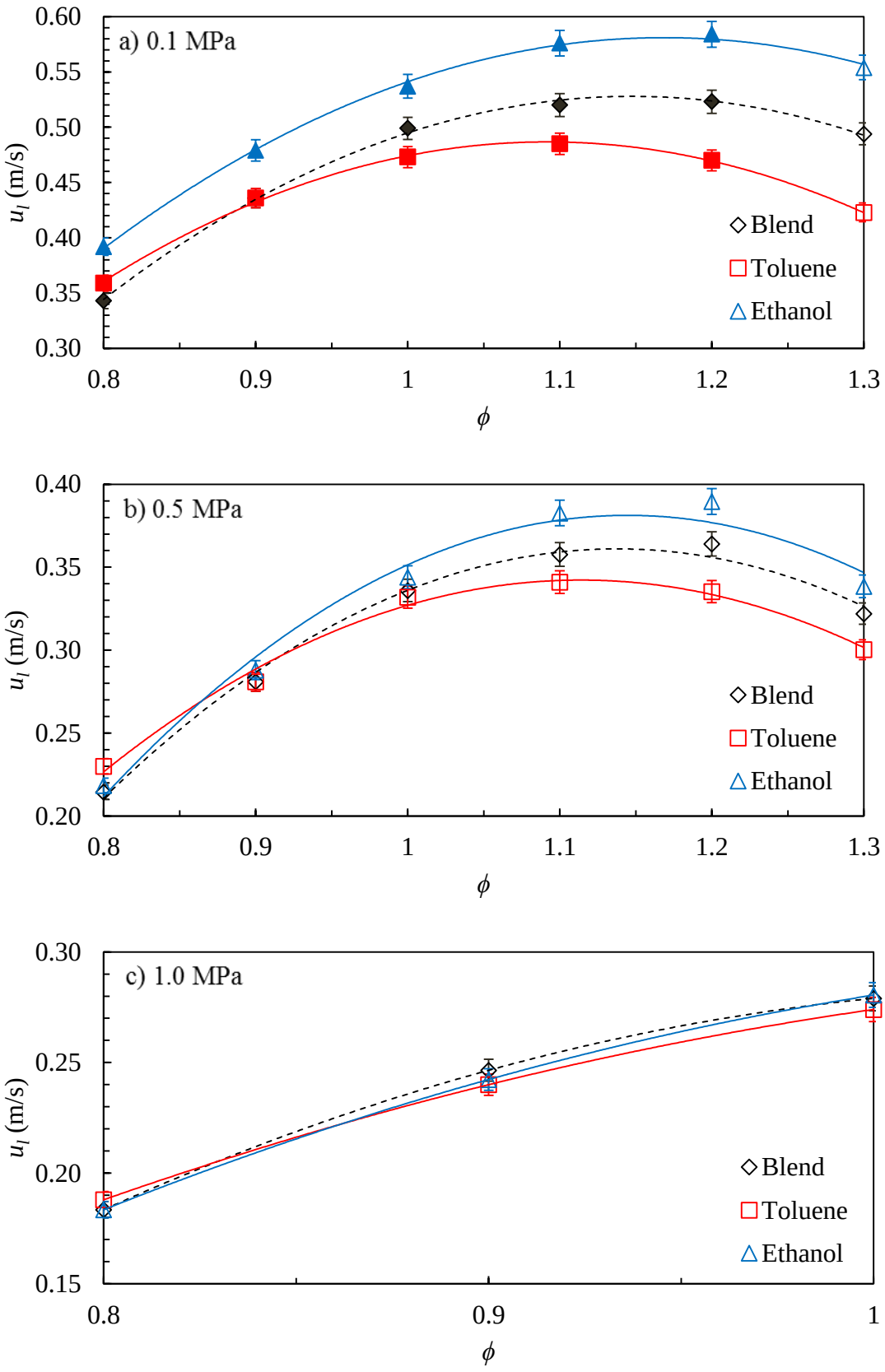

Figure 4.36: Variation of u_l with ϕ for toluene/air, ethanol/air and their relative equimolar binary blend, P_i = a) 0.1 MPa, b) 0.5 MPa, c) 1.0 MPa, T_u = 360K.

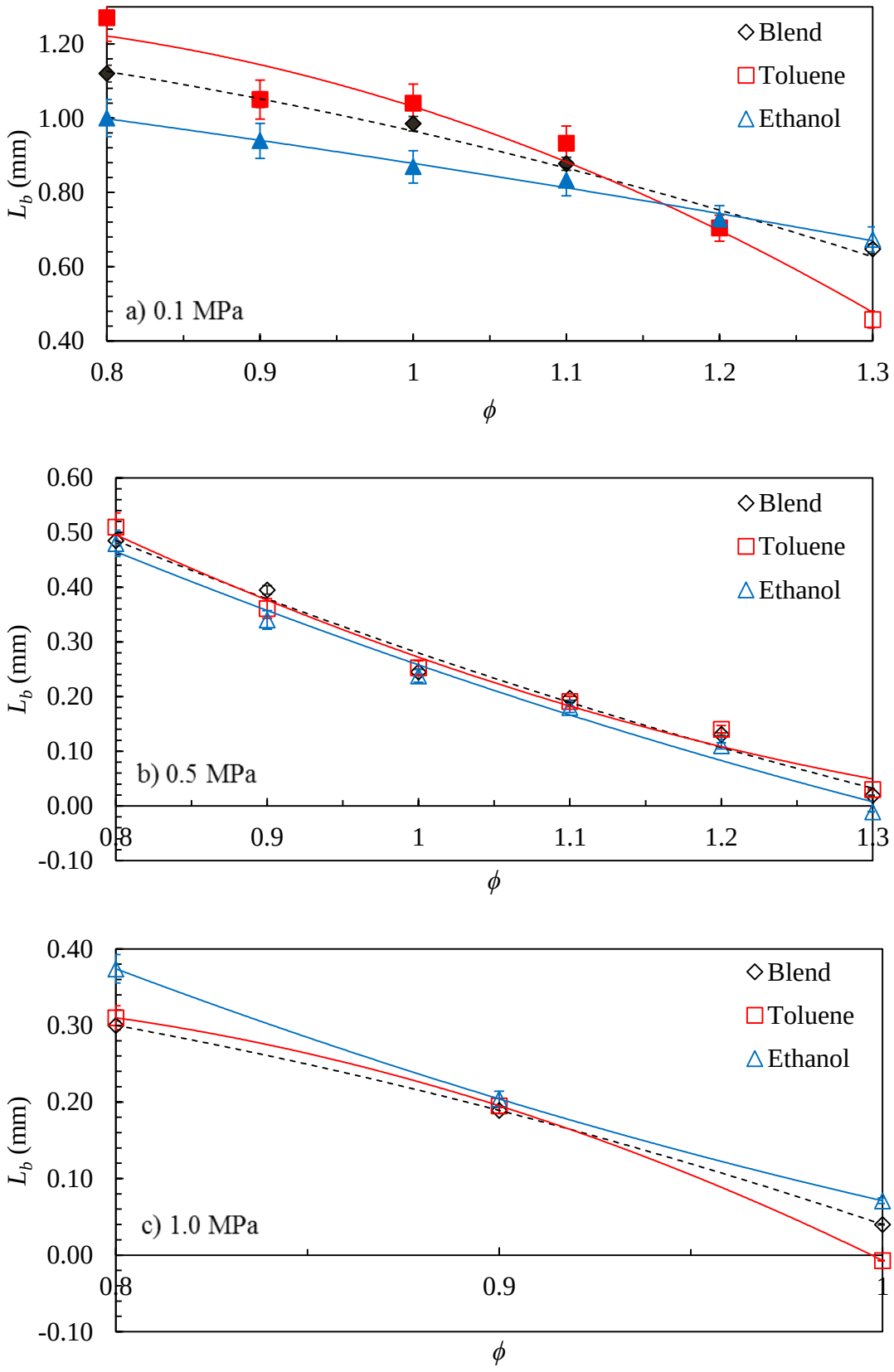

Figure 4.37: Variation of L_b with ϕ for toluene/air, ethanol/air and their relative equimolar binary blend, P_i = a) 0.1 MPa, b) 0.5 MPa, c) 1.0 MPa, T_u = 360K.

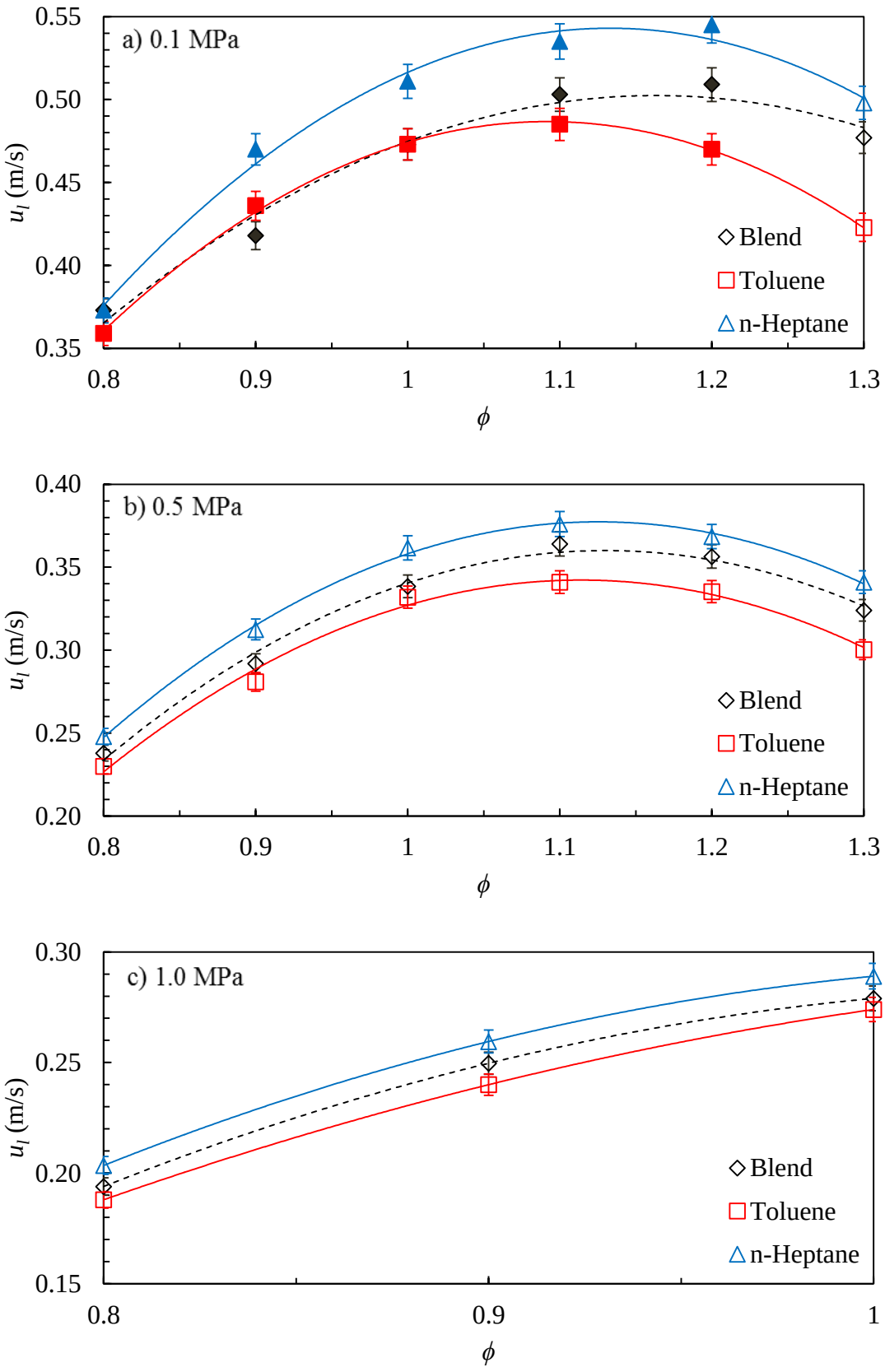

Figure 4.38: Variation of u_l with ϕ for toluene/air, *n*-heptane/air and their relative equimolar binary blend, P_i = a) 0.1 MPa, b) 0.5 MPa, c) 1.0 MPa, T_u = 360K.

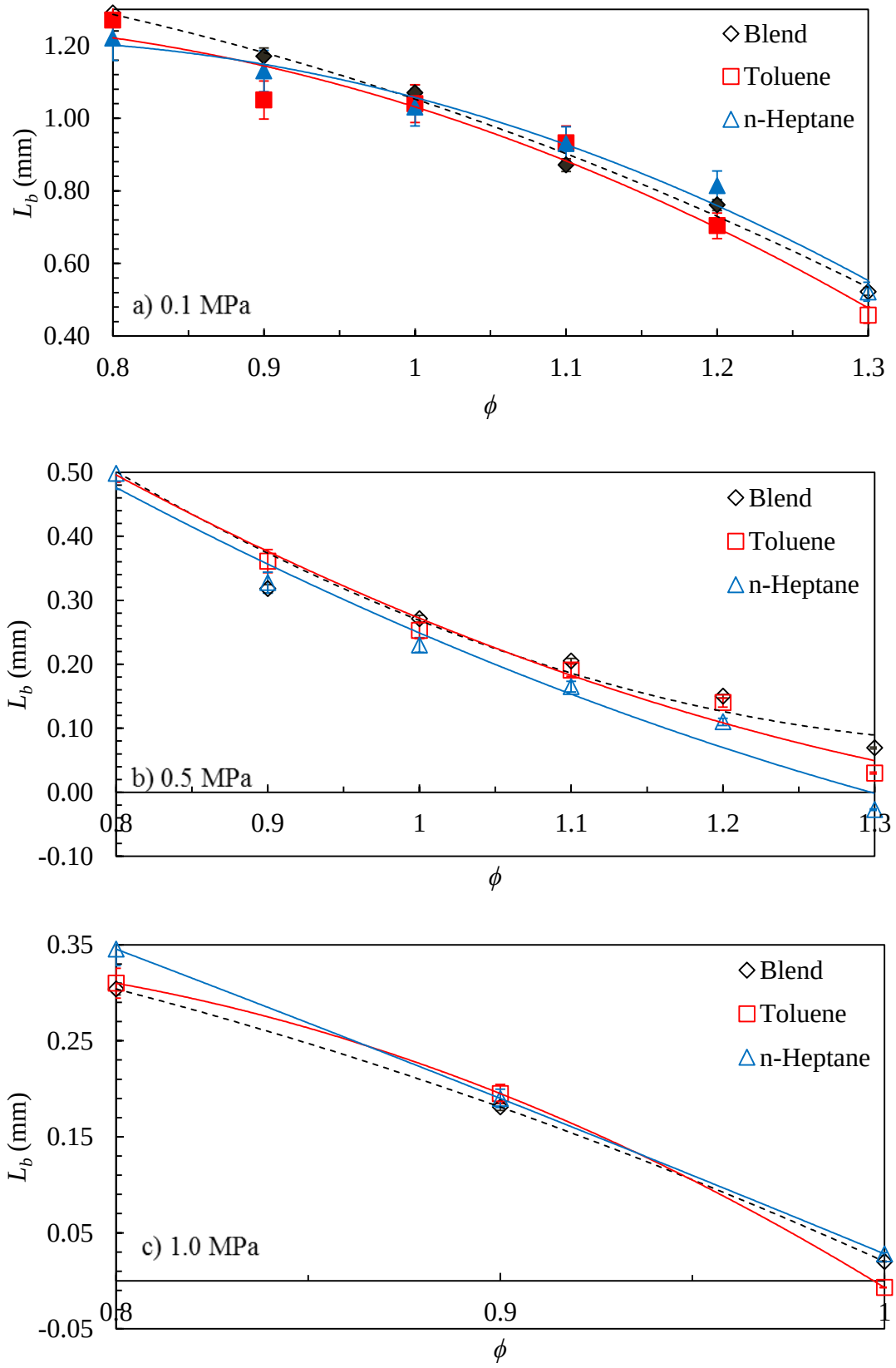

Figure 4.39: Variation of L_b with ϕ for toluene/air, *n*-heptane/air and their relative equimolar binary blend, P_i = a) 0.1 MPa, b) 0.5 MPa, c) 1.0 MPa, T_u = 360K.

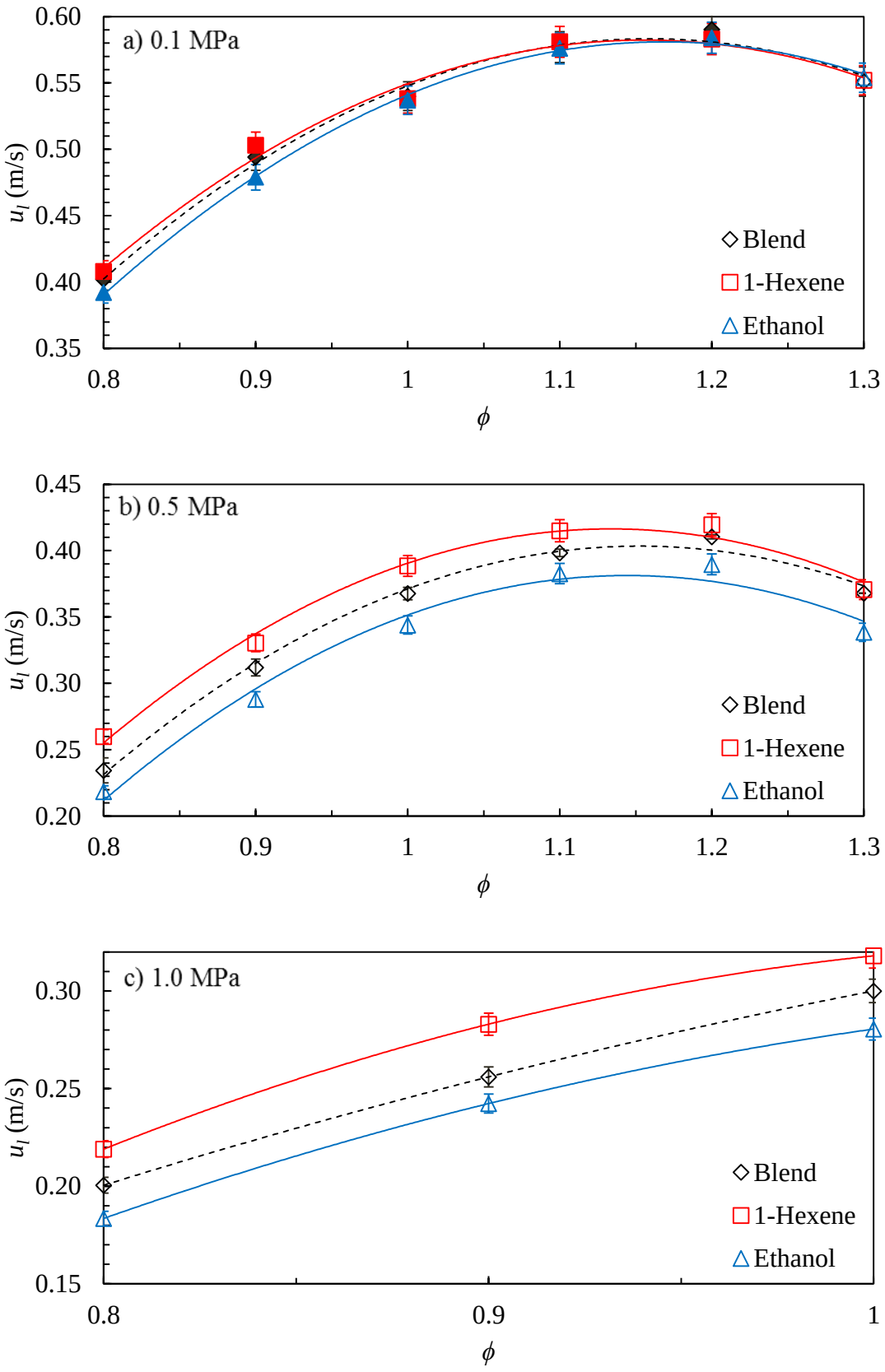

Figure 4.40: Variation of u_l with ϕ for *1*-hexene/air, ethanol/air and their relative equimolar binary blend, P_i = a) 0.1 MPa, b) 0.5 MPa, c) 1.0 MPa, T_u = 360K.

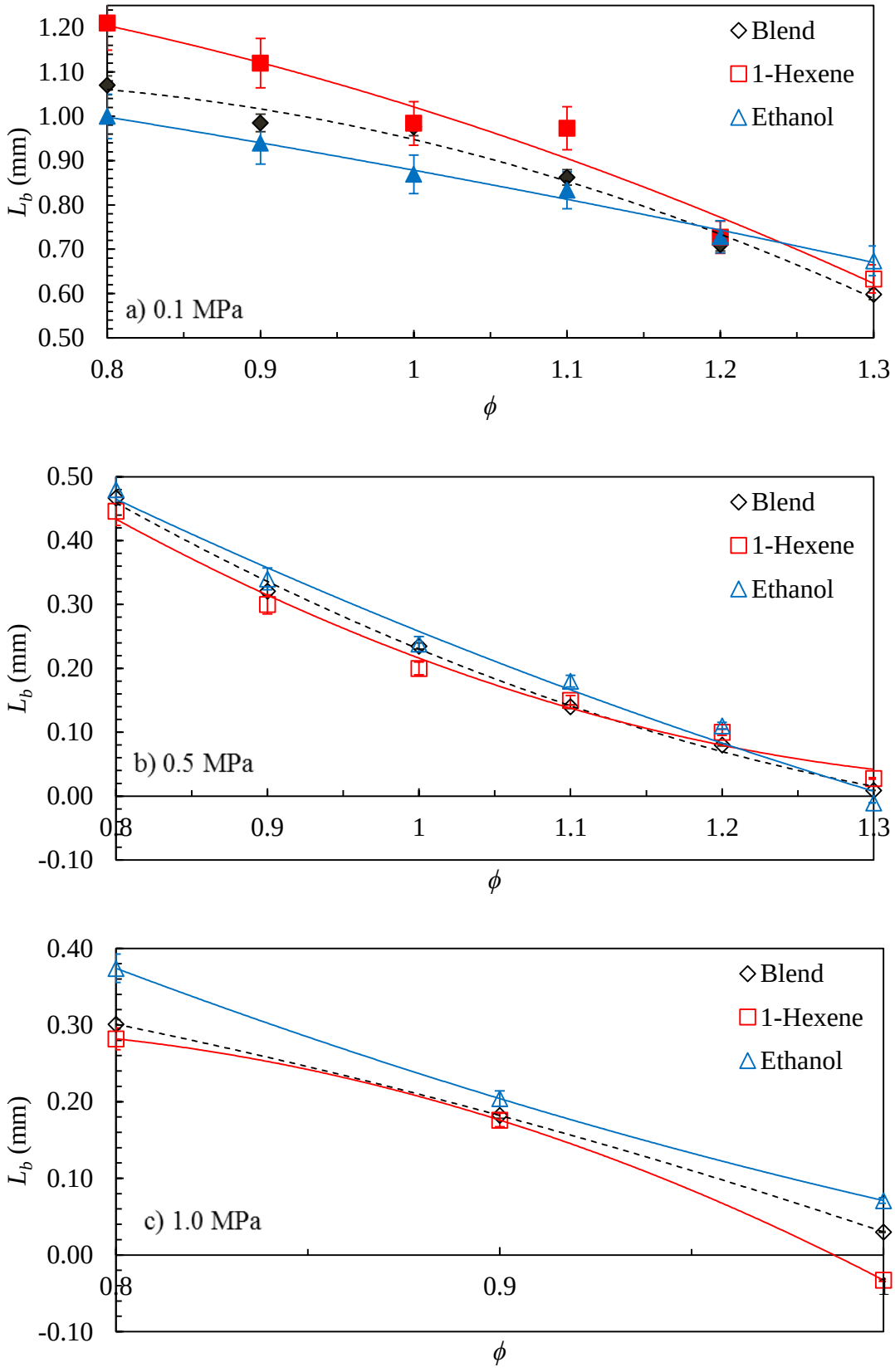

Figure 4.41: Variation of L_b with ϕ for *1*-hexene/air, ethanol/air and their relative equimolar binary blend, P_i = a) 0.1 MPa, b) 0.5 MPa, c) 1.0 MPa, T_u = 360K.

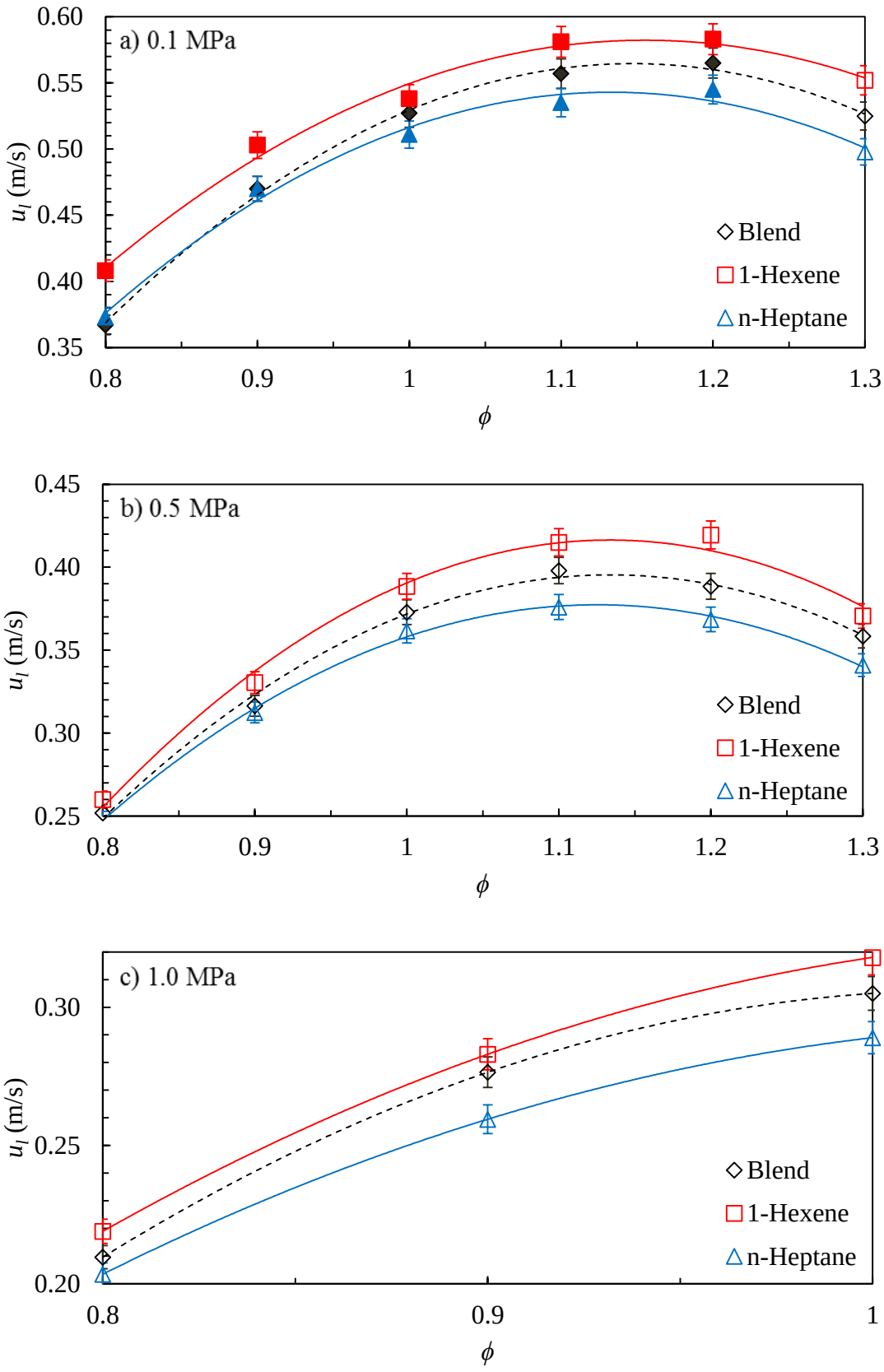

Figure 4.42: Variation of u_l with ϕ for *1*-hexene/air, *n*-heptane/air and their relative equimolar binary blend, P_i = a) 0.1 MPa, b) 0.5 MPa, c) 1.0 MPa, T_u = 360K.

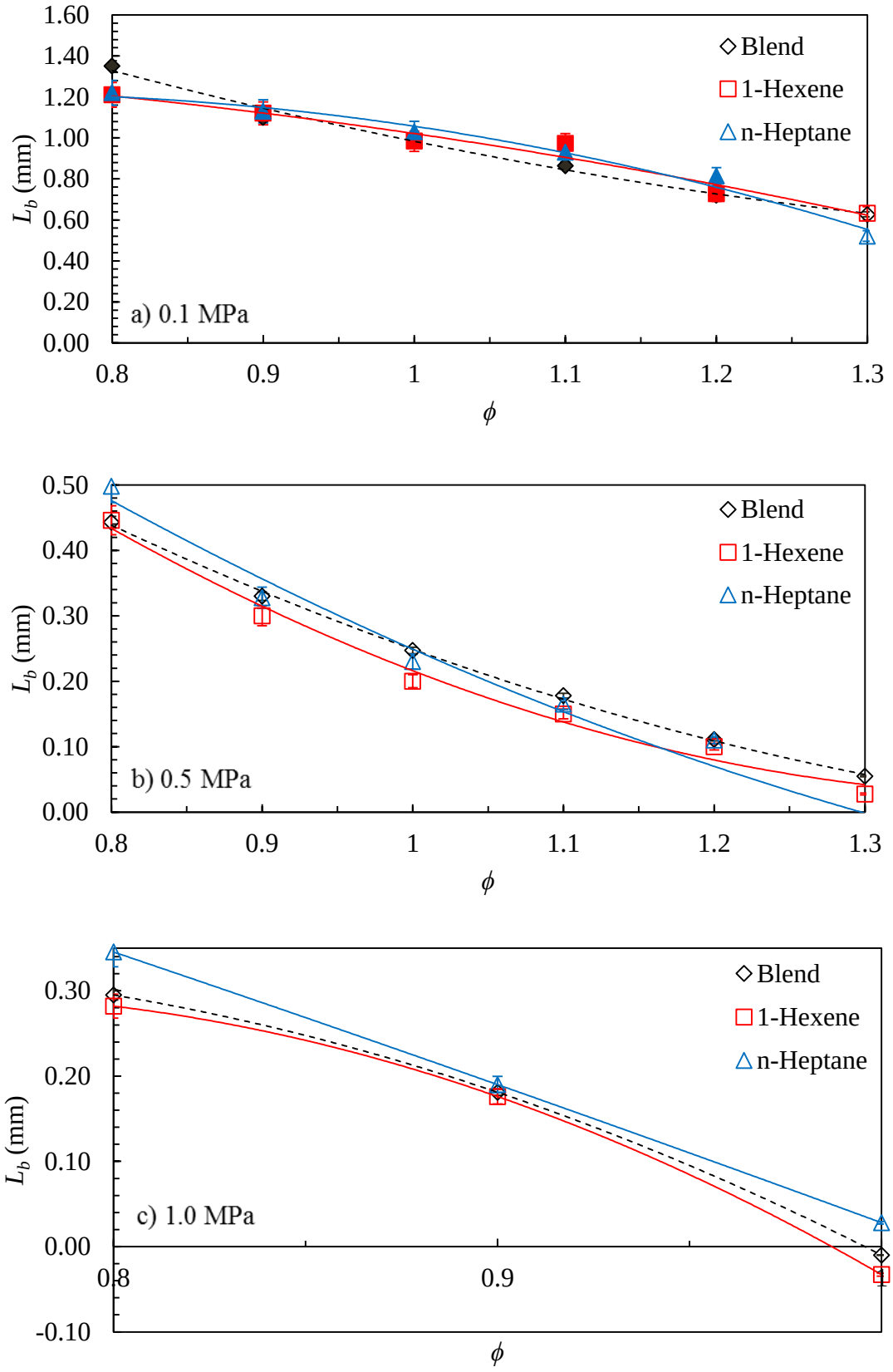

Figure 4.43: Variation of L_b with ϕ for *1*-hexene/air, *n*-heptane/air and their relative equimolar binary blend, P_i = a) 0.1 MPa, b) 0.5 MPa, c) 1.0 MPa, T_u = 360K.

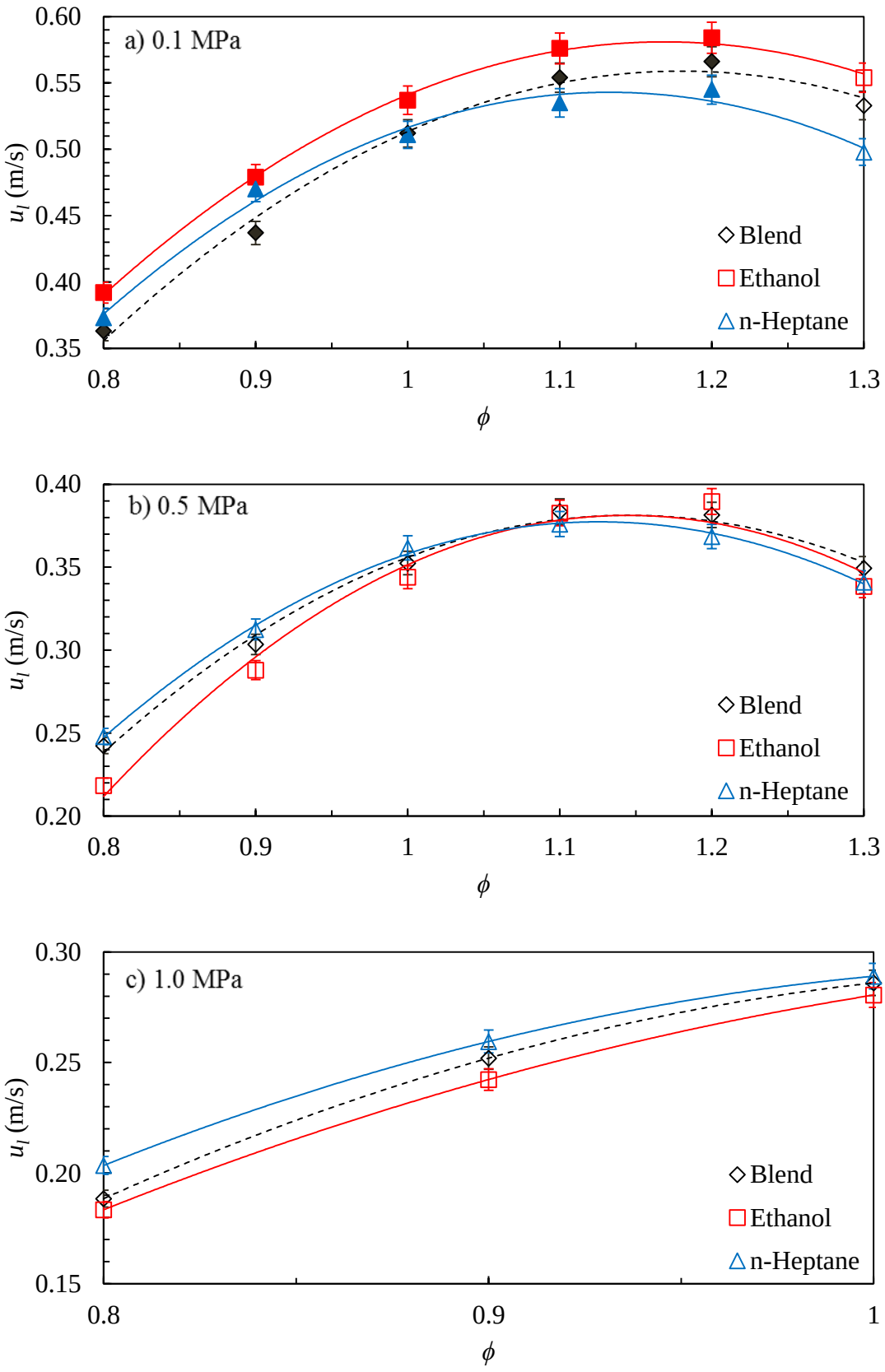

Figure 4.44: Variation of u_l with ϕ for ethanol/air, *n*-heptane/air and their relative equimolar binary blend, P_i = a) 0.1 MPa, b) 0.5 MPa, c) 1.0 MPa, T_u = 360K.

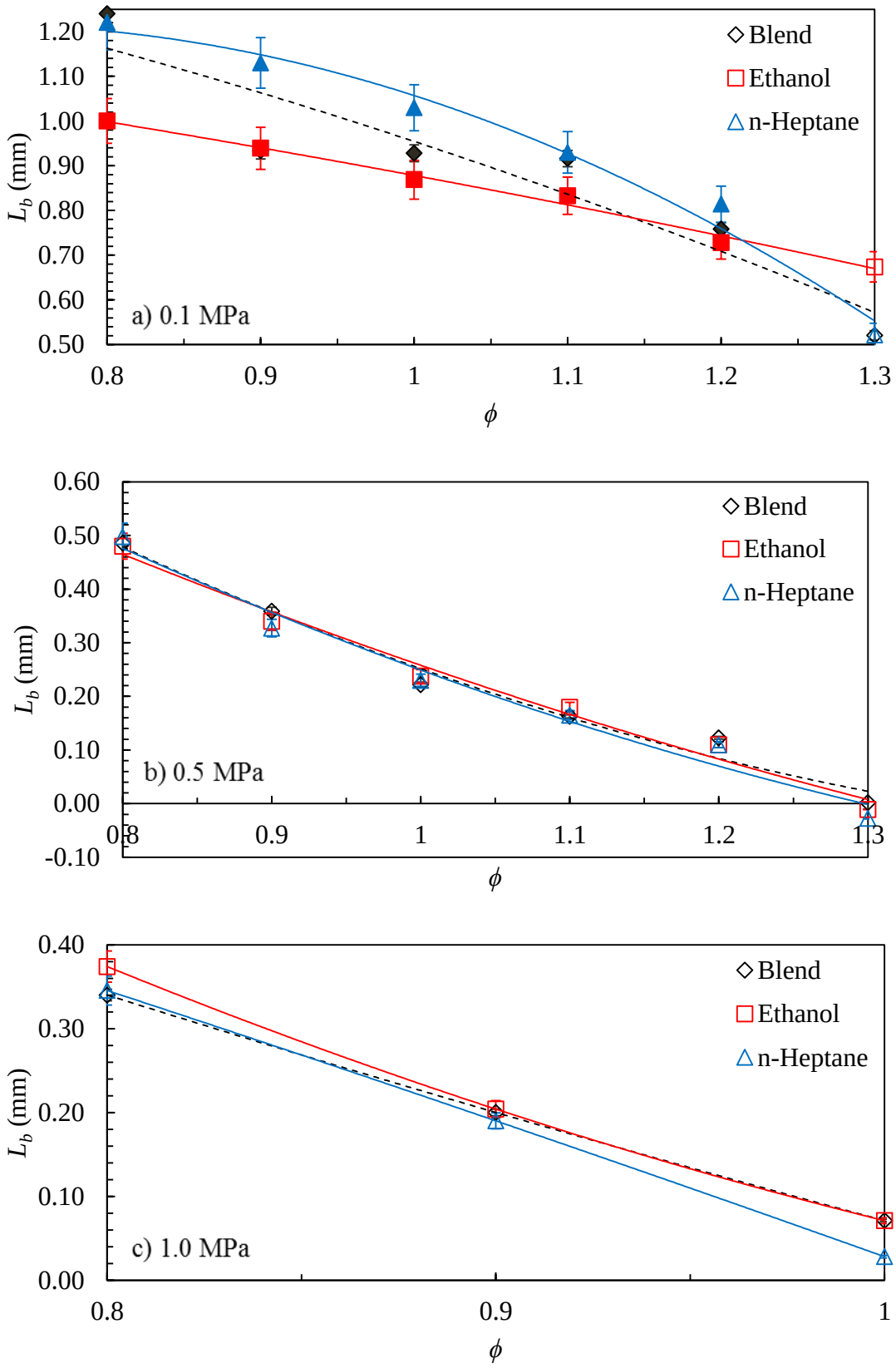

Figure 4.45: Variation of L_b with ϕ for ethanol/air, *n*-heptane/air and their relative equimolar binary blend, P_i = a) 0.1 MPa, b) 0.5 MPa, c) 1.0 MPa, T_u = 360K.

4.4 TRF and Alcohol Blends

The blending of gasoline with bio-derived alcohols in the quest to mitigate demand on petroleum based fuels and reduce CO_2 emissions is becoming increasingly common. Furthermore, within the combustion research community the use of toluene reference fuels (TRFs) as gasoline surrogates are becoming of increasing importance due to their ability to better emulate key modern gasoline combustion characteristic such, ignition delay time, burning velocity and heat realise rate, over that of traditional PRFs. They are typically a blend of *iso*-octane, toluene and *n*-heptane. However, unlike PRFs there are no industry standards for TRF compositions under agreed test conditions. Typically a TRF blend is tailored to characterise a specific parameter of the real gasoline fuel under specific conditions.

Therefore, it is of great interest and importance to understand how TRF gasoline surrogates respond to the addition of promising bio-derived alcohols such as ethanol and *n*-butanol. During the present work, a joint effort with M. Materego (2015) was made to investigate the comparative effects of these alcohols to a high octane TRF gasoline surrogate, in terms of the two key combustion parameters, u_l and τ_l. Furthermore, the study also provided a comprehensive range of multicomponent blend data, which allowed blending law performances to be analysed on a "blends of blends" basis, whereby the base TRF was considered as a single component. This is of significant relevance to those concerned with commercial fuel blending, whereby real commercial gasoline's comprise of hundreds of constituents, often with a base blend common to a number of tailored blends with specific additives to meet different performance requirements.

The TRF blend selected represented a typical European high octane premium gasoline, Grön 98 MK1, with a RON of 98.5 and MON of 88 (Morgan et al., 2010). The composition was given in terms of the liquid fuel volumetric percentage of each constituent: 75.4% toluene, 18.7% *n*-heptane and 5.8% *iso*-octane. The composition was calculated using a second order response surface model that mapped the required TRF constituent fuel proportions to the RON and MON values of any real gasoline (Morgan et al., 2010). Experimental engines studies showed the surrogate to give very similar pressure traces to that of the real gasoline. This indicates the surrogate's ability to strongly emulate the key combustion parameters of ignition delay, burning velocity and the heat release rate characteristics. Table 4.3 summarises the composition of the TRF

blend, showing the proportion of each constituent, in terms in terms of moles, mass and volume.

TRF Blend Constituents	Fuel Liquid Volume Fraction	Fuel/Air Mole Fraction	Fuel/Air Mass Fraction	Fuel Mole Fraction	Fuel Mass Fraction
Toluene	0.754	0.777	0.778	0.814	0.796
n-Heptane	0.187	0.17	0.169	0.146	0.155
iso-Octane	0.058	0.053	0.053	0.04	0.049

Table 4.3: Composition of TRF Blend, showing the different fractional proportions of each constituent within the blend, as discussed in Chapter 2, Section 2.3. Densities for all fuels are shown in Table 4.1.

Both ethanol and *n*-butanol were separately added to the base TRF in 25% liquid volume increments, with the TRF constituents kept at their original liquid volume proportions. Let prefixes E and B denote ethanol and *n*-butanol. For example, E25/TRF75 implies a blend of 25% ethanol and 75% TRF by liquid fuel volume. Table 4.4 shows the composition of the TRF/Alcohol blends, demonstrating the effect of alcohol addition on various mixture fractions in terms of moles, mass and volume.

Alcohol/TRF Blends	Liquid Volume Fraction of Alcohol	Mole Fraction of Alcohol/Air	Mass Fraction of Alcohol/Air	Mole Fraction of Alcohol	Mass Fraction of Alcohol
E25/TRF75	0.25	0.179	0.177	0.395	0.242
E50/TRF50	0.5	0.395	0.393	0.663	0.49
E75/TRF25	0.75	0.661	0.659	0.855	0.742
B25/TRF75	0.25	0.212	0.212	0.294	0.247
B50/TRF50	0.5	0.446	0.447	0.556	0.496
B75/TRF25	0.75	0.707	0.707	0.789	0.746

Table 4.4: Effects on various mixture fractions of increasing liquid volume of ethanol and *n*-butanol to the base TRF liquid Fuel. All fractional calculations are as discussed in Chapter 2, Section 2.3. Densities for all fuels are shown in Table 4.1.

Figures 4.46-4.51 show u_l and L_b values for the TRF/ethanol/air and TRF/*n*-butanol/air blends at P_i = 0.1, 0.5 and 1.0 MPa, as a function of the LV% of alcohol in the blend.

Again, filled and unfilled symbols denote measurements of u_l derived by nonlinear and linear approaches to L_b, respectively. All u_l measurements at 0.1 MPa, with ϕ = 0.8-1.2 were found to exhibit nonlinear behaviour. At the higher pressures linear behaviour was dominant, as found with all the pure fuel/air mixtures described in Section 4.2.

The effects of adding either of the alcohols to the base TRF/air mixture are most significant at P_i = 0.1 MPa. Here the differences in constituent u_l and L_b values are greatest. Across ϕ = 0.8-1.3, u_l increases with the addition of either ethanol or *n*-butanol, at an increasing rate as ϕ increase. Peak u_l values for all blends are observed to be in the region where ϕ = 1.1-1.2, with a tendency towards ϕ = 1.2 as either alcohol fraction was increased.

Under lean conditions, particularly, where ϕ = 0.8, the addition of ethanol or *n*-butanol has little effect on the u_l of TRF/air mixture, exhibiting only a gradual linear increase, but with a significant linear decrease in corresponding L_b values. This is most pronounced with the ethanol blends. Under stoichiometric conditions, values of u_l continue to increase relatively linearly with the addition of either alcohol, but at an increased rate. The corresponding L_b values for ethanol addition, continue to decrease, but at a decreased rate, whilst for *n*-butanol addition, L_b values become relatively similar. Under rich conditions the addition of either alcohol begins to have a more pronounced effect on u_l values, from as low as 25% LV, with ethanol addition exhibiting a more significant nonlinear increase. This was particularly so under the richest condition, ϕ = 1.3. The corresponding L_b values become relatively similar with addition of either alcohol where ϕ = 1.1-1.2. However, at the richest condition, ϕ = 1.3, L_b values increase with either alcohol addition, with *n*-butanol addition exhibiting a gradual linear increase, and ethanol addition, a sharp nonlinear increase from 50% LV.

At P_i = 0.5 MPa, the difference between constituent mixture u_l and L_b values is reduced, and the effect of addition of either alcohol is suppressed. Under lean conditions, where ϕ = 0.8-0.9, the addition of either alcohol has little effect on the u_l value of the TRF/air mixture up to 50% LV. Beyond this u_l values decrease with the addition of ethanol, whilst u_l values remain relatively stable with the addition of *n*-butanol. Under stoichiometric to rich conditions, where ϕ = 1.0-1.3, u_l values increase with the addition

of either alcohol, reflecting trends similar to that at P_i = 0.1 MPa, but with decreased severity. The corresponding L_b values at P_i = 0.5 MPa, across ϕ = 0.8-1.3, become remarkably similar due to very little difference between the constituent L_b values.

Again, at P_i = 1.0 MPa, the equivalence ratio range now becomes limited to stoichiometric conditions due to the early onset of cellularity. Beyond this, the application of L_b is not possible. The difference between constituent u_l values is further reduced, thus suppressing the effect of addition of either alcohol even further. However, the difference between constituent L_b values becomes slightly greater, and the corresponding L_b values show a relatively marginal decrease with the addition of either alcohol.

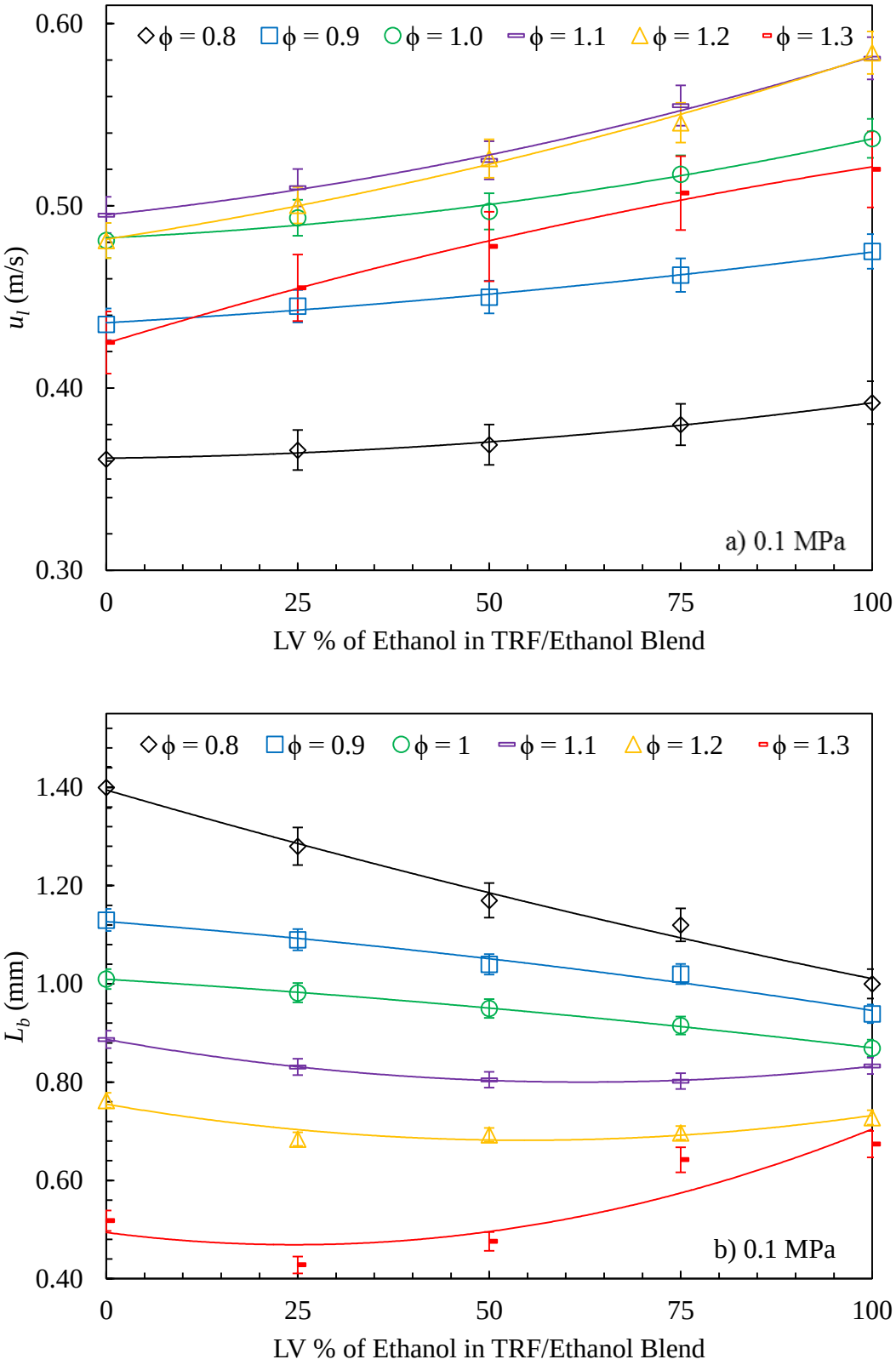

Figure 4.46: Variation of a) u_l and b) L_b with ethanol addition to TRF/air mixtures, P_i = 0.1 MPa and T_u = 360K.

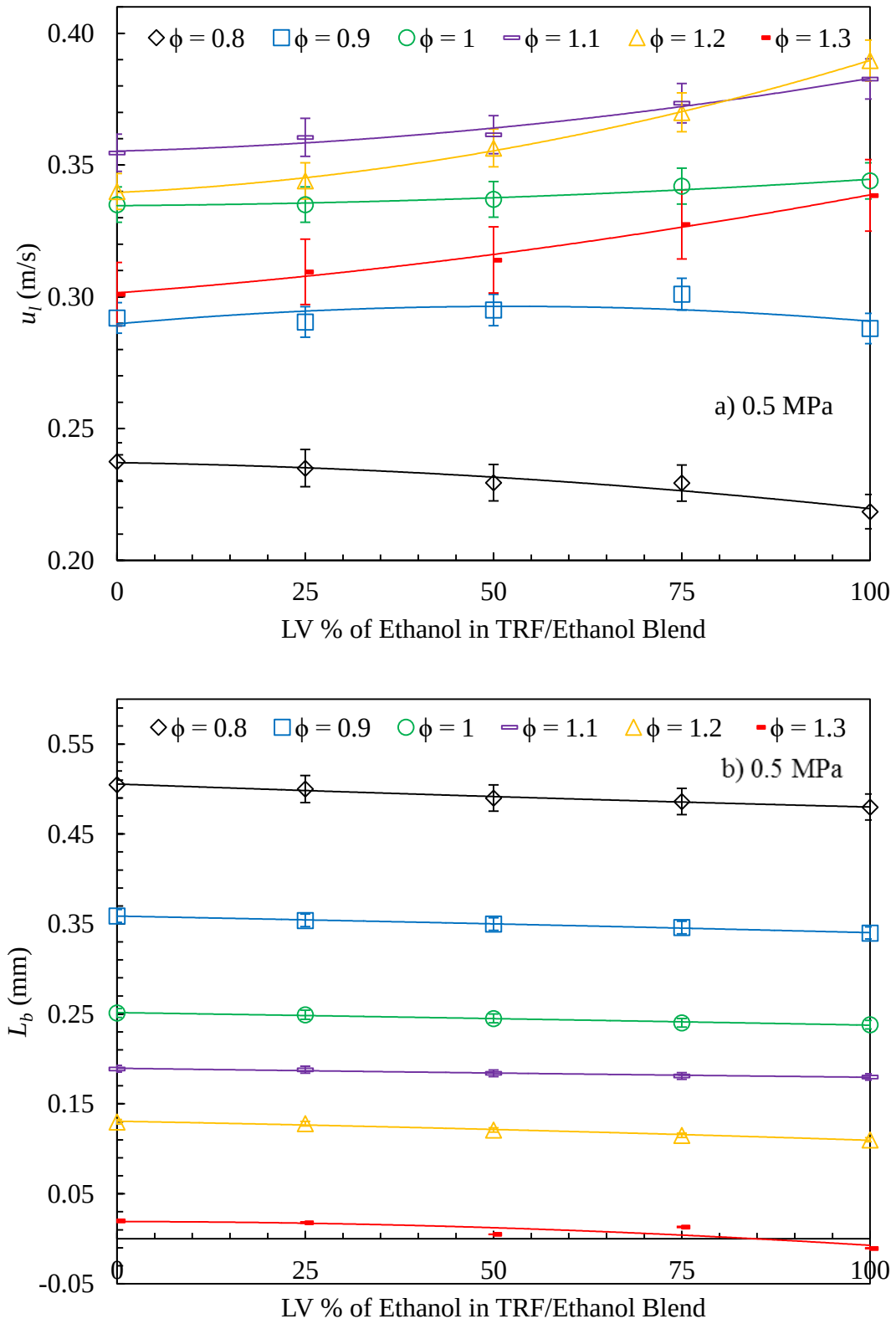

Figure 4.47: Variation of a) u_l and b) L_b with ethanol addition to TRF/air mixtures, P_i = 0.5 MPa and T_u = 360K.

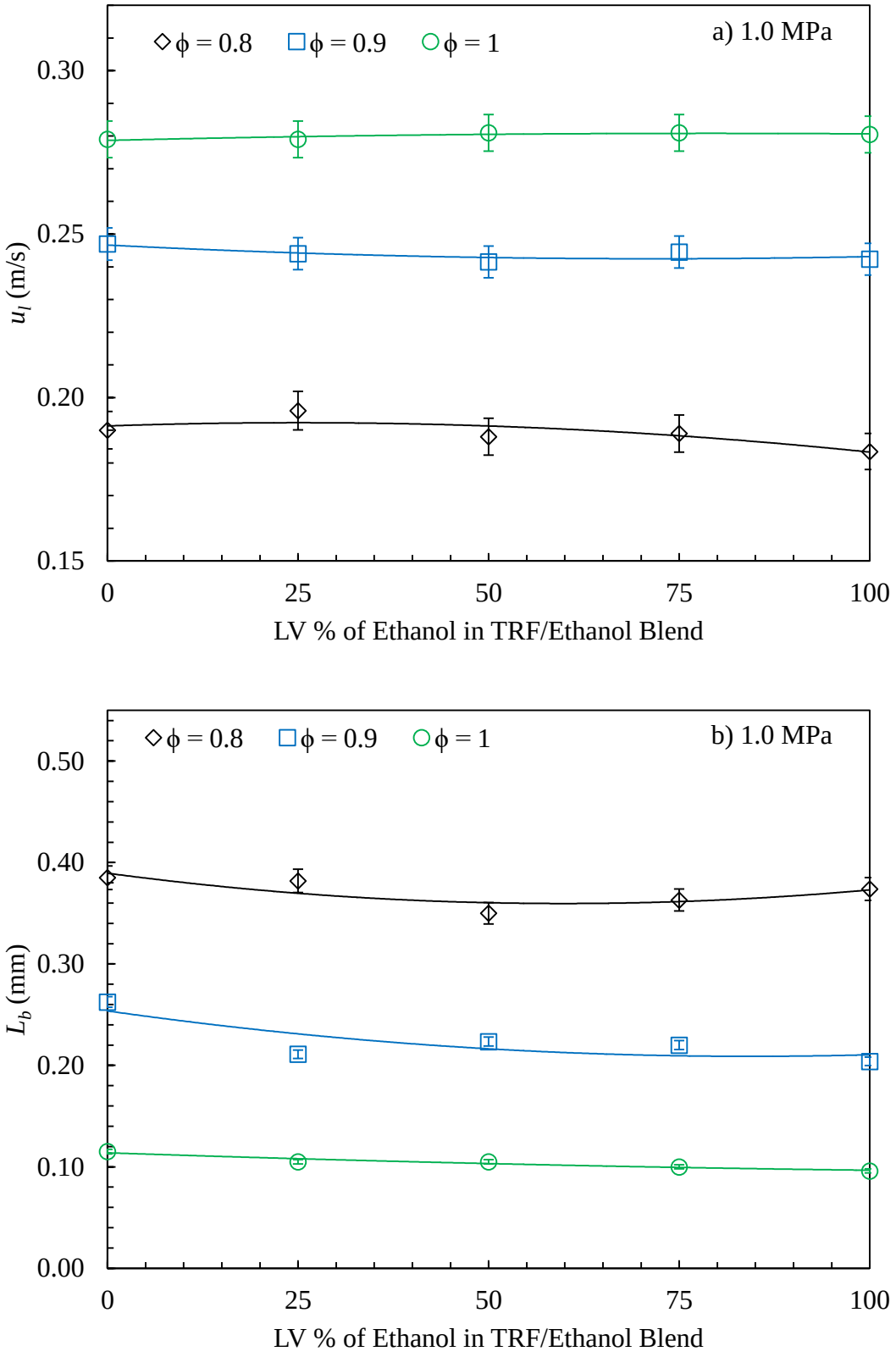

Figure 4.48: Variation of a) u_l and b) L_b with ethanol addition to TRF/air mixtures, P_i = 1.0 MPa and T_u = 360K.

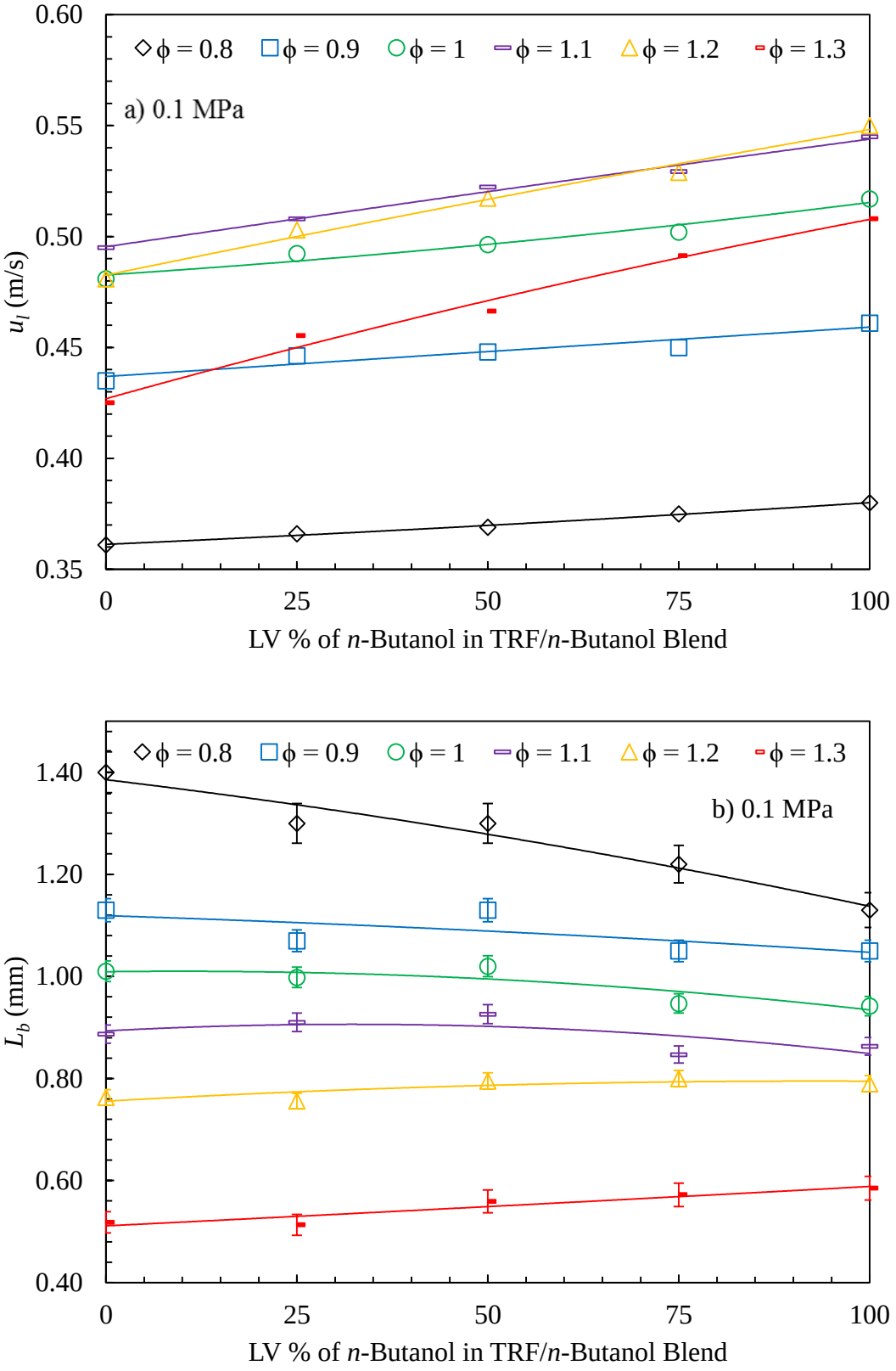

Figure 4.49: Variation of a) u_l and b) L_b with *n*-butanol addition to TRF/air mixtures, P_i = 0.1 MPa and T_u = 360K.

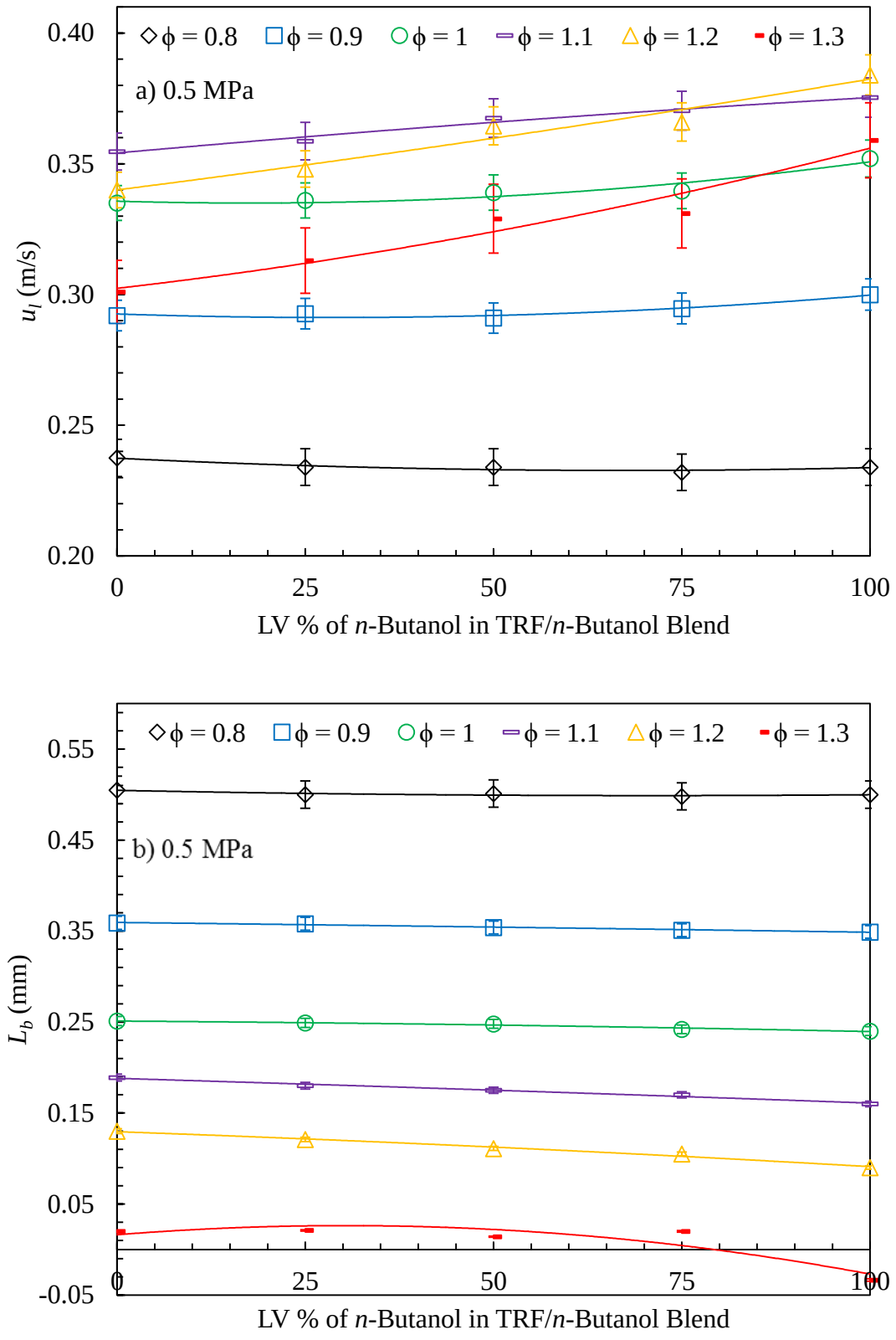

Figure 4.50: Variation of a) u_l and b) L_b with *n*-butanol addition to TRF/air mixtures, P_i = 0.1 MPa and T_u = 360K.

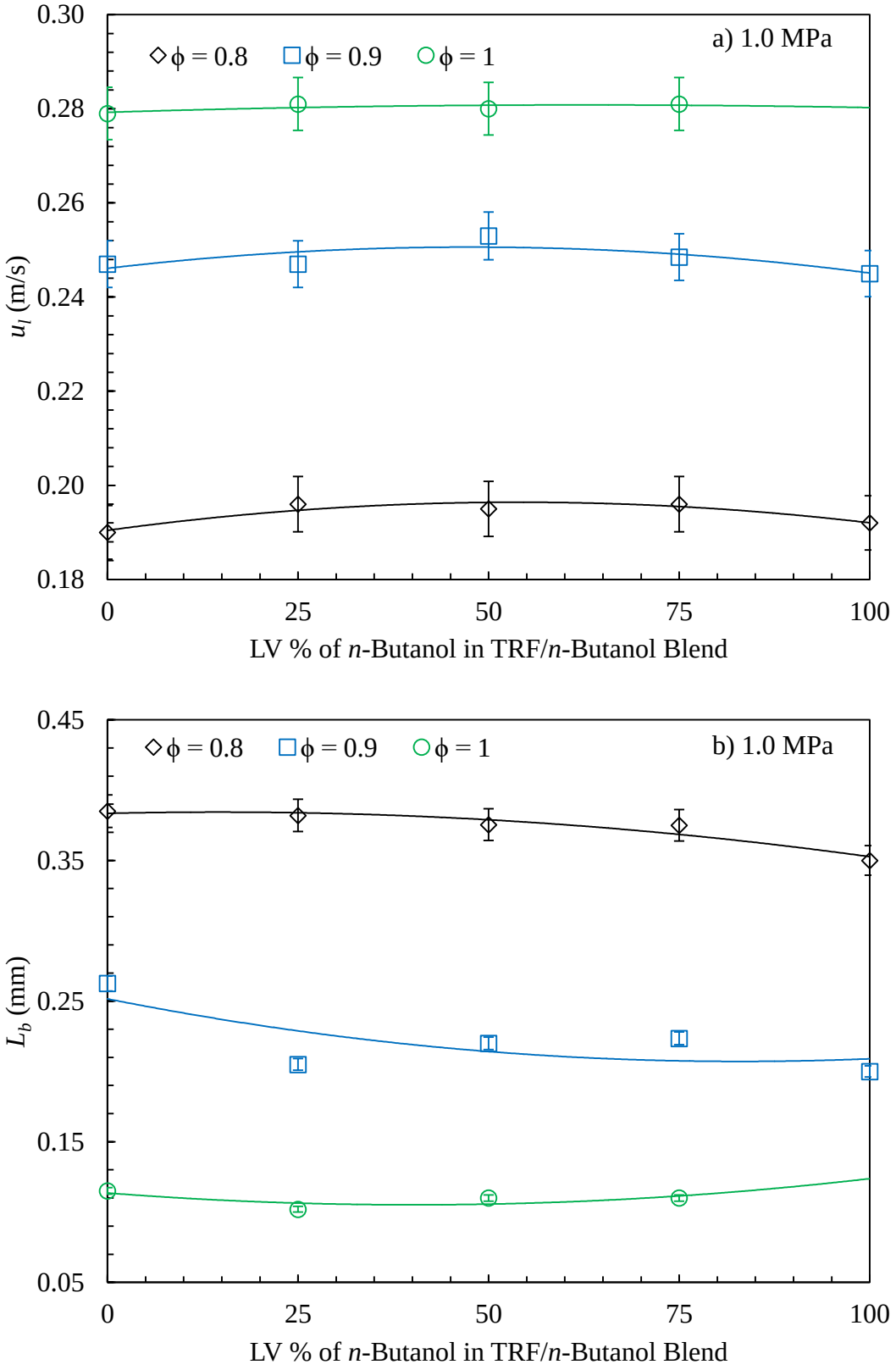

Figure 4.51: Variation of a) u_l and b) L_b with *n*-butanol addition to TRF/air mixtures, P_i = 1.0 MPa and T_u = 360K.

4.5 Methane and Hydrogen Blends

The burning velocities of hydrogen/air and methane/air and their blends have received attention as an aspect of a hydrogen economy, with hydrogen being added to the natural gas distribution system. Burning velocity data is plentiful: (Bauer and Forest, 2001; Halter et al., 2005; Hu et al., 2009; Karim et al., 1996; Shrestha and Karim, 1999). Their radically contrasting chemical composition and kinetics are especially challenging for the development of their blending laws. As pure fuels, u_l and L_b data over extensive equivalence ratio ranges, at different initial temperatures and pressures are plentiful, whereas comprehensive blend data are less so.

However, the blend u_l and L_b data of Hu et al., (2009), provide a suitable and challenging check for the different predictive blending laws. Their experiments were performed in a constant volume combustion vessel, at the initial temperature and pressure of 303K and 0.1 MPa, employing a schlieren technique to measure the flame propagation, with u_l derived via extrapolation to zero stretch, using a justifiable linear approach. The H_2 concentration in the CH_4/H_2 fuel blend was increased in fractional fuel mole increments of 0.1. In terms of the mixing of the H_2/air and CH_4/air both constituent mixtures have the same ϕ, equal of course to the blend ϕ. Table 4.5 summarises the composition of the CH_4/H_2 blends, showing the proportion of each constituent, in terms of moles and mass, as discussed in Chapter 2, Section 2.3.

Figures 4.52a and b show u_l for hydrogen/air, methane/air and their blends over the range of ϕ = 0.6-1.3. The addition of hydrogen increases u_l, whilst shifting the peak value towards richer conditions. Hu et al., (2009), observed that the blend fractions may be classified into three regimes: a methane dominated regime when the hydrogen fraction is less than 60%, a transition regime between 60-80% and finally a hydrogen dominated regime at fractions over 80%. The methane and hydrogen dominated regimes both exhibit linear trends between the addition of hydrogen and increasing burning velocity, whilst the transition regime exhibits an exponential trend in burning velocity increase relative to hydrogen addition.

Figures 4.53a and b show the corresponding L_b measurements for methane, hydrogen and their blends. The values for methane are positive across the entire equivalence ratio range, whilst values for hydrogen become negative under lean conditions. L_b for both methane/air and hydrogen/air mixtures increase with equivalence ratio, with methane/air

exhibiting a significantly increased rate under rich conditions. As the hydrogen fuel mole fraction of a blend increases, L_b decreases. Under lean conditions, particularly in the hydrogen dominated regime, with fractions over 0.8, blend L_b values become markedly negative.

Mole Fraction of H_2 in CH_4+H_2	Mass Fraction of H_2 in CH_4+H_2	Mole Fraction of H_2/Air in (CH_4+H_2)/Air	Mass Fraction of H_2/Air in (CH_4+H_2)/Air
0.1	0.014	0.034	0.026
0.2	0.031	0.074	0.057
0.3	0.051	0.121	0.094
0.4	0.077	0.176	0.139
0.5	0.112	0.243	0.196
0.6	0.159	0.325	0.267
0.7	0.227	0.428	0.362
0.8	0.335	0.562	0.493
0.9	0.531	0.743	0.686

Table 4.5: **A compositional list of the CH4/H2/air blends, showing the proportion of each constituent within the blend by different units of measurement, as discussed in Chapter 2, Section 2.3.**

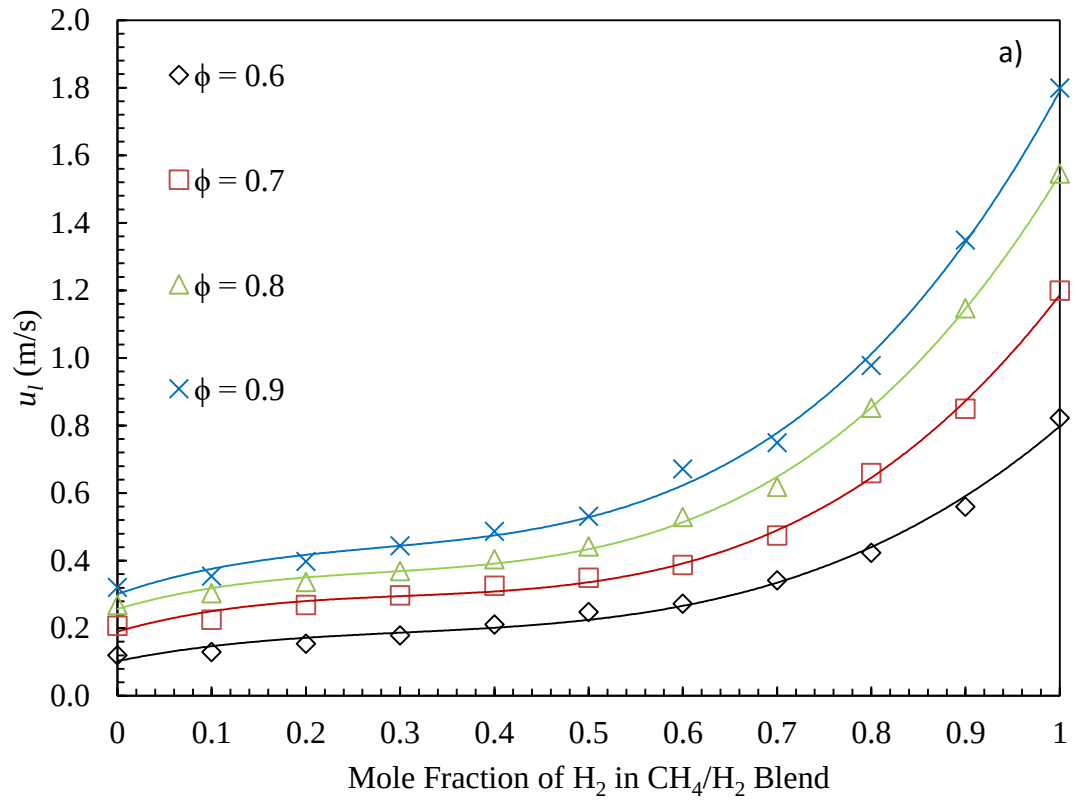

.

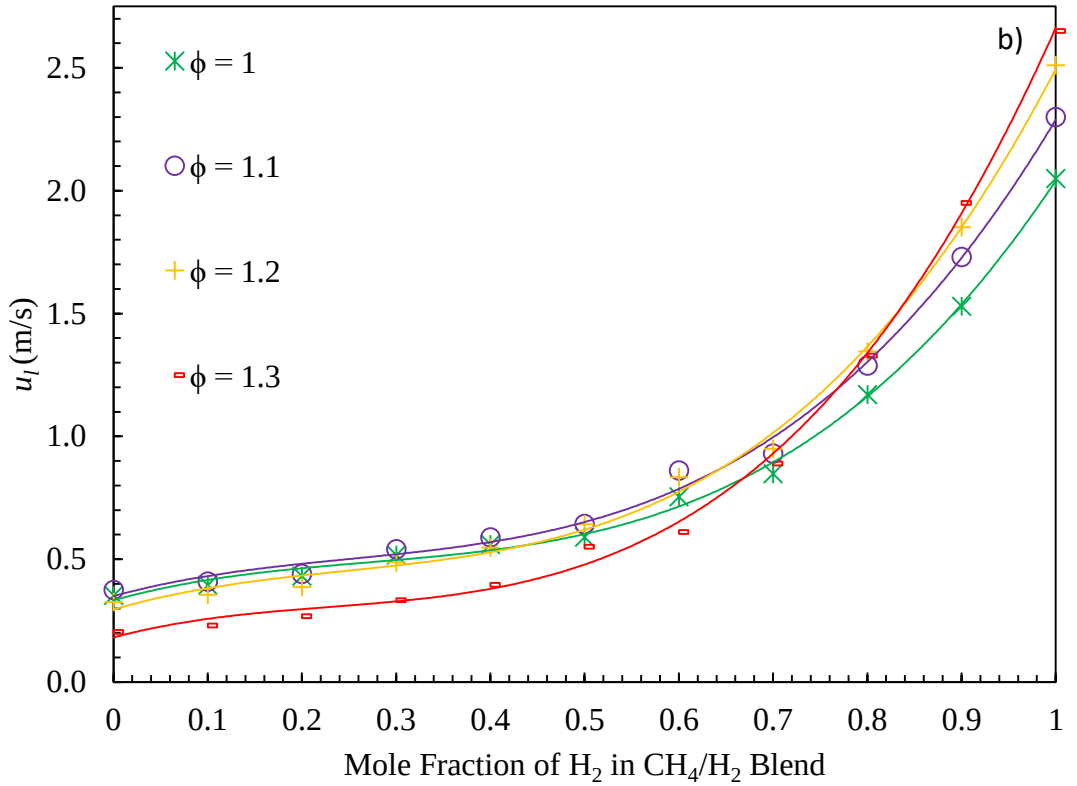

Figure 4.52: Variation of u_l with hydrogen addition to methane/air mixtures, P_i = 0.1 MPa, T_u = 303K, a) ϕ = 0.6-0.9, b) ϕ = 1-1.3.

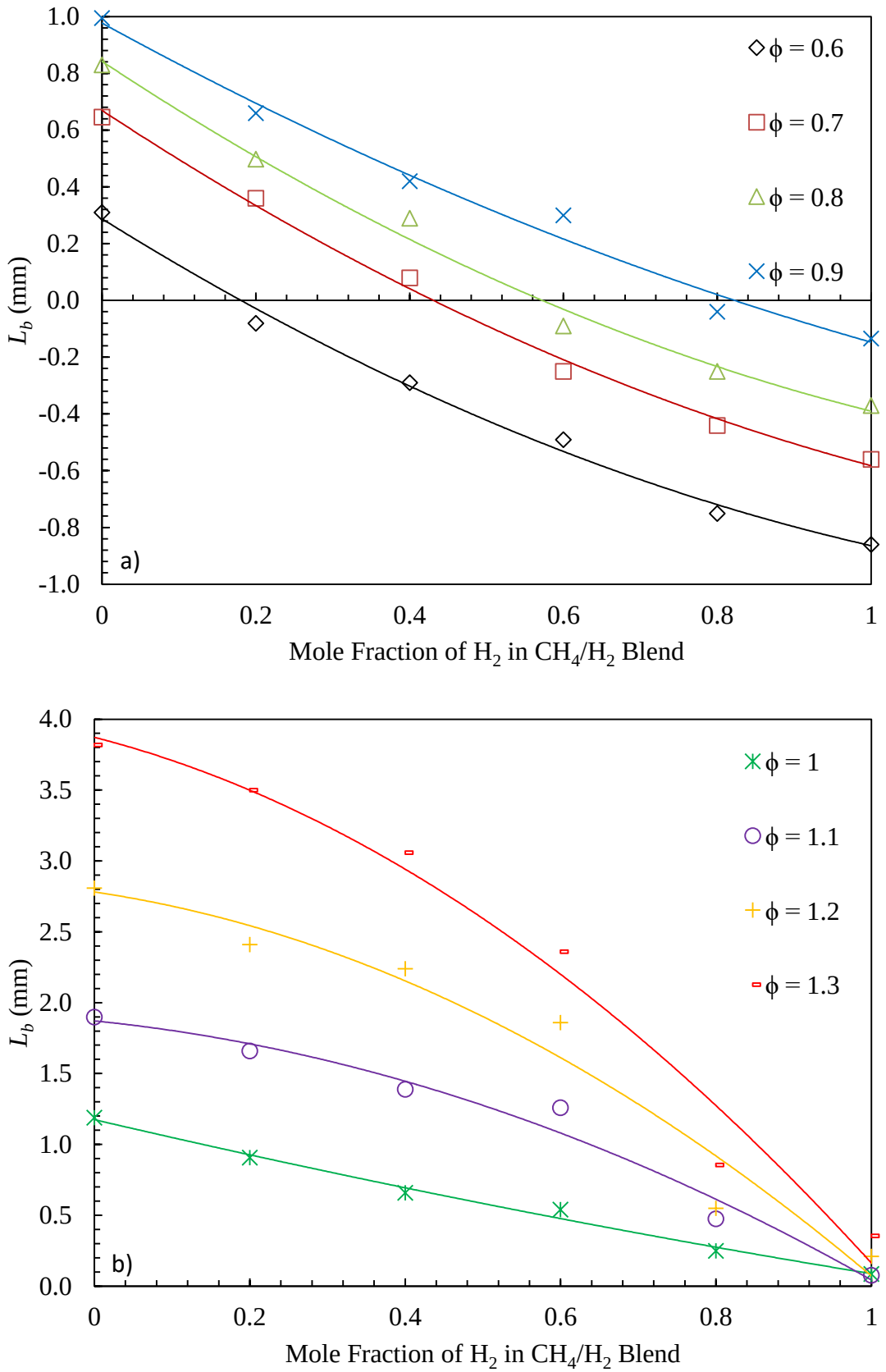

Figure 4.53: Variation of L_b with hydrogen addition to methane/air mixtures, P_i = 0.1 MPa, T_u = 303K, a) ϕ = 0.6-0.9, b) ϕ = 1.0-1.3.

Chapter 5 - Discussions of Measured Pure Fuel/Air Mixtures and Blend Behaviour

5.1 Introduction

This Chapter presents various discussions on the measured data for the pure constituent fuel/air mixtures and their blends presented in Chapter 4, considering the influence of fuel type, pressure and the equivalence ratio.

Section 5.2 discusses observations of linear and nonlinear flame speed/stretch rate relations, and analyses the potential over estimation error associated in the linear extrapolation methodology, when used for mixtures exhibiting distinct nonlinear flame speed/stretch rate behaviour.

Section 5.3 discusses the onset of cellularity indicative of Darrieus-Landau and thermo-diffusive instabilities that occurred at elevated pressure, and the correlation of the critical Peclet and Karlovitz numbers with Markstein numbers. The potential for laboratory combustion vessels at elevated pressure to emulate such parameters for large-scale atmospheric explosions was also investigated.

Comparisons of the pure fuel/air mixtures are made with existing literature in Section 5.4. Section 5.5 discusses the comparative effects of blending a TRF with ethanol and *n*-butanol. Subsection 5.5.1 focuses on laminar burning velocities and Markstein lengths, whilst subsection 5.5.2 focuses on the ignition delay times for the same blends, as part of the conjoint effort into TRF/alcohol blend behaviour with M. Materego (2015), using the newly commissioned RCM, as presented in Appendix A. A summary of the joint investigation is then given in subsection 5.5.3.

Lastly, Section 5.6 discusses methane/air energy flux variations with the addition of hydrogen.

5.2 Linear and Nonlinear Flame Speed vs. Stretch Rate Relationships

As detailed in Chapter 1, all real flames are subject to stretch in the form of strain and/or curvature imposed by their surroundings. As such, the different experimental configurations used in their study impose different degrees of stretch behaviour. Therefore, the notion of decoupling such effects to yield the fictitious laminar burning

velocity, u_l, as a universal parameter has become standardised practise in combustion studies. Therefore, an accurate understanding of the relationship between flame propagation and stretch to ensure an accurate extrapolation to the point of zero stretch is of critical importance to the acquisition of u_l. Flame stretch may be described as a measure of the temporal flame surface deformation and plays a fundamental role in the propagation, stability and structure of any premixed flame.

Kelley and Law (2009) and Halter et al. (2010), have shown the traditional linear methodology is based on assumptions that will not account for distinct nonlinear flame speed/stretch behaviour exhibited by some mixtures under certain conditions. In such cases, the linear approach can give significant over estimation of u_l and calls for the better suited nonlinear methodology. Details of each methodology are introduced in Chapter 1.

During the present study, as presented in Chapter 4, a large number of spherical flame explosions were carried out for a variety of different fuel/air mixtures across an equivalence ratio range of 0.8 to 1.3, for pressures of 0.1, 0.5 and 1.0 MPa. This simultaneously allowed for the analysis of fuel type, equivalence ratio and pressure influence on flame speed/stretch behaviour. Furthermore, the processing of all mixtures u_l values employed both aforementioned linear and nonlinear methodologies, such that any difference in the acquired u_l was quantified. Therefore, an evaluation of any over estimation error caused by the traditional linear methodology was possible.

At the elevated pressures of 0.5 and 1.0 MPa, dominant linear behaviour was observed for all fuel/air mixtures across the full equivalence ratio range. Only at 0.1 MPa was nonlinear behaviour observed, the degree of which decreased with an increase in ϕ. Figures 5.1a and b show the percentage over estimation error for u_l and L_b by linear extrapolation relative to nonlinear extrapolation, as a function of ϕ, for each pure fuel/air mixture. As anticipated, mixtures under the highest degree of stretch show the highest errors.

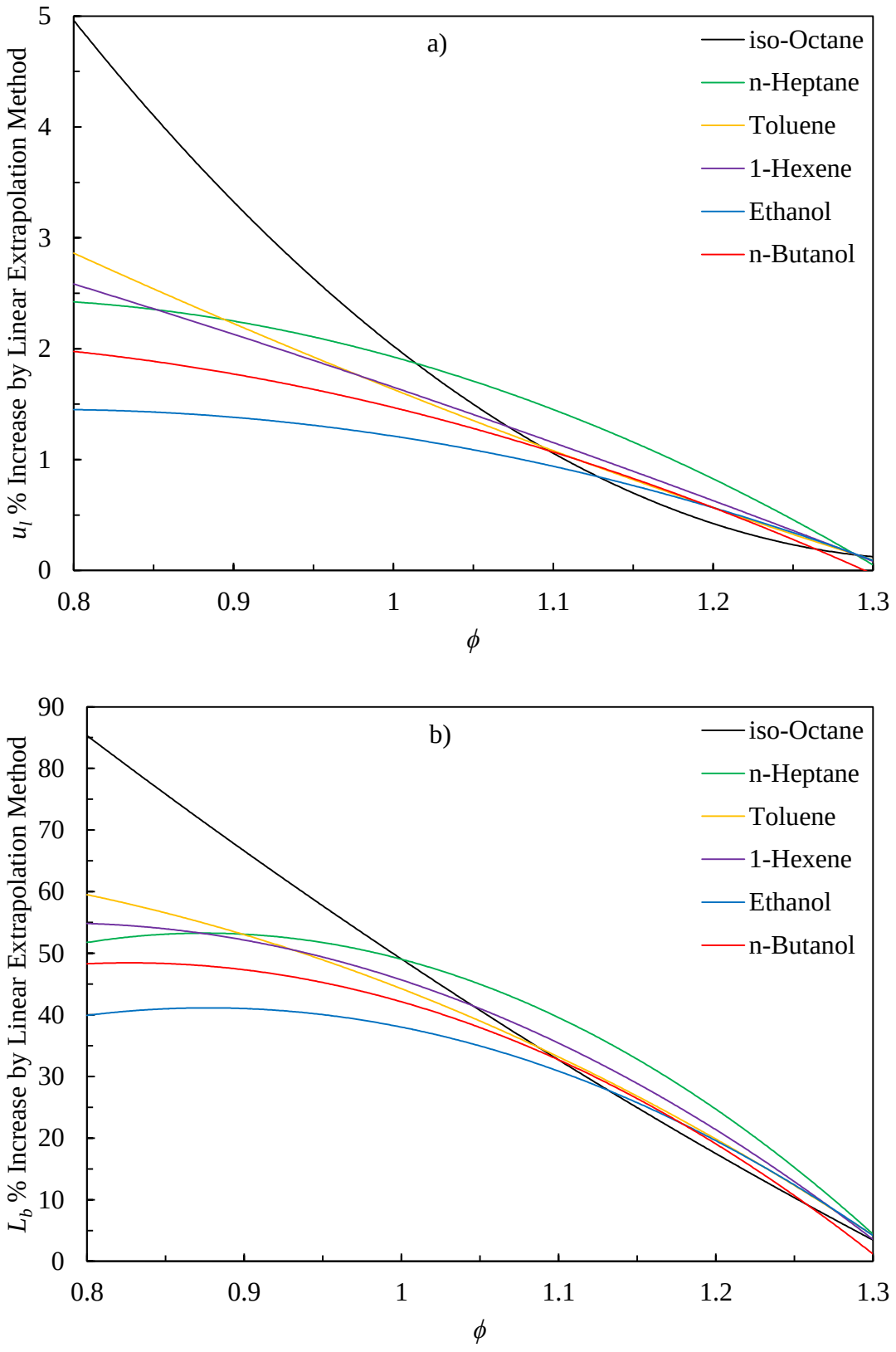

Figure 5.1: Variation of a) u_l and b) L_b percentage increase by linear extrapolation relative to nonlinear extrapolation with ϕ, for all pure liquid fuel/air mixtures, P_i = 0.1 MPa and T_u = 360K.

For the measurement of u_l, at 0.1 MPa, the differences between the two methodologies beyond stoichiometric condition, for all fuel types, are within the experimental error margin of roughly 2%, suggesting the traditional linear approach will suffice. However, under lean conditions, ϕ = 0.8-0.9, all fuels studied were subject to higher degree of stretch. The fuels, *iso*-octane, toluene, *n*-heptane and *1*-hexene, were notably over estimated beyond the experimental error, particularly for the slowest burning fuel, *iso*-octane, peaking with an over estimation error of 5%.

The differences between the two methodologies in terms of L_b are significantly greater. Reflecting that of the u_l data, the over estimation error by the linear methodology relative to the nonlinear methodology reduced with ϕ. Not until ϕ = 1.3, did the error reduce to within the experimental error margin of 5-8%. The highest over estimation error was again exhibited by lean *iso*-octane, ϕ = 0.8, peaking at over 85%.

Whilst u_l overestimations by the linear methodology were found to be relatively low, it is clear, that for the corresponding L_b values, the differences are strikingly high. This demonstrates the need for particular care when assessing the influence of stretch for such hydrocarbon fuels under lean, atmospheric conditions. It is likely that such neglection contributes towards the large degree of scatter for such L_b values in existing literature.

5.3 Cellular Instabilities

When the flame stretch rate in an exploding spherical flame falls below a certain threshold, the Darrieus-Landau and thermo-diffusive instabilities produce severe wrinkling of an initially smooth laminar flame. As the radius of a spherical flame increases, the wrinkling of the flame surface extends to an ever-increasing range of curvatures, resulting in an increasing flame speed and a strengthening of the pressure pulse (Bradley, 2011). The resolution of the wrinkled surface, the derivation of its surface area and its increasing flame speed have presented severe problems in attempts to mathematically model the phenomena, and solutions are not possible beyond a radius of a few cm. Consequently, semi-theoretical studies have involved a combination of fractal analyses (Bradley, 1999; Gostintsev et al., 1988) and experiments (Bradley et al., 1998b; Gu et al., 2000), some on a larger scale of several metres (Bauwens et al., 2015a; Bauwens et al., 2015b; Bradley et al., 2001).

A key parameter for a spherical flame is the critical flame radius, r_{cl}, that marks the onset of flame cellularity with an increasing flame speed. During the present work, measurements of r_{cl} were taken at pressures of 0.5 and 1.0 MPa, at a temperature 360K, and between ϕ = 0.8-1.3 for all pure fuel/air mixtures. Such phenomena was not observed at the lower pressure of 0.1 MPa between ϕ = 0.8-1.2, where flames remained stable within the maximum observable radius of 75 mm. As introduced in Chapter 1, the appropriate dimensionless radius is the Peclet number, Pe_{cl}, comprising r_{cl}, normalised by the flame thickness, δ, equal to the cold mixture kinematic viscosity divided by the u_l.

Due to the thermo-diffusive character of such instabilities, it of rational thought to expect their onset to be dependent upon the Markstein number, Ma_b. Furthermore, if such relationships are not pressure sensitive, it would suggest that high pressure laboratory explosions might be used to predict the effects of large-scale atmospheric explosions. To examine this theory, data from several large-scale atmospheric explosion experiments have been compared to that of data from explosions at elevated pressure in the Leeds combustion vessel during the course of the present work.

Figures 5.2a and b present plots of Pe_{cl} variation with Ma_b for each pure fuel/air mixture form the present work, at 0.5 and 1.0 MPa, respectively, alongside that of corresponding data for large-scale explosions of methane and propane. For the present work data, all symbols are unfilled and represent the mean of at least three explosions. Bearing in mind the inevitable experimental scatter in both of the measured parameters, it is striking that the influences of the fuel and pressure are relatively small.

The black diamond and bar symbols represent the large-scale astmopheric methane and propane explosions, conducted by Shell Research Ltd. in a large vented steel box structure 10m, long, 8.75m wide and 6.25m high (Bradley et al., 2001). Flame speeds were measured up to a radius of 3.5m for CH_4/air, ϕ = 1.1, and C_3H_8/air, ϕ = 1.06. There is a satisfactory correlation, at each of the two presssures, between the Pe_{cl} and Ma_b values of the many different mixtures, irrespective of their value of ϕ. Furthermore, comparison of the two figures shows but a small influence of pressure. Importantly, the two sets of coordinates from the large atmospheric explosions are close to those from the small high pressure explosions at 0.5 MPa, and slightly higher at 1.0 MPa. This suggests that instability data from high pressure laboratory explosions might be used to predict instability effects in large scale atmospheric explosions.

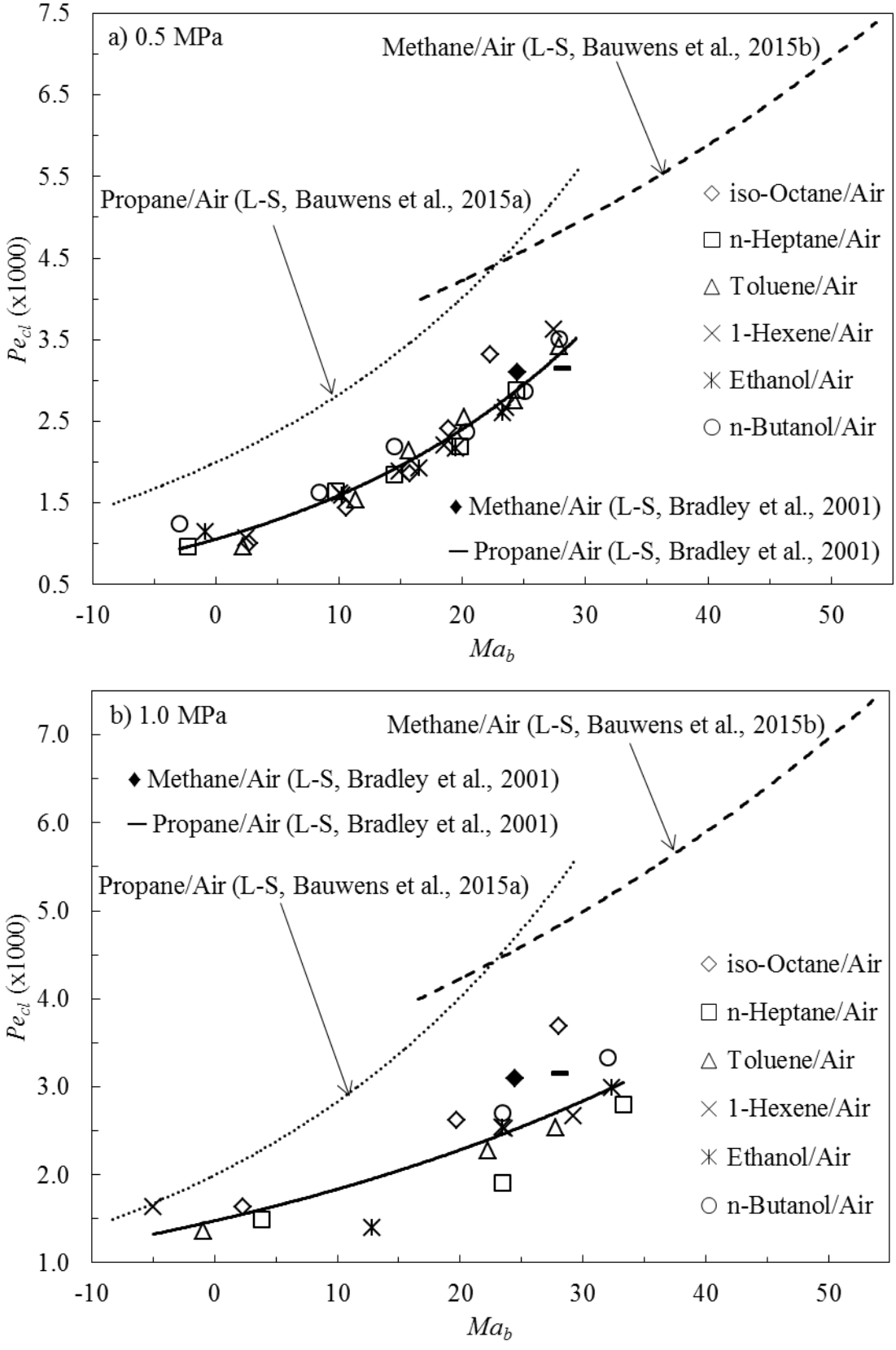

Figure 5.2: Variation of Pe_{cl} with Ma_b for different liquid pure fuel/air mixtures measured in the Leeds CV2, at a) 0.5 MPa and b) 1.0 MPa. Alongside corresponding data of large-scale atmospheric explosions for methane/air and propane/air mixtures. The solid black curve shows the best fit through the Leeds CV2 data.

However, the dotted and dashed curves represent further large-scale atmospheric explosion data for propane (2015a) and methane (2015b), respectively, aquired by Bauwens et al., which does not correlate as well. These flames were up to 2 m diameter, with ϕ ranging between 0.81-1.22. The reported Pe_{cl} values were plotted against values of Markstein numbers that were numerically closer to the strain rate Markstein numbers, Ma_{sr}, rather than the flame speed Markstein numbers, Ma_b. Thus, to compare data from Bauwens et al. more closely with that in the present study, it was assumed that they were those of Ma_{sr} and converted to Ma_b using the tabulated values of the different Markstein numbers in (Gu et al., 2000) for methane, and in (Bradley et al., 1998a) for propane. Necessary data for obtaining δ were taken from (Morley, 2005).

Because of the importance of a necessary minimal stretch rate to stabilise a flame, it was proposed by Bradley et al. (2009), that a more logical criterion for the onset of this type of instability is one based on the flame stretch rate, such as the Karlovitz stretch factor, K, rather than Pe_{cl}. This approach was pursued by Bradley et al (2009), where it was shown that the minimal value of K for which a spherical premixed laminar flame is stable, K_{cl}, is given by:

$$K_{cl} = (2\sigma/Pe_{cl})[1 + (2Ma_b/Pe_{cl})]^{-1}. \qquad \text{(Eq. 5.1)}$$

Values of K_{cl} for all the data of the present work were obtained using Eq. 5.1. Following Figs. 5.2a and b, for the purposes of comparisons, these values of K_{cl} are presented in terms of Ma_b. Figure 5.3a is the counterpart of Fig. 5.2a, and Fig. 5.3b that of Fig. 5.2b. Again, the same symbols are used to represent the large-scale atmospheric explosions of (Bradley et al., 2001). Transformed curves, equivalent to the broken curves that appear in Figs. 5.2a and b, show the data from the large-scale explosions reported by Bauwens et al. (2015a; 2015b) also appear in Figs. 5.3a and b.

Ideally, the three correlation curves on each figure would collapse into a single correlating curve, but there are clearly three different correlations. In explanation, different forms of Markstein number may be relevant, and there can be no certainty that different research groups use the same Markstein number. Furthermore, even with agreement on the corrrect definition of the appropriate Markstein number, there are acute difficulties in obtaining accurate measurements of it. At atmospheric pressures, in some instances there are departures from linearity in the flame speeed/flame stretch rate relationship. In the present work, as discussed in Section 5.2, this was found to diminish as pressure increased.

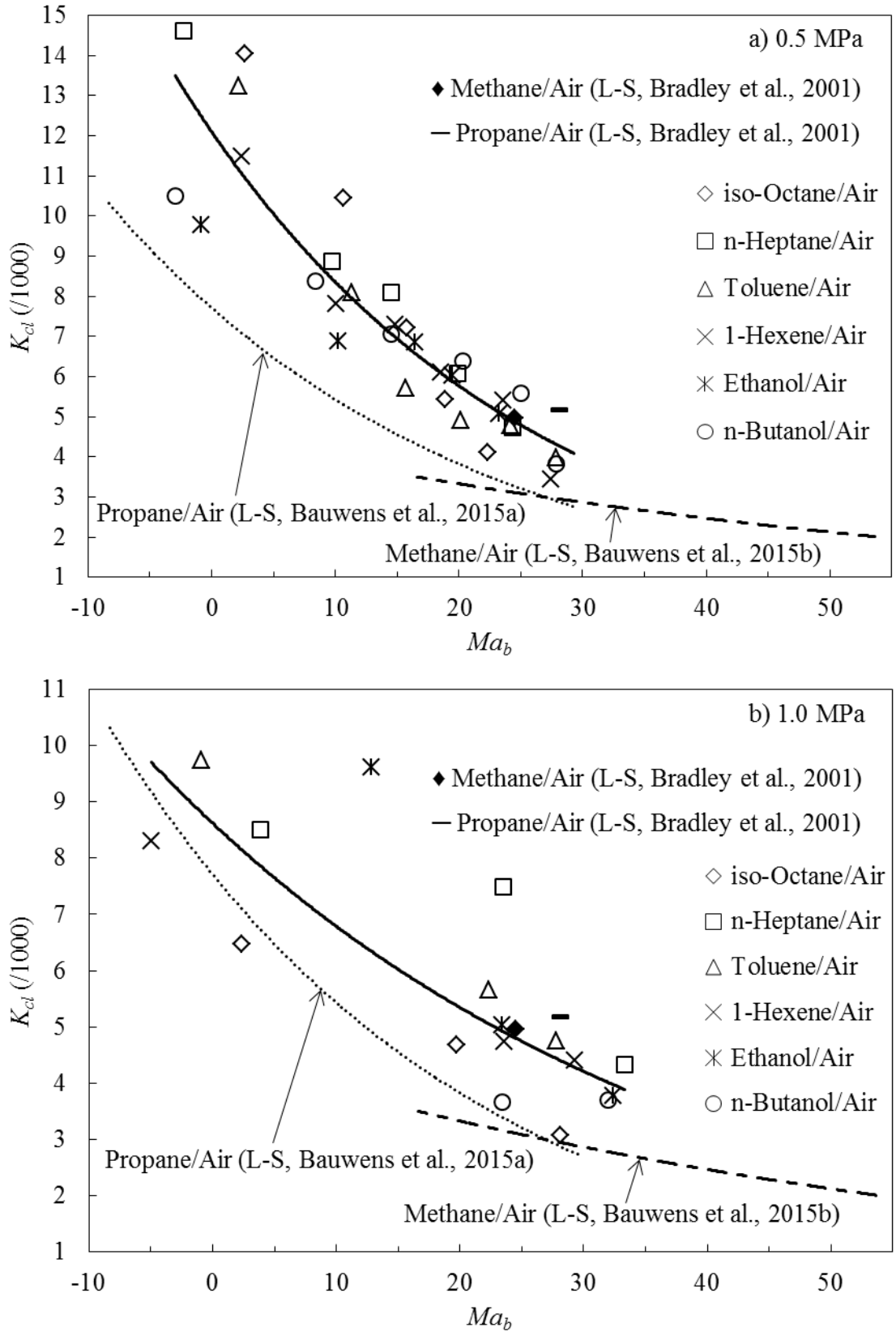

Figure 5.3: Variation of K_{cl} with Ma_b for different liquid pure fuel/air mixtures measured in the Leeds CV2, at a) 0.5 MPa and b) 1.0 MPa. Alongside corresponding data of large-scale atmospheric explosions for methane/air and propane/air mixtures. The solid black curve shows the best fit through the Leeds CV2 data.

Figure 5.4 shows K_{cl} data from different groups, this time expressed entirely in terms of Ma_{sr}. In this case, the high pressure ethanol/air data from explosions at elevated pressures is from the same combustion vessel as that used in the present work (Bradley et al., 2009), and combined with the large-scale atmospheric explosion data for propane and methane from Bawuens et al. (2015a; 2015b), and (Bradley et al., 2001). The three corresponding correlating curves on the figure are in fairly close agreement, and again support the view that small high pressure explosions can give a fairly good indication of the onset of instabilities in large-scale atmospheric explosions. It is, however, clear that, as Ma_{sr} becomes highly negative, the regime of stability is severely narrowed.

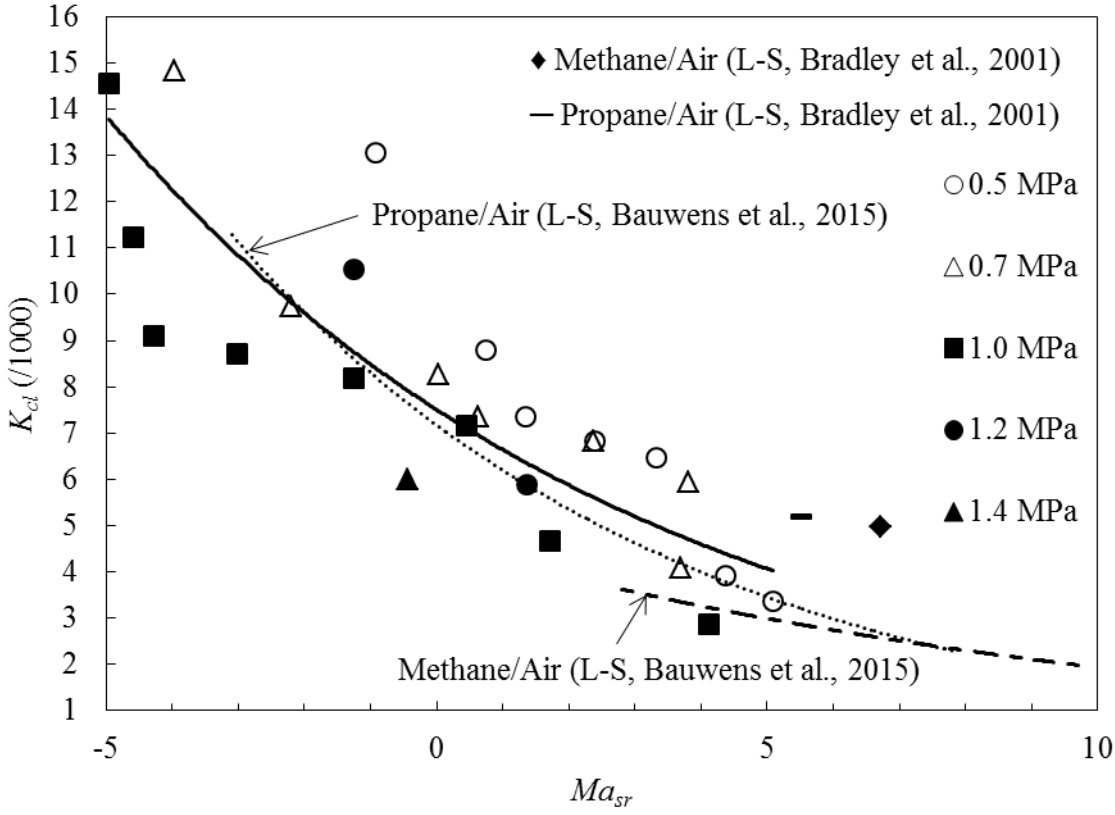

Figure 5.4: Variation of K_{cl} with Ma_{sr}, for ethanol/air mixtures at different elevated pressures, measured in the Leeds CV2 by Bradley et al. (2009). Alongside corresponding data of large-scale atmospheric explosions for methane/air and propane/air mixtures. The solid black curve shows the best fit through the Leeds CV2 data.

5.4 Comparisons of Measured u_l and L_b Values to Existing Data

The author is unaware of any previous data for mixtures of *1*-hexene/air and *n*-butanol/air at comparable conditions. Those for *iso*-octane/air, alongside the present measurements are shown in Figures 5.5-5.7. Agreement for the values of u_l across all pressures amongst the different groups is satisfactory. However, at the lowest pressure of 0.1 MPa, the present measurements are noticeably lower under lean conditions and higher under rich conditions when compared with those of Bradley et al (1998b) and Ormsby (2005) in the same combustion vessel. The difference is likely due to the recent improvements in experimental techniques and upgrades to the Leeds CV2, as discussed in Chapter 3.

Kumar et al (2007) also used a combustion vessel, whereas Dirrenberger et al (2014) and Sileghem et al (2013) used the flat plate adiabatic burner technique, as discussed in Chapter 1. A novel approach was taken by Al-Shahrany et al (2005), using the Leeds CV2, whereby ignition of the mixture occurs from two diametrically opposed spark electrodes near the walls, allowing the final stages of two inwardly propagating flame fronts to be observed at high pressure. However, as with the case of Ormsby (2005) at the high pressure of 1.0 MPa, under rich conditions, the resulting flame cellularity significantly reduces the stable regime of the flame in which in which a Markstein length can be applied and increases the margin of error. The need for high fidelity u_l measurements within the present work was paramount, hence the present study only considered conditions up to ϕ = 1 at 1.0 MPa, where the limit of a sufficient stable flame regime for accurate u_l data acquisition was found.

Reported measurements of L_b are much more scarce, and comparable measurements are only available from the Leeds CV2. All measured values of L_b decrease with an increase in ϕ at all pressures, with all values remaining positive, except for ϕ = 1.3-1.4 at 0.1 and 0.5 MPa and ϕ = 1, at 1.0 MPa. The decrease of L_b with ϕ is associated with the deceasing Lewis number. Variations of L_b values between workers are significantly greater than the corresponding u_l values. A possible explanation of such differences may result from the employment of either a linear or nonlinear extrapolation methodology.

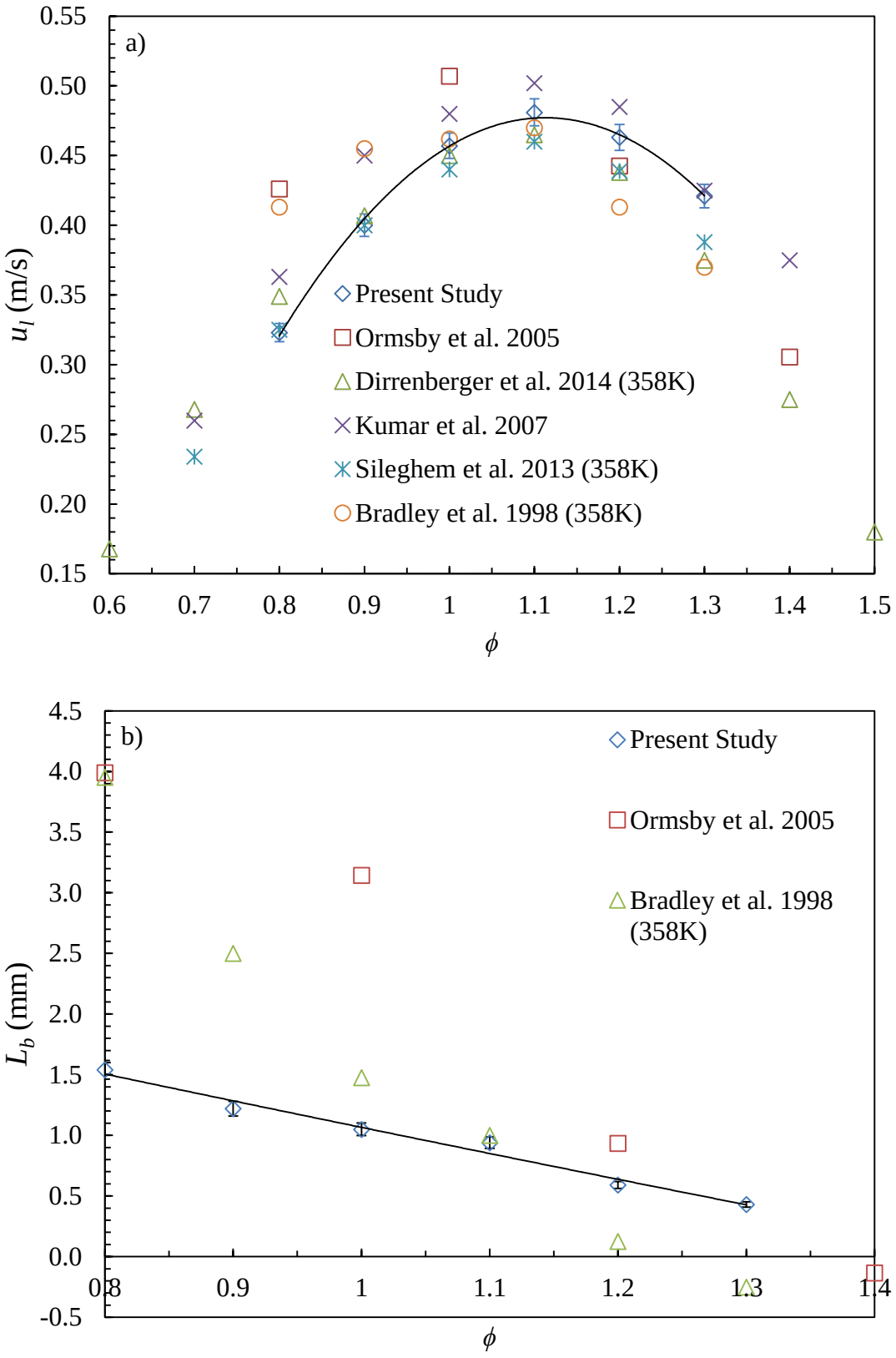

Figure 5.5: Comparison of a) u_l and b) L_b measurements for *iso*-octane/air mixtures at 0.1 MPa, 360K, across ϕ = 0.8-1.3. Solid black curves shows best fit through present data.

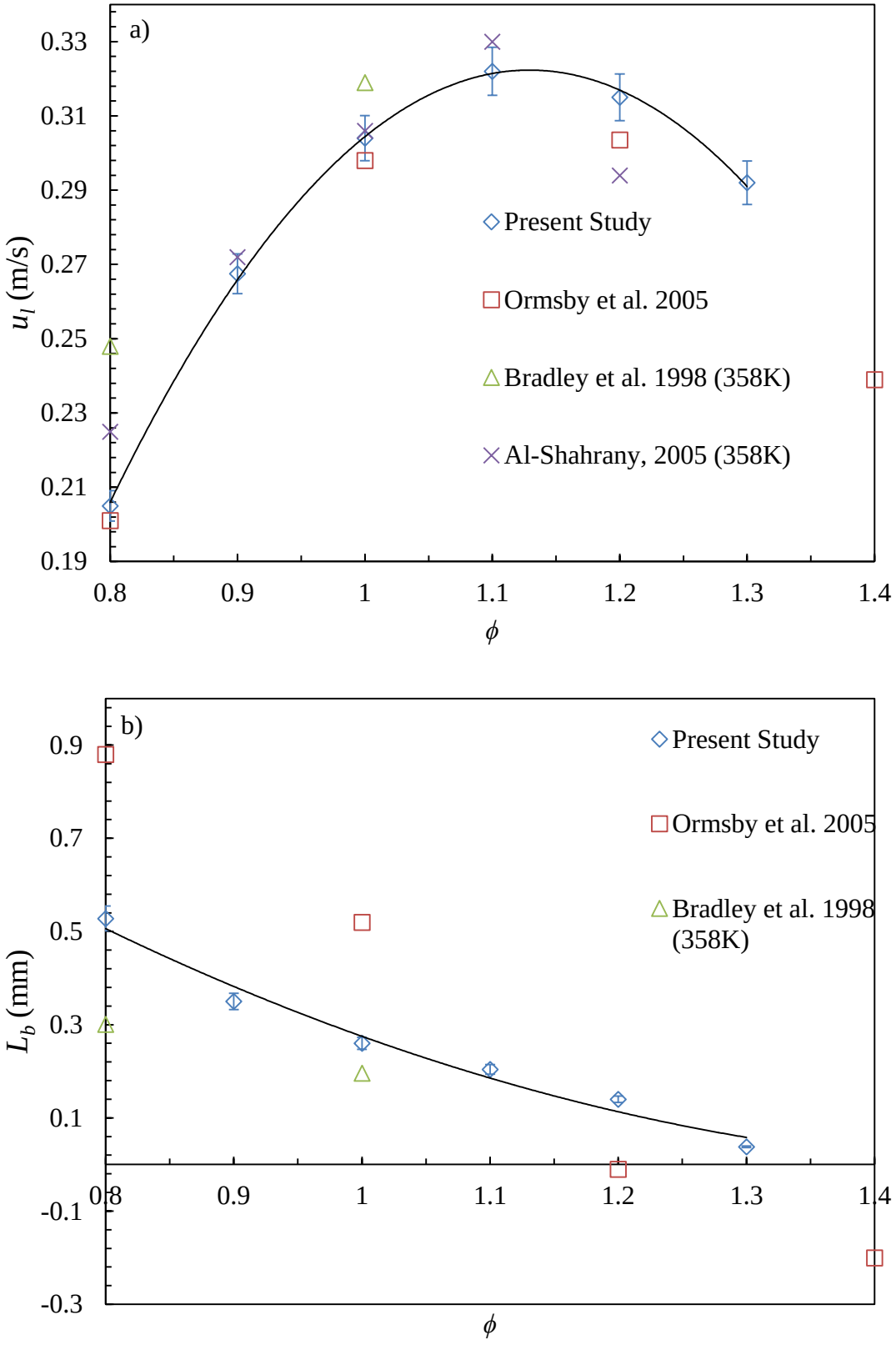

Figure 5.6: Comparison of a) u_l and b) L_b measurements for *iso*-octane/air mixtures at 0.5 MPa, 360K, across ϕ = 0.8-1.3. Solid black curves shows best fit through present data.

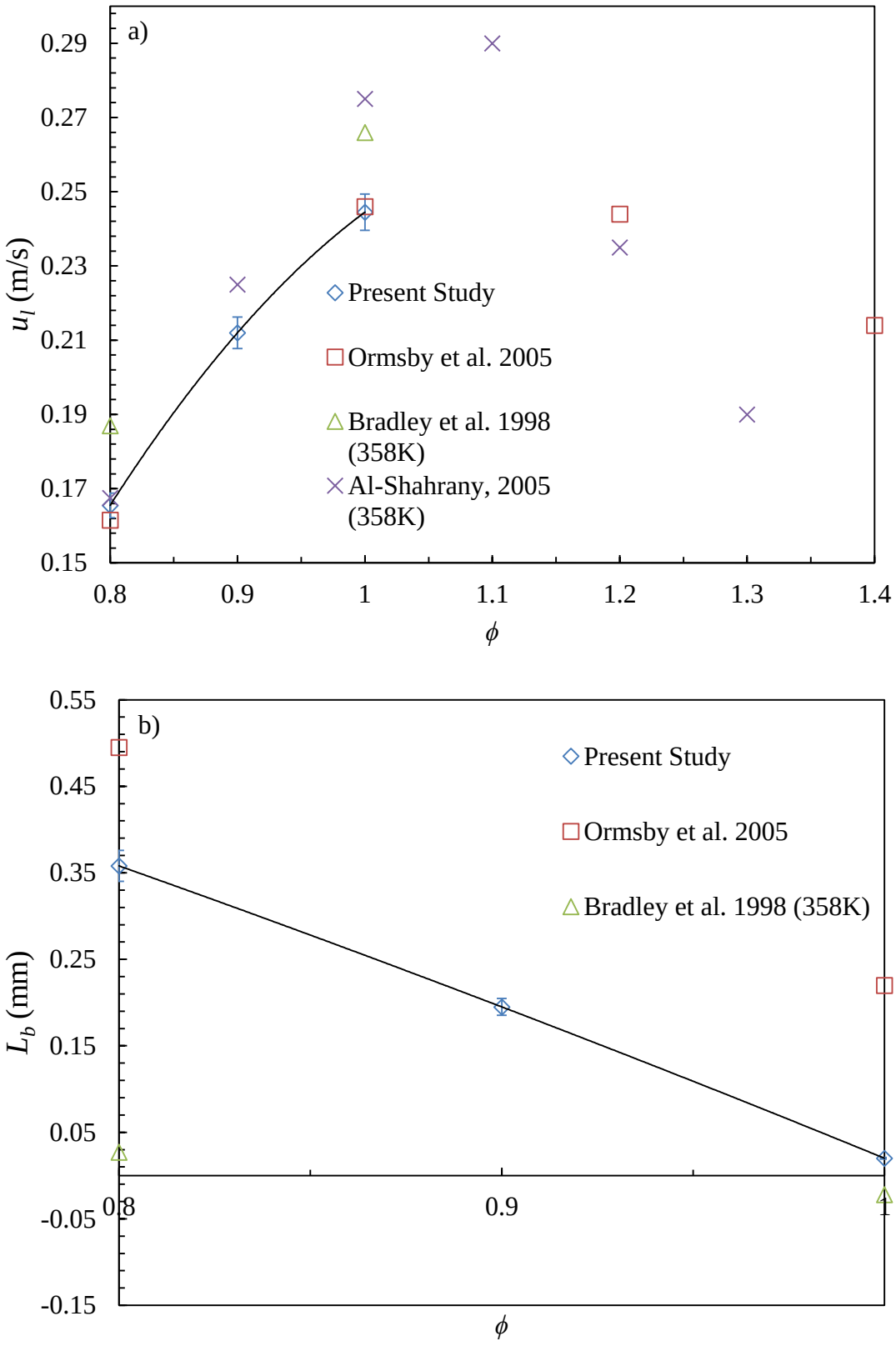

Figure 5.7: Comparison of a) u_l and b) L_b measurements for *iso*-octane/air mixtures at 1.0 MPa, 360K, across ϕ = 0.8-1.3. Solid black curves shows best fit through present data.

Figures 5.8-5.10 show the present and comparable measurements of u_l and L_b, for ethanol/air mixtures by other workers. Agreement of u_l at initial pressures of 0.1 and 0.5 MPa are again satisfactory. However, at 1.0 MPa, present measurements for ethanol/air mixtures are noticeably higher than that of Bradley et al (2009). The corresponding L_b measurements at 0.1 and 0.5 MPa compare well with Bradley et al (2009). However, at 0.1 MPa, data from Liao et al (2007) is significantly higher. At 1.0 MPa, present L_b values are much higher compared to that of Bradley et al (2009). Such variation for both u_l and L_b, particularly at 1.0 MPa, may be attributed to the slightly higher initial temperature, refined experimental technique and improved protocol in handling the hygroscopic nature of ethanol, as discussed in Chapter 3.

Figures 5.11a and b present measurements of u_l for *n*-heptane/air and toluene/air at 0.1 MPa, respectively. Unfortunately no L_b values for either fuel at comparable conditions are available. There is good agreement of u_l for both fuels with values obtained from other combustion vessels (Kumar et al., 2007) and flat plate burners (Sileghem et al., 2013) and (Dirrenberger et al., 2014). Measured values of u_l and L_b for all pure liquid fuels studied can be viewed in Chapter 4, Section 4.2.

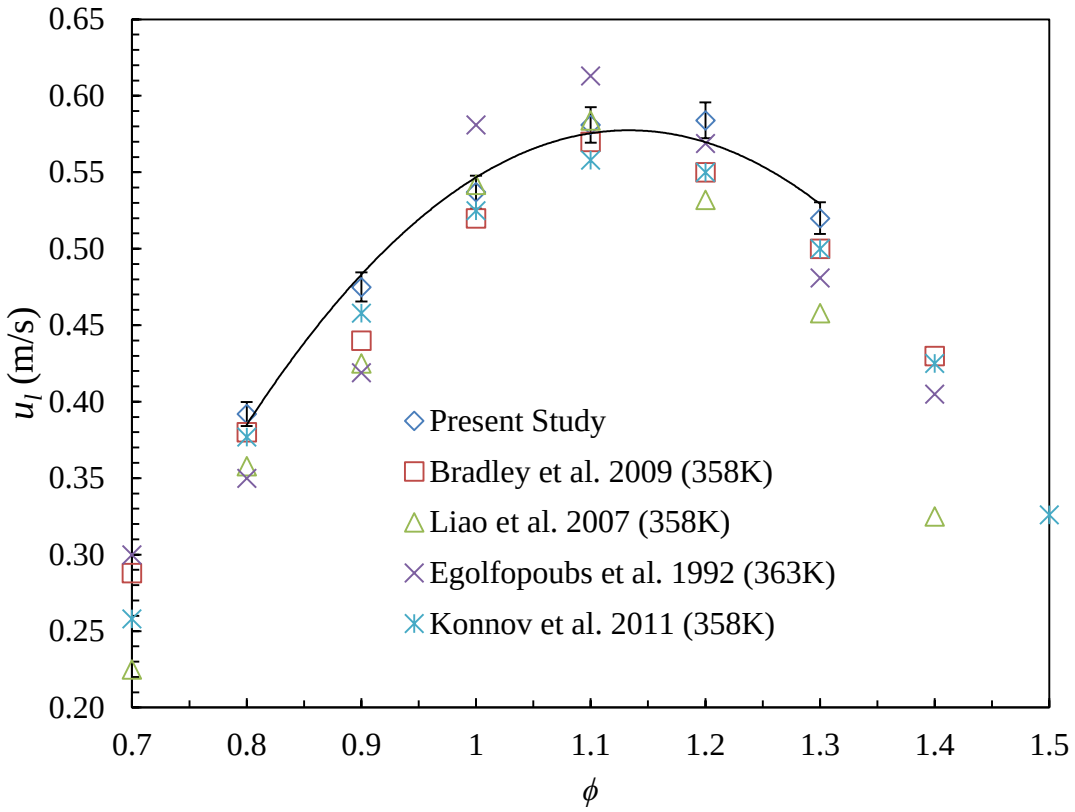

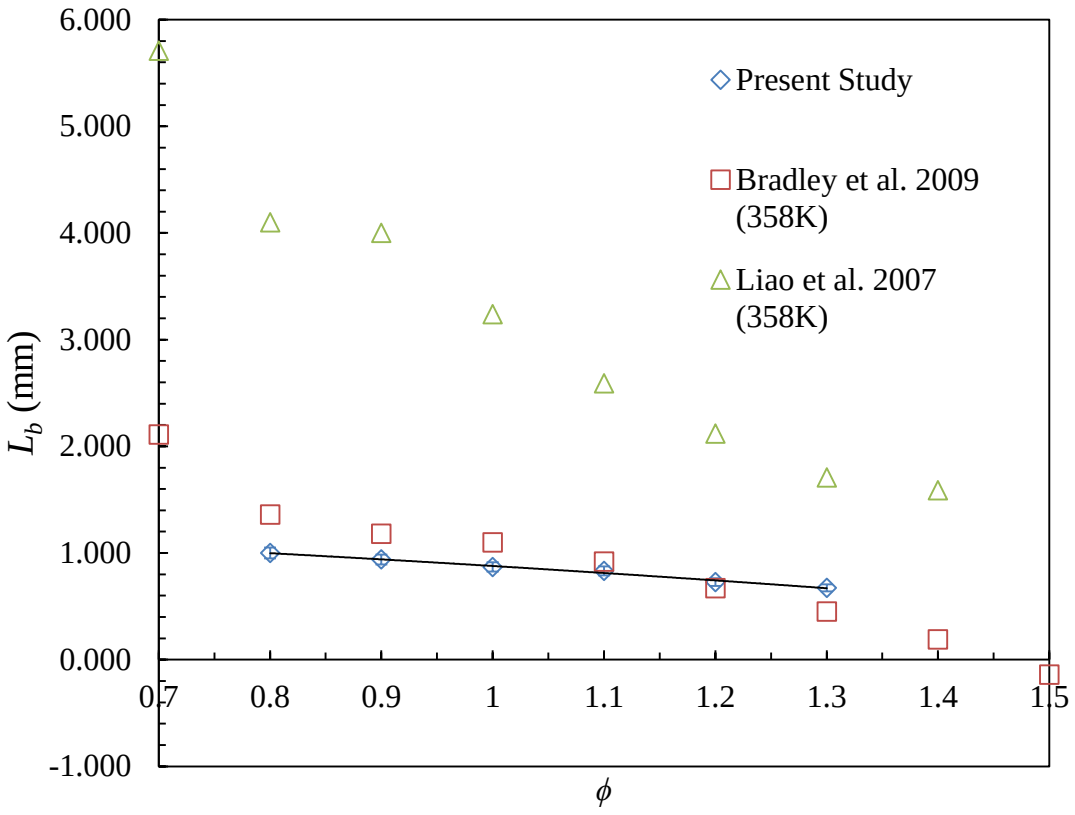

Figure 5.8: Comparison of a) u_l and b) L_b measurements for ethanol/air mixtures at 0.1 MPa, 360K, across ϕ = 0.8-1.3. Solid black curves shows best fit through present data.

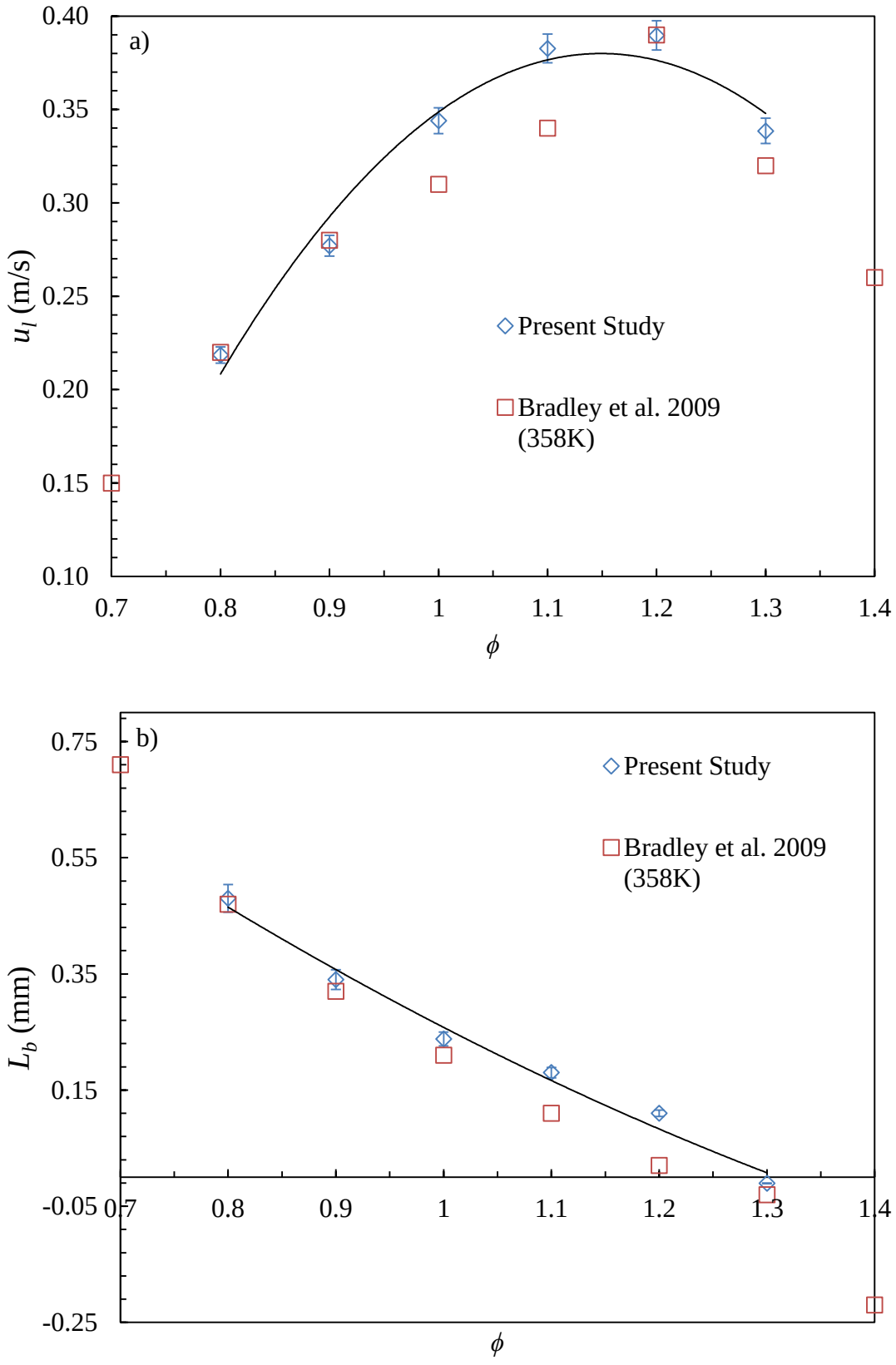

Figure 5.9: Comparison of a) u_l and b) L_b measurements for ethanol/air mixtures at 0.5 MPa, 360K, across ϕ = 0.8-1.3. Solid black curves shows best fit through present data.

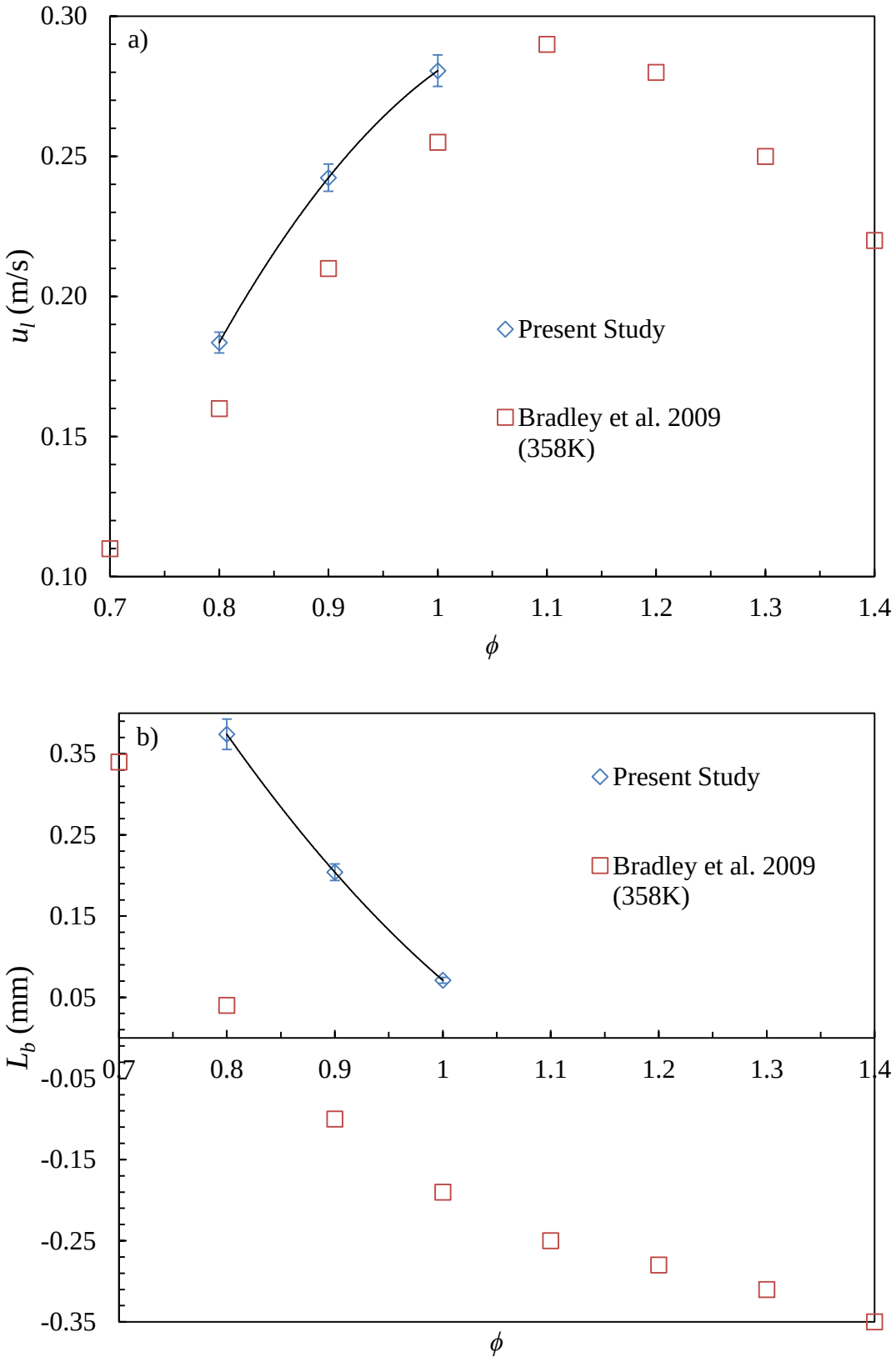

Figure 5.10: Comparison of a) u_l and b) L_b measurements for ethanol/air mixtures at 1.0 MPa, 360K, across ϕ = 0.8-1.3. Solid black curves shows best fit through present data.

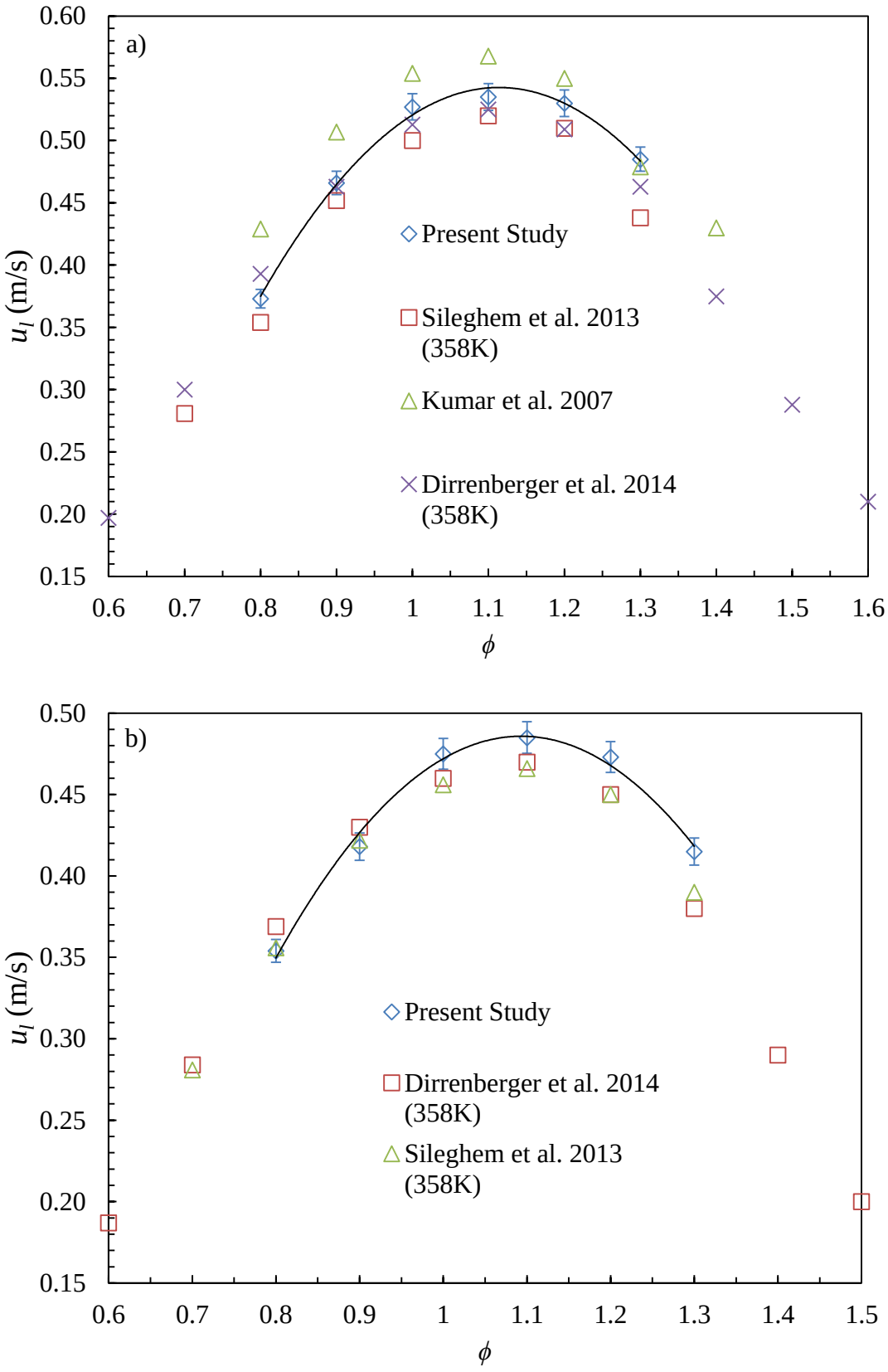

Figure 5.11: Comparison of u_l measurements for a) *n*-heptane/air and b) toluene/air mixtures at 0.1 MPa, 360K, across ϕ = 0.8-1.3. Solid black curves shows best fit through present data.

5.5 Comparative Effects of Ethanol and *n*-Butanol Addition to TRF/Air Mixtures u_l and τ_i Behaviour

As introduced in Chapter 4, the blending of petroleum derived gasoline with promising alternative bio-derived alcohols such as, ethanol and *n*-butanol, can potentially mitigate demand for petroleum and reduce the associated CO_2 emissions. However, considerable care must be taken in assessing how the different properties and blend proportions of such alcohols affect gasoline.

In efforts to further understanding of such blends fundamental combustion characteristics, the concurrent measurement of u_l and τ_i values for a gasoline surrogate TRF/air mixture with the addition of either ethanol or *n*-butanol were made. Subsection 5.5.1 reviews the u_l and L_b measurements as presented in Chapter 4, and subsection 5.5.2 reviews the τ_i measurements made by Materego (2015), via the Leeds RCM, as described in Appendix A, the commissioning of which, formed part of the present work. A summary of the investigation is given in subsection 5.5.3. Furthermore, the investigation gave a vast array of multi-constituent blend data which allowed the blending laws, as presented in Chapter 2, to tested on a 'blends of blends' basis, such that the TRF was considered as one constituent in a binary blend with either alcohol. The predictive performances of which are presented in Chapter 6, Section 6.3.

As detailed in Chapter 4, Section 4.4, the selected TRF gasoline surrogate represents that of a typical high octane European gasoline. Blends of the TRF with either ethanol or *n*-butanol were considered such that the TRF constituents remained constant at their original ratio, with the volumetric addition of either alcohol in 25% increments.

A primary concern with blending such alcohols with gasoline is that of their lower volumetric energy. Figure 5.12 demonstrates the variation of volumetric energy with addition of either ethanol or *n*-butanol to the TRF. Whilst both serve to lower volumetric energy, here *n*-butanol clearly has an advantage. Furthermore, as both alcohols carry oxygen, their stoichiometric FAR's are higher. A typical gasoline FAR is in the region of 0.068, whilst that for ethanol and *n*-butanol are 0.11 and 0.09, respectively, thus, as the proportion of either alcohol, particularly ethanol, within the blend increases, a higher volume of fuel injection is required. Therefore, assuming engine efficiency and fuel tank volume remain the same, the maximum run time would reduce between fuel refills.

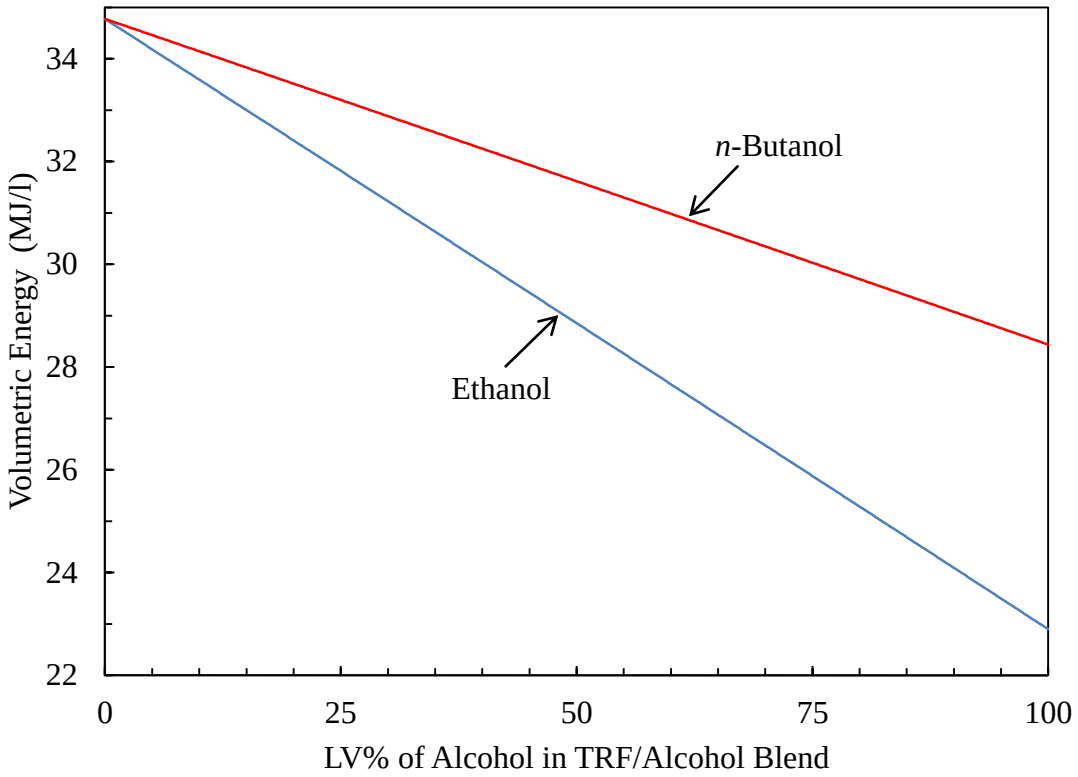

Figure 5.12: Variation of volumetric energy with alcohol addition to TRF.

However, both alcohols, particularly ethanol, have higher enthalpies of evaporation compared to conventional gasoline. Therefore, particularly, in the case of direct injection (DI) they serve to significantly lower the charge temperature, thus reducing the propensity for knock, which in turn, enables a higher compression ratio (CR) and thus higher volumetric efficiency. Furthermore, ethanol has a markedly higher RON value even compared to that of the high octane premium gasoline TRF surrogate, thus being more resistant to knock and again potentially allowing for a higher CR. Countering disadvantages of ethanol in comparisons to *n*-butanol are that of its significantly higher hygroscopic nature and thus increased promotion of phase separation. As a result, blends of high ethanol concentration cannot be distributed in conventional gasoline supply systems and must be locally blended.

5.5.1 Analysis of Measured u_l and L_b Data

Figures 5.13-5.15 shows the u_l and corresponding L_b values for all TRF/alcohol mixtures as a function of initial pressure, under lean, stoichiometric and rich conditions.

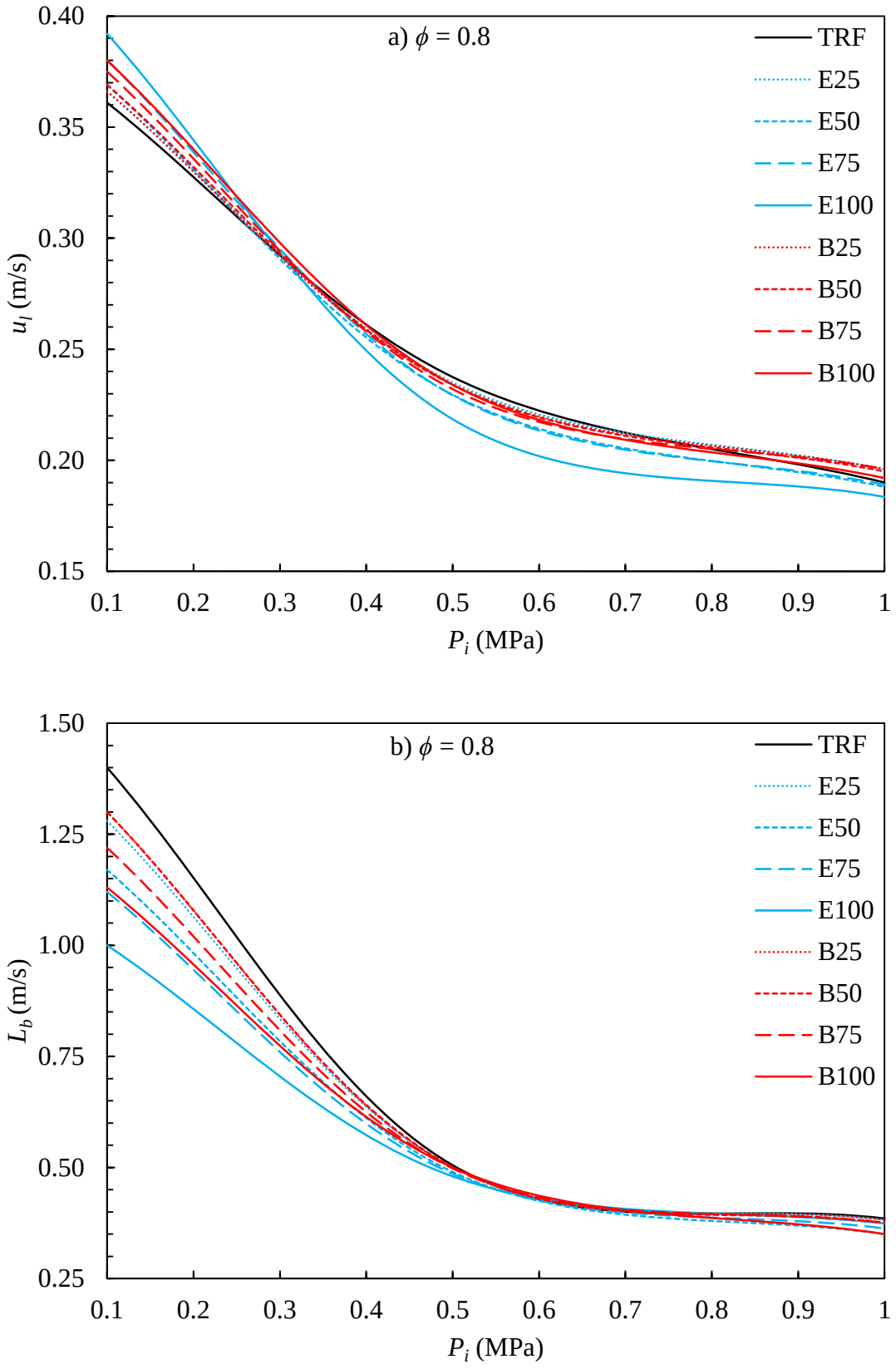

Figure 5.13: Variation of a) u_l and b) L_b with P_i, at ϕ = 0.8, for all TRF/alcohol/air mixtures.

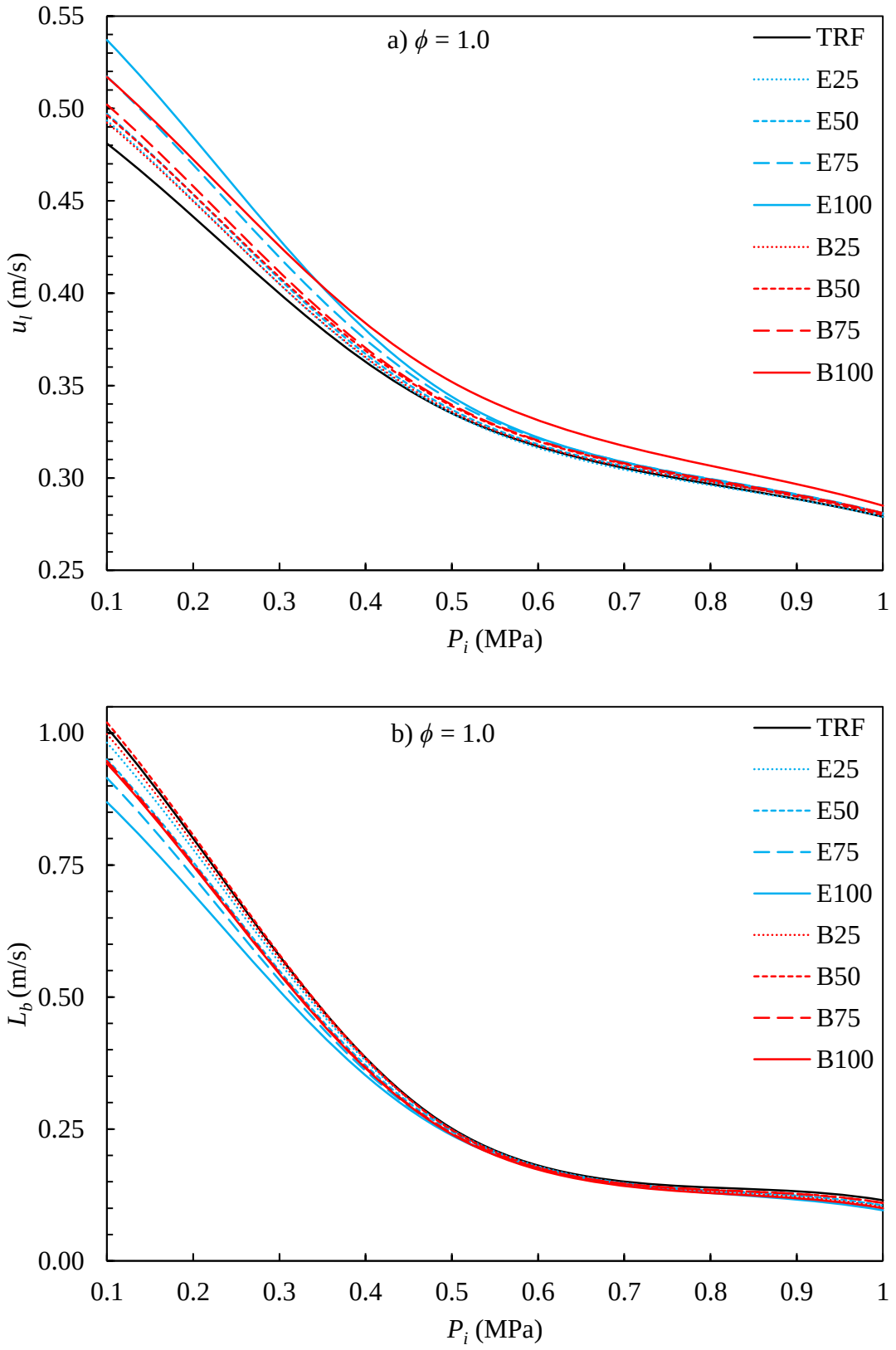

Figure 5.14: Variation of a) u_l and b) L_b with P_i, at ϕ = 1.0, for all TRF/alcohol/air mixtures.

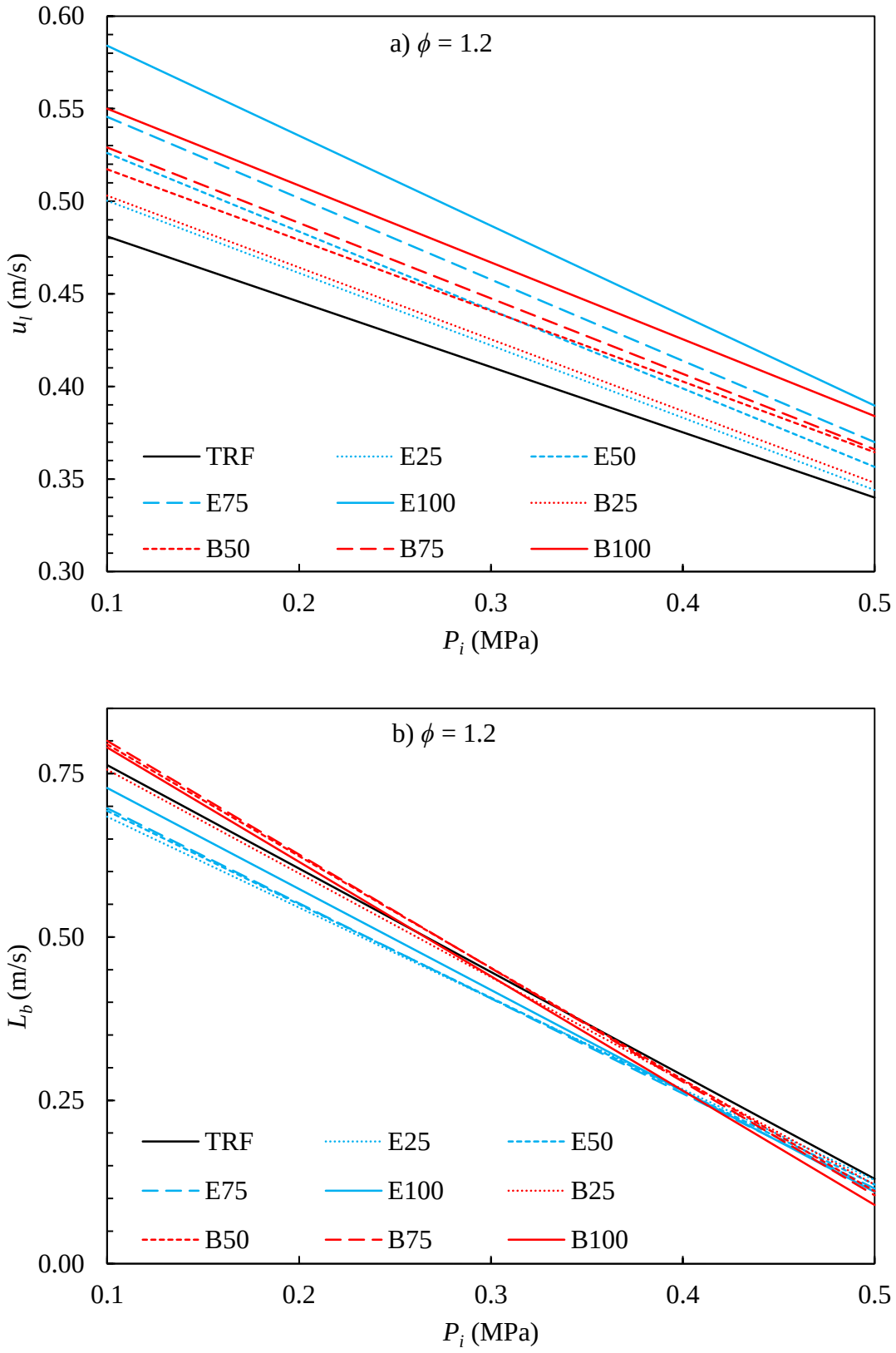

Figure 5.15: Variation of a) u_l and b) L_b with P_i, at ϕ = 1.2, for all TRF/alcohol/air mixtures.

The influence of either alcohol addition, on both the TRF/air mixtures u_l and L_b values, across the ϕ range of 0.8 to 1.3, was most prominent under 0.1 MPa. This was due to the difference between the constituent fuel/air mixtures u_l and L_b values being greater at low pressure and reducing with an increase in pressure.

Measurements at 0.1 MPa show an increase in u_l with the addition of either alcohol, more so for ethanol addition, with increasing effect as ϕ increases. This was anticipated as the u_l difference between toluene, the main TRF constituent, and the alcohols was greatest under rich conditions. The corresponding L_b behaviour, with either alcohol addition, again, particularly ethanol, shows values to decrease under lean conditions, switching to increase values under rich conditions. This is a result of the alcohols being less sensitive to stretch under lean conditions, yet more under rich conditions than that of the TRF blend.

At increased pressure the difference between the u_l and L_b values of the TRF and either alcohol was reduced, therefore the variation of the base TRF u_l and L_b values with the addition of either alcohol becomes less. However, a notable effect, particularly between 0.1 and 0.5 MPa, was that of the high pressure sensitivity of ethanol, which significantly reduced its u_l values to near that of *n*-butanol, in fact, under the lean and rich conditions of ϕ = 0.8 and 1.3, *n*-butanol u_l values became higher. The corresponding L_b values remain remarkably steady with the addition of either alcohol. This was expected, due to such minimal difference between the TRF and alcohol L_b values across the full ϕ range at this increased pressure.

At the pressure of 1.0 MPa, differences between the TRF and alcohol u_l and L_b values became lesser still, as did the ϕ range due to the early onset of cellular instabilities. Values of u_l remain almost steady with the addition of either alcohol, with only a marginal decrease at high proportions under the lean condition of ϕ = 0.8. Whilst, values of L_b are reflective of this, remaining relatively steady.

The high pressure sensitivity of ethanol highlights the need for u_l and L_b data at higher pressure, where u_l values could potentially decrease below that of the TRF. Thus lowering the TRF/alcohol blend u_l values as the ethanol proportion is increased, which is contrary behaviour to what might be inferred by measurements taken at only low pressure. The difficulty with such high pressure measurements is the simultaneous inducing of early onset cellular instabilities, resulting in an insufficient stable flame region to extrapolate to zero stretch, to deduce an accurate u_l value.

5.5.2 Analysis of τ_i Data

All measurements made were stoichiometric at 2.0 MPa, across T_c = 800-952K. Whilst these conditions are different from that of the u_l and L_b measurements, they still serve to highlight valuable comparative ignition delay behaviour between the addition of either alcohol to a high octane gasoline TRF surrogate.

Figure 5.16 shows τ_i values for TRF/air mixtures as a function of temperature. Values of τ_i decrease in the upper and lower temperature range, however, a clear negative temperature coefficient (NTC) region is exhibited in the range of 769-833K. This is symptomatic of many other PFR and TRF surrogates and gasoline mixtures.

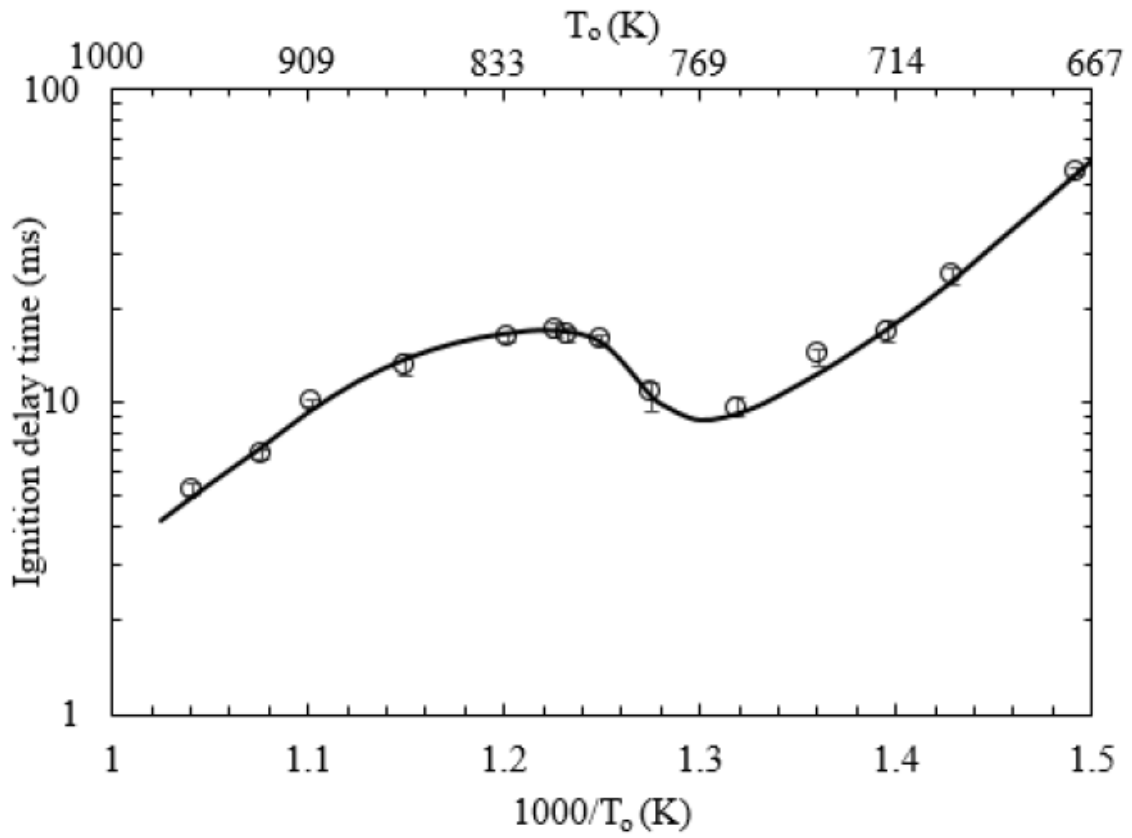

Figure 5.16: Variation of ignition delay with temperature, for TRF/air mixtures at 2.0 MPa and ϕ = 1 (Materego, 2015).

Figure 5.17 shows the variation of τ_i with the addition of either ethanol or *n*-butanol. The zero horizontal line denotes the pure TRF, with each curve showing the difference in τ_i between that and each of the TRF/alcohol blends. In the low temperature range, below 870K, there is significantly contrasting behaviour between the addition of either ethanol or *n*-butanol. Here, ethanol addition serves to significantly increase the resistance to autoignition by increasing τ_i values, whereas, *n*-butanol addition serves to

decrease the resistance to autoignition by decreasing τ_i values. In the mid temperature range, the addition of *n*-butanol is most prominent, casing a reduction in τ_i values. In the higher temperature range, the addition of either alcohol has the similar effect of marginally lowering τ_i values.

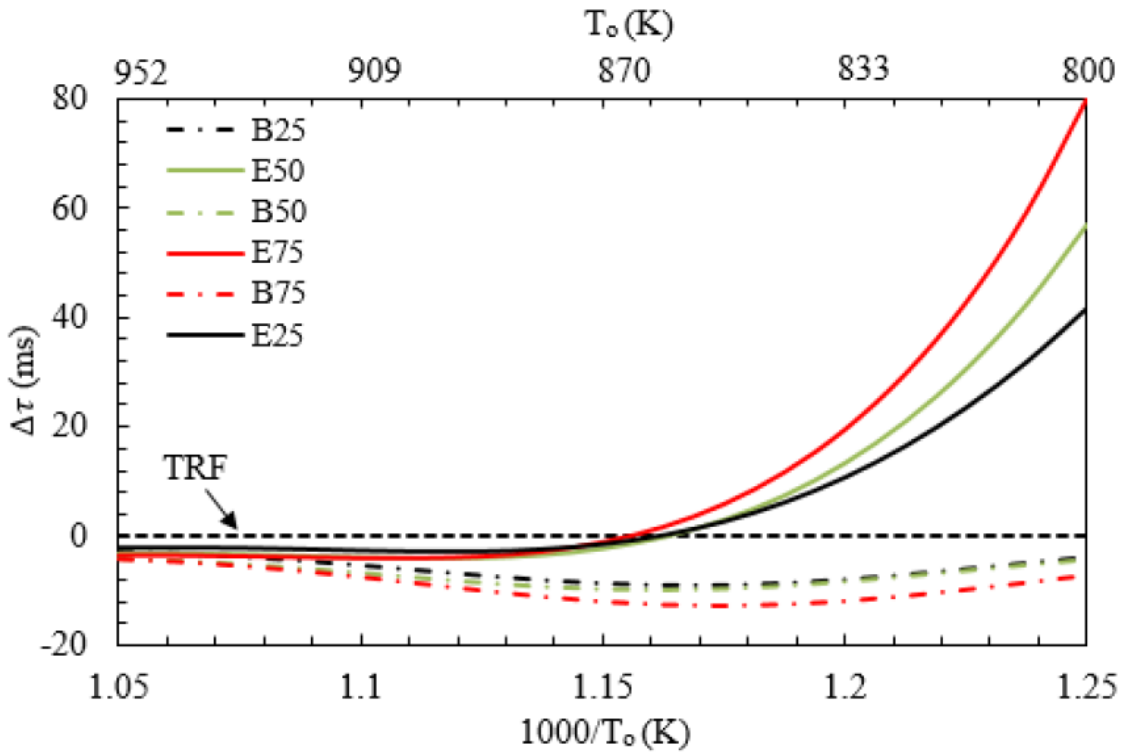

Figure 5.17: Difference in ignition delay between the TRF and the TRF/alcohol blends as a function of temperature, at 2.0 MPa and ϕ = 1 (Materego, 2015).

Unlike the TRF, ethanol exhibits only single stage ignition behaviour and has no NTC region, and its influence even at low LV% results in blends with no definitive NTC. However, all blends of *n*-butanol show two stage ignition behaviour, with a distinctive NTC region for B25 and B50 blends in the mid-temperature range.

5.5.3 Summary of Investigation

The influence of pressure was found to reduce any influence of ethanol or *n*-butanol addition to the base TRR/air mixtures u_l and L_b values, such that near convergence occurred under 1.0 MPa. Assuming such convergence remains to that of SI engine like pressure in the region of 2-2.5 MPa, the burning velocity of high concentration ethanol or *n*-butanol blends will remain similar to that of the base gasoline. Though, it is stressed that ethanol's pressure sensitivity should be investigated further to ensure its u_l values do not reduce below that of the TRF's under higher pressure.

Whilst the present work did not investigate the influence of temperature, the constituents of the TRF, namely, *iso*-octane, *n*-heptane and toluene, and that of ethanol and *n*-butanol have been shown to exhibit very similar temperature exponent powers. Therefore, it is likely that their blends will follow similar exponent powers and thus similar trends will remain.

However, τ_i measurements reveal a striking contrast in the influence of ethanol and *n*-butanol addition in the low temperature region. They suggest that the propensity for autoignition is increased by *n*-butanol addition, indicative of the lower τ_i values, whilst, conversely, it is significantly reduced by the addition of ethanol, which is indicative of its significantly higher τ_i values. Ideally, further τ_i measurements of such blends are required to investigate any influence of pressure and ϕ over the current findings.

In conclusion, despite difficulties arising from ethanol's hygroscopic nature, the findings from the present work suggest that the benefit of ethanol's high resistance to autoignition is an attractive property that would allow for the use of higher CR SI engines and therefore higher volumetric efficiency, whilst maintaining a very similar burning velocity to that of the conventional gasoline under elevated pressure.

5.6 Investigation into Methane/Air Mixtures Energy Flux Variations with Hydrogen Addition.

As discussed in Chapter 4, there have been many previous studies into the effects of u_l and L_b for methane/air mixtures as hydrogen is added, as part of investigations into the feasibility of utilising existing gas supply infrastructures to potentially fuel vehicles and increase domestic heating efficiency. Fortuitously, this has provided a comprehensive range of u_l and L_b measurements for blends of fuel with significantly contrasting chemical kinetics (Hu et al., 2009), that have served to be particularly challenging tests for the predictive u_l and L_b blending laws developed as part of the present work. The predictive performances of which are discussed in Chapter 6, Section 6.4.

Furthermore, the blend data also allowed an investigation into the effect of the energy flux or burn power of methane/air mixtures as hydrogen was added. This is the rate at which heat energy is liberated and a direct function of the mass heat of reaction, Q, the unburned mixture density, ρ_u, and u_l:

$$\text{Energy Flux } (\text{kW/m}^2) = Q u_l \rho_u \qquad (5.2)$$

This is an important fundamental combustion parameter, and has direct relevance to many applications, from small domestic gas cookers and heating boilers, to large industrial smelting burners. Furthermore, it is a particularly interesting parameter for such fuel blends, due to hydrogen/air mixtures having a significantly lower heat of reaction values, yet significantly higher u_l values relative to methane/air mixtures.

Figure 5.18a and b show the energy flux as a function of the hydrogen mole fraction increase, for lean and stoichiometric to rich conditions, respectively. As the mole fraction of hydrogen is increased, the increased u_l of the mixture more than compensates for the lower Q of hydrogen and the energy flux increases, with an increased rate at higher ϕ values. However, in all cases, a plateau exists up to hydrogen mole fractions of 0.5-0.6, therefore, showing hydrogen addition up to such fractions has no influence on the rate of energy liberated.

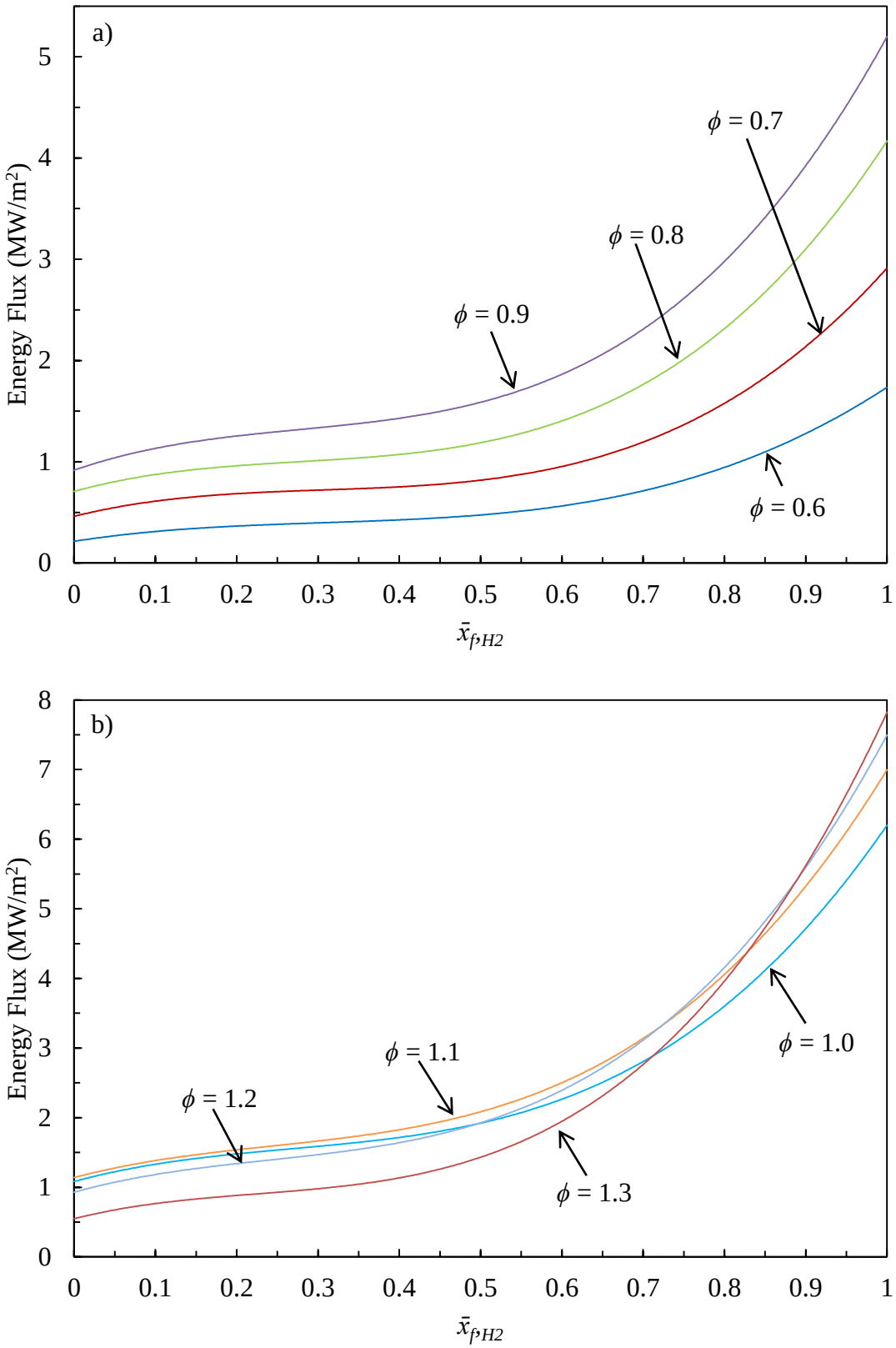

Figure 5.18: Variation of energy flux as a function of hydrogen addition to methane/air mixtures, $\bar{x}_{H2}$, P_i = 0.1 MPa, T_u = 303K, a) ϕ = 0.6-0.9, b) ϕ = 1.0-1.3.

Chapter 6 - Predictive Performance of Laminar Burning Velocity and Markstein Length Blending Laws

6.1 Introduction

This Chapter discusses the predictive performances of the different u_l and L_b blending laws outlined in Chapter 2, for all blends presented in Chapter 4. Section 6.2 starts the assessment with the liquid hydrocarbon binary equimolar blends. Section 6.3 assesses performance on a 'blends of blends' basis, such that the tertiary TRF blend was considered as one constituent in binary blend with either ethanol or *n*-butanol. Section 6.4 examines predictions for the methane and hydrogen blends. Finally, Section 6.5 evaluates the best overall blending laws.

To evaluate the predictive performance of each u_l and L_b blending law the expressions u_{lp}/u_l and L_{bp}/L_b are used respectively, where u_{lp} and L_{bp} represent the predicted values by the blending laws and u_l and L_b the experimentally measured values, with unity denoting 100% agreement. The standard deviation for each average is represented by σ. Assigned symbols are given to each blending law as summarised in Tables 6.1 and 6.2.

Reference	Method	Section	Assigned Symbol
(Payman, 1922)	u_l weighted by mole fraction of constituent mixture.	2.4.1	$\bar{x}$
(van Lipzig, 2010)	u_l weighted by mass fraction of constituent mixture.	2.4.2	x
(Di Sarli and Benedetto, 2007)	u_l weighted by reciprocal fuel mole fraction of constituent mixture	2.4.3	LC
(Spalding, 1956)	Equal T_b assumption.	2.4.4	T_b
(Hirasawa et al., 2002)	$\tilde{T}_a$ weighted by mole fraction of consituent mixture to get blend $\tilde{T}_a$	2.4.5	$\tilde{T}_a$
(Bradley et al., 1991)	u_l plotted against $\bar{Q}$ of consituent mixture.	2.4.6	$\bar{Q}$
Present Work	$u_l\rho_u(Q\bar{c}_p/k_u)^{0.5}$ weighted by mass fraction of constituent mixture.	2.4.7	Q/k

Table 6.1: Summary of all existing and proposed u_l blending laws investigated.

Method	Section	Assigned Symbol
L_b weighted by deficient mole fraction of constituent mixture.	2.5.1	$\bar{x}_d$
L_b weighted by deficient mass fraction of constituent mixture.		x_d
u_lL_b weighted by mass fraction of constituent mixture.	2.5.2	xu_lL_b

Table 6.2: Summary of all proposed L_b blending laws investigated.

6.2 Equimolar Binary Blends

Tables A.1-A.9, within Appendix A present the ratios of predicted to measured burning velocities and Markstein lengths, u_{lp}/u_l and L_{bp}/L_b, for the different blending laws for each of the ten equimolar binary constituent fuel/air blends. The simple equimolar binary blends of pure fuels, each being representative of the major fuel groups within FT synthetic gasoline serve as a good starting point to highlight any particular pure fuel or combination that may challenge the blending laws. Varying the two key combustion parameters of equivalence ratio, over ϕ = 0.8-1.3 and initial pressure, where P_i = 0.1, 0.5

and 1.0 MPa, also serves to identify the blending laws ability in dealing with both lean and rich conditions and pressure sensitive fuels such as ethanol.

For these particular blends and conditions all u_l blending laws, with the exception of the T_b law, are able to predict a large majority of the blends u_l very close to or within the experimental error margin of generally ±2% of the measured value, thus, in such cases rendering any marginal differences between the blending laws negligible or irrelevant. The T_b law consistently over predicted to the order of around 10%, peaking with the *iso*-octane/*n*-heptane/air blend, with a u_{lp}/u_l value of 1.18, at 0.1 MPa and ϕ = 0.9. At 0.1 MPa, under lean conditions, ϕ = 0.8-0.9, a number of the blends presented more of challenge for many of the u_l laws, with over prediction occurring beyond the experimental error, particularly for the *iso*-octane/ethanol/air and *iso*-octane/toluene/air blends as shown in Tables A.3 and A.6, within Appendix A. Notably, maximum stretch rate occurs for all blends at such conditions.

The performance of the L_b blending laws is significantly more varied. As discussed in Chapters 1 and 5, this was expected due to the tentative nature of applying Markstein lengths, where the error margins of measured values can reach ±15%.

On average the best performance was seen by the $\bar{x}_d$ and x_d laws. There was little difference between them under lean to stoichiometric conditions, ϕ = 0.8-1.0, where the deficient reactant was taken to be the fuel fraction. Under rich conditions, where ϕ = 1.1-1.3, the deficient reactant was the oxygen fraction, and the performance becomes identical due to the mole and mass fractions of oxygen being equal. Less success was found with the more empirical law of xu_lL_b, which significantly under predicted for all blends and conditions.

6.3 TRF and Alcohol Blends

Tables A.11-A.22, within Appendix A present the ratios of predicted to measured burning velocities and Markstein lengths, u_{lp}/u_l and L_{bp}/L_b, for the different blending laws, for all TRF/ethanol and TRF/*n*-butanol blends respectively. The assessment was made whereby the three component base TRF blend represents one constituent in a binary blend with either ethanol or *n*-butanol, hence evaluating blending law performance on a ‘blends of blends’ basis, which will be of more interest to those concerned with commercial fuel blending.

A detailed summary of the TRF, TRF/ethanol and TRF/*n*-butanol blends compositions can be found in Table 4.4, Section 4.4 of Chapter 4. As a brief recap, by liquid volumetric percentage of each constituent the TRF blend comprised of: 75.4% toluene, 18.7% *n*-heptane and 0.58% *iso*-octane. For the TRF/alcohol blends, each alcohol was added in 25% liquid volume increments to the base TRF with the TRF constituent fuels kept at their original liquid volume proportions.

The majority of predictions by all u_l laws was very good, with notably better averages in comparison to the binary blends, with predictions falling within or very near to the experimental error margin of the measured value, thus rendering any marginal differences between the blending laws negligible or irrelevant. The L_b laws on average all performed significantly better when comparing their performance to the simpler binary blends, giving relatively similar results. However, predictive performance for all markedly declined under the rich condition, ϕ = 1.3.

6.4 Methane and Hydrogen Blends

Tables A.23-A.30, with Appendix A present the ratios of predicted to measured burning velocities and Markstein lengths, u_{lp}/u_l and L_{bp}/L_b, for the different blending laws, for the CH_4/air and H_2/air blends, for ϕ = 0.6-1.3, as a function of the H_2 fuel mole fraction, $\bar{x}_{f,H2}$ from 0.1-0.9, at 0.1 MPa and 303K. For each Table, at each ϕ, the average predicted to measured ratio over all blends is given for each law at the bottom of each column, alongside the corresponding standard deviation, σ.

Figures 6.1-6.8 present the predicted values of u_l and L_b for blends of CH_4/air and H_2/air compared with the experimentally measured values of u_l and L_b of Hu et al. (2009) at the same conditions. Measured values of u_l and L_b, with maximum standard errors of 8.6% and 16.6% are shown by the dashed lines, while the predicted values by each blending law are shown by the coloured lines. As anticipated the properties of these blends proved to be the most challenging of all the blends for the blending laws to predict.

The best predictions are those of the proposed *Q/k* law. This is not surprising, as it is the only law to account for different constituent mixture heat release rates and thermal conductivities, which as shown in Chapter 4, are markedly different for methane/air and hydrogen/air mixtures. The worst predictions were those from the $\bar{x}$ and $\bar{Q}$ laws. Expectations for the $\bar{Q}$ law were bound to be low. Figure 2.1, in Chapter 2 demonstrates

the consequences of the two fuels belonging to quite different chemical families. Only for ϕ = 0.6 is this law satisfactory. It is rather more surprising that the fractional mole, $\bar{x}$, law was so unsatisfactory and inferior to fractional mass weighting. The $\bar{x}$ law consistently over-estimated u_l, as did the $\bar{Q}$ law, with the exception of blends at ϕ = 0.7, and tended to peak in the region of $\bar{x}_{fH2}$ = 0.5-0.7. Equally consistently, the $\tilde{T}_a$ law under-estimated u_l. This was based on fractional mole weighting. Fractional mass weighting gave even more pronounced under estimations. In contrast, the *LC*, modified Le Châtelier law, which was formulated specifically for CH_4/H_2 blends, both under and over-estimated u_l. This was the only law based on the fraction of fuel, rather than of mixture. All the u_l laws became unsatisfactory for ϕ values of 1.3 and higher.

The prediction of L_b values proved to be more challenging than that of u_l values, this perhaps at least partially attributable to the substantially larger error margin of the measured values at 16.6%. No L_b law was found to be satisfactory over the full equivalence ratio range, however, the xu_lL_b and $\bar{x}_d$ laws performed very well under lean to stoichiometric conditions, where ϕ = 0.6-1.0, particularly the former. Under rich conditions as ϕ increased their performance dramatically declined, more so for the xu_lL_b law, peaking at $\bar{x}_{fH2}$ = 0.4-0.5. However, the $\bar{x}_d$ law performance is satisfactory at $\bar{x}_{f,H2}$ values up to 0.2. The x_d law, was by far the worst performing L_b law, with significant over prediction across the full ϕ range, although peaking at higher values of $\bar{x}_{fH2}$ = 0.7, which is in marked contrast to its performance with the liquid hydrocarbon fuels. Notably under the rich condition, were ϕ = 1.1-1.3, the performance of the x_d and $\bar{x}_d$ law are identical, this is because, the deficient reactant becomes the oxygen, and the oxygen mole and mass ratios become the same.

6.5 Overall Evaluation

An overall evaluation of the predictive performance of each u_l and L_b blending law was made by comparing each laws average predicted to measured ratio, u_{lp}/u_l and L_{bp}/L_b, alongside the standard deviation, for all blends studied at all conditions, as shown by Table 6.3. In the case of u_l blending laws, the proposed *Q/k* law takes first place, closely followed by the *LC* law in second place. The *Q*/*k* having a tendency to slightly over predict, whilst *LC* has a tendency to slightly under predict. The *x* law takes third place, with tendency to over predict. The T_b and $\tilde{T}_a$ laws share fourth place, with the T_b law having a tendency to over predict and the $\tilde{T}_a$ law having a tendency to under predict. The $\bar{Q}$ and $\bar{x}$ laws follow, both with an increased tendency to over predict. For L_b

blending laws, less success was achieved, though, the $\bar{x}_d$ is the better of the three trialled, with a tendency to under predict.

	Average of All Blends Studied									
	u_l Laws							L_b Laws		
	$\bar{x}$	x	LC	T_b	$\tilde{T}_a$	$\bar{Q}$	Q/k	$\bar{x}_d$	x_d	xu_lL_b
Av.	1.07	1.03	0.98	1.04	0.96	1.06	1.01	0.97	0.92	0.68
σ	0.04	0.04	0.02	0.02	0.02	0.04	0.02	0.24	0.63	0.13

Table 6.3: Average u_{lp}/u_l and L_{bp}/L_b values of each u_l and L_b blending law, for all blends studied.

However, these average values are based on a large number of liquid hydrocarbon blends that were successfully predicted by all laws to give ratios close to or of unity. Therefore, the relative difference in blending law performance is best assessed by the average values for exclusively methane/air and hydrogen/air blends, which proved to be significantly more challenging and the only blends to significantly push all the laws beyond the error margins of the experimentally measured values.

Table 6.4 below shows the average predicted to measured ratios for each law, for every methane/hydrogen blend at every condition. The proposed Q/k law again leads, but by a notably higher degree, followed again by the LC and x laws. The $\bar{Q}$ and $\bar{x}$ laws again rank last, showing over prediction, but to a much higher degree. For the L_b blending laws, $\bar{x}_d$ continues to lead. However, as shown by Figs. 6.1-6.5, the empirically based xu_lL_b law performs remarkably well under lean to stoichiometric conditions for all blends.

	Average of All Methane/Air and Hydrogen/Air Blends Studied								
	u_l Laws						L_b Laws		
	$\bar{x}$	x	LC	$\tilde{T}_a$	$\bar{Q}$	Q/k	$\bar{x}_d$	x_d	xu_lL_b
Av.	1.20	1.09	0.92	0.89	1.18	1.01	0.94	0.77	0.77
σ	0.09	0.06	0.04	0.04	0.08	0.03	0.23	1.34	0.14

Table 6.4: Average u_l and L_b blending law performances (u_{lp}/u_l and L_{bp}/L_b), all methane and hydrogen Blends, ϕ = 0.6-1.3, T_u = 303K, P_i = 0.1 MPa.

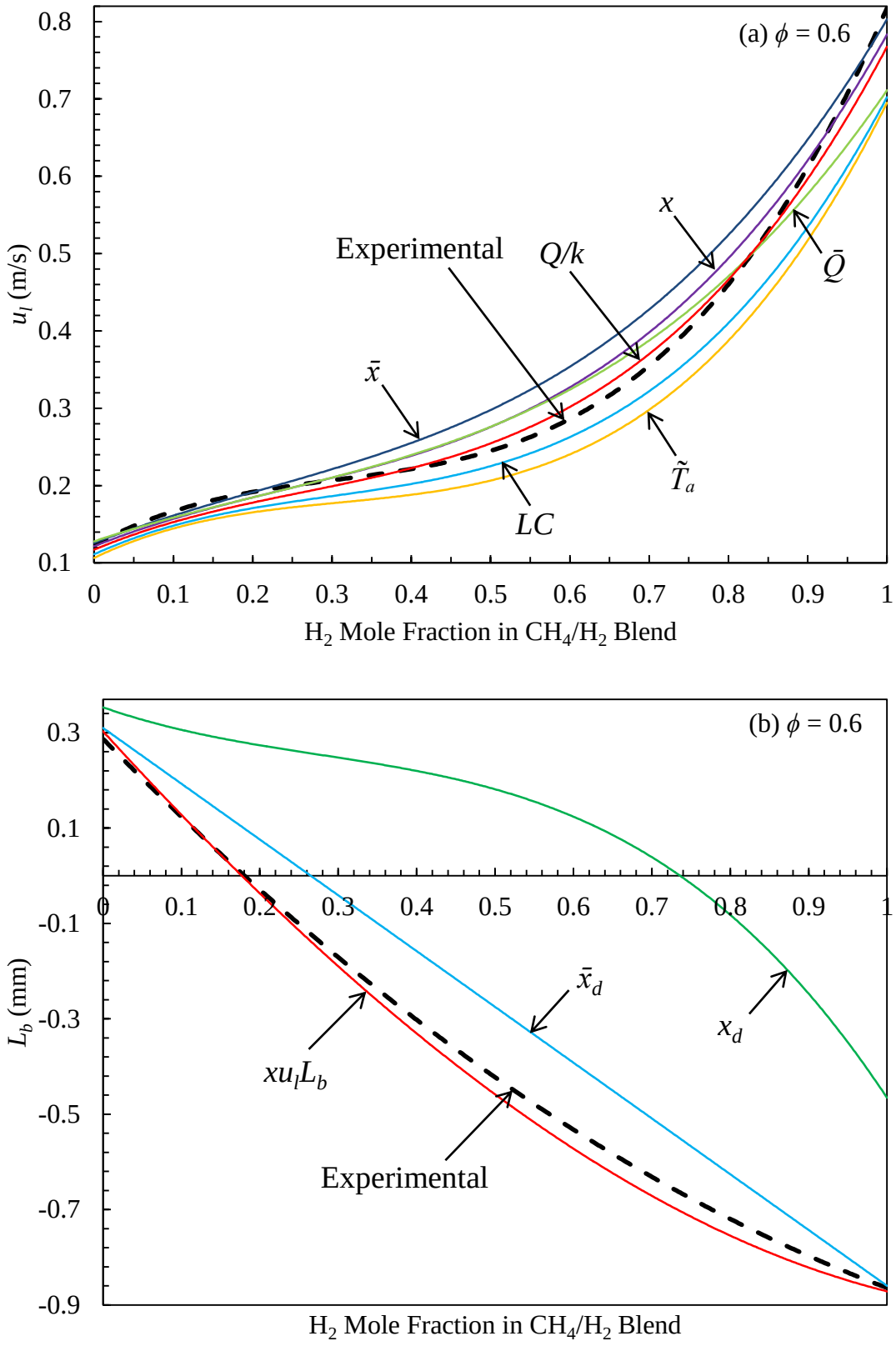

Figure 6.1: Predictive performance of a) u_l and b) L_b laws for blends of methane/hydrogen/air mixtures as a function of $\bar{x}_{fH2}$, P_i = 0.1 MPa, T_u = 303K, ϕ = 0.6.

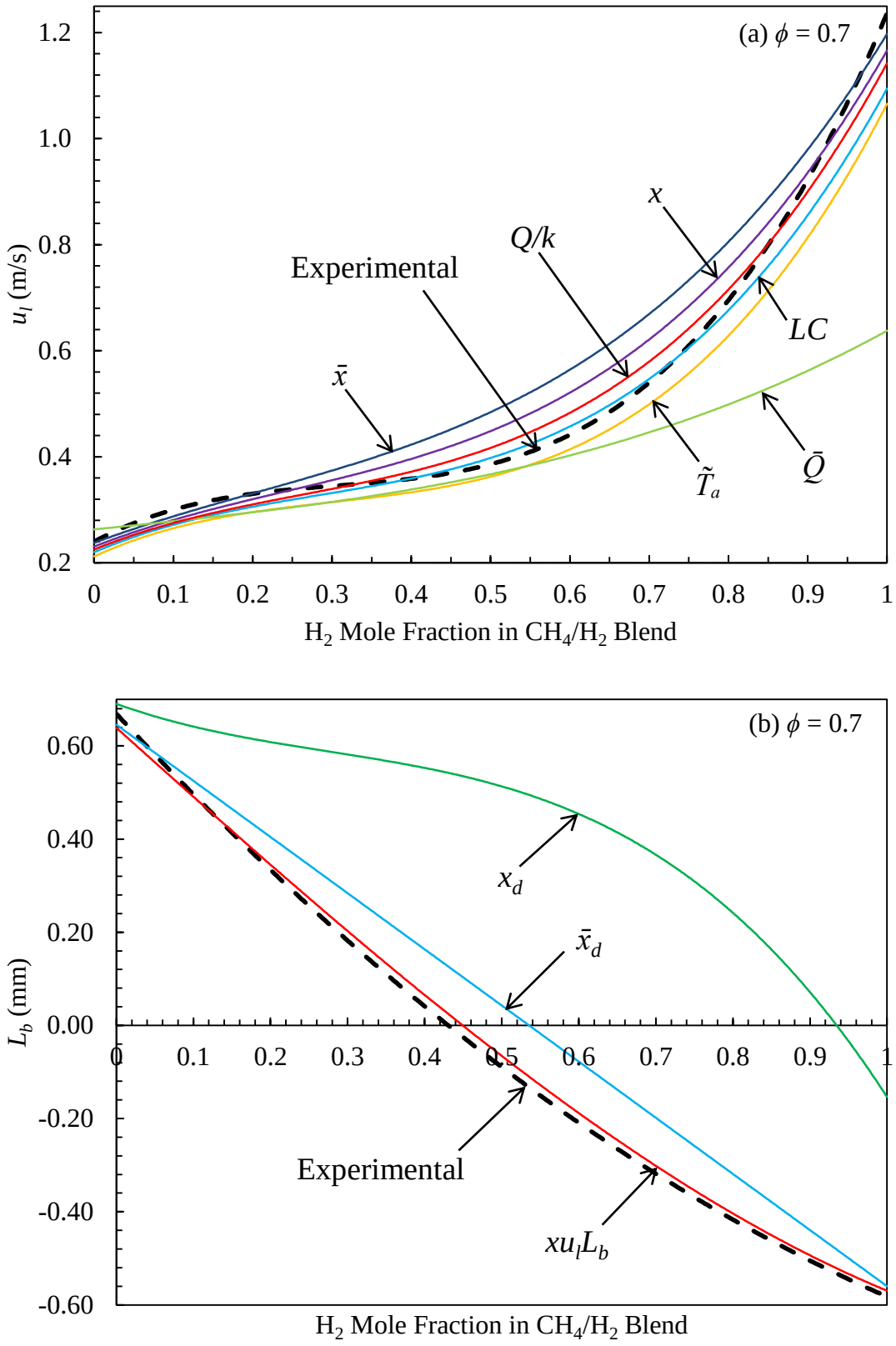

Figure 6.2: Predictive performance of a) u_l and b) L_b laws for blends of methane/hydrogen/air mixtures as a function of $\bar{x}_{fH2}$, P_i = 0.1 MPa, T_u = 303K, ϕ = 0.7.

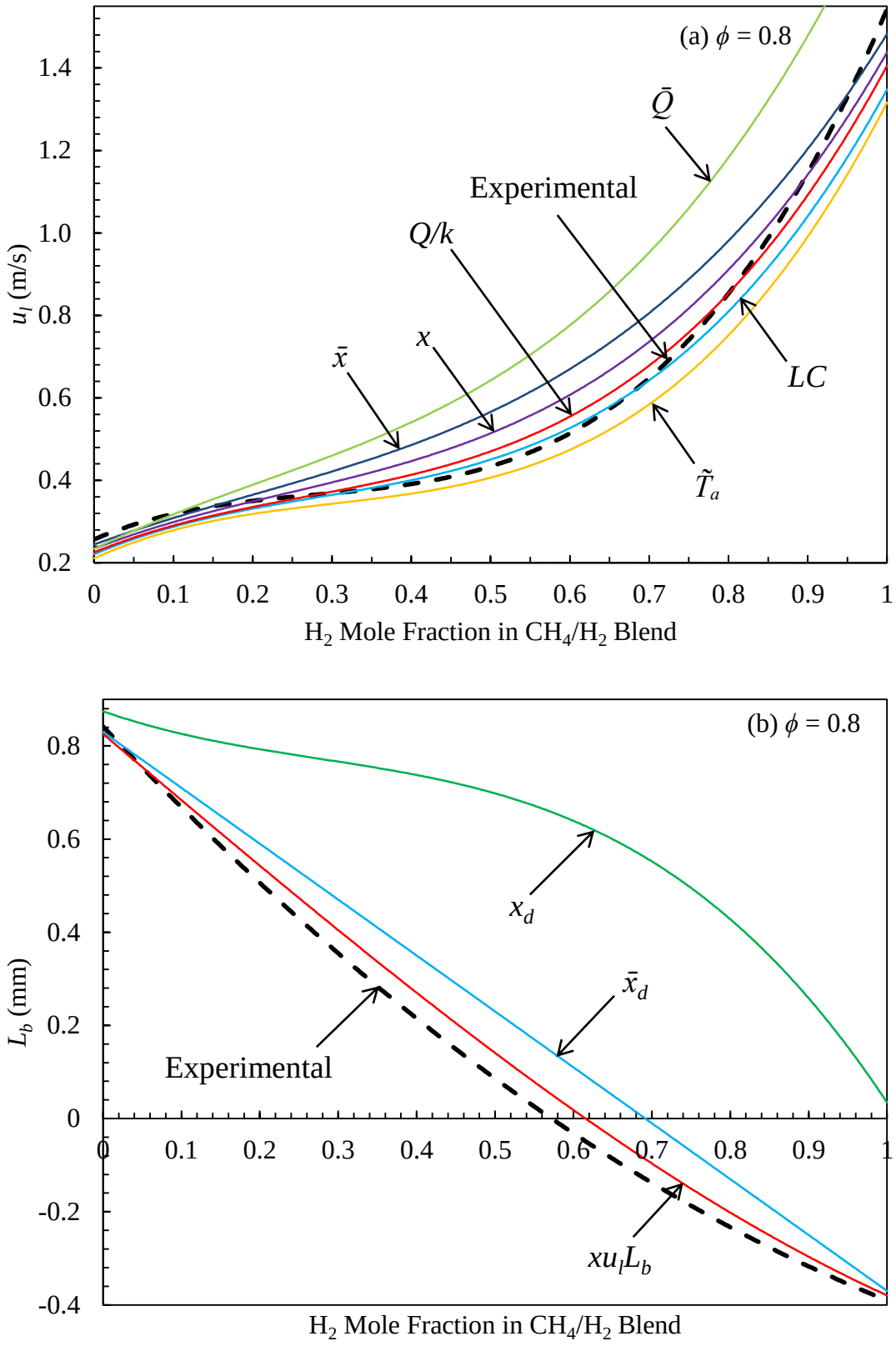

Figure 6.3: Predictive performance of a) u_l and b) L_b laws for blends of methane/hydrogen/air mixtures as a function of $\bar{x}_{fH2}$, P_i = 0.1 MPa, T_u = 303K, ϕ = 0.8.

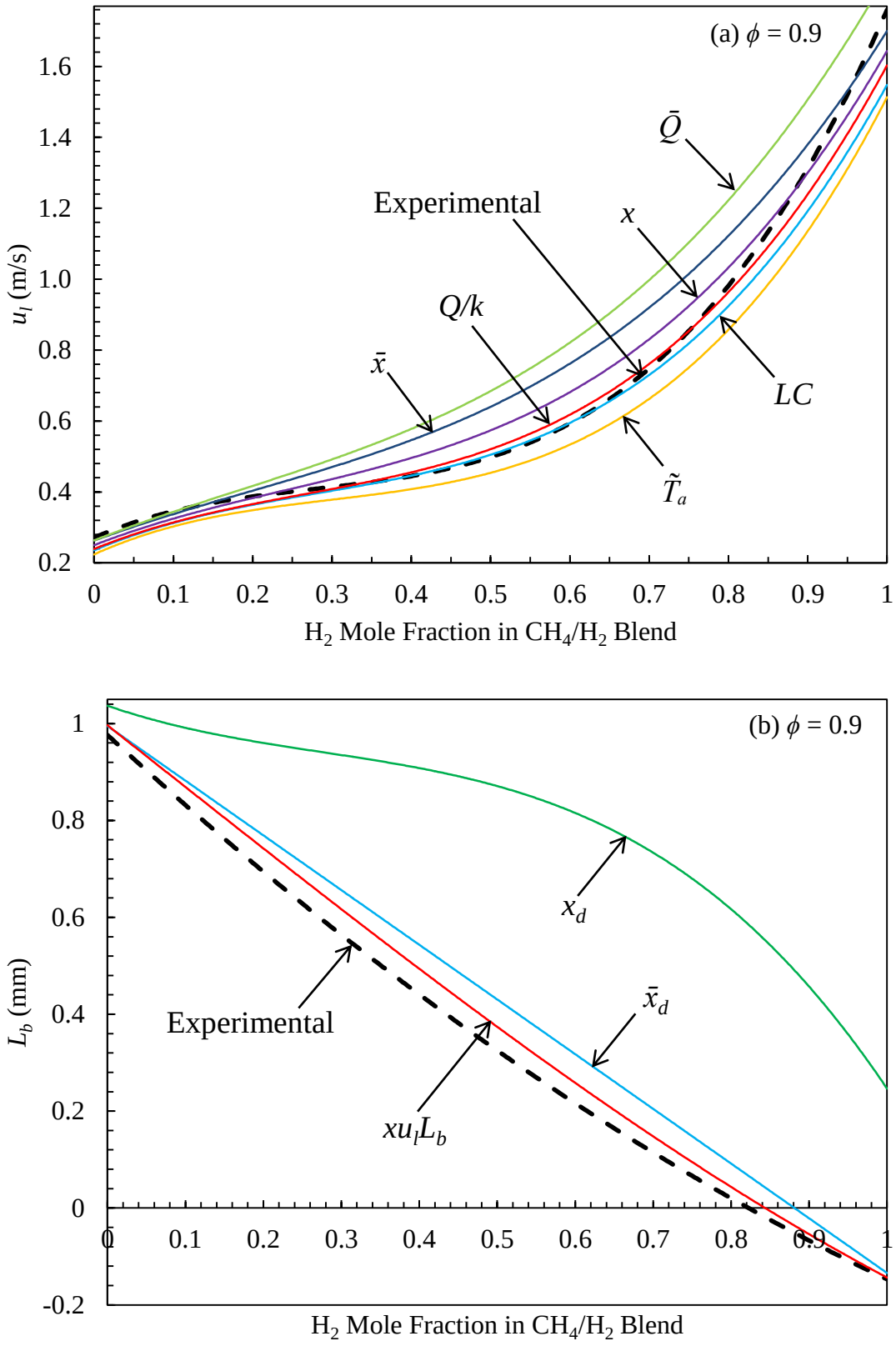

Figure 6.4: Predictive performance of a) u_l and b) L_b laws for blends of methane/hydrogen/air mixtures as a function of $\bar{x}_{fH2}$, P_i = 0.1 MPa, T_u = 303K, ϕ = 0.9.

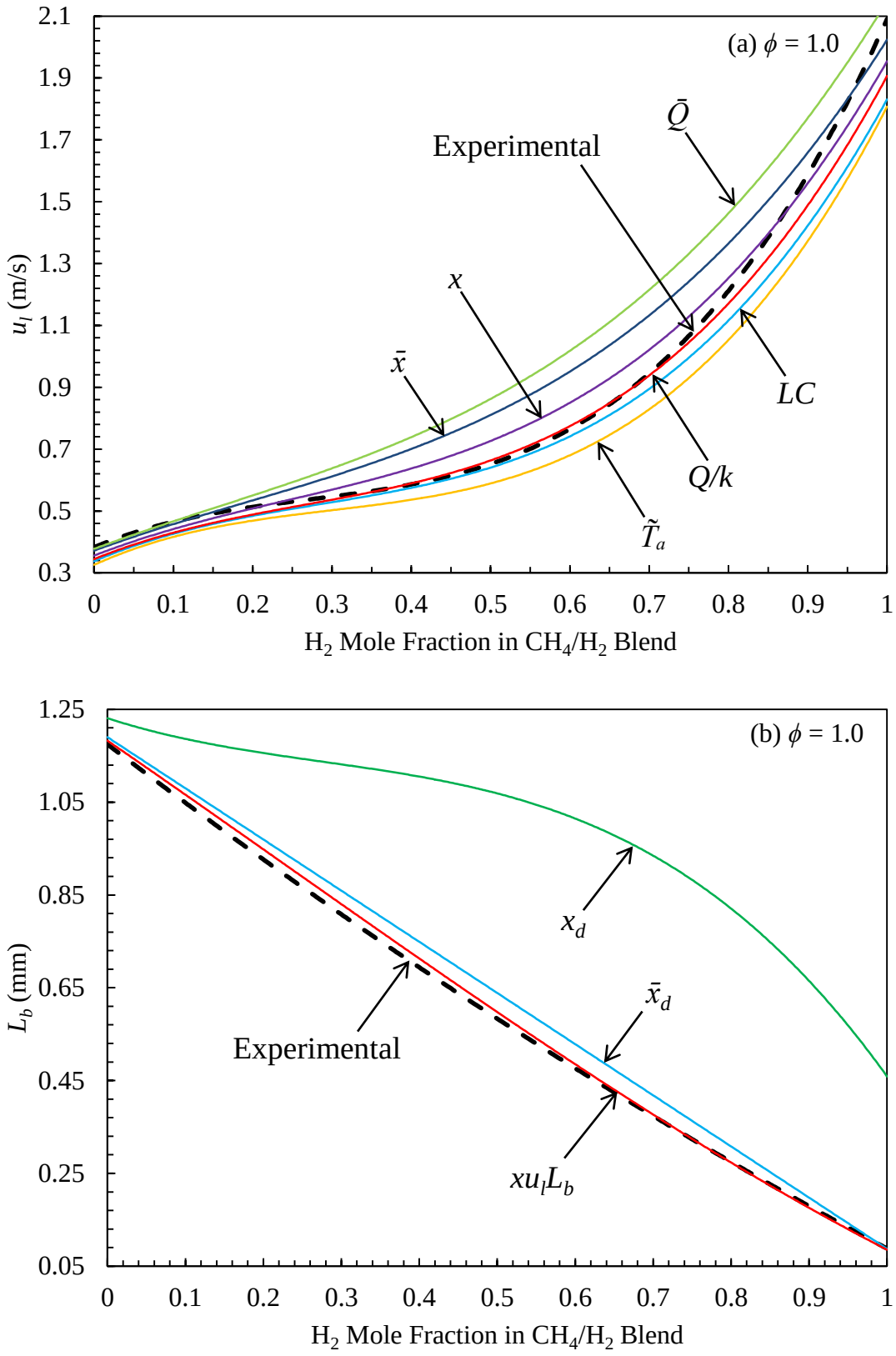

Figure 6.5: Predictive performance of a) u_l and b) L_b laws for blends of methane/hydrogen/air mixtures as a function of $\bar{x}_{fH2}$, P_i = 0.1 MPa, T_u = 303K, ϕ = 1.0.

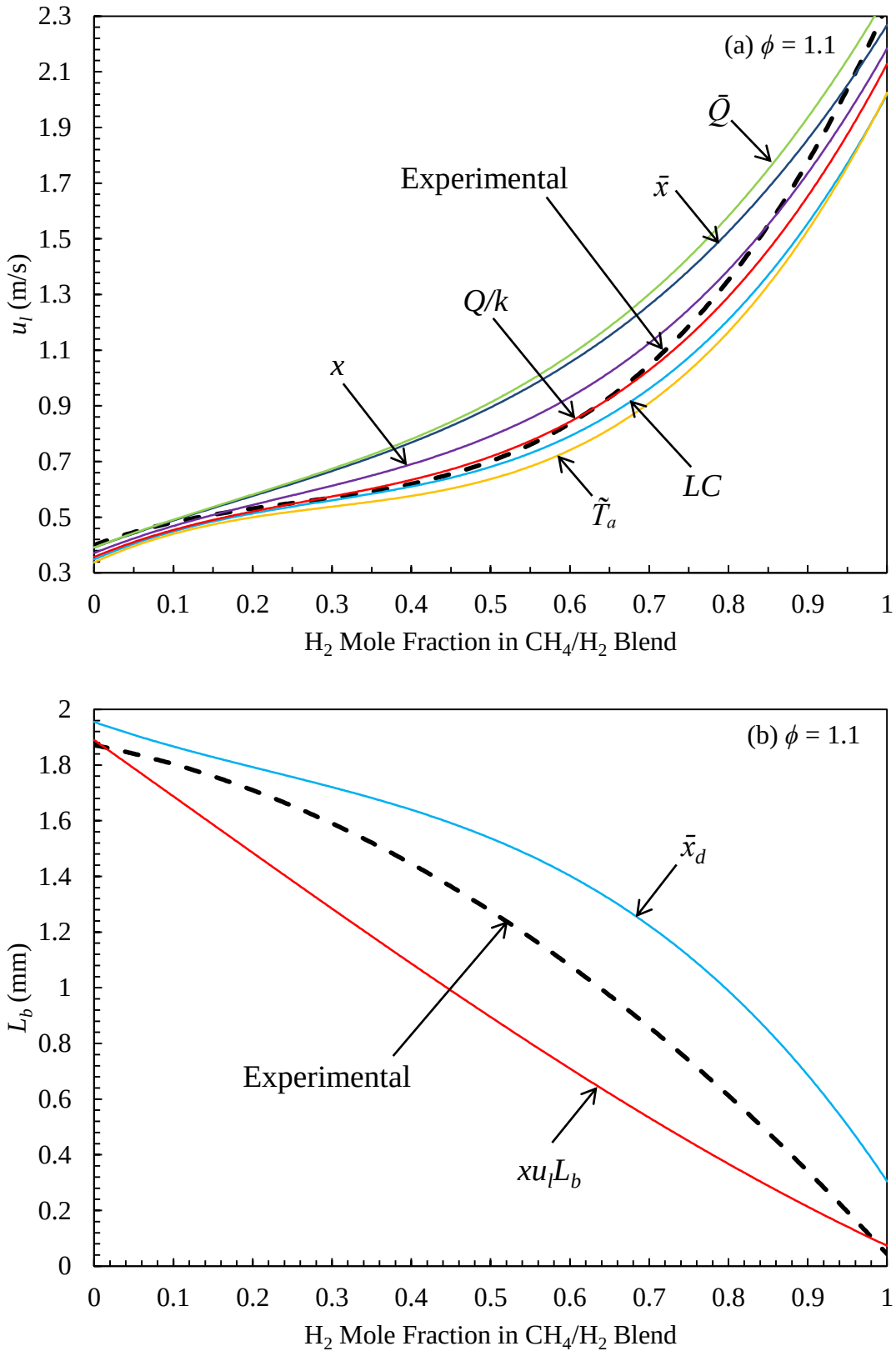

Figure 6.6: Predictive performance of a) u_l and b) L_b laws for blends of methane/hydrogen/air mixtures as a function of $\bar{x}_{fH2}$, P_i = 0.1 MPa, T_u = 303K, ϕ = 1.1.

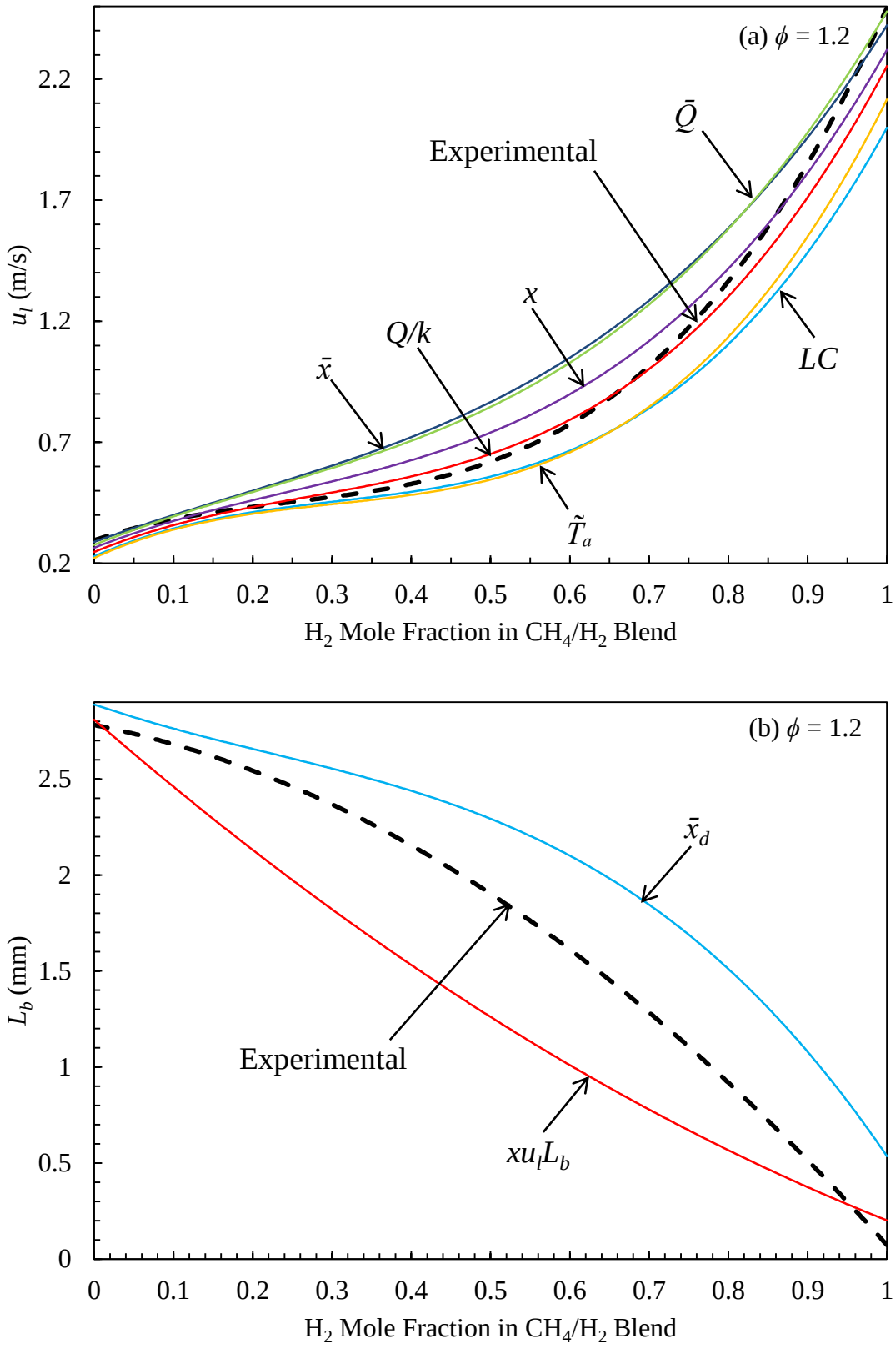

Figure 6.7: Predictive performance of a) u_l and b) L_b laws for blends of methane/hydrogen/air mixtures as a function of $\bar{x}_{fH2}$, P_i = 0.1 MPa, T_u = 303K, ϕ = 1.2.

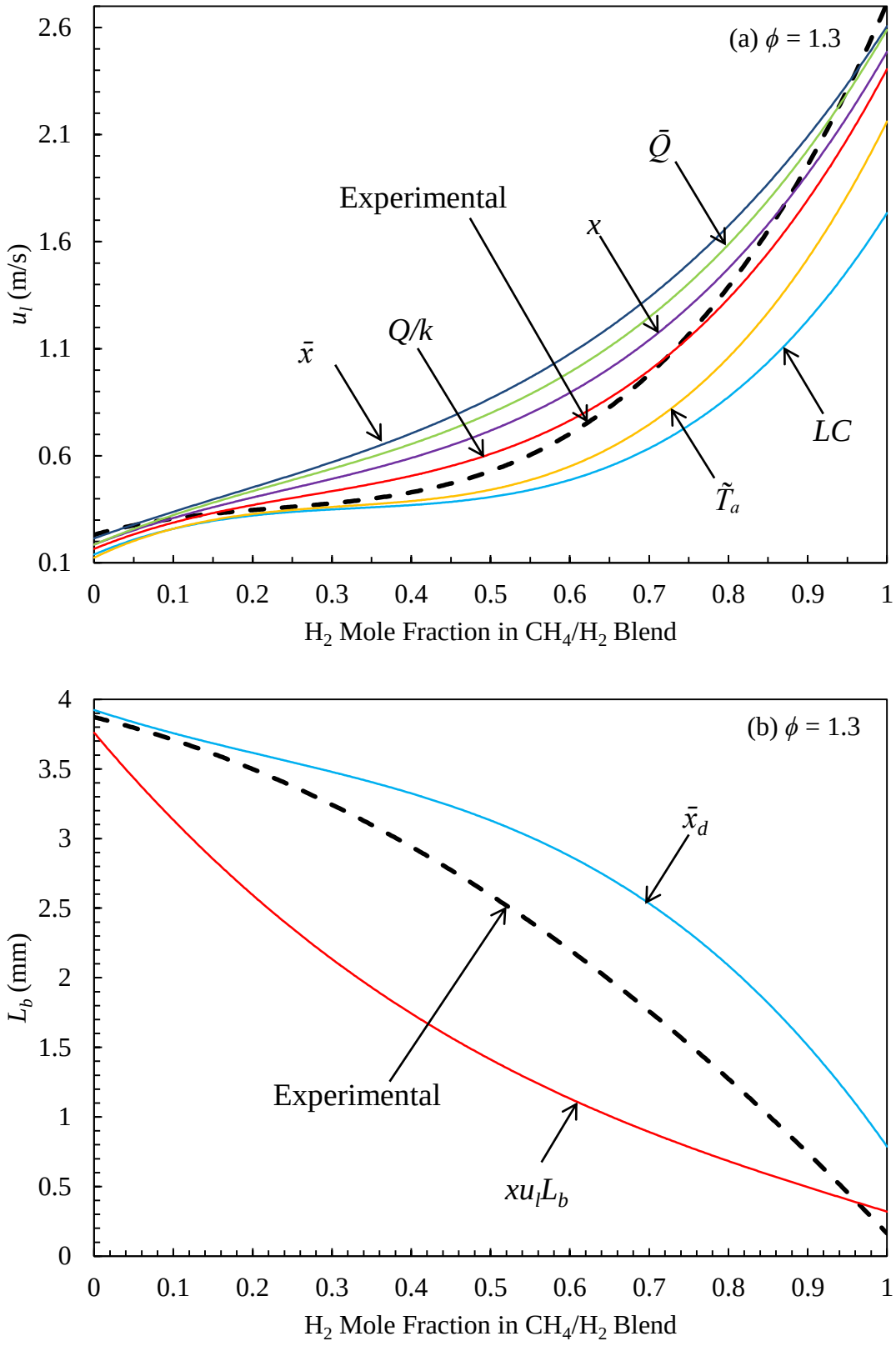

Figure 6.8: Predictive performance of a) u_l and b) L_b laws for blends of methane/hydrogen/air mixtures as a function of $\bar{x}_{fH2}$, P_i = 0.1 MPa, T_u = 303K, ϕ = 1.3.

Chapter 7 - Conclusions and Recommendations for Future Research

7.1 Conclusions

The following subsections serve to summarise the principle findings and conclusions of the present work.

7.1.1 Measurements of u_l and L_b for Pure Hydrocarbon/Air Mixtures and Blends

The initial objective of upgrading the Leeds CV2 heating system and optical setup to improve the accuracy of measured u_l and L_b values at elevated pressure and temperature was achieved. Measurements of pure fuel/air mixtures under the conditions for the present work are in satisfactory agreement with that of existing literature, and therefore validated the experimental apparatus for all subsequent measurements. All fuel/air mixtures were measured between an equivalence ratio range of 0.6 to 1.3 at initial pressures of 0.1, 0.5 and 1.0 MPa and an initial temperature of 360K.

7.1.1.1 Pure Fuels

The pure fuels investigated were representative of the major fuel groups found within commercial gasoline: *iso*-octane, *n*-heptane, toluene and *1*-hexene, and that of promising alternative bio-alcohols, ethanol and *n*-butanol. The primary purpose of their measurement was to allow a relative comparison to that of their blends u_l and L_b values, and the influence of pressure and equivalence ratio. Furthermore, the acquired data for both the pure fuel/air mixtures and their blends also provides valuable experimental data for the validation of chemical kinetic models. The key findings from the pure fuel/air mixtures are summarised below:

i) *iso*-octane/air and *1*-hexene/air mixtures were consistently the slowest and fastest burning mixtures measured for all initial pressure of 0.1, 0.5 and 1.0 MPa, across ϕ = 0.8-1.3.

ii) The greatest difference between each pure fuel/air mixture u_l values occurred at their peak u_l in the region of ϕ = 1.1-1.2. Notably, the alcohols peaked more towards ϕ = 1.2.

iii) The greatest difference in the corresponding L_b values occurred under the leanest condition of ϕ = 0.8. Contrasting to the u_l values, the minimal difference between the L_b values occurred in the peak u_l region.

iv) All liquid fuel/air mixtures studied, showed L_b values to decrease with ϕ. This is associated with a decreasing Lewis number, as the fuels thermal diffusivities were lower relative to the mixture than oxygen.

v) The differences between each pure fuel/air mixtures u_l and L_b values became significantly less with pressure, particularly in the case of L_b.

vi) Ethanol was found to be particularly pressure sensitive, with u_l decreasing with pressure, and was the only fuel to change rank with pressure.

7.1.1.2 Equimolar Binary Blends

Comprising of the pure fuel/air mixtures above, ten binary equimolar blends were measured across the same conditions. They provided a good starting point to identify any u_l and L_b values of blends that do not reflect that of their constituent values. Furthermore, the measured blends provided a foundation for the assessment of existing and proposed u_l and L_b blending laws, for blends of liquid hydrocarbons representative of the major fuel groups found within commercial gasoline.

No significantly unusual u_l and L_b behaviour of the equimolar binary blends were found in comparison to their constituent u_l and L_b values. However, a clear emerged trend was that of the blend to nearer u_l values of the slower burning constituent, particularly under lean conditions.

7.1.1.3 Gasoline Surrogate/Alcohol Blends

The comparative effects of ethanol and *n*-butanol addition to a high octane gasoline surrogate TRF/air mixtures u_l and L_b values were measured, as part of a conjoint investigation into TRF/Alcohol blend behaviour in terms of u_l and τ_i with (Materego, 2015). Measurements of τ_i were undertaken by Materego (2015) for the same blends via the Leeds RCM, the commissioning of which, as described in Appendix A, also formed part of the present work. Furthermore, the multi-constituent blends provided a wealth of data in the assessment of u_l and L_b blending laws, as discussed in Sections 7.1.4 and 7.1.5.

Measurements of u_l and L_b for all TRF/Alcohol/air mixtures were taken at the same conditions as for the pure fuel/air mixtures and their binary blends. The addition of

either alcohol to the TRF base blend was by 25% liquid volume increments, with the TRF constituents fixed at their original ratio.

The investigation showed that the addition of either alcohol markedly increased the u_l value of the base TRF/air mixture, particularly, with ethanol and when beyond 50% LV, at 0.1 MPa. However, an increase in pressure served to supress their effects to the point of negligible difference at 1.0 MPa. The τ_i measurements for the corresponding blends showed the addition of both alcohols to fractionally lower the fuels resistance to autoignition in the high temperature regime of 870-952K, however, in the low temperature regime of 800-850K, that is more reflective of SI engine temperatures, the addition of ethanol served to significantly increase τ_i values, and thus resistance to autoignition. Therefore, the investigation suggests ethanol addition to gasoline will increase autoignition resistance, whilst maintaining a similar burning velocity to that of the base gasoline when under elevated pressures. This would potentially allow for the use of higher compression ratio engines with higher volumetric efficiency, and thus reduce fuel consumption.

7.1.2 Error Analysis of Linear S_n-α Methodology

In deducing the notional u_l of a spherically expanding flame, the methodology of linearly extrapolating the stable regime of the flame on a S_n-α plot to zero stretch became convention for many years. However, it is becoming widely accepted that in the case of strong nonlinear S_n-α behaviour, a nonlinear extrapolation methodology is necessary as to avoid over estimation errors that the traditional methodology would likely incur.

The present work measured a large array of pure fuel/air mixtures and their blends across different pressures and equivalence ratios. This simultaneously gave the opportunity to analyse S_n/α behaviour for different fuel types and the influence of pressure and equivalence ratio, and furthermore, quantify the associated error with use of the linear methodology for mixtures exhibiting distinct nonlinear S_n/α behaviour.

i) Nonlinear behaviour was only observed at 0.1 MPa, particularly under lean conditions and for slower burning fuels, such as *iso*-octane. This showed the largest over predictions of u_l and L_b at $\phi = 0.8$, by 5 and 85%, respectively.

ii) At the elevated pressures of 0.5 and 1.0 MPa, all fuels across the full ϕ range tested, demonstrated distinct linear behaviour, such that any difference between the two methodologies was within the experimental error margin.

7.1.3 Cellular Instability Phenomena

Under elevated pressure, for all fuel/air mixtures studied, cellularity indicative of Darrieus-Landau and thermo-diffusive instabilities was observed. Therefore, alongside the measurement of u_l and L_b, the critical radii, r_c, at onset of cellularity, was also measured. This allowed for comparisons to the onset of such instabilities which occur in large-scale atmospheric explosions. Results have been expressed as values of both the critical Peclet number, Pe_{cl}, and the critical Karlovitz number, K_{cl}, as a function of either the flame speed Markstein number, Ma_b, or the strain rate Markstein number, Ma_{sr}. Plotted in this form, there is surprisingly good correlation, irrespective of the fuel and of the pressure. This suggests that data on the onset of instabilities from small, high pressure, laboratory explosions might be used to predict their onset in large-scale atmospheric explosions. Details of such measurements in the present work are summarised below:

i) Instability phenomena predominately occurred at the elevated pressures of 0.5 and 1.0 MPa for all fuel/mixture across ϕ = 0.8-1.3. However, at 0.1 MPa, flames of all fuel/air mixtures were much more stable, and only at ϕ = 1.3, did some fuel/air mixtures exhibit a measureable r_c within the limited window radii of 75mm.

ii) For all fuel/air mixtures, measurements of r_c were found to decrease with an increase in initial pressure and equivalence ratio. They allowed the calculation of Pe_{cl} and K_{cl}, which when plotted against the Markstein number, Ma_b, revealed a strikingly linear trend between ϕ = 0.8-1.2. At ϕ=1.3 a plateau was reached.

iii) The repeatability of r_c became reduced at higher pressure. At 1.0 MPa, measurements for u_l and L_b were limited to stoichiometric conditions for all fuels. Beyond which the onset of r_c, was near immediate, giving an insufficient stable regime to extrapolate from.

7.1.4 u_l Blending Laws

Historically, empirical fractional mass or mole concentrations have been used to weight the contributions of constituent burning velocities. During the present work, it was found that as long as the mixtures are chemically not dissimilar such approaches are

shown to be reasonably successful. However, difficulties arise when the chemical kinetics and molecular transport processes for the constituent mixtures are dissimilar. In an attack on this problem CH_4/air and H_2/air blends were studied experimentally. Theoretically, blending laws were contemplated that drew heavily on the fundamental theories of burning velocity. Ultimately, with a degree of trial and error a blending law was reached based on heat of reaction and the thermal conductivities of the constituent mixtures.

The predictive performance of the proposed u_l blending law was analysed and compared against that of five existing laws for all liquid hydrocarbon blends measured in the present work, and for existing CH_4/air and H_2/air blend data. The performance of which is summarised below:

i) Overall, the new proposed u_l law, termed the Q/k law, performed best in the prediction of all u_l blend values for all conditions studied in the present work. Having an average predicted to measured ratio of 1.01, with a standard deviation of 0.02.

ii) The measured liquid hydrocarbon blends were generally well predicted by all u_l laws, very close to or within the experimental error margin. This is likely due to their constituents having relatively similar underlying chemistry and u_l values.

iii) As anticipated, the CH_4/air and H_2/air blends proved to be significantly more challenging. This was due to their significantly contrasting chemistry, exhibiting very different heat release rate profiles and u_l values, alongside notably contrasting thermal conductivities. They were the only blends to significantly push all blending laws beyond the experimental error margins, and thereby expose the most comprehensively developed blending law. However, the Q/k law again out performed all existing u_l laws, across ϕ = 0.6-1.3, within an average predicted to measured ratio of 1.01 with a standard deviation of 0.03. Although this ratio is worse than the average ratio for all blends studied, the relative difference to that of the other laws is much greater, thus, highlighting the superior performance of the proposed law. The merit of the Q/k law, particularly for blends such as CH_4/ H_2/air, results from its unique consideration for the influence of each constituent mixtures heat realise rate profile and thermal conductivity.

7.1.5 L_b Blending Laws

The development of an accurate L_b blending law was less successful. This is not surprising due to the relatively tentative nature of measuring L_b and its increased experimental error margin. The predictive performance of all trailed L_b blending laws was analysed over the same blends as that for the u_l blending laws. However, no other existing L_b blending laws were found in literature for comparison. Their performance is summarised below:

i) For the liquid hydrocarbon blends, L_b values were generally well predicted by both the deficient reactant mole and mass fraction based laws, $\bar{x}_d$ and x_d, whilst the more empirically based xu_lL_b law significantly under predicted.

ii) For the CH_4/air and H_2/air blends, conversely, the xu_lL_b law proved to be exceptionally good under lean to stoichiometric conditions, followed closely by the $\bar{x}_d$ law, whilst the x_d law significantly over predicted.

7.2 Recommendations for Future Research

The following subsections give recommendations based on the findings of the present work in terms of further research paths and the experimental apparatus used.

7.2.1 Further Research Paths

i) Full characterisation of the pure fuels and blends studied in the present work requires further measurements at a greater range of pressures, temperatures and equivalence ratios.

ii) Testing of the proposed Q/k law over more conditions, with further fuel types would improve its validity over a greater range. Of particular practical importance, further testing on a "blends of blends" basis with real commercial fuel blends would also be very interesting. Furthermore, testing of the laws performance using blends with gases common to exhaust gas recirculation would potentially be useful in engine studies.

iii) More work into the potential for an L_b law is required. The author recommends following the rational of the deficient reactant based law.

iv) Just as a u_l blending law is highly desirable for the prediction of different alternative fuel blends, so is that of a τ_i blending law, few exist in current literature and often have limited range.

v) Further large-scale explosion data is required to bolster the notion of laboratory combustion vessels being able to simulate their Pe_{cl} and Ka_c values at elevated pressure.

7.2.2 Experimental Apparatus - The Leeds CV2 Bomb

i) Further investigation into mixture temperature uniformity at higher pressures and temperatures is required, particularly under laminar conditions, whereby the degree of temperature uniformity was found to be a function of the time after which the fans are switched off, and the initial pressure and temperature.

ii) A known cool spot of the vessel is that of the bottom port, due to the attaching metal stand which acts as a heat stink. An improvement in the vessels temperature uniformity could be achieved by the use of a gasket made from a high thermally insulating material, such as PTFE, mounted between the bottom port and the metal stand.

iii) Remotely operated electronic solenoid valves on the exhaust line, mixture inlet and static pressure transducer would allow for full operation behind the protected control booth. This would improve safety, particularly during high pressure experiments, as the pressure of the combustion products after combustion could be exhausted without passing the vessel windows.

iv) High fan speeds used to generate high turbulence, limit the lowest initial mixture temperature due to the heat generation from the fan shaft seals. Therefore, the development of an external water cooled jacket would lower mixture temperatures under high turbulence and increase the vessels operating range.

Appendix A - Blending Law Performance League Tables

This Appendix presents the league tables showing the performance of each u_l and L_b blending law, for each blend studied. Section A.1 presents tables for each binary equimolar blend, Section A.2 presents tables for each TRF/alcohol blend, and finally, Section A.3 presents tables for each methane and hydrogen blend.

iso-Octane/Air and Toluene/Air Equimolar Blends											
P_i (MPa)	ϕ	u_l Laws							L_b Laws		
		$\bar{x}$	x	LC	T_b	$\tilde{T}_a$	Q	Q/k	$\bar{x}_d$	x_d	xu_lL_b
0.1	0.8	1.03	1.03	1.03	1.03	1.03	1.03	1.03	0.92	0.93	0.31
	0.9	0.99	0.99	0.99	1.08	0.99	1.00	0.99	0.86	0.87	0.36
	1	1.04	1.04	1.04	1.13	1.04	1.04	1.04	0.99	0.99	0.44
	1.1	1.02	1.02	1.02	1.11	1.02	1.01	1.02	1.03	1.03	0.49
	1.2	1.00	1.00	1.00	1.08	1.00	1.00	1.00	0.83	0.84	0.40
	1.3	1.00	1.00	0.99	1.09	0.99	0.99	1.00	1.04	1.05	0.44
Av.		1.01	1.01	1.01	1.08	1.01	1.01	1.01	0.95	0.95	0.41
σ		0.02	0.02	0.02	0.03	0.02	0.02	0.02	0.09	0.08	0.06
0.5	0.8	1.01	1.01	1.01	1.10	1.01	1.01	1.01	0.94	0.94	0.20
	0.9	1.00	1.00	1.01	1.09	1.00	1.01	1.00	0.94	0.94	0.26
	1	1.02	1.02	1.03	1.11	1.02	1.01	1.02	0.87	0.87	0.27
	1.1	0.99	0.99	0.99	1.07	0.99	1.00	0.99	0.86	0.86	0.29
	1.2	1.01	1.01	1.01	1.10	1.01	1.01	1.01	1.05	1.05	0.34
	1.3	1.02	1.02	1.03	1.12	1.02	1.03	1.02	1.36	1.34	0.38
Av.		1.01	1.01	1.01	1.10	1.01	1.01	1.01	1.01	1.00	0.29
σ		0.01	0.01	0.01	0.02	0.01	0.01	0.01	0.19	0.18	0.06
1.0	0.8	0.98	0.98	0.99	0.98	0.98	0.98	0.98	1.06	1.07	0.19
	0.9	1.01	1.01	1.01	1.10	1.01	1.01	1.01	1.02	1.02	0.23
	1	1.01	1.01	1.02	1.10	1.01	0.95	1.01	8.68	11.60	2.93
Av.		1.00	1.00	1.01	1.06	1.00	0.98	1.00	3.59	4.56	1.12
σ		0.02	0.02	0.02	0.07	0.02	0.03	0.02	4.41	6.09	1.57

Table A.1: u_l and L_b blending law performances (u_{lp}/u_l and L_{bp}/L_b), equimolar fuel/air blend of *iso*-octane/air and toluene/air, ϕ = 0.8-1.3, T_u = 360K, P_i = 0.1, 0.5 and 1.0MPa. Figures 4.26 and 4.27, in Chapter 4 show the related u_l and L_b measured values.

iso-Octane/Air and *1*-Hexene/Air Equimolar Blends											
P_i (MPa)	ϕ	u_l Laws							L_b Laws		
		$\bar{x}$	x	LC	T_b	$\tilde{T}_a$	Q	Q/k	$\bar{x}_d$	x_d	xu_lL_b
0.1	0.8	1.01	1.01	1.01	1.01	1.00	1.01	1.01	0.91	0.92	0.33
	0.9	0.99	0.99	1.00	1.08	0.99	1.00	0.99	0.97	0.97	0.43
	1	1.02	1.02	1.02	1.11	1.01	1.02	1.02	0.94	0.94	0.46
	1.1	1.01	1.01	1.01	1.10	1.00	1.01	1.01	1.01	1.01	0.53
	1.2	0.95	0.95	0.96	1.04	0.95	0.96	0.95	0.77	0.78	0.44
	1.3	0.96	0.96	0.96	1.05	0.95	0.96	0.96	0.78	0.80	0.41
Av.		0.99	0.99	1.00	1.06	0.99	0.99	0.99	0.89	0.91	0.43
σ		0.03	0.03	0.03	0.04	0.03	0.03	0.03	0.10	0.09	0.07
0.5	0.8	0.98	0.98	0.98	1.07	0.97	0.98	0.98	0.97	0.99	0.23
	0.9	1.03	1.03	1.03	1.12	1.02	1.03	1.03	0.90	0.91	0.26
	1	1.02	1.02	1.03	1.11	1.02	1.03	1.02	0.85	0.86	0.29
	1.1	1.03	1.02	1.03	1.11	1.02	1.03	1.02	0.95	0.93	0.33
	1.2	1.02	1.02	1.03	1.11	1.01	1.03	1.02	1.01	0.98	0.34
	1.3	1.03	1.03	1.03	1.12	1.02	1.03	1.03	1.47	1.44	0.45
Av.		1.02	1.02	1.02	1.11	1.01	1.02	1.02	1.03	1.02	0.32
σ		0.02	0.02	0.02	0.02	0.02	0.02	0.02	0.23	0.21	0.08
1.0	0.8	1.02	1.02	1.02	1.02	1.01	1.02	1.02	0.98	1.00	0.19
	0.9	1.01	1.01	1.01	1.10	1.00	1.01	1.01	0.88	0.88	0.21
	1	1.00	1.00	1.01	1.09	1.00	1.01	1.00	0.43	0.27	0.11
Av.		1.01	1.01	1.01	1.07	1.00	1.01	1.01	0.76	0.72	0.17
σ		0.01	0.01	0.01	0.04	0.01	0.01	0.01	0.29	0.39	0.05

Table A.2: u_l and L_b blending law performances (u_{lp}/u_l and L_{bp}/L_b), equimolar fuel/air blend of *iso*-octane/air and *1*-hexene/air, ϕ = 0.8-1.3, T_u = 360K, P_i = 0.1, 0.5 and 1.0MPa. Figures 4.28 and 4.29, in Chapter 4 show the related u_l and L_b measured values.

iso-Octane/Air and Ethanol/Air Equimolar Blends											
P_i (MPa)	ϕ	u_l Laws							L_b Laws		
		$\bar{x}$	x	LC	T_b	$\tilde{T}_a$	Q	Q/k	$\bar{x}_d$	x_d	xu_lL_b
0.1	0.8	1.09	1.09	1.14	1.09	1.08	1.09	1.09	0.75	0.82	0.28
	0.9	1.06	1.06	1.11	1.16	1.06	1.06	1.06	0.93	0.98	0.41
	1	1.04	1.04	1.08	1.13	1.03	1.04	1.03	0.90	0.93	0.45
	1.1	1.03	1.03	1.08	1.12	1.02	1.04	1.03	1.08	1.05	0.54
	1.2	1.01	1.01	1.07	1.10	1.00	1.02	1.01	0.86	0.90	0.48
	1.3	0.99	0.99	1.04	1.09	0.98	0.99	0.99	0.82	0.90	0.46
Av.		1.03	1.03	1.09	1.11	1.03	1.04	1.03	0.89	0.93	0.44
σ		0.04	0.04	0.04	0.03	0.04	0.03	0.04	0.11	0.08	0.09
0.5	0.8	0.99	0.99	1.01	1.09	0.99	0.99	0.99	0.96	0.98	0.21
	0.9	1.04	1.04	1.06	1.14	1.04	1.04	1.04	0.97	0.98	0.26
	1	1.04	1.04	1.08	1.13	1.04	1.05	1.04	0.94	0.95	0.30
	1.1	1.03	1.03	1.08	1.12	1.03	1.08	1.03	0.95	0.93	0.31
	1.2	1.02	1.02	1.08	1.12	1.01	1.05	1.02	1.01	0.97	0.32
	1.3	1.01	1.01	1.05	1.11	1.00	1.01	1.01	-0.70	-0.48	-0.09
Av.		1.02	1.02	1.06	1.12	1.02	1.04	1.02	0.69	0.72	0.22
σ		0.02	0.02	0.03	0.02	0.02	0.03	0.02	0.68	0.59	0.16
1.0	0.8	1.01	1.01	1.04	1.02	1.01	1.01	1.01	1.02	1.02	0.17
	0.9	1.00	1.00	1.04	1.09	1.00	1.00	1.00	0.92	0.91	0.21
	1	1.01	1.01	1.04	1.09	1.00	1.01	1.01	2.07	1.71	0.40
Av.		1.01	1.01	1.04	1.07	1.00	1.01	1.01	1.34	1.21	0.26
σ		0.01	0.01	0.00	0.05	0.01	0.01	0.01	0.64	0.43	0.12

Table A.3: u_l and L_b blending law performances (u_{lp}/u_l and L_{bp}/L_b), equimolar fuel/air blend of *iso*-octane/air and ethanol/air, ϕ = 0.8-1.3, T_u = 360K, P_i = 0.1, 0.5 and 1.0MPa. Figures 4.30 and 4.31, in Chapter 4 show the related u_l and L_b measured values.

iso-Octane/Air and *n*-Heptane/Air Equimolar Blends											
P_i (MPa)	ϕ	u_l Laws							L_b Laws		
		$\bar{x}$	x	LC	T_b	$\tilde{T}_a$	Q	Q/k	$\bar{x}_d$	x_d	xu_lL_b
0.1	0.8	1.03	1.03	1.03	1.03	1.03	1.03	1.03	0.90	0.90	0.30
	0.9	1.08	1.08	1.08	1.18	1.08	1.09	1.08	0.97	0.97	0.39
	1	1.03	1.02	1.02	1.12	1.02	0.44	1.02	0.99	0.99	0.48
	1.1	1.01	1.01	1.01	1.10	1.01	1.01	1.01	1.02	1.02	0.51
	1.2	0.99	0.99	0.99	1.08	0.99	0.99	0.99	0.93	0.94	0.48
	1.3	1.00	1.00	1.00	1.10	1.00	1.00	1.00	1.15	1.16	0.53
Av.		1.02	1.02	1.02	1.10	1.02	0.93	1.02	0.99	1.00	0.45
σ		0.03	0.03	0.03	0.05	0.03	0.24	0.03	0.09	0.09	0.09
0.5	0.8	1.04	1.04	1.04	1.15	1.04	1.04	1.04	1.05	1.05	0.23
	0.9	1.03	1.03	1.03	1.12	1.03	1.04	1.03	0.88	0.88	0.25
	1	1.03	1.03	1.03	1.12	1.03	1.05	1.03	0.96	0.96	0.31
	1.1	0.98	0.98	0.98	1.06	0.98	0.97	0.98	1.01	1.00	0.35
	1.2	1.00	1.00	1.00	1.09	1.00	1.01	1.00	1.57	1.56	0.53
	1.3	1.02	1.02	1.02	1.12	1.02	1.02	1.02	0.11	0.08	0.01
Av.		1.02	1.02	1.02	1.11	1.01	1.02	1.02	0.93	0.92	0.28
σ		0.02	0.02	0.02	0.03	0.02	0.03	0.02	0.47	0.48	0.17
1.0	0.8	1.02	1.02	1.01	1.02	1.01	1.01	1.02	0.95	0.95	0.17
	0.9	0.99	0.99	0.99	1.08	0.99	0.99	0.99	0.97	0.97	0.23
	1	0.99	0.99	0.98	1.07	0.98	0.99	0.99	1.21	1.20	0.33
Av.		1.00	1.00	1.00	1.06	0.99	0.99	1.00	1.04	1.04	0.24
σ		0.02	0.02	0.01	0.04	0.02	0.01	0.02	0.15	0.14	0.08

Table A.4: u_l and L_b blending law performances (u_{lp}/u_l and L_{bp}/L_b), equimolar fuel/air blend of *iso*-octane/air and *n*-heptane/air, ϕ = 0.8-1.3, T_u = 360K, P_i = 0.1, 0.5 and 1.0MPa. Figures 4.32 and 4.33, in Chapter 4 show the related u_l and L_b measured values.

Toluene/Air and *1*-Hexene/Air Equimolar Blends											
P_i (MPa)	ϕ	u_l Laws							L_b Laws		
		$\bar{x}$	x	LC	T_b	$\tilde{T}_a$	Q	Q/k	$\bar{x}_d$	x_d	xu_lL_b
0.1	0.8	1.03	1.03	1.02	1.03	1.03	1.03	1.03	0.95	0.95	0.35
	0.9	1.03	1.03	1.03	1.13	1.03	1.04	1.03	0.98	0.98	0.43
	1	1.00	0.99	0.99	1.08	0.99	1.00	1.00	1.03	1.03	0.53
	1.1	1.01	1.01	1.00	1.10	1.01	1.01	1.01	1.11	1.12	0.59
	1.2	1.00	1.00	0.99	1.09	1.00	1.00	1.00	0.96	0.96	0.50
	1.3	0.98	0.98	0.97	1.07	0.98	0.98	0.98	0.88	0.89	0.43
Av.		1.01	1.01	1.00	1.08	1.01	1.01	1.01	0.99	0.99	0.47
σ		0.02	0.02	0.02	0.03	0.02	0.02	0.02	0.08	0.08	0.08
0.5	0.8	1.00	1.00	0.99	1.09	0.99	1.00	1.00	0.98	0.98	0.24
	0.9	1.00	1.00	0.99	1.09	1.00	1.00	1.00	0.95	0.95	0.29
	1	1.02	1.02	1.02	1.11	1.02	1.02	1.02	0.82	0.83	0.29
	1.1	1.00	1.00	0.99	1.09	1.00	1.01	1.00	0.90	0.89	0.33
	1.2	1.01	1.01	1.00	1.10	1.00	1.01	1.01	0.89	0.88	0.33
	1.3	1.00	1.00	0.99	1.09	0.99	1.25	0.99	0.47	0.46	0.16
Av.		1.01	1.01	1.00	1.09	1.00	1.05	1.00	0.83	0.83	0.27
σ		0.01	0.01	0.01	0.01	0.01	0.10	0.01	0.19	0.19	0.07
1.0	0.8	1.01	1.01	1.00	1.01	1.00	1.01	1.01	1.09	1.09	0.22
	0.9	1.00	1.00	0.99	1.09	0.99	1.00	1.00	1.08	1.09	0.28
	1	1.00	1.00	1.00	1.09	1.00	1.00	1.00	0.73	0.71	0.22
Av.		1.00	1.00	1.00	1.06	1.00	1.00	1.00	0.97	0.96	0.24
σ		0.00	0.00	0.01	0.05	0.00	0.00	0.00	0.21	0.22	0.04

Table A.5: u_l and L_b blending law performances (u_{lp}/u_l and L_{bp}/L_b), equimolar fuel/air blend of toluene/air and *1*-hexene/air, ϕ = 0.8-1.3, T_u = 360K, P_i = 0.1, 0.5 and 1.0MPa. Figures 4.34 and 4.35, in Chapter 4 show the related u_l and L_b measured values.

Toluene/Air and Ethanol/Air Equimolar Blends											
P_i (MPa)	ϕ	u_l Laws							L_b Laws		
		$\bar{x}$	x	LC	T_b	$\tilde{T}_a$	Q	Q/k	$\bar{x}_d$	x_d	xu_lL_b
0.1	0.8	1.09	1.09	1.11	1.09	1.08	1.08	1.09	0.96	0.99	0.35
	0.9	1.02	1.02	1.05	1.12	1.02	1.07	1.02	0.92	0.94	0.41
	1	1.01	1.01	1.04	1.11	1.01	1.03	1.01	0.93	0.95	0.48
	1.1	1.03	1.02	1.06	1.12	1.02	1.08	1.02	1.03	1.02	0.52
	1.2	1.01	1.01	1.05	1.10	1.00	0.97	1.01	1.00	1.01	0.53
	1.3	0.95	0.95	0.99	1.04	0.94	0.93	0.95	0.79	0.84	0.44
Av.		1.02	1.02	1.05	1.10	1.01	1.03	1.02	0.94	0.96	0.45
σ		0.04	0.05	0.04	0.03	0.05	0.06	0.05	0.08	0.06	0.07
0.5	0.8	1.05	1.05	1.03	1.15	1.05	1.05	1.05	1.01	1.01	0.22
	0.9	1.01	1.01	1.02	1.11	1.01	1.01	1.01	0.87	0.88	0.25
	1	1.01	1.01	1.01	1.10	1.01	1.01	1.01	0.99	1.00	0.34
	1.1	1.01	1.01	1.04	1.10	1.01	0.98	1.01	0.96	0.95	0.34
	1.2	1.00	1.00	1.03	1.09	0.99	0.99	1.00	1.01	0.97	0.34
	1.3	0.99	0.99	1.02	1.09	0.99	0.99	0.99	1.02	0.70	0.14
Av.		1.01	1.01	1.02	1.10	1.01	1.00	1.01	0.97	0.92	0.27
σ		0.02	0.02	0.01	0.02	0.02	0.03	0.02	0.05	0.12	0.08
1.0	0.8	1.01	1.01	1.01	1.01	1.01	1.01	1.01	1.19	1.16	0.21
	0.9	0.98	0.98	0.98	1.07	0.98	0.98	0.98	1.07	1.06	0.26
	1	0.99	0.99	1.00	1.08	0.99	1.00	0.99	1.74	1.34	0.31
Av.		0.99	0.99	1.00	1.05	0.99	1.00	0.99	1.33	1.19	0.26
σ		0.02	0.02	0.01	0.04	0.02	0.02	0.02	0.36	0.14	0.05

Table A.6: u_l and L_b blending law performances (u_{lp}/u_l and L_{bp}/L_b), equimolar fuel/air blend of toluene/air and ethanol/air, ϕ = 0.8-1.3, T_u = 360K, P_i = 0.1, 0.5 and 1.0MPa. Figures 4.36and 4.37, in Chapter 4 show the related u_l and L_b measured values.

Toluene/Air and *n*-Heptane/Air Equimolar Blends											
P_i (MPa)	ϕ	u_l Laws							L_b Laws		
		$\bar{x}$	x	LC	T_b	$\tilde{T}_a$	Q	Q/k	$\bar{x}_d$	x_d	xu_lL_b
0.1	0.8	0.97	0.97	0.97	0.97	0.97	0.97	0.97	0.97	0.97	0.36
	0.9	1.06	1.06	1.05	1.15	1.06	1.01	1.06	0.93	0.93	0.39
	1	1.06	1.06	1.05	1.15	1.06	1.07	1.06	0.97	0.97	0.46
	1.1	1.01	1.01	1.01	1.10	1.01	1.04	1.01	1.07	1.07	0.54
	1.2	1.00	1.00	0.99	1.09	1.00	0.99	1.00	1.00	1.00	0.50
	1.3	1.00	1.00	0.99	1.09	1.00	1.00	1.00	0.94	0.94	0.42
Av.		1.02	1.02	1.01	1.09	1.02	1.01	1.02	0.98	0.98	0.44
σ		0.03	0.03	0.03	0.07	0.03	0.03	0.03	0.05	0.05	0.07
0.5	0.8	1.00	1.00	1.00	1.10	1.00	1.00	1.00	0.95	0.95	0.23
	0.9	1.02	1.02	1.01	1.11	1.01	1.01	1.02	1.09	1.09	0.32
	1	1.02	1.02	1.02	1.11	1.02	1.04	1.02	0.90	0.89	0.30
	1.1	0.97	0.97	0.97	1.05	0.97	0.96	0.97	0.86	0.86	0.32
	1.2	0.99	0.99	0.98	1.07	0.98	0.83	0.98	0.82	0.83	0.30
	1.3	0.99	0.99	0.98	1.08	0.99	0.99	0.99	-0.02	0.00	0.00
Av.		1.00	1.00	0.99	1.09	1.00	0.97	1.00	0.77	0.77	0.24
σ		0.02	0.02	0.02	0.02	0.02	0.07	0.02	0.40	0.39	0.12
1.0	0.8	1.01	1.01	1.00	1.01	1.01	1.01	1.01	1.07	1.07	0.21
	0.9	1.00	1.00	0.99	1.09	1.00	1.00	1.00	1.06	1.06	0.27
	1	1.01	1.01	1.01	1.09	1.01	1.03	1.01	0.44	0.47	0.15
Av.		1.01	1.01	1.00	1.06	1.00	1.01	1.01	0.86	0.87	0.21
σ		0.00	0.01	0.01	0.05	0.01	0.02	0.00	0.36	0.34	0.06

Table A.7: u_l and L_b blending law performances (u_{lp}/u_l and L_{bp}/L_b), equimolar fuel/air blend of toluene/air and *n*-heptane/air, ϕ = 0.8-1.3, T_u = 360K, P_i = 0.1, 0.5 and 1.0MPa. Figures 4.38 and 4.39, in Chapter 4 show the related u_l and L_b measured values.

1-Hexene/Air and Ethanol/Air Equimolar Blends											
P_i (MPa)	ϕ	u_l Laws							L_b Laws		
		$\bar{x}$	x	LC	T_b	$\tilde{T}_a$	Q	Q/k	$\bar{x}_d$	x_d	xu_lL_b
0.1	0.8	1.00	1.00	0.99	1.00	1.00	1.00	0.99	0.99	1.01	0.42
	0.9	0.98	0.98	0.97	1.07	0.98	0.98	0.98	1.00	1.02	0.52
	1	1.01	1.01	1.00	1.10	1.01	1.01	1.01	0.92	0.94	0.51
	1.1	1.01	1.01	1.01	1.10	1.01	1.01	1.01	1.09	1.07	0.60
	1.2	0.99	0.99	0.99	1.08	0.99	0.99	0.99	1.02	1.02	0.60
	1.3	0.99	0.99	0.99	1.09	0.99	0.99	0.99	1.08	1.09	0.58
Av.		0.99	0.99	0.99	1.07	0.99	1.00	0.99	1.02	1.02	0.54
σ		0.01	0.01	0.01	0.04	0.01	0.01	0.01	0.06	0.05	0.07
0.5	0.8	1.02	1.02	0.97	1.12	1.02	1.02	1.02	1.01	1.00	0.23
	0.9	0.99	0.99	0.95	1.08	0.99	1.00	0.99	1.03	1.01	0.31
	1	1.00	1.00	0.96	1.09	1.00	1.00	1.00	0.97	0.95	0.34
	1.1	1.00	1.00	0.98	1.09	1.00	1.00	1.00	1.13	1.15	0.47
	1.2	0.99	0.99	0.97	1.08	0.99	0.99	0.99	1.28	1.30	0.54
	1.3	0.99	0.99	0.96	1.09	0.99	0.99	0.99	1.98	1.42	0.38
Av.		1.00	1.00	0.97	1.09	1.00	1.00	1.00	1.23	1.14	0.38
σ		0.01	0.01	0.01	0.02	0.01	0.01	0.01	0.38	0.19	0.11
1.0	0.8	1.00	1.00	0.95	1.01	1.00	1.01	1.00	1.16	1.12	0.22
	0.9	1.03	1.03	0.98	1.12	1.02	1.03	1.03	1.08	1.06	0.27
	1	1.00	1.00	0.96	1.09	1.00	1.00	1.00	2.09	1.53	0.27
Av.		1.01	1.01	0.97	1.07	1.01	1.01	1.01	1.45	1.24	0.25
σ		0.02	0.02	0.01	0.06	0.01	0.01	0.02	0.56	0.25	0.03

Table A.8: u_l and L_b blending law performances (u_{lp}/u_l and L_{bp}/L_b), equimolar fuel/air blend of *1*-hexene/air and ethanol/air, ϕ = 0.8-1.3, T_u = 360K, P_i = 0.1, 0.5 and 1.0MPa. Figures 4.40 and 4.41, in Chapter 4 show the related u_l and L_b measured values.

1-Hexene/Air and *n*-Heptane/Air Equimolar Blends											
P_i (MPa)	ϕ	u_l Laws							L_b Laws		
		$\bar{x}$	x	LC	T_b	$\tilde{T}_a$	Q	Q/k	$\bar{x}_d$	x_d	xu_lL_b
0.1	0.8	1.06	1.06	1.07	1.06	1.06	1.06	1.06	1.02	1.02	0.37
	0.9	1.02	1.02	1.02	1.11	1.02	1.02	1.02	1.02	1.02	0.48
	1	1.02	1.02	1.02	1.11	1.02	1.02	1.02	1.01	1.01	0.53
	1.1	1.00	1.00	1.01	1.09	1.00	1.01	1.00	1.10	1.10	0.61
	1.2	0.98	0.98	0.99	1.07	0.98	0.99	0.98	1.07	1.07	0.60
	1.3	0.98	0.98	0.98	1.07	0.98	0.98	0.98	0.91	0.92	0.48
Av.		1.01	1.01	1.01	1.09	1.01	1.01	1.01	1.02	1.02	0.51
σ		0.03	0.03	0.03	0.02	0.03	0.03	0.03	0.06	0.06	0.09
0.5	0.8	1.01	1.01	1.01	1.11	1.01	1.01	1.01	1.06	1.06	0.27
	0.9	1.02	1.02	1.02	1.11	1.02	1.02	1.02	0.95	0.95	0.30
	1	1.01	1.01	1.01	1.09	1.01	1.01	1.01	0.86	0.87	0.32
	1.1	0.98	0.98	0.98	1.07	0.98	0.98	0.98	0.89	0.89	0.35
	1.2	1.01	1.01	1.02	1.10	1.01	1.02	1.01	0.95	0.95	0.37
	1.3	0.99	0.99	0.99	1.08	0.99	0.99	0.99	-0.04	0.00	0.01
Av.		1.00	1.00	1.00	1.09	1.00	1.00	1.00	0.78	0.79	0.27
σ		0.01	0.01	0.01	0.02	0.01	0.01	0.01	0.41	0.39	0.13
1.0	0.8	1.01	1.01	1.01	1.01	1.01	1.01	1.01	1.05	1.06	0.22
	0.9	0.98	0.98	0.98	1.07	0.98	0.98	0.98	1.01	1.01	0.28
	1	1.00	1.00	1.00	1.08	0.99	1.00	0.99	0.54	0.28	0.12
Av.		0.99	0.99	1.00	1.05	0.99	1.00	0.99	0.87	0.78	0.21
σ		0.01	0.01	0.01	0.04	0.01	0.01	0.01	0.28	0.44	0.08

Table A.9: u_l and L_b blending law performances (u_{lp}/u_l and L_{bp}/L_b), equimolar fuel/air blend of *1*-hexene/air and *n*-heptane/air, ϕ = 0.8-1.3, T_u = 360K, P_i = 0.1, 0.5 and 1.0MPa. Figures 4.42 and 4.43, in Chapter 4 show the related u_l and L_b measured values.

Ethanol/Air and *n*-Heptane/Air Equimolar Blends											
P_i (MPa)	ϕ	u_l Laws							L_b Laws		
		$\bar{x}$	x	LC	T_b	$\tilde{T}_a$	Q	Q/k	$\bar{x}_d$	x_d	xu_lL_b
0.1	0.8	1.05	1.05	1.07	1.06	1.05	1.05	1.05	0.85	0.87	0.32
	0.9	1.02	1.02	1.03	1.12	1.02	1.02	1.02	1.05	1.08	0.51
	1	1.01	1.01	1.02	1.11	1.01	1.01	1.01	0.98	1.00	0.54
	1.1	1.01	1.01	1.03	1.10	1.01	1.01	1.01	0.99	0.97	0.53
	1.2	0.98	0.98	1.01	1.08	0.98	0.99	0.98	1.05	1.03	0.57
	1.3	0.98	0.98	0.99	1.07	0.97	0.98	0.98	1.07	1.11	0.59
Av.		1.01	1.01	1.02	1.09	1.01	1.01	1.01	1.00	1.01	0.51
σ		0.03	0.03	0.03	0.02	0.03	0.03	0.03	0.08	0.09	0.10
0.5	0.8	0.96	0.96	0.93	1.06	0.96	0.96	0.96	1.00	1.00	0.24
	0.9	0.99	0.99	0.97	1.08	0.99	0.99	0.99	0.94	0.93	0.28
	1	1.00	1.00	0.99	1.09	1.00	1.00	1.00	1.06	1.06	0.37
	1.1	0.98	0.98	0.99	1.06	0.98	0.96	0.98	1.03	1.05	0.41
	1.2	0.99	0.99	1.01	1.09	0.99	1.03	0.99	0.89	0.89	0.34
	1.3	0.97	0.97	0.97	1.07	0.97	0.97	0.97	-11.75	-10.41	-3.32
Av.		0.98	0.98	0.97	1.08	0.98	0.98	0.98	-1.14	-0.91	-0.28
σ		0.01	0.01	0.03	0.01	0.02	0.03	0.01	5.20	4.65	1.49
1.0	0.8	1.03	1.03	1.00	1.03	1.03	1.03	1.03	1.08	1.07	0.20
	0.9	1.00	1.00	0.98	1.09	1.00	0.99	1.00	1.00	0.99	0.25
	1	1.00	1.00	0.99	1.09	1.00	0.99	1.00	1.14	0.98	0.25
Av.		1.01	1.01	0.99	1.07	1.01	1.00	1.01	1.07	1.01	0.23
σ		0.02	0.02	0.01	0.03	0.02	0.02	0.02	0.07	0.05	0.03

Table A.10: u_l and L_b blending law performances (u_{lp}/u_l and L_{bp}/L_b), equimolar fuel/air blend of ethanol/air and *n*-heptane/air, ϕ = 0.8-1.3, T_u = 360K, P_i = 0.1, 0.5 and 1.0MPa. Figures 4.44 and 4.45, in Chapter 4 show the related u_l and L_b measured values.

TRF/Air and Ethanol/Air Blends, ϕ = 0.8											
P_i (MPa)	LV% of Eth.	u_l Laws							L_b Laws		
		$\bar{x}$	x	LC	T_b	$\tilde{T}_a$	Q	Q/k	$\bar{x}_d$	x_d	xu_lL_b
0.1	25	1.00	1.00	1.02	1.00	1.00	0.99	1.00	0.97	1.02	1.03
	50	1.01	1.01	1.03	1.01	1.01	1.00	1.01	0.97	1.03	1.05
	75	1.00	1.00	1.02	1.01	1.00	1.00	1.01	0.94	0.99	1.00
Av.		1.01	1.01	1.02	1.01	1.00	1.00	1.01	0.96	1.01	1.03
σ		0.01	0.00	0.01	0.01	0.00	0.00	0.01	0.01	0.02	0.02
0.5	25	1.00	1.00	0.98	1.00	1.00	1.00	1.00	0.99	1.00	1.00
	50	1.00	1.00	0.98	1.00	1.00	1.01	1.00	1.00	1.01	1.01
	75	0.98	0.98	0.96	0.98	0.98	0.98	0.98	1.00	1.00	1.00
Av.		0.99	0.99	0.97	0.99	0.99	1.00	0.99	0.99	1.00	1.00
σ		0.01	0.01	0.01	0.01	0.01	0.01	0.01	0.00	0.00	0.00
1.0	25	0.96	0.96	0.96	0.96	0.96	0.96	0.96	1.00	1.00	0.83
	50	1.00	1.00	0.99	1.00	1.00	1.00	1.00	1.08	1.09	0.66
	75	0.98	0.98	0.98	0.98	0.98	0.98	0.98	1.03	1.04	0.36
Av.		0.98	0.98	0.97	0.98	0.98	0.98	0.98	1.04	1.04	0.61
σ		0.02	0.02	0.02	0.02	0.02	0.02	0.02	0.04	0.04	0.24

Table A.11: u_l and L_b blending law performances (u_{lp}/u_l and L_{bp}/L_b), TRF/ethanol blends, ϕ = 0.8, T_u = 360K, P_i = 0.1, 0.5 and 1.0MPa. Figures 4.46-4.48, in Chapter 4 show the related u_l and L_b measured values.

TRF/Air and Ethanol/Air Blends, ϕ = 0.9											
P_i (MPa)	LV% of Eth.	u_l Laws							L_b Laws		
		$\bar{x}$	x	LC	T_b	$\tilde{T}_a$	Q	Q/k	$\bar{x}_d$	x_d	xu_lL_b
0.1	25	0.99	0.99	1.01	0.99	0.99	1.01	1.00	0.97	0.99	1.00
	50	1.00	1.00	1.02	1.00	1.00	1.02	1.01	0.96	1.00	1.00
	75	1.00	1.00	1.01	1.00	1.00	1.02	1.01	0.95	0.97	0.97
Av.		1.00	1.00	1.02	1.00	1.00	1.01	1.00	0.96	0.99	0.99
σ		0.00	0.00	0.01	0.00	0.00	0.01	0.01	0.01	0.02	0.02
0.5	25	1.00	1.00	1.00	1.00	1.00	1.00	1.00	0.99	1.00	1.00
	50	0.98	0.98	0.98	0.99	0.98	0.99	0.99	0.99	1.00	1.00
	75	0.96	0.96	0.96	0.96	0.96	0.96	0.97	0.99	1.00	1.00
Av.		0.98	0.98	0.98	0.98	0.98	0.99	0.99	0.99	1.00	1.00
σ		0.02	0.02	0.02	0.02	0.02	0.02	0.02	0.00	0.00	0.00
1.0	25	1.01	1.01	1.00	1.01	1.01	1.01	1.01	1.13	1.18	1.19
	50	1.02	1.01	1.01	1.02	1.02	1.02	1.02	1.00	1.05	1.07
	75	1.00	1.00	0.99	1.00	1.00	1.00	1.00	0.97	1.00	1.01
Av.		1.01	1.01	1.00	1.01	1.01	1.01	1.01	1.03	1.07	1.09
σ		0.01	0.01	0.01	0.01	0.01	0.01	0.01	0.09	0.09	0.09

Table A.12: u_l and L_b blending law performances (u_{lp}/u_l and L_{bp}/L_b), TRF/ethanol blends, ϕ = 0.9, T_u = 360K, P_i = 0.1, 0.5 and 1.0MPa. Figures 4.46-4.48, in Chapter 4 show the related u_l and L_b measured values.

TRF/Air and Ethanol/Air Blends, ϕ = 1.0											
P_i (MPa)	LV% of Eth.	u_l Laws							L_b Laws		
		$\bar{x}$	x	LC	T_b	$\tilde{T}_a$	Q	Q/k	$\bar{x}_d$	x_d	xu_lL_b
0.1	25	0.99	1.00	1.02	1.00	0.99	1.00	1.00	0.97	0.99	1.00
	50	1.01	1.01	1.04	1.02	1.01	1.02	1.02	0.96	0.99	0.99
	75	1.00	1.00	1.02	1.01	1.00	1.01	1.01	0.97	0.99	0.99
Av.		1.00	1.00	1.03	1.01	1.00	1.01	1.01	0.97	0.99	0.99
σ		0.01	0.01	0.01	0.01	0.01	0.01	0.01	0.00	0.00	0.00
0.5	25	1.00	1.01	1.01	1.01	1.00	1.01	1.01	0.99	0.99	1.00
	50	1.00	1.01	1.01	1.01	1.00	1.01	1.01	0.99	1.00	1.00
	75	1.00	1.00	1.00	1.00	1.00	1.00	1.00	1.00	1.01	1.00
Av.		1.00	1.00	1.01	1.00	1.00	1.01	1.01	0.99	1.00	1.00
σ		0.00	0.00	0.01	0.00	0.00	0.00	0.00	0.01	0.01	0.00
1.0	25	1.00	1.00	1.00	1.00	1.00	1.00	1.00	1.02	1.05	1.02
	50	0.99	1.00	1.00	1.00	0.99	1.00	1.00	0.98	1.01	0.94
	75	1.00	1.00	1.00	1.00	1.00	1.00	1.00	0.99	1.01	0.88
Av.		1.00	1.00	1.00	1.00	1.00	1.00	1.00	1.00	1.02	0.95
σ		0.00	0.00	0.00	0.00	0.00	0.00	0.00	0.03	0.02	0.07

Table A.13: u_l and L_b blending law performances (u_{lp}/u_l and L_{bp}/L_b), TRF/ethanol blends, ϕ = 1.0, T_u = 360K, P_i = 0.1, 0.5 and 1.0MPa. Figures 4.46-4.48, in Chapter 4 show the related u_l and L_b measured values.

TRF/Air and Ethanol/Air Blends, ϕ = 1.1											
P_i (MPa)	LV% of Eth.	u_l Laws							L_b Laws		
		$\bar{x}$	x	LC	T_b	$\tilde{T}_a$	Q	Q/k	$\bar{x}_d$	x_d	xu_lL_b
0.1	25	1.00	1.00	1.03	1.00	1.00	1.03	1.00	1.03	1.02	1.05
	50	1.01	1.01	1.05	1.01	1.00	1.06	1.02	1.08	1.07	1.07
	75	0.99	1.00	1.02	1.00	0.99	1.04	1.00	1.10	1.09	1.05
Av.		1.00	1.00	1.03	1.00	1.00	1.04	1.01	1.07	1.06	1.06
σ		0.01	0.01	0.01	0.01	0.01	0.01	0.01	0.04	0.04	0.01
0.5	25	1.00	1.00	1.01	1.00	1.00	0.99	1.00	0.98	0.97	0.99
	50	1.01	1.01	1.03	1.01	1.01	1.00	1.02	1.01	1.00	1.00
	75	1.00	1.00	1.01	1.00	1.00	0.98	1.01	1.04	1.03	1.00
Av.		1.00	1.00	1.02	1.01	1.00	0.99	1.01	1.01	1.00	1.00
σ		0.01	0.01	0.01	0.01	0.01	0.01	0.01	0.03	0.03	0.01

Table A.14: u_l and L_b blending law performances (u_{lp}/u_l and L_{bp}/L_b), TRF/ethanol blends, ϕ = 1.1, T_u = 360K, P_i = 0.1, 0.5 and 1.0MPa. Figures 4.46-4.48, in Chapter 4 show the related u_l and L_b measured values.

TRF/Air and Ethanol/Air Blends, ϕ = 1.2											
P_i (MPa)	LV% of Eth.	u_l Laws							L_b Laws		
		$\bar{x}$	x	LC	T_b	$\tilde{T}_a$	Q	Q/k	$\bar{x}_d$	x_d	xu_lL_b
0.1	25	1.00	1.00	1.03	1.00	0.99	0.98	1.00	1.08	1.08	1.10
	50	0.99	1.00	1.04	1.00	0.99	0.96	1.00	1.08	1.07	1.07
	75	1.01	1.01	1.04	1.01	1.00	0.98	1.01	1.09	1.08	1.05
Av.		1.00	1.00	1.04	1.00	0.99	0.97	1.01	1.09	1.08	1.08
σ		0.01	0.01	0.00	0.01	0.01	0.01	0.01	0.00	0.00	0.02
0.5	25	1.01	1.02	1.04	1.02	1.01	1.01	1.02	0.92	0.90	0.98
	50	1.01	1.01	1.04	1.01	1.00	1.00	1.01	1.02	0.99	1.00
	75	1.01	1.01	1.03	1.01	1.00	1.00	1.01	1.11	1.09	1.00
Av.		1.01	1.01	1.04	1.01	1.01	1.00	1.01	1.02	0.99	0.99
σ		0.00	0.00	0.01	0.00	0.00	0.00	0.00	0.09	0.09	0.01

Table A.15: u_l and L_b blending law performances (u_{lp}/u_l and L_{bp}/L_b), TRF/ethanol blends, ϕ = 1.2, T_u = 360K, P_i = 0.1, 0.5 and 1.0MPa. Figures 4.46-4.48, in Chapter 4 show the related u_l and L_b measured values.

TRF/Air and Ethanol/Air Blends, ϕ = 1.3											
P_i (MPa)	LV% of Eth.	u_l Laws							L_b Laws		
		$\bar{x}$	x	LC	T_b	$\tilde{T}_a$	Q	Q/k	$\bar{x}_d$	x_d	xu_lL_b
0.1	25	0.97	0.97	1.01	0.98	0.97	0.96	0.98	1.43	1.49	1.29
	50	0.97	0.97	1.01	0.97	0.96	0.95	0.98	1.20	1.25	1.24
	75	0.96	0.97	0.99	0.97	0.96	0.95	0.97	0.84	0.87	0.98
Av.		0.97	0.97	1.00	0.97	0.96	0.95	0.97	1.16	1.20	1.17
σ		0.00	0.00	0.01	0.00	0.01	0.01	0.00	0.30	0.31	0.17
0.5	25	0.99	1.00	1.02	1.00	0.99	0.99	1.00	0.08	-0.18	0.75
	50	1.01	1.01	1.03	1.01	1.00	1.00	1.01	1.94	0.87	1.27
	75	1.00	1.00	1.02	1.00	0.99	0.99	1.00	1.19	0.92	-0.12
Av.		1.00	1.00	1.02	1.00	1.00	0.99	1.00	1.07	0.54	0.63
σ		0.01	0.01	0.01	0.01	0.01	0.01	0.01	0.93	0.62	0.70

Table A.16: u_l and L_b blending law performances (u_{lp}/u_l and L_{bp}/L_b), TRF/ethanol blends, ϕ = 1.3, T_u = 360K, P_i = 0.1, 0.5 and 1.0MPa. Figures 4.46-4.48, in Chapter 4 show the related u_l and L_b measured values.

TRF/Air and *n*-Butanol/Air Blends, ϕ = 0.8											
P_i (MPa)	LV% of But.	u_l Laws							L_b Laws		
		$\bar{x}$	x	LC	T_b	$\tilde{T}_a$	Q	Q/k	$\bar{x}_d$	x_d	xu_lL_b
0.1	25	1.00	1.00	1.00	1.00	1.00	1.00	1.00	1.02	1.02	1.03
	50	1.00	1.00	1.01	1.00	1.00	1.00	1.01	0.96	0.97	0.97
	75	1.00	1.00	1.00	1.00	1.00	1.00	1.01	0.97	0.98	0.98
Av.		1.00	1.00	1.00	1.00	1.00	1.00	1.01	0.98	0.99	0.99
σ		0.00	0.00	0.00	0.00	0.00	0.00	0.00	0.03	0.03	0.03
0.5	25	1.01	1.01	1.01	1.01	1.01	1.01	1.01	1.01	1.01	1.01
	50	1.01	1.01	1.01	1.01	1.01	1.01	1.01	1.00	1.00	1.00
	75	1.01	1.01	1.01	1.01	1.01	1.01	1.02	1.01	1.01	1.00
Av.		1.01	1.01	1.01	1.01	1.01	1.01	1.02	1.01	1.01	1.00
σ		0.00	0.00	0.00	0.00	0.00	0.00	0.00	0.00	0.00	0.00
1.0	25	0.97	0.97	0.97	0.97	0.97	0.97	0.97	0.98	0.98	0.98
	50	0.98	0.98	0.98	0.98	0.98	0.98	0.98	0.97	0.98	0.98
	75	0.98	0.98	0.98	0.98	0.98	0.98	0.99	0.95	0.96	0.95
Av.		0.98	0.98	0.98	0.98	0.98	0.98	0.98	0.97	0.97	0.97
σ		0.00	0.00	0.00	0.00	0.00	0.01	0.01	0.01	0.02	0.02

Table A.17: u_l and L_b blending law performances (u_{lp}/u_l and L_{bp}/L_b), TRF/*n*-butanol blends, ϕ = 0.8, T_u = 360K, P_i = 0.1, 0.5 and 1.0MPa. Figures 4.49-4.51, in Chapter 4 show the related u_l and L_b measured values.

TRF/Air and *n*-Butanol/Air Blends, ϕ = 0.9											
P_i (MPa)	LV% of But.	u_l Laws							L_b Laws		
		$\bar{x}$	x	LC	T_b	$\tilde{T}_a$	Q	Q/k	$\bar{x}_d$	x_d	xu_lL_b
0.1	25	0.99	0.99	0.99	0.99	0.99	0.99	0.99	1.03	1.04	1.02
	50	1.00	1.00	1.00	1.00	1.00	1.00	1.01	0.96	0.97	0.92
	75	1.01	1.01	1.01	1.01	1.01	1.01	1.02	1.02	1.02	0.95
Av.		1.00	1.00	1.00	1.00	1.00	1.00	1.01	1.00	1.01	0.96
σ		0.01	0.01	0.01	0.01	0.01	0.01	0.01	0.04	0.04	0.05
0.5	25	1.00	1.00	1.01	1.00	1.00	1.00	1.01	0.99	0.99	0.98
	50	1.02	1.02	1.02	1.02	1.02	1.02	1.02	1.00	1.00	0.96
	75	1.01	1.01	1.01	1.01	1.01	1.01	1.02	1.00	1.00	0.94
Av.		1.01	1.01	1.01	1.01	1.01	1.01	1.02	1.00	1.00	0.96
σ		0.01	0.01	0.01	0.01	0.01	0.01	0.01	0.00	0.00	0.02
1.0	25	1.00	1.00	1.00	1.00	1.00	1.00	1.00	1.19	1.20	1.21
	50	0.97	0.97	0.97	0.97	0.97	0.97	0.98	1.04	1.05	1.06
	75	0.99	0.99	0.99	0.99	0.99	0.99	1.00	0.95	0.96	0.97
Av.		0.99	0.99	0.99	0.99	0.99	0.99	0.99	1.06	1.07	1.08
σ		0.01	0.01	0.01	0.01	0.01	0.01	0.01	0.12	0.12	0.12

Table A.18: u_l and L_b blending law performances (u_{lp}/u_l and L_{bp}/L_b), TRF/*n*-butanol blends, ϕ = 0.9, T_u = 360K, P_i = 0.1, 0.5 and 1.0MPa. Figures 4.49-4.51, in Chapter 4 show the related u_l and L_b measured values.

TRF/Air and *n*-Butanol/Air Blends, ϕ = 1.0											
P_i (MPa)	LV% of But.	u_l Laws							L_b Laws		
		$\bar{x}$	x	LC	T_b	$\tilde{T}_a$	Q	Q/k	$\bar{x}_d$	x_d	xu_lL_b
0.1	25	0.99	0.99	1.00	0.99	0.99	0.99	1.00	0.99	0.99	0.98
	50	1.00	1.00	1.01	1.00	1.00	1.00	1.01	0.95	0.96	0.93
	75	1.01	1.01	1.01	1.01	1.01	1.01	1.03	1.01	1.01	0.97
Av.		1.00	1.00	1.01	1.00	1.00	1.00	1.01	0.98	0.99	0.96
σ		0.01	0.01	0.01	0.01	0.01	0.01	0.01	0.03	0.03	0.03
0.5	25	1.01	1.01	1.01	1.01	1.01	1.01	1.01	1.00	1.00	0.99
	50	1.01	1.01	1.02	1.01	1.01	1.01	1.02	0.99	0.99	0.97
	75	1.02	1.02	1.03	1.02	1.02	1.02	1.04	1.00	1.00	0.97
Av.		1.01	1.01	1.02	1.01	1.01	1.01	1.02	0.99	1.00	0.97
σ		0.01	0.01	0.01	0.01	0.01	0.01	0.01	0.01	0.01	0.01

Table A.19: u_l and L_b blending law performances (u_{lp}/u_l and L_{bp}/L_b), TRF/*n*-butanol blends, ϕ = 1.0, T_u = 360K, P_i = 0.1, 0.5 and 1.0MPa. Figures 4.49-4.51, in Chapter 4 show the related u_l and L_b measured values.

TRF/Air and *n*-Butanol/Air Blends, ϕ = 1.1											
P_i (MPa)	LV% of But.	u_l Laws							L_b Laws		
		$\bar{x}$	x	LC	T_b	$\tilde{T}_a$	Q	Q/k	$\bar{x}_d$	x_d	xu_lL_b
0.1	25	1.00	1.00	1.00	1.00	0.99	1.00	1.00	0.96	0.96	0.97
	50	0.99	0.99	1.00	0.99	0.99	0.99	1.00	0.95	0.94	0.95
	75	1.00	1.00	1.01	1.00	1.00	1.01	1.02	1.04	1.04	1.03
Av.		1.00	1.00	1.00	1.00	0.99	1.00	1.01	0.98	0.98	0.98
σ		0.01	0.01	0.00	0.01	0.01	0.01	0.01	0.05	0.05	0.04
0.5	25	1.00	1.00	1.01	1.00	1.00	1.00	1.01	0.94	0.93	1.04
	50	0.99	0.99	1.00	0.99	0.99	1.00	1.00	1.01	1.00	1.06
	75	1.00	1.00	1.00	1.00	1.00	1.00	1.01	1.08	1.07	1.07
Av.		1.00	1.00	1.00	1.00	1.00	1.00	1.01	1.01	1.00	1.06
σ		0.01	0.01	0.00	0.01	0.01	0.00	0.01	0.07	0.07	0.02

Table A.20: u_l and L_b blending law performances (u_{lp}/u_l and L_{bp}/L_b), TRF/*n*-butanol blends, ϕ = 1.1, T_u = 360K, P_i = 0.1, 0.5 and 1.0MPa. Figures 4.49-4.51, in Chapter 4 show the related u_l and L_b measured values.

TRF/Air and *n*-Butanol/Air Blends, ϕ = 1.2											
P_i (MPa)	LV% of But.	u_l Laws							L_b Laws		
		$\bar{x}$	x	LC	T_b	$\tilde{T}_a$	Q	Q/k	$\bar{x}_d$	x_d	xu_lL_b
0.1	25	0.99	0.99	0.99	0.99	0.98	0.99	0.99	1.03	1.04	1.01
	50	0.99	0.99	1.00	0.99	0.99	1.00	1.00	0.97	0.98	0.96
	75	1.00	1.00	1.01	1.00	1.00	1.01	1.02	0.96	0.96	0.95
Av.		0.99	0.99	1.00	1.00	0.99	1.00	1.00	0.99	0.99	0.97
σ		0.01	0.01	0.01	0.01	0.01	0.01	0.01	0.04	0.04	0.03
0.5	25	1.00	1.01	1.01	1.01	1.00	1.01	1.01	0.84	0.83	1.03
	50	0.99	0.99	1.00	0.99	0.98	1.00	1.00	1.01	0.99	1.08
	75	1.01	1.02	1.02	1.02	1.01	1.03	1.03	1.16	1.14	1.09
Av.		1.00	1.00	1.01	1.00	1.00	1.01	1.01	1.00	0.99	1.07
σ		0.01	0.01	0.01	0.01	0.01	0.01	0.02	0.16	0.16	0.03

Table A.21: u_l and L_b blending law performances (u_{lp}/u_l and L_{bp}/L_b), TRF/*n*-butanol blends, ϕ = 1.2, T_u = 360K, P_i = 0.1, 0.5 and 1.0MPa. Figures 4.49-4.51, in Chapter 4 show the related u_l and L_b measured values.

TRF/Air and *n*-Butanol/Air Blends, ϕ = 1.3											
P_i (MPa)	LV% of But.	u_l Laws							L_b Laws		
		$\bar{x}$	x	LC	T_b	$\tilde{T}_a$	Q	Q/k	$\bar{x}_d$	x_d	xu_lL_b
0.1	25	0.97	0.98	0.98	0.98	0.97	0.98	0.98	1.10	1.11	1.09
	50	0.99	1.00	1.00	1.00	0.98	1.00	1.01	0.98	0.99	1.07
	75	0.98	0.99	0.99	0.99	0.98	0.99	1.00	0.93	0.94	1.12
Av.		0.98	0.99	0.99	0.99	0.98	0.99	1.00	1.00	1.01	1.09
σ		0.01	0.01	0.01	0.01	0.01	0.01	0.01	0.09	0.09	0.02
0.5	25	1.00	1.00	1.01	1.01	1.00	1.01	1.01	-0.85	-0.97	0.58
	50	0.99	1.00	1.01	1.00	0.99	1.00	1.01	-0.27	-0.50	0.32
	75	1.03	1.04	1.04	1.04	1.03	1.04	1.05	0.44	0.32	-0.14
Av.		1.01	1.01	1.02	1.01	1.00	1.02	1.02	-0.23	-0.38	0.25
σ		0.02	0.02	0.02	0.02	0.02	0.02	0.03	0.64	0.65	0.36

Table A.22: u_l and L_b blending law performances (u_{lp}/u_l and L_{bp}/L_b), TRF/*n*-butanol blends, ϕ = 1.3, T_u = 360K, P_i = 0.1, 0.5 and 1.0MPa. Figures 4.49-4.51, in Chapter 4 show the related u_l and L_b measured values.

Methane/Air and Hydrogen/Air Blends, ϕ = 0.6									
H_2 Fuel Mole Fraction	u_l Laws						L_b Laws		
	$\bar{x}$	x	LC	$\tilde{T}_a$	$\bar{Q}$	Q/k	$\bar{x}_d$	x_d	xu_lL_b
0.1	1.10	1.07	1.02	0.99	1.08	1.05	-	-	-
0.2	1.09	1.04	0.94	0.90	1.05	0.99	-0.95	-3.41	0.46
0.3	1.11	1.05	0.91	0.85	1.05	0.98	-	-	-
0.4	1.12	1.04	0.87	0.80	1.04	0.96	0.54	-0.76	1.14
0.5	1.13	1.04	0.85	0.78	1.04	0.96	-	-	-
0.6	1.23	1.14	0.91	0.83	1.12	1.04	0.80	-0.25	1.17
0.7	1.19	1.10	0.88	0.81	1.07	1.02	-	-	-
0.8	1.18	1.11	0.90	0.84	1.06	1.04	0.83	0.11	1.01
0.9	1.13	1.08	0.93	0.90	1.00	1.04	-	-	-
Av.	1.14	1.07	0.91	0.86	1.06	1.01	0.31	-1.08	0.94
σ	0.05	0.03	0.05	0.07	0.03	0.03	0.85	1.59	0.33

Table A.23: u_l and L_b blending law performances (u_{lp}/u_l and L_{bp}/L_b), methane and hydrogen blends, ϕ = 0.6, T_u = 303K, P_i = 0.1 MPa. Figures 6.1a and b show the corresponding measured u_l and L_b values alongside the predicted values from each blending law.

Methane/Air and Hydrogen/Air Blends, ϕ = 0.7									
H_2 Fuel Mole Fraction	u_l Laws						L_b Laws		
	$\bar{x}$	x	LC	$\tilde{T}_a$	$\bar{Q}$	Q/k	$\bar{x}_d$	x_d	xu_lL_b
0.1	1.07	1.04	1.01	0.98	1.02	1.02	-	-	-
0.2	1.03	0.99	0.93	0.88	0.91	0.95	1.12	1.69	0.96
0.3	1.08	1.02	0.93	0.87	0.88	0.96	-	-	-
0.4	1.15	1.07	0.95	0.87	0.89	0.99	2.04	6.91	0.82
0.5	1.25	1.15	1.01	0.92	0.91	1.07	-	-	-
0.6	1.33	1.23	1.07	0.96	0.91	1.13	0.31	-1.82	0.75
0.7	1.30	1.20	1.04	0.94	0.83	1.11	-	-	-
0.8	1.14	1.06	0.93	0.86	0.68	0.99	0.72	-0.55	0.92
0.9	1.10	1.05	0.96	0.91	0.60	1.01	-	-	-
Av.	1.16	1.09	0.98	0.91	0.85	1.02	1.05	1.56	0.86
σ	0.11	0.08	0.05	0.04	0.13	0.06	0.74	3.85	0.09

Table A.24: u_l and L_b blending law performances (u_{lp}/u_l and L_{bp}/L_b), methane and hydrogen blends, ϕ = 0.7, T_u = 303K, P_i = 0.1 MPa. Figures 6.2a and b show the corresponding measured u_l and L_b values alongside the predicted values from each blending law.

Methane/Air and Hydrogen/Air Blends, ϕ = 0.8									
H_2 Fuel Mole Fraction	u_l Laws						L_b Laws		
	$\bar{x}$	x	LC	$\tilde{T}_a$	$\bar{Q}$	Q/k	$\bar{x}_d$	x_d	xu_lL_b
0.1	1.03	1.00	0.97	0.94	1.06	0.97	-	-	-
0.2	1.07	1.02	0.96	0.91	1.13	0.97	1.18	1.69	1.09
0.3	1.13	1.06	0.97	0.91	1.24	0.99	-	-	-
0.4	1.20	1.11	0.99	0.92	1.34	1.03	1.21	6.91	0.93
0.5	1.29	1.18	1.04	0.94	1.46	1.08	-	-	-
0.6	1.27	1.16	1.01	0.91	1.48	1.06	-1.22	-1.82	-0.20
0.7	1.30	1.19	1.03	0.94	1.53	1.09	-	-	-
0.8	1.14	1.06	0.93	0.86	1.38	0.99	0.52	-0.55	0.81
0.9	1.05	1.00	0.91	0.87	1.29	0.96	-	-	-
Av.	1.16	1.08	0.98	0.91	1.32	1.02	0.42	1.56	0.66
σ	0.11	0.08	0.04	0.03	0.16	0.05	1.14	3.85	0.58

Table A.25: u_l and L_b blending law performances (u_{lp}/u_l and L_{bp}/L_b), methane and hydrogen blends, ϕ = 0.8, T_u = 303K, P_i = 0.1 MPa. Figures 6.3a and b show the corresponding measured u_l and L_b values alongside the predicted values from each blending law.

Methane/Air and Hydrogen/Air Blends, ϕ = 0.9									
H_2 Fuel Mole Fraction	u_l Laws						L_b Laws		
	$\bar{x}$	x	LC	$\tilde{T}_a$	$\bar{Q}$	Q/k	$\bar{x}_d$	x_d	xu_lL_b
0.1	1.05	1.02	0.99	0.96	1.07	0.99	-	-	-
0.2	1.08	1.02	0.97	0.92	1.11	0.97	1.17	1.45	1.12
0.3	1.12	1.04	0.96	0.90	1.17	0.97	-	-	-
0.4	1.19	1.08	0.98	0.90	1.25	1.00	1.29	2.16	1.18
0.5	1.27	1.15	1.02	0.93	1.35	1.05	-	-	-
0.6	1.18	1.07	0.94	0.85	1.27	0.97	1.06	2.72	0.86
0.7	1.26	1.14	1.01	0.92	1.37	1.05	-	-	-
0.8	1.17	1.08	0.96	0.89	1.27	1.00	-2.29	-15.42	-1.08
0.9	1.05	0.99	0.91	0.87	1.14	0.95	-	-	-
Av.	1.15	1.06	0.97	0.91	1.22	1.00	0.31	-2.27	0.52
σ	0.08	0.06	0.03	0.03	0.11	0.04	1.73	8.78	1.08

Table A.26: u_l and L_b blending law performances (u_{lp}/u_l and L_{bp}/L_b), methane and hydrogen blends, ϕ = 0.9, T_u = 303K, P_i = 0.1 MPa. Figures 6.4a and b show the corresponding measured u_l and L_b values alongside the predicted values from each blending law.

Methane/Air and Hydrogen/Air Blends, ϕ = 1.0									
H_2 Fuel Mole Fraction	u_l Laws						L_b Laws		
	$\bar{x}$	x	LC	$\tilde{T}_a$	$\bar{Q}$	Q/k	$\bar{x}_d$	x_d	xu_lL_b
0.1	1.04	1.01	0.98	0.96	1.07	0.98	-	-	-
0.2	1.11	1.04	0.98	0.94	1.15	0.99	1.07	1.27	1.05
0.3	1.08	0.99	0.91	0.86	1.13	0.93	-	-	-
0.4	1.17	1.05	0.94	0.88	1.23	0.97	1.13	1.67	1.08
0.5	1.30	1.16	1.02	0.94	1.38	1.06	-	-	-
0.6	1.20	1.07	0.93	0.85	1.29	0.97	0.98	1.88	0.90
0.7	1.27	1.14	0.99	0.91	1.37	1.04	-	-	-
0.8	1.12	1.02	0.89	0.84	1.20	0.94	1.23	3.29	1.09
0.9	1.05	0.99	0.91	0.87	1.13	0.95	-	-	-
Av.	1.15	1.05	0.95	0.89	1.22	0.98	1.10	2.03	1.03
σ	0.09	0.06	0.04	0.04	0.11	0.04	0.11	0.88	0.09

Table A.27: u_l and L_b blending law performances (u_{lp}/u_l and L_{bp}/L_b), methane and hydrogen blends, ϕ = 1.0, T_u = 303K, P_i = 0.1 MPa. Figures 6.5a and b show the corresponding measured u_l and L_b values alongside the predicted values from each blending law.

Methane/Air and Hydrogen/Air Blends, ϕ = 1.1									
H_2 Fuel Mole Fraction	u_l Laws						L_b Laws		
	$\bar{x}$	x	LC	$\tilde{T}_a$	$\bar{Q}$	Q/k	$\bar{x}_d$	x_d	xu_lL_b
0.1	1.08	1.04	1.00	0.98	1.09	1.01	-	-	-
0.2	1.18	1.10	1.02	0.99	1.20	1.04	1.08	1.08	0.89
0.3	1.13	1.03	0.93	0.88	1.15	0.95	-	-	-
0.4	1.22	1.09	0.96	0.90	1.24	1.00	1.18	1.18	0.78
0.5	1.32	1.17	1.00	0.94	1.35	1.06	-	-	-
0.6	1.17	1.03	0.87	0.82	1.20	0.93	1.11	1.11	0.56
0.7	1.30	1.15	0.97	0.92	1.34	1.05	-	-	-
0.8	1.14	1.03	0.88	0.85	1.18	0.95	2.08	2.08	0.77
0.9	1.05	0.98	0.88	0.86	1.09	0.93	-	-	-
Av.	1.18	1.07	0.95	0.90	1.21	0.99	1.36	1.36	0.75
σ	0.09	0.06	0.06	0.06	0.09	0.05	0.48	0.48	0.14

Table A.28: u_l and L_b blending law performances (u_{lp}/u_l and L_{bp}/L_b), methane and hydrogen blends, ϕ = 1.1, T_u = 303K, P_i = 0.1 MPa. Figures 6.6a and b show the corresponding measured u_l and L_b values alongside the predicted values from each blending law.

Methane/Air and Hydrogen/Air Blends, ϕ = 1.2									
H_2 Fuel Mole Fraction	u_l Laws						L_b Laws		
	$\bar{x}$	x	LC	$\tilde{T}_a$	$\bar{Q}$	Q/k	$\bar{x}_d$	x_d	xu_lL_b
0.1	1.14	1.08	1.00	0.99	1.12	1.04	-	-	-
0.2	1.28	1.16	1.02	1.00	1.26	1.08	1.10	1.10	0.88
0.3	1.23	1.09	0.90	0.88	1.21	0.99	-	-	-
0.4	1.32	1.15	0.91	0.89	1.30	1.03	1.09	1.09	0.68
0.5	1.36	1.17	0.90	0.88	1.33	1.04	-	-	-
0.6	1.27	1.09	0.82	0.81	1.24	0.97	1.13	1.13	0.54
0.7	1.35	1.17	0.88	0.88	1.33	1.05	-	-	-
0.8	1.17	1.04	0.80	0.82	1.16	0.95	2.75	2.75	1.03
0.9	1.06	0.98	0.81	0.85	1.07	0.93	-	-	-
Av.	1.24	1.10	0.89	0.89	1.23	1.01	1.52	1.52	0.79
σ	0.10	0.07	0.08	0.07	0.09	0.05	0.82	0.82	0.22

Table A.29: u_l and L_b blending law performances (u_{lp}/u_l and L_{bp}/L_b), methane and hydrogen blends, ϕ = 1.2, T_u = 303K, P_i = 0.1 MPa. Figures 6.7a and b show the corresponding measured u_l and L_b values alongside the predicted values from each blending law.

Methane/Air and Hydrogen/Air Blends, ϕ = 1.3									
H_2 Fuel Mole Fraction	u_l Laws						L_b Laws		
	$\bar{x}$	x	LC	$\tilde{T}_a$	$\bar{Q}$	Q/k	$\bar{x}_d$	x_d	xu_lL_b
0.1	1.27	1.16	0.98	0.98	1.22	1.08	-	-	-
0.2	1.48	1.28	0.93	0.95	1.39	1.14	1.03	1.03	0.74
0.3	1.54	1.30	0.85	0.88	1.45	1.12	-	-	-
0.4	1.66	1.37	0.82	0.87	1.53	1.16	1.09	1.09	0.57
0.5	1.50	1.23	0.69	0.75	1.38	1.04	-	-	-
0.6	1.69	1.40	0.75	0.85	1.56	1.19	1.22	1.22	0.48
0.7	1.45	1.22	0.65	0.77	1.34	1.06	-	-	-
0.8	1.21	1.06	0.59	0.73	1.14	0.95	2.44	2.44	0.80
0.9	1.05	0.96	0.62	0.77	1.02	0.90	-	-	-
Av.	1.43	1.22	0.76	0.84	1.34	1.07	1.44	1.44	0.65
σ	0.21	0.14	0.14	0.09	0.18	0.10	0.67	0.67	0.15

Table A.30: u_l and L_b blending law performances (u_{lp}/u_l and L_{bp}/L_b), methane and hydrogen blends, ϕ = 1.3, T_u = 303K, P_i = 0.1 MPa. Figures 6.8a and b show the corresponding measured u_l and L_b values alongside the predicted values from each blending law.

Appendix B - Commissioning a Rapid Compression Machine

B.1 Introduction

The ignition delay time, τ_i, is a fundamental combustion parameter required in the characterisation of a fuels performance. Measurements of τ_i have been made for both liquid and gaseous fuels, at various temperatures, pressures and equivalence ratios, using a range of experimental methods and apparatus (Griffiths et al., 1993; Spadaccini and Colket Iii, 1994; Vasu et al., 2008). Established and common methods include shock tubes (Davidson et al., 2005; Hawthorn and Nixon, 1966; Zhu et al., 2015), rapid compression machines (Gersen et al., 2008; Mittal et al., 2014; Park and Keck, 1990) and flow reactors (Beerer et al., 2009; Dryer and Chaos, 2008). Rapid compression machines are, in general, capable of maintaining the required autoignition pressures and temperatures for longer periods, thus allowing sufficient time for the measurement of relatively long τ_i values across a wide range of fuels and conditions. This coupled with their potential for high accuracy and continuity make the RCM the preferred choice for measuring τ_i values at Leeds.

This Appendix presents the Leeds RCM and the significant modifications undertaken during the present work, to achieve the high end of compression (EOC) pressures, P_c, and temperatures, T_c, associated with modern SI engines and the accurate and efficient acquisition of τ_i values. The ideal and real behaviour of RCM's are first discussed in Section B.2, followed by an overview of the Leeds RCM in Section B.3, giving details of each main section and the principle operations. Section B.4 presents a detailed description of the modifications and developments to the rig during the present work. Section B.5 presents the experimental procedure, detailing the mixture preparation and operating techniques. Finally, Section B.6 presents τ_i values for *iso*-octane acquired from the Leeds RCM as part of an international collaboration investigating the discrepancies between different RCM's.

B.2 Ideal and Real RCM Behaviour

The ideal RCM would instantaneously and isentropically compress a given combustible mixture, with spatial uniformity, to a thermally stable constant volume. However, in practice, the laws of thermodynamics prevail, making this a physical impossibility. Therefore, the main aims for any RCM are to approach such an ideal by compressing

the combustible mixture as rapidly as possible, to a constant EOC volume with minimised heat loss to its surroundings. Subsequently, key challenges are rapidly accelerating the piston, then arresting and absorbing its considerable kinetic energy such that no significant turbulence generation, vibration and piston rebound occur. These should be achieved whilst, simultaneously minimising the inevitable influence of the inner cylinder and chamber thermal boundary layer, such that the rate of heat loss is minimised and an adiabatic core region can be approximated. Figure B.1 shows the step change pressure trace behaviour of the ideal RCM in comparison to a typical real RCM, in which compression is far from instantaneous and heat loss at the EOC results in a decreasing pressure.

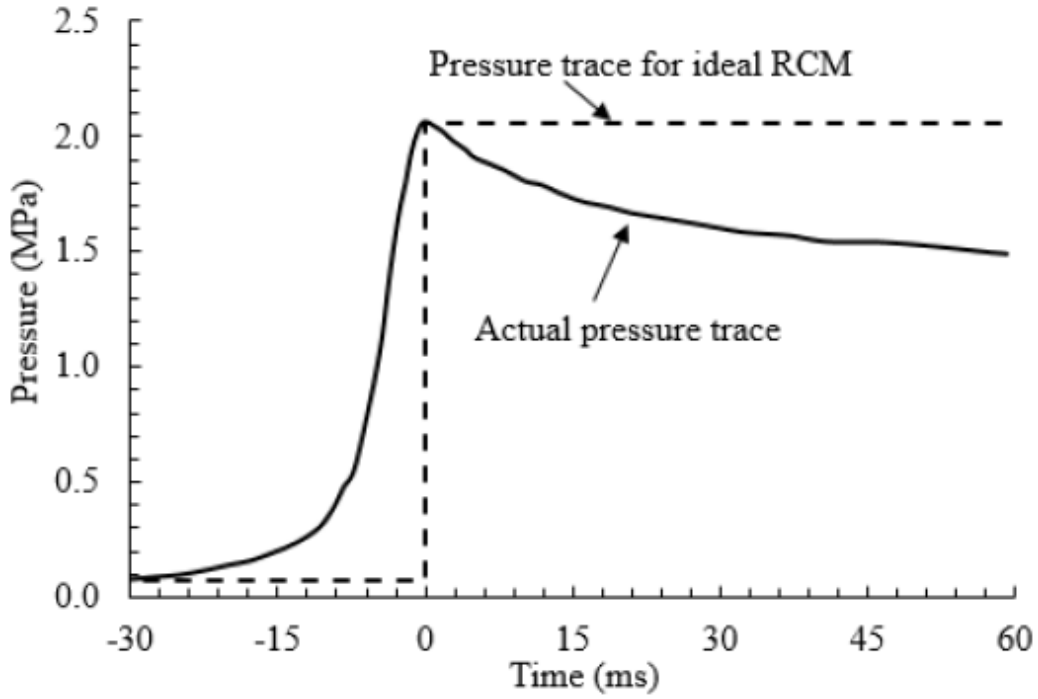

Figure B.1: Ideal vs typical RCM pressure trace.

The importance of rapid compression is to ensure reduced time for pre-reactions to occur before EOC and reduced mixture exposure time to cooler thermal boundary layers (Cox et al., 1996; Griffiths et al., 1993). The speed of the latter half of compression is most crucial due to the higher pressures and temperatures that increase the likelihood of pre-reaction and heat loss rate via the higher temperature differentials. For this reason, a universal RCM parameter of interest is the time taken to reach the last 50% of P_c, known as t_{50}. These times are typically in the region of 1-5ms, as appose to typical full compression times in the region of 20-50ms.

After compression, the rate of pressure drop due to heat loss must be carefully considered, such that the ignition delay time of the combustible mixture occurs within a period of minimal heat loss from the combustion chamber, to prevent excessive deviation from the intended EOC conditions. In extreme cases, significant pressure and temperature drops can reduce the chemical reactivity of the mixture and totally inhibit the onset of combustion. The use of varying diluent gases with different specific heat capacitance and thermal diffusivity to help counter the EOC heat loss is common practise and is discussed in Section B.5.1.

Furthermore, several past studies have shown that the homogeneity of compressed mixtures is compromised by the generation of roll up vortices at the edge of the rapidly accelerated piston, causing the mixing of the cold cylinder wall boundary layer into the core region of the mixture, as shown by Fig. B.2.

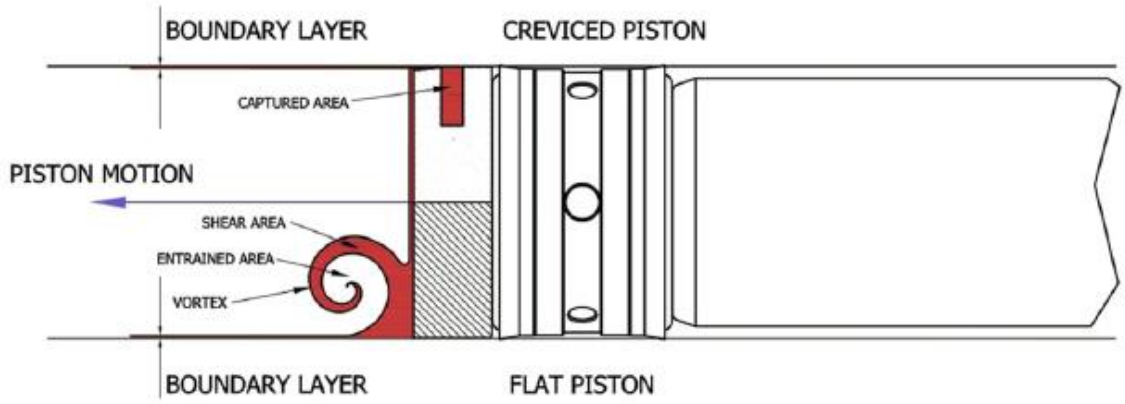

Figure B.2: Illustration of creation of roll up vortex due to piston motion during compression (lower section) and containment of boundary layer through crevice (upper section) through proper design (Sung and Curran, 2014).

Using CFD, as shown in Fig. B.3, Würmel (2004), demonstrated that the use of a creviced piston allows entrapment of the cold boundary layer, giving much improved temperature uniformity in comparison to conventional pistons.

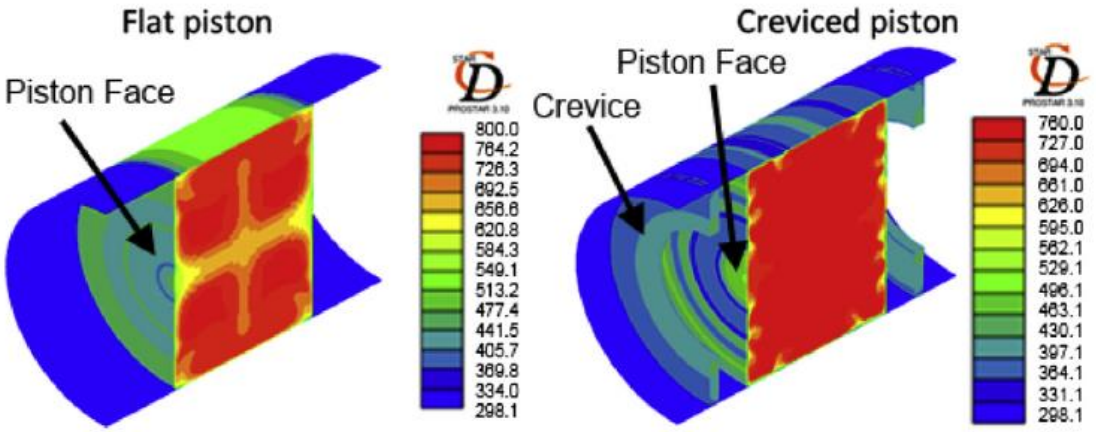

Figure B.3: Computed mixture temperature uniformity for conventional and creviced piston design, using N_2 at 10.4ms (Würmel, 2004).

However, it was latter shown by Mittal and Bhari (2013), that at the EOC the mixture homogeneity may be compromised by the movement of the crevice collected cooler gas back into the combustion chamber. Therefore, the use of creviced pistons should, ideally, employ an EOC crevice containment feature, such that, the crevice volume is isolated from the combustion chamber volume at the EOC. Figure B.4 shows how a simply O-ring can be used to contain the crevice at the EOC.

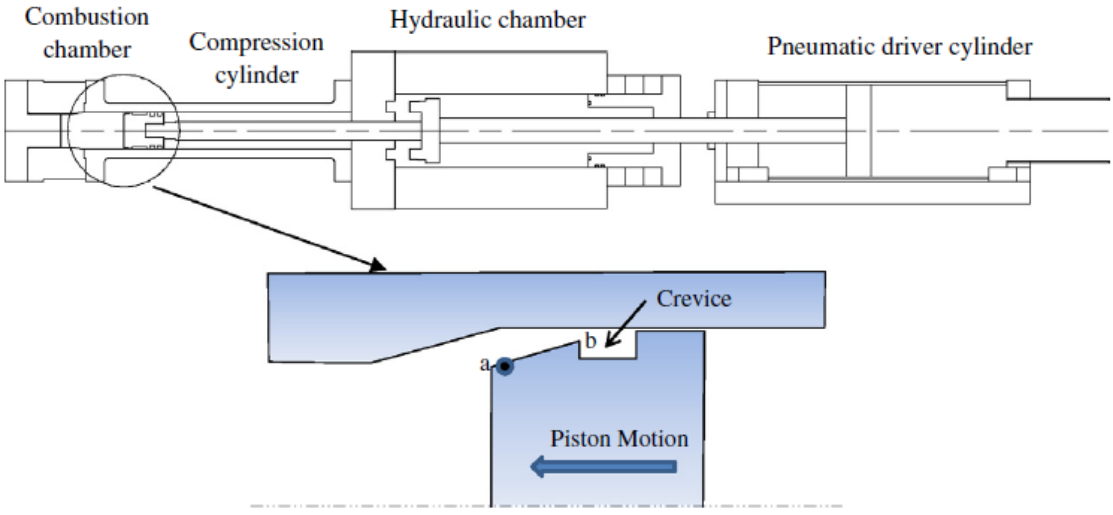

Figure B.4: Crevice containment via O-ring sealing at EOC (Mittal and Bhari, 2013)

The direct accurate temperature measurement of the mixture during and after compression is extremely challenging. Any internal temperature probe is likely to induce complex aerodynamic effects that detract from the adiabatic core region assumption. Furthermore, a temperature probe of sufficient response rate is unlikely to have the structural integrity for such repeated extreme conditions. Optical temperature measurement methods are possible but the inherent vibration of RCM's present timely calibration issues. Therefore, it is common practise to exploit the adiabatic core region hypothesis and indirectly deduce temperature measurements from the pressure trace. This approach has been both experimentally and computationally validated by Das et al. (2012) and Mittal et al. (2011), respectively.

For isentropic compression, the EOC adiabatic temperature, T_{ad}, is expressed as:

$$\int_{T_u}^{T_{ad}} \frac{1}{\gamma - 1}\left(\frac{dT}{T}\right) = \ln(CR), \tag{B.1}$$

where T_u is the initial mixture temperature, CR, the compression ratio and γ, the ratio of specific heat capacitances.

However, as discussed above, isentropic compression is impossible due to heat loss and therefore the real values of P_c and T_c will always be below this ideal. Desgroux et al. (1995) and Griffiths et al. (1993) showed that an approximate EOC adiabatic core gas temperature can be attained by the use of an effective CR, that accounts for heat loss during compression, by knowledge of the actual P_c value:

$$\frac{P_c}{Pi} = CR^{\gamma} \tag{B.2}$$

Therefore, using this assumption, Eq. B.2 may substituted into Eq. B.1 to yield Eq. B.3:

$$\int_{T_u}^{T_c} \frac{1}{\gamma - 1}\left(\frac{dT}{T}\right) = \ln\left(\frac{P_c}{P_i}\right) \tag{B.3}$$

B.3 The Leeds RCM

The RCM was originally designed and built in 1968 as one half of a dual opposed piston design by Affleck and Thomas (1968) at Shell Thornton Research Centre. Shortly after, it was acquired by the School of Chemistry at the University of Leeds, where a number of studies were undertaken by Prof. J. Griffths (Griffiths et al., 1997; Griffiths et al., 1993; Griffiths and Hasko, 1984; Griffiths et al., 2002; Griffiths and

Nimmo, 1985; Westbrook et al., 1998). Later, in 2010 the RCM was transferred to the University's School of Mechanical Engineering, where it has undergone significant development by the present author in the quest for the high fidelity measurements of τ_i values at higher pressures and temperatures that are reflective of modern SI engine conditions.

The Leeds RCM uses a pneumatically driven and hydraulically arrested piston assembly to compress a premixed and preheated combustible mixture to a constant volume combustion chamber. Here, a dynamic pressure transducer records any pressure rises from combustion, allowing the acquisition of the combustible mixtures τ_i value to be calculated from the difference in time between the EOC and the onset of a pressure rise. The following subsections give an overview of the RCM's configuration, principle operations and details of the main sections. During the RCM's development in the present work, all existing auxiliary systems were modified, alongside the introduction of new systems, the validation and details of which are presented in Section B.4.

B.3.1 Configuration and Operation Overview

Figure B.5 shows an external photograph of the RCM alongside a virtual SolidWorks model cross section to show an internal perspective of the RCM, highlighting the three main sections that are interconnected by the piston assembly. Details of these main sections are discussed in the following subjections. Figure B.6 shows SolidWorks model cross section views of the RCM with the piston rod assembly at the start of compression (SOC) and EOC.

The fundamental operation involves hydraulically locking the piston assembly at the SOC, metering the combustible mixture into the combustion chamber, pressurising the driving reservoir with compressed air, arming the recording devices, and initiating the rapid piston movement by the sudden drop of hydraulic pressure via a high speed hydraulic solenoid valve. Nearing the EOC, a hydraulic oil displacement damping mechanism was used to absorb the kinetic energy of the piston rod assembly. Subsequent autoignition pressure traces were then automatically saved to file for processing outside the laboratory. A more detailed description of the operating technique, including mixture preparation is given in Section B.5.

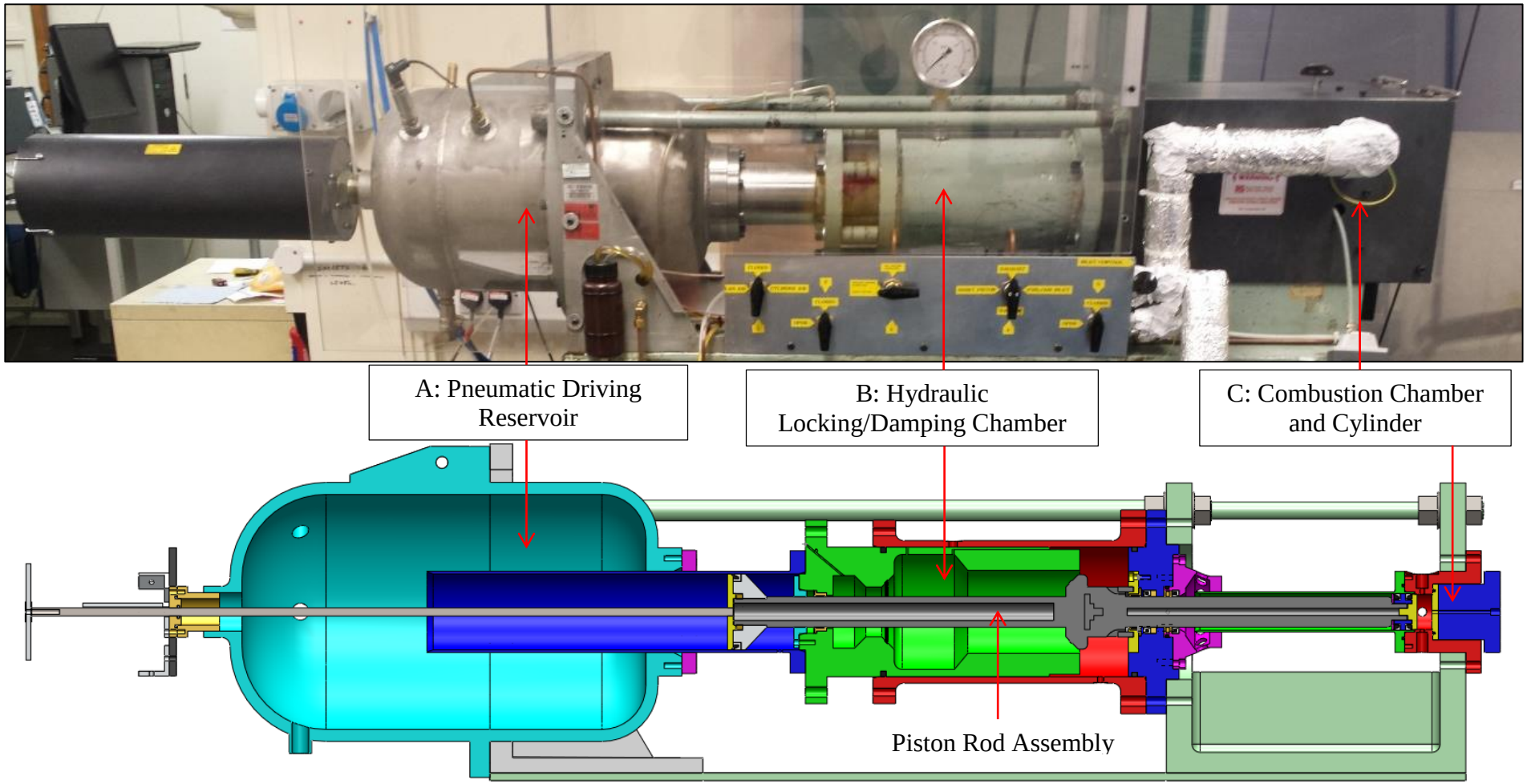

Figure B.5: Photograph of external view of Leeds RCM and SolidWorks model cross section internal perspective view, with different coloured parts to highlight main section interfaces (Piston assembly at EOC). Increased detail of each section can be viewed in Figs. B.7-B.10.

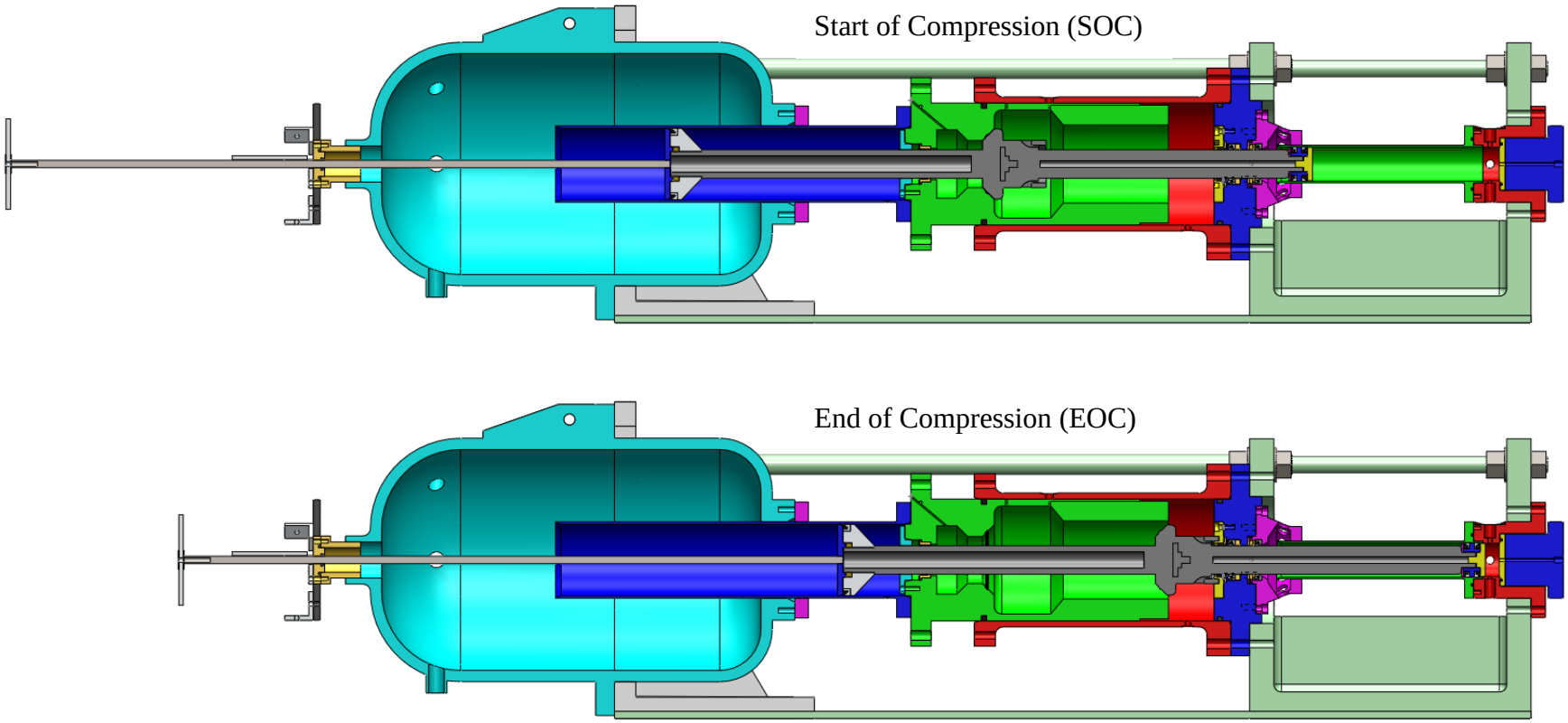

Figure B.6: SolidWorks model cross section view to show piston rod assembly in SOC (top view) and EOC (bottom view).

B.3.2 Pneumatic Driving Reservoir

The driving reservoir, shown as section A, in Fig. B.5, and detailed in Fig. B.7, uses compressed air to provide the energy to rapidly move the piston assembly and hold it at the end of its stroke. The reservoir was supplied with two air lines, one from the laboratory compressor, limited to 0.7 MPa, and the other from a BOC cylinder regulated to just under the 2 MPa maximum safe working pressure of the reservoir. As a further safety precaution, a pressure relief valve (PRV) was also fitted to the reservoir and set to activate at just under 2 MPa. In practice, the reservoir was only pressured to a maximum of 1.6 MPa, beyond which there was insufficient force from the hydraulic locking mechanism (Section B.3.3) to hold the piston assembly back before firing.

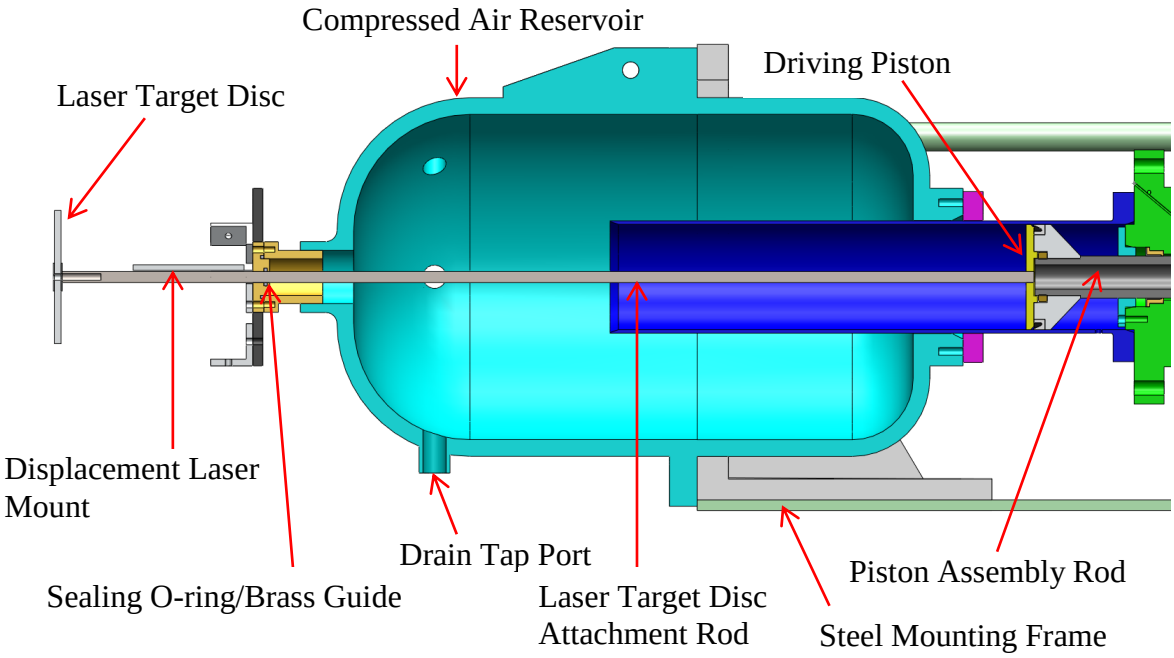

Figure B.7: SolidWorks model cross section of section A: Pneumatic driving reservoir (Piston assembly at EOC).

B.3.3 Hydraulic Locking and Damping Chamber

Shown as section B, in Fig B.5, and detailed in Fig. B.8, the hydraulic section has two main purposes, to lock the piston rod assembly in position at the SOC, and dampen its arrest just before the EOC. The piston assembly was locked in position by pressuring the containing hydraulic oil to 4 MPa via a hand pump, forcing a seal between the rear of the damping ring section on the piston rod assembly and an O-ring within the inner hydraulic chamber wall.

The principle operation of the original damping system was the displacement of oil from the fixed ringed groove in the hydraulic chamber, as the insertion of the slightly smaller corresponding ringed protrusion on the piston rod assembly entered to a depth of 6mm. Thus, the kinetic energy of the piston rod assembly was absorbed by the frictional forces opposing the oil that was forced out between the narrow gap of the ringed groove and the ringed protrusion on the piston rod assembly. This concept is common in many other RCM designs due to its reliability and potential to absorb very high energy. However, as with many other RCM's, the original Leeds RCM damping system was not adjustable. Section B.4.6 details the modifications to the system that allowed variable damping control.

The ratio between the pneumatic driving and hydraulic locking/dampening piston area was 1:0.93. The compression ratio could be altered between 10.5 and 13.93 by varying the quantity of spacers between the inner and outer hydraulic chamber and, therefore, varying the piston assembly stroke between 170 and 230mm.

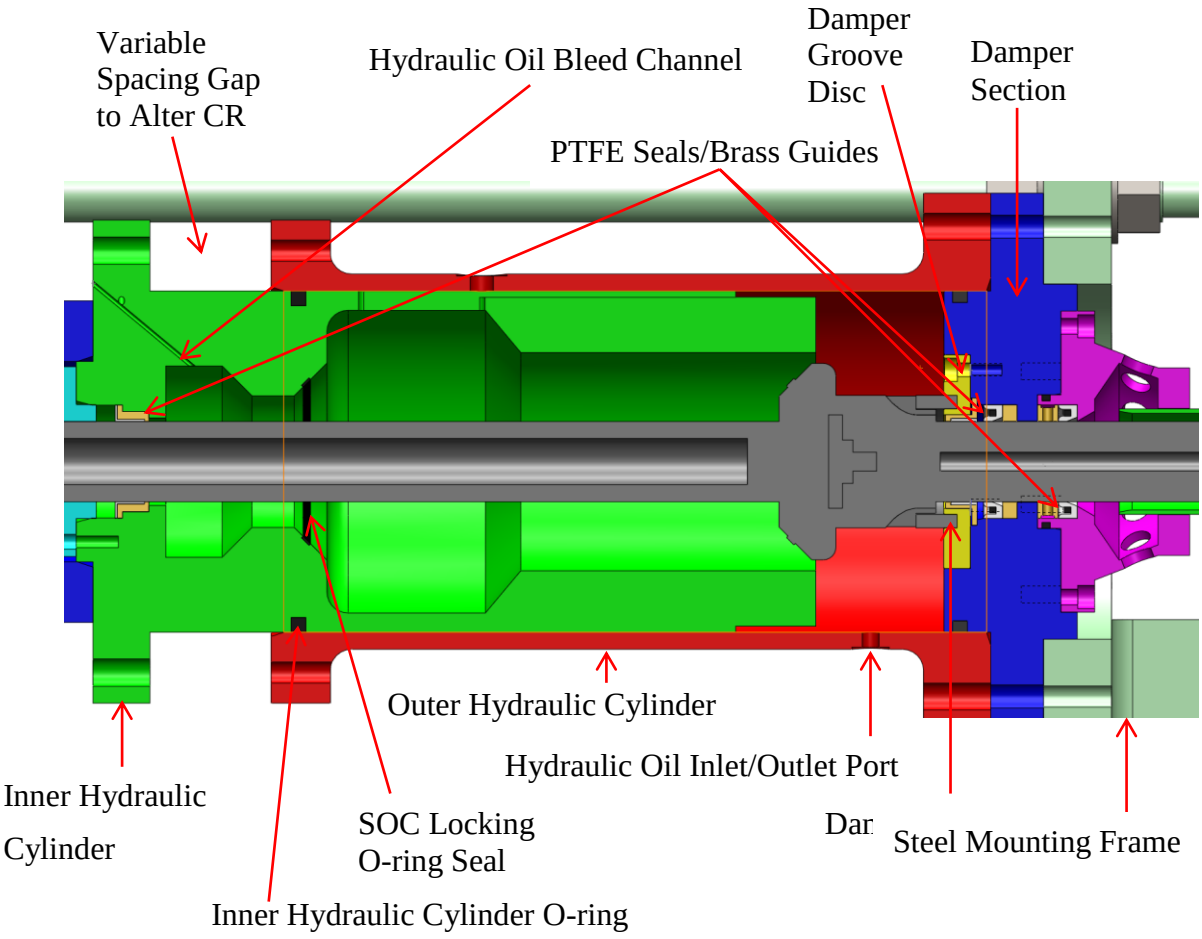

Figure B.8: SolidWorks model cross section of section B: Hydraulic locking/damping chamber (Piston assembly at EOC).

B.3.4 Combustion Chamber and Cylinder

The combustion chamber and cylinder are shown as section C, in Fig. B.5, and detailed in Fig. B.9. They were designed to withstand pressures associated with the compression and autoignition of combustible mixtures. The modular design of the chamber allows different end plugs to be employed, such as transparent quartz plugs for optical work and fanned plugs for turbulence generation. However, the present work used a large heated end plug to ensure uniform heating of the combustible mixtures at high temperatures. Both the cylinder and chamber were machined from 304 stainless steel, where the larger cylinder diameter creates a step to the chamber diameter, in which the piston enters by 2.25mm at EOC. Orbiting the chamber are four ports, the top port was used as an inlet for the combustible mixture via a poppet valve, whereby, the static pressure transducer was connected via a 'T' section joint. The rear port was used to flush mount the dynamic pressure transducer and the front and bottom ports were not used so they were blanked off with flush mounted chamber wall plugs.

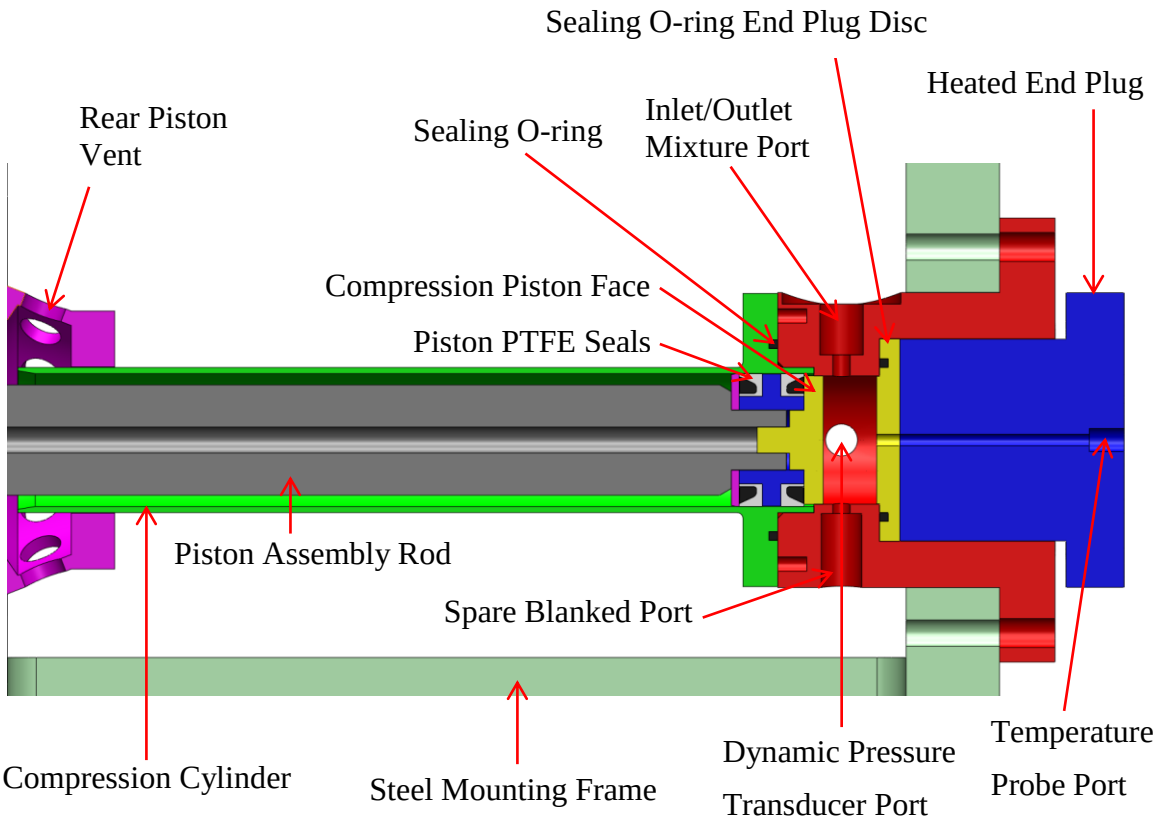

Figure B.9: SolidWorks model cross section of section C: Combustion chamber and cylinder (Piston assembly at EOC).

B.3.5 Piston Assembly

Figure B.10 shows the entire piston assembly which interconnects the three main sections A, B and C in Fig. B.5. The piston assembly mass was minimised to reduce its inertia, hence, aiding its acceleration and de-acceleration. Thus, it has been machined from two lightweight 6061 billet aluminium tubes that join in the middle of the hydraulic damping ring section. Both the driving and the compression piston were also machined from aluminium using PTFE seals. The area ratio between the driving piston and the compression piston is 4:1, hence, only a quarter of the EOC pressure was required to drive the piston to the end of its stroke. However, nearly three times that amount was required to ensure rapid acceleration of the piston assembly.

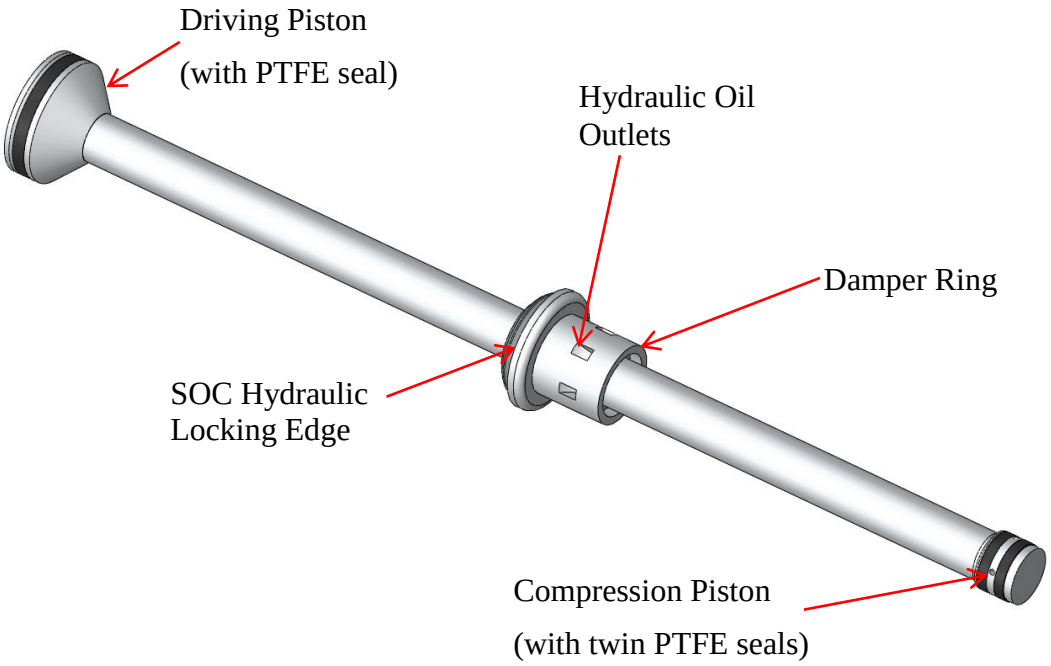

Figure B.10: SolidWorks model of Leeds RCM piston rod assembly.

B.4 Modifications and Developments

The section provides a detailed description of the modifications and developments made to the RCM during the present work. The aims and objectives are first presented, with the following subsections detailing the methods in which they were achieved.

B.4.1 Aims and Objectives

The main development aims were to increase the EOC pressure, P_i, and temperature, T_i, to emulate that of modern high compression ratio SI engines, with an emphasis on increased accuracy in the acquisition of τ_i, whilst having an efficient operating procedure.

Subsequently, the following objectives arose:

1 Create 3D virtual model to aid design process, track modifications and demonstrate internal mechanisms.
2 Acquire accurate piston position monitoring within +/- 1mm, to quantify piston dynamics in relation to combustion chamber pressure dynamics.
3 Increase piston driving pressure to allow higher initial combustion chamber pressures to be used under the same compression ratio, with reduced piston rebound.
4 Revise damping mechanism to reduce piston bounce and allow optimisation with varying driving to combustion chamber pressure ratios.
5 Investigate credibility of combustion chambers dynamic pressure transducer and quantify effect of thermal shock.
6 Design variable combustion chamber heating system with accurate temperature control.
7 Design mixing chamber to allow batches of pre-vaporised, preheated and homogenous combustible mixtures to be safely and accurately regulated to the combustion chamber at the required temperature.
8 Develop LabVIEW interface, with data synchronisation and acquisition upon triggering.

B.4.2 Initial Performance

The EOC pressure, P_c is primarily a function of the CR and the initial pressure, P_i, to which a sufficient driving pressure, P_d, must be applied in order to achieve rapid acceleration and minimum rebound of the piston assembly, whilst not exceeding the tolerance of the damping mechanism. Thus, at any fixed CR, there was an optimal P_d/P_i ratio that was critical to the dynamic behaviour of the piston assembly. Throughout the present work, the CR was set to the maximum of 13.93, as discussed in section B.3.3.

Figure B.11 shows a typical pressure trace with the corresponding piston movement near EOC (piston position monitoring is discussed in Section B.4.4) for the compression of dry air, using a P_d/P_i ratio of 10 and P_i of 0.1 MPa.

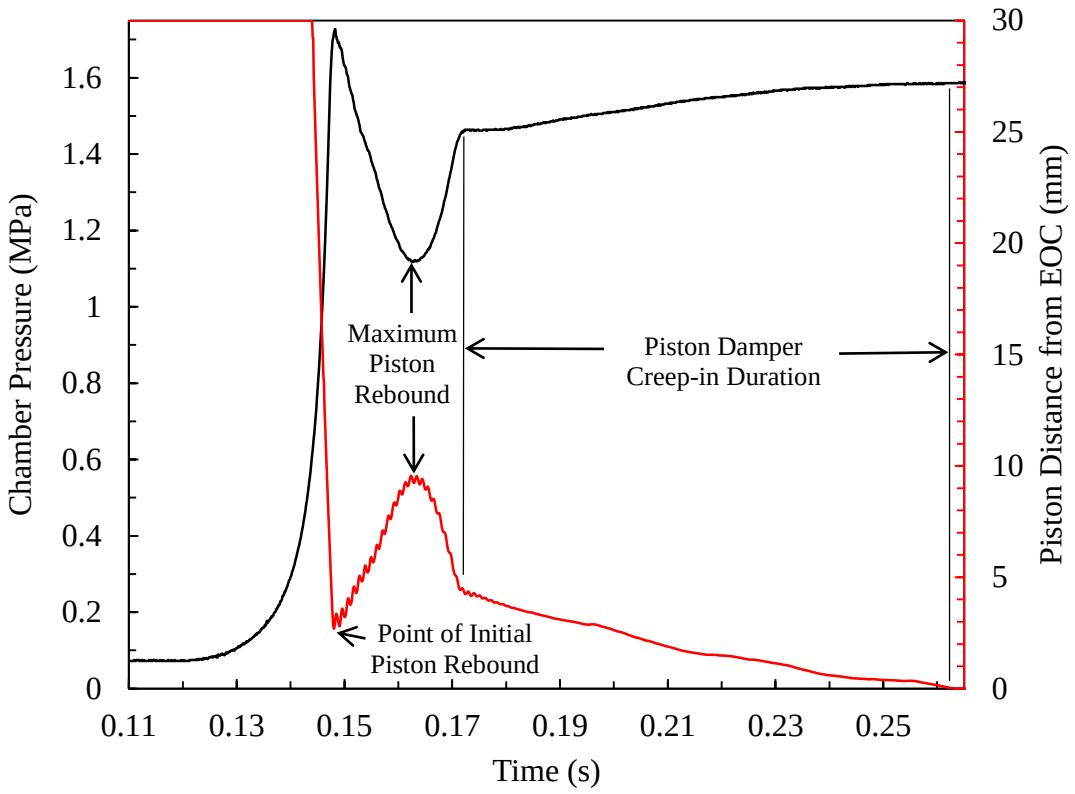

Figure B.11: Example of initial performance, prior to modification, using air. P_d/P_i = 10, with a driving pressure of 0.7 MPa.

A single large piston rebound of 9.48mm from the EOC occurred, resulting in a pressure drop of 0.58 MPa. Following this, a further 93ms was taken for the piston to come to rest as the damper ring engaged in the damper groove, over a 6mm stroke. This period of time was termed the damper creep-in duration. Minimising both piston rebound and damper creep-in duration is paramount to desirable piston dynamics and thus pressure traces. Furthermore, a finite distance from the EOC at the point of the inevitable initial piston rebound must always be maintained to ensure the damper ring does not simply crash into the end of the damper groove, which could potentially cause permanent structural damage. Using the original maximum driving pressure of 0.7 MPa, a series of experiments were performed whereby P_i was altered between 0.117 and 0.023 MPa. This allowed the dynamic behaviour of the piston to be examined under P_d/P_i ratios between 6-30. However, the subsequent lowering of P_i to increase the P_d/P_i ratio, naturally lowered P_c. Figures B.12a and b show the corresponding combustion chamber pressure traces and piston movement near EOC, as the P_d/P_i ratio was varied. As anticipated, under this limited P_d, increasing the P_i, such that the P_d/P_i ratio decreased, induced significant piston rebound and creep-in duration that was unacceptable. In contrast, reducing P_i increased the P_d/P_i ratio and reduced piston

rebound to more acceptable levels. However, prolonged creep-in duration still persisted.

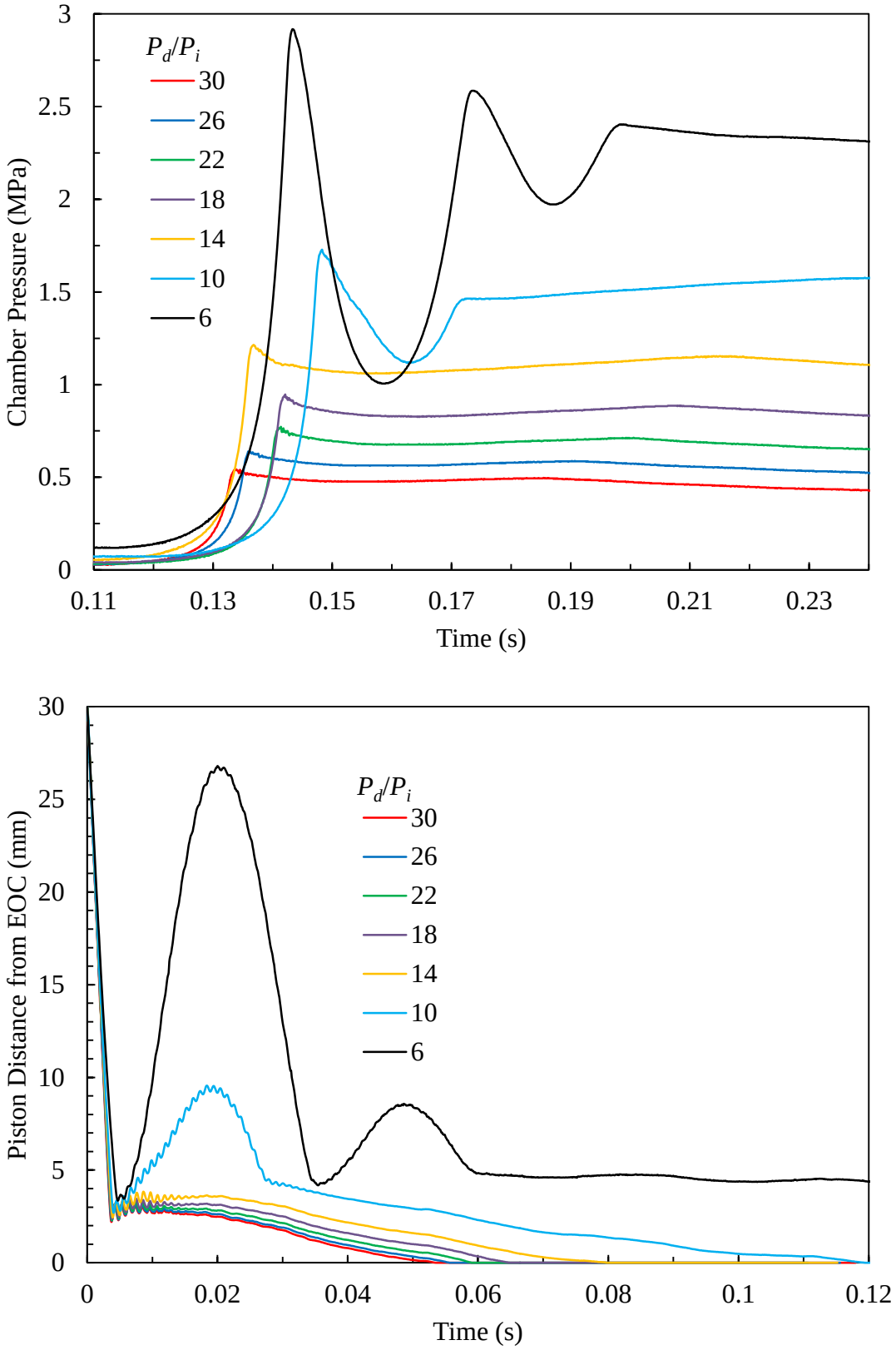

Figure B.12: Performance, prior to modifications, showing variation of a) combustion chamber pressure and b) piston distance from EOC with time, for compression of air, with varying P_d/P_i ratio between 6-30, at a fixed driving pressure of 0.7 MPa.

Figure B.13 shows the maximum piston rebound, damper ring creep-in duration and the distance from EOC at the point of initial rebound as a function of the P_d/P_i ratio. A significant decrease in the maximum piston rebound and creep-in duration was shown between P_d/P_i ratios of 7 and 13, beyond which a plateau was reached, whilst the point of initial rebound remained relatively constant at ~3mm, across the entire P_d/P_i ratio range tested. However, even at a P_d/P_i ratio of 14, the prolonged damper creep-in duration, resulted in a well sustained pressure deviation. Not until a P_d/P_i ratio of 30 was an acceptable pressure trace acquired, at which P_c was a mere 0.5 MPa. Therefore, the RCM clearly required significant modification, primarily, in the form of increased driving pressure, and a revised damping system, to attain the required P_c values with acceptable piston dynamics/post EOC pressure traces.

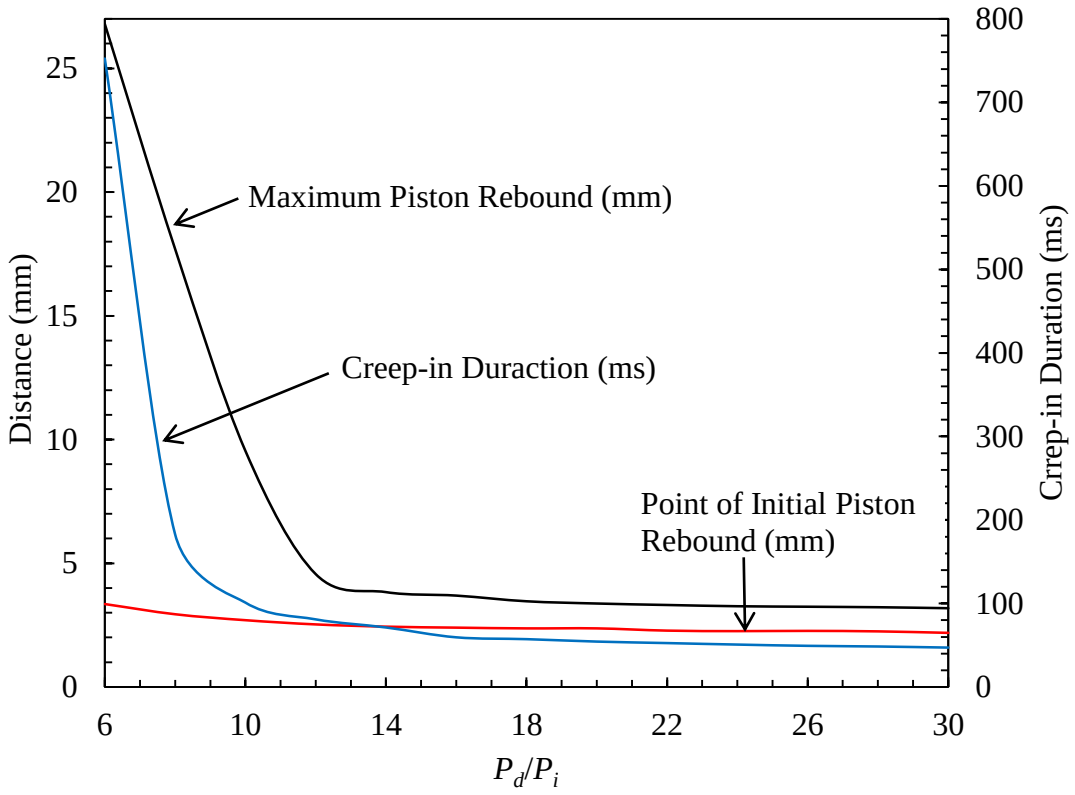

Figure B.13: Maximum piston rebound and creep-in duration as a function of P_d/P_i.

B.4.3 Generation of Virtual Model

To aid the design process of modifications, a 3D scaled virtual model of every component in the RCM was drawn using the solid modelling computer aided design (CAD) program of SolidWorks. This required the complete dismantling of the rig in order to measure and identify the material of each component, which simultaneously allowed a comprehensive inspection for any damage or wear. An assembly of all the

drawn components was then made to create the virtual model. This allowed the interconnectivity of each component to be shown though any cut through plane specified. For example, this was particularly useful in the development of the damping system, whereby the required angle and tolerances for oil channels was instantly shown by the model. Furthermore, the model demonstrates all the internal workings, which are otherwise hidden. Figures B.14 shows example screen shots of the assembled 3D virtual model.

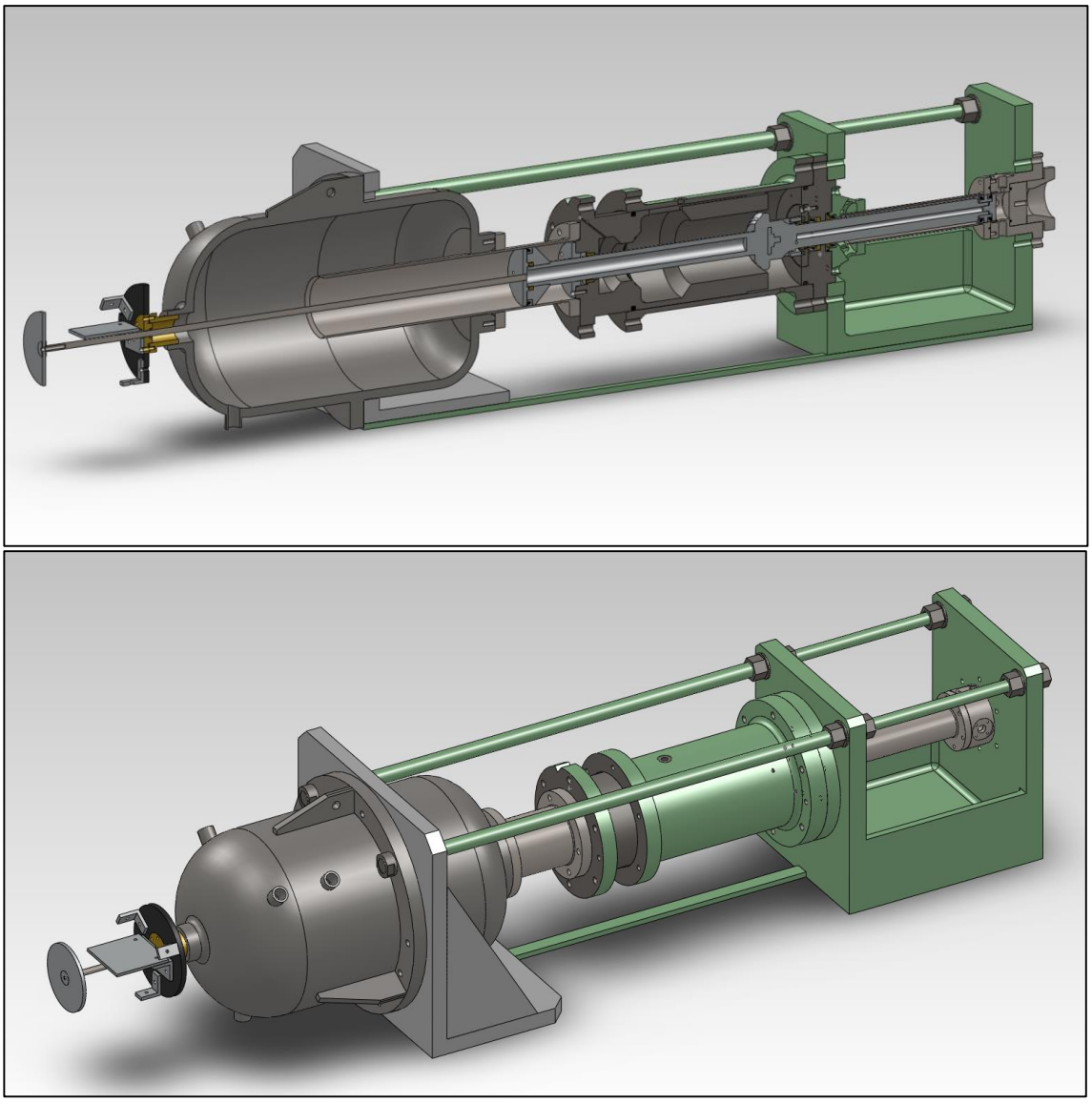

Figure B.14: Example 3D screen shots of Leeds RCM SolidWorks model.

B.4.4 Piston Position Monitoring

The ability to directly and accurately monitor the piston position and movement allows the damping system to be optimised to varying P_d/P_i ratios. Furthermore, it allows inevitable piston rebound to be quantified and the associated pressure drop can to be

calculated. Initially, as shown in Fig. B.15, a piston position measuring device was trialled in the form of a linear potentiometer that connected to a steel rod that attached through the air driving cylinder to the back end of the piston rod assembly. However, the device was found to frequently fail under the extreme de-acceleration of the piston rod assembly.

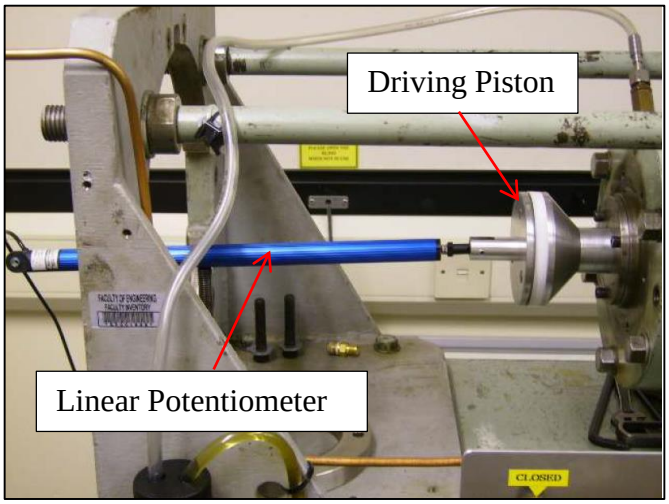

Figure B.15: Photo of side view of linear potentiometer setup used as first piston position monitoring method trailed.

As shown in Fig. B.16, a non-contact approach was then trialled by means of a high speed camera filming an exposed steel rod that attached to the back end of the piston rod assembly against a fixed scaled ruler. However, the limited rod diameter resulted in excessive vibration, giving tentative readings that were extremely time consuming to analyse.

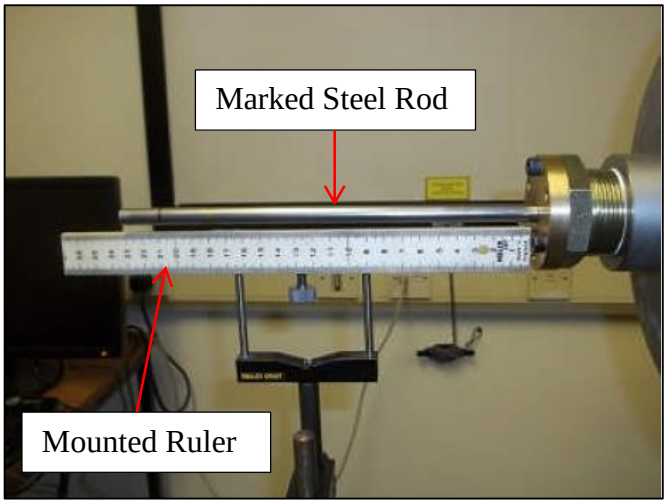

Figure B.16: Photo of side view of high speed camera and ruler setup as second piston position monitoring method trailed.

The solution came in the form of a 2D linear displacement laser that focused on an aluminium disc attached to a stainless steel rod that attached to the back end of the piston rod assembly. Figures B.17 shows the how the displacement laser was mounted, such that the disc moves towards the laser head during compression. The principle being that the linear distance between the laser head and the target disc was calculated by the change in angle between that of the linearly emitted laser beam and the reflected beam from the target disc that was picked up by a RS-CMOS sensor in the laser head. The disc shaped target was essential due to the susceptible nature of the entire piston rod assembly to rotate during operation, thus the disc always provided a target regardless of the piston rods rotation. As a safety guard, the system was enclosed by a large plastic tube, such that the area of the rapid moving target disc was always isolated along with the laser beam.

The selected laser system was supplied by Keyence, model LK-G82, with a maximum power output of 0.95mW, wavelength of 650nm, and a potential sampling rate of up to 20kHz at a resolution of 0.2μm over a distance of 30mm. The system was controlled via an independent control unit with built-in calibrating software that converted the digitally measured 30mm range to a proportional analogue +/- 10v output, hence 1.5mm/volt, which allowed compatibility with existing National Instrument hardware and software. The maximum measureable distance of 30mm was clearly short of the full piston stroke of 230mm, however, the measurable distance of interest was that in which rebound occurs, which was always well within 30mm from the EOC.

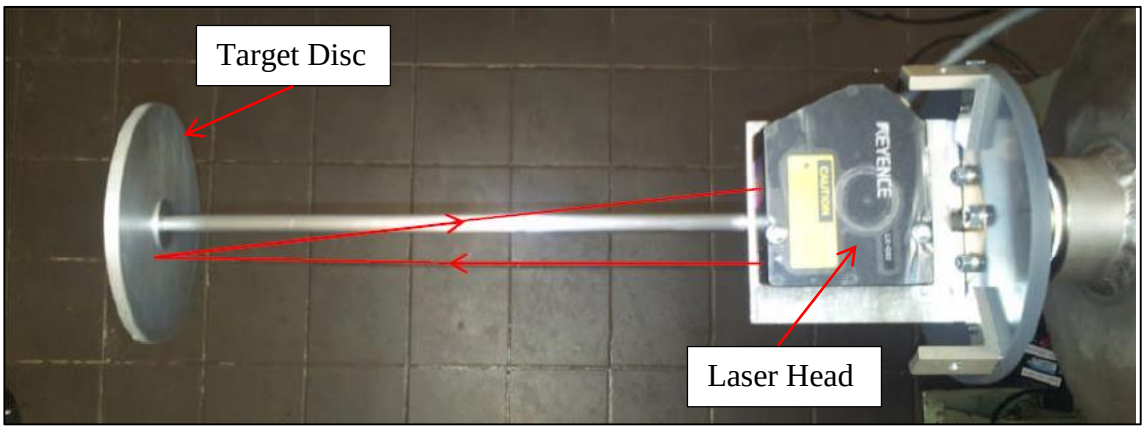

Figure B.17: Photo of overhead view of Keyence LK-G32 linear displacement laser, mount and target disc attached to rear of piston rod assembly, with safety guard removed. Red lines show the laser beam direction.

B.4.5 Increasing Piston Driving Pressure

As detailed in Section B.4.2, the P_d/P_i ratio was critical to optimum piston dynamics, and thus to desirable compression pressure traces. To attain the target P_c of ~2.5 MPa under the maximum CR of 13.58, a P_i value of ~0.9 MPa was required. Therefore, a substantial increase in driving pressure was required in order to maintain a sufficiently high P_d/P_i ratio. To achieve higher driving pressure, a secondary high pressure air supply from a regulated 2 MPa BOC cylinder was coupled to the driving reservoir. As was a static pressure transducer, RS3100, having an increased range of 0-2.5 MPa, coupled to a four digit digital display in the main control box. Further details of the reservoir are discussed in Section B.3.2.

Figures B.18a and b show combustion chamber pressure traces and piston movement near the EOC, for a series of experiments using air, with P_i fixed at 0.1 MPa and P_d increasing from 0.7 to 1.4 MPa, thus varying the P_d/P_i ratio from 7-14. The target P_c of 2.5 MPa was met, and as expected, increasing the P_d/P_i ratio significantly reduced both piston rebound and creep-in duration. However, it was clear the piston assembly was being over damped, such that the creep-in duration was too long, causing the noticeable pressure dip after peak P_c. At a P_d/P_i ratio of 14, the creep-in duration was still 40ms, whilst the distance from EOC at the point of initial piston rebound was only a mere 1mm, indicating the near upper P_d/P_i ratio limit. Thus, the need to adjust the level of piston damping was essential.

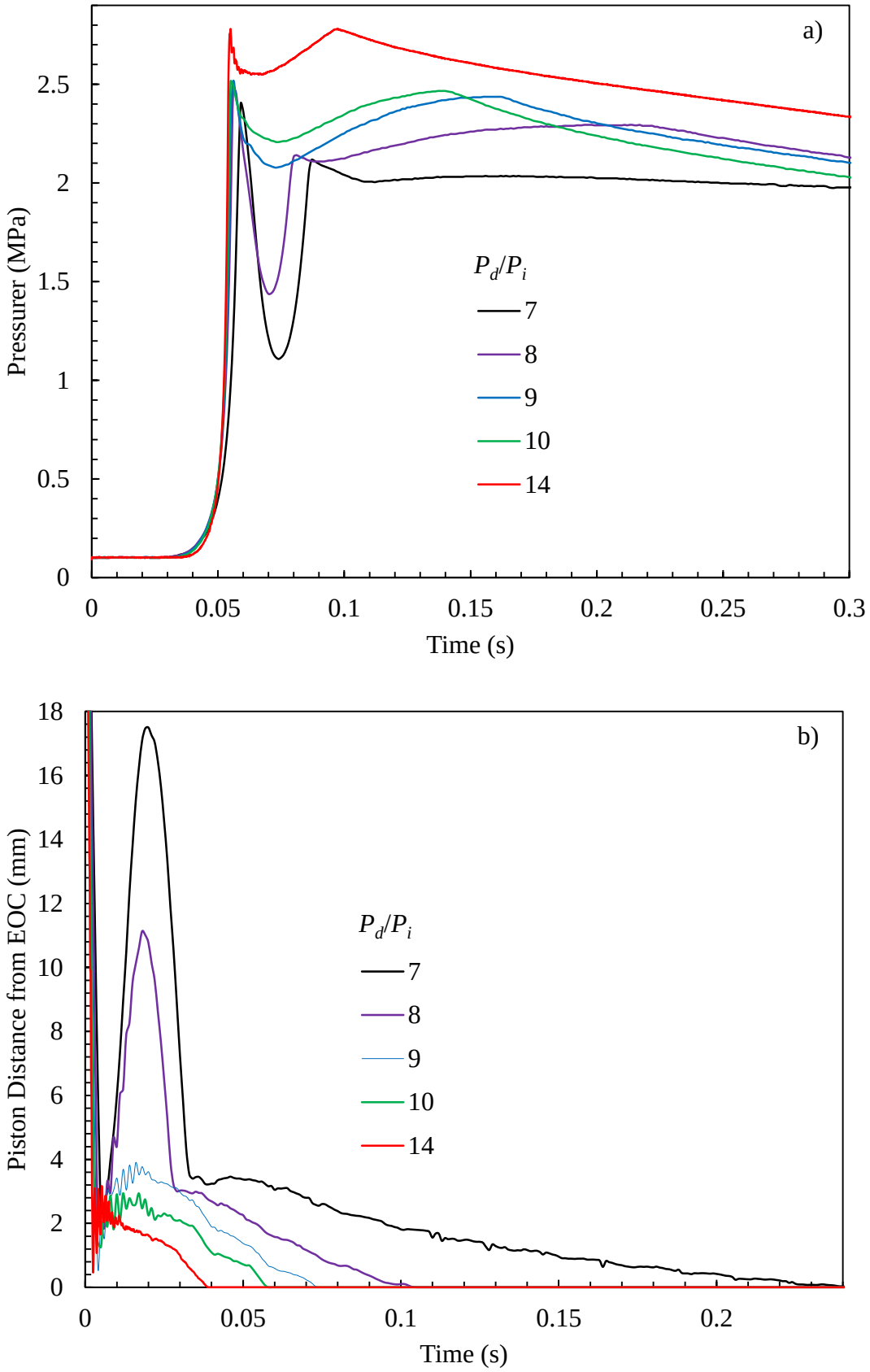

Figure B.18: a) Chamber pressure and b) piston laser displacement measurements for varying P_d/P_i ratios, with P_i fixed at 0.1 MPa, and P_d varying between 7-14.

B.4.6 Adaptable Piston Damping

Arresting and absorbing the kinetic energy from the rapidly fired piston assembly is a key challenge in the design of any RCM, with the P_d/P_i ratio being critical to the piston assembly dynamic behaviour. As the ratio between these pressures is altered, so is, the acceleration, peak velocity and de-acceleration of the piston assembly, which in turn affects the required level of damping. Therefore, to allow full optimisation of the piston rod assembly dynamics in the Leeds RCM, adjustable damping was required. However, as discussed in Section B.3.3 the original damping system was not adjustable. As shown by Fig. B.19, adjustability to the system was achieved via the introduction of a needle valve that regulated the flow of oil from a conduit on the back side of the damping groove to the oil reservoir. This gave potential for a variable and increased flow rate of oil out of the damping groove in a controlled manor. Preliminary tests proved the single needle valve to have negligible effect, so two more needle values were introduced, such that each value was offset by 120 degrees around the damping section. Due to the high operating hydraulic oil pressures, a steel guard band was used to cover the needle valve heads as a safety precaution.

An optimum P_d/P_i ratio of 16.67 was found, such that P_i = 0.9 MPa and P_d = 1.5 MPa. A series of compression experiments were then performed at these conditions, using air, with the needle valves incrementally turned out to increase the oil displacement flow rate from the damper groove. Figure B.20a and b show the pressure traces and piston movement near EOC as a function of the number of needle valve turns, with 0 indicating fully closed. Opening the needle valves by 18 turns successfully reduced the creep-in duration by 94%, to a mere 10ms, giving the post peak P_c pressure curve a much more desirable plateau. Figure B.21 shows the creep-in duration and distance from EOC at the point of initial rebound as a function of needle valve turns. The first five opening turns show a sudden decrease in creep-in duration, followed by a steady decline to the limit of 18 turns. Beyond this, the distance from EOC at the point of initial rebound became too small, as not ensure crashing of the damper ring and groove.

To further enhance the variability of the system, higher viscosity hydraulic oils were trialled: Shell Tellus 22, 68 and 220, the latter being the highest viscosity. This allowed further optimisation such that the P_d/P_i ratio could be slightly increased without the risk of the damping mechanism crashing. Figure B.22 shows the highest P_c value of 2.6MPa acheived whilst maintaining good damping characteristics.

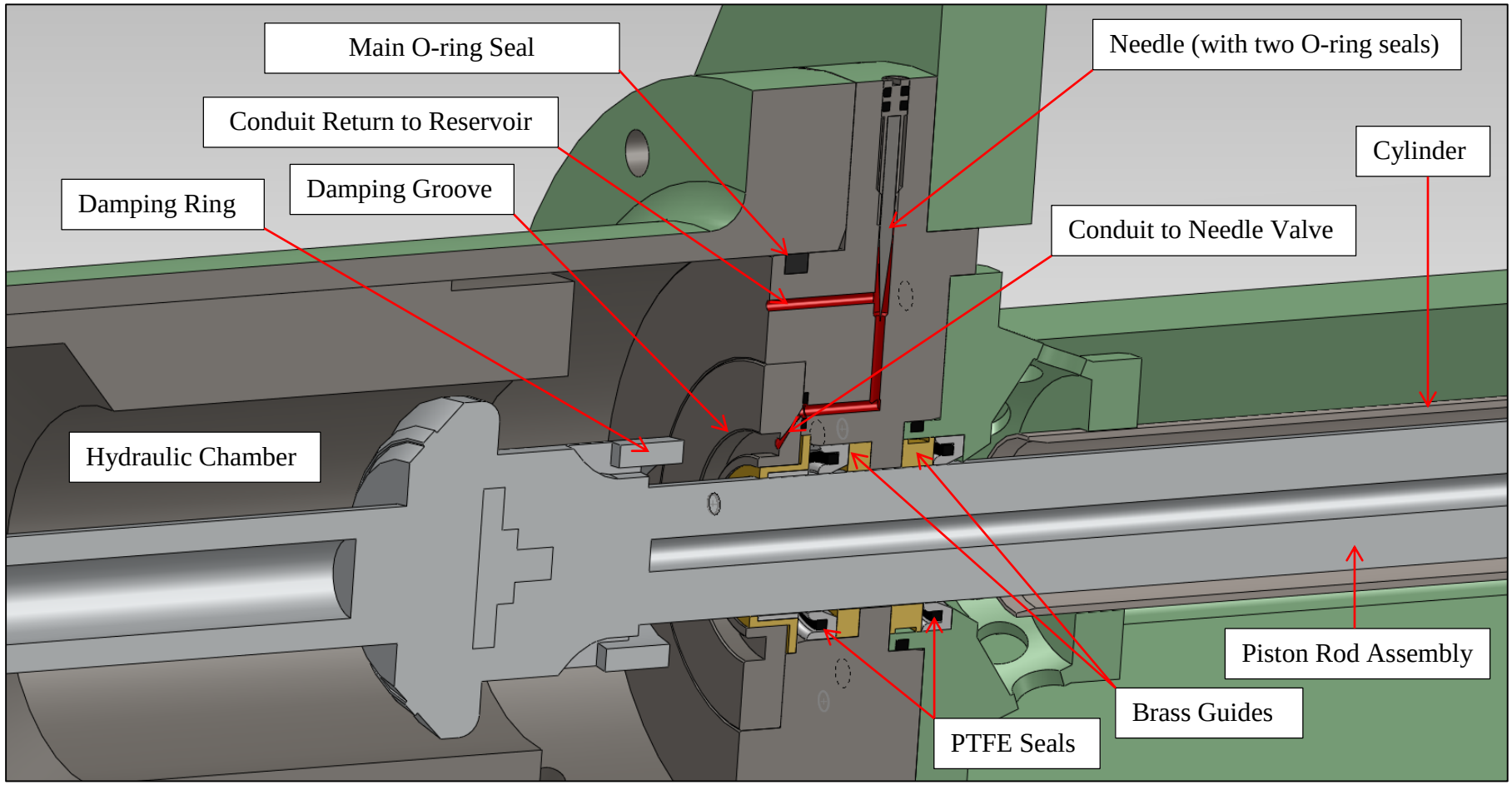

Figure B.19: SolidWorks model cross section view of internal dampening mechanism, with the hydraulic oil conduits highlighted in red. This system is circumferentially employed three times over at 120° offsets.

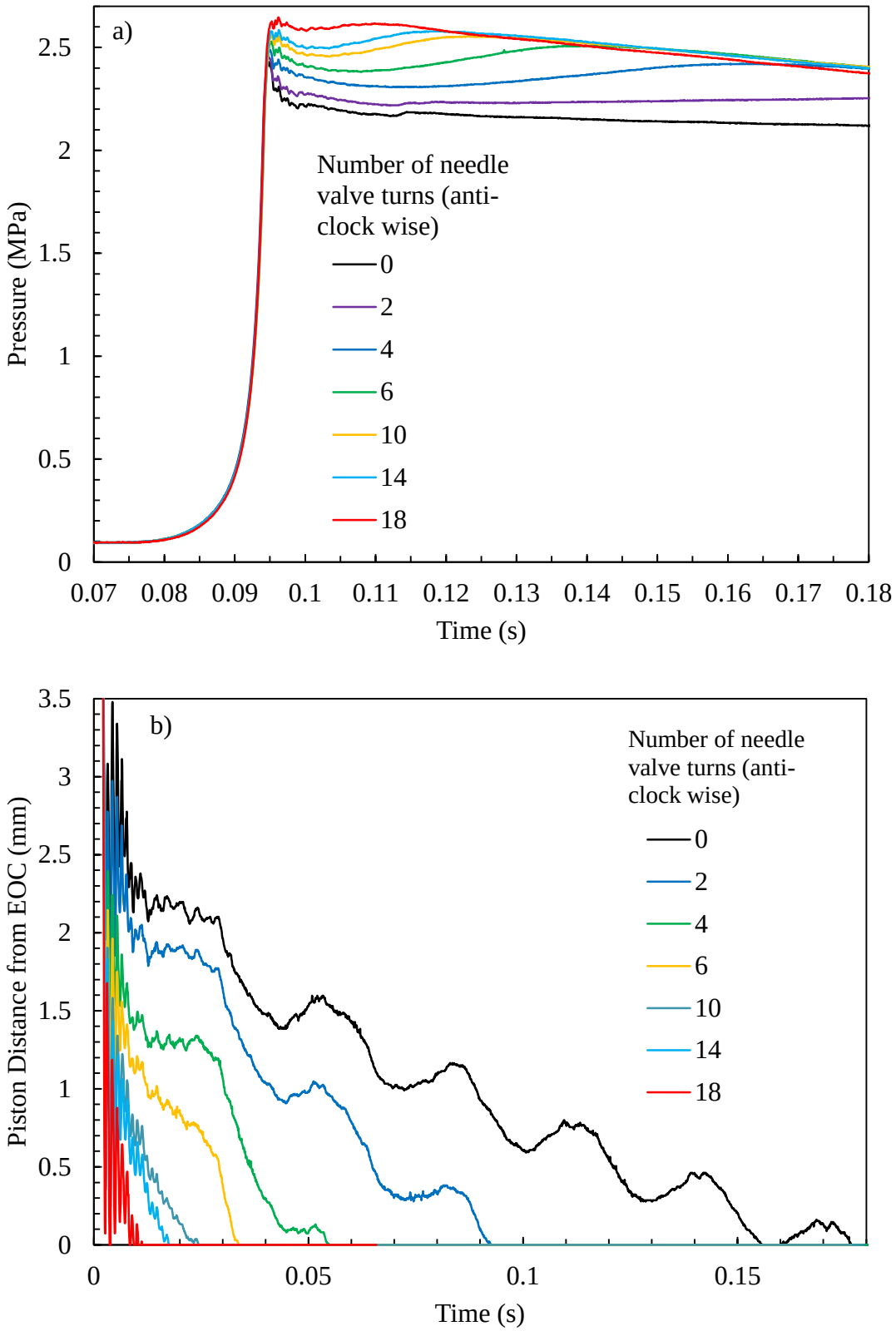

Figure B.20: a) Chamber pressure and b) piston laser displacement measurements for varying needle valve positions, where 0 = fully closed, with P_i and P_d fixed at 0.9 and 1.5 MPa, respectively.

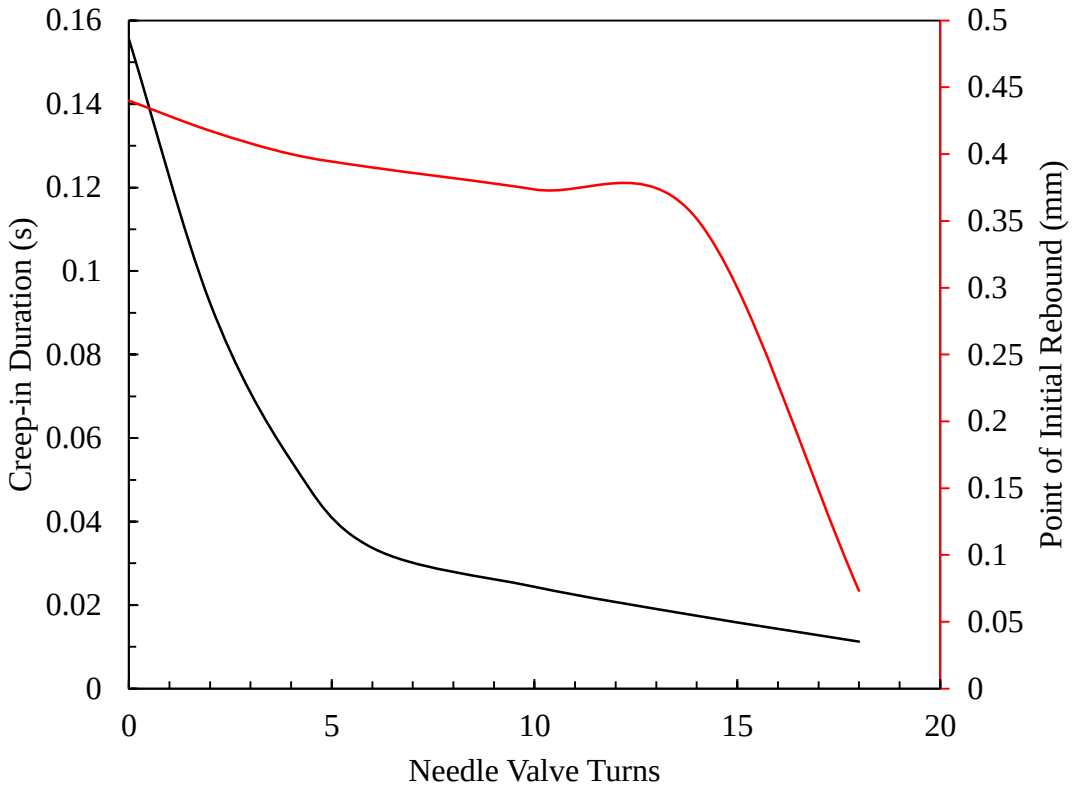

Figure B.21: Creep-in duration and point of initial piston rebound as a function of needle values turns for with P_i and P_d fixed at 0.9 and 1.5 MPa, respectively.

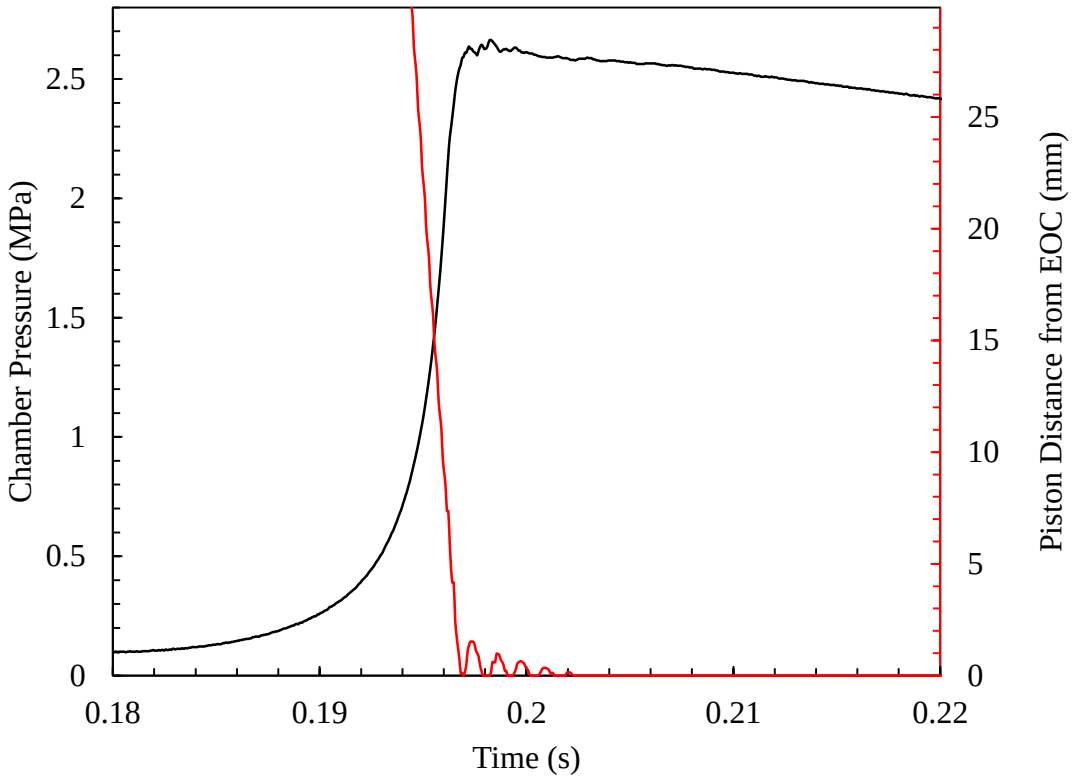

Figure B.22: Chamber pressure and piston laser displacement measurements for P_i = 0.9 MPa, and P_d = 1.5 MPa.

B.4.7 Investigation into Thermal Shock Error of Dynamic Pressure Transducers

The accurate acquisition of the combustion chamber and cylinder pressure rise during the compression and ignition of a combustible mixture was critical to the accurate derivation of temperature and measurement of τ_i values. As common to most RCM's, a piezoelectric dynamic pressure transducer was employed in the combustion chamber to measure such pressure rises, due to their accuracy, high frequency response, durability and repeatability. Figure B.23 shows the cross section of a typical piezoelectric dynamic pressure transducer. Quartz crystals are typically preloaded within a housing to ensure stable, repeatable and linear operation. When a pressure is applied to the diaphragm, the compression of the crystals induces a charge which is then amplified to a measurable voltage. Their electrical insulation is generally very high, however, the charge inevitable leaks to zero, thus the charge leak rate is a function of the electrical insulation resistance and the capacitance of the crystal and its supporting electronics. It is important to ensure this discharge rate is under the heat loss rate at the EOC as to not give an erroneous pressure reading.

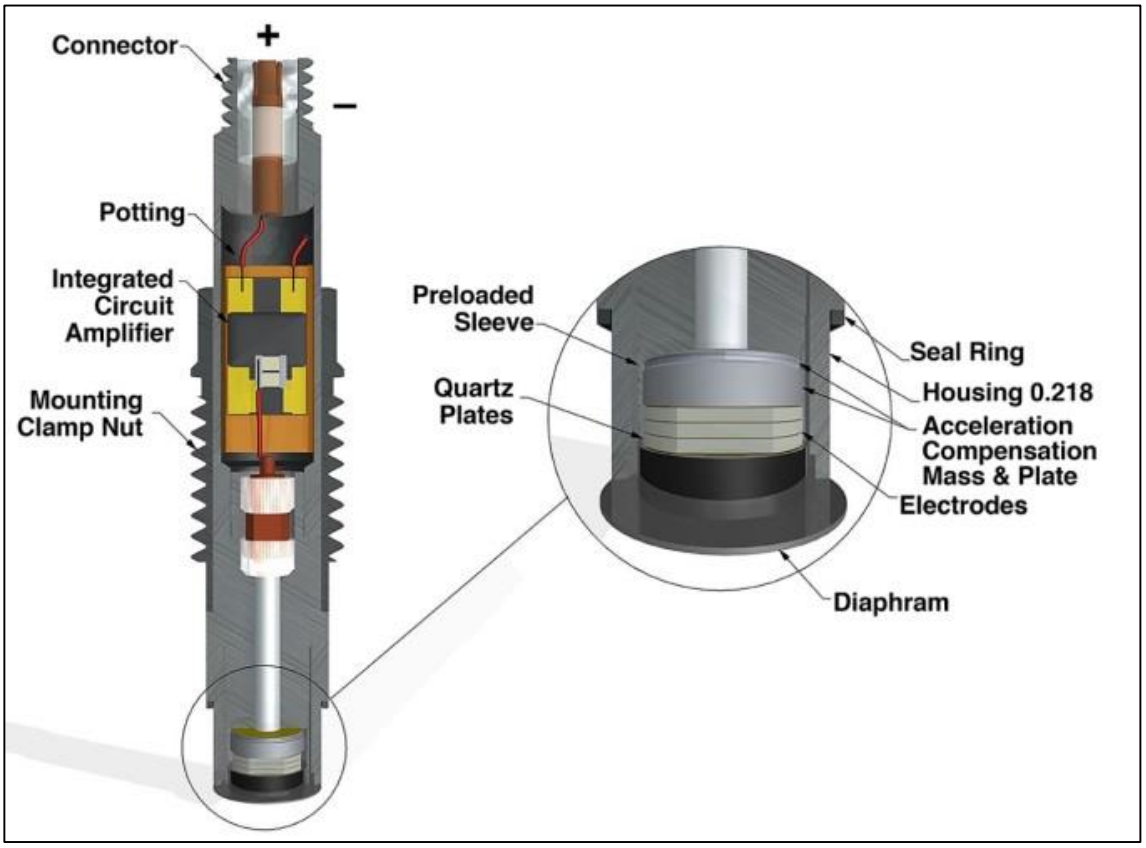

Figure B.23: Cross section view of typical piezoelectric dynamic pressure transducer (PCB, 2015).

Under steady thermal conditions the sensitivity change of such transducers is very small, typically less than 1%, however, their ability is compromised by rapid temperature gradients – thermal shock. The sensitivity of quartz to thermal shock is low, however, its housing and preloaded diaphragm is not. Localised heat can cause expansion and unloading of the quartz to give an erroneous negative signal. Techniques to help counter such effects are suggested by manufactures PCB Ltd. (2015), these include, recess mounting, and a variety of coatings: silicone grease, RTV and vinyl tape. However, reduced sensitivity is often the trade-off.

High temperature gradients and thus thermal shock are intrinsic to the rapid compression of any mixture within in an RCM, typically reaching gradients of over 100K/ms. Mittal and Bhari (2013), showed thermal shock errors to reduce P_c by as much as 0.5 MPa (18.5%) when no protection measures were taken in the compression of nitrogen using an RCM. Further significant pressure drops associated with thermal shock have also been reported in combustion vessel and engines. Therefore, thermal shock error must be quantified to ensure accurate pressure measurement within the RCM. The original Leeds RCM pressure transducer was a Kistler 601A, flush mounted in the bottom port of the combustion chamber. A consultation with Kistler Instruments Ltd. concluded that this transducer was not ideally suited and likely prone to thermal shock error. Therefore, a series of experiments were performed, whereby, a specifically designed thermal shock resistant transducer, the Kistler 6045A, with a known thermal shock error of less than ±1% was acquired and used as a reference to quantify any thermal shock error of the original 601A, alongside other existing and potentially viable pressure transducers available in the laboratory, as shown in Table B.1. The charge from each transducer was amplified by a Kistler 5007 charge amplifier. Further details of signal processing and data acquisition are given in Section B.4.10.

Kistler dynamic pressure transducer model	Features
6045A (Reference)	Low thermal shock error < ± 1% for high temperature gradients
601A	High natural frequency for high vibration
701A	High sensitivity for increased accuracy
7005	Reinforced diaphragm for high pressure use
6061B	Water cooled for constant high temp environments

Table B.1: Summary of all Kistler dynamic pressure transducers examined in the present work.

A further series of experiments were also carried out to investigate the effects of the various manufacture recommend thermal shock protection techniques, as described above, for each of the four questionable transducers. To ensure an accurate comparative analysis, two specially designed end plugs were manufactured to simultaneously mount the pressure transducers in either a flush or recessed position. Figures B.24a and b show SolidWorks models with dimensions of the custom machined multi dynamic pressure transducer flush and recess mounted end plugs.

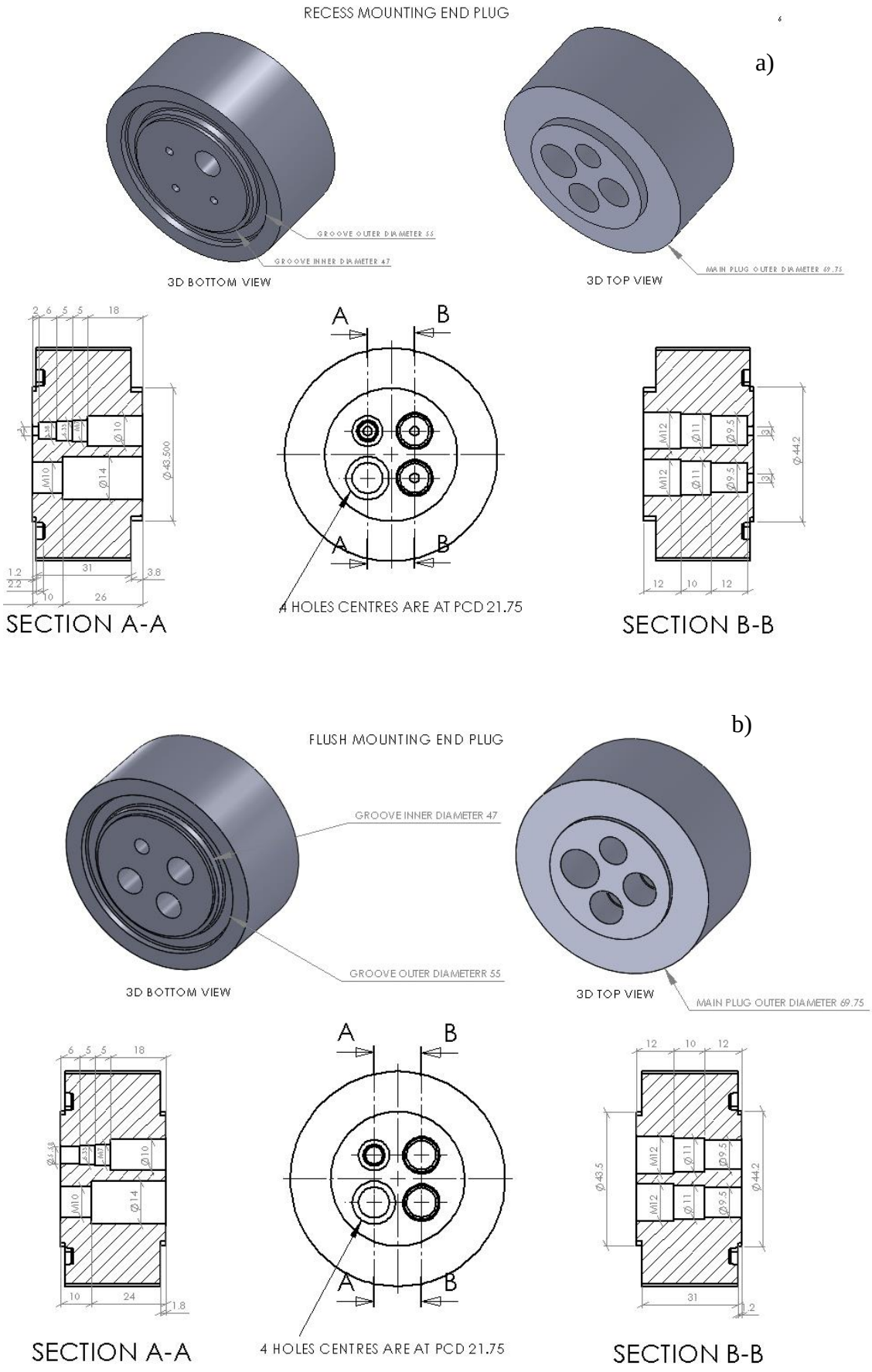

Figure B.24: SolidWorks model of custom machined multi a) recess and b) flush mounted dynamic pressure transducer end plugs.

B.4.7.1 Quantification of Thermal Shock Error

A series of air compression experiments at atmospheric pressure and temperature were first conducted to quantify the thermal shock error of each pressure transducer, with reference to the 6045A, which was specifically designed to reduce thermal shock error. This was flush mounted in the rear port of the combustion chamber and the other four transducers were flush mounted in the specially manufactured end plug as shown in Fig. B.24, allowing simultaneous pressure measurements of all pressure transducers.

Figure B.25 shows each transducers pressure trace, whilst Fig. B.26 shows the difference in pressure between each tested transducer and the reference transducer, hence, quantifying their thermal shock error relative to the reference transducer with a known thermal shock error of less than ± 1%.

At the EOC, the original 601A and the 701A show the most significant pressure deviation from the reference transducer, by circa -0.12 MPa (4%), followed closely by the 7005. The water cooled 6061B fares significantly better with a mere deviation of circa -0.025 MPa (0.8%).

B.4.7.2 Flush Mounting with Coatings

As recommend by pressure transducer manufactures, PCB Ltd. (2015), the first thermal shock protection techniques trailed were that of applying either vinyl tape or a 1mm coating of RTV Silicone directly to the surface of the pressure transducer diaphragm, that was flush mounted to the chamber wall. The vinyl tape used was Scotch Supper 33+ electrical tape, of 0.177mm thickness and the RTV silicone used was Loctite 5399. A flat steel bar with a 1mm cut out was used to accurately level off the silicone and ensure an evenly distributed coat across the diaphragm, and at least 24hrs curing time was given.

Figures B.27-B.30 show the pressure traces for each flush mounted pressure transducer, with and without the two different coatings. For the 601A and 701A transducers, both coatings have negligible effect. For the water-cooled 6061B transducer, both coatings, particularly the vinyl tape, consistently reduce pressure at EOC and thereafter, indicating an ability to reduce thermal shock error but blighted by reduced sensitivity. In contrast, the 7005 transducer shows consistently increased pressure readings for both coatings, particularly the vinyl tape at EOC.

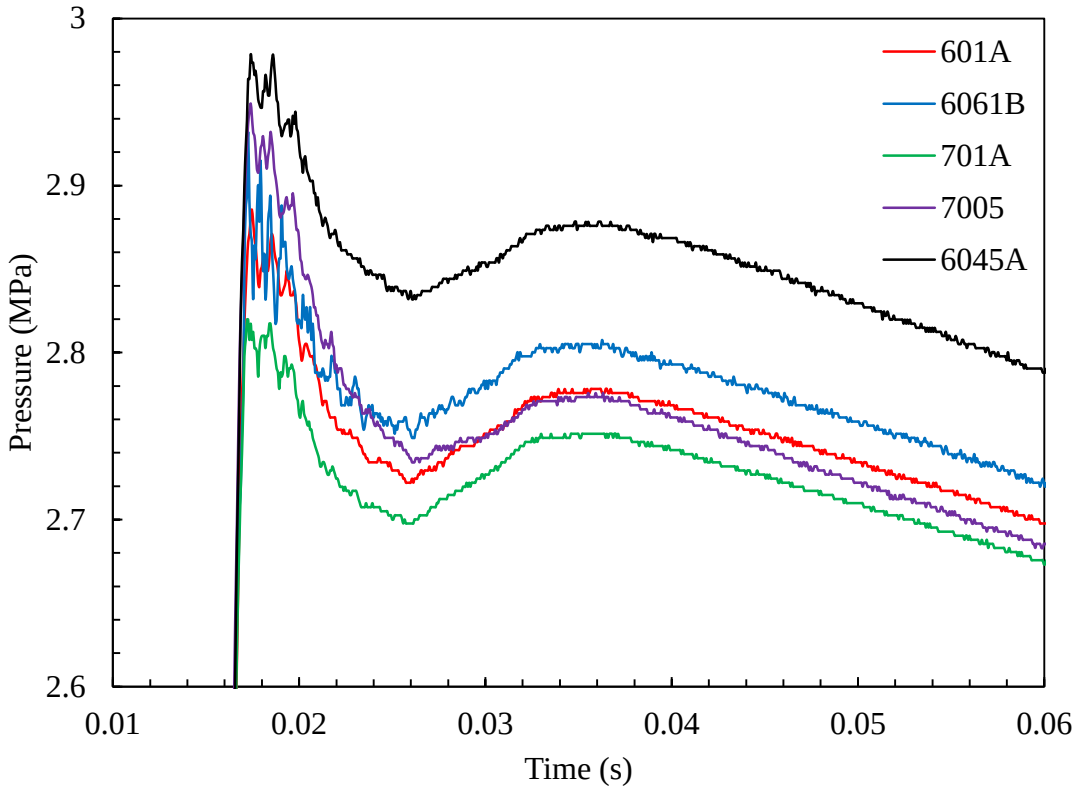

Figure B.25: Chamber pressure traces for all dynamic pressure transducers tested.

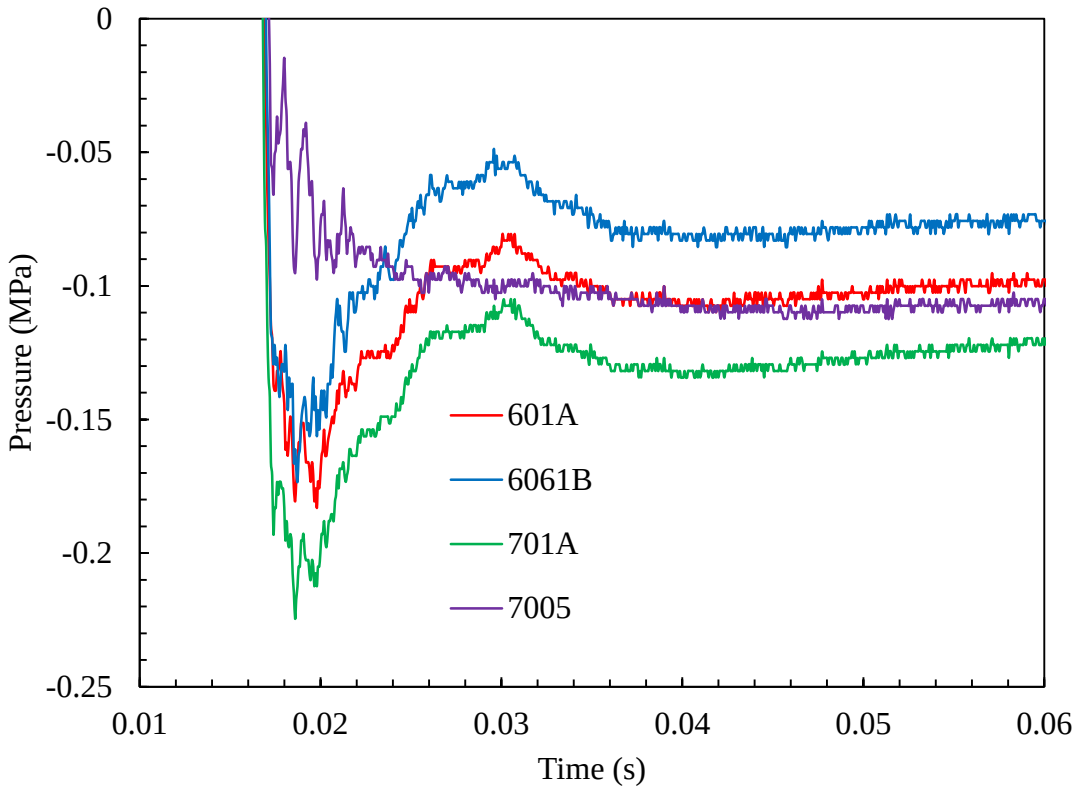

Figure B.26: Pressure difference between each pressure transducer and reference transducer 6045A.

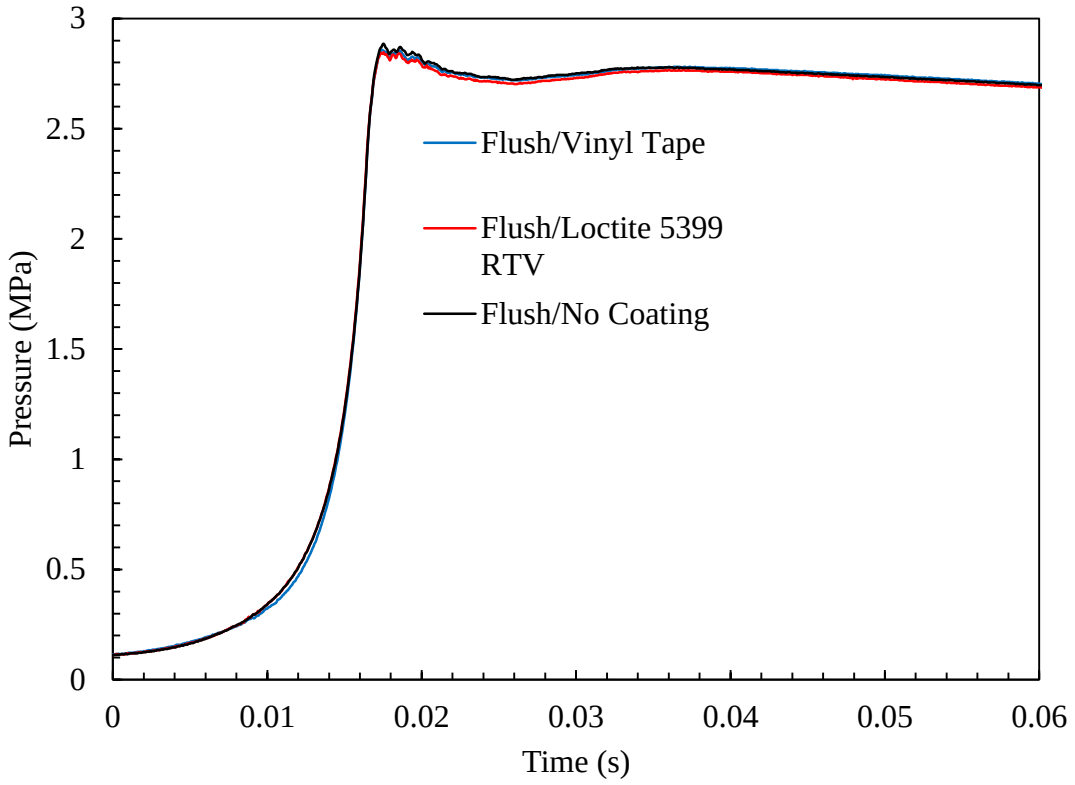

Figure B.27: Chamber pressure traces for flush mounted 601A transducer with different coatings.

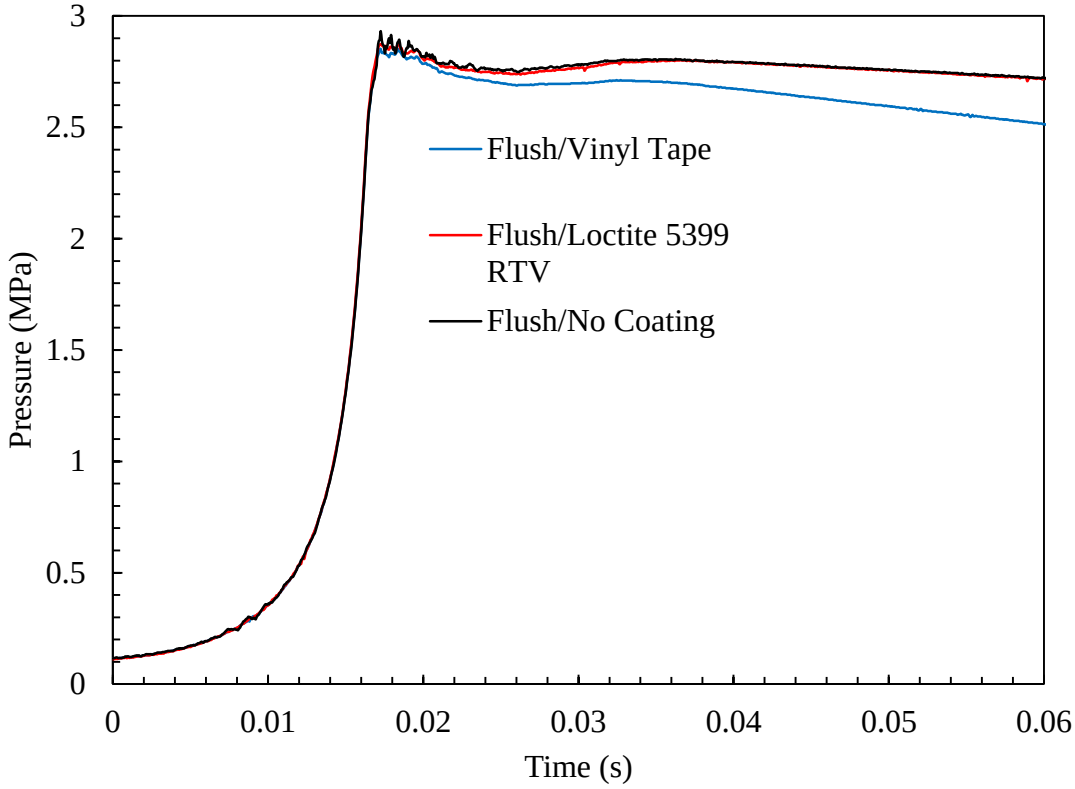

Figure B.28: Chamber pressure traces for flush mounted 6061B transducer with different coatings.

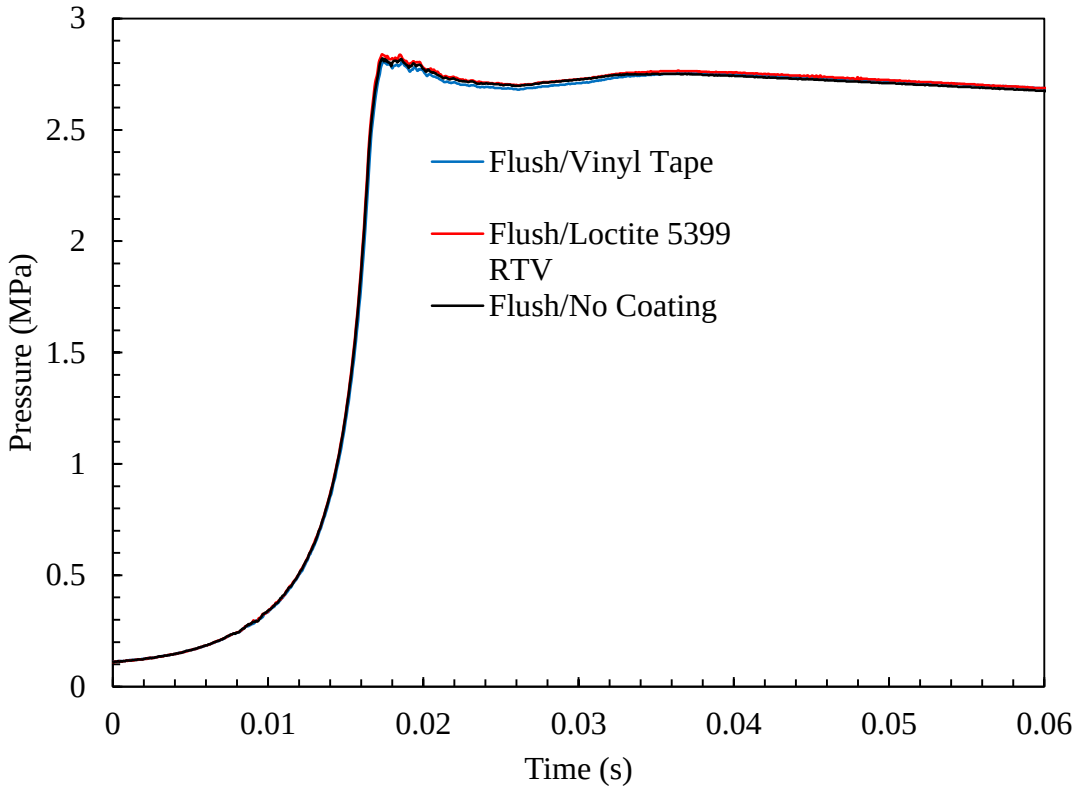

Figure B.29: Chamber pressure traces for flush mounted 701A transducer with different coatings.

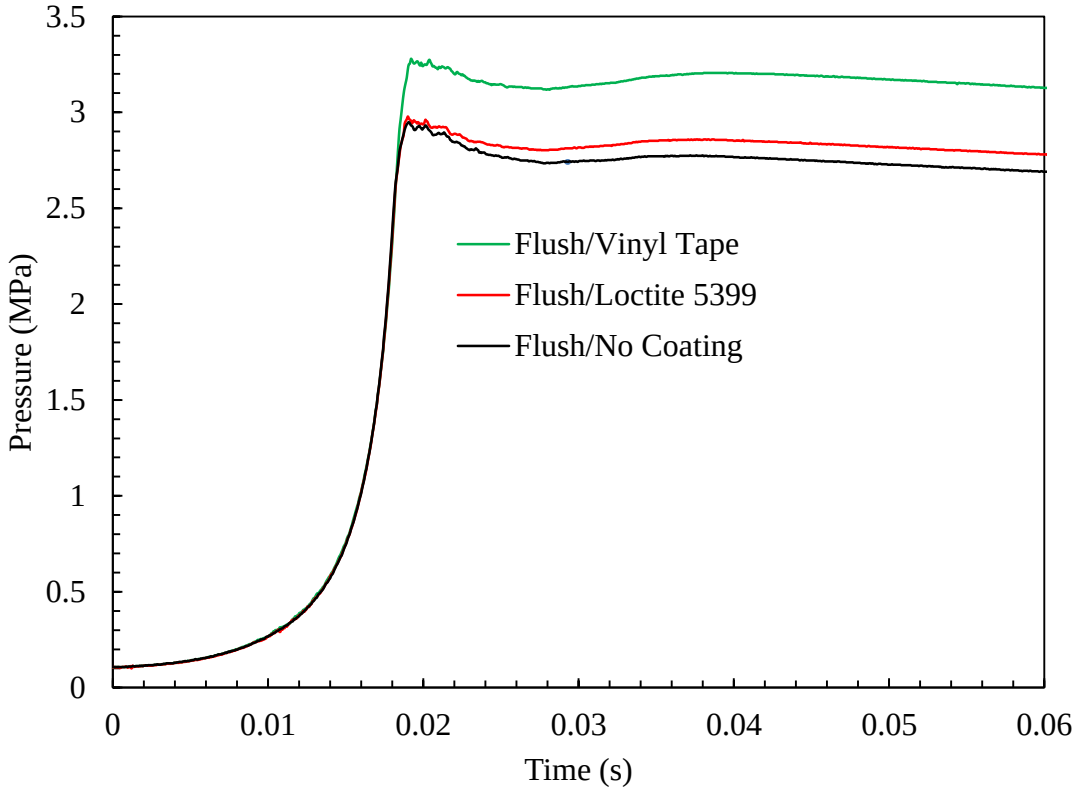

Figure B.30: Chamber pressure traces for flush mounted 7005 transducer with different coatings.

B.4.7.3 Recessed Mounting with Silicone Fillings

The second thermal shock protection technique trailed, again, recommend by PCB Ltd. (2015), and common practice within engine studies, was that of recess mounting the pressure transducer diaphragm from the chamber wall such that it was less exposed to hot gases, flames etc. Further to this, a silicone filling can be added for increased thermal protection. In the present work, three types of silicone fillings were trailed: Loctite 5399 (as previously used in the flush mounted coating tests), 2 Pack RTV and silicone grease.

Figures B.31-B.33 show the pressure traces for each recess mounted pressure transducer; both unfilled and filled with the three types of silicone. For comparison, the corresponding flush mounted pressure traces as described in section B.4.7.3 are also shown. The open recessed mounting technique reduced the readings of all transducers in comparison to the standard flush mounting technique. Both the Loctite 5399 and 2 Pack RTV silicone recess filled techniques significantly reduced all transducer readings, particularly for the 701A and 7005, where the 2 Pack RTV reduced EOC pressure by 79% and 73%, respectively. The silicone grease filled recess technique was the only technique to show an increase in pressure readings above the standardised flush mounted technique, which consistently occurred for all transducers. In the case of the 601A and 7005, this technique gave results close to that of the flush mounted reference transducer. This indicates the technique was effective in reducing thermal shock error without reducing sensitivity. However, in practice, the silicone grease was prone to dislodging after repeated compressions and therefore was not considered a practical solution. As a result the specifically designed thermal shock resistant reference 6045A transducer was chosen for use in the Leeds RCM.

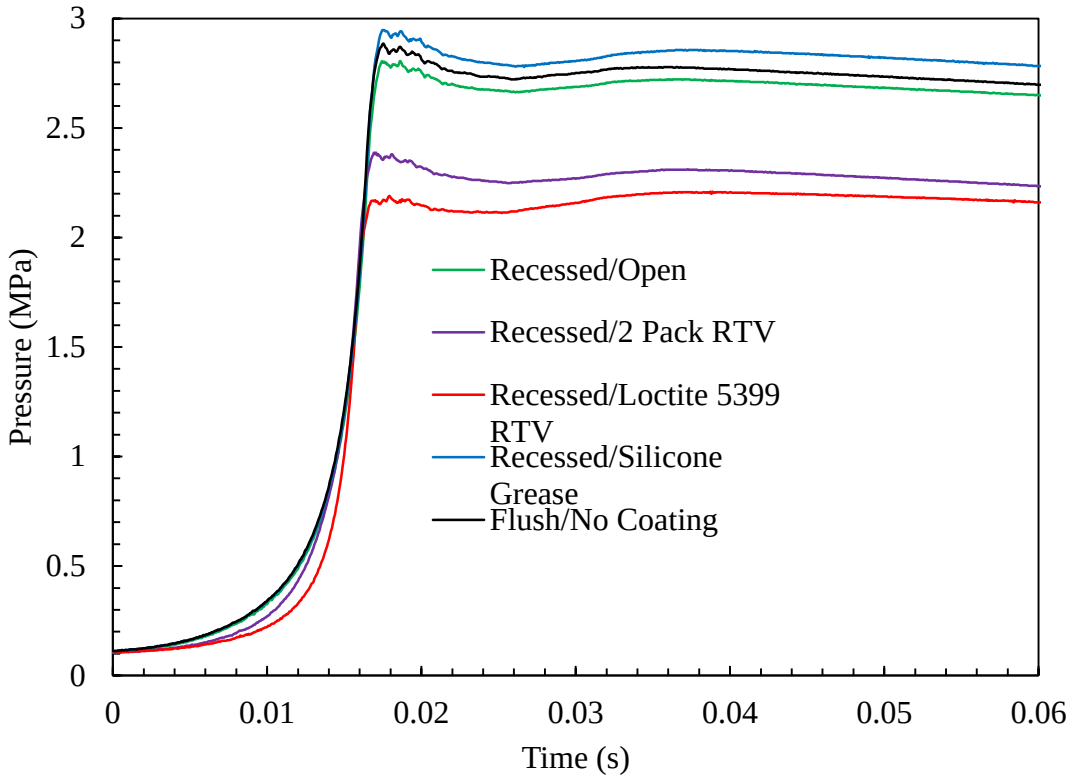

Figure B.31: Chamber pressure traces for recess mounted 601A transducer with different silicone fillings.

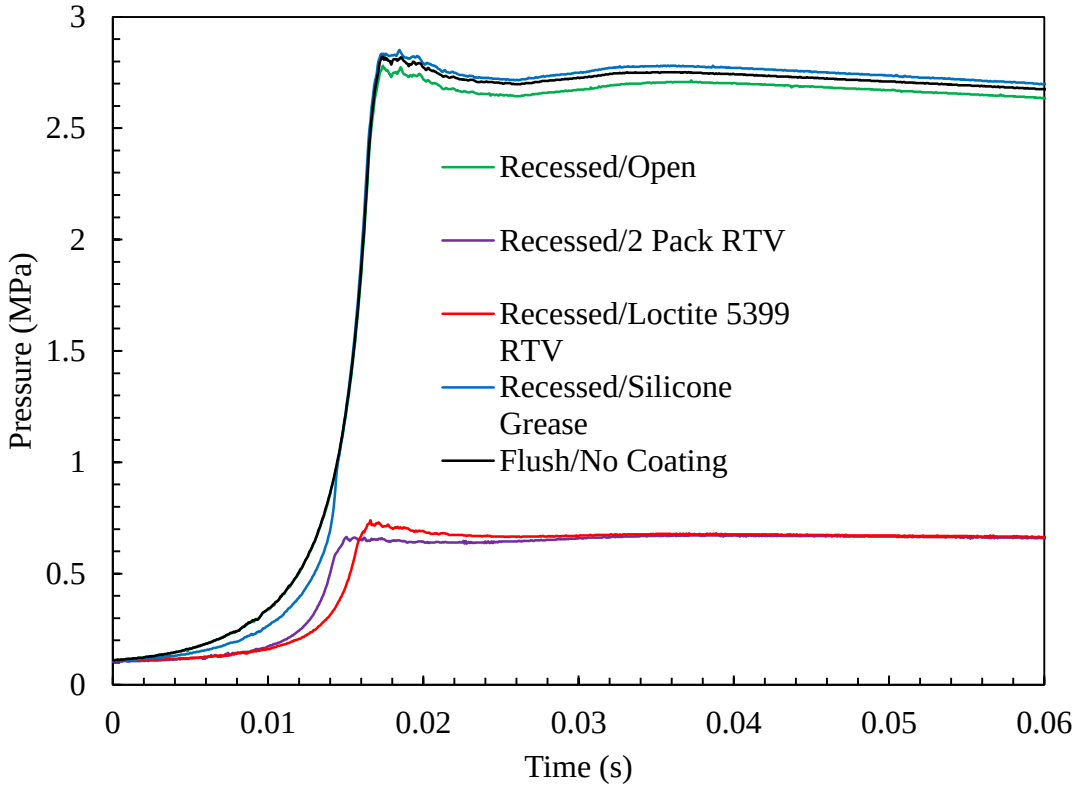

Figure B.32: Chamber pressure traces for recess mounted 701A transducer with different silicone fillings.

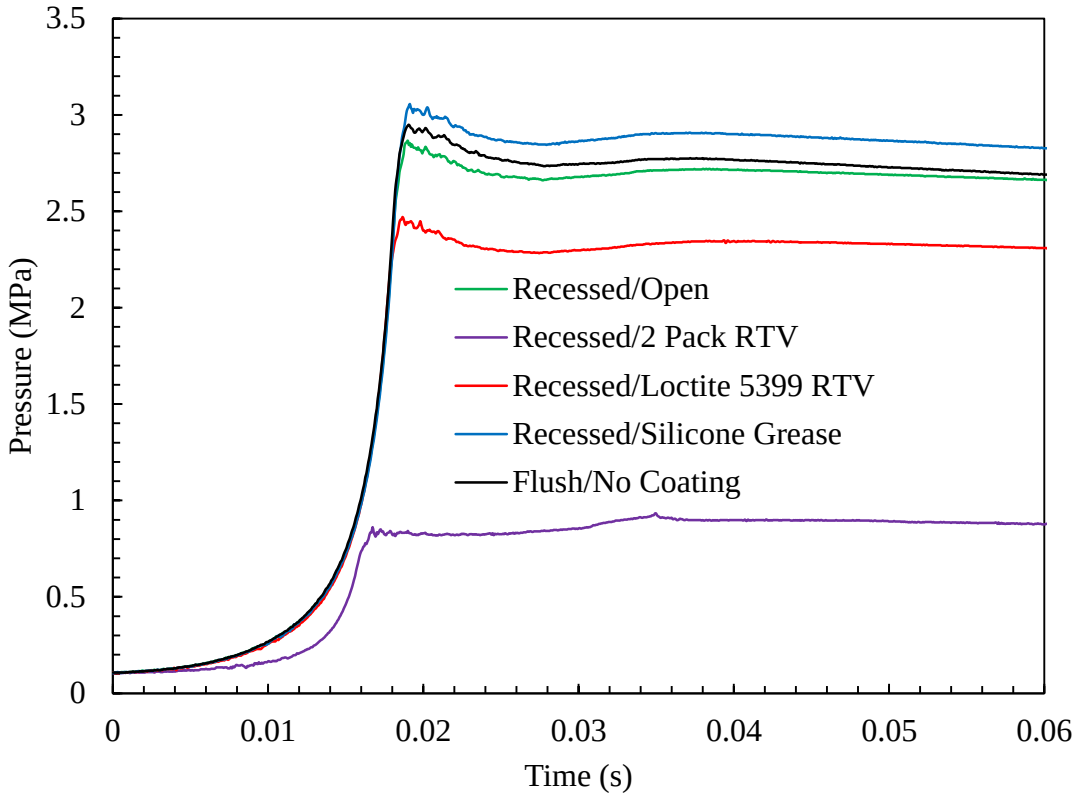

Figure B.33: Chamber pressure traces for recess mounted 7005 transducer with different silicone fillings.

B.4.8 Combustion Chamber Heating and Temperature Control

As discussed in Chapter 1, the autoignition of a combustible mixture is not only a function of its composition and pressure, but temperature. Therefore, the accurate and precise control of the initial mixture temperature, T_u, within the combustion chamber and cylinder was crucial to accurate acquisition of τ_i data.

As shown in Fig. B.34, the original heating system was limited to five 75W heating bands positioned around the cylinder. Whilst being more than powerful enough, their operation caused significant temperature gradients between the cylinder, which tended to overheat, and the unheated combustion chamber, which tended to under heat, due to its larger mass and mounting to the heavy gauge steel frame, acting as a heat sink.

Figure B.35 shows a custom manufactured temperature probe to allow temperature measurements to be taken internally, down the central length of the cylinder and combustion chamber. This comprised of an exposed K-type thermocouple junction at the end of a 4mm outer diameter ceramic twin core tube that was fed through a specially machined end plug with an O-ring sealing access port. This ensured temperature measurements could be taken in line with intended P_i values that were below

atmospheric pressure. The ceramic tube was externally marked at 20mm intervals to accurately position the thermocouple junction within the cylinder and chamber.

To increase heating of the combustion chamber, a specially designed end plug was machined out of mild steel that circumferentially embedded six 50W heating cartridges and a central sealing access port for the internal temperature probe. Figure B.36 shows a photograph of the installed end plug, whilst Fig. B.9 shows a SolidWorks model cross section view. The long 'top hat' design gave both a large surface area of contact between the end plug and the combustion chamber and a high thermal mass to ensure uniform and stable heating. Separate control of the band and cartridge heaters was achieved via two CAL3200 PID temperature controllers mounted in the main control box, with feedback from two K type thermocouples. The band heaters thermocouple was placed under the central band heater, and the cartridge heaters thermocouple was centrally embedded into the end plug.

A series of experiments were performed, trailing different heater configurations and temperature target set points. Figure B.37 shows three temperature profiles from measurements taken within the cylinder and chamber using the internal custom temperature probe, for two different heater configurations. 0mm indicates the chamber end face and 245mm the piston face at SOC. The dashed line shows the temperature profile for the use of two of the original band heaters at either end of the cylinder, the notion being, that two bands at higher set points nearer the cooler regions would help dissipate heat more uniformly. However, whilst measurements within the cylinder remained relatively stable and uniform, temperatures measurements dived towards the unheated chamber, rendering this configuration insufficient. The two other solid lines show temperature profiles for both high and low temperature set points, using both the five original band heaters on low power and the heated end plug that incorporated six cartridge heaters. This configuration was found to give the best internal gas temperature uniformity for both low and high temperatures, with variation typically no more than 5% from the target temperature.

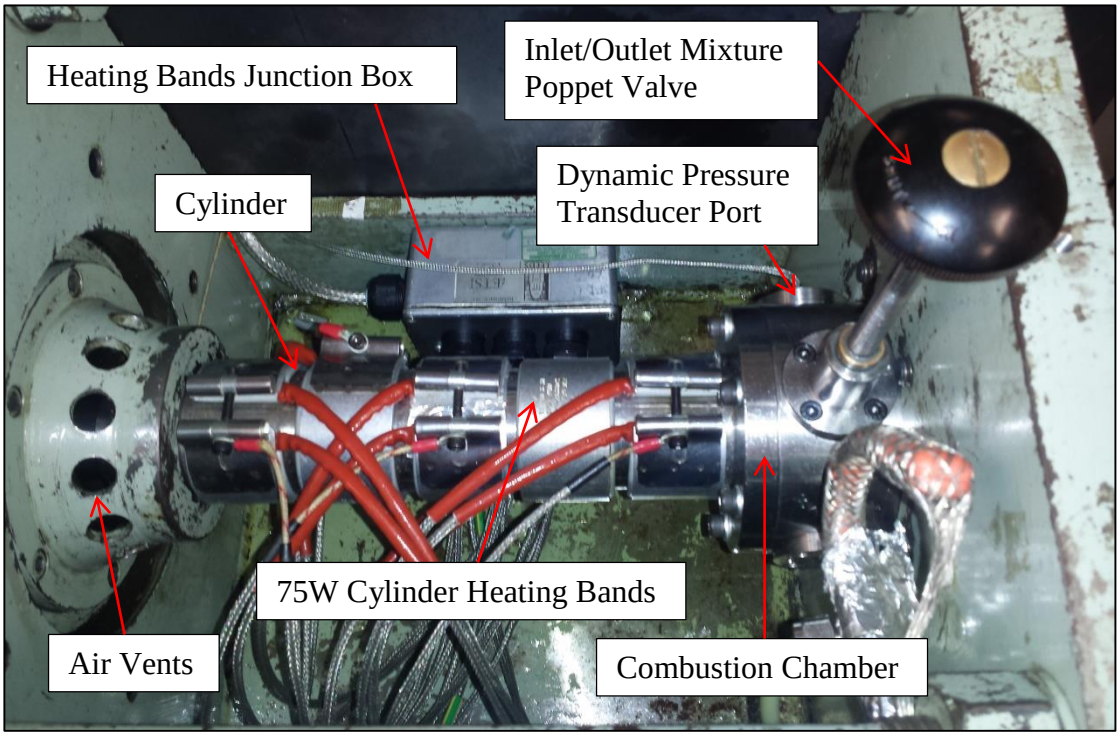

Figure B.34: Photo of the original five 75W cylinder heating bands.

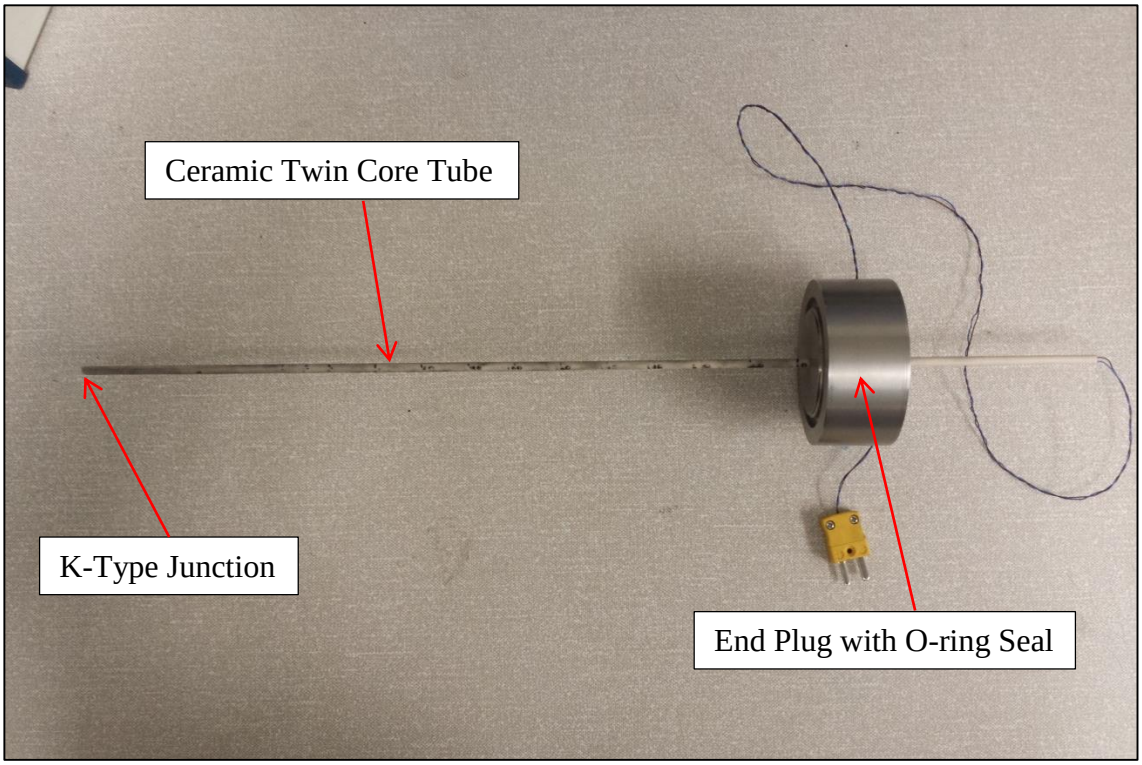

Figure B.35: Photo of custom manufactured internal combustion cylinder and chamber temperature measurement probe.

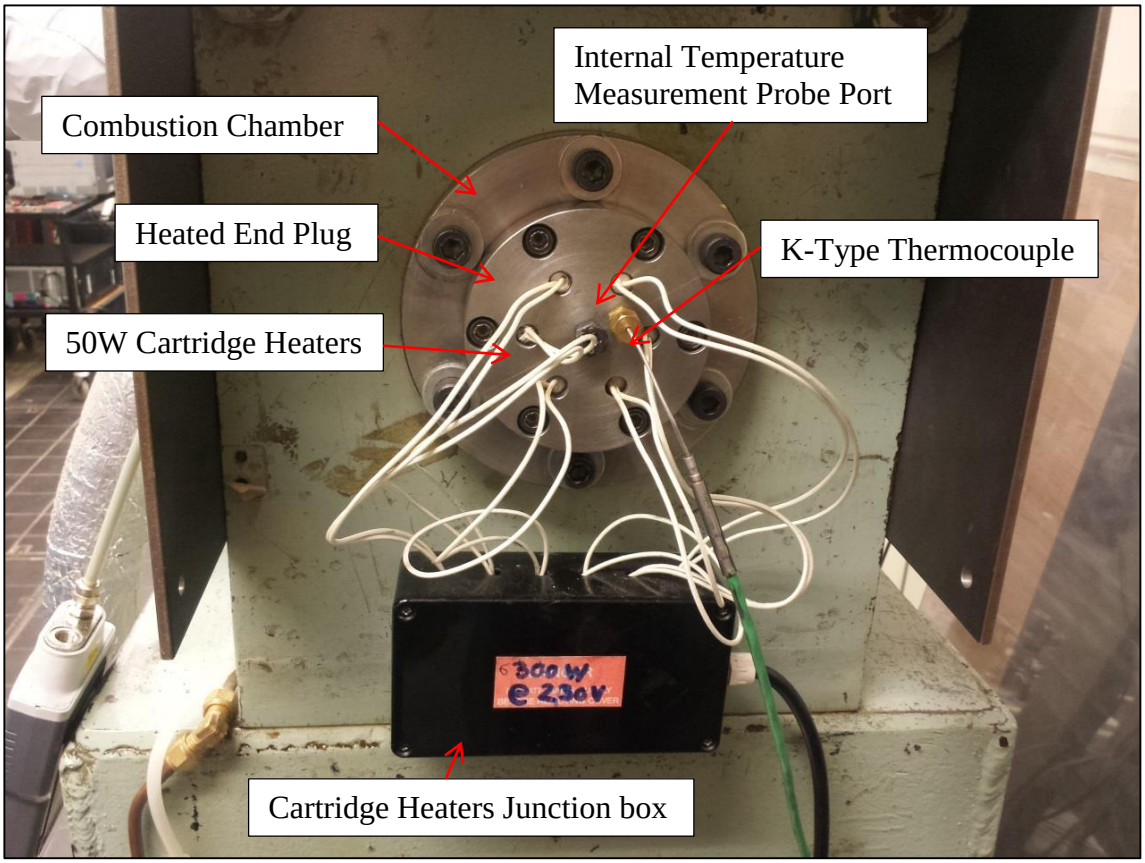

Figure B.36: Photo of combustion chamber end view, with inserted heated end plug containing six 50W cartridge heaters.

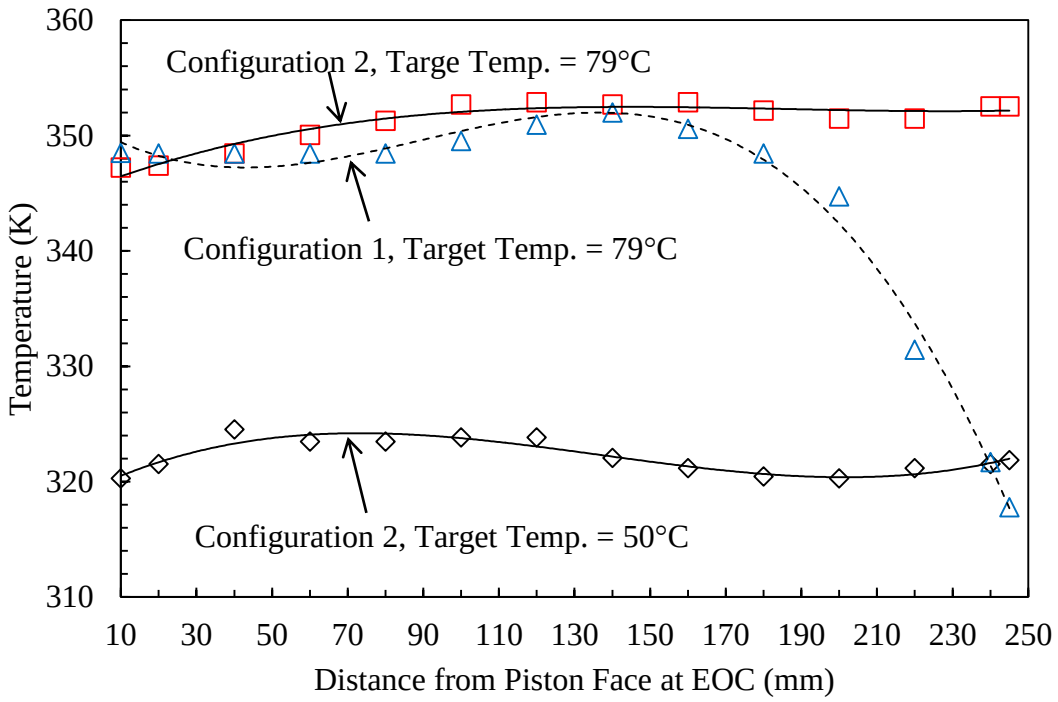

Figure B.37: Combustion chamber and cylinder temperature measurements, using custom internal temperature probe. Config. 1: 2x75W cylinder band heaters, config. 2: 5x75W cylinder band heaters and 6x50W cartridge heaters in large end plug.

B.4.9 Fuel/Oxidiser/Diluent Mixing Chamber and Delivery System

A mixing chamber was designed and manufactured to allow batches of homogenous and preheated fuel/oxidiser/diluent mixtures to be made-up in one procedure. This dramatically increased productivity, reduced fuel handling, and increased the consistency of the mixture. Figure B.38 shows a SolidWorks drawing of the completed mixing chamber. It comprised of a seamless stainless steel 316 cylinder with two O-ring sealed stainless steel 304 end plates held in place by eight external high carbon steel bolts.

Stress calculations for the mixing chamber are presented in Appendix C. A simple mild steel support frame was then used to mount the mixing chamber nearby the combustion chamber, within the main frame work of the RCM, minimising the length of the required delivery system pipework. The internal volume of the chamber was 1.7671 x 10^{-3} m³ and had a maximum working chamber pressure of 0.5 MPa. This would typically allow 15-25 mixture shots for experimentation, dependant on fuel type, equivalence ratio, temperature and the initial combustion chamber pressure. A static pressure transducer, UNIK 5000, was used to measure pressure in the mixing chamber, having a range of 0-0.4 MPa. This was wired to a four digit digital display mounted in the main control box.

Heating was achieved by an external Mica 2kW band heater wrapped around the inner cylinder, with the temperature controlled via a PID CAL3200 mounted in the main control box, using feedback from a K-type thermocouple positioned under the heating element. There were four frontal ports, the top was connected the combustion chamber delivery line, the bottom port was connected to a pressure relieve valve, set to just below 0.5 MPa and venting to the exhaust line, the left port was connected to the gaseous inlet manifold, with the static pressure transducer fitted to an intercepting T-section, and finally, the right port was connected to a luer lock fuel injection port. The delivery line consisted of a main open and shut ball valve and a precision needle valve for accurately controlling the mixture flow when filling the combustion chamber. A handheld static pressure transducer, Comark C9557, connected to the front port of the combustion chamber was used to monitor the initial combustion chamber pressure, P_i, and thus quantify the incoming mixture.

To ensure preheated mixtures did not condense within the 4mm ID stainless steel delivery line, it was heated using RS 50W/m heating element cable that was also controlled by another CAL3200 PID controller, mounted in the main control box, using

a K-type thermocouple attached midway between the mixing and combustion chamber as feedback. The entire line was also heavily insulated with specialist thermal pipe foam and wrapped in aluminium insulation tape to help maintain an evenly distributed temperature.

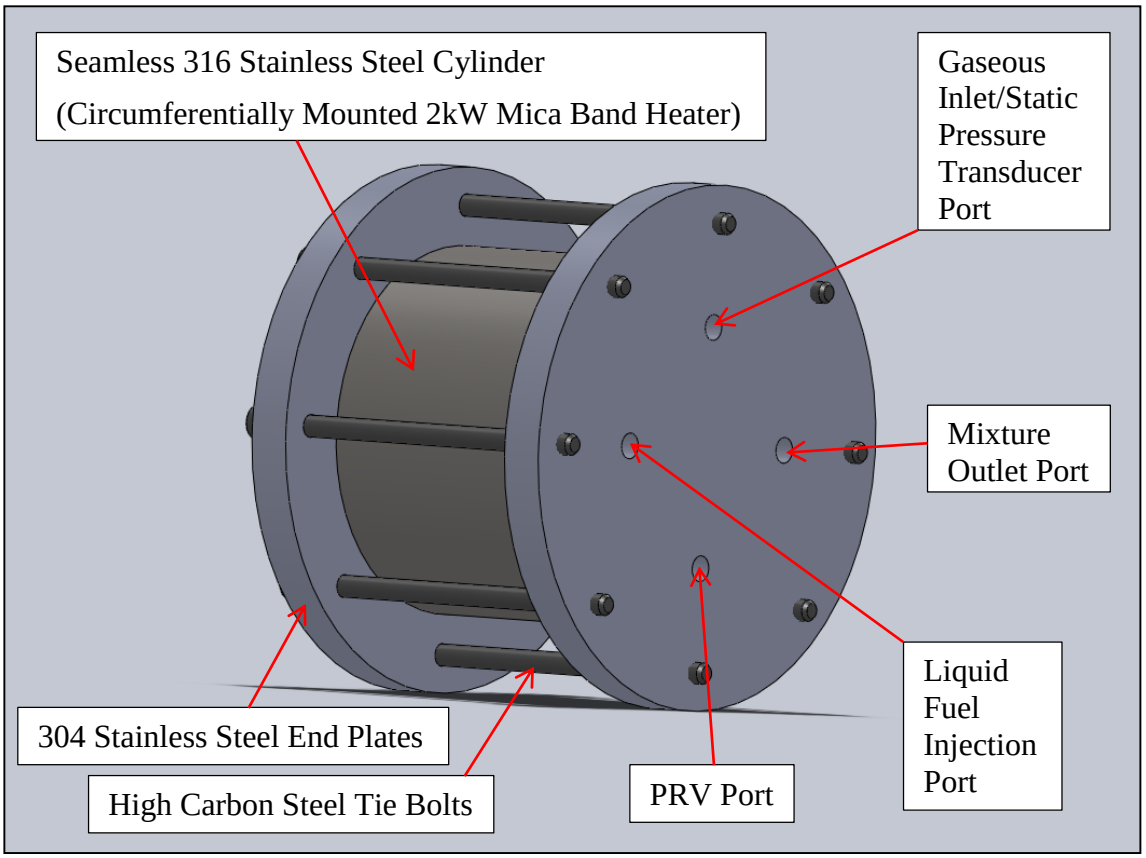

Figure B.38: SolidWorks model of mixing chamber. Dimensions and stress calculations can be found in Appendix C.

B.4.10 Triggering, Synchronisation and Data Acquisition System

In order to simultaneously record the piston movement and the associated pressure rise in the combustion chamber, synchronisation of the piston linear displacement laser, combustion chamber dynamic pressure transducer and the rapid opening hydraulic solenoid valve was required. This was achieved via a custom built triggering system, using a push to make switch to simultaneously activate the opening of the rapid response hydraulic solenoid valve to initiate firing and generate a +5v TTL signal, in which the rising edge triggered the recording of the two analogue channels used for the piston linear displacement laser and dynamic pressure transducer data acquisition. These two ±10v analogue signals were then digitised by a National Instruments DAQ card, NI PCI-6110, which was interpreted by a custom virtual Instrument (VI) using LabVIEW software, to graphically display and record both the pressure trace and piston

position, at a sampling frequency of 50kHz. The DAQ card had a 12 bit resolution, therefore, with the charge amplifier set to 2 MPa/volt, increments of pressure measurement were 2.44mV, thus, 4.88×10^{-4} MPa.

B.5 Experimental Procedure

B.5.1 Mixture Preparation

All fuel/oxidiser/diluent mixtures were made up in batches within the specifically designed preheated mixing chamber as discussed in Section B.4.9. Details of the laboratory liquid fuel handling and preparation protocol prior to injection are as discussed in Chapter 3.

In order to achieve different T_c values, the initial mixture temperature was varied alongside the ratio of different inert diluent gases, with varying specific heats, thermal conductivities and diffusivities, for an increased range. The practise of using such gases to manipulate T_c is common within RCM studies, and are assumed to be chemically inactive to the main combustion reactions, with the proportion of reactants typically below 2%.

Using an RCM, a series of experiments were performed by Würmel et al. (2007) investigating the pressure effects of compressing: argon, helium, nitrogen and xenon, under the same CR and P_i. Table B.2 shows their thermal characteristics.

Species	ρ (kg m^{-3})	c_P (J K^{-1} mol^{-1})	k (W m^{-1} K^{-1})	α (m^2 s^{-1})
He	0.179	20.786	0.1520	1.635×10^{-4}
Ar	1.783	20.786	0.0177	1.908×10^{-5}
Xe	5.900	20.786	0.0057	6.102×10^{-6}
N_2	1.251	29.125	0.0260	1.999×10^{-5}

Table B.2: Thermal properties for common diluents gases (Würmel et al., 2007).

Figure B.39 shows the pressure traces for the compression of each gas. Notably, the nitrogen shows significantly lower P_c and therefore T_c values in comparison to the other gases as a result of its relatively high specific heat capacitance. Xenon, argon and helium all reach similar and much higher P_c values due to their lower specific heat capacitance. However, in comparison, helium suffers from a much higher rate of post compression pressure decline from a higher rate of heat loss due to its high thermal diffusivity. Such aggressive heat loss rates are not desirable in RCM's and therefore helium is not recommended.

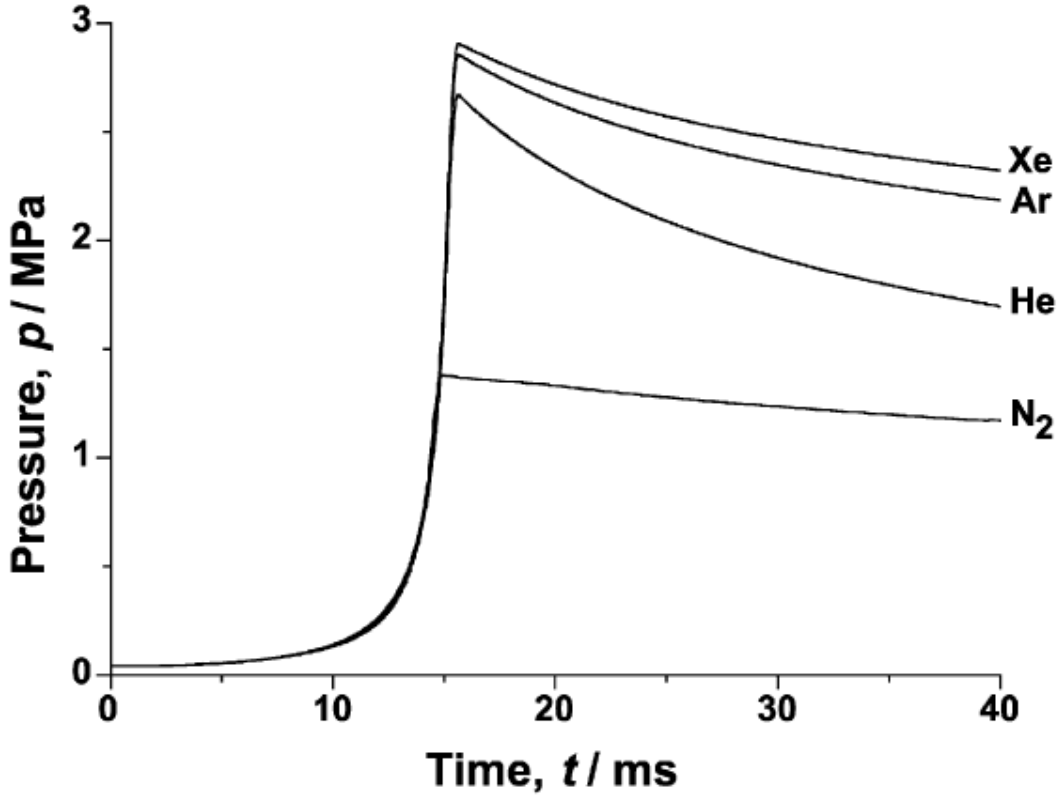

Figure B.39: Pressure traces for the compression of different gases with an RCM (Würmel et al., 2007).

As shown in Fig B.40, Würmel et al. (2007) also demonstrated the direct effect of such diluents on the ignition delay time for 2,3-dimethlypentane (DMP). As anticipated, when using helium, the high rate of heat loss, lowers the reactivity and therefore increases the ignition delay time. This emphasises the need to carefully select appropriate diluents and ratios to ensure post compression heat loss rates are minimised.

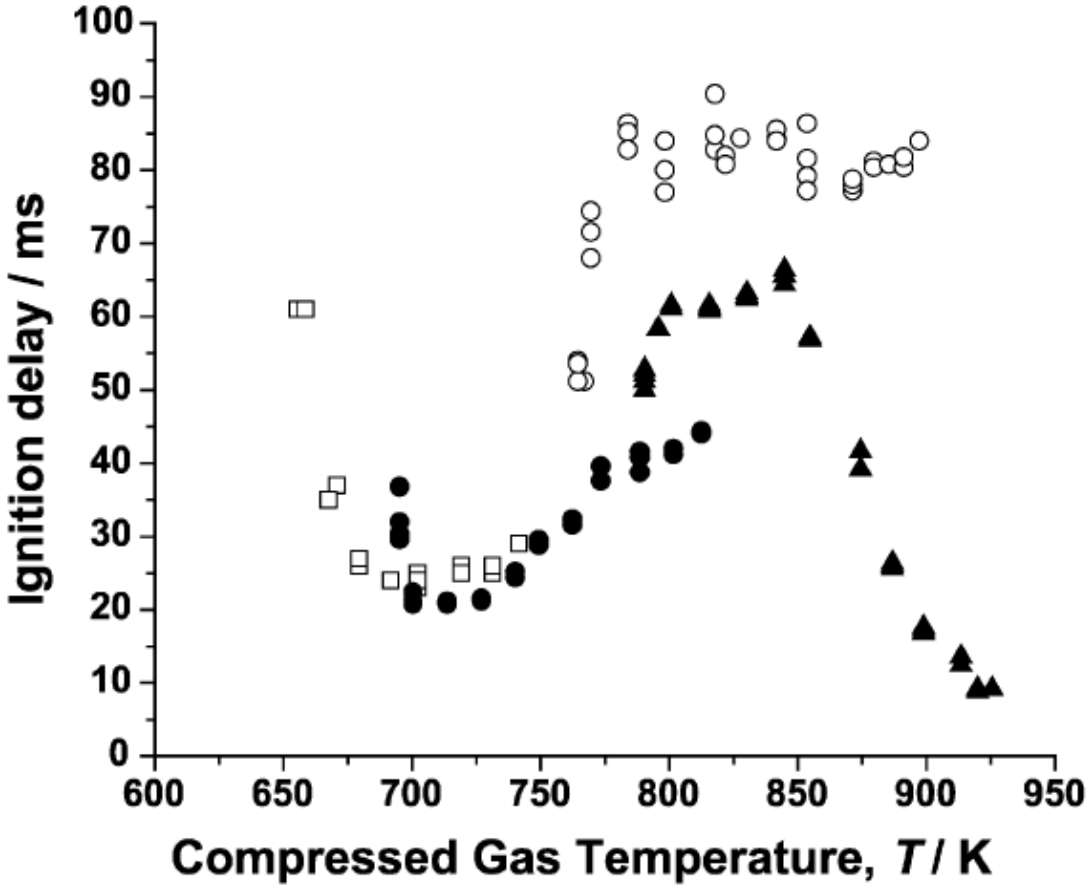

Figure B.40: Ignition delay time variation with reciprocal T_c, for stoichiometric dimethylepentane (DMP), for different dilutent gases, at P_i = 1.5MPa, □ = N_2, ○ = He, ▲= Ar, • = N_2:Ar (Würmel et al., 2007).

B.5.2 Operating Technique

First, with the piston at the SOC position, the end plug was removed and the combustion chamber was examined to ensure it was free from any soot build ups or any other foreign particulates. Acetone was found to be an effect cleaning agent when required. The combustion chamber, mixing chamber and its delivery pipe work was then sufficiently heated to the required target temperature. Typically, for a target temperature of 360K, it would take circa 2hrs for all systems to reach a steady state.

The combustion chamber was purged of any potential exhaust gas residuals from previous experiments, by vacuuming down to 0.05 MPa from atmospheric pressure, filling with dry air to 2 MPa, and again vacuuming down to 0.05 MPa. This ensured any gaseous residuals were kept to a maximum of 0.3%. The piston was then hydraulically locked in the SOC position under the maximum safe working pressure of 0.4 MPa, via the hydraulic hand pump. The combustible mixture from the mixing chamber was then

delivered to the combustion chamber via a high precision needle valve up to the required initial combustion chamber pressure. The driving reservoir was then filled with laboratory compressed air, up to the limited 0.7 MPa line pressure, and then with dry cylinder air up to the 1.4 MPa.

Ensuring the combustion chamber temperatures were stable, the LabView software was armed to record incoming data, a verbal warning of "firing" was given, and the machine was triggered to initiate the rapid compression of the combustible mixture via the push to make firing button. All recorded data was then saved to file.

The combustion product gases were then evacuated to the main exhaust line and the piston reset to the start of compression position by pressuring the combustion chamber with lab air to 0.7 MPa, which simultaneously aided the exhausting process. The combustion chamber was then purged as above and prepared for the next experiment.

B.6 *Iso*-Octane Ignition Delay Data for International Collaborative

In the effort to further understanding of non-ideal RCM behaviour and evaluate the discrepancies between different RCM's, an international collaborative of thirteen research groups, consisting of experimentalists, modellers and theoreticians was formed at the 1st International RCM Workshop at Argon National Laboratory (Goldsborough, 2012). The newly commissioned Leeds RCM was one of seven RCM's to participate in the collection of *iso*-octane ignition delay data under set conditions, to help highlight any correlations in ignition delay variation with any particular RCM characteristics.

The equivalence ratio was stoichiometric with a fixed oxygen content of 21%, P_c = 2.0 MPa, and T_c = 650-950K. The variation of T_c could be achieved via altering T_i, CR or the ratio of the following diluent gases: argon, nitrogen and carbon dioxide. Table B.3 shows the composition of each mixture, P_i and T_i for each T_c measurement made using the Leeds RCM. Figure B.41 shows the Leeds RCM τ_i results in comparison to the other six RCM's that participated. This data was first presented at the 2nd RCM International Workshop (Goldsborough, 2014).

As anticipated, results show considerable spread between the different RCM's, particularly at lower temperatures, and much speculation as to the nature of these discrepancies continues. However, efforts by Materego (2015) to decouple the varying

characteristic causes of heat loss from each RCM to reveal universal ignition delay data have since been made at Leeds and are pending review by the consortium.

Composition	P_i (MPa)	T_i (K)	T_c (K)
$C_8H_{18}+12.5O_2+11.98CO_2+35.02N_2$	0.0789	304	640
	0.0792	310	650
$C_8H_{18}+12.5O_2+5.99CO_2+41.01N_2$	0.0766	312	676
	0.0771	322	694
$C_8H_{18}+12.5O_2+47N_2$	0.074	318	713
	0.0744	328	731
$C_8H_{18}+12.5O_2+11.9Ar+35.1N_2$	0.0708	319	752
	0.0712	328	769
$C_8H18+12.5O_2+30.95Ar+16.05N_2$	0.0644	306	802
	0.065	321	833
	0.0661	353	900
$C_8H_{18}+12.5O_2+47Ar$	0.0589	321	925
	0.0591	328	941

Table B.3: Mixture composition and initial conditions for *iso*-octane experiments at P_c = 2.0 MPa and T_c = 640-941K.

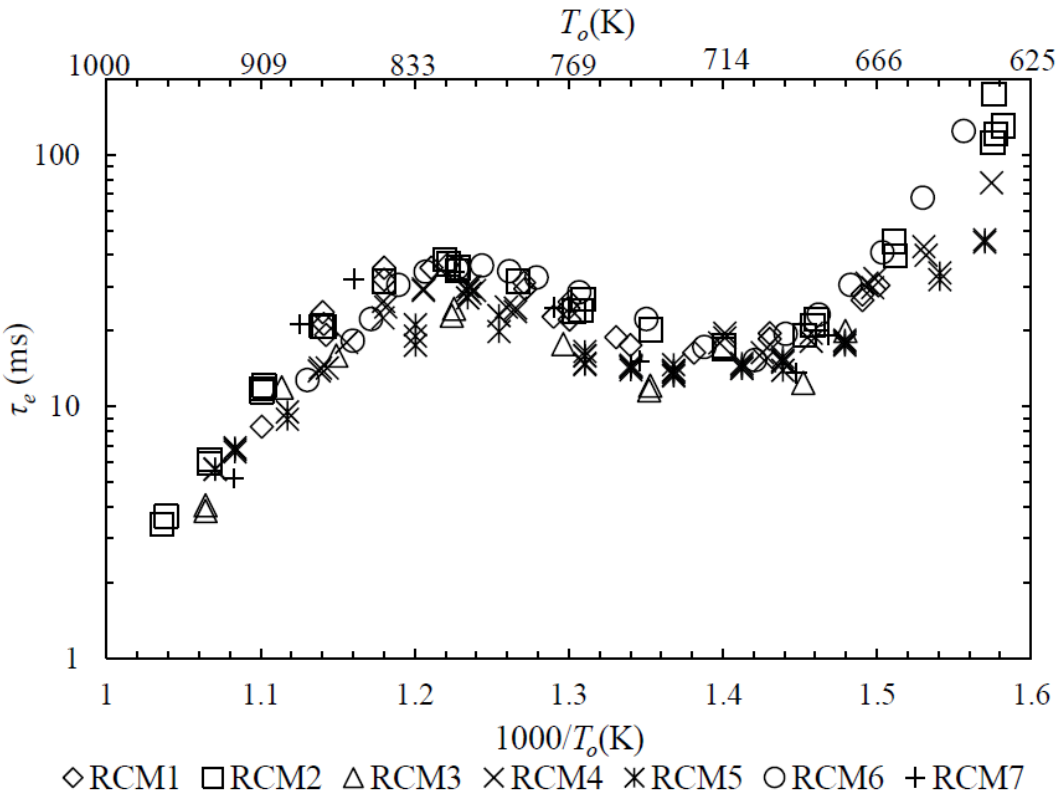

Figure B.41: Ignition delay time variation with reciprocal T_c, for stoichiometric iso-octane, at P_i = 2.0 MPa (Goldsborough, 2012). Table B.4 shows legend for the different RCM's.

RCM	Participant
1	Argon National Laboratory
2	National University of Galway
3	University of Akron
4	University of Lille
5	University of Leeds
6	University of Connecticut
7	University of Akron

Table B.4: Summary of participants who provided *iso*-octane τ_i data via a RCM for 1st international RCM Workshop (Goldsborough, 2012).

Appendix C - Stress Calculations for RCM Mixing Chamber

The following equations are in relation to the dimensions shown in Fig. C.1, and based on equivalent case examples by Roark, J. R. (Roark, 1975).

Assumptions:

- Poisson's ratio = ν = 0.3
- Uniform thicknesses of materials
- Maximum working pressure of 5 MPa
- Combustion pressure increase factor of 6
- Yield stress of stainless steel 303 = 240 MPa
- Yield stress of stainless steel 316L = 170 MPa

Front and Rear Flange Bending Stress:

Force exerted on the flange due to pressure (including combustion factor):

$F = P\pi r^2 = 5 \text{ x } 10^5 \text{ x } \pi \text{ x } 0.075^2 \text{ x } 6 = 53.014\text{kN}$

Maximum bending moment equation: $M_{b-max} = \frac{F}{4\pi}[(1+\nu)\ln\frac{r_o}{r_i} + 1]$

$M_{b-max} = \frac{53014}{4\pi}[(1+0.3)\ln\frac{0.1025}{0.075} + 1] = 7.198\text{kN}$

Bending Stress = $\delta_b = \frac{6M_{b-max}}{z^2} = \frac{6\ x\ 7198}{0.02^2} = 107.97$ MPa

Safety Factor = $\frac{240}{107.97} = 2.223$

Front and Rear Flange Shear Stress:

Shear Area = $A_s = \pi dz = \pi \text{ x } 0.15 \text{ x } 0.02 = 9.425x10^{-3}\text{m}^2$

Shear Stress = $\delta_s = \frac{F}{A_s} = \frac{53014}{9.425x10^{-3}} = 5.625\text{MPa}$

Safety Factor = $\frac{240}{5.625} = 42.667$

Main Tube Body Hoop Stress:

Hoop Stress = $\delta_h = \frac{6Pd}{2z} = \frac{6\ x\ 5 \text{ x } 10^5 \text{ x } 0.15}{2\ x\ 9.13 \text{ x } 10^{-3}} = 24.644$ MPa

Safety Factor = $\frac{170}{24.644} = 6.898$

Tie Bolts:

Industry Specification and Assumptions:

- M10 x 1.25 x 180mm (35mm of thread)
- Class 12.9 = Tensile Strength = 1220 MPa
- Preload Torque = 43.85kN

$F = 6PA = 6 \times 5 \times 10^5 \times \pi \times 0.075^2 = 53.014\text{kN}$

$F_b = \frac{F}{Number\ of\ Bolts} = \frac{53014}{8} = 6.627\text{kN}$

Safety Factor = $\frac{43850}{6627} = 6.617$

Front and Rear Flange Bending Stress (with bolt preload):

$M_{b-max} = \frac{w r_o^{\,2}}{r_i} \times \frac{C_9}{C_8}$

$C_9 = \frac{r_i}{r_o}\left\{\frac{1+\nu}{2}\ln\left(\frac{r_o}{r_i}\right) + \frac{1-\nu}{4}\left[1 - \left(\frac{r_i}{r_o}\right)^2\right]\right\}$

$C_9 = \frac{0.075}{0.1025}\left\{\frac{1+0.3}{2}\ln\left(\frac{0.1025}{0.075}\right) + \frac{1-0.3}{4}\left[1 - \left(\frac{0.075}{0.1025}\right)^2\right]\right\} = 0.208$

$C_8 = \frac{1}{2}\left[1 + \nu + (1-\nu)\left(\frac{r_i}{r_o}\right)^2\right]$

$C_8 = \frac{1}{2}\left[1 + 0.3 + (1-0.3)\left(\frac{0.075}{0.1025}\right)^2\right] = 0.837388$

$W = \frac{F}{\pi d} = \frac{43850}{\pi \times 0.205} = 68.087\text{kN/m}$

$M_{b-max} = \frac{68087 \times 0.1025^2}{0.075} \times \frac{0.208}{0.837388} = 2.369\text{kN}$

Bending Stress = $\delta_b = \frac{6M_{b-max}}{z^2} = \frac{6 \times 2369}{0.02^2} = 35.535\ \text{MPa}$

Safety Factor = $\frac{240}{35.535} = 6.754$

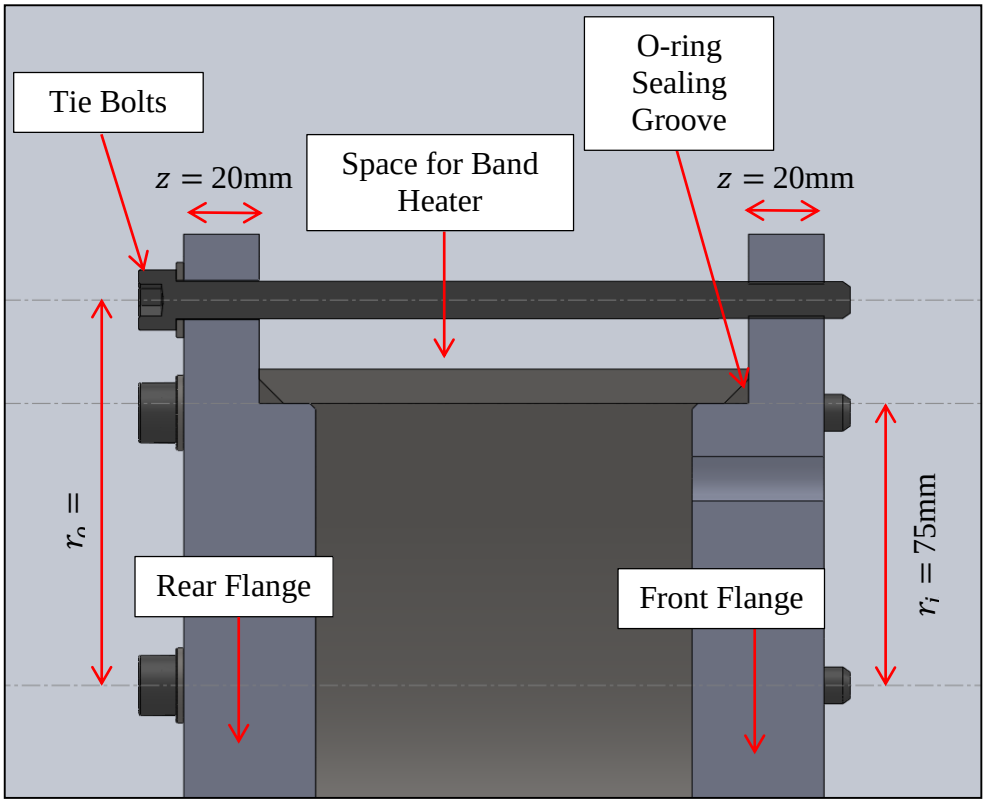

Figure C.1: SolidWorks virtual model of RCM mixing chamber – radial cross section.

References

Affleck, W., Thomas, A., 1968. An opposed piston rapid compression machine for preflame reaction studies. Proceedings of the Institution of Mechanical Engineers 183, 365-387.

Al-Shahrany, A.S., Bradley, D., Lawes, M., Woolley, R., 2005. Measurement of unstable burning velocities of iso-octane–air mixtures at high pressure and the derivation of laminar burning velocities. Proceedings of the Combustion Institute 30, 225-232.

Barnard, J.F.G.a.J.A., 1995. Flame and Combustion, Third Edition ed. Blackie Academic and Professional, an imprint of Chapman and Hall.

Bauer, C.G., Forest, T.W., 2001. Effect of hydrogen addition on the performance of methane-fueled vehicles. Part I: effect on S.I. engine performance. International Journal of Hydrogen Energy 26, 55-70.

Bauwens, C.R., Bergthorson, J.M., Dorofeev, S.B., 2015a. Experimental study of spherical-flame acceleration mechanisms in large-scale propane–air flames. Proceedings of the Combustion Institute 35, 2059-2066.

Bauwens, C.R., Bergthorsonb, J.M., Dorofeeva, S.B., 2015b. Critical Peclet Numbers for the Onset of Darrieus-Landau Instability in Atmospheric-Pressure Methane-Air Flames, 25th ICDERS, University of Leeds.

Beerer, D., McDonell, V., Samuelsen, S., Angello, L., 2009. Interpretation of Flow Reactor Based Ignition Delay Measurements, ASME Turbo Expo 2009: Power for Land, Sea, and Air. American Society of Mechanical Engineers, pp. 1011-1026.

Bosschaart, K.J., De Goey, L., 2003. Detailed analysis of the heat flux method for measuring burning velocities. Combustion and Flame 132, 170-180.

Botha, J.P., Spalding, D.B., 1954. The Laminar Flame Speed of Propane/Air Mixtures with Heat Extraction from the Flame. Proceedings of the Royal Society of London A: Mathematical, Physical and Engineering Sciences 225, 71-96.

Bradley, D., 1999. Instabilities and flame speeds in large-scale premixed gaseous explosions. Philosophical Transactions of the Royal Society of London A: Mathematical, Physical and Engineering Sciences 357, 3567-3581.

Bradley, D., Cresswell, T., Puttock, J., 2001. Flame acceleration due to flame-induced instabilities in large-scale explosions. Combustion and Flame 124, 551-559.

Bradley, D., Dowling, A.P., Morgans, A.S., , 2011. Combution Instabilities in Turbulent Premixed Flames. Eds. N. Swaminathan and K. N. C. Bray Cambridge University Press. , 151-243.

Bradley, D., Gaskell, P., Gu, X., 1996. Burning velocities, Markstein lengths, and flame quenching for spherical methane-air flames: a computational study. Combustion and Flame 104, 176-198.

Bradley, D., Gaskell, P., Gu, X., 1998a. The modeling of aerodynamic strain rate and flame curvature effects in premixed turbulent combustion, Symposium (International) on Combustion. Elsevier, pp. 849-856.

Bradley, D., Habik, S.E.-D., El-Sherif, S.A., 1991. A generalization of laminar burning velocities and volumetric heat release rates. Combustion and Flame 87, 336-345.

Bradley, D., Hicks, R.A., Lawes, M., Sheppard, C.G.W., Woolley, R., 1998b. The Measurement of Laminar Burning Velocities and Markstein Numbers for Iso-octane–Air and Iso-octane–n-Heptane–Air Mixtures at Elevated Temperatures and Pressures in an Explosion Bomb. Combustion and Flame 115, 126-144.

Bradley, D., Lawes, M., Liao, S., Saat, A., 2014. Laminar mass burning and entrainment velocities and flame instabilities of i-octane, ethanol and hydrous ethanol/air aerosols. Combustion and Flame 161, 1620-1632.

Bradley, D., Lawes, M., Mansour, M.S., 2009. Explosion bomb measurements of ethanol–air laminar gaseous flame characteristics at pressures up to 1.4 MPa. Combustion and Flame 156, 1462-1470.

Broustail, G., Seers, P., Halter, F., Moréac, G., Mounaim-Rousselle, C., 2011. Experimental determination of laminar burning velocity for butanol and ethanol iso-octane blends. Fuel 90, 1-6.

Campbell, M.F., Wang, S., Goldenstein, C.S., Spearrin, R.M., Tulgestke, A.M., Zaczek, L.T., Davidson, D.F., Hanson, R.K., 2015. Constrained reaction volume shock tube study of n-heptane oxidation: Ignition delay times and time-histories of multiple species and temperature. Proceedings of the Combustion Institute 35, 231-239.

Chang, C., Thompson, A., Winship, R., 1958. Ignition delay of propane in air between 725–880° C under isothermal conditions, Symposium (International) on Combustion. Elsevier, pp. 431-435.

Clavin, P., 1985. Dynamic behavior of premixed flame fronts in laminar and turbulent flows. Progress in Energy and Combustion Science 11, 1-59.

Cox, A., Griffiths, J., Mohamed, C., Curran, H., Pitz, W., Westbrook, C., 1996. Extents of alkane combustion during rapid compression leading to single-and two-stage ignition, Symposium (International) on Combustion. Elsevier, pp. 2685-2692.

Darrieus, G., 1938. Propagation d'un front de flamme: assai de theorie des vitesses anomales de deflagration par developpement spontane de la turbulence. 6th Int. Cong. Appl. Mech., Paris.

Das, A.K., Uddi, M., Sung, C.-J., 2012. Two-line thermometry and H 2 O measurement for reactive mixtures in rapid compression machine near 7.6 μm. Combustion and Flame 159, 3493-3501.

Davidson, D.F., Gauthier, B.M., Hanson, R.K., 2005. Shock tube ignition measurements of iso-octane/air and toluene/air at high pressures. Proceedings of the Combustion Institute 30, 1175-1182.

Desgroux, P., Gasnot, L., Sochet, L., 1995. Instantaneous temperature measurement in a rapid-compression machine using laser Rayleigh scattering. Applied Physics B 61, 69-72.

Di Sarli, V., Benedetto, A.D., 2007. Laminar burning velocity of hydrogen–methane/air premixed flames. International Journal of Hydrogen Energy 32, 637-646.

Dirrenberger, P., Glaude, P.A., Bounaceur, R., Le Gall, H., da Cruz, A.P., Konnov, A.A., Battin-Leclerc, F., 2014. Laminar burning velocity of gasolines with addition of ethanol. Fuel 115, 162-169.

Dixon-Lewis, G., Williams, A., 1963. Some observations on the structure of a slow burning flame supported by the reaction between hydrogen and oxygen at atmospheric pressure, Symposium (International) on Combustion. Elsevier, pp. 576-586.

Dryer, F.L., Chaos, M., 2008. Ignition of syngas/air and hydrogen/air mixtures at low temperatures and high pressures: Experimental data interpretation and kinetic modeling implications. Combustion and Flame 152, 293-299.

Egolfopoulos, F.N., Du, D.X., Law, C.K., 1992. A study on ethanol oxidation kinetics in laminar premixed flames, flow reactors, and shock tubes. Symposium (International) on Combustion 24, 833-841.

Gersen, S., Anikin, N., Mokhov, A., Levinsky, H., 2008. Ignition properties of methane/hydrogen mixtures in a rapid compression machine. International Journal of Hydrogen Energy 33, 1957-1964.

Gillespie, L., Lawes, M., Sheppard, C., Woolley, R., 2000. Aspects of laminar and turbulent burning velocity relevant to SI engines. SAE Technical Paper.

Gnansounou, E., Dauriat, A., Villegas, J., Panichelli, L., 2009. Life cycle assessment of biofuels: energy and greenhouse gas balances. Bioresource technology 100, 4919-4930.

Goldsborough, S.S., 2012. 1st International RCM Workshop, Meeting Report. Argon National Laboratory

Goldsborough, S.S., 2014. 2nd International RCM Workshop, Meeting Report. Argon National Laboratory

Gostintsev, Y.A., Istratov, A., Shulenin, Y.V., 1988. Self-similar propagation of a free turbulent flame in mixed gas mixtures. Combustion, Explosion, and Shock Waves 24, 563-569.

Griffiths, J.F., Halford-Maw, P.A., Mohamed, C., 1997. Spontaneous ignition delays as a diagnostic of the propensity of alkanes to cause engine knock. Combustion and Flame 111, 327-337.

Griffiths, J.F., Halford-Maw, P.A., Rose, D.J., 1993. Fundamental features of hydrocarbon autoignition in a rapid compression machine. Combustion and Flame 95, 291-306.

Griffiths, J.F., Hasko, S.M., 1984. Two-Stage Ignitions During Rapid Compression: Spontaneous Combustion in Lean Fuel-Air Mixtures.

Griffiths, J.F., MacNamara, J.P., Sheppard, C.G.W., Turton, D.A., Whitaker, B.J., 2002. The relationship of knock during controlled autoignition to temperature inhomogeneities and fuel reactivity. Fuel 81, 2219-2225.

Griffiths, J.F., Nimmo, W., 1985. Spontaneous ignition and engine knock under rapid compression. Combustion and Flame 60, 215-218.

Grogan, K.P., Goldsborough, S.S., Ihme, M., 2015. Ignition regimes in rapid compression machines. Combustion and Flame.

Gu, X., Haq, M., Lawes, M., Woolley, R., 2000. Laminar burning velocity and Markstein lengths of methane–air mixtures. Combustion and Flame 121, 41-58.

Halter, F., Chauveau, C., Djebaïli-Chaumeix, N., Gökalp, I., 2005. Characterization of the effects of pressure and hydrogen concentration on laminar burning velocities of methane–hydrogen–air mixtures. Proceedings of the Combustion Institute 30, 201-208.

Halter, F., Tahtouh, T., Mounaïm-Rousselle, C., 2010. Nonlinear effects of stretch on the flame front propagation. Combustion and Flame 157, 1825-1832.

Haq, Z., 1998. Fundamental Studies of Premixed Combustion, School of Mechanical Engineering. University of Leeds, Leeds.

Harker, M.R., 2009. Experimental Study of Turbulent Flame Structure School of Mechanical Engineering. University of Leeds, Leeds.

Hawthorn, R.D., Nixon, A.C., 1966. Shock tube ignition delay studies of endothermic fuels. AIAA Journal 4, 513-520.

Hill, P., Hung, J., 1988. Laminar burning velocities of stoichiometric mixtures of methane with propane and ethane additives. Combustion Science and Technology 60, 7-30.

Hinshelwood, C., 1940. The kinetics of chemical change, Clarendon. Oxford.

Hirasawa, T., Sung, C.J., Joshi, A., Yang, Z., Wang, H., Law, C.K., 2002. Determination of laminar flame speeds using digital particle image velocimetry: Binary Fuel blends of ethylene, n-Butane, and toluene. Proceedings of the Combustion Institute 29, 1427-1434.

http://biofuel.org.uk/third-generation-biofuels.html, 2015.

Hu, E., Huang, Z., He, J., Jin, C., Zheng, J., 2009. Experimental and numerical study on laminar burning characteristics of premixed methane–hydrogen–air flames. International Journal of Hydrogen Energy 34, 4876-4888.

IEA, 2015. 2015 Key World Energy Statistics. International Energy Agency

Jayachandran, J., Lefebvre, A., Zhao, R., Halter, F., Varea, E., Renou, B., Egolfopoulos, F.N., 2015. A study of propagation of spherically expanding and counterflow laminar flames using direct measurements and numerical simulations. Proceedings of the Combustion Institute 35, 695-702.

Jerzembeck, S., Peters, N., Pepiot-Desjardins, P., Pitsch, H., 2009. Laminar burning velocities at high pressure for primary reference fuels and gasoline: Experimental and numerical investigation. Combustion and Flame 156, 292-301.

Karim, G.A., Wierzba, I., Al-Alousi, Y., 1996. Methane-hydrogen mixtures as fuels. International Journal of Hydrogen Energy 21, 625-631.

Karlovitz, B., Denniston, D., Knapschaefer, D., Wells, F., 1953. Studies on Turbulent flames: A. Flame Propagation Across velocity gradients B. turbulence Measurement in flames, Symposium (International) on Combustion. Elsevier, pp. 613-620.

Kelley, A., Law, C., 2009. Nonlinear effects in the extraction of laminar flame speeds from expanding spherical flames. Combustion and Flame 156, 1844-1851.

Konnov, A.A., Meuwissen, R.J., de Goey, L.P.H., 2011. The temperature dependence of the laminar burning velocity of ethanol flames. Proceedings of the Combustion Institute 33, 1011-1019.

Kumar, K., Freeh, J.E., Sung, C.J., Huang, Y., 2007. Laminar Flame Speeds of Preheated iso-Octane/O2/N2 and n-Heptane/O2/N2 Mixtures. Journal of Propulsion and Power 23, 428-436.

Kuo, K.K., 2005. Principles of Combustion. 2 nd. New York: John Wiley and Sons.

Landau, L., 1944. On the theory of slow combustion. Acta physicochim. URSS 19, 77-85.

Larsson, G., 2008. Turbulence Related Cycle Variation in Combustion, School of Mechanical Engineering. University of Leeds, Leeds.

Law, C., 1989. Dynamics of stretched flames, Symposium (International) on Combustion. Elsevier, pp. 1381-1402.

Lawes, M., 2002. Laminar Premixed Flames. University of Leeds.

Lee, J.W., 2012. Advanced biofuels and bioproducts. Springer Science & Business Media.

Lee, R.A., Lavoie, J.-M., 2013. From first-to third-generation biofuels: challenges of producing a commodity from a biomass of increasing complexity. Animal Frontiers 3, 6-11.

Lezberg, E.A., 1957. PRELIMINARY INVESTIGATION OF PROPANE COMBUSTION IN A.

Liao, S.Y., Jiang, D.M., Huang, Z.H., Zeng, K., Cheng, Q., 2007. Determination of the laminar burning velocities for mixtures of ethanol and air at elevated temperatures. Applied Thermal Engineering 27, 374-380.

Mallard, Chatelier, L., 1883. Recherches expérimentales et théoriques sur la combustion des mélanges gazeux explosifs. Dunod.

Mallard, E., Le Chatelier, H., 1883. Combustion of explosive gas mixtures. Ann. mines 8, 274.

Mansour, M.S., 2011. Fundamental Study of Premixed Combustion Rates at Elevated Pressure and Temperature, School of Mechanical Engineering. University of Leeds, Leeds.

Markstein, G., 1964. Nonsteady Flame PropagationPergamon. New York.

Marshall, S.P., Taylor, S., Stone, C.R., Davies, T.J., Cracknell, R.F., 2011. Laminar burning velocity measurements of liquid fuels at elevated pressures and temperatures with combustion residuals. Combustion and Flame 158, 1920-1932.

Materego, M., 2015. Autoignition characterisation of synthetic fuels via rapid compression machine, School of Mechanical Engineering. University of Leeds, Leeds.

Miller, R., 1958. Some factors governing the ignition delay of a gaseous fuel, Symposium (International) on Combustion. Elsevier, pp. 417-424.

Minns, E.D., 2005. Future Fuel for the APEC Region.

Mittal, G., 2006. A Rapid Compression Machine - Design, Characterization, and Autoignition Investigations, Department of of Mechanical and Aerospace Engineering. Case Western Reserve University.

Mittal, G., Bhari, A., 2013. A rapid compression machine with crevice containment. Combustion and Flame 160, 2975-2981.

Mittal, G., Burke, S.M., Davies, V.A., Parajuli, B., Metcalfe, W.K., Curran, H.J., 2014. Autoignition of ethanol in a rapid compression machine. Combustion and Flame 161, 1164-1171.

Mittal, G., Raju, M.P., Bhari, A., 2011. A numerical assessment of the novel concept of crevice containment in a rapid compression machine. Combustion and Flame 158, 2420-2427.

Morgan, N., Smallbone, A., Bhave, A., Kraft, M., Cracknell, R., Kalghatgi, G., 2010. Mapping surrogate gasoline compositions into RON/MON space. Combustion and Flame 157, 1122-1131.

Morley, C., 2005. Gaseq: a chemical equilibrium program for Windows. http:// www. gaseq. co. uk.

Mullins, B.P., 1951. Studies on the spontaneous ignition of fuels injected into a hot air stream. Part II. The effect of physical factors upon the ignition delay of Kerosine-air mixtures. Ministry of Aviation.

Ormsby, M.P., 2005. Turbulent flame development in a high-pressure combustion vessel., School of Mechanical Engineering. University of Leeds, Leeds.

Park, P., Keck, J.C., 1990. Rapid compression machine measurements of ignition delays for primary reference fuels. SAE Technical Paper.

Payman, W., and Wheeler, R. V., 1922. The Composition of Gaseous Fuels in Relation to their Utilisation. Fuel in Science and Practice, 185-196.

PCB, 2015. Introduction to Dynamic Pressure Sensors

Pepiot-Desjardins, P., Pitsch, H., 2008. An efficient error-propagation-based reduction method for large chemical kinetic mechanisms. Combustion and Flame 154, 67-81.

Peters, N., Williams, F.A., 1987. The asymptotic structure of stoichiometric methane · air flames. Combustion and Flame 68, 185-207.

Poinsot, T., Veynante, D., 2005. Theoretical and numerical combustion. RT Edwards, Inc.

Roark, R.J., 1975. Formulas for stress and strain / Raymond J. Roark, Warren C. Young. McGraw-Hill, New York :.

Ronney, P.D., Sivashinsky, G.I., 1989. A theoretical study of propagation and extinction of nonsteady spherical flame fronts. SIAM Journal on Applied Mathematics 49, 1029-1046.

Saeed, K., Stone, C.R., 2004. Measurements of the laminar burning velocity for mixtures of methanol and air from a constant-volume vessel using a multizone model. Combustion and Flame 139, 152-166.

Semenov, N., 1935. Chemical kinetics and chemical reactions. Clarendon Press, Oxford.

Semenov, N., 1942. translated as NACA Tech. Memo 1026, 433.

Sethian, J.A., 1999. Level set methods and fast marching methods: evolving interfaces in computational geometry, fluid mechanics, computer vision, and materials science. Cambridge university press.

Sharpe, G., 2011. Private Communications

Shrestha, S.o.B., Karim, G.a., 1999. Hydrogen as an additive to methane for spark ignition engine applications. International Journal of Hydrogen Energy 24, 577-586.

Sileghem, L., Alekseev, V.A., Vancoillie, J., Van Geem, K.M., Nilsson, E.J.K., Verhelst, S., Konnov, A.A., 2013. Laminar burning velocity of gasoline and the gasoline surrogate components iso-octane, n-heptane and toluene. Fuel 112, 355-365.

Spadaccini, L.J., Colket Iii, M.B., 1994. Ignition delay characteristics of methane fuels. Progress in Energy and Combustion Science 20, 431-460.

Spalding, D., 1956. A mixing rule for laminar flame speed. Fuel 35, 347-351.

Spalding, D.B., 1957a. I. Predicting the laminar flame speed in gases with temperature-explicit reaction rates. Combustion and Flame 1, 287-295.

Spalding, D.B., 1957b. II. One-dimensional laminar flame theory for temperature-explicit reaction rates. Combustion and Flame 1, 296-307.

Speight, J.G., 2008. Synthetic fuels handbook: properties, process, and performance. McGraw-Hill.

Sung, C.-J., Curran, H.J., 2014. Using rapid compression machines for chemical kinetics studies. Progress in Energy and Combustion Science 44, 1-18.

Tripathi, N., 2012. Dynamics of Confined Premixed Laminar Explosion Flames, School of Mechanical Engineering. University of Leeds, Leeds.

van Lipzig, J., 2010. Flame speed investigation of ethanol, n-heptane and iso-octane using the heat flux method. Division of Combustion Physics, Lund Institute of Technology, Lund, Sweden, Master Thesis.

van Lipzig, J.P.J., Nilsson, E.J.K., de Goey, L.P.H., Konnov, A.A., 2011. Laminar burning velocities of n-heptane, iso-octane, ethanol and their binary and tertiary mixtures. Fuel 90, 2773-2781.

Vasu, S.S., Davidson, D.F., Hanson, R.K., 2008. Jet fuel ignition delay times: Shock tube experiments over wide conditions and surrogate model predictions. Combustion and Flame 152, 125-143.

Westbrook, C.K., Curran, H.J., Pitz, W.J., Griffiths, J.F., Mohamed, C., Wo, S.K., 1998. The effects of pressure, temperature, and concentration on the reactivity of alkanes: Experiments and modeling in a rapid compression machine. Symposium (International) on Combustion 27, 371-378.

Williams, G., 1985. Combustion theory.

Würmel, J., 2004. Detailed Chemical Kinetics Combined with a Computational Fluid Dynamics Study of a Twin Piston Rapid Compression Machine. PhD Thesis, Dept. Chem., Natl. Univ. Ireland Galway, Ireland.

Würmel, J., Silke, E.J., Curran, H.J., Ó Conaire, M.S., Simmie, J.M., 2007. The effect of diluent gases on ignition delay times in the shock tube and in the rapid compression machine. Combustion and Flame 151, 289-302.

Yamaoka, I., Tsuji, H., 1985. Determination of burning velocity using counterflow flames. Symposium (International) on Combustion 20, 1883-1892.

Zeldovich, Y.B., Barenblatt, G., 1959. Theorv of flame propagation. Combustion and Flame 3, 61-74.

Zeldovich, Y.B., Frank-Kamenetskii, D., 1938. A theory of thermal propagation of flame. Zh. Fiz. Khim 12, 100-105.

Zhu, Y., Li, S., Davidson, D.F., Hanson, R.K., 2015. Ignition delay times of conventional and alternative fuels behind reflected shock waves. Proceedings of the Combustion Institute 35, 241-248.